ISSN 2542-1565

Vol. 16 2023 No. 04

GEOGRAPHY ENVIRONMENT SUSTAINABILITY

Special issue «Dust in the environment: a hazard to human health and society»

«The journal GEOGRAPHY, ENVIRONMENT, SUSTAINABILITY was founded in 2008 by Russian Geographical Society, the Lomonosov Moscow State University Geography Department, and the Russian Academy of Sciences Institute of Geography. Since that time the journal publishes **4 issues per year**, containing original research papers and reviews. The journal issues are open source and distributed through subscriptions, library exchanges of leading universities, and via the website through the world»

FOUNDERS OF THE JOURNAL: Russian Geographical Society, Faculty of Geography, Lomonosov Moscow State University and Institute of Geography of the Russian Academy of Sciences

The journal is published with financial support of the Russian Geographical Society.

The journal is registered in Federal service on supervision of observance of the legislation in sphere of mass communications and protection of a cultural heritage. The certificate of registration: ПИ № ФС77-67752, 2016, December 21.

PUBLISHER
Russian Geographical Society
Moscow, 109012 Russia
Novaya ploshchad, 10, korp. 2
Phone 8-800-700-18-45
E-mail: press@rgo.ru
www.rgo.ru/en

EDITORIAL OFFICE
Lomonosov Moscow State University
Moscow 119991 Russia
Leninskie Gory, 1,
Faculty of Geography, 1806a
Phone 7-495-9391552
Fax 7-495-9391552
E-mail: ges-journal@geogr.msu.ru
www.ges.rgo.ru

DESIGN
Layout designer: Tereshkin Anton
Moscow, 115088,
26 Simonovsky Val str., bldg. One
Phone: +7 (903) 108-04-44
E-mail: smile.tai@gmail.com

DOI prefix: 10.24057

Format A4 (210x297mm)

"GEOGRAPHY, ENVIRONMENT, SUSTAINABILITY" is the only original English-language journal in the field of geography and environmental sciences published in Russia. It is supposed to be an outlet from the Russian-speaking countries to Europe and an inlet from Europe to the Russian-speaking countries regarding environmental and Earth sciences, geography and sustainability. The main sections of the journal are the theory of geography and ecology, the theory of sustainable development, use of natural resources, natural resources assessment, global and regional changes of environment and climate, social-economical geography, ecological regional planning, sustainable regional development, applied aspects of geography and ecology, geoinformatics and ecological cartography, ecological problems of oil and gas sector, nature conservations, health and environment, and education for sustainable development.

Date of publication: December 31st, 2023.

EDITORIAL BOARD

EDITORIAL OFFICE

CONTENTS

Vadim Yu. Grigorev, Inna N. Krylenko, Alexander I. Medvedev, Victor M. Stepanenko
EVALUATION OF TERRESTRIAL WATER STORAGE PRODUCTS FROM REMOTE SENSING, LAND SURFACE MODEL AND REGIONAL HYDROLOGICAL MODEL OVER NORTHERN EUROPEAN RUSSIA 6

Dung Trung Ngo, Khanh Nguyen Quoc, Ngoc Thi Dang, Cuong Hung Dang, Lan Linh Tran, Hoi Dang Nguyen
ANALYSIS OF THE MANGROVE STRUCTURE IN THE DONG RUI COMMUNE BASED ON MULTISPECTRAL UNMANNED AERIAL VEHICLE IMAGE DATA 14

Pankaj Kumar, Swati Thakur, Surajmal Junawa, Subhash Anand
ALTITUDINAL APPRAISAL OF LAND USE LAND COVER AND SURFACE TEMPERATURE CHANGE IN THE SATLUJ BASIN, INDIA 26

Rafael Brugnolli Medeiros, Luiz Carlos Araujo dos Santos, Jose Fernando Rodrigues Bezerra, Ana Rosa Marques, Gabriel Irvine Ferreira Alves dos Santos
LANDSCAPE CARTOGRAPHY IN THE MARANHENSE AMAZON: THE CASE OF THE LOWER COURSE OF THE PINDARÉ RIVER BASIN 39

Nina V. Reutova, Tatiana V. Reutova, Fatima R. Dreeva, Akhed M. Khutuev
ARSENIC IN SURFACE WATERS AND GEOCHEMICAL ANOMALIES IN THE CENTRAL PART OF THE NORTH CAUCASUS 52

Nilufer Yazici, Tatyana P. Novikova, Arthur I. Novikov, Nebi
GENE DIVERSITY IN SEED CROP OF TAURUS CEDAR (CEDRUS LIBANI A. RICH.) OVER AN ALTITUDINAL RANGE 63

Andrei V. Korobkov, Svyatoslav S. Kuzovlev, Elena S. Rykunova, Nikolay A. Sluka
LEADING GLOBAL CITIES IN THE RUSSIAN-LANGUAGE SEGMENT OF INTERNET: HOW DO THEY LOOK LIKE AT THE BEGINNING OF THE 21ST CENTURY 72

Anna A. Romanovskaya
TRENDS IN EXTREME WEATHER EVENTS WITH SOCIO-ECONOMIC DAMAGE IN RUSSIA 82

Nikita S. Zdravchev, Alexey V. Bobrov, Mikhail S. Romanov, Iurii M. Lebedev, Alexey N. Sorokin, Anton S. Timchenko, Anna A. Mikhaylova, Natalia D. Vasekha, Maxim V. Kandidov, Kirill V. Kuptsov, Petr S. Iovlev
PHYLOGENY AND HISTORICAL BIOGEOGRAPHY OF THE ORDER PANDANALES 91

Usfa Asif, Aqsa Munir Ahmad, Muhammad Asif Javed, Muhammad Nasar-u-Minallah
GROUNDWATER QUALITY AND QUANTITY ANALYSIS FOR IRRIGATION PURPOSES IN OKARA, SAHIWAL AND KHANEWAL DISTRICTS OF PUNJAB, PAKISTAN 105

Victor I. Gornyy, Olga V. Balun, Andrey V. Kiselev, Sergey G. Kritsuk, Iskander Sh. Latypov, Andrey A. Tronin
MULTIYEAR VARIATIONS OF SOIL MOISTURE AVAILABILITY IN THE EAST EUROPEAN PLAIN 120

Morad Mirzaei, Manouchehr Gorji Anari, Maurício Roberto Cherubin, Nermina Saronjic, Seyed Mohammad Nasir Mousavi, Azin Rooien, Mohammad Zaman, Andrés Caballero-Calvo
CROP RESIDUES STIMULATE YIELD-SCALED GREENHOUSE GAS EMISSIONS IN MAIZE-WHEAT CROPPING ROTATION IN A SEMI-ARID CLIMATE 125

Abed AlFanatseh
A GEOGRAPHIC GIS-BASED APPROACH FOR ASSESSING SPATIAL DISTRIBUTION AND ACCESSIBILITY OF PUBLIC PRIMARY SCHOOLS IN MAFRAQ CITY, JORDAN 133

SPECIAL ISSUE
«DUST IN THE ENVIRONMENT: A HAZARD TO HUMAN HEALTH AND SOCIETY»

Andrew V. Shevchenko, Andrian A. Seleznev, Georgy P. Malinovsky, Ilia V. Yarmoshenko
MODELING SEDIMENT PRODUCTION IN URBAN ENVIRONMENTS: CASE OF RUSSIAN CITIES 144

Dmitriy A. Samulenkov, Maxim V. Sapunov
THE AEROSOL POLLUTION OF THE ATMOSPHERE ON THE EXAMPLE OF LIDAR SENSING DATA IN ST. PETERSBURG (RUSSIA), KUOPIO (FINLAND), MINSK (BELARUS) 156

Yang He, Dongfang. Qi, V M. Bure
LONG-TERM AIR QUALITY EVALUATION SYSTEM IN CHINA PREDICTING BY MULTINOMIAL LOGISTIC REGRESSION METHOD 164

Anna P. Luzhetskaya, Ekaterina S. Nagovitsyna, Vassily A. Poddubny
IMPACT OF METEOROLOGICAL PARAMETERS ON THE DAILY VARIABILITY OF THE GROUND-LEVEL $PM_{2.5}$ CONCENTRATIONS ACCORDING TO MEASUREMENTS IN THE MIDDLE URALS 172

Anna V. Talovskaya, Tamara E. Adil'bayeva, Egor G. Yazikov
MONITORING FOR ELEMENTAL COMPOSITION OF PARTICULATE MATTER DEPOSITED IN SNOW COVER AROUND COAL-FIRED THERMAL POWER PLANT (KARAGANDA, CENTRAL KAZAKHSTAN) 180

Irina E. Subbotina, Alexander G. Buevich, Alexander P. Sergeev, Elena M. Baglaeva, Andrey V. Shichkin, Anastasia S. Butorova, Marina V. Sergeeva
CONCENTRATION, COMPOSITION AND SIZE DISTRIBUTION DATA OF THE ATMOSPHERIC AIR DUST AT BREATHING HEIGHTS IN EKATERINBURG 193

RESEARCH PAPER

EVALUATION OF TERRESTRIAL WATER STORAGE PRODUCTS FROM REMOTE SENSING, LAND SURFACE MODEL AND REGIONAL HYDROLOGICAL MODEL OVER NORTHERN EUROPEAN RUSSIA

Vadim Yu. Grigorev[1,2*], Inna N. Krylenko[1,2], Alexander I. Medvedev[3,4], Victor M. Stepanenko[1,3,4]
[1]Lomonosov Moscow State University, Faculty of Geography, Leninskie Gory, Moscow, 119991, Russia
[2]IWP RAS, Gubkina str., Moscow, 119234, Russia
[3]Lomonosov Moscow State University, Research Computing Center, Leninskie Gory, Moscow, 119991, Russia
[4]Hydrometeorological Research Center of the Russian Feleration, 123242, Moscow, Russia
***Corresponding author:** vadim308g@mail.ru
Received: May 20th, 2023 / Accepted: November 14th, 2023 / Published: December 31st, 2023
https://DOI-10.24057/2071-9388-2023-2899

ABSTRACT. Water storage is one of the key components of terrestrial water balance, therefore its accurate assessment is necessary for a sufficient description of hydrological processes within river basins. Here we compare terrestrial water storage using calibrated hydrological model ECOMAG forced by gauge observations, uncalibrated INM RAS–MSU land surface model forced by reanalysis and GRACE satellite-based data over Northern Dvina and Pechora River basins. To clearly identify differences between the datasets long-term, seasonal and residual components were derived. Results show a predominance of the seasonal component variability over the region (~64% of the total) by all datasets but INM RAS–MSU shows a substantial percentage of long-term component variability as well (~31%), while GRACE and ECOMAG demonstrate the magnitude around 18%. Moreover, INM RAS–MSU shows lowest magnitude of annual range. ECOMAG and INM RAS–MSU is distinguished by earliest begin of TWS decline in spring, while GRACE demonstrates latest dates. Overall, ECOMAG has shown the lowest magnitude of random error from 9 mm for Northern Dvina basin to 10 mm for Pechora basin, while INM RAS–MSU has shown largest one.

KEYWORDS: TWS, GRACE, LSM, hydrological model, cold climate, three-cornered hat method

CITATION: Grigorev V. Yu., Krylenko I. N., Medvedev A. I., Stepanenko V. M. (2023). Evaluation Of Terrestrial Water Storage Products From Remote Sensing, Land Surface Model And Regional Hydrological Model Over Northern European Russia. Geography, Environment, Sustainability, 4(16), 6-13
https://DOI-10.24057/2071-9388-2023-2899

ACKNOWLEDGEMENTS: The study was funded by the Russian Science Foundation, grant No. 21-47-00008 (terrestrial water storage change analysis), the statistical analysis was carried out under the Development Program of the Interdisciplinary Scientific–Educational School of Moscow State University "Cosmos". Part of data were collected and processed under Russian Science Foundation Project 21-17-00181

Conflict of interests: The authors reported no potential conflict of interest.

INTRODUCTION

Terrestrial water storage (*TWS*), containing surface water, soil moisture, groundwater, canopy, snowpack and glaciers, is one of the key components of the hydrological cycle. Accurate estimation of *TWS* at various temporal and spatial scales is important for global change research and water resources monitoring (Frolova et al. 2021). Many extreme hydrological events such as floods and droughts are accompanied and followed by extreme TWS magnitude (Tapley et al. 2019). Besides, *TWS* change (*TWSC*) can also be employed in the validation and calibration process of climate, land surface and hydrological models (Gupta and Dhanya 2021; Massoud et al. 2022; Scanlon et al. 2019; Wu et al. 2021). Occurrences of arid and humid periods in river catchments lead to fluctuations in *TWS*, whose changes, even over a multi-year period, can be significant compare to other water balance components. Thus, imbalance caused by ignoring storage change accounts for 7% (3%) of precipitation in arid (humid) catchments for a typical 10-year period (Han et al. 2020).

In situ measurements of *TWS* components, such as soil moisture, surface water, and snowpack, provide the most accurate and precise estimate of TWS at a local scale. However, the observations are often both sparse and heterogeneous in space and time. This applies especially to the Arctic region for which data are limited. The observations can be complemented by remote sensing or model output, but tracking of the variations of deep soil moisture and groundwater is still a challenge.

Variations of the Earth's gravity field on a century timescales are mainly driven by air and water mass redistributions within the Earth's climate system. The Gravity Recovery and Climate Experiment (GRACE) and GRACE-FO satellite missions, since 2002 and 2018 respectively (Landerer et al. 2020), constitutes the variations and provide monthly, decadal and daily values of *TWS*. Hence GRACE retrieved data are independent of land surface properties, meteorological and hydrological observations, it provides an excellent opportunity for model evaluation. The GRACE derived *TWS* (TWS_{GR}) has been recognized to be reliable as the reference data to validate accuracy of models.

Different types of the models exist, such as global land surface models, whose main purpose is to sufficiently establish interconnection between atmosphere and land as the parts of climate system, or regional hydrological models, which have to derive accurate streamflow estimates under different conditions. As mentioned before, *TWS* plays an essential role in both climate system and streamflow generation process, so there are no clear signs of what kind of model should perform better. Besides, models differ in initial data, parametrization of river basin, meteorological forcing, etc. In the present study a regional hydrological model ECOMAG (EM) (Kalugin and Motovilov 2018) and the global land surface model INM RAS–MSU (IM) (Volodin and Lykosov 1998) were used as the main research tools.

So far, climate and land surface models showed larger range of *TWS* annual cycle in cold regions and smaller range in tropical and (semi)arid basins compared to GRACE (Scanlon et al. 2019; Wu et al. 2021). Moreover, the models have tendency to underestimate long-term *TWSC*, both positive and negative (Scanlon et al. 2018). However, in the absence of the ground truth TWS measurements there are great uncertainties for such assessments. On a basin scale (~10^5 km^2) the random errors of monthly TWS_{GR} have been estimated using different methods from 10 to 20 mm (Chen et al. 2021; Ferreira et al. 2016). An assessment of bias in TWS_{GR} over river basins can be performed for some areas and seasons by water balance equation. Thus, during snowmelt streamflow is the main source of *TWS* variation, and it can be measured in situ, while precipitation and evaporation assessment errors are neglectable. However, in general, precipitation and evaporation bias estimates are required to *TWS* estimate.

Current research on Arctic rivers is mainly aimed at investigating possible future changes in the water balance. Less attention is paid to the assessment of the current water balance. Thus, Nasonova et al. (2022) showed that the Northern Dvina basin (NDB) receives about 665 mm of precipitation annually, 295 mm of which leaves the river basin as river runoff. At the same time, the river runoff is likely to increase by 10% during the 21st century. The main component of the *TWS* variability over the Arctic region is seasonal snowpack formation and melting (Scanlon et al. 2019). Long-term *SWE* in late winter varies across the basin from 80-100 mm in the southwest to 200-220 mm in the east and northeast. Basin average *SWE* at the end of March (approximately maximum of *SWE*) in the NDB showed that they ranged from 126 mm to 221 mm according to ground measurements (Popova et al. 2021).

A GRACE-based assessment of the impact of precipitation *(P)*, evaporation *(E)*, and runoff *(R)* on *TWSC* was performed at a global scale earlier (Zhang et al. 2019). It was shown that *P, ET,* and *R* at the global scale explain 42.6%, 43.2%, and 4.2% of *TWSC*, respectively. However, over the Arctic region, *ET* and *R* are the key components explaining *TWSC*. Thus, in the NDB *ET* explains over 80% of *TWSC*. In the Pechora basin (PB) *ET* and *R* each explains 40-60% of *TWSC*. Comparison of seasonal *TWS* variation to global hydrological models and LSM was evaluated by Scanlon et al. 2019. A GRACE-derived estimate of seasonal amplitude in the NDB showed 191 mm with uncertainty around 15 mm. Similar results were obtained in the PB – 190±20 mm. On average models overestimated the seasonal amplitude of *TWS* by 22 and 27% in the NDB and PB, accordingly. However, there are significant variations in the ratio depending on the model and forcing. Thus, the ratio ranges between 1.17–1.26 in the NDB and between 1.12–1.49 in the PB.

The main objectives of this study were to: (1) evaluate GRACE, ECOMAG and INM RAS–MSU retrieved TWS variation over the Northern Dvina River basin (NDB) and the Pechora River basin (PB); (2) estimate systematic and random errors in the series. The overarching goal of this study is to provide an assessment that will allow more sophisticated validation of land surface and hydrological models against GRACE retrieved observations.

MATERIALS AND METHODS

The study area

The entire NDB and most part of the PB are covered with taiga. Northern part of the PB is characterised by tundra. Human impact on TWS variation is neglectable – there are no water reservoirs or significant water demand. Although flat terrain prevails in both catchments, a narrow stretch on the eastern edge of the PB belongs to the western slopes of the Nether-Polar Ural and Northern Ural Mountains. Mean annual air temperature in the NDB and PB is 1.2°C and -3.3°C accordingly. Magnitude of the annual precipitation is around 550 mm for the both basins. The northeastern part of the PB is occupied by permafrost. Flood period, which accounts for 2/3 of the runoff, in the NDB typically occurs in April to June, while in the PB occurs from May to July. During the summer-autumn period, 21% of the annual runoff is formed in the NDB, and 20% in the PB (Georgiadi and Groisman 2022).

Materials

We used the state of the art GRACE ITSG-Grace2018 daily dataset (Kvas et al. 2019). As in the standard processing of monthly GRACE gravity field models, not *TWS* mass variations are removed by subtracting the output of geophysical background models. The limited satellite ground track coverage during one day (15 tracks per day) does not allow for a stable global gravity field inversion so that additional information has to be employed. The time series is therefore processed by a Kalman smoother approach and auto-regressive model of order 3 which apply information about spatio-temporal variations of gravity field at sub-monthly time scale (Eicker et al. 2020; Kvas et al. 2019). Spatial resolution of the data is approximately 500 km, though it is provided as 0.5° grid.

ECOMAG is an integrated hydrological and channel routing model (Motovilov et al. 1998; Kalugin and Motovilov 2018). It calculates the characteristics of snow cover; soil moistening, freezing, and thawing; surface, subsurface, and groundwater flow; water motion through channel network with one-day time step and with a spatial resolution of the size of elementary watersheds. USSR soil and landscape maps as well as regional reference books of agrohydrological soil properties were used to estimate soil properties. Daily air temperature, precipitation and vapor pressure deficit series at 200 weather stations were used to force the model. Model parameters were calibrated and verified by daily water discharge series at 12 and 7 gauges within the NDB and PB accordingly. Depending on available observation data, NDB model was calibrated for 1994–2003 and verified for 2004–2013, while 1984–1993 and 1994–2003 were chosen for calibration and verification of PB model. ECOMAG showed good results in reproducing monthly mean runoff in both the Northern Dvina (Nash–Sutcliffe coefficient is 0.88) and Pechora (Nash–Sutcliffe coefficient is 0.76) basins.

INM RAS–MSU is a grid-based model with spatial resolution of 0.5° and hourly time stepping (Volodin and Lykosov 1998; Machul'skaya and Lykosov 2009). The model takes into account snow cover accumulation and melting, evaporation of intercepted water; surface, subsurface, and groundwater flow; freezing, and thawing of the soil; water uptake and transpiration by vegetation. The soil is discretized into 23 layers, resulting in a total depth of 10 m. The depth of the first soil layer is 1 cm and the last one is 5 m. GLCC was used to specify land cover properties (Loveland et al. 2000). Soil texture is derived from (Wilson and Henderson-Sellers 1985). Hourly ERA5 datasets were used to force the model (Hersbach et al. 2020). Computation was performed starting with 01.01.2000 and full saturated soil. No calibration was applied to the model.

Methods

Decomposition of TWS series

In order to separate a systematic and random components from TWS_{GR}, TWS_{EM} and TWS_{IM} signals we separated them into a long-term (TWS^{long}), seasonal (TWS^{seas}) and subseasonal/residual components (TWS^{res}). The decomposition was accomplished by STL method (seasonal-trend decomposition using locally estimated scatterplot smoothing). The key idea of the method is to consistently apply seasonal and long-term smoothing filters that are based on local regression (Cleveland et al. 1990). Since the method requires the length of seasonal cycle as constant, we have dismissed February 29 from further computations. The parameters of the decomposition were adopted from (Humphrey et al. 2016) as a polynomial of degree 2 was chosen to filter seasonal cycle and linear function was employed to obtain a long-term component. The width of smoothing window of local regression for seasonal cycle separation was set to 45 days. The parameter of long-term component separation was set to 548 days. The number of iterations in an inner loop have been 5 and we assumed that 3 iterations in an outer loop would be sufficient. We preferred STL over simple seasonal averaging because STL allows to reduce weight of outliers in series so they have limited effect on seasonal and long-term components. Thus, the weights of TWS^{res} values after the first inner loop decrease from 1 to 0 as their absolute values increase from the median to 6 medians.

The relative variation of each component can be calculated as the ratio of mean absolute deviation (MAD) of a single component to the sum of the MAD. This metric was proposed in (Kim et al. 2009) and is called the component contribution ratio (CCR). As an example, for TWS^{long}

$$CCR^{long}, \% = \frac{MAD\,(TWS^{long}) \times 100}{MAD\,(TWS^{long}) + MAD\,(TWS^{seas}) + MAD\,(TWS^{long})}$$

Seasonal and long-term components of *TWS* and *TWSC* were estimated based on their deviation from the ensemble mean.

Three-cornered hat method

The residual component of *TWS* contains a short periodic signal and random noise. Assuming that all three datasets include a short-period component we applied the generalized three-cornered hat method (TCH) to estimate the magnitude of short periodic signal and noise. The generalized three-cornered hat method (TCH) is similar to the classical TCH or triple collocation (TC) approach. TC as well as TCH allows to estimate random error in time series if there are at least three time series with common signal but different noises. Consider TWS series to be $\{TWS_i: i \in (1, 2, 3)\}$ and split each time series as $TWS_i = TWS_{true} + \varepsilon_i$ where TWS_{true} denotes a true value of *TWS* and ε_i is a random error. Let's also denote

$$TWS_i - TWS_j = \varepsilon_i - \varepsilon_j = \varepsilon_{ij} i,j \in (1,2,3) \text{ and } i \neq j$$

with standard deviation of ε_{ij} and ε_i as σ_{ij} and σ_i accordingly.

Then if all ε_i are independent, TC is follows as

$$\sigma_i^2 = 0.5\left(\sigma_{ik}^2 + \sigma_{ij}^2 - \sigma_{jk}^2\right) i,j,k \in (1,2,3) \text{ and } i \neq j \neq k$$

The system includes 3 unknown variables and 3 algebraic equations. However, if ε_i are dependent, so as $cov(\varepsilon_i, \varepsilon_j) \neq 0$, there are 6 unknown variables and 3 algebraic equations. TCH, unlike TC, under some assumptions can be used to solve the underdetermined problem. TCH as proposed in (Premoli and Tavella, 1993) used three key assumptions/requirements: ε_i is normally distributed $\varepsilon_i \sim N(0,\sigma_i^2)$ and the covariance matrix of ε_i is positive definite. The third assumption is the minimum of the sum

$$\sum cov\left(\varepsilon_{ij}^2\right) i,j,k \in (1,2,3) \text{ and } i \neq j \neq k$$

TCH was previously used to estimate accuracy of several monthly TWS_{GR} and *ET* products (Ferreira et al. 2016; Xu et al. 2019).

RESULTS

Over the NDB TWS_{GR}^{long} and TWS_{EM}^{long} have shown good agreement with Pearson correlation coefficient *(r)* equals to 0.82, while *r* between TWS_{IM}^{long} and TWS_{GR}^{long} and TWS_{EM}^{long} have been 0.77 and 0.51 accordingly (Fig. 1). The PB has similar magnitudes of *r*, from 0.42 (TWS_{GR}^{long}-TWS_{IM}^{long}) to 0.69 (TWS_{EM}^{long}-TWS_{IM}^{long}).

There are no clear signs of decrease or increase *TWS* over the basins in 2003–2014. Negative anomalies of *TWS* took place over both basins in 2005–2006 and in 2011 over the PB as well. Each dataset showed pronounce seasonal cycle of *TWS* with one phase of growth and one phase of decline (Fig. 2).

Generally, the maximum of *TWS* in NDB occurs at the end of March, almost a month early than over the PB. The dates of *TWS* minimum in both basins lay in the first half of August (Tab. 1).

There are a few patterns in the dates of seasonal peaks obtained from different datasets. Firstly, GRACE extremums occur later than the others. The tendency is most pronounced for the maximums over NDB and minimums over PB. Despite up to one month lag between the maximums around the basins, minimums occur almost at the same time. Over the NDB, ECOMAG and GRACE have showed largest difference between the maximum dates reaching 20 days, whereas the minimums showed 7 days range. Over the PB, GRACE showed minimum of TWS 15 days later than ECOMAG and IM did. INM RAS - MSU demonstrate earliest begin of *TWS* spring decline over the PB, more than three weeks earlier than the other datasets.

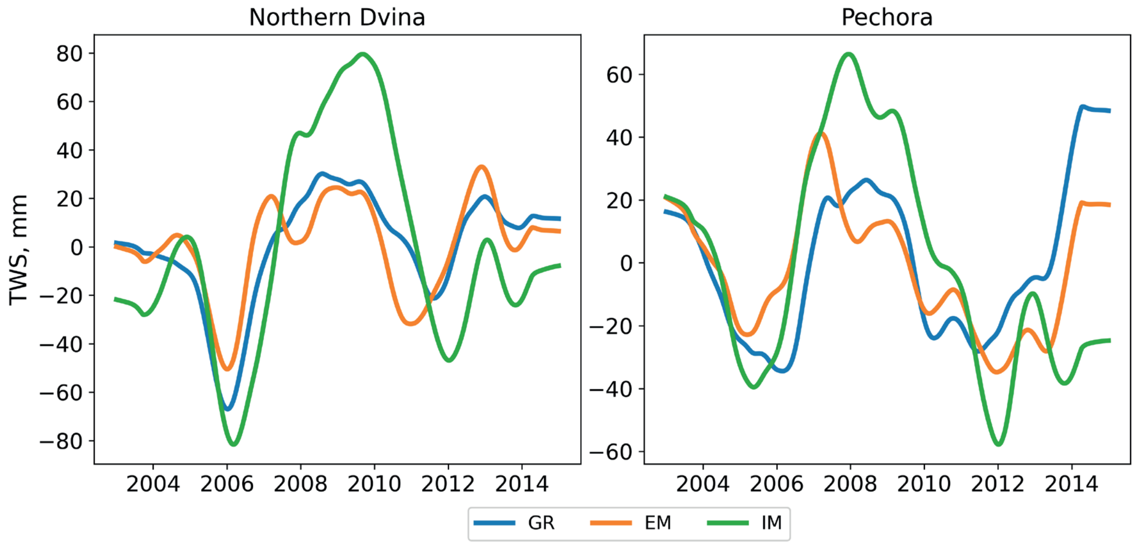

Fig. 1. Change of TWS^{long} over Northern Dvina and Pechora basins, mm.

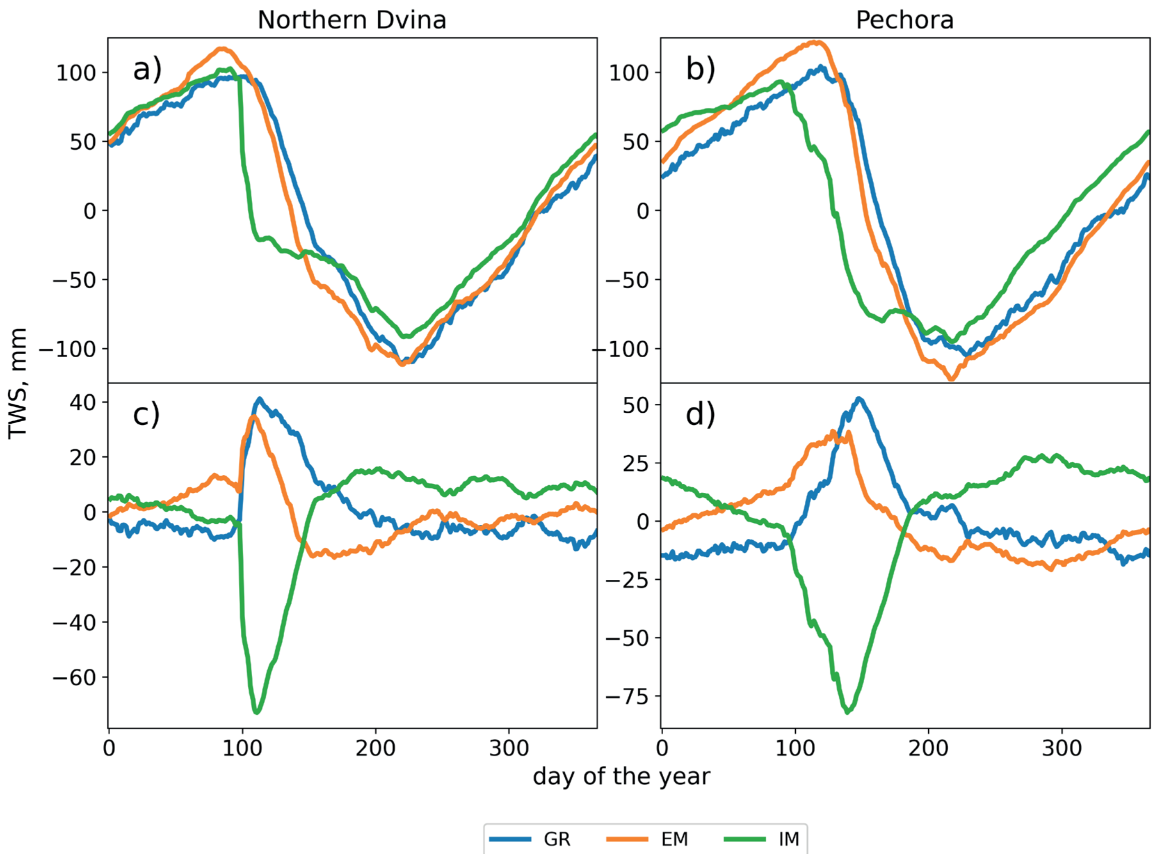

Fig. 2. Mean annual cycle of total water storage (TWS^{seas}) over Northern Dvina (a) and Pechora (b) basins and deviations from ensemble mean for Northern Dvian c) and Pechora d), mm.

Table 1. The average dates of maximum/minimum *TWS* and their respective standard deviation (in days) in Northern Dvina and Pechora basins according to ECOMAG, GRACE and INM RAS – MSU

The average date of max/min	ECOMAG	GRACE	INM RAS – MSU
Northern Dvina	24.03 (1.7)/7.08 (3.4)	13.04 (4.3)/ 14.08 (9.3)	28.03 (5.4)/ 11.08 (5.6)
Pechora	24.04 (7.0)/4.08 (1.4)	26.04 (6.6)/ 19.08 (6.5)	3.04 (6.1)/ 4.08 (1.1)

ECOMAG showed the least variability in the date of the extremums occur and GRACE showed the most. Also, *TWS* extremums are rather flattened - for about 7 days around them *TWS* change for less than 4 mm.

In the NDB, in terms of magnitude, TWS_{IM}^{seas} and TWS_{EM}^{seas} differ the most, while GRACE has intermediate position between them. Relative to average over three datasets, ECOMAG overestimates *TWS* from the beginning of a year to mid-April and underestimates from mid-April to the early August. IM shows opposite to ECOMAG signs of bias. From mid-August to late December ECOMAG and IM have shown similar magnitude with difference not more than 15 mm. The minimum of TWS^{seas} is in range from -93 mm (IM) to -113 mm (ECOMAG and GRACE). Maximums of TWS_{GR}^{seas} and TWS_{IM}^{seas} are close (99 mm and 104 mm accordingly) while TWS_{EM}^{seas} maximum is significantly higher – 118 mm. Consequently, the range of TWS_{EM}^{seas} variations exceeds GRACE by 8% and IM by 17%.

The dynamic of TWS_{EM}^{seas} differs most from TWS_{IM}^{seas} and TWS_{GR}^{seas} during period of rapid *TWS* decline from April to May. Thus, maximum of a 10-days average rate of TWS_{EM}^{seas} decline is 4.2 mm/day against 3.2 mm/day and 10.4 mm/day for GRACE and IM accordingly. Every TWS^{seas} series shows that rate of TWS decline starts to decrease from April 24th (TWS_{IM}^{seas}) to June 3rd (TWS_{EM}^{seas} and TWS_{GR}^{seas}), so it is less pronounce for TWS_{GR}^{seas}. From the occurring of *TWS* minimum until the second half of winter, all three datasets show almost identical trajectories.

The differences among the datasets are more distinguish within the PB. Maximum difference was retrieved for pair TWS_{IM}^{seas} - TWS_{GR}^{seas} at the second half of May when it reaches 128 mm. The range of TWS^{seas} variate from 193 mm to 247 mm according to IM and ECOMAG. GRACE has shown magnitude and the range close to average between IM and ECOMAG. Unlike the NDB, TWS_{IM}^{seas} within the PB does not show the highest 10-day *TWS* decline rate (5.1 mm/day). The TWS_{EM}^{seas} and TWS_{IM}^{seas} both shows significantly higher decline rate than in NDB – 6.1 mm/day and 4.7 mm/day, respectively.

Overall, the datasets do not differ much in MAD TWS^{res} magnitude (Fig. 3). The seasonal component is the most pronounced in EM dataset and the least pronounced in IM's. IM has though shown some differences with less pronounced seasonal component and more substantial long-term component.

Within the NDB, GRACE and ECOMAG have shown similar results as CCR^{seas} is around 67–70%, whereas CCR^{long} is 14.5% and CCR^{res} is roughly 17%. GRACE and ECOMAG also showed similar ratio of *MAD* TWS^{seas}/*MAD* TWS^{res} (the ration of seasonal component variation to residual component variation) – 4.6 and 4.8, while the ratio of IM is significantly less - 3.8. The most noticeable difference of INM RAS - MSU from other datasets is the significant TWS^{long} component (34 mm), which MAD is more than twice as large as GRACE and ECOMAG. The datasets' performance over the PB is similar to NDB one, but IM shows a less pronounced TWS^{long} component (29.3 mm) and GRACE more pronounced (20.5 mm).

Overall, the difference, between how dominant particular components are, among the datasets can be seen. GRACE is taking middle position having CCR^{long} more than ECOMAG, but less than IM. However, GRACE has the lowest *MAD* TWS^{seas}/*MAD* TWS^{res} ratio, as GRACE ratio is less IM one by 6% and less than ECOMAG one by 28%.

Over both basins, ECOMAG showed smallest random error (Tab. 2). GRACE and INM RAS – MSU presented similar performance with error (σ_{err}) more than that of ECOMAG by 33-42% and 52-53% in NDB and PB respectively.

Table. 2. Random error of TWS estimation by GRACE, ECOMAG and INM RAS – MSU datasets, in mm, and its ratio to variation of TWSres, %.

ECOMAG also showed smallest $\sigma_{err}/\sigma_{res}$ ratio in both basins. Over the PB GRACE and IM have showed similar ratio, while over the NDB GRACE appeared to be worse than IM.

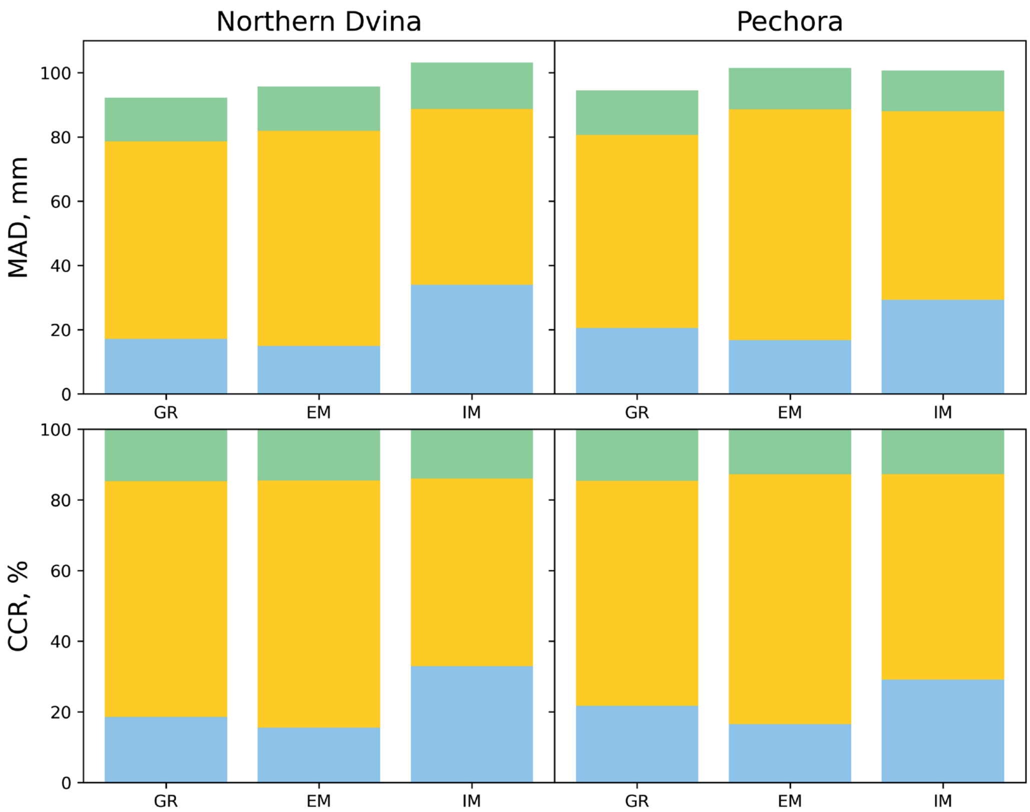

Fig. 3. Contribution of each temporal component to TWS variation. Blue – long-term, orange – seasonal, green – residual

Table 2. Random error σ_{err} of TWS estimation by GRACE, ECOMAG and INM RAS – MSU datasets, in mm, and its ratio to variation of TWS^{res}, %

	Basin	GRACE	ECOMAG	INM RAS - MSU
σ_{err}, mm	NDB	12.8	9.0	13.8
	PB	13.4	10.1	15.4
$\sigma_{err}/\sigma_{res}$, %	NDB	68	48	65
	PB	73	56	81

DISCUSSION

Predominance of seasonal component in *TWS* variation over cold regions based on the monthly series was evaluated worldwide in previous works (Humphrey et al. 2016; B. R. Scanlon et al. 2019). However, *TWS* variations over the Northern Dvina and Pechora basins differ from each other both in magnitude and timing. PB has later date of the maximum and faster rate of *TWS* decline during spring flood. However, despite higher snowfall magnitude, rate of *TWS* accumulation during cold period in the PB is close to NDB rate – less than 80 mm. Occasionally, it can be explained by higher runoff during the period.

In (Scanlon et al. 2019) it was shown that LSM have tendency to overestimate (compared to GRACE) variations of TWS^{seas} over cold regions. Our results are rather opposite. IM showed smallest range of TWS^{seas} in both basins, while hydrological model ECOMAG showed largest range. It's probably not related to the difference in forcing data. Thus, the annual precipitation in the NDB (PB) basin used in ECOMAG was 605 (704) mm, while in the INM RAS – MSU it was 706(719) mm. INM RAS-MSU obtained *TWS* begins to differ from that of ECOMAG in February-March, which is associated with overestimation of river discharge during the winter low flow period in INM RAS-MSU, which is more noticeable in the PB. A much sharper decline in *TWS* compared to other data sets is characteristic of INM RAS-MSU in the NDB. This is due to both overestimation of water discharge during the flood period (maximum discharge is overestimated by 50%) and annual water discharge (by 13%). The sharp decline in the rate of *TWS* decrease in the first decade of June is associated with the beginning of low flow period. INM RAS - MSU shows a short period of flood recession, about 45 days, while ECOMAG shows an average duration of 75 days. One reason for these differences may be the use of the water-holding capacity of snow in ECOMAG, which delays the start of flood season, as well as the use of more detailed vegetation and land surface properties maps over Russia, which caused the snowmelt process in the model to be less synchronous compare to INM RAS - MSU. Overestimation of river discharge during winter may be related to overestimation of the groundwater supply, which may also be related to the high magnitude of MAD TWS^{long}.

Over the PB according to INM RAS – MSU spring flood period starts approximately 16 days early and more smoothly compared to ECOMAG. In spite of this, over the PB the models perform more similar in terms of shape and volume of flood runoff than over the NDB. Therefore, the dynamics of *TWS* in the PB according to the INM RAS - MSU dataset differs from the others mainly by the presence of a shift by 15-20 days.

Magnitudes of MAD TWS^{res} over the basins are similar according to all datasets. That is rather surprising since daily resolution of GRACE series is the result of an approximation that should lead to partially loss of *TWS* signal, that was not eliminated in EM and IM datasets.

Over the NDB the datasets have shown the smaller random error σ_{err} as well as its ratio to σ_{res}. Probably it is related to a large number of weather stations and less complicated features of the basin like absence of permafrost and mountain regions. GRACE also shows higher random error in the PB, which is probably related to a less than the NDB area. In the PB, the random error of GRACE is larger than that in the NDB by only 0.6 mm, while for other datasets it is 1.1 mm and 1.6 mm.

The results obtained here have a number of limitations. Two catchments selected in this study are located in the cold climates. For these catchments, the relative contribution of river runoff and evapotranspiration is approximately equal, which is not the case for most of the Earth. Therefore, the effect of calibrating a hydrological model to discharge data may not have as much effect on the *TWS* in other regions. Also, the ECOMAG calibration was aimed at improving the accuracy of spring flood, which for the area under consideration means also accuracy in reproducing the seasonal *TWS*. Moreover, the Northern Dvina and Pechora basins do not have a significant economic impact such as irrigation and pumping that models cannot always take under consideration. Therefore, the choice of the study area is mostly a favorite of ECOMAG. However, the large size of the basins and the absence of large-scale intense rains are mostly favorable to GRACE, which is not able to catch short-term variations of *TWS*.

CONCLUSION

Results show a predominance of the seasonal component variability over the region (64% of the total) by all datasets but INM RAS–MSU shows a substantial percentage of long-term component variability as well (~31%), while GRACE and ECOMAG demonstrate the magnitude almost twice as low. Hydrological model ECOMAG showed the highest magnitude of the seasonal maximum and minimum, while LSM INM RAS – MSU showed the lowest. However, INM RAS – MSU showed most rapid decline of *TWS* over the NDB during approximately the first half of spring flood period, while GRACE's rate was lowest. ECOMAG is distinguished by earliest begin of TWS decline in spring, while GRACE demonstrates latest dates.

ECOMAG has shown the lowest magnitude of random error from 9 mm for Northern Dvina basin to 10 mm for Pechora basin, while INM RAS – MSU has shown the highest magnitude. However, none of the datasets showed a significantly higher than 1 signal-to-noise ratio in the residual *TWS* component. The question remains open to what extent the obtained errors are related to the models themselves and to what extent the accuracy of input precipitation data since short-period changes in *TWS* are related to precipitation.

Over three datasets ECOMAG showed the best performance considering the lowest rate of random error and the most accurate spring flood hydrograph. However, calibration to discharge data may not be so effective in evaporation-predominant regions without snowmelt floods. The region also lacks significant economic impacts on water resources, which greatly simplifies model development for this area. The large size of the basins and predominance of seasonal component in *TWS* variation are favorable to GRACE.

It should be noted that the advantages of using GRACE data in hydrology are related not so much to the accuracy of this product as to its independence from ground observation data and physiographic features of river basins.

REFERENCES

Chen J., Tapley B., Tamisiea M.E., Save H., Wilson C., Bettadpur S. and Seo K.W. (2021). Error Assessment of GRACE and GRACE Follow-On Mass Change. Journal of Geophysical Research: Solid Earth, 126(9), e2021JB022124, DOI: 10.1029/2021JB022124

Cleveland R.B., Cleveland W.S., McRae J.E. and Terpenning I. (1990). STL: A Seasonal-Trend Decomposition Procedure Based on Loess (with Discussion). Journal of Official Statistics, 6, 3–73.

Eicker A., Jensen L., Wöhnke V., Dobslaw H., Kvas A., Mayer-Gürr T. and Dill R. (2020). Daily GRACE satellite data evaluate short-term hydro-meteorological fluxes from global atmospheric reanalyses. Scientific Reports 2020 10, 4504, DOI: 10.1038/s41598-020-61166-0

Ferreira V.G., Montecino H.D.C., Yakubu C.I. and Heck B. (2016). Uncertainties of the Gravity Recovery and Climate Experiment time-variable gravity-field solutions based on three-cornered hat method. Journal of Applied Remote Sensing, 10(1), 015015, DOI: 10.1117/1.JRS.10.015015

Frolova N.L., Grigorev V.Y., Krylenko I.N. and Zakharova E.A. (2021). State-of-the-art potential of the GRACE satellite mission for solving modern hydrological problems. Vestnik of Saint Petersburg University. Earth Sciences, 66(1), 107–122 (in Russian with English summary), DOI: 10.21638/SPBU07.2021.107

Georgiadi A.G. and Groisman P.Y. (2022). Long-term changes of water flow, water temperature and heat flux of two largest arctic rivers of European Russia, Northern Dvina and Pechora. Environmental Research Letters, 17(8), 085002, DOI: 10.1088/1748-9326/AC82C1

Gupta D. and Dhanya C.T. (2021). Quantifying the Effect of GRACE Terrestrial Water Storage Anomaly in the Simulation of Extreme Flows. Journal of Hydrologic Engineering, 26(4), 04021007, DOI: 10.1061/(ASCE)HE.1943-5584.0002072

Han J., Yang Y., Roderick M.L., McVicar T.R., Yang D., Zhang S. and Beck H.E. (2020). Assessing the Steady-State Assumption in Water Balance Calculation Across Global Catchments. Water Resources Research, 56(7), e2020WR027392. DOI: 10.1029/2020WR027392

Hersbach H., Bell B., Berrisford P., Hirahara S., Horányi A., Muñoz-Sabater J., Nicolas J., Peubey C., Radu R., Schepers D., Simmons A., Soci C., Abdalla S., Abellan X., Balsamo G., Bechtold P., Biavati G., Bidlot J., Bonavita M., … Thépaut J. (2020). The ERA5 global reanalysis. Quarterly Journal of the Royal Meteorological Society, 146(730), 1999–2049, DOI: 10.1002/qj.3803

Humphrey V., Gudmundsson L. and Seneviratne S.I. (2016). Assessing Global Water Storage Variability from GRACE: Trends, Seasonal Cycle, Subseasonal Anomalies and Extremes. Surveys in Geophysics, 37(2), 357–395, DOI: 10.1007/S10712-016-9367-1

Kalugin A.S. and Motovilov Y.G. (2018). Runoff Formation Model for the Amur River Basin. Water Resources, 45(2), 149–159, DOI: 10.1134/S0097807818020082

Kim H., Yeh P.J.F., Oki T. and Kanae S. (2009). Role of rivers in the seasonal variations of terrestrial water storage over global basins. Geophysical Research Letters, 36(17), DOI: 10.1029/2009GL039006

Kvas A., Behzadpour S., Ellmer M., Klinger B., Strasser S., Zehentner N. and Mayer-Gürr T. (2019). ITSG-Grace2018: Overview and Evaluation of a New GRACE-Only Gravity Field Time Series. Journal of Geophysical Research: Solid Earth, 124(8), 9332–9344, DOI: 10.1029/2019JB017415

Landerer F.W., Flechtner F.M., Save H., Webb F.H., Bandikova T., Bertiger W.I., Bettadpur S. V., Byun S.H., Dahle C., Dobslaw H., Fahnestock E., Harvey N., Kang Z., Kruizinga G.L.H., Loomis B.D., McCullough C., Murböck M., Nagel P., Paik M., … Yuan D.N. (2020). Extending the Global Mass Change Data Record: GRACE Follow-On Instrument and Science Data Performance. Geophysical Research Letters, 47(12), e2020GL088306, DOI: 10.1029/2020GL088306

Loveland T.R., Reed B.C., Ohlen D.O., Brown J.F., Zhu Z., Yang L. and Merchant J.W. (2000). Development of a global land cover characteristics database and IGBP DISCover from 1 km AVHRR data. International Journal of Remote Sensing, 21(6–7), 1303–1330, DOI: 10.1080/014311600210191

Machul'skaya E.E. and Lykosov V.N. (2009). Mathematical modeling of the atmosphere-cryolitic zone interaction. Izv. Atmos. Ocean. Phys., 45, 687–703, DOI: 10.1134/S0001433809060024

Massoud E.C., Bloom A.A., Longo M., Reager J.T., Levine P.A. and Worden J.R. (2022). Information content of soil hydrology in a west Amazon watershed as informed by GRACE. Hydrol. Earth Syst. Sci, 26, 1407–1423, DOI: 10.5194/hess-26-1407-2022

Motovilov, Yu., Gottschalk, L., Engeland, K. and Belokurov, A. (1998). ECOMAG — regional model of hydrological cycle. Application to the NOPEX region. Department of Geophysics, University of Oslo.

Nasonova O.N., Gusev Y.M. and Kovalev E. (2022). Climate change impact on water balance components in Arctic river basins. Geography, Environment, Sustainability, 15(4),148–157, DOI: 10.24057/2071-9388-2021-144

Popova V.V., Turkov D.V. and Nasonova O.N. (2021). Estimates of recent changes in snow storage in the river Northern Dvina basin from observations and modeling. Ice and Snow, 61(2), 206–221 (in Russian with English summary), DOI: 10.31857/S2076673421020082

Premoli A. and Tavella P. (1993). A Revisited Three-Cornered Hat Method for Estimating Frequency Standard Instability. IEEE Transactions on Instrumentation and Measurement, 42(1), 7–13, DOI: 10.1109/19.206671

Scanlon B.R., Zhang Z., Rateb A., Sun A., Wiese D., Save H., Beaudoing H., Lo M.H., Müller-Schmied H., Döll P., van Beek R., Swenson S., Lawrence D., Croteau M. and Reedy R.C. (2019). Tracking Seasonal Fluctuations in Land Water Storage Using Global Models and GRACE Satellites. Geophysical Research Letters, 46(10), 5254–5264, DOI: 10.1029/2018GL081836

Scanlon Bridget R., Zhang Z., Save H., Sun A.Y., Schmied H.M., Van Beek L.P.H., Wiese D.N., Wada Y., Long D., Reedy R.C., Longuevergne L., Döll P. and Bierkens M.F.P. (2018). Global models underestimate large decadal declining and rising water storage trends relative to GRACE satellite data. Proceedings of the National Academy of Sciences of the United States of America, 115(6), E1080–E1089, DOI: 10.1073/PNAS.1704665115

Tapley B.D., Watkins M.M., Flechtner F., Reigber C., Bettadpur S., Rodell M., Sasgen I., Famiglietti J.S., Landerer F.W., Chambers D.P., Reager J.T., Gardner A.S., Save H., Ivins E.R., Swenson S.C., Boening C., Dahle C., Wiese D.N., Dobslaw H., … Velicogna I. (2019). Contributions of GRACE to understanding climate change. Nature Climate Change, 9(5), 358–369, DOI: 10.1038/s41558-019-0456-2

Volodin E.M. and Lykosov V.N. (1998). Parametrization of heat and moisture transfer in the soil-vegetation system for use in atmospheric general circulation models: 1. Formulation and simulations based on local observational data. Izvestiya, Atmospheric and Oceanic Physics, 37(4), 405–416.

Wilson M.F. and Henderson-Sellers A. (1985). A global archive of land cover and soils data for use in general circulation climate models. Journal of Climatology, 5(2), 119–143, DOI: 10.1002/JOC.3370050202

Wu R.J., Lo M.H. and Scanlon B.R. (2021). The Annual Cycle of Terrestrial Water Storage Anomalies in CMIP6 Models Evaluated against GRACE Data. Journal of Climate, 34(20), 8205–8217, DOI: 10.1175/JCLI-D-21-0021.1

Xu T., Guo Z.X., Xia Y.L., Ferreira V.G., Liu S.M., Wang K.C., Yao Y., Zhang X. and Zhao C. (2019). Evaluation of twelve evapotranspiration products from machine learning, remote sensing and land surface models over conterminous United States. Journal of Hydrology, 578, 124105. DOI: 10.1016//J.JHYDROL.2019.124105

Zhang Y., He B., Guo L., Liu J. and Xie X. (2019). The relative contributions of precipitation, evapotranspiration, and runoff to terrestrial water storage changes across 168 river basins. Journal of Hydrology, 579, 124194. DOI: 10.1016/J.JHYDROL.2019.124194

RESEARCH PAPER

ANALYSIS OF THE MANGROVE STRUCTURE IN THE DONG RUI COMMUNE BASED ON MULTISPECTRAL UNMANNED AERIAL VEHICLE IMAGE DATA

Dung Trung Ngo[1,*], Khanh Nguyen Quoc[1], Ngoc Thi Dang[2], Cuong Hung Dang[1], Lan Linh Tran[3] and Hoi Dang Nguyen[1,*]

[1]Institute of Tropical Ecology, Joint Vietnam-Russia Tropical Science and Technology Research Center, № 63, Nguyen Van Huyen Str., Cau Giay District, Hanoi, Vietnam.

[2]University of Science, Vietnam National University, No. 334, Nguyen Trai Str., Thanh Xuan District, Hanoi, Vietnam.

[3]Quang Ninh Department of Natural Resources and Environment, W4VF+P3 V, Nguyen Van Cu Str., Ha Long District, Quang Ninh, Vietnam.

***Corresponding author:** ngotrungdung266@gmail.com, danghoi110@gmail.com

Received: November 20th, 2022 / Accepted: November 14th, 2023 / Published: December 31st, 2023

https://DOI-10.24057/2071-9388-2023-2641

ABSTRACT. Mangroves are one of the most important types of wetlands in coastal areas and perform many different functions. Assessing the structure and function of mangroves is a premise for the management, monitoring and development of this most diverse and vulnerable ecosystem. In this study, the unmanned aerial vehicle (UAV) Phantom 4 Multispectral was used to analyse the structure of a mangrove forest area of approximately 50 hectares in Dong Rui commune, Tien Yen district, Quang Ninh Province – one of the most diverse wetland ecosystems in northern Vietnam. Based on the visual classification method combined with the results of field taxonomic sampling, a mangrove tree classification map was established for UAV with three species, *Bruguiera gymnorrhiza, Rhizophora stylosa,* and *Kandelia obovata*, achieving an overall accuracy = 86.28%, corresponding to a Kappa coefficient =0.84. From the images obtained from the UAV, we estimated and developed maps and assessed the difference in tree height and four vegetation indices, including the normalized difference vegetation index (NDVI), green normalized difference vegetation index (GNDVI), enhanced vegetation index (EVI), and green chlorophyll index (GCI), for three mangrove plant species in the flying area. *Bruguiera gymnorrhiza* and *Rhizophora stylosa* reach an average height of 4 to 5 m and are distributed mainly in high tide areas. Meanwhile, *Kandelia obovata* has a lower height (ranging from 2 to 4 m), distributed in low-tide areas, near frequent flows. This study confirms the superiority of UAV with red edge and near-infrared wave bands in classifying and studying mangrove structures in small-scale areas.

KEYWORDS: Wetland; Tree height; Near infrared; Tree species classification; Biodiversity assessment

CITATION: Ngo D. T., Quoc K. N., Dang N. T., Dang C. H., Tran L. L. and Nguyen H. D. (2023). Analysis Of The Mangrove Structure In The Dong Rui Commune Based On Multispectral Unmanned Aerial Vehicle Image Data. Geography, Environment, Sustainability, 4(16), 14-25

https://DOI-10.24057/2071-9388-2023-2641

ACKNOWLEDGEMENTS: This work was performed with the support of the project «Application of remote sensing technology and unmanned aerial vehicle to assess the change of wetland ecosystems» chaired by the Institute of Tropical Ecology, Joint Vietnam-Russia Tropical Science and Technology Research Center.

Conflict of interests: The authors reported no potential conflict of interest.

INTRODUCTION

With an area of approximately 7-9 million km^2, accounting for approximately 4-6% of the land surface, wetlands play a very important role in human life, including approximately 45% of the natural value of ecosystems (Costanza et al. 1997; Mitsch et al. 2000). Despite the importance of flooding, approximately 50% of the world's wetlands have been lost since the 1900s (Nicholls 2004). In Vietnam, mangrove areas have also been significantly reduced, with approximately 4/5 of the total mangrove area disappearing between 1943 and 2003 (IUCN 2012). Therefore, classification and assessment of the structure and status of mangroves are considered the basis for developing management, monitoring and conservation measures (Pellegrini et al. 2009).

Mangroves are ecosystems with a diverse level of salt-tolerant species composition, mainly woody trees commonly found in intertidal, tropical and subtropical coastal areas (Polidoro et al. 2010). Mangroves play a huge role in preventing coastal erosion, mitigating wave impacts, and protecting coastal habitats (Nguyen, H. H. et al. 2020). In addition, mangroves have other important functions, such as breeding and nesting grounds, shelter areas, nurseries, and feeding habitats (Nagelkerken et al. 2008). For mangrove ecosystems, the distribution of species is different, mainly along the slopes of tidal flat terrain (Watson 1925). Based on the properties and capabilities of mangroves, it is possible to classify different mangrove biomes, thereby providing an overview of the types of mangrove biomes and the dominant interactions that form them (Saenger 2002).

In the past, the method of dividing cells and establishing cross sections was commonly used to study mangrove structures such as species composition, tree density and tree height, trunk diameter, root density, and tree height (Dawes 1999; Ly et al. 2016). LiDAR technology has the ability to provide height and canopy structure parameters and is also widely used in forest plant taxonomy studies (Andersen et al. 2005; Brennan et al. 2006; Maltamo et al. 2004; Zhang 2020). In addition to field measurements, satellite images are effective tools for analysing and assessing the structure, function and area fluctuations of mangrove biomes (Nguyen, H. H. et al. 2020; Nguyen, L. D. et al. 2019). At Kecebing Bay, Sentinel-2 satellite imagery was applied to analyse the vertical and horizontal structure as well as the abundance of mangrove biomes (Nur W et al. 2017). However, satellite images are often low resolution, leading to errors in the results of structural analysis of mangroves.

To limit the errors caused by low image resolution, unmanned aerial vehicles (UAV) are considered an effective solution for providing ultrahigh-resolution images (Bandini et al. 2017; Lorenz et al. 2017). UAV are capable of providing resolutions of up to several centimetres, allowing them to determine the detailed structure of forest vegetation, such as measuring forest canopy gaps (Nguyen, D. H. et al. 2021), identifying vegetation index types (Mallmann et al. 2020; Ngo et al. 2020), creating tree classification maps (Hese et al. 2019), and constructing forest routes (Buğday 2018). With the improvement of cameras mounted on UAV, especially UAV with multispectral cameras, including near-infrared wave bands, many different types of vegetation indices can be identified (Hunt et al. 2013). Types of UAV with sensors, including red-edge and near-infrared (NIR) wave bands, for measuring vegetation indices have recently been introduced in agricultural research (Yeom et al. 2019). Vegetation indicators are important indicators in determining the health status of crops and types of vegetation (Modi et al. 2019). For UAV data, some types of vegetation indicators are commonly used in vegetation studies, such as the normalized difference vegetation index (NDVI) (Pal et al. 2020; Song et al. 2020), enhanced vegetation index (EVI), soil-adjusted vegetation index (SAVI) (Rhyma et al. 2019), and soil-atmospherically resistant vegetation index (SARVI) (Qiao et al. 2022).

In addition to the ability to provide various types of vegetation indicators for determining the health and structure of vegetation, the images obtained from UAV are also capable of classifying tree species and determining the height of dominant plant biomes (Deng et al. 2022; Huang et al. 2019; Okojie 2017). In the wetland area of Florida, UAV are applied in the classification of seven land use mantle objects using object-based image analysis (OBIA) (Liu et al. 2018). In the rich Central European forest area, UAV are used to classify plants based on the reflection spectrum of each plant species with an accuracy of 78.4% (Richter et al. 2016). In India, UAV are also used in the classification of detailed coating types with up to 95% accuracy (Richter et al. 2016; Tiwari et al. 2020). In Luozhuang, Changziying town, China, the authors used images obtained from UAV to classify eight mantle objects, including six different tree species (Yunjun et al. 2019). Tree height determination studies from the Digital Surface Model (DSM) after image processing UAV were also applied in various regions (Huang et al. 2019). In India, UAV were tested to determine the height of oil palm trees (Abdullah et al. 2022). In the Czech Republic, UAV are used to determine the height of *Picea abies L., Larix decidua, Pinus sylvestris,* and *Betula* lines ranging from 11.42 to 12.62 m (Panagiotidis et al. 2018).

In addition to being able to provide ultrahigh-resolution images, UAV also have significant advantages in studying the structure of mangrove vegetation. The images obtained from UAV are optimal methods for accurately mapping mangrove characteristics with canopy characteristics, biome types, and coverage (Kamal et al. 2014). UAV with multispectral sensors can provide and determine correlations between the NDVI vegetation index, canopy height, and canopy coverage (Yaney-Keller et al. 2019; Zahra et al. 2022). Combining the sensors available on UAV and LiDAR technology enables the detection and measurement of tree height and canopy diameter and the determination of cluster density (ma et al. 2017; Prasetyo et al. 2019; Yin et al. 2019). High-resolution imagery from UAV allows accurate identification of forest canopy gaps and assessment of their fluctuations over periods for mangrove ecosystems, thereby serving as a basis for monitoring the recovery of tree canopies (Lassalle et al. 2022). For wetland areas, the advantage of UAV is that they can be used to capture images actively at any time, right at local flooding or at low tide (Dezhi et al. 2018). However, the use of UAV in vegetation research also faces some limitations in adverse weather conditions, such as the effects of wind and rain conditions due to small loads (Matese et al. 2015; Nex et al. 2014).

Dong Rui commune mangroves are regarded as one of the two most diversified mangrove habitats in northern Vietnam that must be properly maintained (Huan 2021). However, past research has solely concentrated on measuring species composition, biodiversity levels, and area variations caused by aquaculture operations and local fishing. One of the key markers controlling the development of this ecosystem is the structure and distribution of mangrove plant species (Sarno et al. 2015). The use of UAV for the structural evaluation of mangrove ecosystems will provide a more comprehensive picture of the structure, variety, and species composition of wetland ecosystems in Dong Rui commune. In particular, this research has applied multispectral UAV for the first time in studying plant structure and classification in mangrove forests in Dong Rui commune. This result is the basis for the planning and conservation of mangrove plant biomes belonging to the wetland ecosystem for the Dong Rui commune area.

In this study, a Phantom 4 Multispectral UAV was used to photograph mangrove biomes outside the dike in the wetlands of Dong Rui commune, Tien Yen district, Quang Ninh province, Vietnam. Here, the distribution and structure of each plant biome from the dike to the outside of the estuary are markedly different. The main goal of the study is to determine the structure of mangrove biomes based on the following criteria: tree subspecies, tree height and several different vegetation indicators.

MATERIALS AND METHODS

Study area

The Dong Rui commune wetland area covers an area of 4902 hectares, with geographical coordinates from 21°11'N to 21°33'N and from 107°13'E to 107°32'E (Figure 1). This is a coastal accretion area with low terrain, gradually moving to the sea and an average elevation from 1.5 meters to 3 meters. Many places are renovated into arable land and aquaculture lagoons, and the rest are parrot beaches and coastal dunes flooded with tidal water. The saline soil group dominates the research area, and the alluvial soil in the central area is where the local population is concentrated.

In estuary biomes, abundant mangroves appear in tidal wetlands, adapt to unstable conditions of the environment and are affected by low and high tides. Due to the terrain conditions of the narrow estuary marshes distributed along the riverbank, this type of carpet is a group of trees that grow scattered and take the form of strips. Characteristic plant biomes include Aegiceras corniculatum superior plant biomes with the plant associations of *Aegiceras corniculatum, Kandelia obovata, Bruguiera gymnorhiza, and Rhizophora stylosa, Aegiceras corniculatum, and Kandelia obovata,* and *Kandelia obovata, Bruguiera gymnorhiza, and Rhizophora stylosa.*

Flight procedures for capturing and processing UAV

This study used a DJI Phantom 4 Multispectral UAV with 6 cameras combined with RTK positioners that provide a multispectral imaging system consisting of 1 RGB camera and a multispectral camera array with 5 cameras covering the following bands: Blue (R_b): 450 nm ± 16 nm, Green (R_g): 560 nm ± 16 nm, Red (R_r): 650 nm ± 16 nm, Red edge (R_{re}): 730 nm ± 16 nm, and Near-infrared (R_{nir}): 840 nm ± 26 nm – all at 2 MP.

The UAV flight route was built with DJI GPS Pro software with the following flight parameters: UAV flight altitude: 60 m; photo coverage: 80%; flight time: 7h00 to 8h00 at the lowest tide; flight date: July 15, 2022.

After flying, UAV image data will be processed using Pix4Dmapper Enterprise 4.4.12 software according to the process in Fig. 3.

Tree-species classification

Tree-species classification

Based on field surveys, a set of image sequences were collected from mangrove tree taxonomic samples consisting of three species: *Bruguiera gymnorrhiza, Rhizophora stylosa,* and *Kandelia obovata*. Next, the image interpretation key is fed into the eCognition software that implements the multiresolution segmentation algorithm. Baatz (2000) developed and used the multiresolution

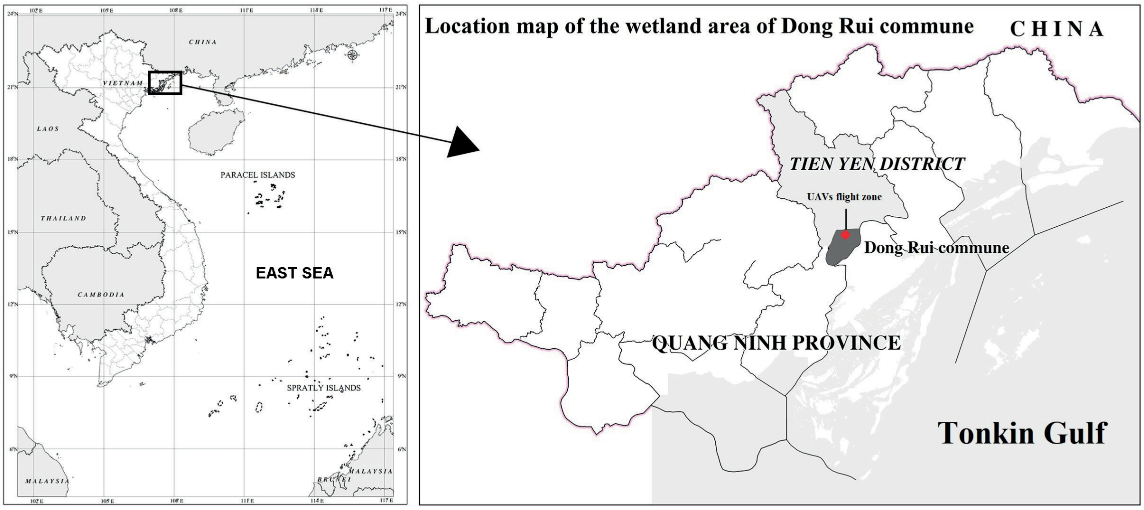

Fig. 1. Map of the location of the Dong Rui commune wetland area

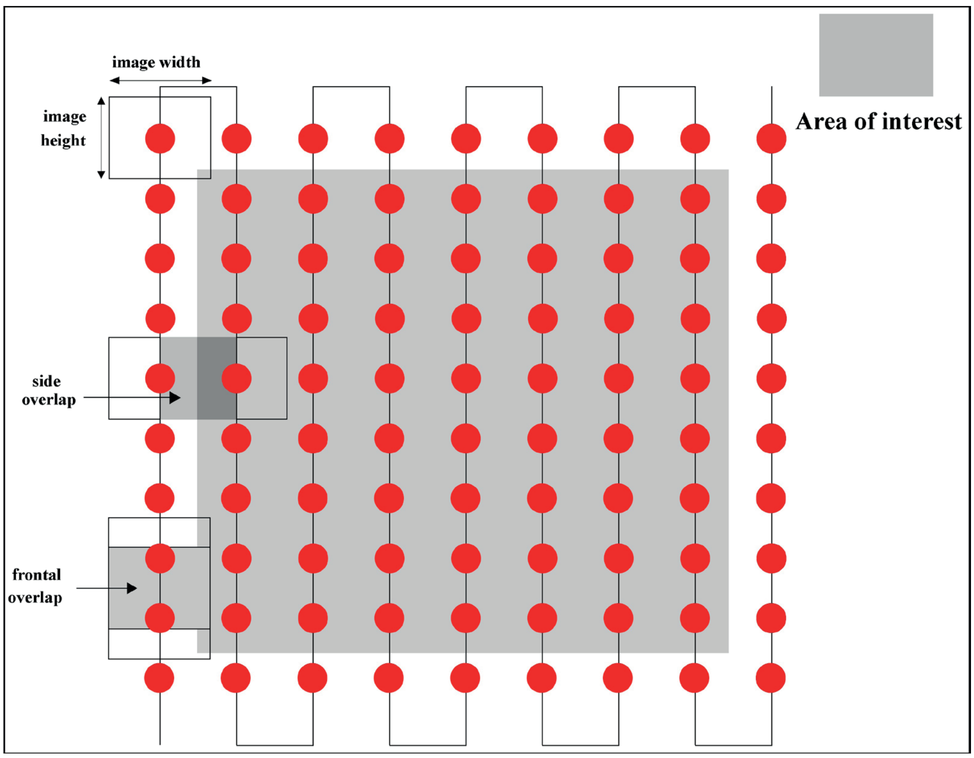

Fig. 2. Flight routes for UAV

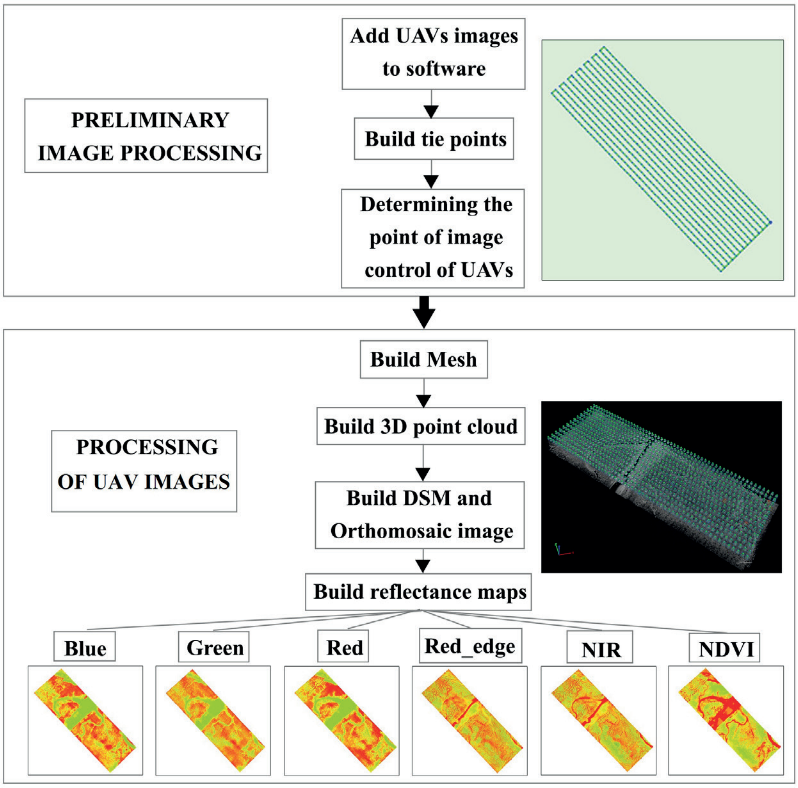

Fig. 3. UAV image processing process

segmentation algorithm, which is a fusion technique for grouping regions with similar pixels and adjacent points into objects by considering the homogeneity criteria of existing pixels or image objects (Baatz et al. 2000). Multiresolution segmentation algorithms are based on the principle of maximizing uniformity in objects and heterogeneity between objects (Chen et al. 2019). Photo segmentation is used to locate objects and boundaries between objects (Kavzoglu et al. 2014). In the next steps, smaller image objects are merged into larger objects.

To enhance the accuracy of mangrove vegetation classification maps in the Dong Rui commune, this study used the random forest algorithm. Random forests, proposed by Breiman, allow the classification of forest trees by the regression method (Breiman L. 2001). The random forest algorithm includes two additional pieces of information: a measure of the importance of the predictor variables and a measure of the internal structure of the data (the proximity of different data points to one another). Currently, the random forest algorithm is widely used in classification, forest inventory mapping, and forest tree classification, helping to enhance the accuracy of different types of thematic maps (Francke et al. 2008; Prinzie et al. 2007).

Map accuracy assessment

The error matrix (confusion matrix) between the classification results and the control sample was constructed, and the kappa coefficient (K) was evaluated. Kappa was first introduced in 1960 by Cohen as a reliability statistic when two judges classified targets into categories on a nominal variable (Cohen, 1960). The Kappa coefficient is a suitable tool for assessing the reliability of maps based on preliminary results and factual verification results and is used in many studies of remote sensing-based mapping (Nguyen, D. H. et al. 2022; Pardo-Iguzquiza et al. 2018).

Accordingly, 20% of the total number of photo reference samples collected in the field (corresponding to 558 photo reference samples) was used to assess map accuracy (Fig. 4). The kappa coefficient was used as a measure of classification accuracy. This is the utility factor of all the primes from the error matrix. It is the essential distinction between what is true about the matrix's deviation error and the total number of changes reflected by the rows and columns. The formula for determining the kappa index is as follows:

$$K = \frac{N\sum_{i=1}^{r} X_{ii} - \sum_{i=1}^{r}\left(X_{i+} - X_{+i}\right)}{N^2 - \sum_{i=1}^{r}\left(X_{i+} - X_{+i}\right)} \qquad (1)$$

Here, r is the number of columns in the image matrix, X_{ii} is the number of pixels observed in row i and column i (on the main diagonal), X_{i+} is the total pixels observed in row i, and N is the total number of pixels observed in the image matrix.

The kappa coefficient is usually between 0 and 1; values in this range indicate acceptable accuracy of the classification. Kappa can be classified into three groups of values: $K \geq 0.8$: high accuracy; $0.4 \leq K < 0.8$: moderate accuracy; and $K < 0.4$: low accuracy (US Geological Survey).

Determination of mangrove vegetation structure based on UAV

Determination of tree height

To determine the height of the mangrove biome in the study area, a terrain number model (DTM) and surface number model (DSM) (Fig. 5) were constructed from point cloud data from images obtained by UAV (Al-Najjar et al. 2019). To improve the accuracy of the DTM model, in addition to the GPS measurement data in the field, this study identified ground points directly based on forest canopy gaps obtained from UAV images. The tree height in the study area is calculated by subtracting the DSM value from the DTM value (Lisein et al. 2013).

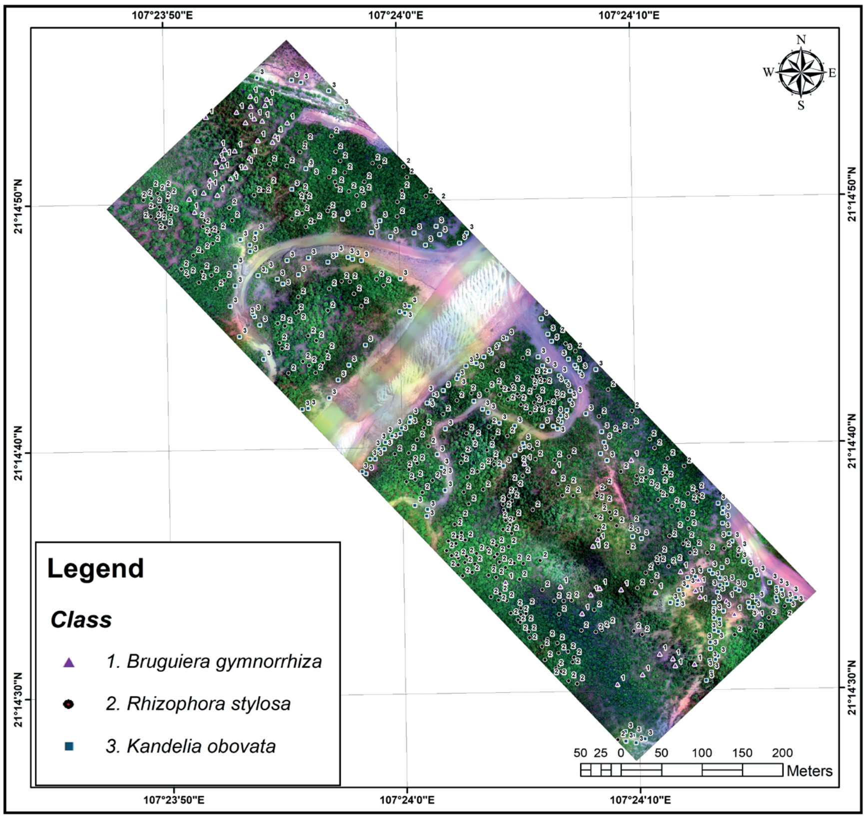

Fig. 4. 558-point image lock diagram for map accuracy assessment

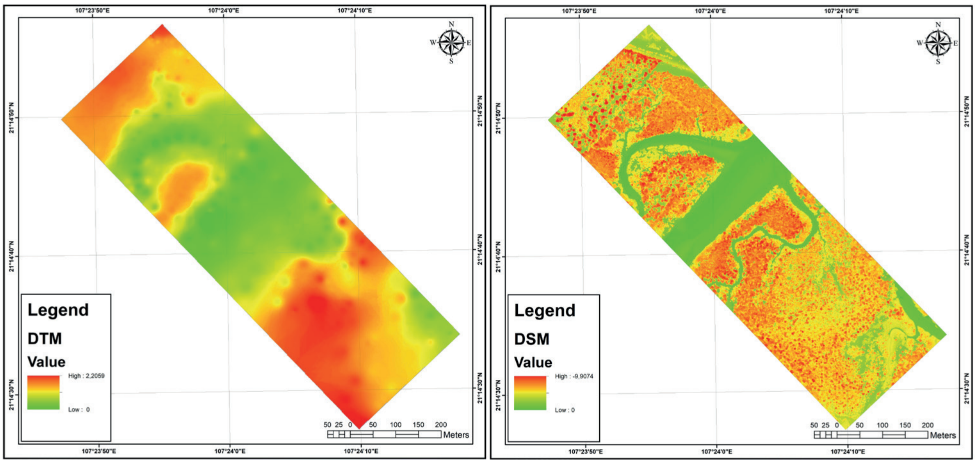

Fig. 5. Model DTM and DSM flight area capture UAV

Identification of vegetation indices

Based on 5 monochrome spectral channels obtained after UAV image processing (blue (R_b): 450 nm ± 16 nm, green (R_g): 560 nm ± 16 nm, red (R_r): 650 nm ± 16 nm, red edge (R_{re}): 730 nm ± 16 nm, near-infrared (R_{nir}): 840 nm ± 26 nm)), several vegetation indices for mangrove areas were identified, including the following:

Normalized Difference Vegetation Index (NDVI). This is an important indicator in studies of ecology, growth, development and fluctuations in plant cover. In addition, this indicator also contributes to warnings about crop disease status, yield and crop yields when combined with other indicators. The NDVI index has many applications in agriculture and forestry. In particular, applications to detect plant cover fluctuations between different periods on one fixed range. In addition, in the field of agriculture, the NDVI index also contributes to the assessment of crop development and the forecast of yield. The NDVI index is calculated by the formula (Tucker, 1979):

$$NDVI = \frac{R_{nir} - R_r}{R_{nir} + R_r} \tag{2}$$

Green Normalized Difference Vegetation Index (GNDVI). Similar to the NDVI, the GNDVI further enhances the variability in chlorophyll in plant leaves. The GNDVI is calculated by the following formula (Hunt et al. 2013):

$$GNDVI = \frac{R_{nir} - R_g}{R_{nir} + R_g} \tag{3}$$

The enhanced vegetation index (EVI) was invented by Liu and Huete to simultaneously calibrate the value of NDVI against atmospheric influence and ground reflection, particularly in areas with dense canopies. The value range of the EVI is -1 to 1; for healthy vegetation, the EVI value ranges between 0.2 and 0.8. The formula for calculating the EVI index is as follows (Huete et al. 2002):

$$EVI = 2.5\frac{R_{nir} - R_r}{R_{nir} + 6R_r - 7.5R_b + 0.16} \tag{4}$$

Green Chlorophyll Index (GCI). In remote sensing, the green chlorophyll index is used to estimate the chlorophyll content in various plant species. The chlorophyll content reflects the physiological state of vegetation; it decreases in stressed plants and thus can be used as a measurement of plant health. The GCI index is calculated by the formula (Hunt et al. 2013):

$$GCI = \frac{R_{nir}}{R_g} - 1 \quad (5)$$

RESULTS

Mangrove tree-species classification map

Map accuracy assessment

Based on the 558 reference samples used to assess the map accuracy and classification results of each mangrove plant species at the UAV flying area, a matrix table was developed to assess the accuracy of the mangrove species classification map (Tab. 1).

Accordingly, the overall accuracy of the UAV classification map is 86.28%, corresponding to K=0.84 (according to formula 1). Compared to the K range given by the US Geological Survey, what is the high accuracy (K ≥ 0.8).

For user accuracy, *Kandelia obovata* had the highest value, reaching 98.06%, and the lowest belonged to the species *Bruguiera gymnorrhiza*, with a value of only 71.88%. For producer accuracy, the highest value belonged to *Rhizophora stylosa*, which scored 93.69%, while *Kandelia obovata* had the lowest value, reaching 81.28% (Tab. 1). According to Table 1, only 14% of the total number of samples (corresponding to 8/54 samples) of *Bruguiera gymnorrhiza* were misinterpreted as *Rhizophora stylosa*. Meanwhile, 5.36% of all specimens of *Rhizophora stylosa* were misinterpreted as *Bruguiera gymnorrhiza*, accounting for 17/317. For samples of the species *Kandelia obovata*, 18.13% of the total samples were misinterpreted as *Rhizophora stylosa*, corresponding to 34 of the 187 total samples of the species *Kandelia obovata* identified in the field.

Tree-species classification map

Based on the process of mapping mangrove vegetation taxonomy, taxonomic mapping was established, and the distribution was determined for 3 mangrove plant species, including *Bruguiera gymnorrhiza, Rhizophora stylosa*, and *Kandelia obovata*, in the UAV flight area (Fig. 6).

Table 1. Error matrix evaluates map accuracy

		Ground Reference			Total
		Bruguiera gymnorrhiza	*Rhizophora stylosa*	*Kandelia obavata*	
Classification	Bruguiera gymnorrhiza	46	8		54
	Rhizophora stylosa	17	297	3	317
	Kandelia obavata	1	34	152	187
Total		64	339	155	558
User Accuracy (%)		71.88	87.61	98.06	85.85
Producer Accuracy (%)		85.19	93.69	81.28	86.72
Overall Accuracy (%)					86.28

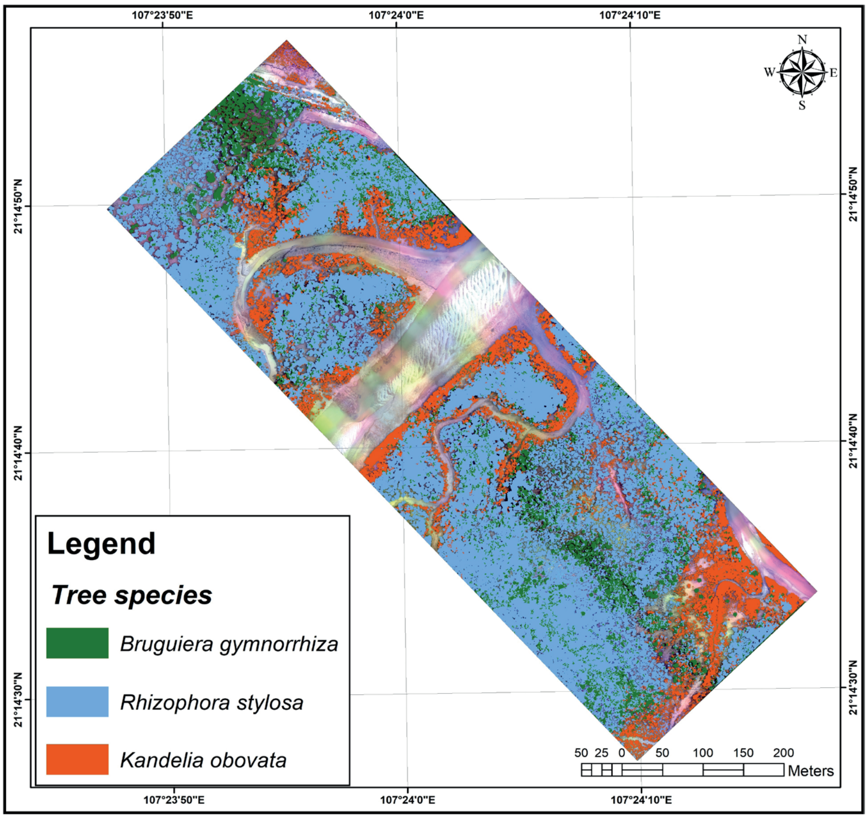

Fig. 6. Tree-species classification map of flying areas capturing UAV

In the study area, *Rhizophora stylosa* predominates, often with an alternating distribution with *Bruguiera gymnorrhiza* at high tide flats, creating vegetation populations that characterize not only UAV but also the western area of Dong Rui commune (Fig. 6). Meanwhile, *Kendelia obovata* is distributed mainly in low tide areas, riverine areas and areas along frequent streams (Fig. 6).

According to Fig. 7, the canopy coverage rate of *Rhizophora stylosa* is the highest of the 3 species identified in the UAV flight area, reaching 65.89% of the total area covered. Next, the coverage areas of *Bruguiera gymnorrhiza* and *Kendelia obovata* species were relatively low compared to *Rhizophora stylosa*, at 14.44% and 19.67%, respectively.

Mangrove structure

Tree height

Based on the established DSM and DTM models using UAV flight imagery data, a tree height map for the study area was developed (Fig. 8).

According to Fig. 8 and Tab. 2, the *Bruguiera gymnorrhiza* population has the largest height in the study area, particularly in the northern and central areas of the UAV (average height ranges from 4.41 ± 0.51 m). For *Rhizophora stylosa*, the height of some individuals in the northern region is also relatively large, and the average height reaches approximately 4.28 ± 0.68 m. The biome of *Bruguiera gymnorrhiza* and *Rhizophora stylosa* reaching an average height of 2 m to 4 m is concentrated mainly in the south and southeast of the UAV flying area, occupying most of the area.

Meanwhile, *Kendelia obovata* populations are distributed in low-tide areas at lower elevations than those of *Bruguiera gymnorrhiza* and *Rhizophora stylosa*, averaging only 3.47 ± 0.63 m. Some of the *Kendelia obovata* bodies located in the north and south of the flight area capture UAV with a height of only approximately 1.5 m (Fig. 8).

According to Figs. 6 - 8, the strong growth of *Bruguiera gymnorrhiza* and *Rhizophora stylosa* biomes can be seen in the UAV, with a predominance in both area distribution and tree height. Meanwhile, *Kendelia obovata* predominates in low-tide, riparian or frequent streams.

Vegetation indices of mangroves

According to the formula for calculating vegetation indices (Formulas 2-5), four maps have been developed showing the value of vegetation indices for UAV, including NDVI (Fig. 9a), GNDVI (Fig. 9b), EVI (Fig. 9c), and GCI (Fig. 9d).

According to Fig. 9a, areas with the distribution of *Bruguiera gymnorrhiza* and *Rhizophora stylosa* species have higher NDVI values than areas with only the distribution of

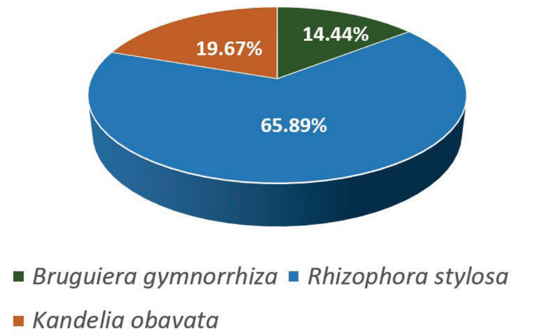

Fig. 7. The canopy coverage ratio of 3 types of flying area plants captured by the UAV

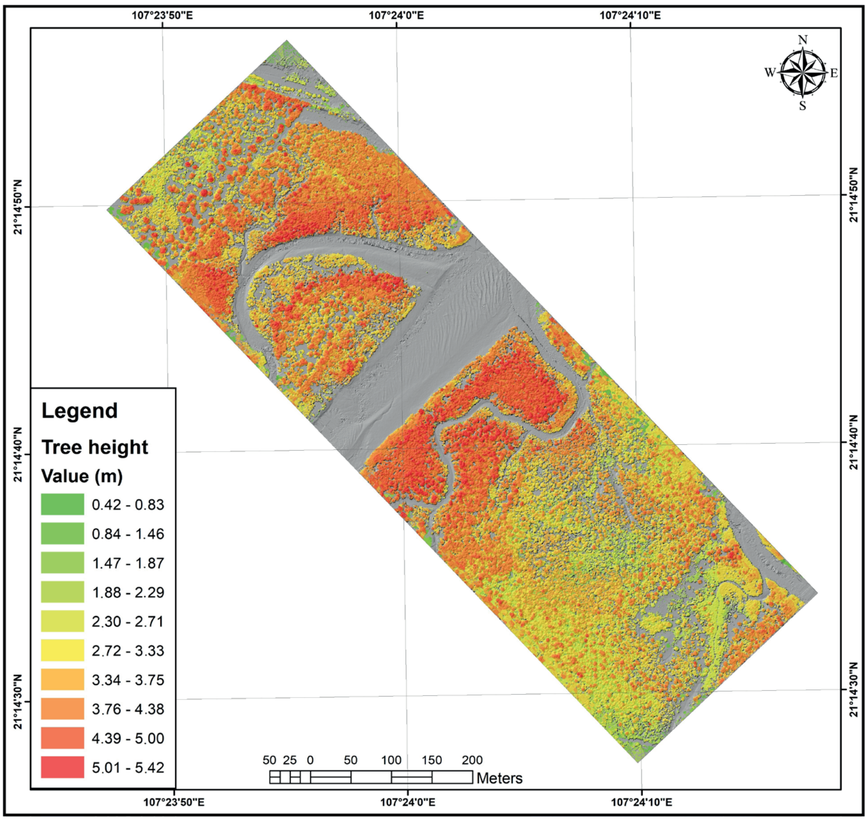

Fig. 8. Tree height map of flying area capturing UAV

Table 2. Number of individuals, mean ± standard deviation, minimum and maximum tree height

Species	Number of individuals	Mean height ± S.D. (m)	Min. - Max. Height (m)
Bruguiera gymnorrhiza	54	4.41 ± 0.51	3.54 – 5.42
Rhizophora stylosa	317	4.28 ± 0.68	1.25 – 5.42
Kendelia obovata	187	3.47 ± 0.63	1.46 – 5.21

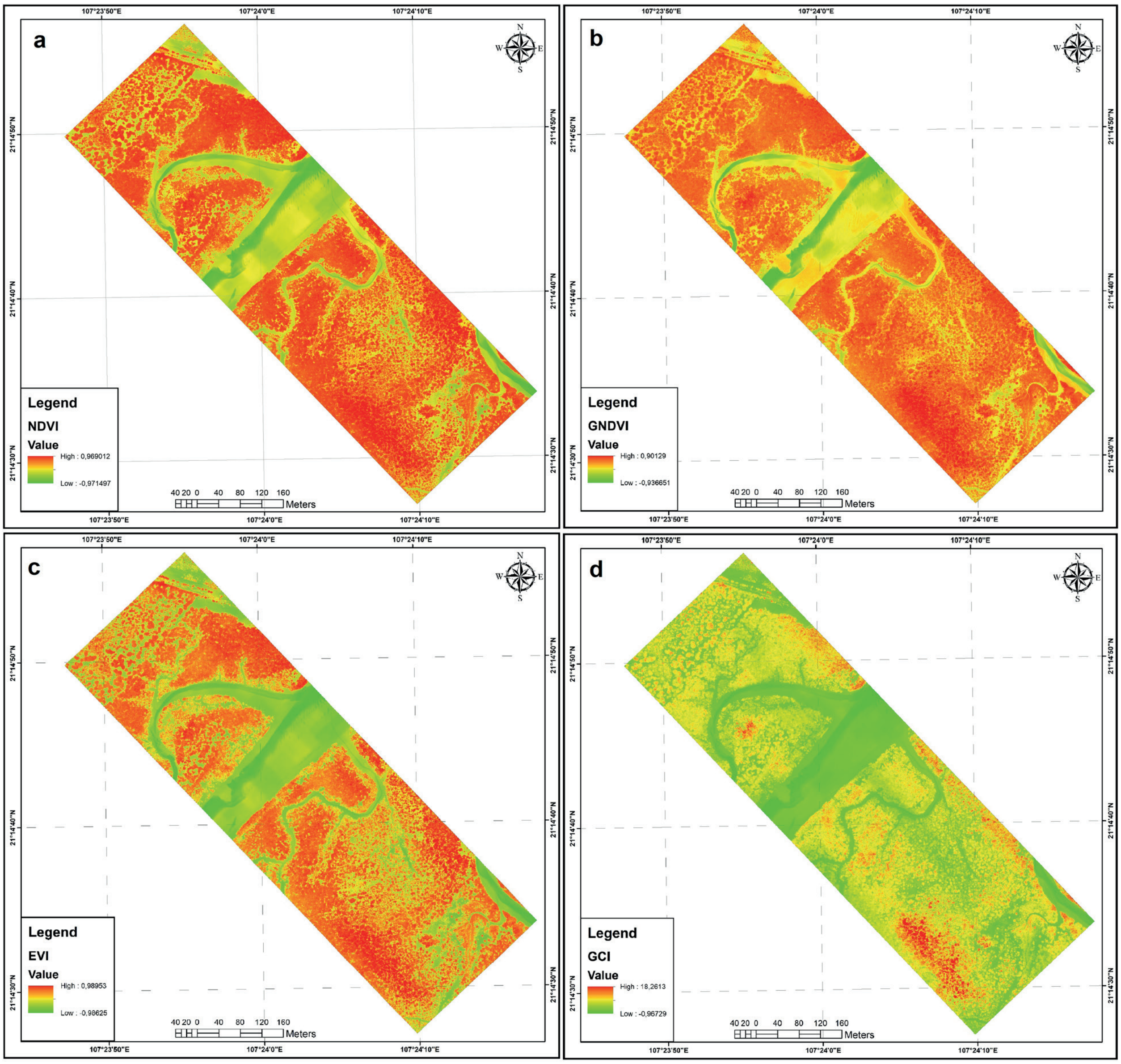

Fig. 9. Values of some vegetation indices in the UAV flying area

Kendelia obovata species. In particular, areas with high NDVI values in the mangrove biome area have a large height (ranging from 4 m to 5 m) and large coverage. Similar to the NDVI value, the high GNDVI and EVI values in this area are also concentrated in the *Bruguiera gymnorrhiza* and Rhizophora stylosa biomes, which have reached a stable state, high height, and high coverage (Fig. 9b, 9c). For the GCI value, the flora consists of *Bruguiera gymnorrhiza* and *Rhizophora stylosa* species distributed in the south and northeast of the most valuable UAV flight area (Fig. 9d).

Based on 558 field sampling points, 4 types of vegetation index values (NDVI, GNDVI, EVI, and GCI) were extracted from each point to compare the values of vegetation index types between mangrove species. According to Fig. 10, the NDVI and EVI values of *Bruguiera gymnorrhiza* and *Rhizophora stylosa* are similar, achieving mean values of 0.82 and 0.76, respectively, higher than those of *Kendelia obovata* (average NDVI value reaches 0.68, EVI reaches 0.62). The EVI of vegetation at all sampling sites was greater than 0.2, indicating that the state of mangrove health at the UAV was good. For the GNDVI value, the value of the above three species is relatively large, reaching between 0.62 and 0.68, of which the highest is the species *Bruguiera gymnorrhiza* (Fig. 10). The GCI values of these three plants varied widely, with the mean GCI values of *Bruguiera gymnorrhiza*, *Rhizophora stylosa*, and *Kendelia obovata* being 4.4, 3.7, and 3.2, respectively (Fig. 10).

DISCUSSION

This study provides a method for classifying mangrove trees based on data obtained from UAV and analyses the mangrove structure in the Dong Rui commune based on height parameters and vegetation indicators determined by the results of multispectral UAV. This is the advantage of photos taken because UAV have a multispectral camera with

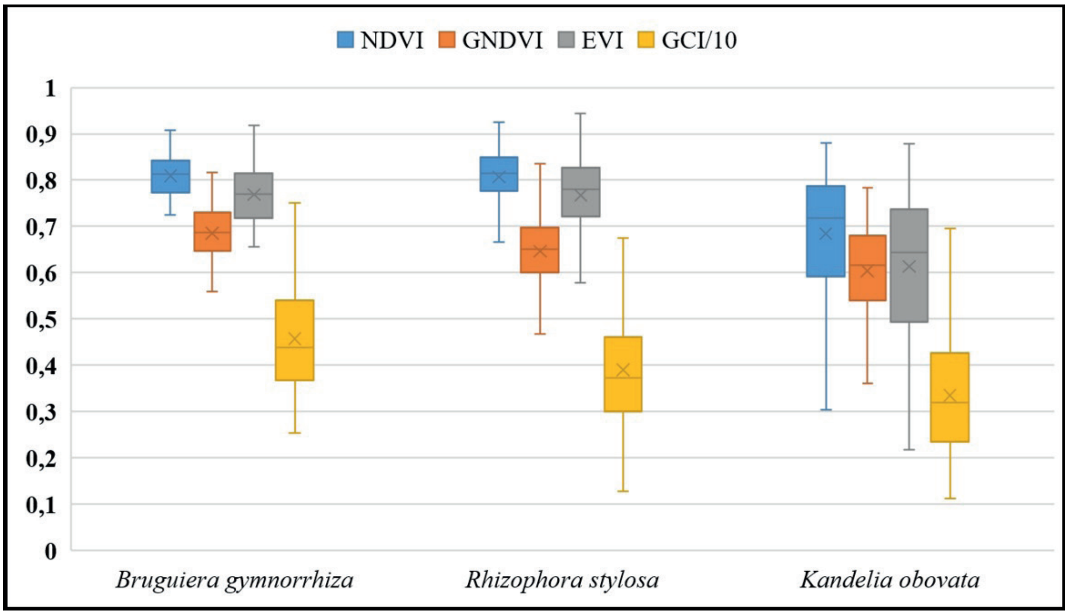

Fig. 10. Value of vegetation indices of three species of mangrove trees flying area shooting UAV

5 monochrome wave bands (green, blue, red, red_edge, and NiR), allowing up to 21 different vegetation indicators to be identified (Hunt et al. 2013), while conventional UAV only mount cameras with RGB wavebands that only allow the identification of some vegetation indicators, such as VARI and TGI (Ngo et al. 2020). Analysis of vegetation indicators is considered an effective method in the classification and assessment of mangrove vegetation texture (Cao et al. 2018).

Combining imaging and random forest algorithms with the characteristic spectra of each plant allows for enhanced accuracy of mangrove classification maps (Jiang et al. 2021). In the UAV flight area, 3 species of trees, including *Bruguiera gymnorrhiza, Rhizophora stylosa,* and *Kendelia obovata,* were classified with an overall accuracy of 86.28%, corresponding to K=0.84. These are 3 species of mangrove plants common in the tidal flat area of the Dong Rui commune. Almost all mangrove species are distinguishable in the visible and near-infrared infrared because of the dispersion in porous mesenchymal cells in plants (Zulfa et al. 2021; Zulfa et al. 2020). In addition to the image classification method combined with random forest terminology, the determination of chlorophyll content in plant leaves according to plant indicators based on spectroscopic measurements is also a common method for classifying plants (Meivel et al. 2023; Xue et al. 2009). Botanical indicators using a wave range from 550 nm to 730 nm are suitable for plant classification purposes due to the different leaf structures of each species (Zhao et al. 2019). The wavelengths of 549 nm, 559 nm, 702 nm, 722 nm, 742 nm, and 763 nm are the most sensitive to the chlorophyll of mangrove tree species (George et al. 2020).

The average NDVI value of mangrove vegetation in Dong Rui commune in both summer and winter ranges from 0.7 to 0.8, which is higher than the average NDVI value of mangrove forest areas in Dodola and Guraping of North Maluku Province (Singgalen 2022) or North Halmahera, Indonesia (Singgalen et al. 2021) when the average NDVI value in these areas is only 0.3 to 0.4. The NDVI value of mangroves in the Dong Rui commune is greater when compared to the NDVI value of the Can Gio mangrove forest region, a typical mangrove forest area in southern Vietnam (Hoa et al. 2020). Dong Rui commune mangroves have NDVI and GNDVI values that are comparable to those found on Sumatra's eastern coast (NDVI = 0.738 and GNDVI = 0.641) (Samsuri et al. 2021) and greater than those found in the Banten, Jakarta, and West Java Ecotone Zones (NDVI: 0.39 – 0.61 and GNDVI: 0.25 – 0.48) (Asy'Ari et al. 2022).

According to the results of the biodiversity survey of the research team in the wetland area of the Dong Rui commune, the level of species diversity here is relatively large when compared to other wetland areas in northern Vietnam, such as the Cat Ba mangrove forest, Phu Long – Gia Luan mangrove forest, and Hai Phong Province (Pham et al. 2017; Thinh et al. 2008). In Xuan Thuy National Park (Nam Dinh Province), the wetland ecosystem is considered the most diverse in northern Vietnam, and the biodiversity level of the species composition of the Dong Rui commune wetland area is equivalent to over 1500 species of organisms (Huan 2021; Nhan et al. 2015).

In the wetland area of the Dong Rui commune, the height of mangrove plant biomes is relatively low. For the biomes of *Bruguiera gymnorrhiza, Rhizophora stylosa* tidal flats, their average height is only 4 – 5.5 m. Compared with the mangrove areas of southern Vietnam, such as U Minh Ha National Park (*Melaleuca alternifolia* height can be up to 10-12 m) (Safford et al. 1998) or Tram Chim National Park (Viet et al. 2020), this is a much lower tree height. There are many reasons for the difference in the structure of mangrove flora between southern and northern Vietnam, mainly because the sediment layer of mud and sand in the northern region is thinner than that in the southern area (Huan 2021). In addition, northern Vietnam is subject to many impacts from typhoons (average 5.2 typhoons/year) (Toan, 2014). Therefore, the mangrove plant biomes here cannot reach great heights (People's Committee of Tien Yen district 2015; Van et al. 2022). Similarly, when compared to some mangrove areas in Southeast Asia, such as in Perak Province, Malaysia (Otero et al. 2018), Indonesia (FAO 2007) or in the world, such as in the Czech Republic (Panagiotidis et al. 2018), the average height of mangroves in Dong Rui commune is much smaller.

The classification of plants based on UAV imagery is still mainly based on spectral values and canopy morphology on the resulting images, which do not show other morphological forms, such as stem and root structures. These are the limitations of classifying plants based on UAV data, which do not represent tree structures below the foliage, which are already obscured by the canopy. To limit errors when classifying mangrove trees based on satellite imagery, verifiable field surveys are indispensable. In addition, lidar sensors are also suitable tools for analysing mangrove structures (Doughty et al. 2021).

CONCLUSIONS

In this study, based on multispectral UAV image data, tree classification maps and mangrove structure analysis through tree height values and vegetation index values were developed for UAV flight zones in the Dong Rui commune wetland ecosystem. Combined with collecting tree taxonomy samples through field surveys and image processing methods of UAV on GIS software, we propose that UAV are effective tools for small-scale mangrove structure classification and assessment.

However, the limitation of UAV is that the range of operations is limited to only approximately 200 hectares. Therefore, mapping large-scale areas is more efficient when combined with high-resolution satellite imagery along with UAV that are "key points" to identify details for small areas. In addition, the enhanced combination with lidar sensors will help to establish a more detailed model of the structure of vegetation.

Based on the findings of this research, local managers may create programs and strategies to examine the present state of the structure, number, and function of each species participating in the Dong Rui commune mangrove ecosystem. Furthermore, the findings of this research may be used to measure the amount of growth of each species in various intertidal locations, which can then be utilized to pick restored mangrove seedlings for each appropriate site. UAVs are also useful for assessing and monitoring topography alterations as well as the sedimentation of estuary sediments based on seasonal or yearly cycles. With the development of UAV technology in the future, such as enhanced image resolution, resistance to extreme weather conditions or increased flight time, UAV will be a powerful support tool for researchers as well as managers in managing and conserving wetland ecosystems. ■

REFERENCES

Abdullah, S., Tahar, K. N., Abdul Rashid, M. F., & Osoman, M. (2022). ESTIMATING TREE HEIGHT BASED ON TREE CROWN FROM UAV IMAGERY. Malaysian Journal of Sustainable Environment, 9, 99. doi: 10.24191/myse.v9i1.17294

Al-Najjar, H., Kalantar, B., Pradhan, B., Saeidi, V., Abdul Halin, A., Ueda, N., & Mansor, S. (2019). remote sensing Land Cover Classification from fused DSM and UAV Images Using Convolutional Neural Networks. Remote Sensing, 2019, 1461. doi: 10.3390/rs11121461

Andersen, H.-E., McGaughey, R., & Reutebuch, S. (2005). Estimating forest canopy fuel parameters using LIDAR data. Remote Sensing of Environment, 94, 441-449. doi: https://doi.org/10.1016/j.rse.2004.10.013

Asy'Ari, R., Rahmawati, A., Sa'diyya, N., Gustawan, A., Setiawan, Y., Zamani, N., & Pramulya, R. (2022). Mapping mangrove forest distribution on Banten, Jakarta, and West Java Ecotone Zone from Sentinel-2-derived indices using cloud computing based Random Forest. Jurnal Pengelolaan Sumberdaya Alam dan Lingkungan (Journal of Natural Resources and Environmental Management), 12, 97-111. doi: https://doi.org/10.29244/jpsl.12.1.97-111

Baatz, M., & Schape, A. (2000). Multiresolution segmentation: an optimization approach for high quality multi-scale image segmentation. Angew. Geogr. Info. verarbeitung, Wichmann-Verlag, Heidelberg, 12-23.

Bandini, F., Butts, M., Jacobsen, T., & Bauer-Gottwein, P. (2017). Water level observations from Unmanned Aerial Vehicles for improving estimates of surface water-groundwater interaction. Hydrological Processes, 31. doi: https://doi.org/10.1002/hyp.11366

Breiman L. (2001). Random forests. Machine Learning, 1(45), 5–32.

Brennan, R., & Webster, T. (2006). Object-oriented land cover classification of LIDAR-derived surfaces. Canadian Journal of Remote Sensing, 32. doi: https://doi.org/10.5589/m06-015

Buğday, E. (2018). Capabilities of using UAVs in Forest Road Construction Activities. 4, 56-62. doi: https://doi.org/10.33904/ejfe.499784

Cao, J., Leng, W., Liu, K., Liu, L., he, Z., & Zhu, Y. (2018). Object-Based Mangrove Species Classification Using Unmanned Aerial Vehicle Hyperspectral Images and Digital Surface Models. Remote Sensing, 10, 89. doi: https://doi.org/10.3390/rs10010089

Chen, Y., Chen, Q., & Jing, C. (2019). Multi-resolution segmentation parameters optimization and evaluation for VHR remote sensing image based on mean NSQI and discrepancy measure. Journal of Spatial Science, 66, 1-26. doi: 10.1080/14498596.2019.1615011

Cohen, J. (1960). A Coefficient of Agreement for Nominal Scales. Educational and Psychological Measurement, 20, 37-46. doi: https://doi.org/10.1177/001316446002000104?journalCode=epma

Costanza, R., Arge, Groot, R., Farberk, S., Grasso, M., Hannon, B., . . . Belt, M. (1997). The Value of the World's Ecosystem Services and Natural Capital. Nature, 387, 253-260. doi: https://doi.org/10.1016/S0921-8009(98)00020-2

Dawes, C. (1999). Mangrove structure, litter and macroalgal productivity in a northern-most forest of Florida. Mangroves and Salt Marshes, 3, 259-267. doi: 10.1023/A:1009976025000

Deng, T., Fu, B., Liu, M., He, H., Donglin, F., Li, L., . . . Gao, E. (2022). Comparison of multi-class and fusion of multiple single-class SegNet model for mapping karst wetland vegetation using UAV images. Scientific Reports, 12. doi: 10.1038/s41598-022-17620-2

Dezhi, W., Wan, B., Qiu, P., Su, Y., Guo, Q., Wang, R., . . . Wu, X. (2018). Evaluating the Performance of Sentinel-2, Landsat 8 and Pléiades-1 in Mapping Mangrove Extent and Species. Remote Sensing, 10, 1468. doi: https://doi.org/10.3390/rs10091468

Doughty, C. L., Ambrose, R. F., Okin, G. S., & Cavanaugh, K. C. (2021). Characterizing spatial variability in coastal wetland biomass across multiple scales using UAV and satellite imagery. Remote Sensing in Ecology and Conservation, 7(3), 411-429. doi: https://doi.org/10.1002/rse2.198

FAO. (2007). The world's mangroves 1980-2005 Food and Agriculture Organization of the United Nations. Rome.

Francke, T., López-Tarazón, J. A., & Schröder, B. (2008). Estimation of suspended sediment concentration and yield using linear models, Random Forests and Quantile Regression Forests. Hydrological Processes, 22, 4892-4904. doi: https://doi.org/10.1002/hyp.7110

George, R., Padalia, H., Kumar, S., & Sinha, S. (2020). Evaluating sensitivity of hyperspectral indices for estimating mangrove chlorophyll in Middle Andaman Island, India. Environmental Monitoring and Assessment, 191. doi: 10.1007/s10661-019-7679-6

Hese, S., Thiel, C., & Henkel, A. (2019). UAV based Multi Seasonal Deciduous Tree Species Analysis in the Hainich National Park using Multi Temporal and Point Cloud Curvature Features. Int. Arch. Photogramm. Remote Sens. Spatial Inf. Sci., XLII-2/W13, 363–370. doi: https://doi.org/10.5194/isprs-archives-XLII-2-W13-363-2019

Hoa, L., Tran, T., Gyeltshen, S., Nguyen, C., Tran, D., Luu, T., & Mán, D. (2020). Characterizing Spatiotemporal Patterns of Mangrove Forests in Can Gio Biosphere Reserve Using Sentinel-2 Imagery. Applied Sciences, 10, 4058. doi: https://doi.org/10.3390/app10124058

Huan, N. C. (2021). Established Dong Rui Wetland Reserve, Tien Yen, Quang Ninh Province (pp. 348). Quang Ninh: Department of Natural Resources and Environment of Quang Ninh province.

Huang, H., He, S., & Chen, C. (2019). Leaf Abundance Affects Tree Height Estimation Derived from UAV Images. Forests, 10, 931. doi: 10.3390/f10100931

Huete, A., Didan, K., Miura, T., Rodriguez, E., Gao, X., & Ferreira, L. G. (2002). Overview of the Radiometric and Biophysical Performance of the MODIS Vegetation Indices. Remote Sensing of Environment, 83, 195-213. doi: https://doi.org/10.1016/S0034-4257(02)00096-2

Hunt, J. E., Doraiswamy, P., McMurtrey, J., Daughtry, C., Perry, E., & Akhmedov, B. (2013). A visible band index for remote sensing leaf Chlorophyll content at the Canopy Scale. International Journal of Applied Earth Observation and Geoinformation, 21, 103–112. doi: https://doi.org/10.1016/j.jag.2012.07.020

Jiang, Y., Zhang, L., Yan, M., Qi, J., Fu, T., Fan, S., & Chen, B. (2021). High-Resolution Mangrove Forests Classification with Machine Learning Using Worldview and UAV Hyperspectral Data. Remote Sensing, 13, 1529. doi: https://doi.org/10.3390/rs13081529

Kamal, M., Phinn, S., & Johansen, K. (2014). Characterizing the Spatial Structure of Mangrove Features for Optimizing Image-Based Mangrove Mapping. Remote Sensing, 6, 984-1006. doi: 10.3390/rs6020984

Kavzoglu, T., & Yildiz, M. (2014). Parameter-Based Performance Analysis of Object-Based Image Analysis Using Aerial and Quikbird-2 Images. Paper presented at the Remote Sensing and Spatial Information Sciences, Gottingen.

Lassalle, G., & Souza Filho, C. (2022). Tracking canopy gaps in mangroves remotely using deep learning. Remote Sensing in Ecology and Conservation. doi: 10.1002/rse2.289

Lisein, J., Deseilligny, M., Bonnet, S., & Lejeune, P. (2013). A Photogrammetric Workflow for the Creation of a Forest Canopy Height Model from Small Unmanned Aerial System Imagery. Forests, 4, 922-944. doi: 10.3390/f4040922

Liu, T., & Abd-Elrahman, A. (2018). Multi-view object-based classification of wetland land covers using unmanned aircraft system images. Remote Sensing of Environment, 216. doi: https://doi.org/10.1016/j.rse.2018.06.043

Lorenz, S., Zimmermann, R., & Gloaguen, R. (2017). The Need for Accurate Geometric and Radiometric Corrections of Drone-Borne Hyperspectral Data for Mineral Exploration: MEPHySTo—A Toolbox for Pre-Processing Drone-Borne Hyperspectral Data. Remote Sensing, 9. doi: https://doi.org/10.3390/rs9010088

Ly, T. N., Van, P. D. T., Le, T. L., Jun, S., & Hisamichi, N. (2016). Mangrove structure variation under influences of tidal-inundation in the Bac Lieu coastal zone. Journal of Science and Technology.

ma, Q., Su, Y., & Guo, Q. (2017). Comparison of Canopy Cover Estimations From Airborne LiDAR, Aerial Imagery, and Satellite Imagery. IEEE Journal of Selected Topics in Applied Earth Observations and Remote Sensing, PP, 1-12. doi: 10.1109/JSTARS.2017.2711482

Mallmann, C. L., Zaninni, A. F., & Filho, W. P. (2020). Vegetation Index Based In Unmanned Aerial Vehicle (Uav) To Improve The Management Of Invasive Plants In Protected Areas, Southern Brazil. 2020 IEEE Latin American GRSS & ISPRS Remote Sensing Conference (LAGIRS), 66-69.

Maltamo, M., Eerikäinen, K., Pitkänen, J., Hyyppä, J., & Vehmas, M. (2004). Estimation of timber volume and stem density based on scanning laser altimetry and expected tree size distribution functions. Remote Sensing of Environment, 90, 319-330. doi: https://doi.org/10.1016/j.rse.2004.01.006

Matese, A., Toscano, P., Di Gennaro, S., Genesio, L., Vaccari, F., Primicerio, J., . . . Gioli, B. (2015). Intercomparison of UAV, Aircraft and Satellite Remote Sensing Platforms for Precision Viticulture. Remote Sensing, 7, 2971-2990. doi: https://doi.org/10.3390/rs70302971

Meivel, s., & Banu, D. (2023). Design and Method of an Agricultural Drone System Using Biomass Vegetation Indices and Multispectral Images (pp. 343-373).

Mitsch, W., & Gosselink, J. (2000). The Value of Wetlands: Importance of Scale and Landscape Setting. Ecological Economics, 35, 25-33. doi: https://doi.org/10.1016/S0921-8009(00)00165-8

Modi, A., & Das, P. (2019). Multispectral Imaging Camera Sensing to Evaluate Vegetation Index from UAV. Research & Reviews: Journal of Space Science & Technology, 8(2), 30-42.

Nagelkerken, I., Blaber, S. J. M., Bouillon, S., Green, P., Haywood, M., Kirton, L. G., . . . Somerfield, P. J. (2008). The habitat function of mangroves for terrestrial and marine fauna: A review. Aquatic Botany, 89(2), 155-185. doi: https://doi.org/10.1016/j.aquabot.2007.12.007

Nex, F., & Remondino, F. (2014). UAV for 3D mapping applications: A review. Applied Geomatics, 6. doi: https://doi.org/10.1007/s12518-013-0120-x

Ngo, D., Nguyen, H., Dang, C., & Kolesnikov, S. (2020). UAV application for assessing rainforest structure in Ngoc Linh nature reserve, Vietnam. E3S Web Conf., 203, 03006.

Nguyen, D. H., & Ngo, T. D. (2021). Seasonal Dynamics of Tropical Forest Vegetation in Ngoc Linh Nature Reserve, Vietnam Based on UAV Data. Forest and Society, 5(2), 376-389. doi: https://doi.org/10.24259/fs.v5i2.13027

Nguyen, D. H., Ngo, T. D., Vu, V. D., & Du, Q. V. V. (2022). Establishing distribution maps and structural analysis of seagrass communities based on high-resolution remote sensing images and field surveys: a case study at Nam Yet Island, Truong Sa Archipelago, Vietnam. Landscape and Ecological Engineering. doi: https://doi.org/10.1007/s11355-022-00502-0

Nguyen, H. H., Nghia, N. H., Nguyen, H. T. T., Le, A. T., Ngoc Tran, L. T., Duong, L. V. K., . . . Furniss, M. J. (2020). Classification Methods for Mapping Mangrove Extents and Drivers of Change in Thanh Hoa Province, Vietnam during 2005-2018. Forest and Society, 4(1), 225-242. doi: 10.24259/fs.v4i1.9295

Nguyen, L. D., Nguyen, C. T., Le, H. S., & Tran, B. Q. (2019). Mangrove Mapping and Above-Ground Biomass Change Detection using Satellite Images in Coastal Areas of Thai Binh Province, Vietnam. Forest and Society, 3(2), 248-261. doi: 10.24259/fs.v3i2.7326

Nhan, H. T. T., Hai, H. T., & Canh, L. X. (2015). Biological deversity in Xuan Thuy National Park, Nam Dinh Province. Paper presented at the The 5th National Scientific Conference on Ecology and Biological Resources, Ha Noi.

Nicholls, R. (2004). Coastal Flooding and Wetland Loss in the 21st Century: Changes Under the SRES Climate and Socio-Economic Scenarios. Global Environmental Change, 14, 69-86. doi: 10.1016/j.gloenvcha.2003.10.007

Nur W, M., Hapsara, R., Cahyo, R., Wahyu, G., Syarif, A., Umarhadi, D., . . . Widyatmanti, W. (2017). Mangrove Structure Mapping Model Using Sentinel-2A Satellite Imagery. Paper presented at the International Symposium on Remote Sensing Japan.

Okojie, J. (2017). Assessment of the relative accuracy of canopy height models developed from UAV and LiDAR sourced datasets for forest tree height estimation in temperate forests. Paper presented at the Geospatial Systems for Apps Development and Research in Africa, Asokoro, Abuja.

Otero, V., Van De Kerchove, R., Satyanarayana, B., Martínez-Espinosa, C., Fisol, M. A. B., Ibrahim, M. R. B., . . . Dahdouh-Guebas, F. (2018). Managing mangrove forests from the sky: Forest inventory using field data and Unmanned Aerial Vehicle (UAV) imagery in the Matang Mangrove Forest Reserve, peninsular Malaysia. Forest Ecology and Management, 411, 35-45. doi: https://doi.org/10.1016/j.foreco.2017.12.049

Pal, S., Mishra, A., & Singh, P. (2020). Assessment of Normalized Difference Vegetation Index by The Use of UAV Remote Sensing. International Journal of Advanced Science and Technology, 29, 4907-4914.

Panagiotidis, D., Abdollahnejad, A., Surovy, P., & Chiteculo, V. (2018). High resolution airborne UAV imagery to determine tree height and crown diameter.

Pardo-Iguzquiza, E., Dowd, P., Ruiz-Constán, A., Martos-Rosillo, S., Luque-Espinar, J. A., Rodriguez-Galiano, V., & Pedrera, A. (2018). Epikarst mapping by remote sensing. Catena, 165, 1-11. doi: https://doi.org/10.1016/j.catena.2018.01.026

Pellegrini, J., Soares, M., Chaves, F., Estrada, G., & Cavalcanti, V. (2009). A Method for the Classification of Mangrove Forests and Sensitivity/Vulnerability Analysis. Journal of Coastal Research, SI56, 443-447.

People's Committee of Tien Yen district. (2015). General report on socio-economic development master plan of Tien Yen district to 2020, orientation to 2030. Quang Ninh.

Pham, T. D., Yoshino, K., & Kaida, N. (2017). Monitoring Mangrove Forest changes in Cat Ba Biosphere Reserve using ALOS PALSAR Imagery and a GIS-based Support Vector Machine Algorithm. Paper presented at the International Conference on Geo-Spatial Technologies and Earth Resource.

Polidoro, B., Carpenter, K., Collins, L., Duke, N., Ellison, A., Ellison, J., . . . Yong, J. (2010). The Loss of Species: Mangrove Extinction Risk and Geographic Areas of Global Concern. PloS one, 5, e10095. doi: https://doi.org/10.1371/journal.pone.0010095

Prasetyo, L., Nursal, W., Setiawan, Y., Rudianto, Y., Wikantika, K., & Irawan, B. (2019). Canopy cover of mangrove estimation based on airborne LIDAR & Landsat 8 OLI. IOP Conference Series: Earth and Environmental Science, 335, 012029. doi: 10.1088/1755-1315/335/1/012029

Prinzie, A., & Van den Poel, D. (2007). Random Multiclass Classification: Generalizing Random Forests to Random MNL and Random NB (Vol. 4653).

Qiao, L., Tang, W., Dehua, G., Zhao, R., An, L., Li, M., . . . Song, D. (2022). UAV-based chlorophyll content estimation by evaluating vegetation index responses under different crop coverages. Computers and Electronics in Agriculture, 196, 106775. doi: 10.1016/j.compag.2022.106775

Rhyma, P. P., Kamarudin, N., Omar, H., Faridah-Hanum, I., & Wahab, Z. (2019). Integration of normalised different vegetation index and Soil-Adjusted Vegetation Index for mangrove vegetation delineation. Remote Sensing Applications: Society and Environment, 17, 100280. doi: 10.1016/j.rsase.2019.100280

Richter, R., Reu, B., Wirth, C., Doktor, D., & Vohland, M. (2016). The use of airborne hyperspectral data for tree species classification in a species-rich Central European forest area. International Journal of Applied Earth Observation and Geoinformation, 52, 464-474. doi: 10.1016/j.jag.2016.07.018

Saenger, P. (2002). Mangrove Structure and Classification (pp. 183-205).

Safford, R. J., Tran, T., Maltby, E., & Ni, D. (1998). Status, biodiversity and management of the U Minh wetlands, Vietnam. Tropical Biodiversity, 5, 217-244.

Samsuri, S., Zaitunah, A., Meliani, S., Hasnanda Syahputra, O., Budiharta, S., Susilowati, A., . . . Azhar, I. (2021). Mapping of mangrove forest tree density using SENTINEL 2A satelit image in remained natural mangrove forest of Sumatra eastern coastal. IOP Conference Series: Earth and Environmental Science, 912, 012001. doi: https://doi.org/10.1088/1755-1315/912/1/012001

Sarno, Rujito, A. S., Zulkifli, D., Munandar, & Moh. Rasyid, R. (2015). Primary Mangrove Forest Structure and Biodiversity. Int J Agri Sys, 2, 135–141. doi: http://dx.doi.org/10.20956/ijas.v3i2.102

Singgalen, Y. (2022). Vegetation Index and Mangrove Forest Utilization through Ecotourism Development in Dodola and Guraping of North Maluku Province. Jurnal Manajemen Hutan Tropika (Journal of Tropical Forest Management), 28, 150-161. doi: https://doi.org/10.7226/jtfm.28.2.150

Singgalen, Y., Gudiato, C., Prasetyo, S., & Fibriani, C. (2021). Mangrove monitoring using normalized difference vegetation index (NDVI): case study in North Halmahera, Indonesia. Jurnal Ilmu dan Teknologi Kelautan Tropis, 13, 2. doi: https://doi.org/10.29244/jitkt.v13i2.34771

Song, B., & Park. (2020). Detection of Aquatic Plants Using Multispectral UAV Imagery and Vegetation Index. Remote Sensing, 12, 387. doi: 10.3390/rs12030387

Thinh, N., Huan, N., Pham, U., & Sơn Tùng, N. (2008). Landscape ecological planning based on change analysis: A case study of mangrove restoration in Phu Long-Gia Luan area, Cat Ba Archipelago. VNU Journal of Science, Earth Sciences, 24, 133-144.

Tiwari, A., Sharma, S., Dixit, A., & Mishra, V. (2020). UAV Remote Sensing for Campus Monitoring: A Comparative Evaluation of Nearest Neighbor and Rule-Based Classification. Journal of the Indian Society of Remote Sensing, 49. doi: https://doi.org/10.1007/s12524-020-01268-4

Toan, D. (2014). Statistical assessment of the properties of the East Sea and the coast of Vietnam in the period 1951-2013. Estuarine and Coastal Marine Science, 12, 13.

Tucker, C. (1979). Red and Photographic Infrared Linear Combinations for Monitoring Vegetation. Remote Sensing of Environment, 8. doi: https://doi.org/10.1016/0034-4257(79)90013-0

Van, T., Nguyen Dang, M., Khiem, M., Duong, T. H., Van, K., Thanh, T., . . . Minh, T. (2022). Climatic Factors Associated with Heavy Rainfall in Northern Vietnam in Boreal Spring. Advances in Meteorology, 2022, 1-14. doi: https://doi.org/10.1155/2022/5917729

Viet, H., Potokin, A., Anh, D., Nguyen, T., & Nguyen, T. (2020). Forest Vegetation Cover in Tram Chim National Park in Southern Vietnam. IOP Conference Series: Earth and Environmental Science, 574, 012014. doi: https://doi.org/10.1088/1755-1315/574/1/012014

Watson, J. (1925). Mangrove Forests of the Malay Peninsula. Malays. For. Rec., 6, 1-275.

Xue, L., & Yang, L. (2009). Deriving leaf chlorophyll content of green-leafy vegetables from hyperspectral reflectance. Isprs Journal of Photogrammetry and Remote Sensing - ISPRS J PHOTOGRAMM, 64, 97-106. doi: 10.1016/j.isprsjprs.2008.06.002

Yaney-Keller, A., Tomillo, P., Marshall, J., & Paladino, F. (2019). Using Unmanned Aerial Systems (UAS) to assay mangrove estuaries on the Pacific coast of Costa Rica. PloS one, 14, e0217310. doi: 10.1371/journal.pone.0217310

Yeom, J., Jung, J., Chang, A., Ashapure, A., Maeda, M., Maeda, A., & Landivar, J. (2019). Comparison of Vegetation Indices Derived from UAV Data for Differentiation of Tillage Effects in Agriculture. Remote Sensing, 11, 1548. doi: 10.3390/rs11131548

Yin, D., & Wang, L. (2019). Individual mangrove tree measurement using UAV-based LiDAR data: Possibilities and challenges. Remote Sensing of Environment, 223, 34-49. doi: 10.1016/j.rse.2018.12.034

Yunjun, Y., Deng, H., Liu, Y., & Zhu. (2019). Application of UAV-Based Multi-Angle Hyperspectral Remote Sensing in Fine Vegetation Classification. Remote Sensing, 11, 2753. doi: https://doi.org/10.3390/rs11232753

Zahra, N., Setiawan, Y., & Prasetyo, L. (2022). Estimation of Mangrove Canopy Cover Using Unmanned Aerial Vehicle (UAV) in Indramayu Regency, West Java. IOP Conference Series: Earth and Environmental Science, 950, 012032. doi: 10.1088/1755-1315/950/1/012032

Zhang, C. (2020). Assessing the Effects of Hurricane Irma on Mangrove Structures in the Coastal Everglades using Airborne Lidar Data Multi-sensor System Applications in the Everglades Ecosystem (1st Edition ed., pp. 289-302).

Zhao, Y., Yan, C., Lu, S., Wang, P., Qiu, G., & Li, R. (2019). Estimation of chlorophyll content in intertidal mangrove leaves with different thicknesses using hyperspectral data. Ecological Indicators, 106, 105511. doi: 10.1016/j.ecolind.2019.105511

Zulfa, A. W., Norizah, K., Hamdan, O., Faridah-Hanum, I., Rhyma, P. P., & Fitrianto, A. (2021). Spectral signature analysis to determine mangrove species delineation structured by anthropogenic effects. Ecological Indicators, 130, 108148. doi: https://doi.org/10.1016/j.ecolind.2021.108148

Zulfa, A. W., Norizah, K., Hamdan, O., Zulkifly, S., Faridah-Hanum, I., & Rhyma, P. P. (2020). Discriminating trees species from the relationship between spectral reflectance and chlorophyll contents of mangrove forest in Malaysia. Ecological Indicators, 111, 106024. doi: https://doi.org/10.1016/j.ecolind.2019.106024

RESEARCH PAPER

ALTITUDINAL APPRAISAL OF LAND USE LAND COVER AND SURFACE TEMPERATURE CHANGE IN THE SATLUJ BASIN, INDIA

Pankaj Kumar[1], Swati Thakur[2*], Surajmal Junawa[1], Subhash Anand[1]
[1]Department of Geography, Delhi School of Economics, University of Delhi, Delhi, India
[2]Department of Geography, Dyal Singh College, University of Delhi, New Delhi
*Corresponding author: swatithakur.dsc@gmail.com
Received: July 29th, 2023 / Accepted: November 14th, 2023 / Published: December 31st, 2023
https://DOI-10.24057/2071-9388-2023-2958

ABSTRACT. The land use change has affected nearly 32% of the global landscape from 1960 to 2019. Several studies have examined the impacts of land use land cover (LULC) on the surface temperature. Still, the spatiotemporal variation of LULC and LST with altitude is a less researched area. In the current study, we assess the LULC dynamics and its relation to altitudinal LST in the Himalayan Satluj River basin in Himachal Pradesh across the altitudinal range of 332 to 6558 meters. LULC, LST, NDVI, and NDMI were derived from Landsat data for 1980-2020. The spatial pattern was analyzed using Support Vector Machine (SVM) and a mono-window algorithm. The results of LULC denote that snow covered area (SCA) have decreased by nearly 56.19% since 1980 and vegetation cover has increased. However, a decline in vegetation density is pronounced at the same time. The mean surface temperature of the Satluj basin has amplified by 6°C (0.25°C/year) from 1996 to 2020. Mostly Zone 3 and 4 are under high hilly and temperate dry regions in Lahaul Spiti and Kinnaur district of Himachal Pradesh. The most important sign is that the mean surface temperature for Zone 3 (3000m-4500m) and Zone 4 (above 4500m) was the highest increase to 6°C (0.26°C/year) and 8°C (0.31°C/year) from 1996 to 2020. The increase in LST values is attributed to land cover dynamics precisely the decline of snow cover area and the emergence of vegetation zone at higher above the 4500 altitudes. Our study facilitates regional analysis.

KEYWORDS: Land use land cover; Land surface temperature; Altitudinal Variation; Satluj Basin; Climate changes

CITATION: Pankaj Kumar, Swati Thakur, Surajmal Junawa, Subhash Anand (2023). Altitudinal Appraisal Of Land Use Land Cover And Surface Temperature Change In The Satluj Basin, India. Geography, Environment, Sustainability, 4(16), 26-38
https://DOI-10.24057/2071-9388-2023-2958

Conflict of interests: The authors reported no potential conflict of interest.

INTRODUCTION

Among geographical regions mountains are the most sensitive to climate changes (Xystrakis et al. 2017). Witnessing some of the clearest evidences such as melting of glaciers, rise of temperature and increasing intensity of extreme events (Bandyopadhyay et al. 2023), mountains not only are at risk but they affect the adjacent lowland population and environment too. Moreover, the implications are likely to be faced by entire geosystem (Lutz et al., 2013) due to inter regional linkages involving mass and energy exchange. One of the prime drivers affecting mountain ecosystem is the pressure of land use and land cover (LULC) change leading to compromises in its capacity to provide its ecosystem services (Husain et al. 2023; John et al. 2022; Pang et al. 2022). Mountains being home to 15 per cent of world's population the changing climate and demography are bound to have environmental and societal consequences transversely elevations. Land transformations are mainly altered by anthropogenic pressure to maximize the economic benefits of human. The main drivers of the land transformations and global climate are amplified by the urbanization, over population, expansion of settlement, construction of roads, deforestation, changing agriculture pattern, exploitation of natural resources, tourism, demand of energy especially hydro projects in mountain regions (Chauhan et al., 2021; Chhogyel et al., 2020; Roy et al., 2022; Upadhayaya, 2015). Global climate change and increasing anthropogenic pressure are affecting regional biodiversity ecosystem and sustainable development. Climate change, and increasing intensity and frequency of natural events have effects on SDGs such as SDG 1 (no poverty), SDG 3 (good health and wellbeing), SDG 11(sustainable communities) SDG 13 (Climate action), and availability & accessibility of resources.

Himalayan mountain geosystem provides millions of lowland and downstream populations with life sustaining vital nutrients such as water and soil. The changes in land utilization pattern (land use) viz. deforestation and intensification of agricultural areas by humans and biophysical cover of surfaces (land cover) are dominant transitions which have impacted the historiography of landscape patterns. The worry is that the recent transitions coupled with natural climatic changes have challenged the long term ecosystem services (Young, 2014). Detailed multi temporal change studies will provide better understanding of the challenges posed due to changes in landscape making regional sustainability complex as people's livelihoods depend on natural resources in mountain areas. Land Surface Temperature (LST) provides useful information regarding water, heat and land surface processes (Bindajam et al. 2020). It is one of the most effective factors for understanding the regional climate, surface energy balance, vegetation change in the highland-lowland regions (Holzman et al. 2014; Taripanah et al. 2021). The evaluation of LST hence is another significant factor pertinent to environmental change studies.

The whole Himalayas doesn't respond the same to alterations of the landscape and character of surface temperature and encompass variation at the regional level (Rani et al. 2022). It is affected by changes in many ways such as degradation of land, increasing climatic variability, landslide hazards, depletion of groundwater, soil erosion, etc. (Ali et al. 2019; Grêt-Regamey et al. 2014; Swain et al. 2022; Vannier et al. 2019; Wen et al. 2020). The spatial temporal distribution of energy exchange is also affected by topographical, metrological, vegetation and soil character shaping the geophysical setting (Li et al. 2015).

Among the different river basins which connect the highland lowland interactive systems, the Satluj basin comprises a landscape with distinct climatic condition, elevation gradient, intense agriculture matrix, expanding hydro power and urban centres in lowland area, all posing pressure to native ecosystem and its services. It is not far from these changes, the rising surface temperatures at the river's higher altitudes make sustainability difficult at local level.

The analysis of landuse land cover dynamics from available public domain data by elevation and geographic setting and to integrate with changes in land surface temperature characteristics would be first step to the study of its ecosystem service dynamics and challenges to its sustainability. Within this context our study presents the first element of this framework and specifically addresses two research objectives: i) to analyse LULC and Land Surface Temperature (LST) change pattern across biophysical and altitudinal settings of Sutlej basin in terms of rate, magnitude and direction of change, ii) to contextualise the environmental and anthropogenic driving factors to explain the transition. This can be valuable input to the management in the context of vulnerability of highland landscape to changing climatic condition affecting the ecosystem services and hence adaptive capacity of the natives.

We put forward that increase in vegetation cover at higher altitudes have changed surface temperature character resulting in warming. This can further threaten the melting of smaller glaciers at the higher altitude challenging the water supply system of a river basin putting the allied resource and services at risk.

STUDY AREA

The Satluj river is the longest tributary of the Indus River with the geographical extent of basin from 30°45' N to 33°00' N latitude to 76°15′ E to 79°00′ E longitude (Figure 1). It spreads within altitudinal range of 332m to 6558m. Covering an area of 18325 km^2 in Himachal Pradesh, it is geographically divided into Spiti valley, Tibet plateau, Khab to Nathpa, and Nathpa dam to Bhakhra Dam (R. Zhang et al., 2020) as upper, middle and lower Sutluj basin respectfully. It exhibits sub-humid tropical to arid temperate climate type and receives rainfall from western disturbances and heavy monsoon downpour as received in outer Himalayas. Heavy snowfall is also evident in Tibet plateau indicating most of the rainfall to be concentrated in the lower Satluj basin (Singh et al. 1997). The basin is known for variation in biodiversity due to variations in elevation. The Upper Satluj basin has less vegetation but a positive change is sort according to the India State of Forest Report 2021, where approximately 915 km^2 of the recorded forest area has shown an increase from 2019 data. The evidence for climate change is of 18.52% decline in snow cover during the year 2020 and 2021(Zhongming et al., 2021).

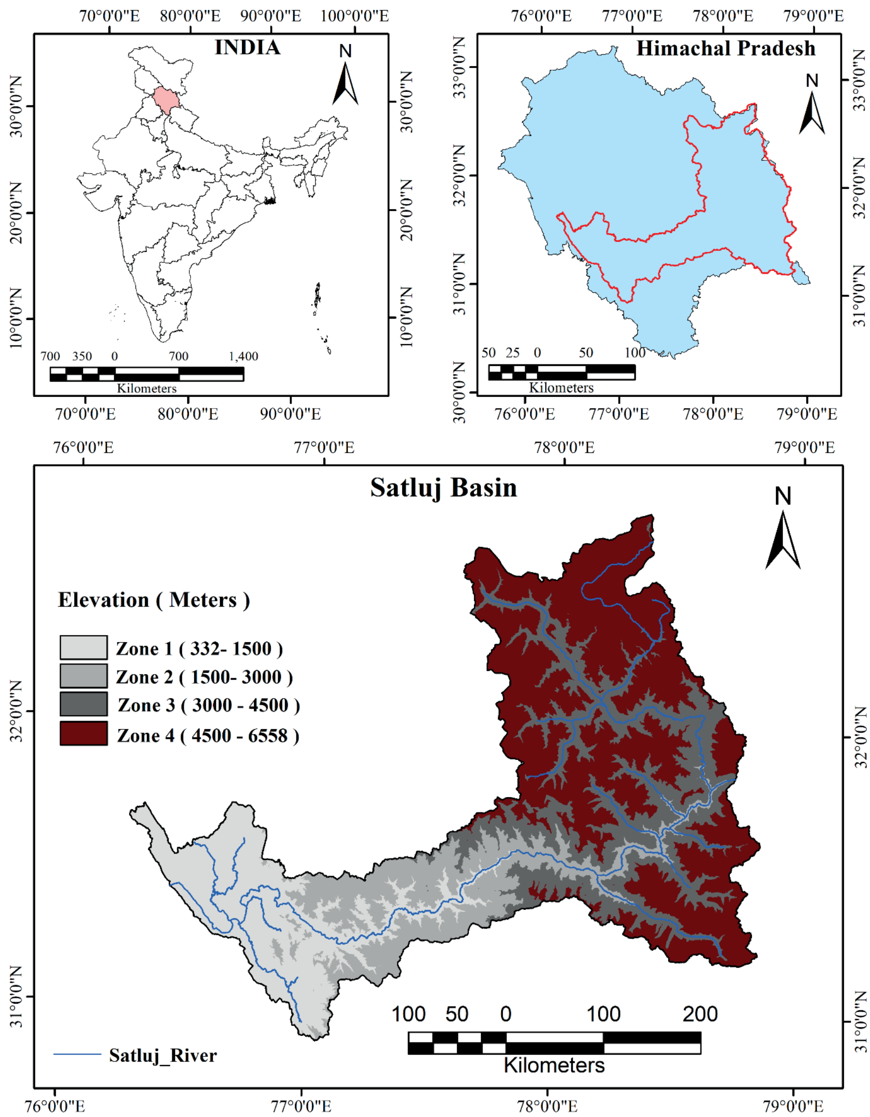

Fig. 1. Study area: Satluj Basin in Himachal Pradesh

METHODOLOGY

Datasets

To evaluate the land use change LANDSAT imageries were taken from the open-source data set available on the USGS website (https://earthexplorer.usgs.gov/) for 1980, 1996, 2011, and 2020 time periods (Table 1). The LST and NDVI were calculated for the years 1996, 2011, and 2020 due to weather appropriate availability of respected spectral bands in month of September and October. DEM (SRTM) 90M Resolution database (https://www.earthdata.nasa.gov/sensors/srtm)was utilized for analyzing the altitude wise change in land cover, LST, NDVI, and NDMI. ArcGIS environment was used for data retrieval, mapping, and analysis.

To ensure quality of data source an accuracy assessment of the 1980 LULC classification was done. The results of user and producer accuracy indicated that the highest classified LULC was recorded for snow cover for all the years. The Kappa coefficient evaluates the relative progress of the class over random assigning to classes (Pal et al. 2017), and the accuracy of the producer and user calculates the proportion of the map that is the correct pixel from the producer and user viewpoints. The average kappa coefficient was 0.79 and overall accuracy was 85.41% for 1996, 2011, and 2020 respectively. A kappa coefficient

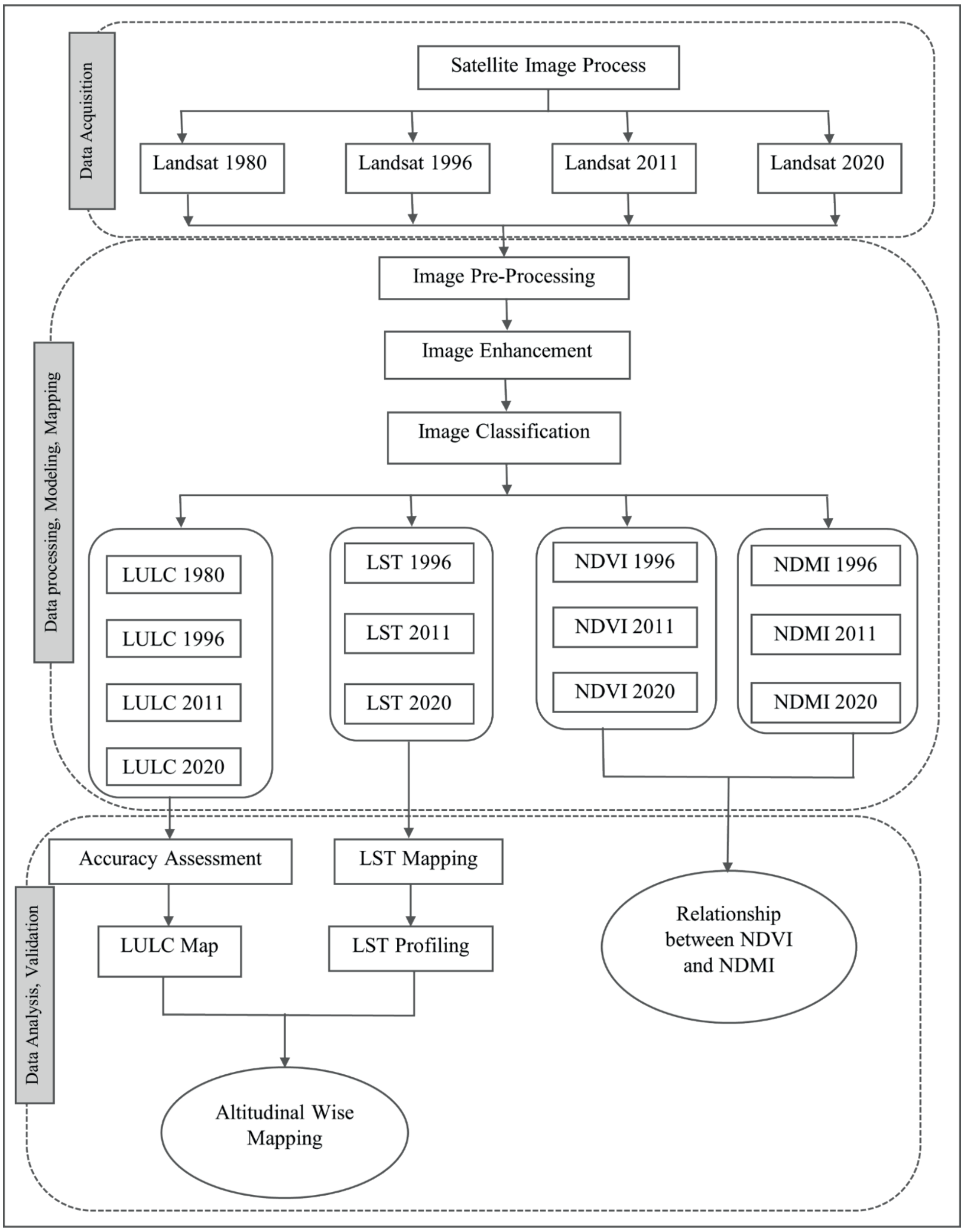

Fig. 2. Methodological framework for study

Table 1. Landsat datasets

Year	Satellite	Sensor	Acquisition Month	Path/Row	Spatial Resolution
1980	Landsat 3	1-5MSS	September-October	158/37,158/38,159/38, 157/38,158/39	80m
1996	Landsat 5	4-5TM	September-October	147/37,147/38,147/39,146/38	30m
2011	Landsat 5	4-5TM	September-October	147/37,147/38,147/39,146/38	30m
2020	Landsat 8	OLI	September-October	147/37,147/38, 146/38	30m

value greater than 0.7, indicates high conformity and is considered very good for research (Monserud et al. 1992). The confusion matrix was used for the accuracy of the LULC classification which is shown in Table 2.

LULC classifications

The LULC has been classified into 4 major classes namely, snow cover, vegetation, water body, and barren land. Supervised classification was done with the help of the Support Vector Machine (SVM) technique in ArcGIS 10.8. For testing and training of the SVMs model, detected that SVMs give reliable results with small training groups (Pal et al. 2006). In this study around 150 to 200 training samples for four classes were randomly taken from the LANDSAT imagery. The main benefits of SVM are that it creates less noise than other techniques and requires only a few training datasets for classification (Mountrakis et al. 2011).

Methods of LST computation from Landsat images

To calculate Land surface temperature from thermal image firstly the Digital Number (DN) is converted to Spectral Radiance (Lλ) utilizing equation 1 (Zhang et al. 2006).

$$L\lambda = \text{" } gain \text{ "} \times QCAL + \text{" } offset \text{ "} \tag{1}$$

Where, *bias* = the intercept of the radiance/DN conversion function. *gain* =the slope of the radiance/DN conversion function *DN* =the digital number of a given pixel

The respective values are substituted in equation 1 as given in equation 2:

$$L\lambda = 0.037059 \times DN + 3.2 \tag{2}$$

The second step is regarding the conversion of spectral radiance to the brightness of satellite temperatures using equation 3 (Artis et al. 1982).

$$TB = \frac{K_2}{In\left(\frac{K_1}{L\lambda} + 1\right)} \tag{3}$$

Where K_1 and K_2 denote the correction constant in $Wm^{-2} sr^{-2} \mu m^{-2}$ (The value of K_2 is 1260.56 and K_1 is 607.76 for Landsat TM). TB is at-satellite brightness temperature (K), and L_λ is the Spectral radiance of the thermal band at radar aperture in $Wm^{-2} sr^{-2} \mu m^{-2}$.

The third step is At-satellite brightness temperature corrected by land surface emissivity (ε) therefore equation 4 was adopted (Snyder et al. 1998).

$$\varepsilon = 0.004 * Pv + 0.986 \tag{4}$$

Here, P_v denote as the Percentage of vegetation and it can be estimated using equation 5.

$$P_v = \left(\frac{NDVI_{jr} - NDVI_{MIN}}{NDVI_{MAX} + NDVI_{MIN}} \right) \tag{5}$$

The final step is a retrieval of Land Surface Temperature and it's computed following equation 6 (Artis et al. 1982).

$$LST = \frac{T_B}{\left[1 + \{ (\lambda \times TB/\rho) \times In\varepsilon \} \right]} \tag{6}$$

Where LST is the surface temperature (Kelvin), λ is the wavelength of produced radiance in meters (for which the highest reply and the regular of the preventive wavelengths (*λ=11.5µm* (Markham and Barker 1985) is utilized, *p=h*c/σ (1.438*10*$^{-2}$*mK)*, σ is Boltzmann constant (*1.38*10*$^{-23}$*j/k*), h is indicated to Planck's constant (*6.626*10*$^{-34}$*J K*$^{-1}$) and *ε*= surface emissivity c is the velocity of light (*2.998*10*^{8}*m/s*). The conversion of surface temperature from Kelvin to degree Celsius (°C) 273 is done where 15 is subtracted from Eq.6 where 0 °C is equivalent to 273.15 K.

Calculation of NDVI and NDMI

The Normalized Difference Vegetation Index (NDVI) is estimated with help of Near and Visible Infrared Sensors (NIR & VIS) bands of satellite data (TOWNSHEND et al. 1986). NDVI is as follows:

NDVI = (NIR - VIS) / (NIR + VIS)

Normalized Difference Moisture Index (NDMI) is estimated with help of Near and Mid Infrared Bands (NIR & MIR) of satellite datasets(Jin et al. 2005). NDMI equation includes:

NDMI= (NIR-MIR) / (NIR+MIR)

RESULTS

Spatiotemporal Pattern of Land Use and Land Cover Changes

An evaluation of land use dynamics for a period of 40 years has been done. Figure 3 shows that barren land is the dominant land cover representation in the area which shows a decrease of 2.33 per cent since 1980 to 2020. Vegetation land cover represents the second largest leading class, ranging from 34.86 per cent (1980) to 42.49 per cent

Table 2. LULC Confusion Matrix

Year	1996		2011		2020	
LULC	U/A (%)	P/A (%)	U/A (%)	P/A (%)	U/A (%)	P/A (%)
Snow cover	96.42	100	95.45	95.45	88	100
Vegetation	91.89	70.83	96.42	79.41	100	75.51
Barren land	85.18	92	75	100	80	100
Water Body	65.78	83.33	77.14	79.41	76.31	87.87
Overall Accuracy	83.84		85.74		86.66	
Kappa Coefficient	0.78		0.80		0.81	

Where U/A and P/A indicate User accuracy and Producer accuracy respectively.

in 2020 (Table 3). It was continuously increasing over time, but was poorly represented in the initial observed years (1980-96 with meagre 3.47 per cent) but the second phase was high with 11 per cent positive change representing nearly 40 per cent of area covered under this category indicative of a 26-fold increase from 1980. The natural ecosystem dominant in higher latitudes by snow cover LULC class which decreased from 9.95 per cent of total area in 1980 to 4.35 per cent in 2020 whereas the water body has noted high perseverance from 131.26km^2 to 184.68km^2 over the period of analysis.

The dynamics of landscape across the study area showed heterogeneous patterns through time but still a geographic pattern can be sorted. The north and north eastern part of the region predominantly characterises decline in snow cover whereas the southern and south western part dominates with expansion of agricultural and vegetation area. The changed detection map has been produced from the post-classification of Land Sat imageries (1980–2020) for different LULC categories. After subtracting the total area of loss from the total gross gains, the net change of each landscape has been mapped (Figure 4). The conversion of barren land to vegetation cover (1642.92km^2) was more dominant in the area and was followed by snow cover to barren land (1084.83km^2) in the last 40 years.

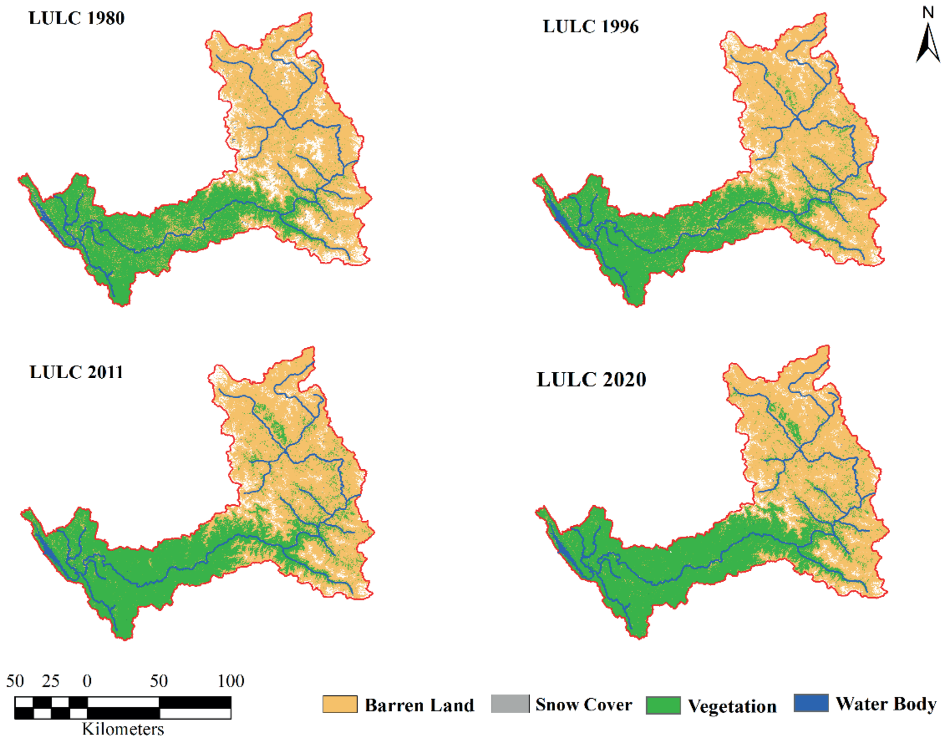

Fig. 3. Spatial pattern of LULC in the Satluj basin in 1980, 1996, 2011, and 2020

Table 3. Percentage of the LULC Area in different periods

LULC	1980 (Km^2)	Area in percentage	1996 (Km^2)	Area in percentage	2011 (Km^2)	Area in percentage	2020 (Km^2)	Area in percentage
Snow Cover	1823.22	9.95%	1042.42	5.69%	1017.06	5.54%	798.58	4.35%
Vegetation	6386.85	34.86%	6608.76	36.07%	7327.97	39.98%	7785.27	42.49%
Water Body	131.263	0.71%	211.09	1.15%	177.10	0.96%	184.68	1.00%
Barren Land	9977.73	54.46%	10456.64	57.08%	9805.86	53.50%	9550.39	52.13%

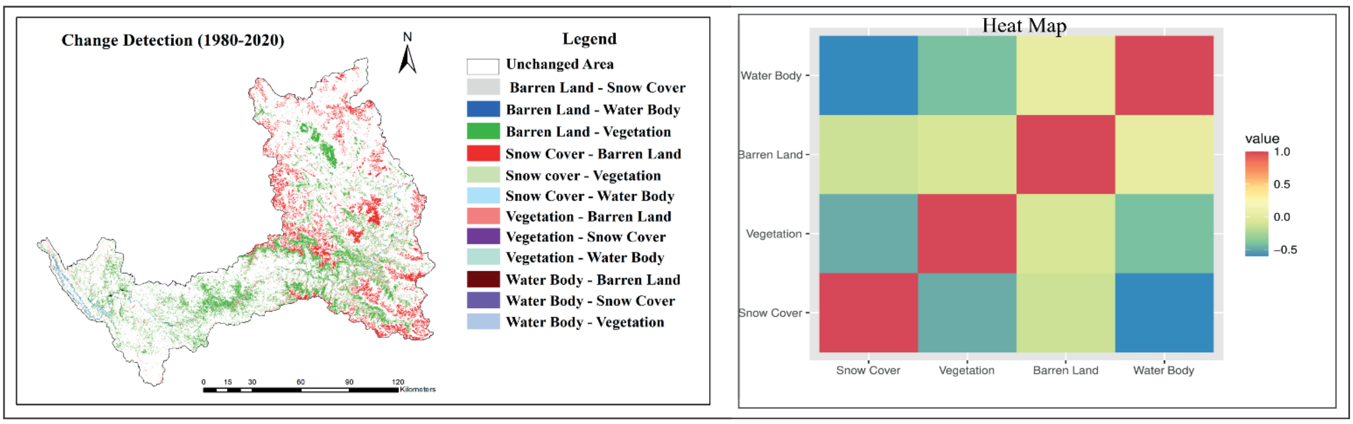

Fig. 4. Change detection map and Heat map of LULCC

LULC transitions along the altitude

The stability of respective classes of LULC is decreasing throughout the study period. The changes are more evident when studied along elevation bands. The study area is classified into four altitudinal zones based on SRTM DEM and delimited based on Natural Break in ArcGIS 10.8. Zone 1 is less than 1500 meters above sea level and is sub-tropical wet and consists of foothills and has more potential for the cultivation of cash crops such as paddy and off-season vegetables etc. Zone 2 is between 1500 and 3000 meters. Dense forest and high populated density are found in zone 1 and & 2. Zone 3 is between 3000 and 4500 meters, and zone 4 is higher than 4500 meters. Mostly Zone 3 & 4 are under high hilly and temperate dry region in Lahaul Spiti and Kinnaur district of state. Alphin vegetation, Glaciers, and low population density of state are found in these zones. Precipitation occurs from western disturbance and short warm summer in high altitude. Vegetation, water bodies, and barren land LULC classes are found in all four zones, and snow cover is found in only zones 3 and 4. Elevation plays an important role in the LULC changes because of rainfall and temperature variation. Temperature variations are influenced by many factors, including slope gradient and exposure.

Zone 1(Figure 5) is the area of lower basin of the Satluj river. Vegetation was dominated by LULC class at 2902.16km^2 (83.09%) but it increased over the area of 3205.82km^2 (91.73%) in 2020. Water bodies have increased by 3.05 per cent to 4.60 over the years from 1980 to 2020. The barren land area has drastically decreased from 483.54km^2 (13.84%) to 128km^2 (3.66%) in the last 40 years. It remained at only 3.66 per cent of the total area of zone 1in 2020.

Zone 2(Figure 5) is almost similar to Zone 1 where vegetation occupied 83.63 per cent of total area in 1980 and increased to 2749.83 sq. kms (93.67%) in 2020 whereas barren land decreased to almost 63.82 per cent of total area in the last four decades and the decreasing rate was high after 1996. This zone holds a smaller proportion of water bodies. Zone 3(Figure 5) is situated in the high-altitude and predominantly has snow cover showing a drastic decrease of 53.87km^2 in 1980 and to only 7.47km^2 in 2020 in absolute areal extend.

Zone 4 (Figure 5) is part of the upper Satluj basin. Snow cover and barren land were the most dominant LULC class in 1980, with 23.40 per cent and 75.20 per cent of total area respectively. Out of which the snow cover area decreased by 55.26 per cent, barren land slightly increased and occupied 15.51 per cent in last four decades. The vegetation area increased from 81.74km^2 to 198.43km^2 (142.75%) from 1980 to 2020. Vegetation is increasing in higher altitudes due to decreasing snow cover land is converting into barren land and rising surface temperature. It gives suitable conditions to grow shrubs in the higher altitude of the western Himalayas (Kumar et al., 2018).

Zones 3 and 4 were more vulnerable to change at higher altitudes (Figure 6). The conversion of barren land to vegetation cover is more dominant in Zone 3 from 1996–2011 and 2011–2020. In Zone 4, snow cover to barren land conversion is highest at 226.37km^2 (21.96%), and barren land to vegetation cover has converted to 174.35km^2 from 1996-2011. And the snow cover to barren land conversion rate was highest compared to the previous years, 2011–2020. It was 337.05km^2 (33.64%) in the last 10 years. The change in vegetation is prominent in all zones and notable for zone 3 and 4 in recent 15 years span. Within the reference period of 40 years long term positive change of more than 150 per cent in vegetation is evident in zone 4. The other landscape categories' conversion was lower with respect to their area. The rates of change of snow cover, vegetation, water body, and barren land in 4 different regions are shown in a table 4.

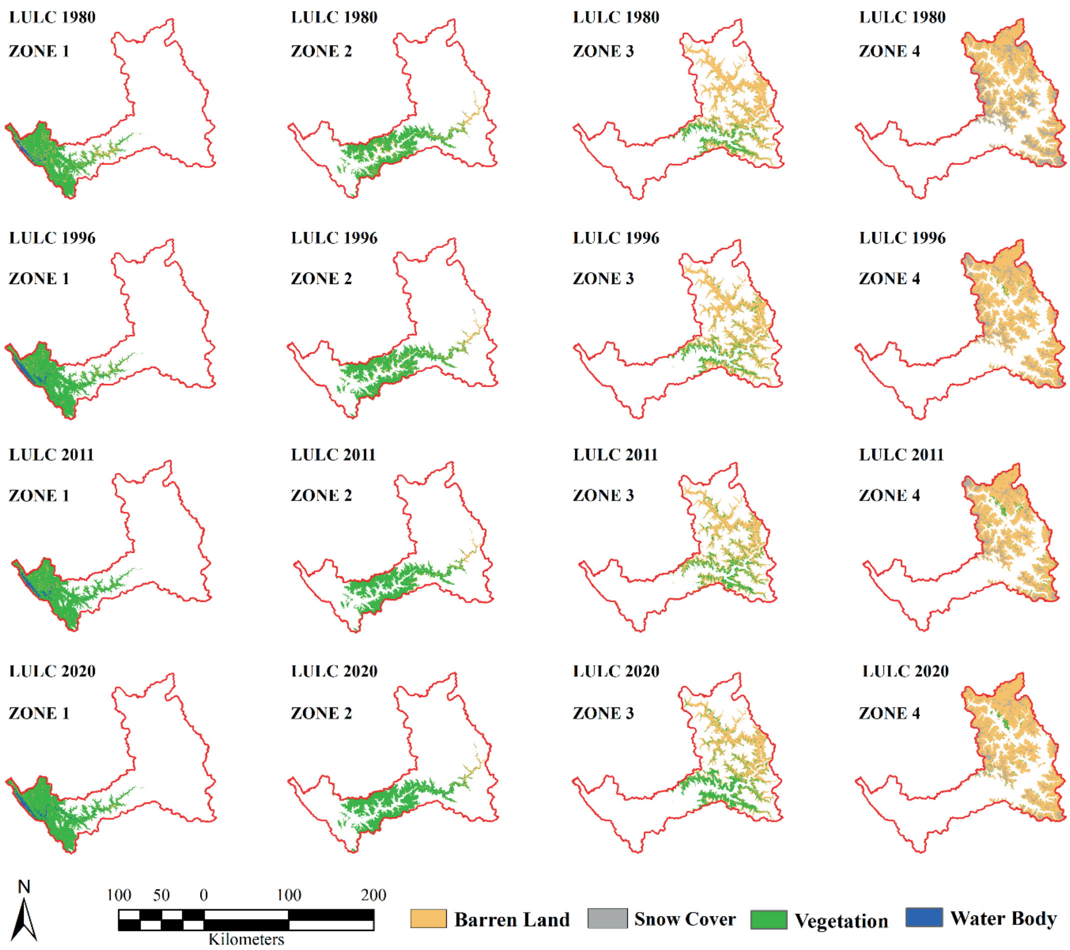

Fig. 5. Land cover change detection as per Elevation; Zone 1, Zone 2, Zone 3, Zone 4

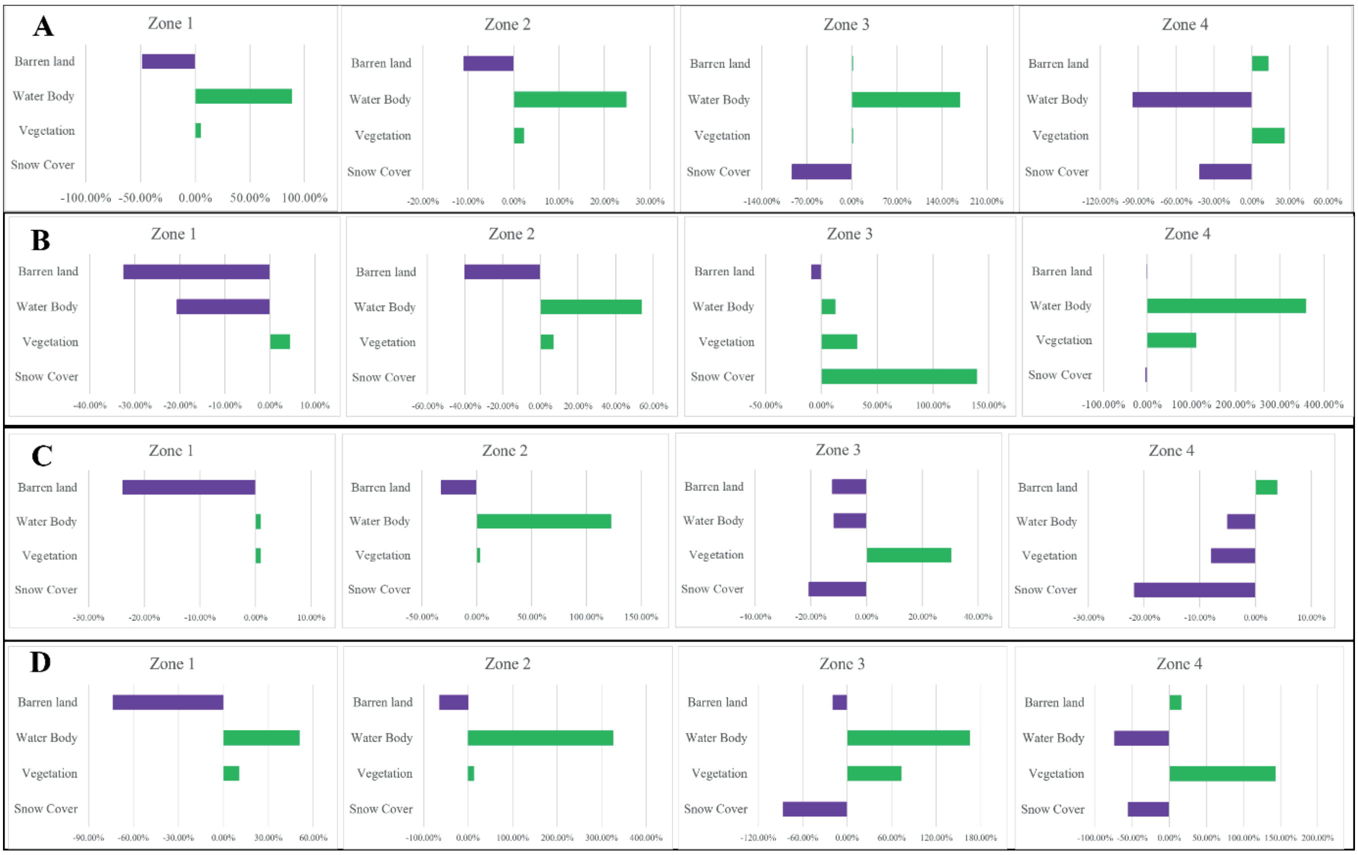

Fig. 6. Gain & Losses of LULC classes in percentage, A) 1980-1996, B) 1996-2011, C) 2011-2020, D) 1980-2020

Table 4. Rate of change (%) area under the different altitudinal-wise LULC

Zone	Class	1980-1996(%)	1996-2011(%)	2011-2020(%)	1980-2020(%)
Zone 1	Snow cover	0	0	0	0
	Vegetation	4.94	4.33	0.88	10.46
	Water Body	88.16	-20.63	0.87	50.64
	Barren Land	-48.53	-32.49	-23.8	-73.52
Zone 2	Snow cover	0	0	0	0
	Vegetation	2.19	6.84	2.68	12.12
	Water Body	24.91	53.8	121.84	326.22
	Barren Land	-10.87	-40.05	-32.3	-63.82
Zone 3	Snow cover	-92.7	139.44	-20.61	-86.13
	Vegetation	0.95	31.4	30.29	72.84
	Water Body	168.1	12.09	-11.69	165.4
		1.12	-9.08	-12.15	-19.23
Zone 4	Snow cover	-41.13	-2.89	-21.73	-55.26
	Vegetation	25.71	109.712	-7.92	142.75
	Water Body	-94.03	361.94	-5	-73.8
	Barren Land	12.88	-1.43	3.82	15.51

Transitions of native vegetation ecosystem

In general, the stability of vegetation is increasing over the study period across the river basin (Figure 7), with increasing traces of open forest above 4500 m, primarily in the Spiti valley and Kinnaur district. The sparse vegetation which was 26.74% in 1996 and increased to 41.55% of the total forest area as estimated from values of NDVI which is approx. 0.39 (1996) to 0.31(2020) in higher altitude. This is an indicator of decrease in reflectance from the available green cover hence decrease of its spatial extent. Native forest density is also decreasing in the entire river basin.

The total dense forest area has reduced from 119.72km^2 to almost null value (table 5). As evident from table the scale of representation of NDVI highest value has reduced from 0.75 (1996) to 0.61 (2020). The spatial extent of decrease in the range is much evident in lower altitude of the basin in less than 4500m. Figure 7 shows the decrease in south western part in district of Bilaspur, Mandi. The possible explanation would be change to open forest type (Table 5). The barren land of LULC class has been changed to vegetation area (approximately 1642.92km^2) and snow cover class has also changed to vegetation covering around 13.65km^2 in the study period. The early trace of open vegetation types is found in upper river basin (Figure7).

Spatiotemporal pattern of LST

The spatiotemporal pattern of LST was vital for considering to evaluate the influence of changes in mountain land use. LST deducts the radiative skin temperature produced from the earth's surface, including bare earth, paved surfaces, building roofs, vegetation, and water (Voogt et al. 2003). The thermal map was produced by using Landsat imagery of 1996, 2011, and 2020 (Figure 8). The mean LST of the Satluj basin was noted as 10.3°C in 1996, but it increased by more than 2°C and reached 13.64°C in 2011. In the latter half of the study LST rapidly increased to reach 16.55°C in 2020.

When evaluated based on elevation zones we found that zone 1 existed above the 10°C temperature range (Figure 10). The result shows that the 10°C to 20°C LST belt area is moving towards the 20°C to 30°C LST belt as evaluated during 1996 to 2020 (Figure 10). The area representing more than 30°C in zone 1 was 2.17 km^2 in 1996, but it increased about forty-fold in 25 years (Figure 10). In zone 2, meagre area is recorded under the 0°C LST whereas the 0°C to 10°C temperature belt almost disappeared from 1996 to 2020 (Figure 9, Figure 10). The mean LST of zone 2 was 15.85°C, 17.10°C, and 20.06°C in 1996, 2011, and 2020 respectively.

Zones 3 and 4 are situated in the high altitudinal zone. The results show that zone 3 is more sensitive to changes in LST. The area under less than -10 °C temperature was 49.97 km2 in 1996 reduced to 2.5 km2 in 2011 and none of it extend were traceable in 2020 (Figure 9, Figure 10). From 1996 to 2020, zone 4 mean LST increased more than zone 3.

Transition pattern of NDMI

The NDMI indicates the characteristic of earth vegetation dynamics and is closer to tracking changes in plant biomass (Delgado et al. 2022; Jin et al. 2005) The results of the NDMI calculation ranged from 0.96 to -0.95 in 1996 and 0.95 to -0.81 in 2011, but it rapidly changed after 2011, from 0.73 to -0.43 in 2020 (Figure 11). It can be understood from the map that a snow-covered area is present at a high altitude. NDMI values are low, the same as NDVI values in the lower river basin of 2020. The variation in NDMI values can see in (figure 11).

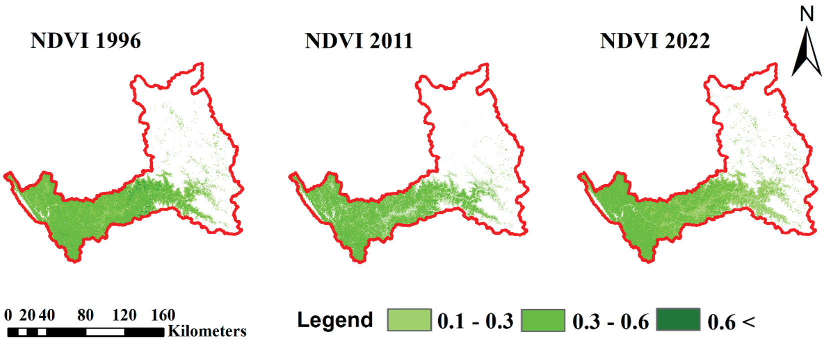

Fig. 7. Spatial pattern of NDVI in 1996, 2011, and 2020

Table 5. Matrix of type of Vegetation

Vegetation/Year	1996 (km^2)	2011 (km^2)	2022 (km^2)
Open Vegetation (0.1-0.3)	2014.47	2307.75	**3213.67**
Moderate Vegetation (0.3-0.6)	5398.99	5096.28	4519.58
Dense Vegetation (More than 0.6)	119.72	27.31	0.0018

*Bold value denotes positive change

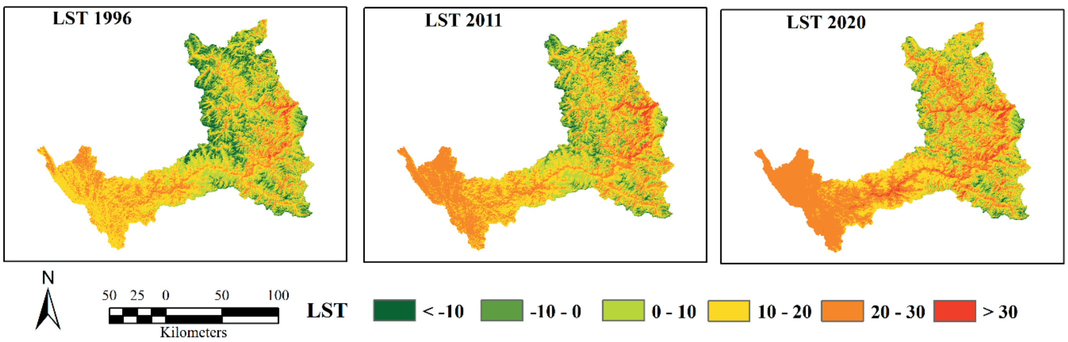

Fig. 8. Spatio-temporal pattern of LST in 1996, 2011, and 2020

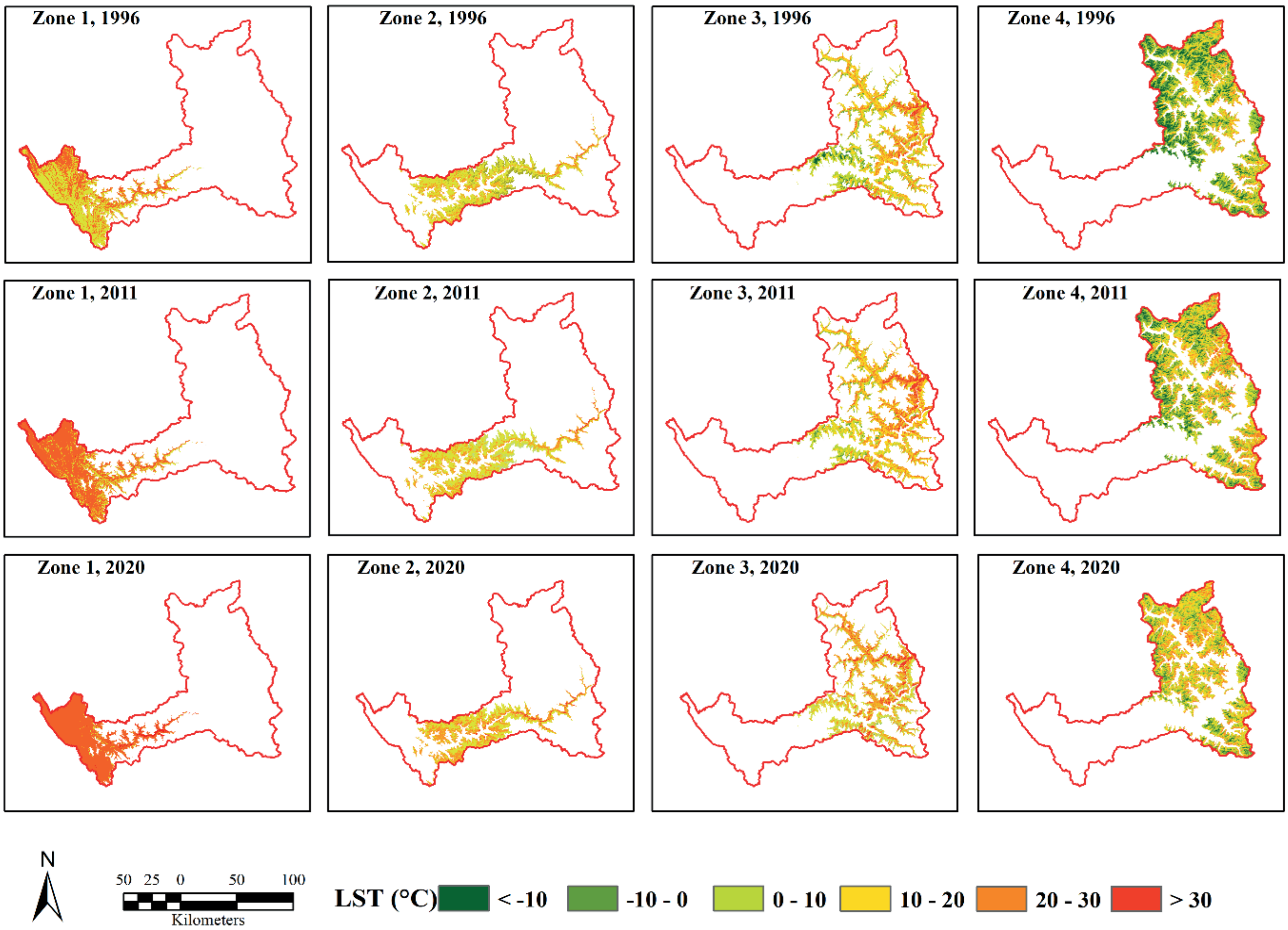

Fig. 9. Map of LST detection along altitudinal zones

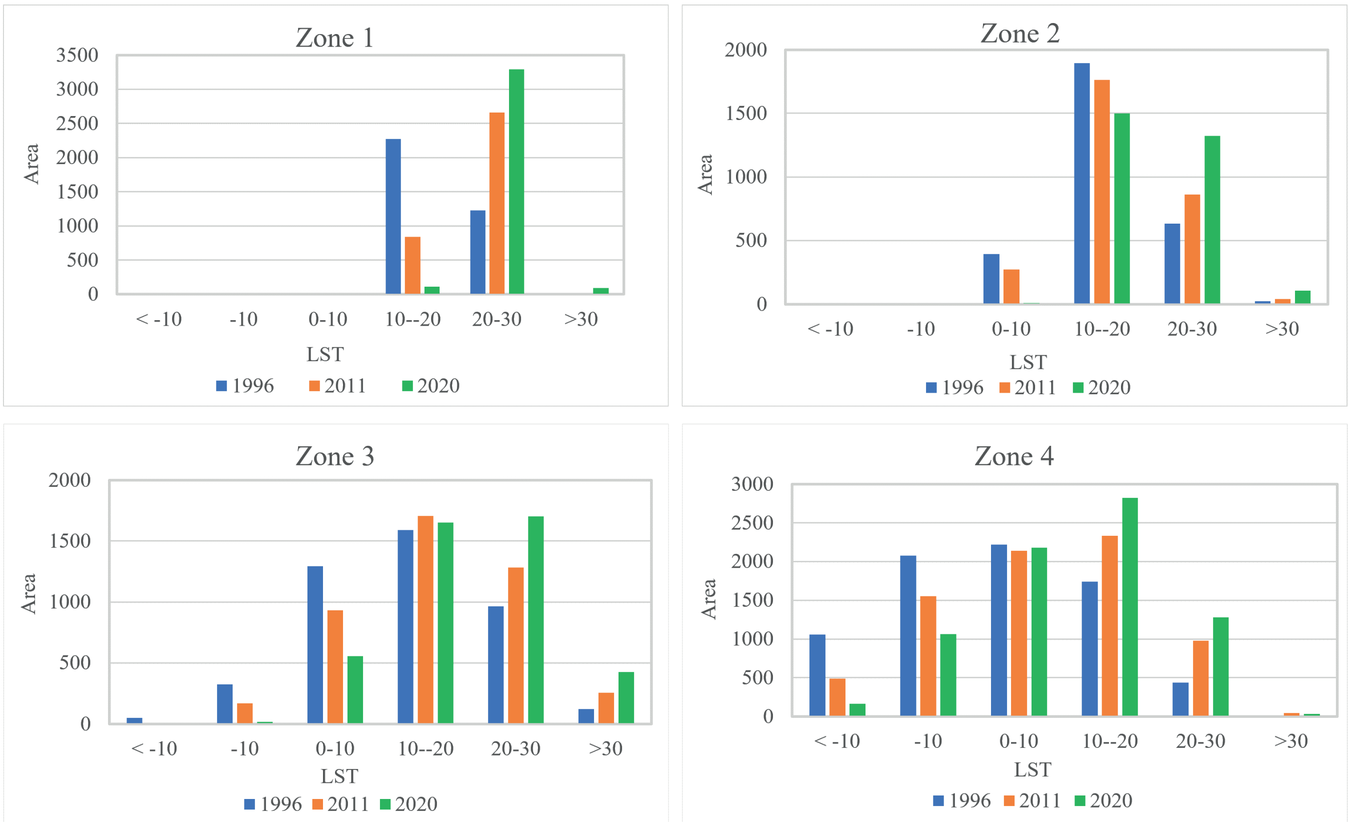

Fig. 10. Bar plot of LST area change along with elevation

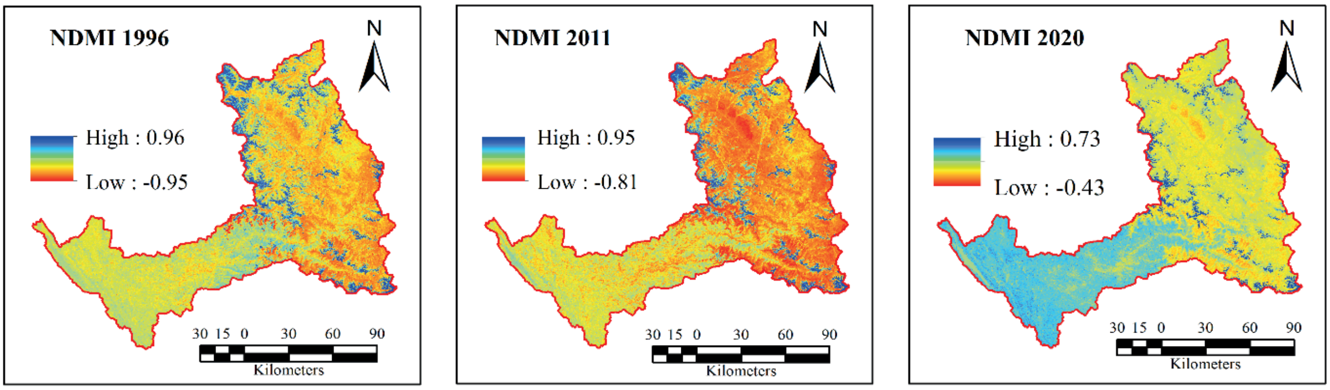

Fig. 11. Spatial pattern of NDMI in 1996, 2011, and 2020 in the study area

DISCUSSION

Temperature variation for different elevation-based zones

Our research finding indicate significantly steady growth in land use change and surface temperature in over the year but this trends more prominent in recent decades. This similar trend also finds in pervious study in Himalayan regions (Khan et al., 2023; Satti et al., 2023). The relationship between LULC and LST along elevation was investigated using a graphical LST profile, which provides a better comprehensive understanding of the dynamics change of LST. Two cross-section lines have been made to obtain each pixel value of LST where zone wise LST was shown, A-B represents all four zones, and C-D represents only zones 3 and 4 (Figure 12). When we see surface temperatures between all LULC types, the LST has profoundly increased across elevation zones. It is found from the cross profile that barren land recorded high LST in all zones (25-27°C in 1996, 29-32°C in 2011, and 33-36°C in 2020), and water bodies recorded the lowest LST in lower attitude (17-19°C in 1996, 21-22°C, 24-25°C in 2020).

The observed trend from the result of LULC reveals that the mean temperature of all zones increased. The probable explanation would be the decrease in forest density and the snow cover at higher altitudes. As per the LST profile map A-B (Figure 12), zone 1 mean temperature was recorded at 19.32°C in 1996 and it increased by 4.4°C (23.72°C) in the last 24 years. The same is evident in zone 2 where the mean surface temperature that was 15.85°C recorded in 1996 increased nearly 4.21°C (17.10°C in 2011 and 20.06°C in 2020) from 1996 to 2020. The spectrally quantified index value demonstrates decreasing density of vegetation with increase in LST (Shahfahad et al., 2020). Several similar studies indicate that snow, vegetation, and water bodies have relatively lower temperatures, whereas sparse vegetation and bare earth have higher temperatures (Das et al. 2020; Kumar et al. 2018; Njoku et al. 2022; Worku et al. 2021).

The snow cover area has decreased but its annual fluctuation is also evident in various studies in the Himalayan region (Haq et al. 2020; Maurya et al. 2021). In our study the LST profile shows that zones 3 and 4 are more vulnerable to changes in LULC and LST. The mean surface temperature for zone 3 & 4 was the had the highest positive increase of 6.46°C during the study period (12.91°C in 1996, 16.10°C in 2011, and 19.37°C in 2020) and 7.59°C (2.73°C in 1996, 7.38°C in 2011, and 19.37°C in 2020) in last 24 years respectively. It has been observed that the highest LST change (Figure 12, C-D) is complementing the decreasing snow cover area and increasing barren land. The changes in the sample LST value for the same vegetation cover pixel was calculated and a progressive increase was evident (18-19°C in 1996, 22-23°C in 2011, and 26-27°C in 2020) in the higher altitude. The ongoing degradation of mountain ecosystem due to anthropogenic pressure and global climate change in the Himalaya region and similar trend also found in the Alpe, Rocky and other global Mountains in several research studies (F. Zhang et al., 2022; H. Zhang et al., 2022). Further the same sample was correlated with NDMI value. A significant correlation was found between NDVI and NDMI (Figure 13).

The Linear Regression between NDVI and NDMI denotes a positive correlation with the correlation coefficient of $R^2 = 0.4077$, $R^2 = 0.5523$, and $R^2 = 0.6995$ in 1996, 2011, and 2020, respectively, indicating that vegetation content has increased along with moisture content over the study period (Figure 13).

The further scenario is not estimating the beyond the scope of the study but that would be taken further with help of modelling tool such as the InVEST model for examine the habitat quality, water balance for river ecosystem. The recognized changed in vegetation are positive way for local communities' livelihood. Agriculture pattern is changed in higher altitude such as apples, potato and etc. farming are altitudinal shifting in this region because global climate change gives suitable condition for this practice and plantation program results are shown in the Spiti region.

CONCLUSION

This study assessed the spatial pattern of LULC change and LST in the Satluj basin, Himachal Pradesh from 1980-2020. It analyzed the dynamics of LULC and LST with changing elevation based on altitudinal zonation of the landscape. The LULC was divided into different classes like vegetation, snow cover, barren land, and water bodies and was evaluated with help of the Support Vector Machine. The results of LULC denote that the Satluj basin has undergone change since 1980. Snow cover has decreased by 56.19% and vegetation cover has increased by 21.89% within the same study period. The spatial and temporal pattern of LST also evidently mark its dynamics in the river basin. The analyses demonstrates that the mean surface temperature of the Satluj basin has amplified by about 0.25°C per year since 1996 and has increased 60.67 per cent (10.3°C to 16.55°C) in the last 24 years. Altitude wise zonation of LST exhibits an increase of 0.18°C/year in zone 1, 0.17°C /year in zone 2, 0.26°C/year in zone 3, and 0.31°C/year in zone 4 respectively. The analyses of this study recommend that LST can be the key factor to LULC character of the landscape. The decrease in NDVI values show the transition in native vegetation. The characteristic expansion in sparse vegetation area and decrease in terms of vegetation density is well evident from the study. Due to the increase in LST and melting of snow cover,

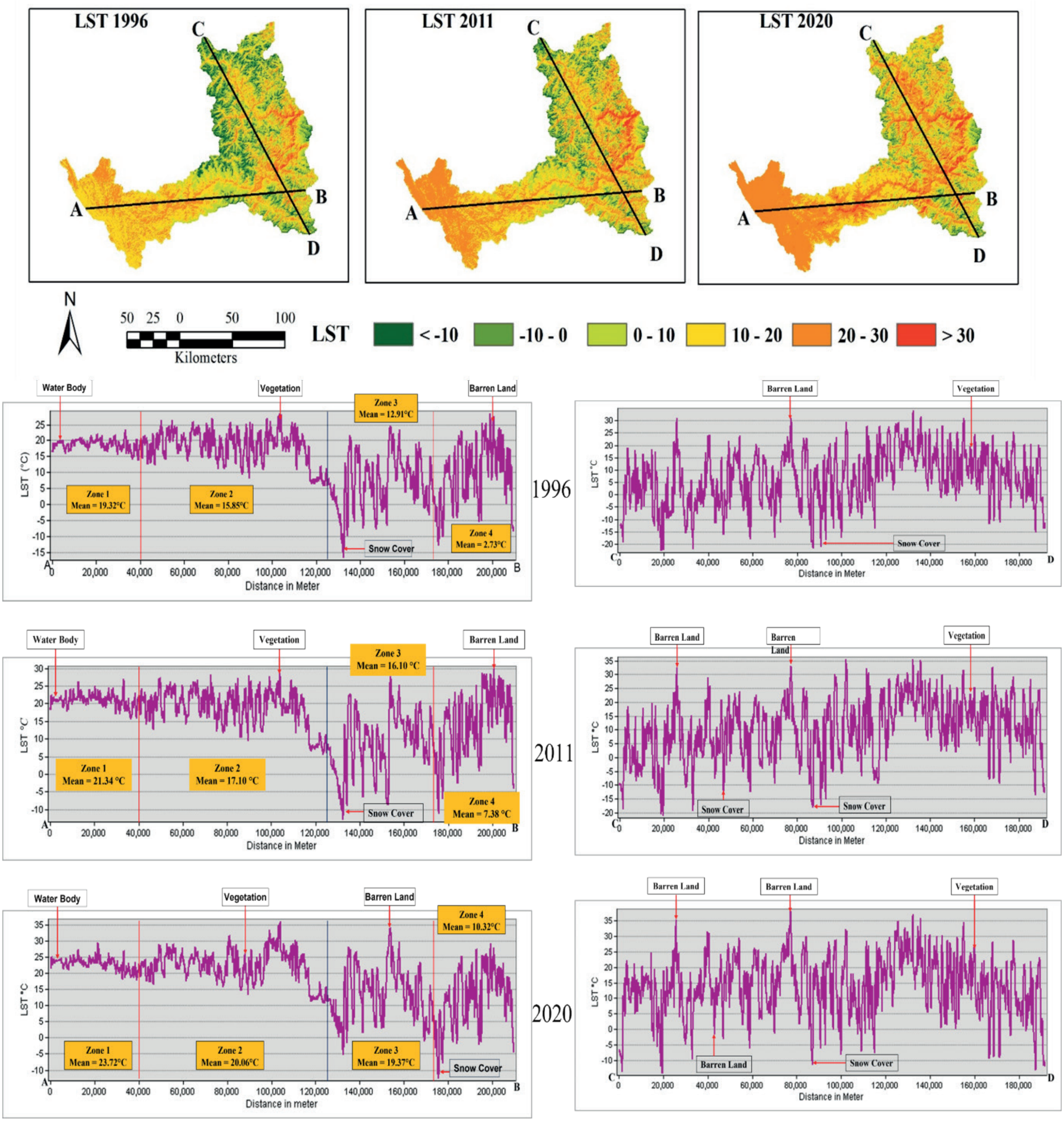

Fig. 12. LST profile (A-B; C-D) over the LST of 1996, 2011, and 2020

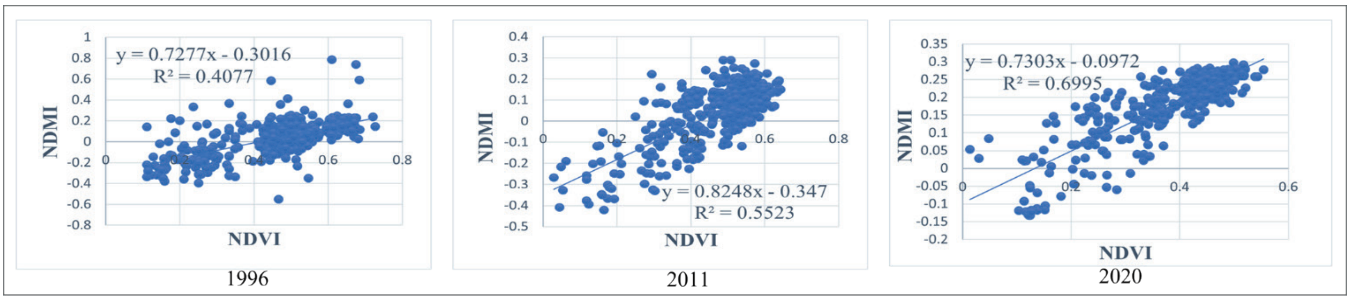

Fig. 13. Correlation between NDVI and NDMI

conditions in the high altitudinal zone are favourable for growth of sparse vegetation. Changing global climate and land transformation have a both positive and negative consequences for the local community. Melting snow would be create water scarcity problem in next coming decades but increasing vegetation land are enhancing local community economy through develop market for the farmers crops. Tourism activity also increase in this region that help in positive way to local community livelihood. Decreasing vegetation density status have strong impact on forest function, biodiversity and sustainability of local people in lower river basin.

Land transformation and LST can change the mountain climate and ecological balance. Society is totally defending on the ecosystem services in the Himalayan Mountain. Change in global climate and anthropogenic pressure have impact on ecosystem services such as water balance, soil quality, food production, habitat quality and carbon storage etc. Many natural disasters can occur such as floods, Glacial Lake Outburst flood, landslides due to environmental change. These changes make difficult to sustain livelihood of community. All these circumstances can lead to migration from mountain region to other place and can be create environmental refuge and disturbance in demographic dividend.

Our study revealed that the potential impact of land transformation and climate change on river basin is becoming a significant issue for all stockholders such as policymakers, local community, river basin engineers, etc. The deterioration of natural resource has increasing vulnerability of local community to absorb shock of frequent natural events due climate change. These results help the identification of potential priority region for more vulnerable exposure level to multiple pressure for the future monitoring activities and decision makers to mitigate possible impact from anthropogenic intervention. Local government authorities can propose better climate risk adaptation plan at attitudinal zone level for the farmers and local community to prevent the global climate change on basis of study findings. ■

REFERENCES

Ali, S. A., Khatun, R., Ahmad, A., & Ahmad, S. N. (2019). Application of GIS-based analytic hierarchy process and frequency ratio model to flood vulnerable mapping and risk area estimation at Sundarban region, India. Modeling Earth Systems and Environment, 5(3), 1083–1102. https://doi.org/10.1007/s40808-019-00593-z

Artis, D. A., & Carnahan, W. H. (1982). Survey of Emissivity Variability in Thennography of Urban Areas. 329, 313–329. https://doi.org/10.1016/0034-4257(82)90043-8.

Bandyopadhyay, D., Mukherjee, S., Singh, G., & Coomes, D. (2023). The rapid vegetation line shift in response to glacial dynamics and climate variability in Himalaya between 2000 and 2014. Environmental Monitoring and Assessment, 195(1). https://doi.org/10.1007/s10661-022-10577-9

Bindajam, A. A., Mallick, J., Alqadhi, S., & Singh, C. K. (n.d.). Impacts of Vegetation and Topography on Land Surface Temperature Variability over the Semi-Arid Mountain Cities of Saudi Arabia. 1–28. Atmosphere, 11(7), 762. https://doi.org/10.3390/ATMOS11070762.

Chauhan, N., Upadhyay, S. K., & Singh, R. (2021). The Himalayan natural resources: Challenges and conservation for sustainable development. Article in Journal of Pharmacognosy and Phytochemistry, 10(1), 1643–1648. www.phytojournal.com

Chhogyel, N., Kumar, L., Bajgai, Y., & Hasan, M. K. (2020). Perception of farmers on climate change and its impacts on agriculture across various altitudinal zones of Bhutan Himalayas. International Journal of Environmental Science and Technology, 17(8), 3607–3620. https://doi.org/10.1007/s13762-020-02662-8

Das, S., & Angadi, D. P. (2020). Land use-land cover (LULC) transformation and its relation with land surface temperature changes: A case study of Barrackpore Subdivision, West Bengal, India. Remote Sensing Applications: Society and Environment, 19(July 2019), 100322. https://doi.org/10.1016/j.rsase.2020.100322

Delgado-Moreno, D., & Gao, Y. (2022). Forest Degradation Estimation Through Trend Analysis of Annual Time Series NDVI, NDMI and NDFI (2010–2020) Using Landsat Images BT - Advances in Geospatial Data Science (R. Tapia-McClung, O. Sánchez-Siordia, K. González-Zuccolotto, & H. Carlos-Martínez (eds.); pp. 149–159). Springer International Publishing.

Grêt-Regamey, A., Weibel, B., Bagstad, K. J., Ferrari, M., Geneletti, D., Klug, H., Schirpke, U., & Tappeiner, U. (2014). On the effects of scale for ecosystem services mapping. PLoS ONE, 9(12), 1–26. https://doi.org/10.1371/journal.pone.0112601

Haq, M. A., Baral, P., Yaragal, S., & Rahaman, G. (2020). Assessment of trends of land surface vegetation distribution, snow cover and temperature over entire Himachal Pradesh using MODIS datasets. Natural Resource Modeling, 33(2). https://doi.org/10.1111/nrm.12262

Holzman, M. E., Rivas, R., & Piccolo, M. C. (2014). Estimating soil moisture and the relationship with crop yield using surface temperature and vegetation index. International Journal of Applied Earth Observation and Geoinformation, 28(1), 181–192. https://doi.org/10.1016/j.jag.2013.12.006

Husain, M. A., Kumar, P., Singh, A., Raman, V. A. V, Dua, R., & Thakur, S. (2023). Snow Cover and Snowline Variation in Relation to Land Surface Temperature in Spiti Valley, Himachal Pradesh, India. International Journal of Ecology and Environmental Sciences, 49, 187–199.

Jin, S., & Sader, S. A. (2005). Comparison of time series tasseled cap wetness and the normalized difference moisture index in detecting forest disturbances. Remote Sensing of Environment, 94(3), 364–372. https://doi.org/10.1016/j.rse.2004.10.012

John, A., Cannistra, A. F., Yang, K., Tan, A., Shean, D., Hille Ris Lambers, J., & Cristea, N. (2022). High-Resolution Snow-Covered Area Mapping in Forested Mountain Ecosystems Using PlanetScope Imagery. Remote Sensing, 14(14), 1–24. https://doi.org/10.3390/rs14143409

Khan, A., Haque, S. M., & Biswas, B. (2023). Altitudinal Shifting of Apple Orchards with Adaption of Changing Climate in the Alpine Himalaya. Journal of the Indian Society of Remote Sensing, 51(5), 1135–1155. https://doi.org/10.1007/s12524-023-01678-0

Kumar, P., Husain, A., Singh, R. B., & Kumar, M. (2018). Impact of land cover change on land surface temperature: A case study of Spiti Valley. Journal of Mountain Science, 15(8), 1658–1670. https://doi.org/10.1007/s11629-018-4902-9

Li, Z., Jia, L., & Lu, J. (2015). On uncertainties of the Priestley-Taylor/LST-Fc feature space method to estimate evapotranspiration: Case study in an arid/semiarid region in northwest China. Remote Sensing, 7(1), 447–466. https://doi.org/10.3390/rs70100447

Lutz, A. F., Immerzeel, W. W., Gobiet, A., Pellicciotti, F., & Bierkens, M. F. P. (2013). Comparison of climate change signals in CMIP3 and CMIP5 multi-model ensembles and implications for Central Asian glaciers. Hydrol. Earth Syst. Sci., 17(9), 3661–3677. https://doi.org/10.5194/hess-17-3661-2013

MARKHAM, B. L., & BARKER, J. L. (1985). Spectral characterization of the LANDSAT Thematic Mapper sensors. International Journal of Remote Sensing, 6(5), 697–716. https://doi.org/10.1080/01431168508948492

Maurya, R., Negi, V. S., & Pandey, B. W. (2021). Spatio-temporal analysis of land use/land cover change through overlay technique in Kinnaur district of Himachal pradesh, Western Himalaya. Sustainability, Agri, Food and Environmental Research, 9(1). https://doi.org/10.7770/safer-v0n0-art2161

Monserud, R. A., & Leemans, R. (1992). Comparing global vegetation maps with the Kappa statistic. Ecological Modelling, 62(4), 275–293. https://doi.org/10.1016/0304-3800(92)90003-W

Mountrakis, G., Im, J., & Ogole, C. (2011). Support vector machines in remote sensing: A review. ISPRS Journal of Photogrammetry and Remote Sensing, 66(3), 247–259. https://doi.org/10.1016/j.isprsjprs.2010.11.001

Njoku, E. A., & Tenenbaum, D. E. (2022). Remote Sensing Applications : Society and Environment Quantitative assessment of the relationship between land use / land cover (LULC), topographic elevation and land surface temperature (LST) in Ilorin , Nigeria. Remote Sensing Applications: Society and Environment, 27, 100780. https://doi.org/10.1016/j.rsase.2022.100780

Pal, M., & Mather, P. M. (2006). Some issues in the classification of DAIS hyperspectral data. International Journal of Remote Sensing, 27(14), 2895–2916. https://doi.org/10.1080/01431160500185227

Pal, S., & Ziaul, S. (2017). Detection of land use and land cover change and land surface temperature in English Bazar urban centre. Egyptian Journal of Remote Sensing and Space Science, 20(1), 125–145. https://doi.org/10.1016/j.ejrs.2016.11.003

Pang, G., Chen, D., Wang, X., & Lai, H. W. (2022). Spatiotemporal variations of land surface albedo and associated influencing factors on the Tibetan Plateau. Science of the Total Environment, 804, 150100. https://doi.org/10.1016/j.scitotenv.2021.150100

Rani, S., & Mal, S. (2022). Trends in land surface temperature and its drivers over the High Mountain Asia. Egyptian Journal of Remote Sensing and Space Science, 25(3), 717–729. https://doi.org/10.1016/j.ejrs.2022.04.005

Roy, P. S., Ramachandran, R. M., Paul, O., Thakur, P. K., Ravan, S., Behera, M. D., Sarangi, C., & Kanawade, V. P. (2022). Anthropogenic Land Use and Land Cover Changes—A Review on Its Environmental Consequences and Climate Change. Journal of the Indian Society of Remote Sensing, 50(8), 1615–1640. https://doi.org/10.1007/s12524-022-01569-w

Satti, Z., Naveed, M., Shafeeque, M., Ali, S., Abdullaev, F., Ashraf, T. M., Irshad, M., & Li, L. (2023). Effects of climate change on vegetation and snow cover area in Gilgit Baltistan using MODIS data. Environmental Science and Pollution Research, 30(7), 19149–19166. https://doi.org/10.1007/s11356-022-23445-3

Shahfahad, Kumari, B., Tayyab, M., Ahmed, I. A., Baig, M. R. I., Khan, M. F., & Rahman, A. (2020). Longitudinal study of land surface temperature (LST) using mono- and split-window algorithms and its relationship with NDVI and NDBI over selected metro cities of India. Arabian Journal of Geosciences, 13(19). https://doi.org/10.1007/s12517-020-06068-1

Singh, P., & Kumar, N. (1997). Impact assessment of climate change on the hydrological response of a snow and glacier melt runoff dominated Himalayan river. Journal of Hydrology, 193(1–4), 316–350. https://doi.org/10.1016/S0022-1694(96)03142-3

Snyder, W. C., & Wan, Z. (1998). BRDF models to predict spectral reflectance and emissivity in the thermal infrared. IEEE Transactions on Geoscience and Remote Sensing, 36(1), 214–225. https://doi.org/10.1109/36.655331

Swain, S., Mishra, S. K., Pandey, A., & Kalura, P. (2022). Inclusion of groundwater and socio-economic factors for assessing comprehensive drought vulnerability over Narmada River Basin, India: A geospatial approach. Applied Water Science, 12(2), 1–16. https://doi.org/10.1007/s13201-021-01529-8

Taripanah, F., & Ranjbar, A. (2021). Quantitative analysis of spatial distribution of land surface temperature (LST) in relation Ecohydrological, terrain and socio- economic factors based on Landsat data in mountainous area. Advances in Space Research, 68(9), 3622–3640. https://doi.org/10.1016/j.asr.2021.07.008

TOWNSHEND, J. R. G., & JUSTICE, C. O. (1986). Analysis of the dynamics of African vegetation using the normalized difference vegetation index. International Journal of Remote Sensing, 7(11), 1435–1445. https://doi.org/10.1080/01431168608948946

Upadhayaya, P. K. (2015). Sustainability Threats to Mountain Tourism with Tourist Mechanized Mobility Induced Global Warming: A Case Study of Nepal. Journal of Tourism & Hospitality, 04(02). https://doi.org/10.4172/2167-0269.1000148

Vannier, C., Lasseur, R., Crouzat, E., Byczek, C., Lafond, V., Cordonnier, T., Longaretti, P. Y., & Lavorel, S. (2019). Mapping ecosystem services bundles in a heterogeneous mountain region. Ecosystems and People, 15(1), 74–88. https://doi.org/10.1080/26395916.2019.1570971

Voogt, J. A., & Oke, T. R. (2003). Thermal remote sensing of urban climates. Remote Sensing of Environment, 86(3), 370–384. https://doi.org/10.1016/S0034-4257(03)00079-8

Wen, X. (2020). Temporal and spatial relationships between soil erosion and ecological restoration in semi-arid regions: a case study in northern Shaanxi, China. GIScience and Remote Sensing, 57(4), 572–590. https://doi.org/10.1080/15481603.2020.1751406

Worku, G., Teferi, E., & Bantider, A. (2021). Assessing the effects of vegetation change on urban land surface temperature using remote sensing data: The case of Addis Ababa city, Ethiopia. Remote Sensing Applications: Society and Environment, 22(April), 100520. https://doi.org/10.1016/j.rsase.2021.100520

Xystrakis, F., Psarras, T., & Koutsias, N. (2017). A process-based land use/land cover change assessment on a mountainous area of Greece during 1945–2009: Signs of socio-economic drivers. Science of the Total Environment, 587–588, 360–370. https://doi.org/10.1016/j.scitotenv.2017.02.161

Young, K. R. (2014). Ecology of land cover change in glaciated tropical mountains. Revista Peruana de Biología, 21(3), 259–270.

Zhang, F., Zeng, B., Yang, T., Zheng, Y., & Cao, Y. (2022). A Multi-Perspective Assessment Method with a Dynamic Benchmark for Human Activity Impacts on Alpine Ecosystem under Climate Change. Remote Sensing, 14(1). https://doi.org/10.3390/rs14010208

Zhang, H., Zhan, C., Xia, J., & Yeh, P. J. F. (2022). Responses of vegetation to changes in terrestrial water storage and temperature in global mountainous regions. Science of the Total Environment, 851(July), 158416. https://doi.org/10.1016/j.scitotenv.2022.158416

Zhang, J., Wang, Y., & Li, Y. (2006). A C++ program for retrieving land surface temperature from the data of Landsat TM/ETM+ band6. Computers and Geosciences, 32(10), 1796–1805. https://doi.org/10.1016/j.cageo.2006.05.001

Zhang, R., Tang, X., You, S., Duan, K., Xiang, H., & Luo, H. (2020). A novel feature-level fusion framework using optical and SAR remote sensing images for land use/land cover (LULC) classification in cloudy mountainous area. Applied Sciences (Switzerland), 10(8), 1–24. https://doi.org/10.3390/APP10082928

Zhongming, Z., Linong, L., Xiaona, Y., Wangqiang, Z., & Wei, L. (2021). Climate change leads to 18.52% decrease in snow cover in Himachal: Study.

RESEARCH PAPER

LANDSCAPE CARTOGRAPHY IN THE MARANHENSE AMAZON: THE CASE OF THE LOWER COURSE OF THE PINDARÉ RIVER BASIN

Rafael Brugnolli Medeiros[1*], Luiz Carlos Araujo dos Santos[1], Jose Fernando Rodrigues Bezerra[1], Ana Rosa Marques[1], Gabriel Irvine Ferreira Alves dos Santos[1]
[1]Universidade Estadual do Maranhão, Programa de Pós-Graduação em Geografia, Natureza e Dinâmica do Espaço
*Corresponding author: rafael_bmedeiros@hotmail.com
Received: January 11th, 2023 / Accepted: November 14th, 2023 / Published: December 31st, 2023
https://DOI-10.24057/2071-9388-2023-2706

ABSTRACT. The landscape cartography assesses the functional, dynamic, structural and morphological aspects of landscapes, regardless of their taxonomic scale. It seeks to use these units to support environmental and territorial planning and management. Thus, the present study sought to apply this line of analysis to the Pindaré River Basin, precisely in its lower course, located in the Brazilian state of Maranhão. The objective was to identify, classify, map and analyze the landscapes of the lower course through the correlation of variables related to geology, relief, soils, land use and land cover providing data to support and promote preservationist and conservationist public policies and actions in the area. The methodology identified four levels of landscape analysis, from morphometric aspects, geoforms and upper units to reaching the final landscape map, using field output, digital elevation models and satellite images to validate information. The procedures allowed to identify the landscape heterogeneity in a unique environment of saturated and periodically flooded soils contrasting with extensive pastures and little native vegetation. As a result, seven first-level landscape units were identified, coming up to fifty-eight sub-units in the final map. The work aims to apply the methodology in an area of the Maranhão State where few studies on landscape cartography have occurred. The target is to comprehend possible relationships between the functional and structural potential of landscapes and their relationship with the current intensity of land use, contributing to physical-territorial planning permeating geoecological sustainability.

KEYWORDS: Landscape Mapping; Geosystems; Amazon Basin; Baixada Maranhense

CITATION: Medeiros R. B., dos Santos L. C. A., Bezerra J. F. R., Marques A. R., dos Santos G. I. F. A. (2023). Landscape Cartography In The Maranhense Amazon: The Case Of The Lower Course Of The Pindaré River Basin. Geography, Environment, Sustainability, 4(16), 39-51
https://DOI-10.24057/2071-9388-2023-2706

ACKNOWLEDGEMENTS: The authors thank CAPES – (Coordination for the Improvement of Higher Education Personnel) for funding the project and granting a Master's and Post-Doc (Author A) Internship scholarship.

Conflict of interests: The authors reported no potential conflict of interest.

INTRODUCTION

Landscape cartography allows the assessment of geosystemic units in the context that they all have an environmental/geoecological, social, economic and cultural functionalities that when overexploited bring environmental problems and irreversible impacts to the natural system. The method and technique seek to enter the geosystemic bias, in which the landscape reflects the relationships between natural (abiotic and biotic), technical-economic, and socio-cultural components. The concept of landscape discussed in this article follows Zonneveld (1995) and Mateo Rodriguez, Silva and Cavalcanti (2013), that is, a complex and open space-time system that originates and evolves through a constant transfer of energy, matter, and information. According to (Littell et al. 2018; Newman et al. 2019), these are complex systems, and the Landscape Cartography is the way to interpret the landscape and comprehend its structure, functioning, dynamics, evolution, and indicators, widely discussed in the works of De Pablo (1988), Mateo Rodriguez, Silva and Cavalcanti (2013) and Cavalcanti (2014). Approaching the landscape as an object of scientific investigation enables to incorporate information that supports environmental diagnoses, even physical-territorial orders, proposing forms of rational use in the face of existing weaknesses and potential. Therefore, the relevance of applying it in the context of a basin. The subject has been widely discussed through the estimation of landscape temporal changes (Cunha et al. 2020), predictive scenarios (Amorim, 2015), landscape heterogeneity and hydrological processes (Gao et al. 2018), assessment of geoecological status (Brugnoli and Salinas Chávez, 2021), geoecological diagnosis (Brugnoli et al. 2022). Several other studies admit the landscape as an operational concept of analysis, and the basin as a territorial unit of study, and both concepts come together when focusing on environmental themes. Systemic analysis based on Society/Nature relationship is essential for its cartography (synthesis, analytical and descriptive) and responds to environmental problems proposing adequate ways to minimize them, and indicate rational ways of land use. Thus, applying such concepts in a degraded area that presents problems and weaknesses is essential to achieve geoecological sustainability.

The Pindaré River Basin comprises thirty-eight municipalities. The present study focusses its lower course, in the so-called Baixada Maranhense, located in a region known for deforestation and landscape fragmentation with wide destruction of native forests, especially ombrophilous with remnants of the Cocais Forest. Especially the Amazon the presented increases in anthropogenic actions on natural environments in the last decades, intensifying processes that replace natural vegetation by other land covers. These interventions had converted extensive and continuous areas covered with forests into agriculture, urban areas, and other covers, causing environmental impacts. In many cases, the lack of planning for these processes threatens water sustainability of basins in the Amazon region (Yesuph & Dagnew 2019; Rocha; de Lima & Adami, 2021).

The lower Pindaré region is an ecologically diverse and complex environment, periodically flooded, and more than 97% of its areas present flat to Smoothly undulating topography, no more than 20% slope. The region presents drainage channels that converge with ponds, lakes and rivers, and intertwine through streams. The meandering and anastomosing drainage channels form a rich hydric and geomorphological structure. According to Costa-Neto (2002), the dynamic is due to the rain seasonality with well- defined dry and rain seasons. The rainy season occurs from January to July over the extensive flat area causing significant floods, due to the little depth of lakes and rivers in the region, thus, water table rises and soils saturate in water. However, during the dry season, the slopes form extensive dry fields and shrubby vegetation, grasses and cyperaceae. Such occurrences and dynamics raised the hypothesis that the flat relief favors this unique seasonality, however, it favors occupation by human beings. Pastures predominate the area replacing the native vegetation, fragmenting the landscape. Facing the landscape functional aspects, this research aims to realize whether these units have been fulfilling their ecological functions, as well as identifying environmental difficulties, using the data collected to propose ways to mitigate weaknesses. The relevant and diversified current data about the Maranhense Amazon present less accuracy and/or incongruity as approaching more local and regional scales of analysis, making it impossible to adapt development/ planning programs to the fragile physical environment. In agreement with Salinas Chávez and Ribeiro (2017) and Brugnolli et al. (2022), landscape cartography according to the methodology proposed here, works to adjust and balance the three geoecological views, geographic, socioeconomic and ecological.

The present work sought to identify, map and analyze the landscape units of the lower course of the Pindaré River Basin (Figure 1), in order to identify the existing correlations between geology, relief, soil, and land use and land cover. The results may contribute to establish the River Basin Committee of the Mearim River - law 9,957 (Maranhão, 2013), which the Pindaré River belongs to, as well as relevant data of a little studied region.

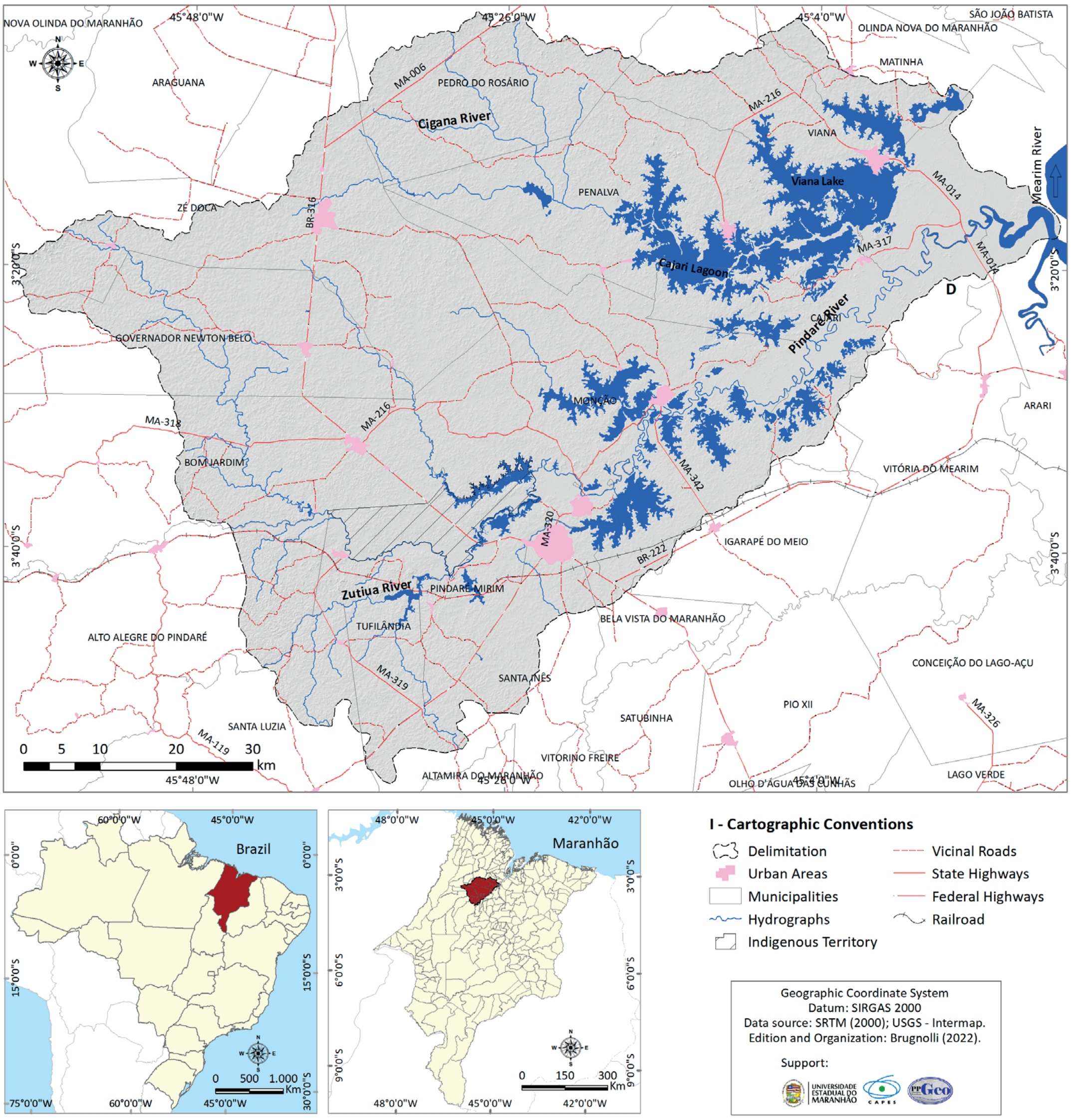

Fig. 1. Location of the lower course of the Pindaré River Basin, Maranhão

METHODOLOGY

The methodology applied here approached two basic steps. The first consists of surveying the landscape components, and the second links to the interactive analysis among them, using basic methodologies of landscape cartography. The procedures start by using the Digital Terrain Model of the Shuttle Radar Topography Mission (DTM/ SRTM), acquired free of charge through the Earth Explorer of the United States Geological Survey. The model went through pre-processing steps to correct noise, spurious pixels, and to fill in existing defaults. The procedures were performed in a Geographic Information System environment, using QGIS Desktop 3.16. In the sequence, we carried out the hypsometric mapping of the study area to identify the elevations and altimetric levels. The same base (DTM/SRTM) was used to generate the slope of the area, using the Brazilian Soil Classification System (Sistema Brasileiro de Classificação de Solos - SIBCS, 2018) to define the slope classes to be compartmentalized: 0.00 to 3.00% - flattened; 3.01 to 8.00% - Smoothly undulating; 8.01 to 20.00% - undulating; 20.01 to 45.00% - strongly undulating. The geology data (morphostratigraphic units) were defined using the base of the Mineral Resources Research Company (Companhia de Pesquisa de Recursos Minerais – CPRM). However, we identified incongruities, and small sand and classification errors, due to its scale. Thus, field works were performed for detailing and support data, as well as the use of DTM/SRTM and satellite images, more precisely the mosaic of images of the QuickMapServices, add-on to QGIS Desktop 3.16. In this matter, the adjustment and the definition and delimitation of polygons (example for the plains) in the area improved and detailed the base with the terrestrial reality. For soils, we used the Ecological-Economic Zoning of Maranhão base. For the adjustment and detailing, the same procedures described in geology were used, such as DTM/SRTM, field work, and mosaic of images to investigate and correct incongruent polygons. Details and corrections that stand out and are necessary for working with landscape cartography. In this first phase, we worked with data from MapBiomas (2020) to classify land use and land cover. The Landsat 8 satellite images allowed to identify mangrove classes, flooded field and swampy area, grassland formation, savanna formation, forest formation, pasture, apicum, other temporary crops, urbanized, area and water. Afterwards, an interactive analysis was carried out at four levels between the landscape components (Figure 2) to identify, classify, and map the landscape units of the lower course of the Pindaré River Basin. The analysis and cartography comprise methodologies in agreement with Salinas Chávez and Ribeiro (2017) and Brugnolli and Salinas Chávez (2021), supported by authors such as Mateo, Silva and Cavalcanti (2013) and Cavalcanti (2014). Comprehending that the units are physical-territorial complexes with relatively homogeneous characteristics with their own geoecological and anthropic functions, allow them to be delimited under the precepts of a geosystemic perspective.

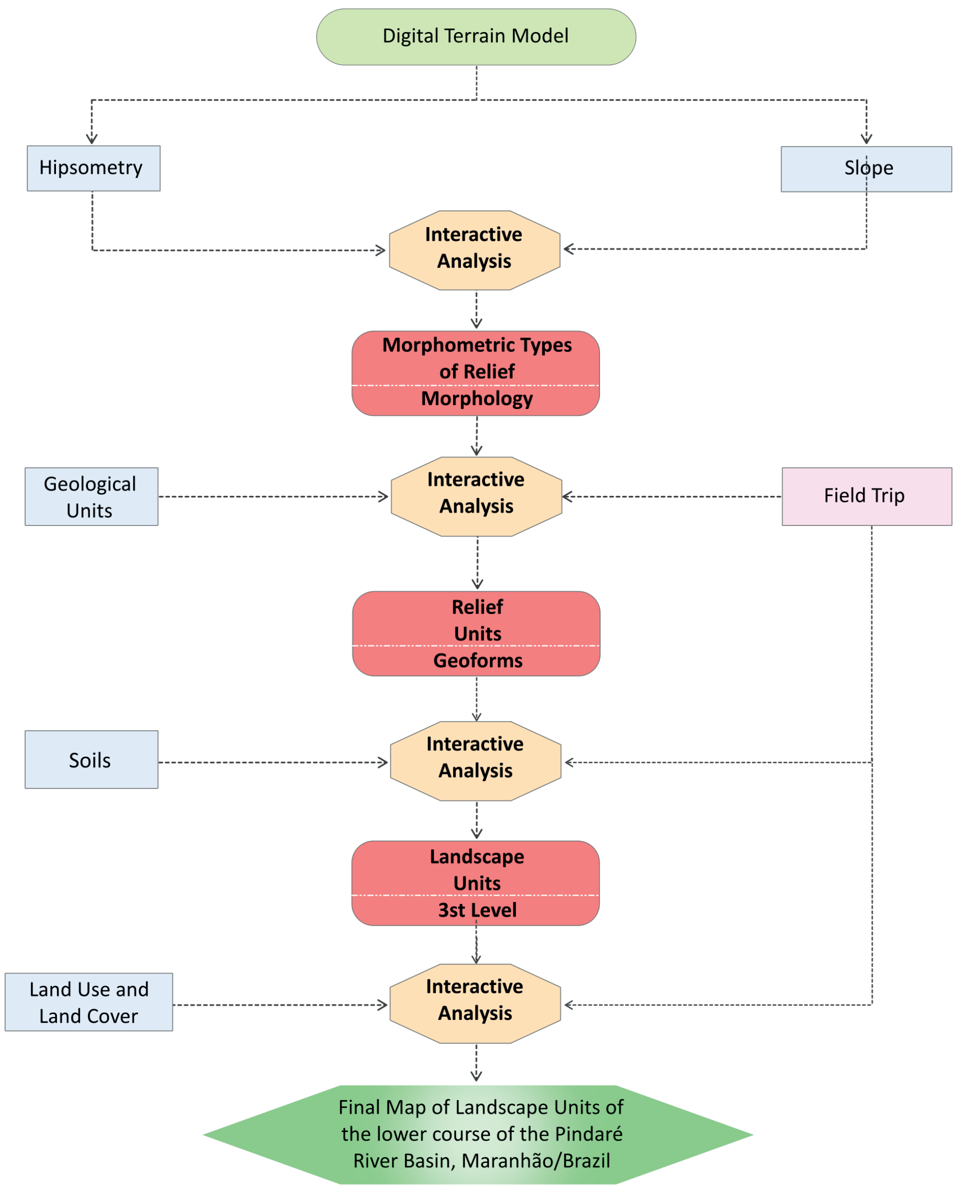

Fig. 2. Methodological flowchart applied to the Pindaré River Basin, Maranhão

We highlight that the levels are the synthesis of integrated variables, and the tabulation results may compartmentalize the study area. Thus, the first compartmentalization occurs through the integration between hypsometry and slope, both derived from the DTM/SRTM. The result of this first level of landscape units are the morphometric aspects of relief/morphology. Subsequently, the result of the first phase and the geological aspects (geological units) are approached, with a field trip to verify the acquired and generated information. In the field trip, we used the Global Positioning System - Garmin eTrex Portable GPS, photographic cameras, and the DJI Mavic Drone, for vertical and oblique photographs of the landscape, leading to the second level of landscape units, called geoforms. The geoforms correlate with soils, reaching the third level and, then, with land use and land cover, ending the fourth and last level, that is, the final map of landscape units of the PRB lower course. The final map allows to use such units for environmental and territorial purposes of management and planning, as they all present unique geoecological and anthropic aspects. The units present their own functionalities, structures, dynamics and evolutions favoring the comprehension of the environmental use-exploitation- services.

It is important to note that the interactive analyses that take landscapes from level to level, relied on automated interpolation via GIS, in a multicriterial assessment and clusterization, in which clustering is performed with a view to finding homogeneous units. From this classification, the empirical role of researchers and knowledge about the study area enters the discussion as a way to validate the data obtained automatically and improve the final quality of the products generated.

ENVIRONMENTAL CHARACTERIZATION OF THE LOWER COURSE OF THE PINDARÉ RIVER BASIN

The Baixada Maranhense presents a unique landscape, seasonally influenced by the water table and precipitation (rain cycle) variation. It is characterized by its large and extensive lake environments and paths/channels that intertwine until reaching the water sources. As the region is adjusted to the general base level, there are areas under the influence of tides through streams (igarapés) making the salinization of the waters a significant negative factor. In this complex hydric and geomorphological structure, the soil partially saturated in water contrasts with areas of pasture, rice plantations, native vegetation, urban areas, and some temporary crops (Figure 3).

In the wetlands predominate recent geological structures with alluvial and fluvial-lacustrine deposits dated from the Quaternary period, recent within the Brazilian geological structure. The structures present large deposits of sand, silicon, clay and gravel. According to Rodrigues et al. (2014), the sediments may be linked to the fluvial course (alluvial) and/or lake environments (fluvial-lacustrine) that were transported and deposited over the last 10 thousand years. In the areas close to the water sources, we identify estuaries and anastomosing channels that flow to the Mearim River, which runs 40 km to the São Marcos Bay, north of Maranhão State. The fact explains the presence of mangroves, the so-called Igapó Forest, recent and water-saturated soils, such as the fluvic neosol and the thiomorphic gleysols, as well as the apparent salinization of the main river and the tributaries close to the mouth of the Pindaré River, as pointed by Machado and Pinheiro (2016) and Almeida et al. (2020). The salinization or marine intrusion occurs altering the riparian zones. The intrusion is due to anthropic interferences, the reduction of riparian vegetation, conversion of native vegetation to pastures and rice crops. Facts that contribute to the silting of upstream areas, and increase of sediments carried to the meanders, changing the local base level and modifying the upstream water structure. The proximity to the general base level contribute to the intrusion and interference in the region, as the northern region of Maranhão is strongly influenced by tide variation. During the high tide, the river waters rise causing impacts on the hydrodynamics and local biodiversity. The native vegetation proves to be resistant in specific areas, however, the entrance of pasture advances and devastate the banks of water sources. Livestock activities are not suitable for the region due to several limitations, such as the soils (haplic, melanic and thiomorphic gleisols, and fluvic neosols) and relief, located in floodplains and plains. The floodable areas contrast with river terraces and Smoothly undulating to undulating surfaces linked to old rocks, such as the Itapecuru Formation, linked to claystones, siltstones and shales interspersed with sandstones deposited in various environments. The deposition presents predominantly continental influence, however, indications of marine transgressions (CPRM, 2013) are present, as well. Deep and well-developed soils predominate the areas, such as plintosols and argisols, common in hot and humid equatorial zones. According to EMBRAPA (2018), these soils exhibit poor drainage, and excess of humidity. Even tough, the area shows agricultural potential, due to its location on flat to Smoothly undulating reliefs. Small patches of native vegetation remain in the area, mainly dense and open ombrophilous forests. The Baixada Maranhense area is predominantly used by pastures, some left fallow, and others for cattle and buffalo. The buffalo livestock has caused a series of environmental problems, due to the weight of the animal. They trample the soil causing the silting of springs and flat, degraded, floodable and fragile slopes. Thus, the Public Ministry of Maranhão sued some municipalities for their lack of control facing the activity, since the region is an Environmental Protection Area - EPA (Área de Proteção Ambiental - APA), according to state decree nº 11.900 (Maranhão, 1991).

We highlight that the region is part of the Golfão Maranhense, in which the occupational process has reached drastic levels. The region has been consolidated as one of those located in the arc of deforestation, due to the anthropic actions and significant disappearance of native vegetation. Anthropic actions are identified even in swamp lands with rice planting in the river plains. In addition, the region presents humid tropical climate with a dry season (July to December) and a rainy season (January to June), favoring the seasonality of floods and droughts in the Baixada Maranhense. The region comprises diverse geosystems, complex and distinct typologies, validating the present proposal of identifying, classifying and mapping the landscape physical-geographical units, analyzing them under the environmental study.

LANDSCAPE UNITS OF THE LOWER COURSE OF THE PINDARÉ RIVER BASIN

The research approached landscape cartography to comprehend the correlations between the natural and social components of the lower course of the Pindaré River Basin, a complex area of Maranhão State. The purpose is to define relatively homogeneous units to facilitate and support the planning and management process of these units. Studying them is a fundamental step towards success in actions and decision-making, as it allows establishing an adequacy between current uses and the support capacity and balanced functioning of the units (Figure 4 and Table 1).

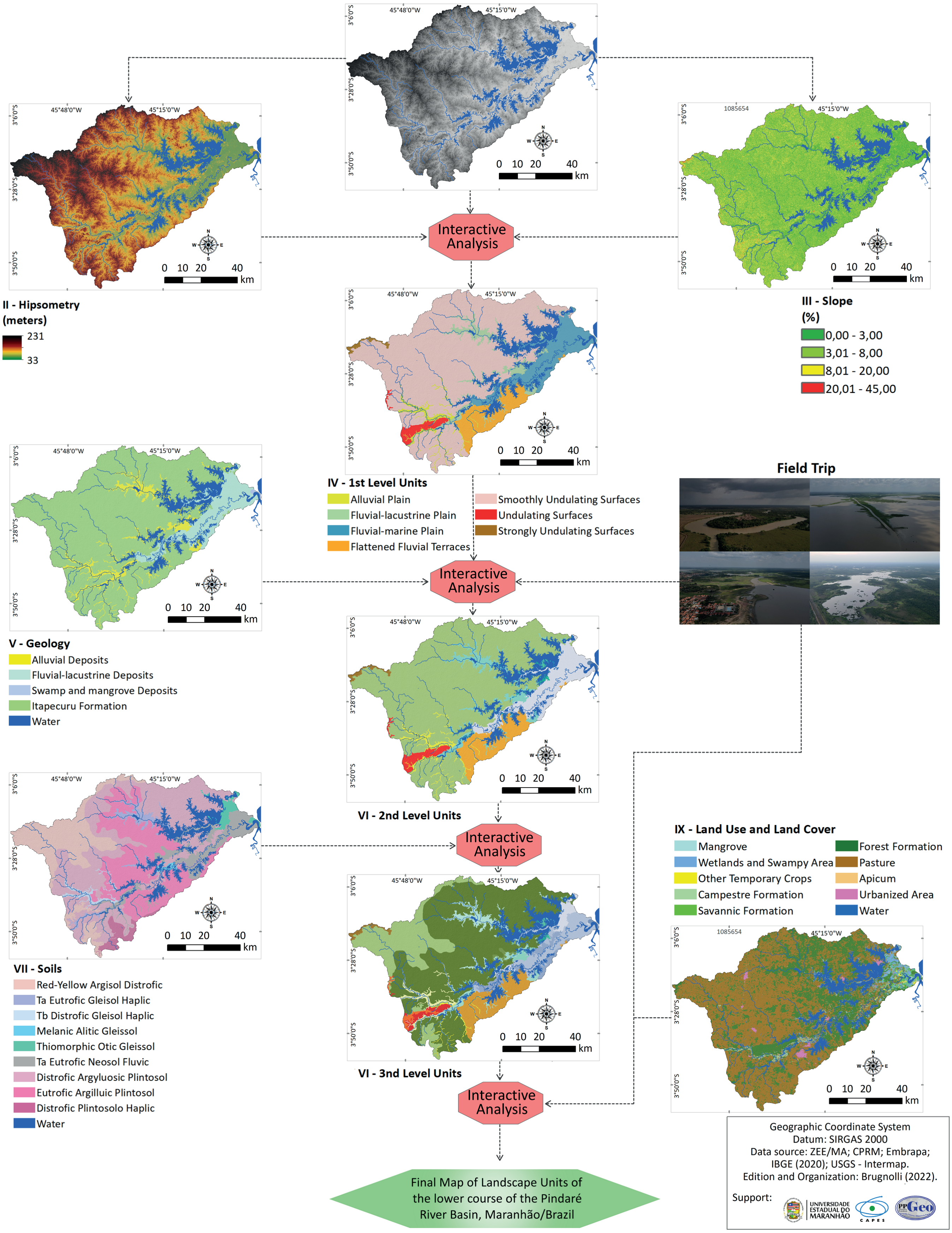

Fig. 3. Physical and anthropic components of the lower course of the PRB, Maranhão

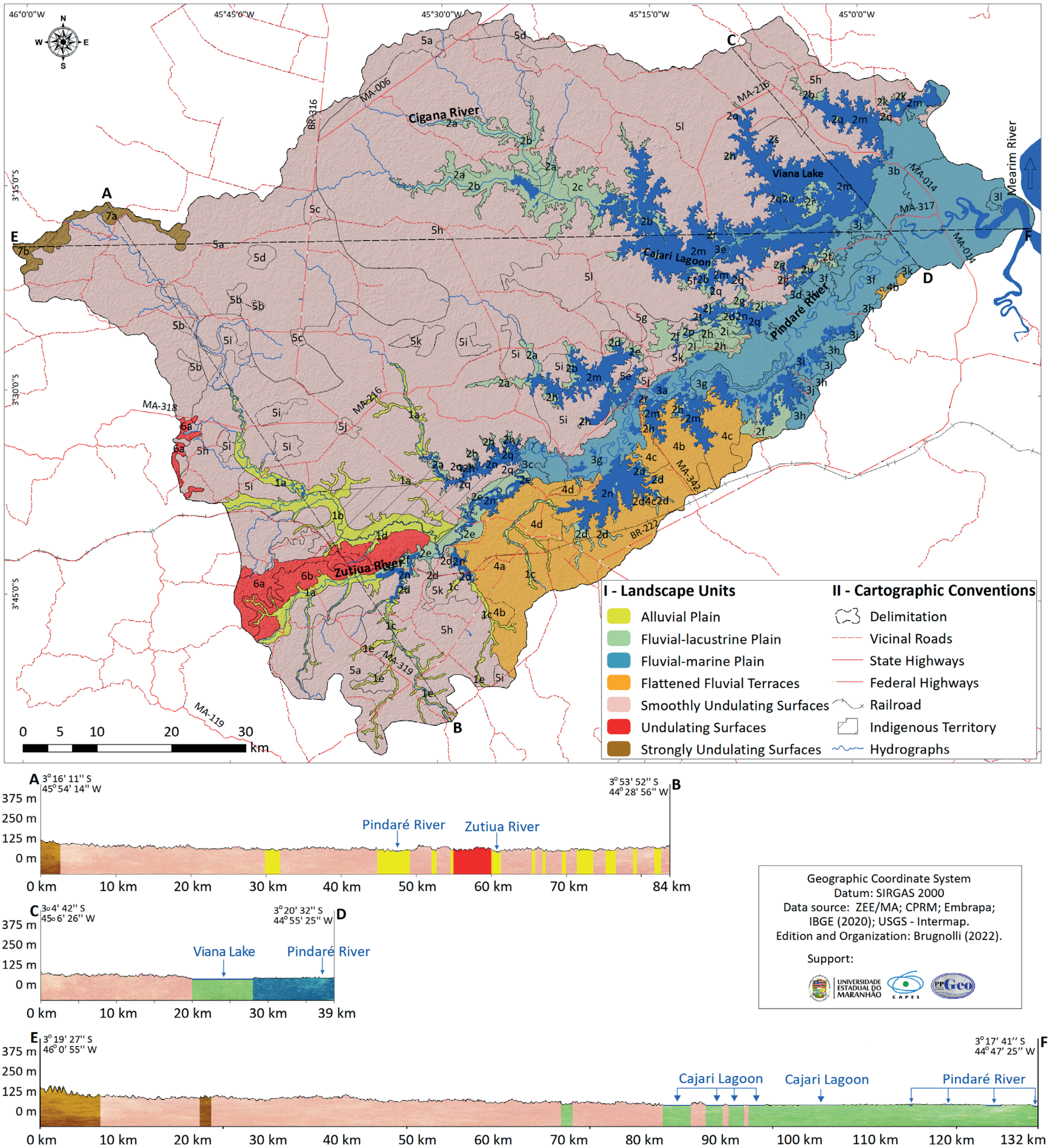

Fig. 4. Landscape Units of the lower course of the Pindaré River Basin, Maranhão

The description of the units follows a hierarchy linked to the relief. According to Serrano (2012), Hernandez et al. (2017), Khoroshev (2019) and Comerlato, Lamour and Silveira (2020), the relief is the essential component in environmental systems as the agent that redistributes the flows of matter and energy in the system. Thus, the relief acts significantly in the distinction and typology of landscape units.

LU1 - Alluvial Plain – The unit associated with water resources, typical of valley bottoms, of receiving property with sediment accumulations. The rocks are predominantly formed by recent sand, silt and gravel (alluvial) deposits, dating from the Quaternary. They cover a total of 195.82 km^2, that is, 2.82% of the study area along five sub-units. The soils vary from gleisol in the areas close to springs, neosols, especially fluvic, and plinthsols. The flattened relief does not exceed 3.00%, and they are periodically flooded, presenting predominance of grassland and forest vegetation in the riparian zones. However, several areas are degraded with pastures and remnants of vegetation forest, and some pastures have already reached the banks of water sources. The plains are not associated with lacustrine environments. The area presents restricted plains at the beginning of the low course, as well as a single extensive plain at the confluence of the Zutiua River with the Pindaré River (Figure 5).

These sub-units present major land use limitations, since they are fragile areas from the pedological, geomorphological, and geological view. The large areas are periodically flooded by the water source overflows, and as permanent preservation areas, restrictions are imposed. The water resources are silted with large and extensive sandbanks, and the riparian zones show wide open gaps with pastures. Therefore, the recommendation

Table 1. Description of the Landscape Units of the Pindaré River Basin

Landscape Units							
Units		Coverage Areas (km^2) (%)		Characteristic of the Unit at Pindaré River Basin			
				Geology	Slope	Soils	Land Use and Land Cover
Alluvial Plain	1a	81,00	1,17	Alluvial Deposits	0,00 a 3,00 %	Gleisols	Pasture with vestiges of forest vegetation
	1b	56,78	0,82	Alluvial Deposits	0,00 a 3,00 %	Gleisols	Grassland and forest vegetation in riparian zones
	1c	24,32	0,35	Alluvial Deposits	0,00 a 3,00 %	Neosols	Pasture with vestiges of forest vegetation
	1d	14,39	0,21	Alluvial Deposits	0,00 a 3,00 %	Neosols	Grassland and forest vegetation in riparian zones
	1e	19,33	0,28	Alluvial Deposits	0,00 a 3,00 %	Plintosols	Pasture with vestiges of forest vegetation
Fluvial-lacustrine Plain	2a	37,35	0,54	Alluvial Deposits	0,00 a 3,00 %	Gleisols	Pasture with vestiges of forest vegetation
	2b	106,54	1,54	Alluvial Deposits	0,00 a 3,00 %	Gleisols	Wetland with dense forest vegetation
	2c	37,20	0,54	Alluvial Deposits	0,00 a 3,00 %	Gleisols	Pastures in the middle of the lagoons with remnants of forest vegetation
	2d	19,62	0,28	Alluvial Deposits	0,00 a 3,00 %	Neosols	Pasture with vestiges of forest vegetation
	2e	37,38	0,54	Alluvial Deposits	0,00 a 3,00 %	Neosols	Grassland and forest vegetation in riparian zones
	2f	37,83	0,55	Alluvial Deposits	0,00 a 3,00 %	Neosols	Open Forest Vegetation
	2g	5,72	0,08	Alluvial Deposits	0,00 a 3,00 %	Neosols	Wetland with dense forest vegetation
	2h	22,38	0,32	Alluvial Deposits	0,00 a 3,00 %	Plintosols	Pasture with vestiges of forest vegetation
	2i	13,18	0,19	Alluvial Deposits	0,00 a 3,00 %	Plintosols	Dense forest vegetation
	2j	1,37	0,02	Alluvial Deposits	0,00 a 3,00 %	Plintosols	Grassland and forest vegetation in riparian zones
	2k	1,34	0,02	Alluvial Deposits	0,00 a 3,00 %	Plintosols	Wetland with dense forest vegetation
	2l	5,79	0,08	Alluvial Deposits	0,00 a 3,00 %	Plintosols	Open Forest Vegetation
	2m	430,93	6,21	Fluvial-lacustrine deposits	0,00 a 3,00 %	Gleisols	Lakes and Lagoons
	2n	111,85	1,61	Fluvial-lacustrine deposits	0,00 a 3,00 %	Neosols	Lakes and Lagoons
	2o	0,61	0,01	Fluvial-lacustrine deposits	0,00 a 3,00 %	Neosols	Dense forest vegetation
	2p	0,91	0,01	Fluvial-lacustrine deposits	0,00 a 3,00 %	Neosols	Dense forest vegetation
	2q	2,58	0,04	Fluvial-lacustrine deposits	0,00 a 3,00 %	Plintosols	Dense forest vegetation
	2r	10,49	0,15	Fluvial-lacustrine deposits	0,00 a 3,00 %	Plintosols	Pasture with vestiges of forest vegetation
	2s	0,57	0,01	Fluvial-lacustrine deposits	0,00 a 3,00 %	Plintosols	Lakes and Lagoons
	2t	5,55	0,08	Itapecuru Formation	0,00 a 3,00 %	Neosols	Pasture with vestiges of forest vegetation
	2u	5,31	0,08	Itapecuru Formation	0,00 a 3,00 %	Plintosols	Pasture with vestiges of forest vegetation
Fluvial-marine Plain	3a	24,36	0,35	Fluvial-lacustrine deposits	0,00 a 3,00 %	Gleisols	Grassland and forest vegetation in riparian zones
	3b	92,06	1,33	Fluvial-lacustrine deposits	0,00 a 3,00 %	Gleisols	Wetland area with grassland and forest vegetation
	3c	11,42	0,16	Fluvial-lacustrine deposits	0,00 a 3,00 %	Neosols	Grassland and forest vegetation in riparian zones
	3d	2,35	0,03	Fluvial-lacustrine deposits	0,00 a 3,00 %	Neosols	Pasture with vestiges of forest vegetation
	3e	1,69	0,02	Fluvial-lacustrine deposits	0,00 a 3,00 %	Neosols	Dense forest vegetation

Fluvial-marine Plain	3f	413,44	5,96	Fluvial-lacustrine deposits	0,00 a 3,00 %	Neosols	Wetland area with grassland and forest vegetation, with some temporary crops, mainly rice plantations.
	3g	89,32	1,29	Fluvial-lacustrine deposits	0,00 a 3,00 %	Plintosols	Grassland and forest vegetation in riparian zones
	3h	77,00	1,11	Fluvial-lacustrine deposits	0,00 a 3,00 %	Plintosols	Pasture with vestiges of forest vegetation
	3i	0,09	0,00	Fluvial-lacustrine deposits	0,00 a 3,00 %	Plintosols	Dense forest vegetation
	3j	25,59	0,37	Fluvial-lacustrine deposits	0,00 a 3,00 %	Plintosols	Open Forest Vegetation
	3k	3,36	0,05	Fluvial-lacustrine deposits	0,00 a 3,00 %	Plintosols	Mixed Vegetation
	3l	7,74	0,11	Swamp and mangrove deposits	0,00 a 3,00 %	Gleisols	Swamps and mangroves
Flattened Fluvial Terraces	4a	308,44	4,45	Itapecuru Formation	0,00 a 3,00 %	Plintosols	Pasture with vestiges of forest vegetation
	4b	53,01	0,76	Itapecuru Formation	0,00 a 3,00 %	Plintosols	Open Forest Vegetation
	4c	63,63	0,92	Itapecuru Formation	0,00 a 3,00 %	Plintosols	Dense forest vegetation
	4d	27,22	0,39	Itapecuru Formation	0,00 a 3,00 %	Plintosols	Urban Area
Smoothly Undulating Surfaces	5a	984,48	14,19	Itapecuru Formation	3,01 a 8,00 %	Argisols	Pasture with vestiges of forest vegetation
	5b	25,87	0,37	Itapecuru Formation	3,01 a 8,00 %	Argisols	Dense forest vegetation
	5c	14,79	0,21	Itapecuru Formation	3,01 a 8,00 %	Argisols	Urban Area
	5d	28,11	0,41	Itapecuru Formation	3,01 a 8,00 %	Argisols	Open Forest Vegetation
	5e	1,25	0,02	Itapecuru Formation	3,01 a 8,00 %	Gleisols	Pasture with vestiges of forest vegetation
	5f	2,17	0,03	Itapecuru Formation	3,01 a 8,00 %	Gleisols	Open Forest Vegetation
	5g	29,68	0,43	Itapecuru Formation	3,01 a 8,00 %	Neosols	Pasture with vestiges of forest vegetation
	5h	2302,30	33,18	Itapecuru Formation	3,01 a 8,00 %	Plintosols	Pasture with vestiges of forest vegetation
	5i	176,03	2,54	Itapecuru Formation	3,01 a 8,00 %	Plintosols	Open Forest Vegetation
	5j	10,75	0,15	Itapecuru Formation	3,01 a 8,00 %	Plintosols	Urban Area
	5k	37,89	0,55	Itapecuru Formation	3,01 a 8,00 %	Plintosols	Dense forest vegetation
	5l	863,02	12,44	Itapecuru Formation	3,01 a 8,00 %	Plintosols	Pastures with large fragments of dense forest vegetation
Undulating Surfaces	6a	50,36	0,73	Itapecuru Formation	8,01 a 20,00%	Argisols	Pasture with vestiges of forest vegetation
	6b	81,32	1,17	Itapecuru Formation	8,01 a 20,00%	Plintosols	Pasture with vestiges of forest vegetation
Strongly Undulating Surfaces	7a	26,93	0,39	Itapecuru Formation	20,01 a 45,00%	Argisols	Pasture with vestiges of forest vegetation
	7b	12,60	0,18	Itapecuru Formation	20,01 a 45,00%	Argisols	Open Forest Vegetation

is to recover the areas with native vegetation, and to intensify the restriction on the entry of cattle on the banks of water sources. Actions that may bring environmental valuation to the region, and, as the "the gateway" to the Baixada of Maranhense, the silting of downstream areas (fluvial-lacustrine and fluvial-marine environments) may be reduced, as well.

LU2 - Fluvial-lacustrine Plain – Unit associated with the bottom of valleys, lakes, ponds, and impoundments of the Baixada Maranhense, as well as the entire plain related to these water bodies. It is a depositional environment characterized by an extremely flat relief and low altimetry amplitude. The extensive areas are periodically flooded by the regular rains that occur from January to July. Due to the lacustrine environments, the substrate rocks are mostly fluvial-lagoon deposits, a recent formation dating from the Quaternary and a result of intense sedimentation processes (sand, silt and gravel) of lagoon and fluvial environments. The soils are diverse, however, all clay-bounded and rich in organic matter. The units encompass 894.51 km^2 or 12.89%, and are distributed over twenty-one subunits. The number of sub-units is explained by the rich geodiversity, varied soils, rock formations, and different forms of land use and land cover. The extensive flat plain relief differs from the fluvial plains, linked to lakes, lagoons and islands (Figure 6). On the islands, it occurs the Itapecuru formation, a distinct rock formation where pasture with remnants of forest vegetation predominate.

Extensive wetlands with dense and open forest vegetation (ombrophilous forest) cover the unit, however, the presence of pastures is a fact, impacting the quantity and quality of water sources. We highlight that on the banks of the units, urban areas of the Baixada Maranhense, such as the cities of Viana, Monção, Cajari and Penalva, are

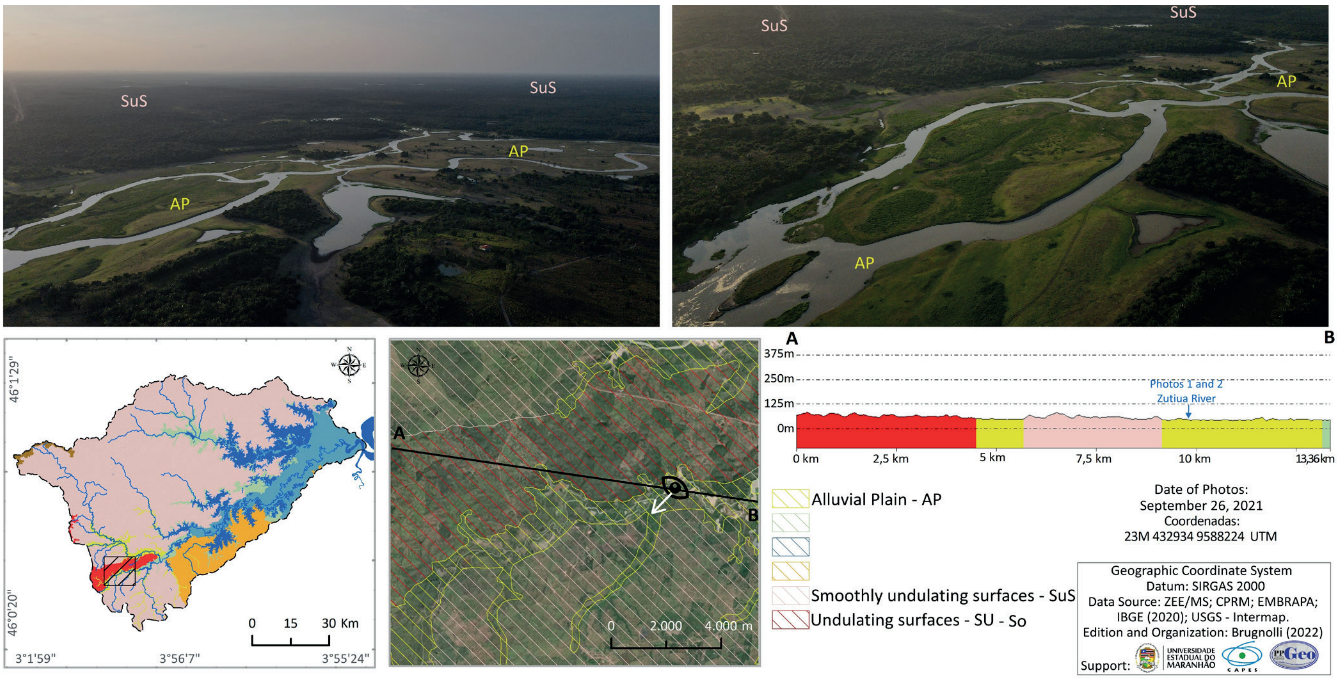

Fig. 5. River Plain near the confluence of the Zutiua River in the Pindaré River

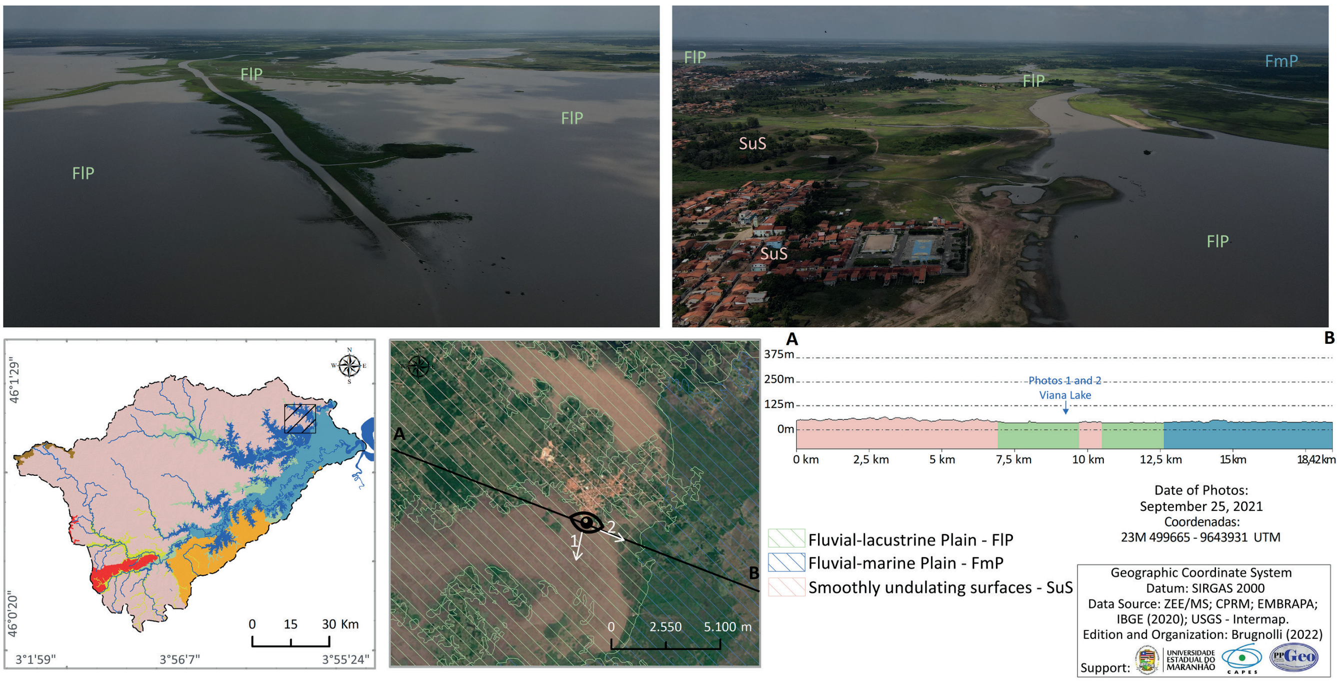

Fig. 6. Fluvial-lacustrine Plain characterized by lagoons, lakes, and islands

affected by the seasonality caused by the floods in the region. The limitations of these sub-units are mainly linked to the saturated soil, and their margins demand protection and preservation. However, the Forest Code (Brasil, 2012), which is responsible to safeguard them, however, it is not applied or supervised. The banks of the lakes have been replaced by pastures as urban areas advance towards them and large part of the population lives from fishing. In addition, the urban areas suffer from recurring floods, causing annual losses for residents. Thus, another issue emerges as the municipalities do not have a municipal sanitation policy, making the ponds dumping sites of solid waste and their waters lose qualitative levels. In this way, it is recommended the restoration of the environmental value of such units by recovering the margins of the lagoons, and retreating the advance of pastures over the wetlands.

LU3 – Fluvial-marine Plain - The unit is linked to the interactions of fluvial and marine processes with coastal sedimentary deposits, swamps, and mangroves with recent colluvium and alluvium (Quaternary) adjusted to the general base level. It presents flat topography, reaching no more than 3%. The extensive plain covers the entire lower course of the Pindaré River, linked to anastomosing and meandering channels that intertwine and interconnect with the fluvial-lacustrine lakes of the unit. The gleysol, neosol, and plinthosol soils present water saturation and floods occur periodically. Therefore, the vegetation that covers the soil offers protection to it due to great amount of natural vegetation, grassland and dense open forest. The ombrophilous vegetation makes the riparian zone the most preserved in the Baixada Maranhense, despite presenting extensive pastures. Salinization occurs in the area affecting the local residents who depend on fishing in the Pindaré River and its tributaries. The LU3 presents 12 sub-units that together cover 748.40 km^2 or 10.79% of the total lower course. An intensive geodiversity occurs in the area with swamps and mangroves (hydrophilic floodplain fields) close to the Pindaré River. Rice is the temporary crop present close to the river mouth, due to the humidity and periodically flooded area. However, it brings environmental damage, such as the construction of drains diverting water runoff, transforming and fragmenting the landscape, as well as over consumption of water available. The sub-units present significant limitations and weaknesses, from the rocky substrate formed by unconsolidated and recent sediments to fragile soils and areas with legal restrictions. Moreover, they present preserved areas, so the recommendation is to maintain the native vegetation with profound restrictions on the advancement of pastures. However, pastures have been identified in the region. In areas where the landscape has already been altered due to crops and/or pastures, a more adequate management may be applied to reduce the construction of drains for crops, and to preserve of the streams that supply the region and regulate the water level of rivers.

LU4 – Flattened fluvial terraces - The unit covers a total of 452.31 km² or just 6.52% of the Baixada Maranhense, and it is represented over four units predominantly formed by the Itapecuru Formation and plinthosols. The terraces occupy higher levels than the plains, showing the periods of evolution. Morphologically, they present flattened levels, lower than 3%, though, not affected by the flood of rivers. The sub-units are located in the southeastern section of the lower course of the Pindaré River, and according to Christofoletti (1980), characterized by the abandonment of the floodplain due to climatic oscillations, mass movements, tectonics, and change in the regime and hydraulic potential of the river. They characterize old units that went through long transformation and sedimentation processes, which left it at higher altimetric levels. It is a watershed between the lower course of the Pindaré and Mearim Rivers that favors occupation, as they are not affected by floods. Pastures predominate the area, and some subunits present open forest vegetation, others present dense vegetation. One unit presents urban area, which corresponds to the municipality of Santa Inês with 77,282 inhabitants, and the highest population in the lower course, according to the Brazilian Institute of Geography and Statistics (Instituto Brasileiro de Geografia e Estatística - IBGE - 2010). The areas present few limitations since their rocks, soils, and relief comprise the current pastures. However, the riparian zones are degraded, many open clearings and pastures entering the water sources, and even the margins of the lakes of the fluvial-lacustrine unit. Thus, we recommend to alter and recompose such areas, but there is no need to change pastures that are out of the Permanent Preservation Areas (PPA) as long as they present land management.

LU5 – Smoothly undulating surfaces - It covers the largest area of the lower course, 4476.33 km² or 64.51% of the total, characterizing the Baixada Maranhense region. Although it presents several sub-units, due to the local geodiversity the topography is Smoothly undulating, below 8% declivity, and the relief linked to an old geological formation, the Itapecuru. They present sandstone, siltstone and shale terrains, subjected to erosional development. The twelve subunits differ by soils (argisols, gleysols, neosols and plinthosols), land use and land cover, displaying extensive degraded areas, pastures that advance to the PPAs, and spaced patches of open forest vegetation. About 70% of the unit present pastures with few remnants of forest vegetation, the rest is divided into urban areas and dense, and open forest vegetation. Pastures predominate the Baixada Maranhense region, part of them in fallow and others with cattle and buffaloes. We highlight two major exceptions, as the dense ombrophilous forests to the north and northwest of the lower course, and a subunit in the central part of the study area which is located in the Pindaré River Indigenous Land. According to satellite images and by the definition of landscape units, this subunit (Indigenous Land) presents the highest density of forest vegetation in the entire Baixada Maranhense. In addition, other typical regional vegetations occur, such as the babassu, characteristic of an ecotone related to the Cocais Forest. Facts that reinforce the relevance exerted by the Indigenous Land. However, the edges of the area present deforestation and the advance of pastures already. Although being suitable for exploration due to its flattened relief, it presents serious environmental problems. Thus, we recommend that the exploration respect the productive potential of the unit. The current functions may proceed as long as conservation practices are taken, and native vegetation preserved.

LU6 – Undulating Surfaces - The unit is located in small territorial portions to the west of the lower course of the Pindaré River Basin. It is a transition area between the medium course (undulating relief) and the lower course, where, according to the Geological Survey of Brazil -CPRM (2013), several geological faults occur, especially directional waste. The sub-units present ancient geological formation, such as the Itapecuru, superimposed by argisols and plinthosols. Subjected to erosional development, the undulating relief of the units reaches 8.01% to 20.00% slope, and pastures predominate the land use with remnants of forest vegetation. The open forest vegetation characterizes the degradation and fragmentation of the unit, covering 131.67 km² or 1.90% of the lower course.

LU7 – Strongly undulating surfaces - The unit is located in the northwest of the lower course of the Pindaré River Basin in areas of watersheds, where high altimetric levels begin. The area characterizes the beginning of the middle course of the PRB with tabular plateaus, and the watershed of the Turiaçu River (to the north). The sub-units face significant deforestation process with pastures covering the region with ombrophilous vegetation. Few remnants of dense forest vegetation remain. The soils are predominantly formed by argisols, which are characteristic of high regions as watersheds, and its geology encompasses the Itapecuru Formation. Despite the significant differences, especially in relief, they cover small territorial portions (39.53 km² or 0.57%), and the delimitation and distinction from the others proved to be necessary due to the strongly undulating topography with slopes reaching up to 45%. Assessing the Pindaré River Basin and its lower course, named Baixada Maranhense, requires entering and researching an area that has been little studied in its environmental context. As in other regions of Maranhão, the researches related to environmental issues and landscape cartography are still scarce. The methodology used in here is not widely applied regionally, making this study relevant from a conceptual, methodological, and application view.

DISCUSSION

The lower course of the Pindaré River Basin presents significant damages. Thus, the resilient capacity of this environmental system may be affected unless urgent measures are taken. We highlight that regardless of the fragile soils, the geoecological stability is present in places with dense ombrophilous forests, wetlands with grassland and/or forest vegetation, lakes, swamps and mangroves, riparian zones with grassland and forest vegetation. These areas correspond to 22% of the total area and free of land use conflicts. Therefore, it is essential to prioritize the vegetation maintenance and to inspect river courses in order to monitor the local water dynamics and surface waters in quantitative and qualitative terms. In medium and long term, the lack of protection and inspection may lead to the domain of pastures all over the region, fragmenting the landscape, affecting surface waters, as well as the entire geoecological stability. The geoecological instability is a concern for those areas that present pastures with few remnants of forest vegetation. According to García-Rivero et al. (2019) and Brugnolli et al. (2022), landscapes undergo significant changes in spatial and functional structure in unstable areas, and may not fulfill their functions and services properly. The flattened relief favors the establishment of pastures in the unstable areas, despite the fragile soils. The intensive land use overlaps the functional capacity of landscapes. These locations cover 60% of the low course of the Pindaré River Basin. The scenario becomes obscure and critical in medium and long-term, generating serious and numerous ecological/environmental, economic and social damages. Similar facts were found in the work of Rocha; de Lima; Adami (2021). Thus, the area demands urgent mitigation measures to restore the geoecological value.

According to Pinton and Cunha (2014), García-Rivero et al. (2019), and Brugnolli and Salinas Chávez (2021), the gradual loss of geoecological functions leads to a high level of instability. The internal relationships between landscape components lose strength, translating into the decrease of productive potential and biological productivity, and the development of intense soil degradation processes and water resources. We highlight that the whole Baixada Maranhense region - the territorial portion in the lower course of the Pindaré River Basin - is defined as an area for preservation with “very high” and “extremely high” priority indices by the Brazilian Institute of Geography and Statistics (IBGE - Instituto Brasileiro de Geografia e Estatística) and the Institute of Socioeconomic and Cartographic Studies of Maranhão (IMESC - Instituto Maranhense de Estudos Socioeconômicos e Cartográficos). Yet, 35% of the lower course of the PRB is located in an Environmental Protection Area - EPA (APA -Área de Proteção Ambiental) in agreement with the National System of Units of Conservation (SNUC - Sistema Nacional de Unidades de Conservação). However, the reality is devoid of social, economic and, environmental preservation and conservation strategies. According to the National System of Units of Conservation (SNUC - BRASIL, 2000), the definition of an EPA is an extensive area with a certain degree of human occupation, endowed with abiotic, biotic, aesthetic or cultural attributes, especially important for the quality of life and well-being of populations. The paramount target is to protect biological diversity, discipline the occupation process, and ensure the sustainability of its natural resources.

Therefore, despite having and allowing human occupation, the impacts on the landscape affect the biological communities and the physical and social components of the area. The Baixada Maranhense region has been seriously impacted, unlinking the basic EPA premise, which is the sustainable use.

CONCLUSIONS

The theories and methods related to landscape cartography and the definition of its units are linked to the integrated analysis and comprehension of the basin as a manifestation of geosystems. Each geosystem with its own structure, dynamics, functioning, and evolution. Studying the Baixada Maranhense through environmental indicators allowed us to apply the methodology described here, supported by field trips and use of a drone to investigate and validate the landscape and other components. Within landscape cartography, the use of these indicators and new ways of correlating data is appropriate, and requires care and validation. Facts that allowed to define the region as a complex landscape in the State of Maranhão, where the heterogeneity of the units is striking and consistent with the water potential and geomorphological complexity. The anastomosing and meandering drainage channels, lakes, lagoons and streams shape and define social and economic characteristics of the region. In the field work, we identified cattle and buffalo pastures; areas with rice plantations that modify and fragment the landscape of units periodically flooded near the mouth of the Pindaré River; and areas where forest vegetation is persistently affected by anthropic action, as the Indigenous Land of the Pindaré River. By applying the methodology and correlating the Synthesis Map, Landscape and water and geomorphological dynamics, we reached the objectives outlined and ratified the hypothesis raised at the beginning of the present article. Agriculture has been impacting and fragmenting the landscape of the lower course of the PRB, changing and reducing the its potential, as well as damaging the landscape functioning.

Based on the analyzes discussed here, an alert has been given to the public bodies, since the Baixada Maranhense presents significant water potential, and its water sources are one of the main income sources for its inhabitants. It is envisaged that this work may bring data and/or solutions to the difficulties identified in the landscape units, permeating geoecological sustainability. This, precisely, is the prism of Landscape Geoecology and Landscape Cartography.

One of the great contributions made by this article regarding the modeling of landscapes through GIS, is to find paths tied to the sequence and mode of interaction of the data. Using the method of landscape levels has enabled us to define relief as a prominent element and that guiding component in the compartmentalization of landscapes. From this, the compartmentalization is carried out according to the taxonomic level one wants to reach. This type of methodology becomes applicable in other areas of the Amazon, in floodable areas, as well as areas that have insufficient data, as is the case of this research region.

For this reason, the study aims to contribute by subsidizing data for the planning and physical-territorial management of the lower course of the Pindaré River, as well as supporting the future adoption of a committee for the Pindaré River Basin, facing its environmental, economic, and social potential.

REFERENCES

Almeida J.L., Silva V.A.R., Santos J.S., Santos J.R.N., Araújo M.L.S., Pyles M.V., Silva F.B. (2020). O cenário de fragilidade ambiental do baixo curso do rio Mearim. Revista Brasileira de Geografia Física, 13(1), 102-120.

Amorim J.A.F. (2015). Análise e modelação da mudança da ocupação e uso do solo: Caso de estudo da bacia hidrográfica do Rio Vez. Dissertação (Mestrado em Gestão Ambiental e Ordenamento do território) - Instituto Politécnico de Viana do Castelo, Escola Superior Agrária, Ponte de Lima.

Brasil. Lei nº 12.651, de 25 de maio de 2012. Dispõe sobre a proteção da vegetação nativa; altera as Leis nºs 6.938, de 31 de agosto de 1981, 9.393, de 19 de dezembro de 1996, e 11.428, de 22 de dezembro de 2006; revoga as Leis nºs 4.771, de 15 de setembro de 1965, e 7.754, de 14 de abril de 1989, e a Medida Provisória nº 2.166-67, de 24 de agosto de 2001; e dá outras providências. Diário Oficial da União, Brasília-DF, 25 de maio de 2012.

Brasil. Lei no 9.985, de 18 de julho de 2000. Regulamenta o art. 225, § 1o, incisos I, II, III e VII da Constituição Federal, institui o Sistema Nacional de Unidades de Conservação da Natureza e dá outras providências. Diário Oficial da União, Brasília-DF, 18 de julho de 2000.

Brugnolli R.M., Salinas Chávez, E., Silva, C.A., Berezuk, A.G. (2022). Geoecological diagnosis of landscapes of the Formoso River Watershed, Bonito/MS, Brazil. Environmental Earth Sciences, 81, 1-19. DOI:10.1007/s12665-022-10247-6.

Brugnolli, R.M. (2020). Zoneamento Ambiental para o Sistema Cárstico da Bacia Hidrográfica do Rio Formoso, Mato Grosso do Sul. Tese (Doutorado em Geografia) - Universidade Federal da Grande Dourados, Dourados.

Brugnolli R.M., Salinas Chávez, E. (2021). Estado geoecológico das paisagens da bacia hidrográfica do córrego Formosinho, Bonito/MS - Brasil: bases para a gestão territorial. Geofronter, 7, 01-26.

Cavalcanti L.C.S. (2014). Cartografia de Paisagens: Fundamentos. São Paulo: Oficina de Textos.

Christofoletti A. (1980). Geomorfologia. São Paulo: Edgard Blücher.

Comerlato T., Lamour M., Silveira C. (2020). Mapeamento digital de formas de relevo no ambiente costeiro do Paraná. Caminhos de Geografia, Uberlândia, 21(73), 477-491. DOI: 10.14393/RCG217349608

Costa-Neto J. P., Barbieri R., Ibañez M.S.R., Cavalcante P.R.S., Piorski N.M. (2002). Limnologia de três Ecossistemas Aquáticos característicos da Baixada Maranhense. Boletim Laboratório de Hidrobiologia, São Luís, 15, 50-67. DOI: https://doi.org/10.18764/.

CPRM, Serviço Geológico do Brasil. Geodiversidade do Estado do Maranhão. Teresina: CPRM. 2013.

Cunha E. R., Santos C. A. G., Silva R. M., Bacani V. M., Teodoro P. E., Panachuki E., Oliveira N. de S. (2020). Mapping LULC types in the Cerrado-Atlantic Forest ecotone region using a Landsat time series and object-based image approach: A case study of the Prata River Basin, Mato Grosso do Sul, Brazil. Environmental Monitoring and Assessment, 24;192(2):136. DOI: 10.1007/s10661-020-8093-9.

De Pablo C.L., Martín de Agar P., Gómez S.A.L, A. (1988). Descriptive capacity and indicative value of territorial variables in ecological cartography. Landscape Ecology 1, 203–211.

Empresa Brasileira de Pesquisa Agropecuária. (2018). Sistema Brasileiro de Classificação de Solos. Brasília, DF: EMBRAPA.

Gao H., Sabo J.L., Chen X., Liu Z., Yank Z., Ren Z., Liu M. (2018). Landscape heterogeneity and hydrological processes: a review of landscape-based hydrological models. Landscape Ecol 33, 1461–1480. DOI: 10.1007/s10980-018-0690-4.

García-Rivero A.E., Miravet B.L.S., Salinas Chávez E., Dominguez A.Z.G. (2019). A cartografia das paisagens com sistemas de informação geográfica como base para o diagnóstico geoecológico da bacia hidrográfica do rio Ariguanabo (Cuba). Revista da ANPEGE, Dourados, 15(27), 169-194. DOI: 10.5418/RA2019.1527.0006.

Hernández J.R.S., Pérez J.L.P.D., Vergés F.R., Villalobos M.D., Méndez A.P.L., Navarro E.S. Clasificación geomorfométrica del relieve mexicano: una aproximación morfográfica por densidad de curvas de nivel y la energía del relieve. Investigaciones Geográficas, 94, 1-15. 2017. DOI: 10.14350/rig.57019.

IBGE. Cidades. 2010. Available at: https://cidades.ibge.gov.br/. Accessed in: 11 feb. 2022.

Khoroshev A.V. (2019). Multiscale Organization of Landscape Structure in the Middle Taiga of European Russia. Landscape Online, 66. DOI: 10.3097/LO.201966.

Littell J.S., Mckenzie D., Wan H.Y., Cushman S.A. (2018). Climate change and future wildfire in the western United States: an ecological approach to nonstationarity. Earth's Future 6, 1097–1111. DOI: 10.1029/2018EF000878.

Machado M.A., Pinheiro C.U.B. (2016). Da água doce à água salgada: mudanças na vegetação de igapó em margens de lagos, rios e canais no baixo curso do rio Pindaré, Baixada Maranhense. Revista Brasileira de Geografia Física, Recife, 9(5), 1410-1427.

Mapbiomas. Plataforma de Mapas e Dados – Coleção 6. 2020. Available at: https://plataforma.brasil.mapbiomas.org/. Accessed in: 12 feb. 2022.

Maranhão. Decreto nº 11.900 de 11 de junho de 1991. Cria, no Estado do Maranhão, a Área de Proteção Ambiental da Baixada Maranhense, compreendendo 03 (três) Sub-Áreas: Baixo Pindaré, Baixo Mearim-Grajaú e Estuário do Mearim-Pindaré – Baía de São Marcos incluindo a Ilha dos Caranguejos. Diário Oficial do Estado do Maranhão, São Luís-MA, 11 de junho de 1991.

Maranhão. Lei Estadual 9.957, de 18 de novembro de 2013. Dispõe sobre a instituição do Comitê da Bacia Hidrográfica do Rio Mearim, de acordo com art. 43, V, da Constituição do Estado do Maranhão, c/c art. 29, III, da Política Estadual de Recursos Hídricos – Lei 8.149, de 15 de junho de 2004. Diário Oficial do Estado do Maranhão, São Luís – MA, 18 de novembro de 2013.

Mateo Rodríguez J.M., Silva E.V. da., Cavalcanti A.P.B. (2013). Geoecologia das Paisagens: uma visão geossistemica da análise ambiental. Fortaleza, CE: Editora UFC.

Newman E. A., Kennedy M. C., Falk D. A., Mckenzie D. (2019). Scaling and complexity in landscape ecology. Frontiers in Ecology and Evolution, 7(293). DOI: 10.3389/fevo.2019.00293

Pinton L.G., Cunha C.M.L. (2014). Diagnóstico do estado geoambiental da área urbana do município de Cubatão (SP). Sociedade & Natureza, 26(2). DOI: 10.1590/1982-451320140211.

Rocha N., de Lima A., Adami M. (2021). Forest Fragmentation And Landscape Structure In The Guamá River Basin, Eastern Amazon. Geography, Environment, Sustainability, 14(3), 32-40. DOI: 10.24057/2071-9388-2020-130.

Rodrigues F.H., Coelho J.M., Santos F.S.M., Amaral A.M.C., Zaine J.E. (2014). Avaliação da possibilidade de erosão natural e induzida na bacia hidrográfica do ribeirão das pedras, Quirinópolis (GO). Geociências, 2, 339-359.

Salinas Chávez E., Ribeiro A.F.N. (2017). La cartografía de los paisajes con el empleo de los Sistemas de Información Geográfica: Caso de estudio Parque Nacional Sierra de Bodoquena y su entorno, Mato Grosso do Sul, Brasil. Geografia y Sistemas de Información Geográfica (GeoSIG), 9(9), 186-205.

Serrano D.G. (2012). El papel del relieve en la definición de unidades de paisaje. el caso de Muntanyes d'Ordal (Barcelona). Cuadernos de Investigación Geográfica, 38(2), 123-145. DOI: 10.18172/cig.1286.

United States Geological Survey. MDT/SRTM. 2000. Available at: https://earthexplorer.usgs.gov/. Accessed in: 23 may. 2021.

Yesuph A.Y., Dagnew A.B. (2019). Land use/cover spatiotemporal dynamics, driving forces and implications at the Beshillo catchment of the Blue Nile Basin, North Eastern Highlands of Ethiopia. Environmental System Research, 8, 21, 1-30, DOI: 10.1186/s40068-019-0148-y.

Zonneveld J.I.S. (1995). Land Ecology, An introduction to Landscape Ecology as a base for Land Evaluation, Land Management and Conservation. Amsterdam: SPB Academic Publ.

AUTHOR CONTRIBUTIONS: Rafael B. Medeiros: Conceptualization, Design. Data collection. Data analysis. Methodology. Manuscript drafting. Review and approval of the final version of the paper. Luiz Carlos A. dos Santos: Conception. Supervision. Data collection. Data analysis. Writing of the manuscript. Review and approval of the final version of the paper. Jose Fernando R. Bezerra: Conception. Data collection. Data analysis. Writing of the manuscript. Review and approval of the final version of the work. Ana Rosa Marques and Gabriel Irvine Ferreira Alves dos Santos: Design. Supervision. Data collection. Validation. Data analysis. Reviewing and Editing.

COMPETING INTERESTS:
Conflicts of interest/Competing interests (include appropriate disclosures): Not applicable.
Ethics approval (include appropriate approvals or waivers): Not applicable.
Consent to participate (include appropriate statements): Not applicable.
Consent for publication (include appropriate statements): Not applicable.
Availability of data and material (data transparency): Not applicable.
Code availability (software application or custom code): Not applicable.

RESEARCH PAPER

ARSENIC IN SURFACE WATERS IN THE CENTRAL PART OF THE NORTH CAUCASUS AND CORRESPONDENT HEALTH RISK ASSESSMENT

Nina V. Reutova*, Tatiana V. Reutova, Fatima R. Dreeva, Akhed M. Khutuev
Kabardino-Balkar Scientific Center of the Russian Academy of Sciences Center for Geographical Research
*Corresponding author: reutova371@mail.ru
Received: January 25th, 2023 / Accepted: November 14th, 2023 / Published: December 31st, 2023
https://DOI-10.24057/2071-9388-2023-2748

ABSTRACT. Arsenic is ranked as a significant global health hazard associated with potable water. The present study assesses the arsenic pollution of the surface waters in the mountainous regions of the central part of the North Caucasus due to the presence of geochemical anomalies and the potential health risk by its consumption for the residents. The studies were carried out from 2016 to 2022. The surface waters of 5 main rivers of the region (Kuban, Malka, Baksan, Chegem and Cherek) with their main tributaries have been studied. Samples were taken during the period of intensive melting of glaciers (summer). The determination of the soluble form of arsenic was carried out using the method of atomic absorption spectrometry. In general, arsenic concentrations in this region are lower than Clark values for river waters. Along with this, watercourses with high and very high concentrations of arsenic have been identified. Elevated concentrations of arsenic in surface waters spatially coincide with the location of geochemical anomalies. The most polluted is the Baksan River. The levels of surface waters pollution from natural and anthropogenic sources are almost the same (up to 100 μg/dm^3). In this regard, an assessment of the health hazard was carried out. For residents receiving drinking water from wells located at the southern foot of Elbrus, the carcinogenic risk for adults was 4.51×10^{-4}, which is unacceptable for the general population. The non–carcinogenic risk was 1.00 - the maximum permissible risk causing concern.

KEYWORDS: arsenic geochemical anomalies, carcinogenic risk, non-carcinogenic risk, North Caucasus, surface waters

CITATION: Reutova N. V., Reutova T. V., Dreeva F. R., Khutuev A. M. (2023). Arsenic In Surface Waters In The Central Part Of The North Caucasus And Correspondent Health Risk Assessment. Geography, Environment, Sustainability, 4(16), 52-62
https://DOI-10.24057/2071-9388-2023-2748

Conflict of interests: The authors reported no potential conflict of interest.

INTRODUCTION

The role of environmental geochemistry in the etiology of many types of cancer and other non-communicable diseases in some countries reaches 70% of cancer deaths worldwide. Their dependence on local geochemistry for drinking water and growing crops is still widespread (Middleton et al. 2020). Water pollution by heavy metals and metalloids is one of the global problems of our time. The problems of arsenic in the environment are recognized and identified in many countries of the world, in a wide range of geological and climatic conditions (Ahamad et al. 2020; Goswami et al. 2020; Murtaza et al. 2020; Wang et al. 2020). Drinking water is the highest single source of exposure to high arsenic levels by humans (Aderibigbe 2018). Arsenic is ranked as a significant global health hazard associated with potable water. This element is considered one of the most toxic to humans and can cause both carcinogenic and non-carcinogenic diseases. Thus, high concentrations of arsenic in potable water (≥50 μg/l) are the cause of lung, liver, kidney, bladder and skin cancers (Saint-Jacques et al. 2014; Goswami et al. 2020; Middleton et al. 2020). Children are more susceptible than adults to As poisoning (Ahamad et al. 2020; Goswami et al. 2020). There is a growing body of evidence that prenatal and early childhood exposure to arsenic from drinking water can have serious long-term health implications (Dauphine et al. 2011; Smith et al. 2012; Farzan et al. 2013). The presence of arsenic in potable water at concentrations ≥5 μg/l pose a threat to child development (Wasserman et al. 2014) and leads to arsenic neuropathy in adults (Chakraborti et al. 2003). A high correlation was found between the presence of arsenic in drinking water and its content in urine, blood (Kladsomboon et al. 2020), nails and hair (Goswami et al. 2020), which indicates the accumulation of this element in the human body.

The dependence of the chemical composition of soils, surface and groundwater on the geochemical characteristics of the region is well known. The chemical composition of these environmental components has a significant impact on public health (Aderibigbe et al. 2018; Middleton et al. 2020). In this regard, the study of the chemical composition of surface waters, which are the main source of potable water, is an urgent task.

The waters of mountain rivers are traditionally considered very clean. But mountains are areas of modern and ancient volcanism, which affects the chemical composition of these waters. The aim of this work is to study the arsenic pollution of the surface waters in the mountainous regions of the central part of the North Caucasus due to the presence of geochemical anomalies and to assess the potential health risk by its consumption for the residents.

The chemical composition of the waters of the Terek and the Kuban has been studied by a number of authors – Reshetnyak O.S., Komarov R.S. (2021), Lurie P.M., Panov V.D., Bazelyuk A.A. (2015), etc. Such data are summarized in the yearbooks "Quality of surface waters of the Russian Federation". But all these data relate only to the low-mountain zone and assess the anthropogenic impact. There are a small number of works with the results of surveys of the Baksan, Chegem and Cherek rivers in the high and mid-mountain zone (Central Caucasus) by a number of authors (Gazaev et al. 2014: Reutova T. et al. 2018; Ermakov et al. 2020), as well as the Kuban and Teberda rivers (Western Caucasus) (Degas et al. 2016; Onishchenko et al. 2016). But in all these works there is no data on the content of arsenic in the waters under study. The only works that provide data on arsenic are studies in the area of the Tyrnyauz tungsten-molybdenum factory (Bortnikov et al, 2013; Vinokurov et al. 2016). Thus, we studied the features of arsenic content in the surface waters of the mountainous zone of the Central and Western Caucasus for the first time.

MATERIALS AND METHODS

Study area

In the Western Caucasus region, we examined the upper reaches of the Kuban River and its main tributaries in mountainous areas. In the Central Caucasus region, the rivers Malka, Baksan, Chegem and Cherek, which are tributaries of the Terek River, were examined. The location of sampling points and As ore mineralization are shown in Fig. 1 and 2. The numbers of sampling points in the figures and in all tables are the same.

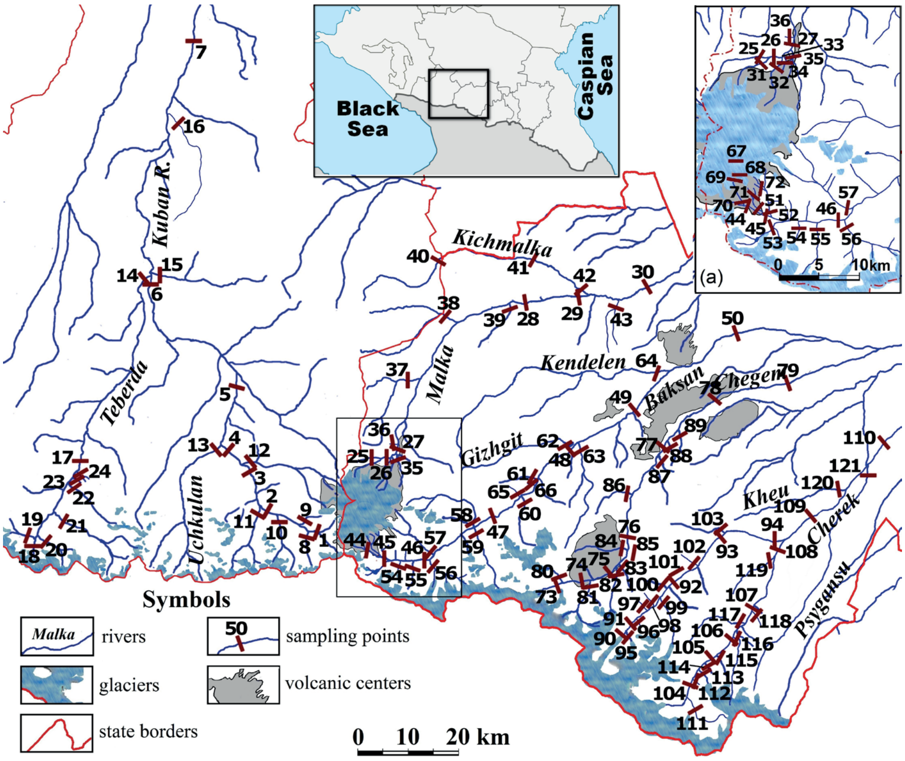

Fig. 1. Schematic map of sampling points

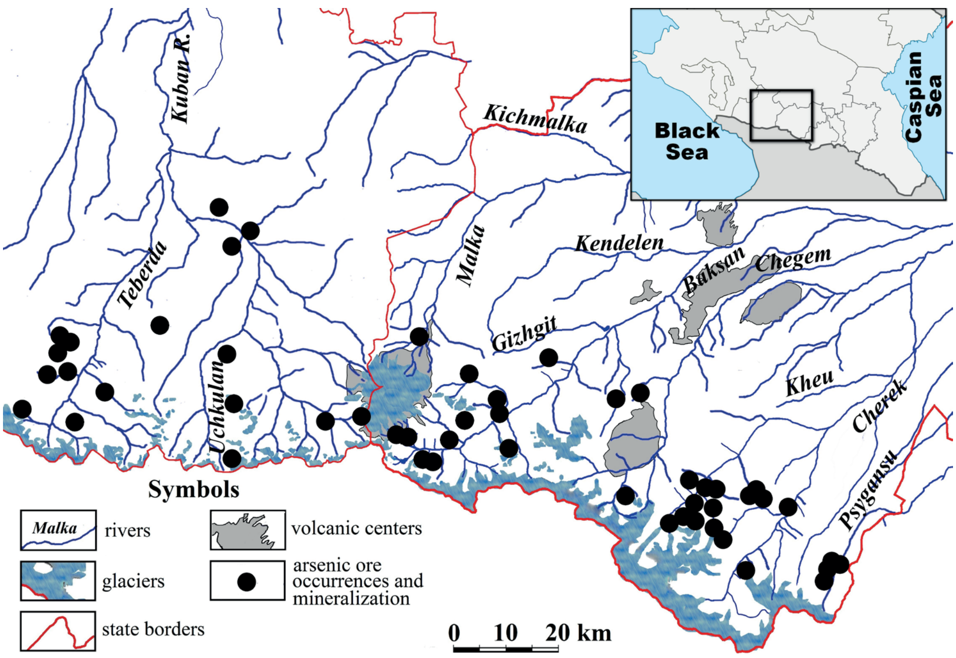

Fig. 2. Schematic map of deposits and ore mineralization of arsenic in the study area (according to Pis`menny`j et al. 2002; Pis`menny`j et al. 2013; Pis`menny`j et al. 2021; Semenukha et al. 2021)

Sample collection and processing

Samples were taken annually, during the summer floods (July – early August). During this period there is an intense melting of glaciers. In this regard, the differences between water bodies of various origins are well expressed. In addition, during the cold season, most of the objects in the highlands are inaccessible. All tables show the average values for 7 years (2016-2022). We determined only the dissolved form of arsenic. Sampling, processing and preservation of samples were carried out in accordance with GOST 17.1.5.05-85, GOST 31861-2012 and GOST R 59024-2020. Samples from a polyethylene sampler with a volume of 1 dm^3 were filtered *in situ* through membrane filters with a pore size of 0.45 microns (using syringe filter cartridges) into polypropylene tubes (15 ml) with screw caps. Preservation of samples for the determination of heavy metals was carried out with nitric acid (High Purity) at the rate of 0.5%. The samples were transported and stored at a temperature of 2°C - 5 °C.

Analysis methods

The hydrogen ion exponent in the samples was measured using a portable pH meter on the day of sampling. Arsenic concentrations were determined using the atomic absorption spectrometry (AAS) in accordance with GOST R 57162-2016. This method is widely used to determine concentrations of potentially toxic elements in natural waters (Ahamad et al. 2020; Brindha et al. 2020; Mallongi et al. 2022).

Statistical data processing was carried out using the Excel 2016 program to calculate the average values and coefficients of variation.

RESULTS AND DISCUSSION

Western Caucasus

Mountain region of the Kuban River basin.

For the Kuban River basin, we provide data on 24 sampling points (Table A.1). Of these, 7 samples were taken directly along the riverbed. For tributaries, data on the arsenic content in their mouth zone are given.

In the rivers waters the pH changes from neutral to weakly alkaline with increasing distance from the sources. We present the pH value in the tables due to the fact that it has a significant effect on the solubility and migration of arsenic in surface waters. Under oxidizing conditions (pH 5.7), As(III) migrates faster than As(V); under neutral conditions, migration of As(V) increases, but As(III) is still more mobile; at pH 8.3, migration of both forms of As increases significantly (Putilina et al. 2011).

Arsenic concentrations both along the riverbed of the Kuban River and its tributaries are lower than Clark for river waters (2 μg/dm^3) (Nikanorov 2008). Only two sampling points have high and very high concentrations of arsenic. These are the waters of the Shumka River (No. 24) and a water pipe on the highway (No. 23). In the latter, the concentration of arsenic is 15 times higher than the MPC for drinking water (10 μg/dm^3). This sampling point is a popular source of drinking water for the residents. In both of these objects, arsenic concentrations are very stable over the years, as evidenced by the low values of the coefficients of variation. Such stability is characteristic of waters of underground origin. The water flow in the water pipe is small. The Shumka River is also a small river. After the confluence of these tributaries, the concentration of arsenic in the waters of the Teberda river does not increase. In this zone there are mineralization points and geochemical arsenic halos associated with hydrothermal gold-arsenic mineralization (As up to 5.74%) (Semenukha et al. 2021). The main ore mineral is arsenopyrite.

Central Caucasus

Mountain region of the Malka river basin

There are 19 sampling points located in the area, 6 of them directly along the riverbed. The data is given in Table A.2.

Most of the river waters in the Malka River basin are neutral and slightly alkaline. There is a tendency to latch down the Malka River. This is typical not only for the waters of the river itself, but also for its tributaries.

Some geochemical anomalies of arsenic are located in the basin of the Malka River. This is the point of mineralization of the arsenic-polymetallic formation of the Sirkh and stream sediment sample with single signs of arsenic in the upper reaches of the Kichmalki River. In the surface waters of the studied area, arsenic concentrations were very low and ranged within 1 μg/dm^3 which is lower than the Clark value. Only in the water of the drinking spring (No. 33) and the Sultangarasu river (No. 34), located near the Sirkh mineralization point (Fig. 1,2), the concentration of arsenic was almost 4 μg/dm^3. We found no elevated concentrations of arsenic in the waters of the Kichmalka River (Reutova et al. 2021). But we took samples starting from the 22nd kilometer, and stream sediment sample with single signs of arsenic were detected in the upper reaches of this river.

Mountain region of the Baksan river basin.

There are 29 sampling points in the Baksan River basin. Table A.3 shows the average values of arsenic concentrations. This table also shows data on the arsenic content in meltwater flowing down the southern slopes of Elbrus.

An excess of 1.4-40.0 times in comparison with Clark values was noted in the water of 10 out of 29 sampling points. This indicates the enrichment of the surface waters with this element, which is due to the presence the rocks with a high arsenic content. One of them is the arsenic ore occurrence "Azau arsenic", which is located on the right, steep side of the Azau River valley, 2 km below the village Terskol. This ore occurrence is represented by three ore zones: Northern, Central and Eastern (Fig. 2). According to the Pis`menny`j (2013), the arsenic content reaches 9.52-10%. The main ore minerals are realgar, auripigment, galena, sphalerite, rarely cinnabar.

During the summer, it is possible to conduct a comparative analysis of arsenic concentrations in thawed streams flowing down from the southern slopes of Elbrus and in the rivers waters originating from these glaciers. Thus, in the meltwater flowing down the snowy slope near of "Priyut 11" (No. 67, Garabashi glacier, altitude 4000 m above sea level), arsenic concentrations ranged from 0.33-1.21 μg/dm^3. In the area of the Garabashi cable car station (No. 68, altitude 3800 m above sea level), where there is snow in summer, arsenic concentrations in meltwater were 0.7-1.69 μg/dm^3. And at the "Mir" station (No. 69, altitude 3500 m above sea level), where meltwater flows directly through the ground, arsenic concentrations become higher – 0.9-9.15 μg/dm^3. The Azau waterfall (No. 70), the waters of which are in contact with the rocks of the southern slopes of Elbrus for about 2 km, is also characterized by high concentrations of arsenic. This distribution of concentrations indicates that the rocks are the main source of arsenic in surface waters. This zone of arsenic mineralization causes extremely high natural arsenic contamination of the Garabashi River waters, originating from the southern slopes of Elbrus, and pollution to a lesser extent of the Terskol River, whose sources are located on the eastern slopes of Elbrus. One of the tributaries of the Garabashi River is the waterfall "Devich`i kosy" (No.

71), located on the southeastern slopes of Elbrus and having an underground origin. The water of this waterfall is characterized by high and very high concentrations of arsenic (2.01-107.78 µg/dm^3).

The sources of the Terskol River are located on the eastern slopes of Elbrus. The right tributary of this river is the waterfall "Terskol". It is located on the other side of the same offshoot of Elbrus mountain range as the waterfall "Devich`i kosy" and is characterized by a relatively high content of arsenic (Table A.3). After the confluence of these rivers into the Baksan River, arsenic concentrations in it also increase (No. 45).

Arsenic mineralization of Alpine age is also represented by the mineralization point "Irikskoye" (Fig. 2) (Pis`menny`j et al., 2013). But we did not find elevated concentrations of arsenic in the water of the Irik River.

Two points of mineralization are located in the area of the Kyrtyk river (Fig.2) (Pis`menny`j et al. 2013). In the water of the Kyrtyk river, we did not detect elevated concentrations of arsenic (Table A.3).

The highest arsenic content in rocks is characterized by the Gitche–Tyrnyauz deposit, where its content reaches 23.1% (Fig.2) (Pis`menny`j et al. 2013). The Tyrnyauz tungsten-molybdenum factory is located here. The extremely high arsenic pollution of the watercourses of this area is anthropogenic. These are the Kamyksu River (No. 61), the Bolshoy Mukulan (No. 65), the "Rudnik" stream (No. 66). Flowing into the Baksan River above the 60th kilometer (No. 48), they lead to an increase in the concentration of arsenic in the waters of the Baksan River (Table A.3).

Thus, the arsenic content in the surface waters of the Baksan River basin is due to its content in rocks and its sources are both natural and anthropogenic. The levels of surface waters pollution from natural and anthropogenic sources are almost the same (up to 100 µg/dm^3).

Mountain region of the Chegem river basin.

For the surface waters of the Chegem river basin, we provide data on 17 sampling points, of which seven are located directly along the riverbed (Table A.4).

All glacial rivers and most non-glacial rivers in the high-altitude zone of the Chegem River basin had a neutral or slightly alkaline reaction. Unlike the Baksan River basin, there are almost no geochemical anomalies with a high arsenic content in the Chegem River basin. Only the Kektash mineralization point in the upper reaches of the left tributary of the Chegem river (As content – 1%) (Pis`menny`j et al. 2021) and the Gubuchhan (Pis`menny`j et al. 2002), located in the basin of the Gara-Aususu river, were noted (Fig. 2). The concentrations of this element in the surface waters of this region are at the level of Clark values (Table A.4.).

A few dozen kilometers east of Elbrus is the ancient Verkhnechegem caldera with an age of about 2.8 million years (Chernyshev et al. 2014; Myshenkova and Koronovsky 2015). In the area of this caldera, the Chegem River flows up to the 30th kilometer. After the 30th to the 88th kilometer, the area of the Nizhnechegemsky plateau is located. It is characterized by the presence of acidic volcanites (tuffs), which are either aerally transferred products of the activity of the Verkhnechegem caldera, or they are associated with an independent center of Pliocene volcanism in this area (Chernyshev et al. 2014). Thus, this part of the Chegem riverbed flows through an area of ancient volcanism. But this did not affect the arsenic content in the surface waters in this region.

Mountain region of the Cherek river basin.

Since the Cherek River has two equivalent sources – the Bezengi Cherek and the Balkar Cherek –we present both of these rivers with their tributaries in Table A.5. There are 14 sampling points located on the Cherek Bezengiysky River, 5 of them along the riverbed. In the basin of the Balkar Cherek and the Cherek River itself, we provide data on 18 sampling points, 7 of which are located along the riverbed.

The majority of river waters are neutral or slightly alkaline, in the high-altitude zone, pH<8, in the lower zones, pH>8, but does not reach 8.5.

Many manifestations of arsenic locate in the upper reaches of the Cherek River basin from the interfluve of the Chegem River and the Bezengiysky Cherek River to the Psygansu (Fig. 2) (Pis`menny`j et al. 2002). There are also polymetallic ore represented by minerals such as chalcopyrite, pyrite, sphalerite, arsenopyrite, etc. (Kaigorodova and Petrov 2016). It affected the distribution of arsenic concentrations in the surface waters of the area. Thus, in two sampling points of the Chegem river basin, the sources of which are located on the border of the Chegem and Cherek Bezengiysky river basins (Nos. 82 and 83), arsenic concentrations are higher than in all other sampling points (Table A.4, Fig. 1,2). From the tributaries of the Cherek Bezengiysky River, higher concentrations of arsenic are characteristic of Nos. 97-99 (Table A.5). But they do not lead to a noticeable increase in arsenic concentrations in the waters of the Bezengiysky Cherek River.

In the basin of the Cherek Balkarsky river, the highest concentrations of arsenic were detected in the waters of a small stream (No. 112). In the waters of the river itself, the arsenic content increases from 33 to 58 km. In two tributaries flowing in this interval (Nos. 117 and 118), arsenic concentrations are also higher (Table A.5, Fig. 1,2). In general, the arsenic content in the surface waters of the Cherek river basin is higher than in the basins of the Kuban, Malka and Chegem rivers, but lower than in the Baksan River basin, which well reflects the geochemical features of these areas.

Thus, the dependence of arsenic concentrations in surface waters on the presence of geochemical anomalies is clearly traced in the mountainous areas of the river basins of the central part of the North Caucasus.

There is another region in the North Caucasus with a high arsenic content in drinking water. This is the Republic of Dagestan, where groundwater is used for water supply. The arsenic content in them ranged from 10-500 µg/l, which is significantly higher than in the study area. But in Dagestan, the arsenic content was estimated in groundwater, not in surface waters (Abdulmutalimova 2019).

Health risk assessment

According to S.F. Vinokurov and co-authors (2016), arsenic (as well as tungsten and molybdenum), unlike other trace elements, is found in the surface waters of this region in dissolved form. Consequently, it enters potable water in the same concentration as in surface waters.

As – code CAS 7440-38-2. According to the classification of carcinogens by the International Agency for Research on Cancer (IARC) and the US Environmental Protection Agency (EPA), arsenic is a carcinogen for humans. The affected organs and systems are the skin, central nervous system, nervous system, cardiovascular system, immune system, hormonal system (diabetes) and the gastrointestinal tract. To quantify the impact of drinking water with a high arsenic content on the health of the population, a methodology for assessing the risk to public health was used, within which an algorithm recommended by WHO and other leading international organizations was used.

The risk assessment for public health was carried out in accordance with the Human Health Risk Assessment from Environmental Chemicals. Manual P 2.1.10.1920—04.

For the mountainous region of the Kuban River basin, very high concentrations are characteristic of the sampling point No. 23 (Table A.1). Although this spring is popular among residents, it is not the main source of potable water. For the residents of the Tyrnyauz tungsten-molybdenum factory, the main source of potable water is the Baksan river. Arsenic concentrations in the river waters are not high, and the water intakes for the city of Tyrnyauz are located above the ore body. Therefore, we did not calculate the health risks to the population in these regions.

Potable water in the geologists' camp located at the Gitche-Tyrnyauz deposit contains 156 µg/dm^3 of arsenic. Potable water in the village Azau is obtained from water pipelines located directly on the southern slope of Elbrus, and the concentration of arsenic in it is about 35 µg / dm^3. Potable water from the well of the village Terskol is received by all hotels located below, contains 6.27-15.41 µg/ dm^3 (on average 11 µg/ dm^3). Therefore, for these areas with a high natural level of arsenic pollution, we calculated the risks to public health in accordance with the Human Health Risk Assessment from Environmental Chemicals. Manual P 2.1.10.1920—04.

The standard values of exposure factors for oral intake of chemicals with potable water for the geologists' camp were: exposure frequency (EF) 180 days/year, since the field season lasts from May to November, and exposure duration (ED) is 5 years (approximate average working time of one employee). The remaining values are standard (average body weight 70 kg and water ingestion rate 2.0 litre for adults). For this contingent, the carcinogenic risk (CR) was 2.35×10^{-4}, which corresponds to the third range (individual lifetime risk of more than 1×10^{-4}, but less than 1×10^{-3}) acceptable for occupational groups and unacceptable for the general population. This is a hazard risk. The non-carcinogenic risk (HQ) for this contingent was 1.22. If HQ > 1, this is a hazard risk. We reported the results to the head of the geologists' camp, the employees began to use bottled water.

For hotels and cafes located in the Azau glade, potable water comes from water pipelines located on the southern slopes of Elbrus. There is no health hazard for tourists living here for a short time. This drinking water can only pose a danger to employees of hotels and cable cars, who are mostly local residents. To calculate individual risks, we used standard values of exposure factors for oral intake of chemicals with drinking water according to Human Health Risk Assessment from Environmental Chemicals (365 days/year, 70 lifetime year for carcinogen and 30 year for adult and 6 years for children for non-carcinogen, average body weight 70 kg for adults and 15 kg for children, water ingestion rate 2.0 litre for adults and 1 litre for children). The carcinogenic risk (CR) for adults was 1.44×10^{-3}, which is unacceptable neither for the population nor for professional groups (extremely hazard, unacceptable risk). The non-carcinogenic risk (HQ) for this contingent was 3.20, which is significantly more than 1. But it should be noted that there are very few people who have been permanently residing in this village for many years.

For Terskol villagers receiving drinking water from the well, the carcinogenic risk for adults was 4.51×10^{-4}, which is unacceptable for the general population. The non–carcinogenic risk was 1.00 - the maximum permissible risk causing concern. Children are more vulnerable to As exposure than adults (Dauphine et al. 2011) and are therefore central to any such assessment. For children, the carcinogenic risk was 1.05×10^{-3}, which is unacceptable neither for the population nor for professional groups. The non-carcinogenic risk was 2.34. If we take into account that in this region there is also aluminum pollution associated with the presence of the Elbrus Neovolcanic Center (Reutova N. et al. 2018), the total risks to public health may be higher. This problem requires further study.

CONCLUSIONS

This study is novel in three ways: (a) it studies As concentrations in the surface waters of mountainous regions of the Central and Western Caucasus; (b) it examines the sources of arsenic entering surface waters; and (c) it evaluates health hazard of natural arsenic pollution for residents.

Arsenic content in surface waters depends on the presence of geochemical anomalies. Concentrations of arsenic in the waters of the rivers are two times lower than Clark values in those areas where there are no arsenic ore. The presence of ancient paleovolcanoes has no effect on arsenic concentrations in surface waters. Natural levels of surface water pollution are the same as anthropogenic. The intake of arsenic is not associated with atmospheric precipitation, but is entirely due to its intake from rocks.

The carcinogenic risk for adult residents of this region was unacceptable for the general population. The non–carcinogenic risk was the maximum permissible risk causing concern. For children, the carcinogenic risk was unacceptable neither for the population nor for professional groups.

REFERENCES

Abdulmutalimova T.O. (2019). Assessment of carcinogenic risk to public health when using groundwater with high arsenic content as sources of drinking water supply on the example of the Republic of Dagestan. Toxicological Bulletin, 6(159), 39-44. DOI: 10.36946/0869-7922-2019-6-39-44 (in Russian with English summary).

Aderibigbe A.D., Stewart A.G., Hursthouse A.S. (2018). Seeking evidence of multidisciplinarity in environmental geochemistry and health: An analysis of arsenic in drinking

water research. Environmental Geochemistry and Health, 40(1), 395-413, DOI: 0.1007/s10653-017-9919-4

Ahamad A., Raju N.J., Madhav S., Khan A.H. (2020). Trace elements contamination in groundwater and associated human health risk in the industrial region of southern Sonbhadra, Uttar Pradesh, India. Environ Geochem Health, 42, 3373-3391, DOI: 10.1007/s10653-020-00582-7

Bortnikov N.S., Bogatikov O.A., Karamurzov B.S., Gurbanov A.G., Shazzo Yu.K., Gazeev V.M., Dokuchaev A.Ya., Leksin A.B., Tsukanova L.E., Petrenko D.B., Shevchenko A.V. (2013). The results of the study of the impact of the buried industrial waste of the Tyrnyauz tungsten-molybdenum plant on the water of the Baksan River and its tributaries (Kabardino-Balkarian Republic, Russia). Bulletin of the Vladikavkaz Scientific Center, 13(3), 22-30 (in Russian).

Brindha K., Paul R., Walter J., Tan M.L., Singh M.K. (2020). Trace metals contamination in groundwater and implications on human health: comprehensive assessment using hydrogeochemical and geostatistical methods. Environ Geochem Health, 42, 3819-3839, DOI: 10.1007/s10653-020-00637-9

Chakraborti D., Mukherjee S.C., Pati S., Sengupta M. K., Rahman M. M., Chowdhury U. K., Lodh D., Chanda Ch. R., Chakraborti A.K. Basu G. K. (2003). Arsenic groundwater contamination in middle Ganga plain, Bihar, India: A future danger. Environ. Health Persp, 111, 1194-1201, DOI: 10.1289/ehp.5966

Chernyshev I.V., Bubnov S.N., Lebedev V.A., Goltsman Yu.V., Bairova E.D., Yakushev A.I. (2014). Two stages of explosive volcanism of the Elbrus area: geochronology, petrochemical and isotopic-geochemical characteristics of the volcanic rocks and their role in the Neogene-Quaternary evolution of the Greater Caucasus. Stratigraphy and Geological Correlation, 22(1), 96-121, DOI: 10.1134/S086959381401002X

Dauphine D.C., Ferreccio C., Guntur S., Yuan Y., Hammond S.K., Balmes J., Smith A.H., Steinmaus C. (2011). Lung function in adults following in utero and childhood exposure to arsenic in drinking water: Preliminary findings. International Archives of Occupational and Environmental Health, 84(6), 591-600, DOI 10.1007/s00420-010-0591-6

Degas N.S., Onishchenko V.V., Shidakov A.K., Logvinenko O.A. (2016). The experience of geomodeling the hydrochemical structure of the surface waters of the Kuban River in the Karachay-Cherkess Republic. Information systems in science and education, 27(2), 55-59 (in Russian).

Ermakov V.V., Tyutikov S.F., Degtyarev A.P., Danilova V.N., Gulyaeva U.A., Dogadkin D.N. (2020). Formation of Biogeochemical Anomalies in the Baksan River Basin. Geochem. Int., 58(10), 1097-1109, DOI: 10.1134/S0016702920100067

Farzan S.F., Karagas., M.R., Chen Y. (2013). In utero and early life arsenic exposure in relation to long-term health and disease. Toxicol. Appl. Pharmacol., 272(2), 384-390, DOI: 10.1016/j.taap.2013.06.030

Gazaev M.A., Agaeva E.A., Zhinzhakova L.Z. (2014). Comparative analysis of river water composition within high land area of the Baksansky and Chereksky gorges. Water: chemistry and ecology, 72(6), 3-7 (in Russian with English summary).

Goswami R., Kumar M., Biyani N., Shea P.J. (2020). Arsenic exposure and perception of health risk due to groundwater contamination in Majuli (river island), Assam, India. Environ. Geochem. Health., 42, 443-460, DOI: 10.1007/s10653-019-00373-9

Human Health Risk Assessment from Environmental Chemicals. Manual P 2.1.10.1920—04). Available at: https://docs.cntd.ru/document/1200037399 [Accessed 11.07.2023].

Kaigorodova E.N. and Petrov V.A. (2016). Arsenic and base metal ore occurrences of Chegem-Cherek Balkar interfluve area (Kabardino-Balkarian Republic). Prospect and protection of mineral resources, (2), 3-8 (in Russian with English summary).

Kladsomboon S., Jaiyen C., Choprathumma Ch., Tusai Th. Apilux A. (2020). Heavy metals contamination in soil, surface water, crops, and resident blood in Uthai District, Phra Nakhon Si Ayutthaya, Thailand. Environ Geochem Health, 42, 545-561, DOI: 10.1007/s10653-019-00388-2

Mallongi A., Rauf A.U., Daud A., Hatt M., Al-Madhoun W., Amiruddin R., Stang S., Wahyu A., Astuti R.D.P. (2022). Health risk assessment of potentially toxic elements in Maros karst groundwater: a Monte Carlo simulation approach. Geomatics, Natural Hazards and Risk, 13(1), 338-363, DOI: 10.1080/19475705.2022.2027528

Middleton D.R.S., McCormack V.A., Watts M.J., Schüz J. (2020). Environmental geochemistry and cancer: a pertinent global health problem requiring interdisciplinary collaboration. Environ. Geochem. Health, 42, 1047-1056, DOI: 10.1007/s10653-019-00303-9(0123

Murtaza B., Amjad N.M., Shahid M., Imran M. Shah N.S., Abbas G., Naeem M.A., Amjad M. (2020). Compositional and health risk assessment of drinking water from health facilities of District Vehari, Pakistan. Environ Geochem Health, 42, 2425-2437, DOI: 10.1007/s10653-019-00465-6

Myshenkova M.S. and Koronovsky N.V. (2015). Bashilsky Shaft - upper Pleistocene extrusive massif in the Verhnechegemskay caldera (Northern Caucasus). Moscow University Geology Bulletin, (6), 28-35 (in Russian with English summary).

Nikanorov A. (2008). Hydrochemistry. Rostov/D: Publishing house «NOK» (in Russian).

Onishchenko V.V., Degas N.S., Gerbekova D.Yu. (2016). Medico-ecological paradigm of a health resort and recreational Teberda River basin of the Karachay-Cherkess Republic. Human Ecology, 10, 3-9, DOI: 10.33396/1728-0869-2016-10-3-9 (in Russian with English summary).

Panov V.., Bazelyuk A. and Lurie P. (2015). The Terek River. Hydrography and flow regime. Rostov-on-Don: Don Publishing House (in Russian).

Pis`menny`j A., Tereshchenko V., Perfiliev V., Marchenko R., Popov S., Tereshchenko L. and Prokuranov P. (2002). State Geological Map of the Russian Federation scale 1:200000. 2nd edition. The Caucasian series. Sheet K-38-VIII, XIV (Soviet). Explanatory note / Ed. Grekova I.. St. Petersburg: Publishing house of St. Petersburg kartfabriki VSEGEI. (in Russian).

Pis`menny`j A., Pichuzhkov A., Zarubina M., Gorbachev S., Vertiy S., Grekov I., Gamasa Yu. and Tereshchenko L. (2013). State Geological Map of the Russian Federation scale 1:200000 Second edition Caucasian Series. Sheet K-38-I, VII (Kislovodsk) Explanatory note / Edited by N., Enna. M.: MF VSEGEI. (in Russian).

Pis`menny`j A., Tereshchenko V., Marchenko R., Popov S., Tereshchenko L., Prokuranov P. and Markus M. (2021). State Geological Map of the Russian Federation scale 1:200000. Second edition. The Caucasian series. Sheet K-38-II (Nalchik). Explanatory note / Ed. Kirichko Yu., Enna N. M.: MF «VSEGEI». (in Russian).

Putilina V., Galitskaya I. and Yuganova T. (2011). Arsenic behaviour in soils, rocks and groundwater. Transformation, adsorption / desorption, migration. Novosibirsk: GPNTB SB RAS. (in Russian).

Reshetnyak O.S., Komarov R.S. (2021). Trends in the variability of the chemical composition and water pollution level in the Kuban river. Water and ecology: problems and solutions, 1(85), 30-40, DOI: 10.23968/2305-3488.2021.26.1.30-40 (in Russian with English summary).

Reutova N.V., Reutova T.V., Dreeva F.R., Khutuev A.M., Kerimov A.A. (2018). Features of aluminum concentrations in rivers of the mountain zone of the Central Caucaus. Russian Journal of General Chemistry, 88(13), 2884-2892, DOI: 10.1134/S1070363218130091

Reutova T.V., Dreeva F.R., Reutova N.V. (2018). Pollutant concentrations in mountain river waters in the upper Baksan area (Prielbrus'e National Park) and their seasonal variations. Water Resources, 45(1), 120-126, DOI: 10.1134/S0097807818010153

Reutova N.V., Reutova T.V., Dreeva F.R., Khutuev A.M. (2021). Microelements in surface waters of the Malka River basin and geochemical features of the region. Geology and Geophysics of Russian South, 11(3), 172-184, DOI: 10.46698/VNC.2021.20.60.014 (in Russian with English summary).

Saint-Jacques N., Parker L., Brown P., Dummer T.JB. (2014). Arsenic in drinking water and urinary tract cancers: a systematic review of 30 years of epidemiological evidence. Environ. Health, 13, 44, http://www.ehjournal.net/content/13/1/44

Semenukha I.N., Chernykh V.I., Sokolov V.V., Derkacheva M.G., Grekov I.I., Enna N.L., Korsakov A.S. (2021). State Geological Map of the Russian Federation scale 1:200 000. Second edition. The Caucasian series. Sheet K-37-VI, (XII) (Karachayevsk). Explanatory note / Ed . Pis`menny`j A. N., M.: MF «VSEGEI». (in Russian).

Smith A.H., Marshall G., Liaw J., Yuan Y., Ferreccio C., Steinmaus C. (2012) Mortality in young adults following in utero and childhood exposure to arsenic in drinking water. Environ. Health Persp., 120(11), 1527-1531, DOI: 10.1289/ehp.1104867

Vinokurov S.F., Gurbanov A.G., Bogatikov O.A., Karamurzov B.S., Gazeev V.M., Leksin A.B., Shevchenko A.V., Dolov S.M., Dudarov Z.I., Gurbanova O.A. (2016). Seasonal fluctuations in concentrations of macro- and microelements and forms of their migration in surface watercourses in the area of the Tyrnyauzsky tungsten-molybdenum plant (Kabardino-Balkarian Republic, Russian Federation). Bulletin of the Vladikavkaz Scientific Center, 16(2), 55-62 (in Russian).

Wang Y., Zhu G., Engel B., Wu Y. (2020). Probabilistic human health risk assessment of arsenic under uncertainty in drinking water sources in Jiangsu Province, China. Environ Geochem Health, 42, 2023-2037, DOI: 10.1007/s10653-019-00476-3

Wasserman G.A., Liu X., Lolacono N.J., Kline J., Factor-Litvak P., Geen A., Mey J.L., Levy D., Abramson R., Schwartz A., Graziano J.H. (2014). A cross-sectional study of well water arsenic and child IQ in Maine school children. Environ. Health., 13, 23, http://www.ehjournal.net/content/13/1/23

APPENDIX

Table A.1. Arsenic in surface waters of the mountainous area of the Kuban River basin

No	Sampling points	Distance from the source, km	$pH_{min} - pH_{max}$	As µg/dm³ (coefficient of variation)
1	Kuban River	7.5	7.15-7.50	0.81 (1.13)
2	Kuban River	20.7	7.19-7.68	1.03 (1.18)
3	Kuban River	31.1	7.16-7.55	2.11 (0.87)
4	Kuban River	38.3	7.23-7.54	1.91 (1.09)
5	Kuban River	54.5	7.24-7.61	2.30 (1.04)
6	Kuban River	89.0	7.47-7.73	1.45 (0.93)
7	Kuban River	150.0	7.37-7.90	1.52 (1.13)
The main tributaries of the Kuban river				
8	R. Kichkinekol	8.0	7.20-7.66	1.40 (1.28)
9	R. Akbash	6.0	7.65-7.89	0.66 (1.56)
10	R. Chirinkol	14.3	6.92-7.50	1.41 (1.11)
11	R. Uzunkol	18.1	6.95-7.42	3.18 (0.47)
12	R. Ullukhurzuk	21.9	7.40-7.80	1.53 (1.08)
13	R. Uchkulan	36.0	7.20-7.35	2.27 (0.96)
14	R. Teberda	72.0	7.15-7.66	1.35 (1.15)
15	R. Mara	31.7	8.23-8.52	1.06 (1.31)
16	R. Dzheguta	30.8	8.12-8.21	1.50 (1.24)
Teberda river, left tributary of the Kuban River at 89 km				
17	R. Teberda	22.6	6.85-7.75	1.61 (1.15)
14	R. Teberda	72.0	7.15-7.66	1.35 (1.15)
Tributaries of the Teberda river				
18	R. Amanauz	3.9	6.66-6.92	0.97 (2.09)
19	R Alibek	8.6	6.64-7.05	1.15 (1.52)
20	R. Dombay Ulgen	8.7	6.77-7.80	1.70 (0.94)
21	R. Gonachhir	20.4	7.01-7.28	1.28 (1.54)
22	R. Ulu-Muruju	15.0	7.18-7.20	5.20 (0.37)
23	water pipe on the highway	0	7.71-7.82	142.00 (0.06)
24	R. Shumka	3.1	7.18-7.35	30.57 (0.16)

Table A.2. Arsenic in surface waters of the mountain region of the Malka river basin

No	Sampling points	Distance from the source, km	$pH_{min} – pH_{max}$	As µg/dm^3 (coefficient of variation)
25	R. Malka (R. Kyzylkol)	10.6	6.53-7.89	0.58 (1.28)
26	R. Malka	12.4	7.26-7.66	0.84 (1.07)
27	R. Malka	15.7	7.53-7.93	1.26 (0.50)
28	R. Malka	65.6	7.84-8.14	2.42 (1.12)
29	R. Malka	79.1	7.83-8.05	1.89 (1.31)
30	R. Malka	93.9	7.91-8.17	2.15 (1.29)
The main tributaries				
31	R.Ullukol	8.6	6.78-7.38	2.03 (0.87)
32	R. Birjaly	6.3	6.70-7.21	0.49 (1.01)
33	Spring-drinking water	0	7.27-7.56	3.74(0.32)
34	R. Sultangarasu	1.9	6.94-7.60	3.61 (0.20)
35	R. Karakayasu	8.0	6.97-7.75	1.13 (0.38)
36	R. Sirkh	1.2	7.95-8.52	0.79 (0.38)
37	R. Harbaz	13.8	7.34-7.94	0.30 (1.20)
38	R. Khasaut	21.7	7.94-8.40	1.89 (1.17)
39	R. Gedmysh	12.8	8.02-8.31	0.75 (0.89)
40	R. Kichmalka	22.0	7.87-8.41	1.12(0.73)
41	R. Kichmalka	45.6	7.82-8.10	0.79(0.62)
42	R. Kichmalka	61.6	7.59-8.39	2.00 (1.13)
43	R. Ekiptsoko	11.5	8.08-8.21	2.78 (0.93)

Table A.3. Arsenic in surface waters of the mountainous region of the Baksan river basin

No	Sampling points	Distance from the source, km	$pH_{min} – pH_{max}$	As μg/dm³ (coefficient of variation)
67	Meltwater "Priyut 11"	0	6.32-6.60	0.77 (0.81)
68	Meltwater on the ground of Garabashi station	0	6.22-8.54	2.09 (1.16)
69	Meltwater on the ground of station "Mir"	0	6.37-7.52	1.25(0.87)
44	R. Baksan (Azau)	3.3	6.60-7.08	2.08 (1.24)
45	R. Baksan	8.1	7.07-7.53	3.67 (0.73)
46	R. Baksan	17.7	7.15-7.55	3.12 (0.95)
47	R. Baksan	35.3	7.07-7.80	1.52 (0.65)
48	R. Baksan	59.4	7.58-7.95	2.96 (0.62)
49	R. Baksan	76.2	7.63-8.14	2.31 (0.56)
50	R. Baksan	112.3	7.70-8.20	2.99 (0.51)
The main tributaries				
70	Azau Waterfall	3.0	6.91-7.03	14.47 (0.84)
51	R. Garabashi	4.3	7.04-7.69	66.38 (0.29)
71	Waterfall «Devich`i kosy`»	1.6	6.85-7.67	79.81 (0,40)
72	Terskol Waterfall	0.8	6.99-7.09	10.06 (0.49)
52	R. Terskol	4.2	6.66-7.73	5.87 (0.61)
53	R. Donguz-Orun	8.0	6.93-7.34	2.71 (0.87)
54	R. Kogutai	3.5	1.15-7.55	2.16 (0.65)
55	R. Yusengi	7.6	7.50-7.59	1.66 (0.71)
56	R. Adylsu	11.8	6.89-7.77	2.35 (1.31)
57	R. Irik	11.8	7.30-7.90	1.62 (0.53)
58	R. Kyrtyk	22.2	7.79-7.88	1.45 (0.92)
59	R. Adyrsu	16.1	7.32-7.80	1.54 (0.70)
60	R. Tyutyusu	11.2	7.06-7.85	1.33 (0.79)
65	Bolshoy Mukulan Stream	4.5	7.76-7.99	70.19 (0.57)
66	"Rudnik" Stream	2.0	7.63-8.24	47.18 (0.15)
61	R. Kamyksu	10.2	8.06-8.41	29.43 (0.67)
62	R. Gizhgit	28.5	8.17-8.45	1.66 (0.67)
63	R. Kestanty	27.6	7.87-8.29	1.77 (0.89)
64	R. Kendelen	58.7	7.88-8.16	2.31 (1.12)

Table A.4. Arsenic in surface waters of the Chegem river basin

No	Sampling points	Distance from the source, km	pH_{min} – pH_{max}	As µg/dm^3 (coefficient of variation)
73	R. Chegem (Bashil)	8.9	7.30-7.55	0.80 (0.58)
74	R. Chegem (Bashil)	14.7	7.32-7.75	0.51 (0.43)
75	R. Chegem	19.3	7.32-7.61	0.60 (0.82)
76	R. Chegem	29.1	7.36-7.72	1.11 (0.56)
77	R. Chegem	55.8	7.68-8.17	0.99 (0.43)
78	R. Chegem	70.2	7.67-8.18	1.13 (0.47)
79	R. Chegem	88.7	7.62-8.14	2.93 (1.16)
The main tributaries				
80	R. Jailyk	7.9	7.45-7.80	1.55(0.65)
81	R. Gara-Aususu	7.7	7.30-7.52	0.83 (0.11)
82	R. Bulungusu	8.5	7.39-7.95	2,98 (0.19)
83	R. Sylyksu	6.4	7.54-7.98	3.22(0.15)
84	R. Jylgysu	11.4	7.15-7.68	1.91 (0.43)
85	R. Cardan	8.4	7.95-8.51	1.92 (0.55)
86	R. Kektash	10.6	8.28-8.59	1.28(0.70)
87	R. Chatysu	6.3	7.96-8.38	1.16 (0.08)
88	R. Adaysu	3.8	7.94-8.45	2.20 (0.33)
89	R. Kiyikchisu	8.0	8.08-8.41	1.99 (0.15)

Table A.5. Arsenic in the surface waters of the Cherek river basin

No	Sampling points	Distance from the source, km	$pH_{min} - pH_{max}$	As µg/dm³ (coefficient of variation)
Cherek Bezengiysky River				
90	R. Cherek Bezengiysky	9.05	7.04-7.51	2.50 (0.73)
91	R. Cherek Bezengiysky	11.0	7.23-7.59	3.71 (0.63)
92	R. Cherek Bezengiysky	24.5	7.19-7.79	2.34 (0.51)
93	R. Cherek Bezengiysky	40.8	7.74-7.80	3.18 (0.63)
94	R. Cherek Bezengiysky	53.3	7.91-8.17	3.66 (0.48)
The main tributaries of the Cherek Bezengiysky River				
95	R. Mizhirgi	3.2	7.06-7.52	2.16 (1.15)
96	Stream Gitche-Naratli	1.9	7.82-7.89	3.12 (0.87)
97	R. Bashkamsu	4.0	8.02-8.20	6.48 (0.84)
98	R. Akkusu	5.3	7.85-7.90	15.30 (1.06)
99	R. Dumala	12.1	7.75*	8.27*
100	Stream Shiki	4.75	7.29-7.66	2.83 (0.19)
101	R. Kishlyksu	6.8	8.25-8.33	1.47 (0.74)
102	R. Shoudorsu	5.9	8.37-8.38	2.49 (0.03)
103	R. Karasu (Bezengi)	15.7	7.98-8.23	2.04 (1.02)
Cherek Balkarsky River				
104	R. Cherek Balkarsky	11.1	7.35-7.58	2.96 (0.78)
105	R. Cherek Balkarsky	17.8	7.38-7.58	3.31 (0.90)
106	R. Cherek Balkarsky	25.6	7.11-7.94	2.80 (0.70)
107	R. Cherek Balkarsky	32.7	7.10-7.76	3.47 (0.65)
108	R. Cherek Balkarsky	47.2	7.07-7.92	4.75 (0.06)
109	R. Cherek	58.0	7.69-8.30	4.05 (0.70)
110	R. Cherek	82.2	7.95-8.13	2.71 (0.71)
The main tributaries of the Cherek River (Balkarsky)				
111	R. Karasu	9.3	7.57-7.57	3.91 (0.53)
112	Stream	2.0	7.72-7.96	10.44 (0.23)
113	R. Zerklisu	4.0	7.30-7.66	2.70 (0.54)
114	stream from Mount Sabalah	2.6	7.88-7.93	5.58 (0.04)
115	R. Gulchisu	4.5	7.35-7.89	3.35 (0.47)
116	R. Ishkirty	16.2	7.47-7.91	2.45 (0.85)
117	R. Chinashki	16.4	7.60-7.88	6.27 (0.93)
118	R. Kurungusu	3.8	8.25-8.47	8.89 (1.03)
119	R. Karasu (Balkarsky)	15.8	7.90-8.34	2.69 (0.87)
120	R. Kheu	28.2	8.05-8.56	2.75 (0.65)
121	R. Psygansu	55.6	8.05-8.26	2.06 (1.21)

*- Arsenic was determined once.

RESEARCH PAPER

GENE DIVERSITY IN SEED CROP OF TAURUS CEDAR *(Cedrus libani* A. Rich.*)* OVER AN ALTITUDINAL RANGE

Nilufer Yazici[1], Tatyana P. Novikova[2], Arthur I. Novikov[2*], Nebi Bilir[1]
[1]Faculty of Forestry, Isparta University of Applied Sciences, Isparta 32260, Turkey
[2]Faculty of Computer Science and Technology (T.N.) Timber Industry Faculty (A.N.), Voronezh State University of Forestry and Technologies named after G.F. Morozov, 8 Timiryazeva street, Voronezh 394087, Russian Federation
***Corresponding author:** arthur.novikov@vglta.vrn.ru

Received: June 1st, 2023 / Accepted: November 14th, 2023 / Published: December 31st, 2023
https://DOI-10.24057/2071-9388-2023-2922

ABSTRACT. There could be many environmental and biological impacts such as edaphic, geographic, climatic, age, tree structure and population on morphological, physiological and genetically seed quality in plant species. Gene diversity is an important mirror of genetically seed quality. Gene diversity in seed crops were estimated based on female and male strobili productions of fifty trees (N) randomly chosen from each population sampled over an altitudinal range as low (1200-400 meters ≤ altitude), middle (1400 m < altitude ≤ 1600 m), high (1600 m < altitude ≤ 1800 m), and very high (1800 m < altitude) in Taurus cedar also known as cedar of Lebanon (*Cedrus libani* A. Rich.) for two consecutive years (2021&2022). The variation in strobilus production was subjected to estimation of female and male fertility variation. The total fertility variation (Ψ) was estimated from the female and male fertility variation. Impacts of some growth characteristics (tree height and diameter at breast height) on strobili productions were also investigated. Strobili productions varied among the populations and individuals within population, and between years. The differences for populations and years were also found for coefficient of variations which were mirror of fertility variation of the strobili productions. Tree height and diameter at breast height seemed more reasonable predictor than age for number of strobili. Fertility variations of female parents were generally higher than that of male in both years. First year showed generally higher parental variations in individual populations. Gene diversity (GD=1-0.5Ψ/N) ranged from 0.967 to 0.974 for the populations and years. The loss of highest gene diversity was 0.004 in low population (0.967 & 0.971) between years. Results of the study indicated that altitudinal gene diversity of seed crop could be used to produce genetically quality seed and their grading. Moreover, data sets can be used to fill the Forest Landscape Restoration library (FLR-Library).

KEYWORDS: co-ancestry, effective number, quality, seed, variation, FLR-Library

CITATION: Yazici N., Novikova T. P., Novikov A. I., Bilir N. (2023). Gene Diversity In Seed Crop Of Taurus Cedar *(Cedrus Libani* A. Rich.) Over An Altitudinal Range. Geography, Environment, Sustainability, 4(16), 63-71
https://DOI-10.24057/2071-9388-2023-2922

ACKNOWLEDGEMENTS: The synthesis of samples and genetic research was carried out by N.Y and N.B. with the support of the Isparta University of Applied Sciences. The development, conceptualization and validation of the FLR-model was carried out by T.N. and A.N. within the framework of the grant of Russian Science Foundation (RSF), grant number 23-26-00102, https://rscf.ru/project/23-26-00102/.

Conflict of interests: The authors reported no potential conflict of interest.

INTRODUCTION

Cedrus libani A. Rich. (Asia Minor, Lebanon, Syria) is one of the four species of the genus *Cedrus* in the family *Pineacea: C. deodora* Loud. (Himalaya Mountains, Nepal), *C. brevifolia* Hen. (Cyprus), and *C. atlantica* Manetti (Atlas Mountains) (Vidakoviç 1982). Taurus cedar also known as cedar of Lebanon (*C. libani* A. Rich.), has its main natural occurrence in the Taurus Mountains in total 23.1 million ha national forest area which of 9.6 million ha is unproductive according to the latest forest inventory of Turkey. The species has also some remain populations in other parts of Anatolia such as Sultandağı-Afyon and in the Black Sea region (Çatalan-Erbaa and Akıncıköy-Niksar) together with Taurus Mountains (Boydak 2003). The species has tall and slender trunks and can grow to old ages over than 1000 years old, impressive size by up to 2.49 m (diameter at breast height) and 46 m height, and appearances. There are also many monumental forests and trees scattered throughout the Taurus Mountains of the species (Boydak 2003). Its reported extent in southern Turkey is 405 424 ha (OGM 2022) which the main natural distribution in whole the world together with endemic to elevated mountains around the Eastern Mediterranean in Lebanon and Syria. The species is classified as one of the socio-culturally, economically and ecologically important tree species for Turkish forestry and the "National Tree Breeding and Seed Production Program" (Koski, Antola 1993). Many biological (i.e., volume, height, diameter, age, stem straight, stand purity) and environmental (i.e., distance to plantation area, altitude, size, location, edaphic and climatic characteristics) criterions are used in selection of seed collection areas from natural forests, and establishment of the areas such as seed orchards, and other forestry purposes. Altitude which is easy and cheap could be also considered as an environmental criterion in these selections for forest managers and owners. Taurus cedar used widely in afforestation practices and conversion of unproductive forest area to productive because of valuable timber species and quite striking specimen plants in the landscape and other purposes. Taurus cedar seems potential forest tree species for potential afforestation, reforestation and restoration areas both except and inside of natural distribution. It is getting importance of quantity and quality of seed supply. Seed procurement and its quality using frontier techniques (Bernardes et al. 2022; Novikova et al. 2022; Novikov et al. 2021a; Novikov et al. 2021b; Novikov et al. 2019) is an important stage of the program and practices. It is also known that quality of seed crop genetically improved together with other morphological (i.e., grading) and physiological characteristics play important roles in economical and biological succession of plantation forestry. Seeds are classified generally morphological and physiological characteristics. However, gene diversity is a mirror of genetically improved seed quality together with the other characteristics. While some studies were carried out on seed science and technology of Taurus cedar (Boydak 2003; Bilir 1997; Odabasi 1990; Saatcioglu 1971; Saatcioglu 1956), gene diversity of seed crops based on fertility variation have not been discussed well, yet. Besides, fertility studies are very limited in the species (Bilir, Kang 2014; Bilir, Ozel 2017; Bilir, Kang 2021; Yazici, Bilir 2017).

Fertility also called fecundity is defined as an ability to produce progeny to next generation. Its estimation is used for many purposes such as seed production, managing of forest genetic resources and gene conservation, and evolutional study. Estimation of fertility variation among genotypes is one of the important tools for plant genetics and breeding purposes (Kang 2001; Kang et al. 2003; Bilir et al. 2005; Kamalakannan et al. 2015; Park et al. 2017; Kang, Bilir 2021). Fertility variation and its linkage parameters (i.e., co-ancestry, effective number, gene diversity, status number) estimated based on reproductive characters is modern, easy, cheap, and light survey in plant science. It is preferred by these advantages in plant science recently in the species and other species (e.g., Bilir, Kang 2014; Bilir, Ozel 2017; Bilir, Kang 2021; Yazici, Bilir 2017; Park et al. 2017).

The practical application of the data from this study may be as follows. The implementation of any forest restoration process will always consist of a set of technological operations. The set of these technological operations can be organized in the form of an enlarged algorithm (FLR-algorithm), decomposed into six main groups (Novikova 2022a). The third group of the FLR-algorithm responsible for the preparation of forest reproductive material includes the "Seed collection, pretreatment" operator preceding the "Seed grading" operator (Appendix A, Figure A.1, *b*). To improve seed collection before their detection and processing using frontier scientific techniques, for example, based on convolution neural networks (Bernardes et al. 2022), it is necessary to include the results presented below in block 10 of the algorithm (Novikova 2022b) (appendix A, fig. A.1, *c*).

The purpose of this study is to estimate the gene diversity in seed crop based on fertility variation among individuals in four populations sampled altitudinal range of Taurus cedar by female and male strobili counts, and to discuss the possibility of it using in genetically characteristics in grading and quality of seeds, and to contribute seed technology of the species.

MATERIALS AND METHODS

Populations and data collection

C. libani generally bears cone at about 30 years old in natural stands. Male flowers appear in July and elongate 3-5 cm in August, while female flowers can be seen in September. Pollination takes place in September or early October, depending on the elevation. The following year between April or May and June, conelets develop to normal cone sizes. Opening of the cone scales begins in October about 25-26 months after flowering. Seed dispersal begins at the end of November or December and continues throughout the winter. Seeds of cones collected in August months after flowering (Boydak 2003). However, the period can vary based on many biotic and a-biotic factors.

C. libani in the Taurus Mountains occurs generally between 800 and 2100 m elevation, but it can be also found at lower (500–600 m) and higher (2400 m) elevations as small populations and groups or individuals (Boydak 2003). Natural distribution of the species at studied area were divided into four altitudinal ranges in the southern part of Turkey as: low (1200-400 meters ≤ altitude), middle (1400 m < altitude ≤ 1600 m), high (1600 m < altitude ≤ 1800m), and very high (1800m < altitude) ranges. Some geographic and climatic characteristics of the populations were given for year 2021 in Tables 1 & 2. Numbers of female (♀21 & ♀22) and male (♂21 & ♂22) strobili productions were counted in four populations sampled altitudinal ranges and fifty trees randomly chosen in each population for two consecutive years (2021 and 2022), while tree height (H), diameter at base (D_0), and age were measured at end of growing period of first year (Table 3).

Within the occurrences of *C. libani* at backwards of the Taurus mountains and inner Anatolia sub-humid and semi-arid climatic conditions prevail, respectively. Its populations rather restricted and mostly in degraded conditions at inner Anatolia. The averages of annual temperatures of the area are between 6 and 12 °C. Mean July temperature is about l8 to 25 °C, generally more than 30 °C. Mean January temperature is ranged from 0 to -5 °C. with an absolute minimum -35 °C. Mean yearly precipitation varies between 600 and 1200 mm. Summer periods are generally rainless. Duration of snow cover period ranges 1-5 months. Relative humidity during the growing season varies from about 40 to 60 % (Boydak 2003).

Data analysis

The following ANOVA model was used to analyses the difference of strobili productions among populations and years by the SPSS software (SPSS 2011).

$$Y_{i_{j_k}} = \mu + F_i + B(F)_{j(i)} + e_{ijk} \tag{1}$$

Table 1. Some geographic details of studied populations

Altitudinal ranges (m)	Population code	Latitude (N)	Longitude (E)	Average altitude (m)
Low (1200-1400)	Low	38°05'	30°42'	1278
Middle (1400-1600)	Middle	37°44'	30°49'	1486
High (1600-1800)	High	37°52'	31°17'	1714
Very high (>1800)	Vhigh	37°51'	31°18'	1884

Table 2. Some climatic characteristics of the studied years

Months	Average temperature (ºC)				Average humidity (%)				Total rainfall (mm/m²)			
	Low & Middle		High & Vhigh		Low & Middle		High & Vhigh		Low & Middle		High & Vhigh	
	2021	2022	2021	2022	2021	2022	2021	2022	2021	2022	2021	2022
J	5.6	2.1	2.9	-0.8	78.5	75.7	76.8	75.7	182.0	104.6	69.2	72.4
F	6.2	3.5	2.5	1.3	69.1	78.1	67.9	78.1	50.6	96.6	7.4	111.4
M	6.8	3.5	3.8	0.8	66.5	70.5	72.3	70.5	60.8	61.8	92.2	80.8
A	12.9	14.3	11.1	13.1	59.1	52.5	55.1	52.5	10.0	25.4	7.4	16.0
M	19.2	16.8	17.2	15.1	52.2	62.3	47.6	62.3	7.0	25.2	5.0	35.2
J	19.9	22.0	17.5	19.8	64.2	64.0	61.6	64.0	90.0	39.0	102.2	65.2
J	25.7	24.8	23.0	20.5	49.7	47.0	44.2	51.3	6.4	8.8	11.0	5.6
A	25.5	25.1	23.1	23.2	47.6	48.5	41.2	42.5	0.0	1.4	11.6	17.2
S	19.8	20.5	17.2	21.7	57.5	48.5	55.2	49.7	15.8	38.6	16.2	28.2
O	14.0	15.0	11.9	16.1	62.6	62.3	55.1	67.3	15.6	25.2	5.2	26.8
N	10.8	10.3	8.1	7.1	70.9	64.7	70.0	69.0	64.4	14.0	42.8	10.6
D	6.2	5.8	1.4	4.7	79.1	76.8	80.4	80.1	185.8	165.7	96.6	13.2

Table 3. Averages and coefficient of variation (CV%) of tree height (H), diameter at base (D_0), and age of the populations

Characteristics	Populations							
	Low		Middle		High		Vhigh	
	x*	CV	$\bar{x}$	CV	$\bar{x}$	CV	$\bar{x}$	CV
H (m)	38.1[c]	1.29	31.9[b]	1.53	21.8[a]	11.48	22.0[a]	2.58
D^0 (cm)	36.5[b]	1.59	31.8[a]	2.48	35.3[b]	26.27	32.5[a]	2.11
Age (year)	61.1[a]	15.60	68.8[bc]	16.96	64.5[ab]	19.47	69.8[c]	14.86

* The same letters showed not significantly different at p>0.05 among altitudinal ranges.

Where Y_{ijk} is the observation from the k^{th} tree of the j^{th} population in the i^{th} year, µ is the overall mean of strobili production, F_i is the effect of i^{th} year, $B(F)_{j(i)}$ is the effect of the j_{th} population in the ith year, and e_{ijk} is the random error.

Phenotypic Pearson' correlations among strobili productions and growth characteristics were estimated in the populations by SPSS software.

The coefficients of variations for female and male fertility were calculated and applied to estimate the fertility variation in female (CV♀) and male (CV♂) parents, respectively.

The female fertility (ψ♀) and male fertility (ψ♂) variations were estimated by coefficient of variation (*CV*) by Kang, Lindgren (1999) as:

$$\psi_{♀} = N\sum_{i=1}^{N} ♀_i^2 = CV_{♀}^2 + 1; \ \psi_{♂} = N\sum_{i=1}^{N} ♂_i^2 = CV_{♂}^2 + 1 \quad (2a\&b)$$

Where *N* is the census number, $♀_i$ is the female fertility of the i^{th} individual, $♂_i$ is the male fertility of the ith individual and CV♀ and CV♂ are the coefficients of variation in female and male fertility among individuals, respectively.

Total fertility variation (Ψ) was calculated by Bilir et al. (2005) as:

$$\psi = \left(\frac{CV_{♀}^2 + CV_{♂}^2}{4}\right) + 0.5\left(N\sum_{n=1}^{N}\frac{♀_n ♂_n}{\sum ♀ \sum ♂} + 1\right) \quad (3)$$

Where *N* is the census number, CV♀ is the coefficient of variation in female fertility, and CV♂ is the coefficient of variation in male fertility, $♀_n$ and $♂_n$ are the number of female and male strobilus of the n^{th} individual; ♀ and ♂ are used as index for the female and male strobilus, respectively.

The effective number of parents were estimated for female [$N_{p(♀)}$] and male [$N_{p(♂)}$] parents and total fertility (N_p) by Kang and Lindgren (1999) as:

$$N_{p(♀)} = N/\psi_{♀}; \ N_{p(♂)} = N/\psi_{♂}; \ N_p = N/\psi \quad (4a, b \& c)$$

Where *N* is the census number, ψ♀ is the female fertility variation, ψ♂ is the male fertility variation, Ψ is the total fertility variation.

Gene diversity (GD) was estimated based on the effective number of parents (N_p) by Kang and Lindgren (1998) as:

$$GD = 1 - 0.5/N_p \quad (5)$$

RESULTS

Strobili productions and relations

Averages of the strobili productions varied for the altitudinal populations and years (Table 4, Figure 1). They showed also large differences among individuals within population and year (Table 4). For instance, the most productive 5 trees (10% of total trees) produced 30.1% of total ♀$_{21}$ and 27.3% of total ♂$_{21}$ in low population, while they were 4.1% and 2.1% for the lowest productive 5 trees in the population and year, respectively. There were about 10 times differences between lowest (48) and highest (486) productive trees in low altitude of ♀$_{21}$ (Table 4). The results were supported by results of analysis of variance that there were significant ($p<0.01$) differences among the populations except of ♂$_{22}$, and between years. Population and year interaction was also found significant ($p<0.01$) based on results of analysis of variance. Middle population was evidently different for ♀$_{21}$ and ♂$_{22}$ based on results of Duncan's multiple range test (Table 4).

Averages of female strobili were higher than that of male in all populations. Vhigh population showed the highest performances for the strobili productions (149.1 for ♀$_{21}$, 912.6 for ♂$_{21}$ and 94.5 for ♂$_{22}$) except of the lowest ♀$_{22}$ (27.0) in the population (Table 4).

Coefficient of variations which were mirror of fertility variation of the strobili productions changed for the populations and years (Table 4, Figure 2).

Table 4. Averages and coefficient of variation (CV%) and range for strobilus production of the populations and years

Characteristics	Low			Middle			High			Vhigh		
	$\bar{x}$*	CV	range	$\bar{x}$	CV	range	$\bar{x}$	CV	range	$\bar{x}$	CV	range
♀21	127.8^{b}	74.3	48-486	73.9^{a}	68.5	25-322	146.7^{b}	49.6	36-323	149.1^{b}	45.6	22-342
♀22	31.7^{a}	58.5	12-105	53.3^{b}	59.2	13-140	31.0^{a}	52.4	9-75	27.0^{a}	46.7	8-75
♂21	589.9^{b}	82.1	100-1800	129.2^{a}	51.5	35-300	647.8^{b}	79.3	60-2020	912.6^{c}	87.4	115-3020
♂22	75.8	61.2	25-242	79.3	44.1	26-225	91.5	36.1	34-205	94.5	60.2	22-252

* The same letters showed not significantly different at p>0.05 within year.

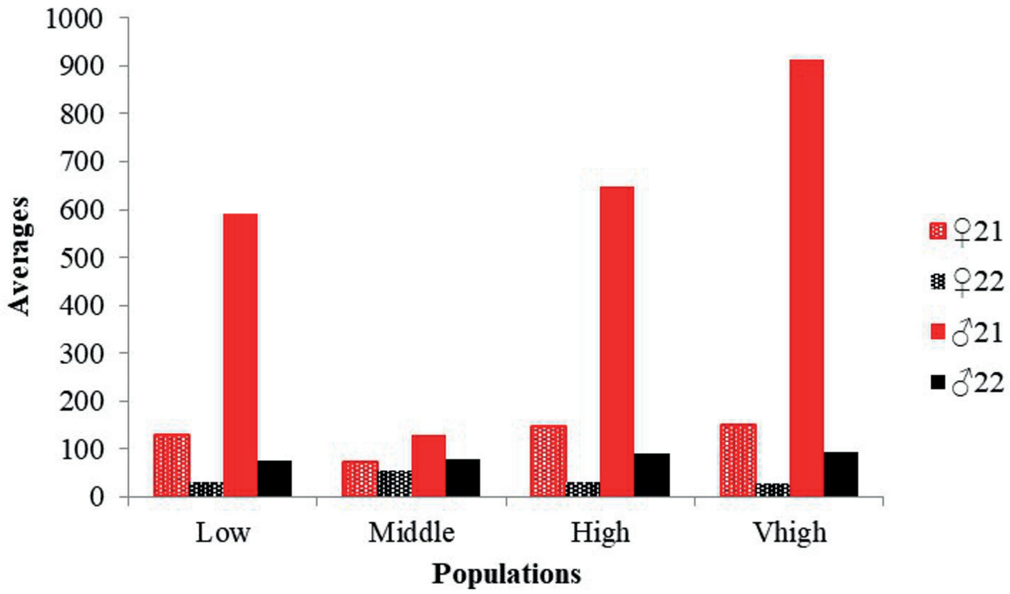

Fig. 1. Averages of strobili productions for the populations and years

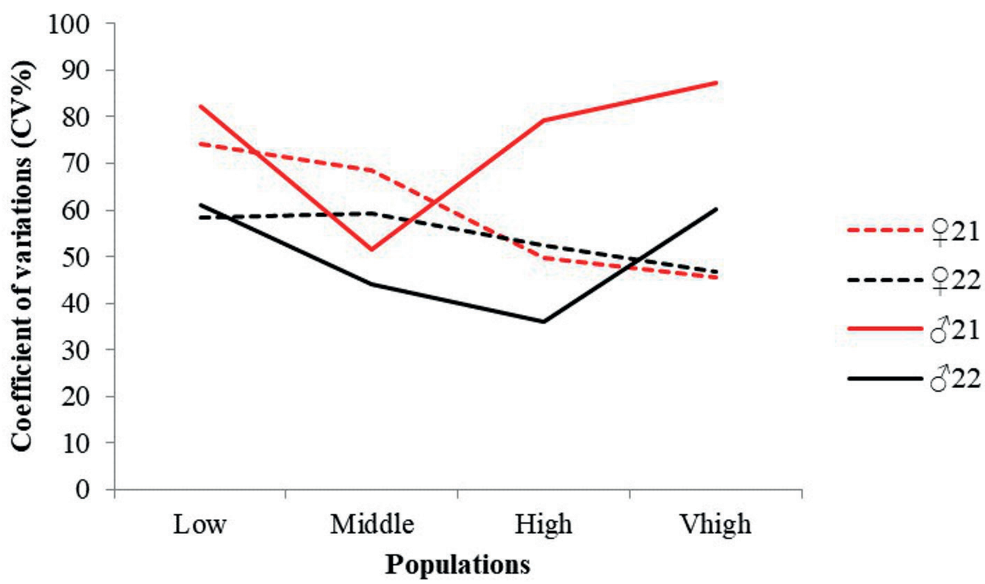

Fig. 2. Coefficient of variations strobili productions for the populations and years

There were positive and significant (p<0.05) correlations between female and male productions in all populations within year, while they were generally significant between years (Table 5). Tree height had negative impacts significantly (*p<0.05*) on strobili productions of first year and on ♂$_{22}$, while it was positive on ♀$_{22}$ in pooled populations (Table 5). While altitude had positive impacts significantly (*p<0.05*) on strobili productions except of negative effect on ♀$_{22}$ in pooled populations of both years, diameter at base had positive effective on strobili productions of first year. Besides, impacts of age varied for the populations and years (Table 5).

Fertility variation, gene diversity and parental balance

Fertility variations of female (ψ♀) parents were higher than that of male (ψ♂) in low and Vhigh populations in both years, and first year of high population (Table 6). First year showed generally higher parental variations (ψ♀ & ψ♂) in individual populations. All populations had higher total fertility variation (Ψ) in first year than second year. It ranged from 2.76 (meaning 36% fertile trees) to 3.32 (30%) in first year, and varied between 2.65 (38%) and 2.92 (34%) in second year (Table 6). The cumulative contribution curve described the relative proportion of trees to the accumulative gamete contribution. The parental cumulative contributions of trees were shown in Figure 3 for the populations and years.

As seen from Figure 3, ♂21 showed skewed evidently distribution in low, high and Vhigh populations.
Gene diversity (GD) varied between 0.967 (first year of low population) and 0.974 (second year of high population) in the populations. The loss of highest gene diversity was 0.004 in low population (0.967 & 0.971) between years (Table 6, Figure 4).

DISCUSSION

Strobili productions and relations

There were large differences for strobili production among populations and among individuals within population, and between years (Table 4, Figure 1). Similar results were also reported for strobili productions in natural populations of Taurus cedar (Bilir, Kang 2021; Yazici, Bilir 2017) and different forest tree species (Kang et al. 2003; Bilir et al. 2005; Kamalakannan et al. 2015; Park et al. 2017; Ozbey, Bilir 2022). It was reported that good seed year of the species in natural stands was once in two or three years (Boydak 2003). Strobili production difference between years was in well accordance with the good flowering year of the species. Differences among populations and between years were also well accordance with results

Table 5. Pearson's correlation coefficients (r) among the strobili productions for the populations and years

	r	N♀21	N♂21	N♀22	N♂22
Low Middle High Vhigh Total	N♂21	.614** .460** .453** .298* .500**	-		
Low Middle High Vhigh Total	N♀22	.436** .187^{NS} 464** .432** .099^{NS}	.501** .220^{NS} .219^{NS} .309* -.035^{NS}	-	
Low Middle High Vhigh Total	N♂22	.356* .225^{NS} .436** .329* .099^{NS}	.446** .234^{NS} .400** .451** .419**	.690** .423** .533** .529** .419**	-
Low Middle High Vhigh Total	H	.111^{NS} .089^{NS} .295* .191^{NS} -.173*	-.001^{NS} .071^{NS} .065 ^{NS} .068^{NS} -.235**	.065^{NS} .161^{NS} .221^{NS} .004^{NS} .186**	-.104^{NS} .092^{NS} .108^{NS} -.149^{NS} -.169*
Low Middle High Vhigh Total	D_0	.444** -.121^{NS} .501** .461** .306**	.386** .206^{NS} .216^{NS} .159^{NS} .151*	.256^{NS} .081^{NS} .538** .368** .098^{NS}	.202^{NS} .142^{NS} .243^{NS} .165^{NS} .082^{NS}
Low Middle High Vhigh Total	Age	.503** .090^{NS} .081^{NS} .306* .188**	.459** .115^{NS} .099^{NS} .178^{NS} .148^{NS}	.336* -.126^{NS} .164^{NS} .186^{NS} .104^{NS}	.358* .123^{NS} .060^{NS} .283* .219**
Low Middle High Vhigh Total	Altitude	-.163^{NS} -.209^{NS} .123^{NS} -.295* .168*	-.312* -.289* .079^{NS} -.274^{NS} .239**	-.175^{NS} -.413** -.171^{NS} -.275^{NS} -.230**	-.224^{NS} .042^{NS} -.056^{NS} -.098^{NS} .151*

**; Correlation is significant at the 0.01 level, *; Correlation is significant at the 0.05 level, ^{NS}; Correlation is not statistically significant *(p<0.05)*.

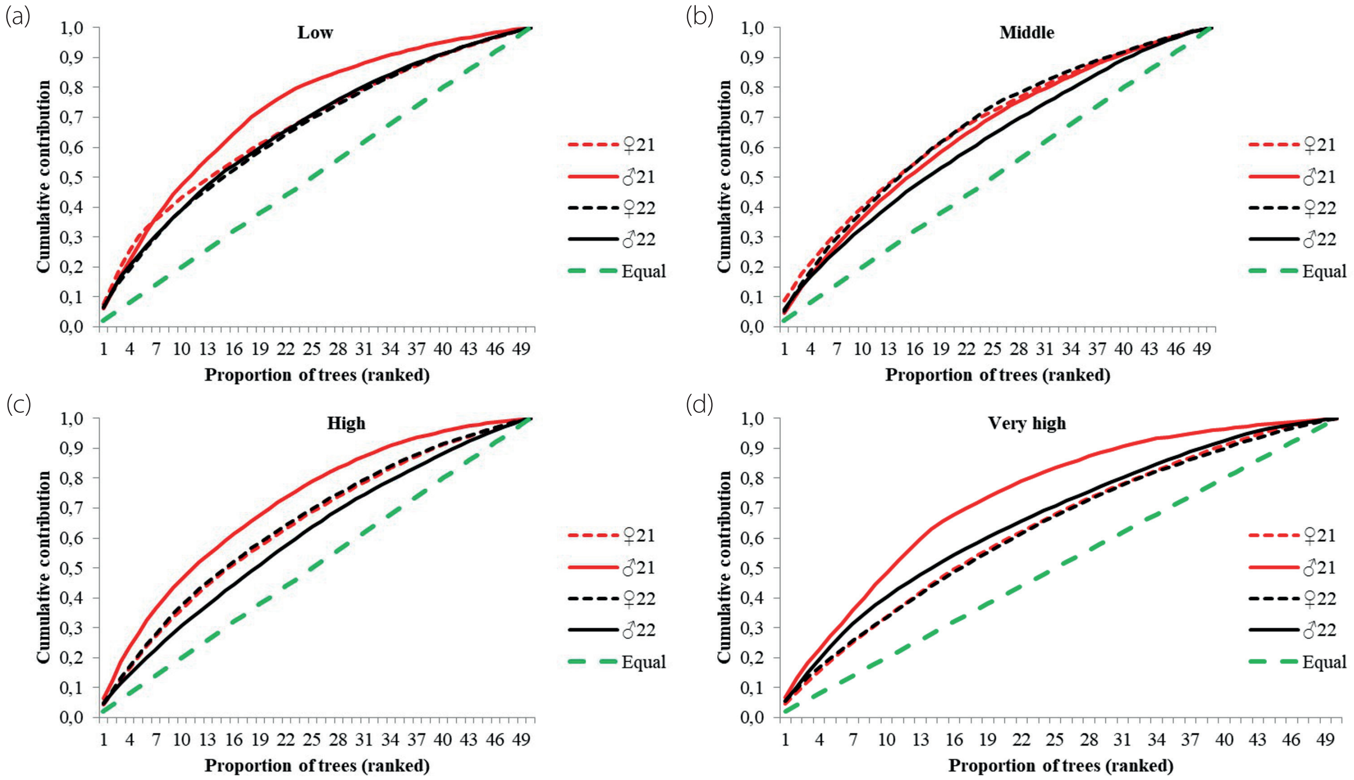

Fig. 3. Parental-balance curves in the populations for the years

Table 6. Female (ψ_f), male (ψ_m), and total fertility variation (Ψ), the female ($N_{p(f)}$) and male ($N_{p(m)}$), and total (N_p) effective number, and gene diversity (GD) for the populations and years

Populations	Low		Middle		High		Vhigh	
Years	2021	2022	2021	2022	2021	2022	2021	2022
ψf*	1.54 (.65)	1.34 (.75)	1.46 (.68)	1.34 (.74)	1.24 (.81)	1.27 (.79)	1.20 (.83)	1.21 (.82)
ψ^m	1.66 (.60)	1.37 (.73)	1.26 (.79)	1.19 (.84)	1.62 (.62)	1.13 (.89)	1.75 (.57)	1.36 (.74)
Ψ	3.32 (.30)	2.92 (.34)	2.93 (.34)	2.75 (.36)	2.82 (.35)	2.65 (.38)	2.76 (.36)	2.70 (.37)
$N_{p(f)}$	32.45	37.45	34.24	37.21	40.30	39.39	41.53	41.21
$N_{p(m)}$	30.11	36.58	39.69	42.00	30.93	44.34	28.59	36.88
N_p	15.05	17.13	17.04	18.18	17.74	18.87	18.13	18.53
GD	0.967	0.971	0.971	0.973	0.972	0.974	0.972	0.973

*; Parentheses indicates the relative effective number of parents (Nr=Np/N).

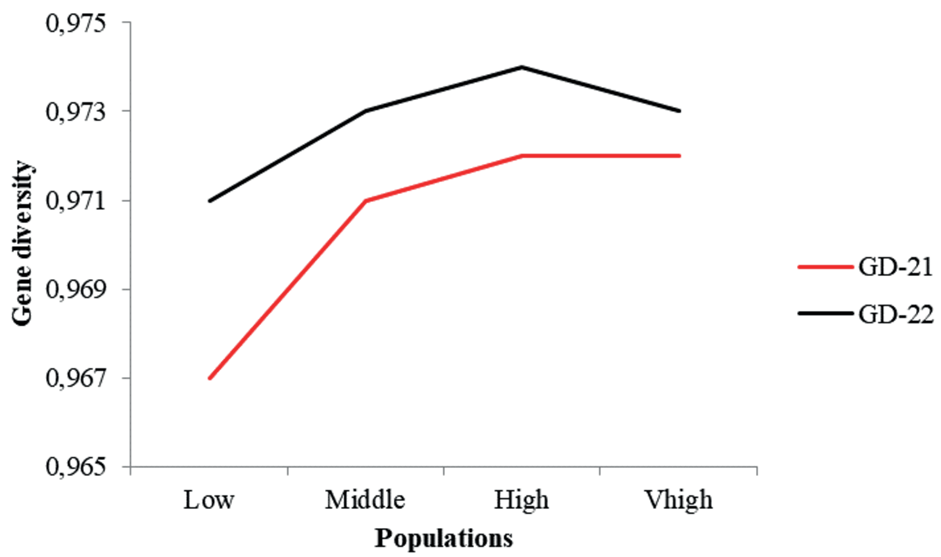

Fig. 4. Gene diversity for the populations and years

of analysis of variance. The results showed also that population and year interaction was significant ($p<0.01$). There could be many environmental or genetical effects in these differences. It was found that age, elevation and crown closure were important factors in seed yield of natural populations of *Pinus brutia* (Eler 1990). Differences in age and environmental variation, mainly in soil properties, may have influenced the observed variation in fruiting and seed set within each population in the natural forest (Bila, Lindgren 1998), or other biological and environmental factors such as population, habitat, aspect, altitude (Yazici, Bilir 2017; Bilir et al. 2005; Bilir 2011) and crown closure (Yazici, Bilir 2023).

Averages of female strobili were higher than that of male in all populations, while their coefficient of variations changed for the populations and years (Table 4, Figure 2). The results were well accordance with findings of strobili production in the species (Bilir, Kang 2021). Low coefficients of variation (CV) were welcomed by forest managers for maintaining higher genetic diversity.

Positive and significant ($p<0.05$) correlations between female and male productions were estimated in all populations within year (Table 5). Similar correlations were also found in natural populations of *C. libani* (Bilir, Kang 2021) and *Pinus brutia* (Bilir et al. 2005) opposite to negative genetic correlation between female and male flowering in *P. sylvestris L.* (Savolainen et al. 1993).

Tree height had generally negative impacts on strobili productions in pooled populations opposite to diameter at base while impacts of age changed for the populations and years (Table 5). It could be said that height and diameter at breast height seemed more reasonable predictor than age for number of strobili. Altitude had positive impacts significantly ($p<0.05$) on strobili productions except of negative effect on $♀_{22}$ in pooled populations (Table 5). However, no significant impact of altitude on strobili production was reported in *Pinus brutia* (Bilir et al. 2005).

Fertility variation, gene diversity and parental balance

Fertility variations of female ($\psi♀$) parents were generally higher than that of male ($\psi♂$) in the populations (Table 6). First year showed mostly higher parental variations ($\psi♀$ & $\psi♂$) in individual populations. All populations had higher total fertility variation (Ψ) in first year than second year (Table 6). Similar fertility variations were reported for strobili (Bilir, Ozel 2017; Bilir, Kang 2021) and cone productions (Bilir, Kang 2014; Yazici, Bilir 2017) in natural populations of Taurus cedar. The results indicated importance of population and years in forestry practices of the species.

The effective number of parent ($N_{p(♀)}$), $N_{p(♂)}$ & N_p) mirrored to the gene diversity showed that about 30% of individuals in the low population of first year behavior as they were under the ideal population, while they were 38% in high population of second year. It showed the size equivalent to the ideal populations was 8% larger in high population than low population based on the fertility variation of individuals in the populations (Table 6). It was suggested as a rough generalized heuristic rule that CV lower than 140% ($\Psi\leq3$) for natural populations (Kang 2001; Kang, Bilir 2021). The low populations were close to the value ($\Psi\leq3$) in both years and first year of middle population (Table 6).

Gene diversity (GD) varied between 0.967 (first year of low population) and 0.974 (second year of high population) in the populations (Table 6, Figure 4). They emphasized importance of seed collection year and population sampled altitudinal range in the study. The result was in well accordance with the report that altitude is an important environmental factor in selection and establishment of seed sources in forestry (Wright 2012). However, the GD could be balanced by different forestry practices. For instance, gene diversity of seed crop could be increased from 0.967 to 0.970 (Ψ=2.73) by removing/uncollected of five the most/lowest productive trees in first year of low population. GD could play important role to establish resistance forest to different environmental conditions.

Seed harvesting and other forestry practices (e.g., natural regeneration practices) were suggested in good seed year. The strobili productions were clearly higher in first year than second year in the populations (Table 4), while GDs were similar between years within population (Table 6, Figure 4). It indicated that poor seed year could be also suitable for forestry practices based on gene diversity.

CONCLUSIONS

Variation of strobili productions among individuals within population indicated importance of individual selection in seed harvesting. Similar gene diversity between years showed that forestry practices (e.g., seed harvesting, natural regenerations) could be also carried out in poor seed year. Gene diversity (GD) was higher in high and very high altitudes than that of low and middle. The result could be a guide in altitudinal forestry practices. However, many ecological (i.e, altitude, aspect, edaphic, climatic) and biological factors (i.e, adaptation capacity and genetic diversity of the species, crown closure, tree size) could impact on gene diversity. The study was carried out in limited area of the species to be decreased effect of other factors. Effects of ecological and other factors which were changed altitudinal on gene diversity could be examined in large area by long term and future studies. Low gene diversity in seed crop could be increased by forest practices such as harvesting from similar productive trees. GD of seed crop should be taken into consideration in seed quality/grading together with other seed characteristics. Relations among the characters can be a guide for future studies, and establishment and management of seed sources. Present study included two-year data and limited area of the species. New studies should be carried out by different populations and years in the species to give accurate conclusions.

REFERENCES

Bernardes R.C., De Medeiros A., da Silva L., Cantoni L., Martins G.F., Mastrangelo T., Novikov A.I. and Mastrangelo C.B. (2022). Deep-learning approach for fusarium head blight detection in Wheat seeds using low-cost imaging technology. Agriculture, 12, 1801. https://doi.org/10.3390/agriculture12111801

Bila A.D. and Lindgren D. (1998). Fertility variation in Milletia stuhlmannii, Brachystegia spiciformis, Brachystegya bohemii and Leucaena leucocephala and its effects on relatedness in seeds. For. Genet. 5, 119–129.

Bilir N. (1997). Nursery stage of provanence on Taurus cedar (*Cedrus libani* A. Rich) in Eastern Black Sea region [MSc. Thesis] Trabzon, Turkey, Black Sea Technical University.

Bilir N. (2011). Fertility variation in wild rose (Rosa canina) over habitat classes. Int. J. Agric. Biol., 13, 110–114.

Bilir N. and Kang K.-S. (2014). Estimation of fertility variation by strobili and cone productions in Taurus cedar (*Cedrus libani* A. Rich.) populations. In: Proceedings of the Proceedings of the IUFRO Forest Tree Breeding Conference; Prague, Czech Republic, 25-29 August, 2014.

Bilir N. and Kang K.-S. (2021). Fertility variation, seed collection and gene diversity in natural stands of Taurus cedar (*Cedrus libani*). Eur. J. For. Res., 140, 199–208. https://doi.org/10.1007/s10342-020-01324-1.

Bilir N. and Ozel H.B. (2017). Fertility variation in a natural stand of Taurus cedar (*Cedrus libani* A. Rich.). In: Proceedings of the International Forestry and Environment Symposium (IFES); Trabzon, Turkey, 7-10 November, 2017.

Bilir N., Kang K.-S. and Lindgren D. (2005). Fertility variation in six populations of Brutian pine (*Pinus brutia* Ten.) over altitudinal ranges. Euphytica, 141, 163-168. https://doi.org/10.1007/s10681-005-6803-6.

Boydak M. (2003). Regeneration of Lebanon cedar (*Cedrus libani* A. Rich.) on karstic lands in Turkey. For. Ecol. Manage, 178, 231-243. https://doi.org/10.1016/S0378-1127(02)00539-X

Eler U. (1990). Seed yield in Calabrian cluster pine (*Pinus brutia* Ten.) by age. In Forest Research Institute, Technical Bulletin; Forest Research Institute: Antalya. Turkey, 53–78. https://doi.org/10.3390/f14061130

Kamalakannan R., Varghese M., Park J.-M., Kwon S-H., Song J.-H. and Kang K.-S. (2015). Fertility variation and its impact on effective population size in seed stands of Tamarindus indica and Azadirachta indica. Silvae Genet., 64, 91-99. https://doi.org/10.1515/sg-2015-0008.

Kang K.-S. (2001). Genetic gain and gene diversity of seed orchard crops [PhD Thesis], Umeå: Swedish University of Agricultural Science.

Kang K.-S. and Bilir N. (2021). Seed orchards (Establishment, Management and Genetics. Ankara, Turkey, OGEM-VAK Press, 189.

Kang K.-S. and Lindgren D. (1998). Fertility variation and its effect on the relatedness of seeds in *Pinus densiflora, Pinus thunbergii* and Pinus koraiensis clonal seed orchards. Silvae Genet., 47, 196–201.

Kang K.-S. and Lindgren D. (1999). Fertility variation among clones of Korean pine (*Pinus koraiensis* S. et Z.) and its implications on seed orchard management. For. Genet., 6, 191-200.

Kang K.-S., Bila A.D., Harju A.M. and Lindgren D. (2003). Estimation of fertility variation in forest tree populations. Forestry, 76, 329-344. https://doi.org/10.1093/forestry/76.3.329.

Koski V. and Antola J. (1993). National tree breeding and seed production programme for Turkey 1994-2003. [online] Available at: https://ortohum.ogm.gov.tr [accessed on Jan 10, 2023].

Novikov A.I., Lisitsyn V.I., Tigabu M., Tylek P. and Chuchupal S. (2021b) Detection of Scots pine single seed in optoelectronic system of mobile grader: mathematical modeling. Forests, 12, 240. https://doi.org/10.3390/f12020240.

Novikov A.I., Sokolov S.V., Drapalyuk M.V., Zelikov V.A. and Ivetić V. (2019). Performance of Scots pine seedlings from seeds graded by colour. Forests, 10, 1064. https://doi.org/10.3390/f10121064.

Novikov A.I., Zolnikov V.K. and Novikova T.P. (2021a) Grading of Scots pine seeds by the seed coat color: how to optimize the engineering parameters of the mobile optoelectronic device. Inventions, 6, 7. https://doi.org/10.3390/inventions6010007.

Novikova T.P. (2022a). Study of a set of technological operations for the preparation of coniferous seed material for reforestation. Forestry Engineering Journal, 11, 150-160. https://doi.org/10.34220/issn.2222-7962/2021.4/13.

Novikova T.P. (2022b). The choice of a set of operations for forest landscape restoration technology. Inventions, 7, 1. https://doi.org/10.3390/inventions7010001.

Novikova T.P., Mastrangelo C.B., Tylek P., Evdokimova S.A. and Novikov A.I. (2022). How can the engineering parameters of the NIR grader affect the efficiency of seed grading? Agriculture, 12, 2125. https://doi.org/10.3390/agriculture12122125

Odabasi T. (1990). Research on cone and seed characteristics of *Cedrus libani*. [online] Available at: https://www.ogm.gov.tr [accessed on Jan 14, 2023].

OGM.gov.tr (2022). Forest inventory of Turkey. [online] Available at: www.ogm.gov.tr. [Accessed Apr 20, 2023].

Ozbey A. and Bilir N. (2022). Block effect on genetic parameters in a 23-year-old progeny trial of *Pinus brutia*. Forestry Engineering Journal. 12, 5-13. https://doi.org/10.34220/issn.2222-7962/2022.2/1.

Park J.M., Kwon S.H., Lee H.J., Na S.J., El-Kassaby Y.A. and Kang K.-S. (2017). Integrating fecundity variation and genetic relatedness in estimating the gene diversity of seed crops: *Pinus koraiensis* seed Orchard as an example. Can. J. For. Res., 47, 366-370. https://doi.org/10.1139/cjfr-2016-0223.

Saatcioglu F. (1956). Research on seeds of cedar of Lebanon. J. For. Fac. Istanbul Univ 1, 35-64.

Saatcioglu F. (1971). Forest tree seeds. Istanbul, Turkey: Forestry Faculty of Istanbul University, 243.

Savolainen O., Karkkainen K., Harju A., Nikkanen T. and Rusanen M. (1993). Fertility variation in *Pinus sylvestris*: a test of sexual allocation theory. Am. J. Bot., 80, 1016-1020. https://doi.org/10.2307/2445748.

SPSS (2011). IBM SPSS Statistics for Windows, Version 20.0., NY: IBM Corp.

Vidakoviç M. (1982). Conifers: morphology and variability. Zagreb, Yugoslavia, Yugoslav Academy of Science and Arts, and Liber University, 710.

Wright J.W. (2012). Introduction to forest genetics. Elsevier, 480.

Yazici N. and Bilir N. (2017). Aspectual fertility variation and its effect on gene diversity of seeds in natural stands of Taurus cedar (*Cedrus libani* A. Rich.). Int. J. Genomics, 2960624, 1-5. https://doi.org/10.1155/2017/2960624.

Yazici N. and Bilir N. (2023). Impact of crown closure on cone production and effective number of parents in natural stands of Taurus cedar (*Cedrus libani* A. Rich.). Forests, 14, 1130. https://doi.org/10.3390/f14061130

APPENDIX A

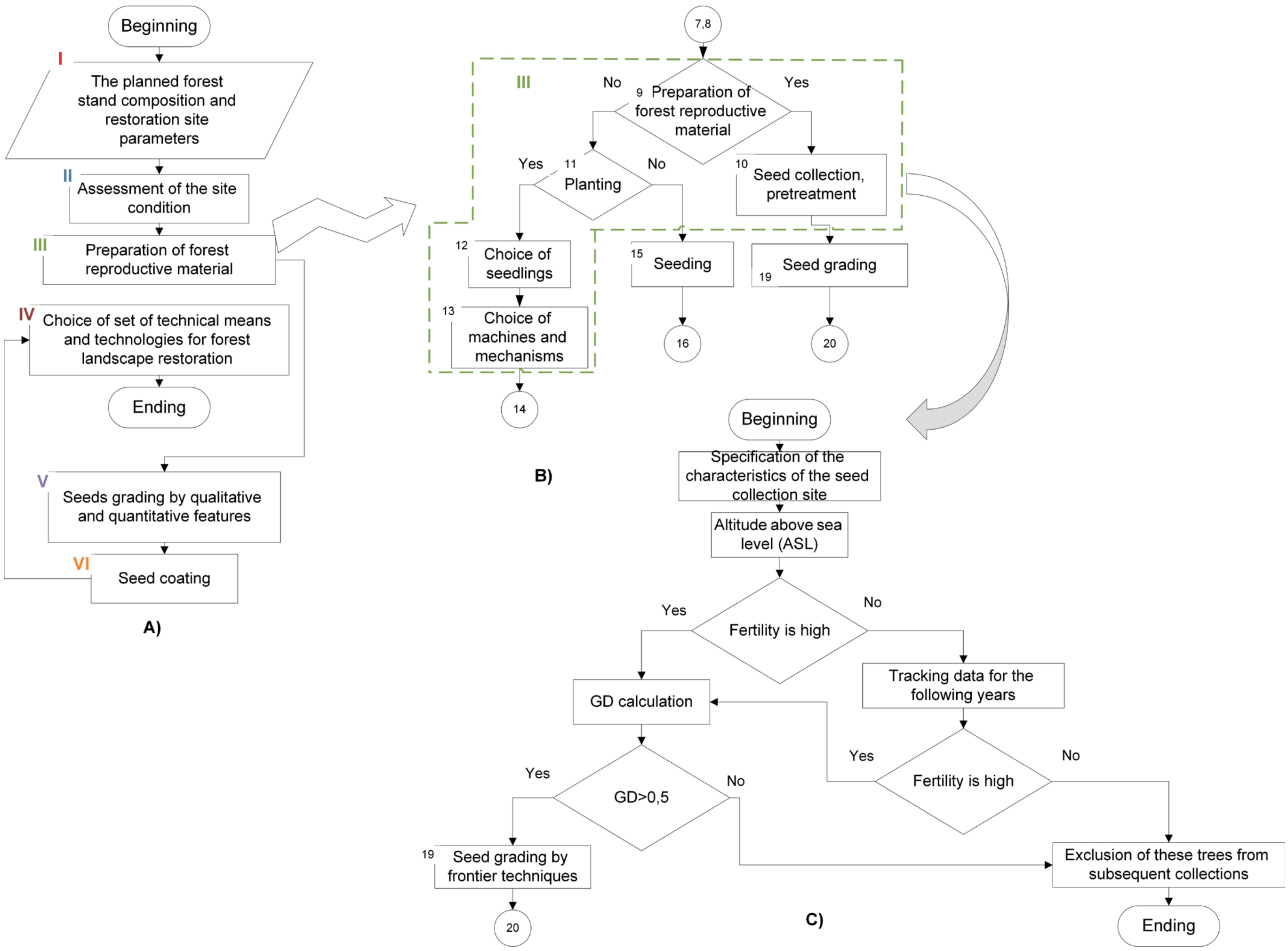

Fig. A.1. Practical application of the parameters of the genetic diversity of seeds (C) in the decomposition of the FLR-model for the preparation of forest reproductive material (B), which is the III-group of the generalized algorithm for choosing the technology of forest restoration (A). Figures A) and B) are adapted from the paper by co-author T.N. (Novikova 2022b), figure C) is the T.N. own composition

RESEARCH PAPER

LEADING GLOBAL CITIES IN THE RUSSIAN-LANGUAGE SEGMENT OF INTERNET: HOW DO THEY LOOK LIKE AT THE BEGINNING OF THE 21ST CENTURY?

Andrei V. Korobkov[1], Svyatoslav S. Kuzovlev[2], Elena S. Rykunova[3*], Nikolay A. Sluka[2]
[1]Middle Tennessee State University, Department of Political Science and International Relations, 37132, Murfreesboro, TN, USA
[2]Lomonosov Moscow State University, Faculty of Geography, 119991, Moscow, Russia
[3]KIMEP University, Faculty of General Education, 050010, Almaty, Kazakhstan
***Corresponding author:** rykunova.es@yandex.ru
Received: December 15th, 2022 / Accepted: November 14th, 2023 / Published: December 31st, 2023
https://DOI-10.24057/2071-9388-2023-2682

ABSTRACT. In the XXI century, the factors of the development of megacities are changing rapidly, the competitiveness of which increasingly depends on their image in different social environments. The purpose of the study is to identify main common features of the current image of the leading global cities (London, Paris, New York and Tokyo) in the Russian–language segment of the Internet (Runet). The research was based on a combination of methods of socio-economic geography, quantitative and qualitative methods of sociology. To reflect the objective reality of megacities, international statistics were used; to assess the role of Internet information resources influencing the formation of the image, the number of search queries in Runet and the context of publications about cities in social media were analyzed; to identify the configuration of the image, the data of a sociological survey were studied. It was revealed that the perception of megacities in Runet is based on a comparable volume of information flow in social networks (the number of published messages is 20 thousand per day for Paris and London, 15 thousand for New York, 4 thousand for Tokyo) and on similarity of publications' context (2/5 are in the categories "entertainment" and "personality"). Despite certain limitations of the methods used and the relevance of the digital artifacts obtained, the image structure of the centers under consideration is characterized by the predominance of objective over subjective and cognitive (knowledge and ideas about "physical" givens) over affective (emotions, feelings, sensations) components with the key role of four collective categories: common features of large cities, idealized imagery of the country, prestigious urban locations and world architectural brands; as well as high stability in time and space. The continuation of research based on the proposed principles, while improving the methodology and involving cities of different classes, will contribute to the adaptation of foreign experience in designing of images of ambitious Russian cities in the face of new global challenges.

KEYWORDS: image geography, leading global cities, image support frame, social media, Runet

CITATION: Korobkov A. V. , Kuzovlev S. S., Rykunova E. S., Sluka N. A. (2023). Leading Global Cities In The Russian-Language Segment Of Internet: How Do They Look Like At The Beginning Of The 21st Century?. Geography, Environment, Sustainability, 4(16), 72-81
https://DOI-10.24057/2071-9388-2023-2682

Conflict of interests: The authors reported no potential conflict of interest.

INTRODUCTION

In the conditions of the information society development, the ratio and structure of endo- and exogenous factors in the formation of a large city, which is recognized as a complex phenomenon in social geography and related disciplines, and traditionally considered as a focus of political, economic and cultural life of territorial systems of various scales, are changing significantly and rapidly. New global challenges, including, in particular, the COVID-19 pandemic and sanctions have sharply limited the possibilities and scope of direct contacts. Such situation vividly reflects the growing dependence of the successfulness and international attractiveness of metropolis not so much on the scale of its economic resources - land, capital, labor (i.e., territory, population and GDP), but on the established reputation. This trend was noticed by a number of well-known scientists who stated that: "in our age of rapid development of mass media, ideas about the world replace the world itself" (Kolosov, Tikunov, Zayats, 2000) and proposed the concept of *symbolic capital* (Bourdieu, 2001; Toffler, 2003). Being formed on the global stage the image of the city determines the attitude towards it, which ultimately finds expression in the development of economic, political, social and other ties at all territorial levels. It is increasingly becoming a necessary tool not only for attracting foreign investment, branches of foreign TNCs, human capital, international tourists, etc., but also for the formation of a sustainable competitiveness of the city in the long term period. As a result, in the age of communication development, the image becomes not an abstract concept, but a specific one; it acquires an important economic meaning.

The image of the city is the totality of ideas about it that exists in the mind, according to Vizgalov, "not necessarily systemic and correct", often not only positive, but also negative, problematic. The most significant of them can be considered as a supporting structure or frame that provides sufficient strength and stability for the image of each metropolis; and their identity for a group of equivalent objects - like a generalizing portrait or a supporting frame[1] - is a kind of bond that gives the proper configuration to the image of cities of a certain class. It shows both generalization, and connections, and differentiation of phenomena, including spatial ones. Identification of the supporting frame of the image of different categories of cities is of not only scientific and educational, but also applied values. It represents a starting line of action for ambitious cities, including Russian, aimed at increasing international influence and increasing role in world politics, economics, and culture.

The study of the image support frame of the modern elite of urban formations and the most eminent world centers becomes to be of great value in determining the main guidelines and specific priorities in constructing the perception of each metropolis in the international community. A special group among them is represented by global cities that are maximally integrated into transnational networks - multidimensional political, economic, social, religious and other interactions over and beyond state and territorial borders. The phenomenon of a global city was theoretically substantiated in the works of S. Sassen (Sassen, 1991) and has got the primary empirical interpretation in the works of the international research group "Globalization and World Cities" (GaWC). According to the founders of the concept, the international significance of the city is directly linked to the quality of service for the transnational capital and is identified by the concentration of headquarters and branches of highly specialized companies and knowledge-intensive services. The leadership definately belongs to four centers - New York, London, Paris and Tokyo (Beaverstock, Smith, Taylor, 1999; Sluka, Karyakin, Kolyasev, 2020). The concept, focused on the assessment of intercity interaction, highlighted the process of increasing cooperation and, at the same time, fierce competition between centers. That actualizes the study of both modern key competencies of megacities that provide competitive advantages, and strategies for achieving them, including by improving the image.

The general ideas and a number of models of symbolic politics as one of the technologies for creating an image are well known. (Efremova, 2015; Potseluev, 2012; Edelman, 1964; Meyer, 1992; Sarcinelli, 1987). The problem of its creation is closely related, on the one hand, to the multiplicity of factors, including territorial affiliation, status, historical past, quality of the environment, the level and quality of the city's power structures, etc., and on the other hand, with the to the multiplicity of target audiences, which requires "the activities of the circle of actors aimed at the production and promotion of certain ways of interpreting social reality" (Malinova, 2010) and the selection of special tools for each "consumer" of the place. The concept of "positive image" and its frame in relation to the city for different categories of people sounds differently.

The purpose of this study is to identify the image support frame of the leading global centers in the Russian-speaking segment of the Internet (Runet) using the capabilities of social media.

MATERIALS AND METHODS

The study is based on the one hand on the theories of a world and global city (Geddes, 1915; Friedmann, 1986; Hall, 1966 and others.) and on the other hand – on a conceptual basis of image geography, marketing and city branding fundamentals (Vizgalov, 2008, 2011; Zamyatin, 2006; Zamyatina, Harutyunyan, 2005; Kalutskov, 2008; Tokbulatova, Kolosov 2018; Okunev, 2020, etc.), as well as the elaborations of foreign research structures (IFUS[2], 2018; Ipsos[3], 2020) and consulting companies (Resonance[4], 2018; Reputation Institute[5], 2018). The conceptual scheme for studying the global city image relies on a large set of objective and subjective factors that characterize the object of perception itself, the carriers of perceptions and the specifics of the relationship between them. Image formation factors reflect the reality. Building the image of an object depends on the transmission link between the real world and the perceived world - a complex of existing mechanisms, among which, along with school and in-depth knowledge, special place belongs to personal experience, electronic media information sources occupy a special place. Some of them (third-party initiative) are aimed at promoting of the properties of the city outwards, and some (personal initiative) are associated with satisfying the interests and preferences of the audience itself. In this case a set of features of the city perception appears, which is built mainly on the basis of three types of categories: cognitive - knowledge and ideas about the "physical" components; *affective* - emotions, feelings, sensations; *behavioral* - actions of the recipient in relation to the image inductor (Kiryanova, 2015).

The lack of recognized ways to verify the image imposes additional obligations on the researcher to verify, clarify and update the findings, which can be achieved by using a set of methods that allow assessing the phenomenon from different angles and relying on different sources. The methodological apparatus of this study is based on a combination of general scientific and classical methods of social geography, including comparative geographical method; as well as qualitative and quantitative methods applied in sociology (public opinion polls). The first set of methods allows obtaining information about the views dominating within the audience directly from their carriers, while the latter methods are focused on the analysis of social media content, which are both a tool for the development of views and their partial reflection (Tokbulatova, 2020). When collecting actual data, the Internet metric method was actively used, combining the use of special Internet services and remote interaction with respondents from social networks. The conceptual scheme for the implementation of the study is shown in Figure 1.

The primary research database was collected on the eve of the COVID-19 pandemic, from March 2017 to February 2018, and consists of four main blocks. The first is a set of statistical data and international ratings, which allow to create a general idea of the leading global cities "portraits" from the standpoint of classical geo-urban studies. The second is the number of search queries in Runet for each center, given by the "Yandex. Choice of words" tool. The third is the frequency and context of mentioning the cities, using a number of qualitative categories such as economy, politics, personalities, entertainment, infrastructure, etc. in the combination of social media, e.g. VK, Facebook,

[1]The idea of the frame approach was actively developed by many russian economic geographers. According to I.M. Maergois, the notion of a frame is highly informative (Lappo, 1983), and by virtue of this alone can and should be effectively incorporated into imaginative geography.

[2]Institure for Urban Strategies (IFUS). City perception survey. https://www.mori-m-foundation.or.jp.

[3]IPSOS https://www.ipsos.com/en

[4]Resonance Consultancy. https://resonanceco.com/

[5]Reputation Institute. Most Reputable Cities 2018. https://www.reputationinstitute.com/city-reptrak.

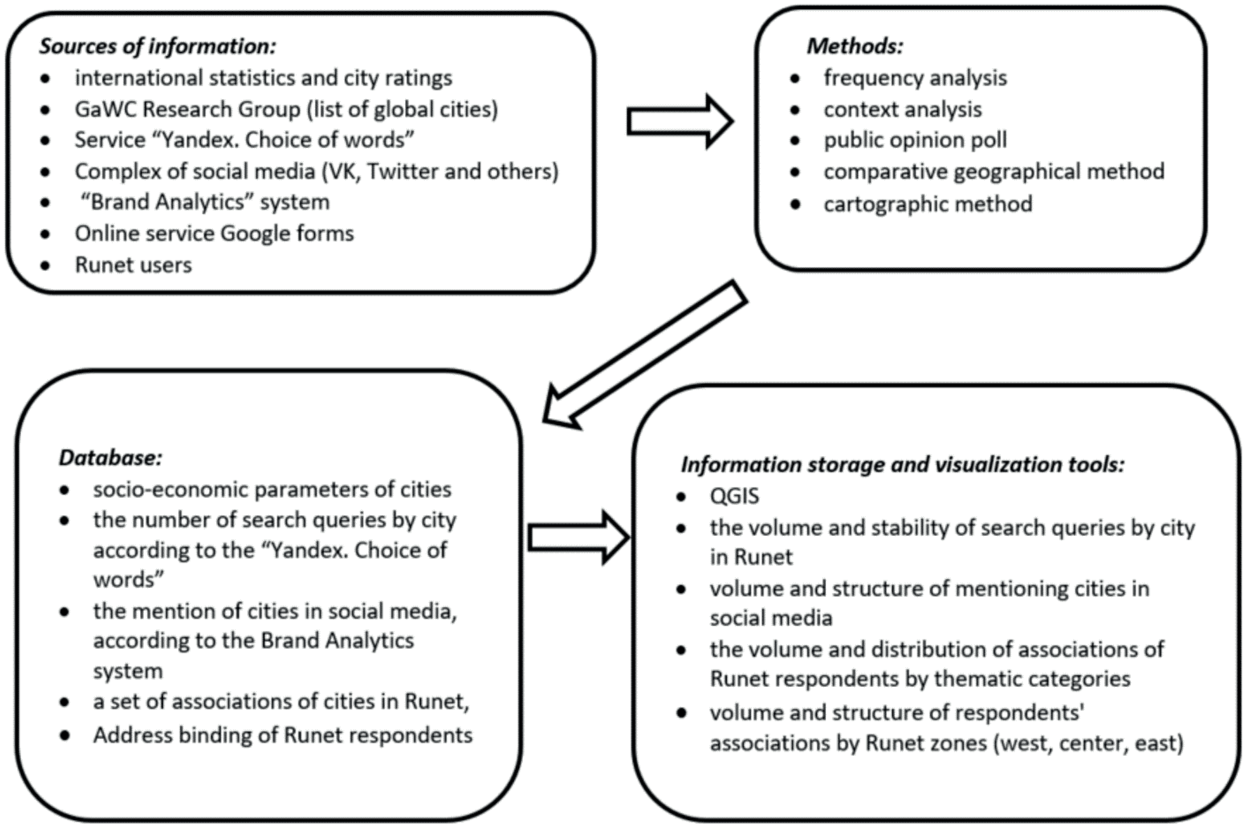

Fig. 1. Image of the leading global cities in Runet: conceptual scheme of the study

Instagram, Twitter and others[6]. These data are obtained with the help of a special setting of the Brand Analytics system[7], a business intelligence and reputation management tool developed by the Russian company I-Teco. The fourth block is presented by the results of a sociological survey among Runet users by a special method using the Google form service and aimed at understanding the main features of the city's image. About 2,000 respondents were involved in the survey, mostly from the regions of Russia[8]. The structure of respondents was distinguished by gender equality, an increased proportion of young people, and a variety of levels of education and qualification. All received data were processed and systematized, summarized in statistical charts and visualized as a system based on the consolidation of tabular data and spatial relationships using the functionality of QGIS.

RESULTS

Four global cities in the system of objective reality indicators

Characteristics that reflect objective reality are the basic component of the image frame of any territory (Vizgalov, 2011). Leading global cities are often comparable to entire countries in terms of geographic size parameters (Sluka N., Tikunov V., Chereshnia, 2019). They occupy special positions in the international division of labor, act as focuses of the globalization process and transnationalization of the economy, and their meaning and identity go far beyond their home countries. The role of *world capitals*, on the one hand, and the multifunctionality of centers and the attractive qualities of the urban environment, on the other hand, are well revealed both by individual quantitative indicators[9] (Table 1) and by numerous complex ratings, e.g. the Global Power City Index, Global City Competitiveness Index, Global Financial Centers Index 29, The Sustainable Cities Index, etc. Dozens of indicators of different qualitative fields and spheres of life and their groups are used while compiling these ratings.

By most indicators, the leading global cities are far ahead of other centers and, as a rule, "share" the leadership among themselves. The hallmark of each of them is the concentration of various government bodies, the large number of international organizations and business structures, leading universities and research institutes, accommodation facilities and cultural institutions, including primarily a rich museum fund. They are clearly distinguished both by the quality of the urban environment and by their integration into the system of global communications and flows. For example, flights are regularly operated from New York to 223 direct air routes, from Paris - 286, and London - 355 (Rating of innovative attractiveness ..., 2023, p. 174). At the same time, against the general background, Tokyo is primarily distinguished by its colossal population, the power of the economy and the development of higher education, New York - by a vast territory of the agglomeration and the representativeness of successful business, and European capitals - by performing a political function, and by the function of hospitality.

The scale and international significance along with multi-dimensionality and originality of the key competences determine a very broad start platform for building the perception of global cities by different audiences and social groups. A number of properties such as status, geographical location, country of origin,

[6]The initial data of the study were collected before the introduction of a ban in Russia on the social networks Facebook and Instagram and the recognition of the American company Meta, which owns them, as extremist along with its products.
[7]Brand Analytics. http://branalytics.ru
[8]Questionnaires of respondents from other countries were selectively taken into account during expert verification and clarification of the features of the «support frame» of the image.
[9]Demographia World Urban Areas. URL: http://www.demographia.com/db-worldua.pdf (access date 30.03.2023).

Table 1. Key Indicators of Leading Global Cities

Indicators	New York	London	Paris	Tokyo
City category in GaWC rating	α++	α++	α+	α+
Population of agglomeration, million people	21,6	10,6	10,9	38,1
Built-Up Land Area, sq.km	12093	1738	2853	8231
GDP, billion dollars 2021 (estimates)	1330	1064	1036	2205
Number of diplomatic missions	93	151	150	146
Number of TNC headquarters	107	75	55	149
Number of headquarters of international organizations	764	1242	1054	295
Number of unicorn companies	110	41	26	8
Number of leading universities	20	22	16	45
Number of scientific publications, 2016–2020, thousand	245	255	205	249
Number of congresses/participants, thousand people	47/…	177/78,8	190/111,7	117/27,9
Number of international tourists, million	14,0	19,6	19,1	10,4
Passenger air traffic, million people	135,5	170,9	105,2	126,3
The most popular cities in the world by the number of hashtags in the Instagram network, million	95,5	107,6	91,7	40,8

Compiled by the authors based on the data of international statistics and city ratings.

history, culture, security, etc. are integral. Part of them are especially significant for the global elite (for example, prestige, functions, business environment, location of the head offices of TNCs), part of them are for various segments of the vast and rapidly progressing global periphery, which has enormous human potential and natural resource base (accessibility, accommodation facilities, prices, tourist attractors).

The City Brand Index 2020[10] is aimed at comparing the perception of the largest cities among the widest possible audience. Its methodology involves the evaluation of 50 centers within 6 categories: *Presence* – international status, *Place* – external attractiveness of the city, *Prerequisites* – accommodation options and accessibility of public spaces, *People* – the friendliness of residents, *Pulse* – the activity of city life, and *Potential* – the prospects for education and business. The research is based on online interviews with 5,000 respondents aged 18 and over from 10 countries: Australia, Brazil, UK, Germany, India, China, Republic of Korea, Russia, USA and France. Online user data is weighted by key demographics and education levels.

Over the past 10 years, the leading group of ranking centers with a predominance of European cities has been fairly stable, but the leadership has changed periodically. According to the Index, calculated on the basis of data on the eve of the COVID-19 pandemic, London was at the head of the hierarchy. The top 10 cities after Sydney included two other leading global cities: Paris and New York. They were followed by Rome, Amsterdam, Vienna, Vancouver, Melbourne and San Francisco. Tokyo took only the 16th line of the rating. At the same time, the leading global cities differed quite significantly in terms of the set and combination of strengths. According to the international audience, London's positions were especially high in the categories *Presence*, *People* and *Potential*; Paris - in the category *Place*; New York - *Pulse* and *Potential*; and Tokyo - *Presence* and *Pulse*.

According to its purpose, the Brand Index contributes to the monitoring of the ranking table of cities, but is not devoid of the subjective component of the formation of respondents' ideas (other people's opinions, stereotypes, rumors), which, however, is very difficult to avoid in general; is not able to take into account the influence of information flows and the ratio of the main operating mechanisms in the perception of the centers (third-party and personal initiative); and besides, it is schematic, which seriously limits the possibilities of indicating the primary element base or the image frame of the studied agglomerations.

Global cities in the Runet information flow

A significant role in the image construction is played by both the traditionally increased creativity and eventfulness of the megacities' environment, and the power of the own mass media industry, which ensures the central positioning of the leading global cities in the international information flow, and their high attractiveness for the *external world*. This, in turn, is expressed by a huge number of relevant hashtags on the Instagram[11] network (Table 1). The capacity of the information base for building the image of the leading global cities in the Runet audience is very significant and surpasses all other large centers, but differs significantly with a high correlation in the distribution of sources of different genesis - the number of search queries and the frequency of mentions in social media (Table 2). In both cases, Paris and London share the lead by a noticeable margin, which can be considered natural, given the specifics of the development of political, business and cultural ties between Great Britain and France, on the one hand, and Russia, on the other. Cities consistently enjoy special prestige among the Russian establishment and popularity among the population as world-class tourist centers. In 2019, each of them was visited by more than 19 million international tourists, including tens of thousands

[10] IPSOS https://www.ipsos.com/en

[11] Social network banned in Russia.

Table 2. Leading global cities in the Runet information flow

City	The mentions of cities in the total social media, according to Brand Analytics, million	The search queries by city, according to Yandex. Selection of words, million	Search queries per number of mentions
Paris	6,522	24,345	3,73
London	5,801	22,358	3,85
New York	4,052	14,931	3,68
Tokyo	1,468	10,392	7,08
Los Angeles	1,138	5,913	5,19
Singapore	1,125	5,680	5,19
Seoul	0,961	2,910	3,03
Hong Kong	0,839	3,971	4,73
Shanghai	0,638	4,233	6,63

Data are given for a number of other global cities for comparison.

from Russia. It is also indicative that, according to our data, 42% of respondents visited the capital of France, and only 25% - the UK capital (Sluka, Kuzovlev, 2020). New York and especially Tokyo are far behind the European centers. The public information in the media about these cities is partly closed through the personal settings of Internet search engines.

Among the permanently acting sources of the cities' image, the influence of the discourse formed by the media is highly important. According to the histogram of published messages on the Internet in Russian (Fig. 2), the information base for building the leading global cities' image is quite stable throughout the year with a slight decrease in the summer period and, however, does not depend on seasonality in general. For example, for Paris and London, it averages about 20,000 messages per day; for New York – 15,000; and for Tokyo - about 4,000 messages a day. It is natural that its total size is largely adjusted by a combination of accidents (terrorist attacks, strikes, Khvorostovsky's[12] death in London) and major international events (presidential elections in France, governmental visits, international exhibitions, economic forums, etc.). Some of them, due to the inertia of forming any object's perception, are left in the minds of the audience and for a long time remain among the important features of the image. For example, Brexit has become a hallmark not only of Great Britain, but also of its capital.

According to Brand Analytics, the structure of published messages on the Internet in Russian is quite specific and generally similar. In the case of the four cities, the category *incidents* accounts for about 10%, the sphere *economics and politics* 10-15%, and the main part - more than 2/5 – is taken by only two nominal thematic areas - "entertainment" and "personality" (Fig. 2). For example, in Paris - 22% each; and London - 16% and 35%, respectively. In the case of Paris, this is determined by the targeted promotion of the strong points of urban infrastructure, services and tourist attractions (sights, museums, hotels, restaurants, cafes, etc.). In the case of London it can be explained by satisfying the existing interest of the audience in famous historical personalities (great military leaders, politicians, artists, architects, artists, etc.) and the modern elite of the creative class (Florida, 2005), serving as a role model and forming public opinion, being actively involved in the global world.

"Support frame" of the global cities' image in Runet

The nature of the information flow, along with some other mechanisms, largely determines the private images or features and properties of the city, which make up its holistic perception in the recognition of the selected audience and the image frame is being formed. You can study them from different perspectives. One possible approach is to rely on two categories. The first one is the "common field" or "richness" of the image as the combination of all private images. Theoretically, their number is infinite and includes many thematic aspects of both the real and imaginary worlds, but in practice it depends on the competence of the respondents and is reasonably limited. The second category is the *focus* of the image - the level of identification or recognition of the object's features by a group of respondents. It can be both mass and very selective. It can occur on the basis of one or more properties of an object. The combination of the "general field" and "focus" scales allows to operate with a series of models of the "support frame" of the image. At one pole there is a model with a large number of features and a high localization of associations around one feature of the city (image-core), at the opposite - with a small and discrete associations. Naturally, there are a number of transitional options between these poles (Fig. 3).

Based on the proposed views and relying on the results of a sociological survey conducted by an Internet questionnaire using the Google Forms service, the *support frame* of the leading global cities' image in Runet is described by a single model with a very wide field richness and a polynuclear structure. They are identified through hundreds of associations, with a maximum for Paris and a minimum for Tokyo, which, when generalized, are reduced to almost two dozen main components of a predominantly cognitive category (Fig. 4). At the same time, the repeatability of the stereotype of ideas about a common modern city as is especially high (beautiful, crowded, multi-ethnic, expensive, fashion, culture) and its main functions - political, business, financial, transport, cultural. In contrast to the City Brand Index, the general construct of perception of global centers in Runet practically does not reflect their international status, accommodation opportunities, the goodwill of residents, the prospects for education and business are not assessed. In addition, there are no mentions of the largest global agents of the economy - parent TNCs and politics - the UN (headquarters

[12]Dmitry Khvorostovsky – famous Russian opera singer.

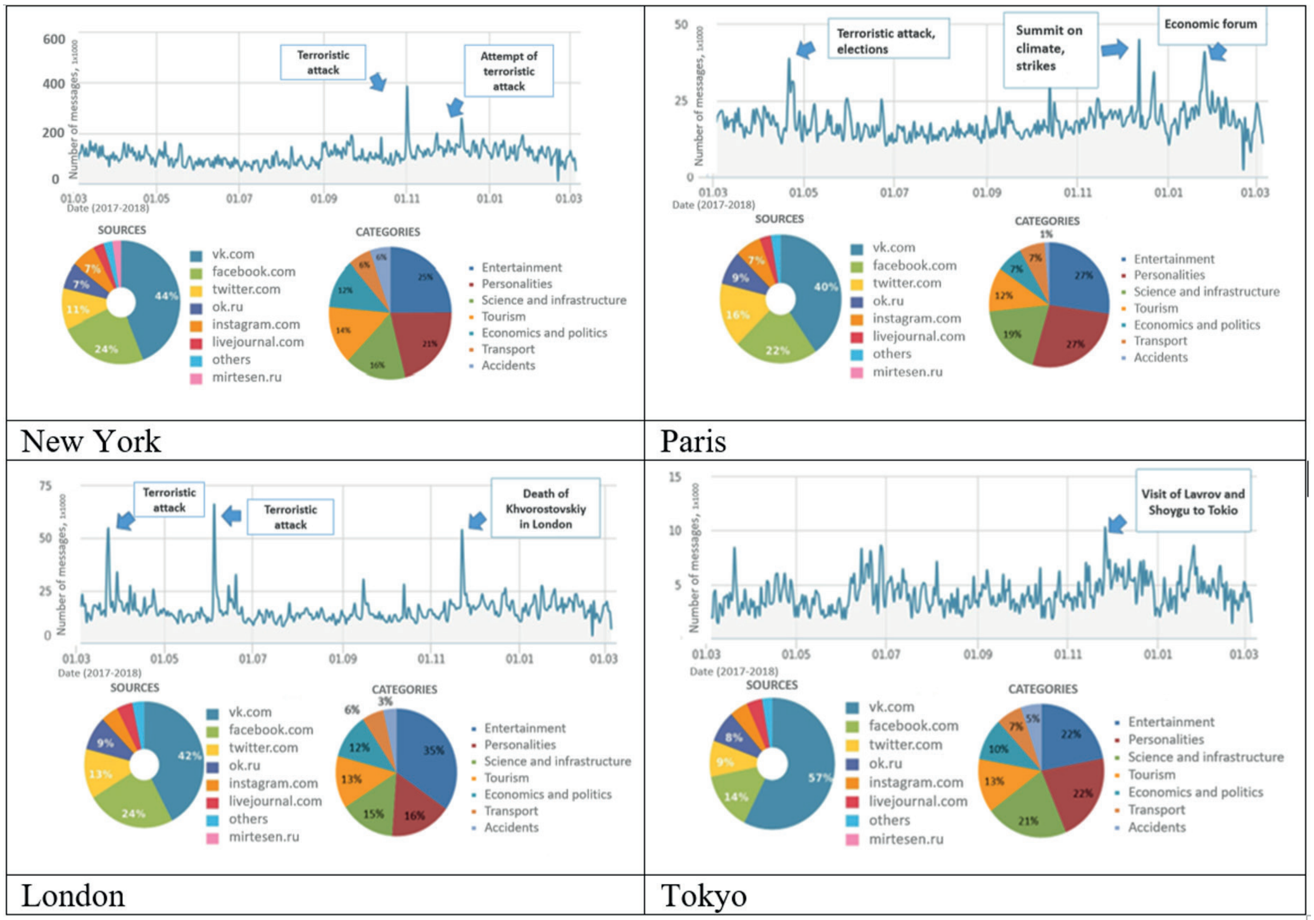

Fig. 2. Distribution of published messages about New York, Paris, London and Tokyo in Russian on the Internet

Features		Image field richness (number of images)		
	Subcategories	High	Medium	Low
Variants of the "image framework"				
Image focus (number of core images)	One	Wide, mononuclear	Limited, mononuclear	Narrow, mononuclear
		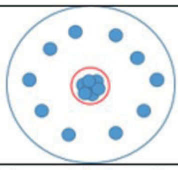	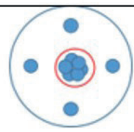	
	Several	Wide, polynuclear	Limited, polynuclear	Narrow, polynuclear
		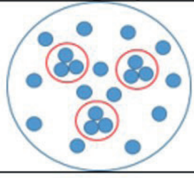	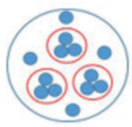	
	None	Wide, amorphous	Limited, amorphous	Narrow, amorphous
		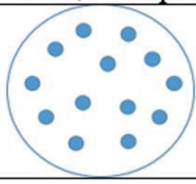	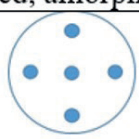	

Fig. 3. Theoretical models of the city's image support frame

in New York) and its specialized agencies such as UNESCO (Paris), the International Maritime Organization (London), the UN University (Tokyo), etc., a very modest number of associations with products of mass culture such as literary heroes, characters of television series and the film industry. It is curious that in the latter case, London is perceived primarily through the characters of fiction books (Sherlock Holmes, Harry James Potter), Paris – through music (classical Moulin Rouge cabaret; singer, composer and poet Charles Aznavour), New York – through cinema (comedy-drama television series Sex and the City, Christmas comedy HOME ALONe), and Tokyo is not identified in any way.

The polynuclear nature of the image support frame of the leading global cities, in addition to the block of above mentioned stereotypes and functions, is determined by at least three more major elements. The first one of them is being an official and unofficial capital. In contrast to the international audience, the Russian-speaking segment of the Internet is characterized by building an idea of the metropolis place not in the entire world, but primarily at the national level. The identification of the city and countries occurs in a variety of ways, starting with physical and geographical data, historical events, political and administrative structure, cultural traditions and ending with the specifics of national cuisine. For example, tags for Paris are croissants, baguettes, onion soup, frog legs, etc., for Tokyo - sakura, anime, fish and seafood, sushi, etc.

The second element is a combination of prestigious urban locations and their parts – business centers, historical districts, shopping streets, parks, etc. The most popular component for New York is Manhattan, for Paris – Montmartre and Champs Elysees, for London – City, for Tokyo – Shibuya. At the same time, for the capital of France, the "local Manhattan" - La Defense, and the nearest

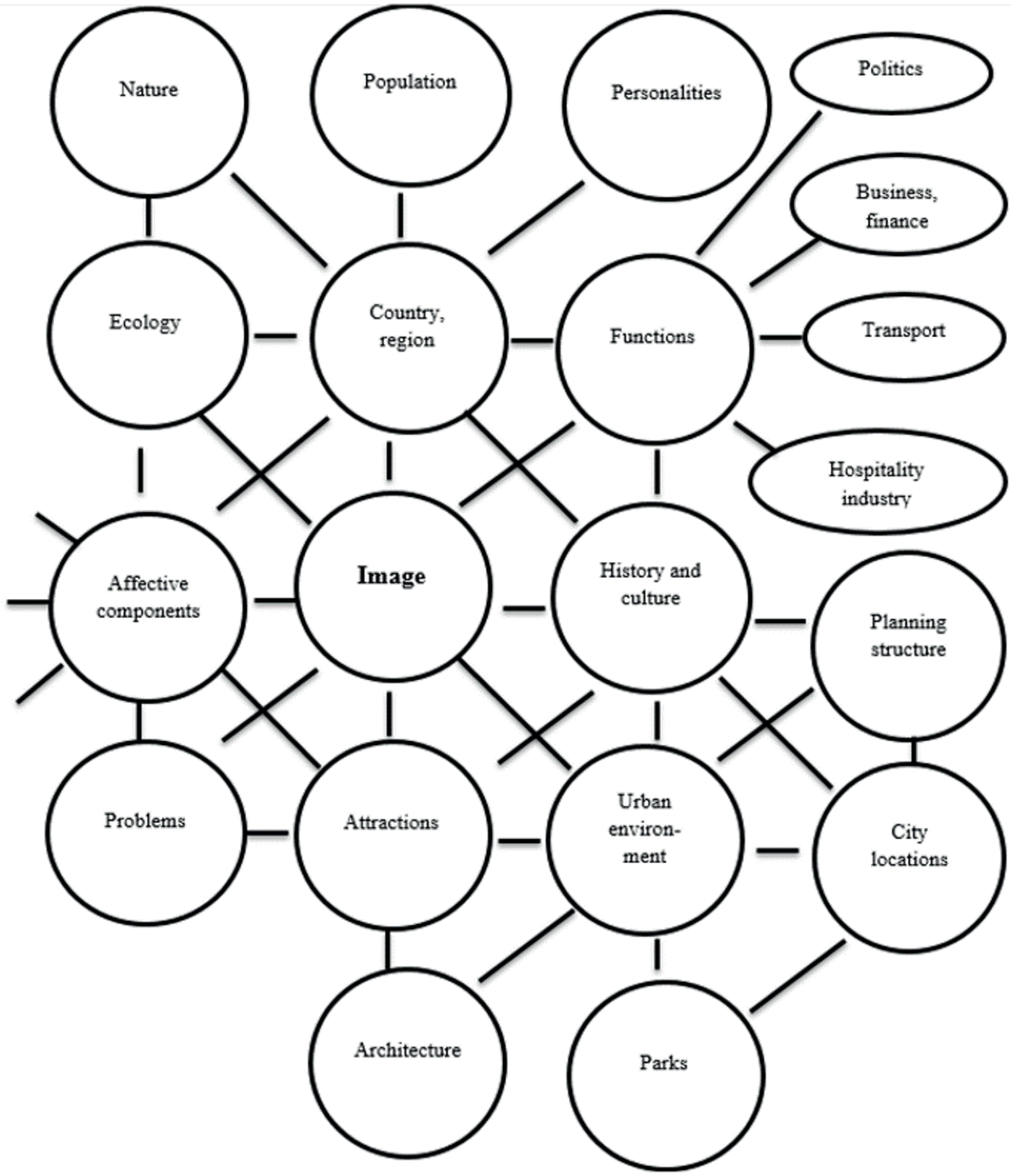

Fig. 4. The construct of the image support frame of the leading global cities in Runet

suburbs, including Versailles, are not mentioned, as well as the Docklands - a young business district, part of which - Canary Wharf, the second financial center of London.

Finally, the third element is the world-famous architectural landmarks of cities, the vast majority of which clearly gravitate towards their historical center (the Louvre, the Eiffel Tower, Big Ben, the Statue of Liberty, etc.). Compared to museum valuables, which require in-depth knowledge to assimilate, it is probably the face-to-face or distance visual acquaintance with the brands of cities and countries that makes a special contribution to their perception.

With a common support frame, the detailed configuration of the leading global cities' image is highly individual. This is already noticeable through a very diverse ratio of the cognitive and affective categories of the image. Thus, with the equivalence of the general field and the structure of the image due to the contribution of emotions, feelings and sensations, the perception of Paris differs noticeably from London, New York and Tokyo, which is well read when visualized through *tag clouds* (Fig. 5). In the first case, there is an emotionally sublime idea of the city (tags - romance, spring, love, etc.), which probably has developed as a result of a long and deep penetration of French culture into the minds of the respondents. In particular, it is known that many generations of Russians were brought up on the outstanding French national historical and adventure novels and their screen adaptations[13]. In other cases, much colder tones of perception of the cities are obvious: for London - with a relative emphasis on political aspects, dating back to the days of the British Empire; for New York with its dry business style; and for Tokyo through technological advancement as a result of the "Japanese economic miracle".

With the overall stability of the image support frame of the leading global cities in Runet space, its configuration is modified in the meridional direction. This may be partly due to both the quality of the audience (age, education, qualifications, etc.) and the distance factor - the remoteness of a particular object from the place of residence of the respondents and, accordingly, the mass tourism, which provides a more critical perception of the city. Thus, according to our data, about 60% of respondents from the regions of the European part of Russia visited Paris, and from the Asian part - less than 40%. As a result, in the western segment of the Runet, in addition to the classic features, a number of aspects are especially marked, including manifestations of environmental and socio-ethnic problems, e.g. traffic jams, dirt, strikes, homeless people, immigrants, etc. In Moscow, national brands in fashion, gastronomic delights and the entertainment industry have an increased weight in the structure of the image of the metropolises. In the east, the capital of France is identified mainly through architectural and historical and cultural attractions such as Eiffel Tower, Louvre, Montmartre, Champs Elysees, etc. (Fig. 6).

DISCUSSION

The proposed research algorithm based on a set of methods and the use of social media analysis capabilities on the eve of the COVID-19 confirmed its efficiency in general and made it possible to identify pandemic following results:

- The high attractiveness of the leading global cities among Runet users and their clear superiority in terms of the information base for building an image over other large

Paris

London

Tokyo

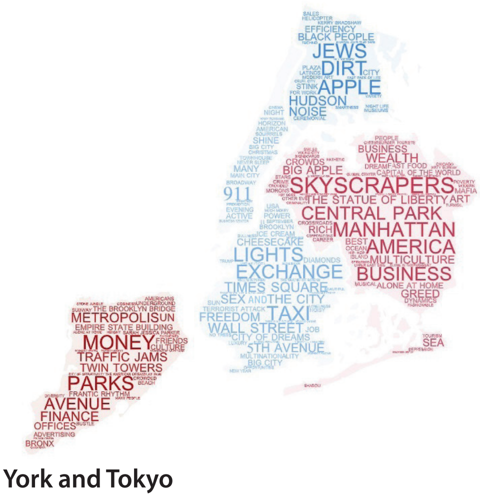

New York

Fig. 5. Image tag clouds of Paris, London, New York and Tokyo

[13]As noted by L.N. Nabilkina: "More has been written about Paris than about any other city in the world. Hemingway and Victor Nekrasov, Balzac and Henry Miller, Ilya Ehrenburg and Alexei Tolstoy, Victor Hugo and Erich Maria Remarque wrote about Paris. ... It is either cold and gloomy, as in the works by Henry Miller, or joyful and affable, like by Ernest Hemingway, or attractive and deceptive, like by Honore de Balzac, or hospitable and attractive, like by Alexandre Dumas» (Nabilkina, 2012).

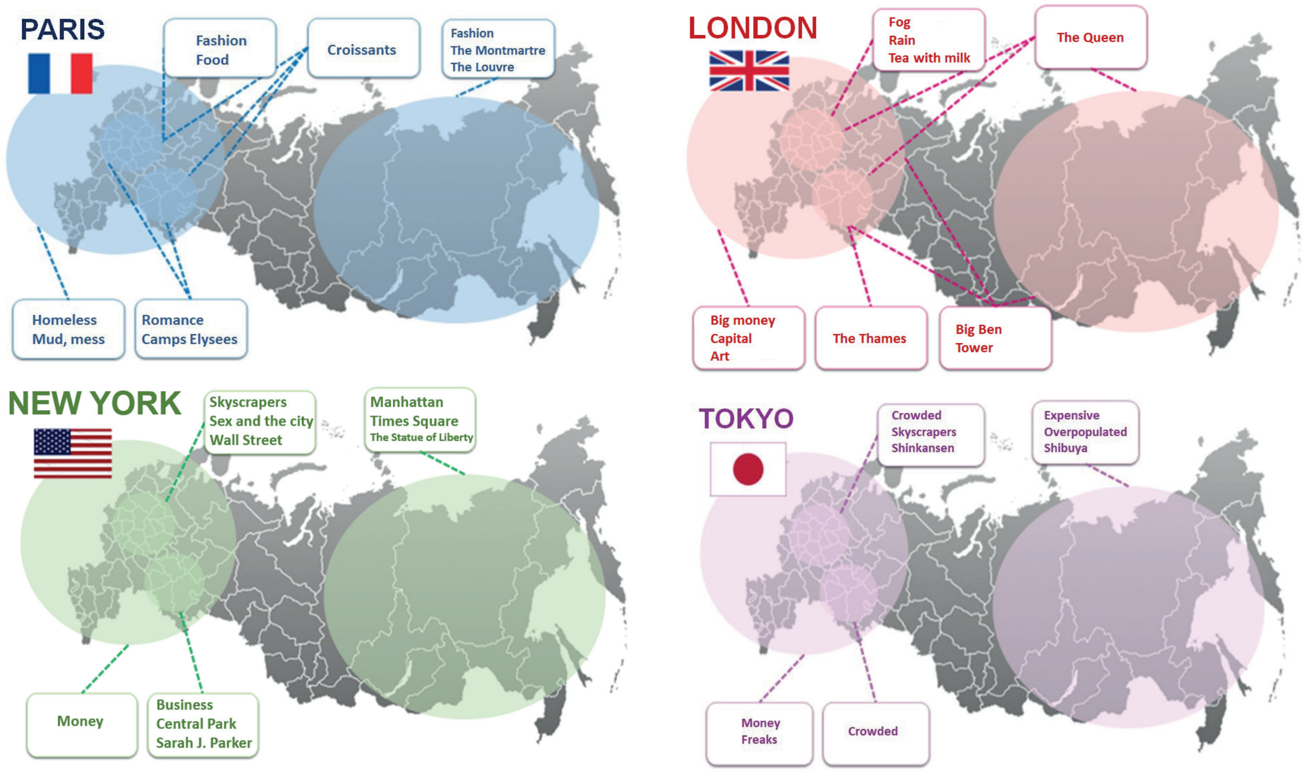

Fig. 6. Priorities in the global cities' image support frame by territorial zones of the Runet (fragments)

agglomerations, with the obvious leadership of European capitals and some backlog of Tokyo;

- The similarity of the structure of the proposed social media content with significant differences in the ideas that dominate the Runet audience, which, with a certain degree of generalization, are largely consistent with the uniqueness of the key competencies of cities;

- A very wide field for the formation of the image frame of the centers, often with a reflection of the "unique, special, individual" (Mironenko, 2001), but with a noticeable predominance of the objective over the subjective component, cognitive over affective components and the tangible weight of the latter in the case of Paris;

- The stability of the image frame in time and space can be partly corrected, on the one hand, by the eventfulness factor within a particular object, and, on the other hand, by the factor of its geographical proximity to the zonal segments of the Runet audience;

- The unity of the model and the relative limitedness of the image support frame, with the key role, on the one hand, of the stereotypes of a large city, and on the other hand, three broad collective categories: official or unofficial "metropolisness", prestigious urban locations and world architectural brands.

At the same time, it should be noted that the used approach cannot claim to be universal and comprehensive. The authors acknowledge: firstly, despite the solid body of scientific work, the incompleteness of the discourse within the framework of the theory of global cities and the absence of a definition and clear criteria for their identification. Although, the authority of the quartet of world centers - New York, London, Paris and Tokyo - is beyond doubt. Secondly, certain limitations of the methods used and the relevance of the resulting digital artifacts. In particular, a big problem is cleaning the raw data from advertising products. Thirdly, the possible variability of the research information base, depending, on the one hand, on the choice of a set of social media, and on the other, on the representativeness and quality of the Runet audience and its territorial zones. The study revealed, for example, significant differences in the perception of cities by respondents who have visited them and those who have not. However, real data on the totality of Runet users and their spatial differentiation are not yet available in reliable sources. Fourthly, the relative inaccessibility of widespread use of the resources of the Brand Analytics system. Fifthly, the analytical capabilities of the proposed approach and research methodology have not been fully studied at the moment; they require further clarification and testing, as well as broad scientific and applied understanding. The authors see prospects in monitoring the image of leading global centers in the post-COVID period, expanding the research area to include cities of different classes, developing and testing methods that make it possible to more accurately select the composition of respondents, attracting new data sources, for example, mobile operators, analyzing international experience and best practices of symbolic politics. The implementation of these directions will allow us to gain new knowledge about the image frame of the largest cities in the world, the features of its formation and to formulate a package of practical recommendations for interested consumers.

CONCLUSION

The revolution of recent decades in the field of communication, production and processing of spatiotemporal information has led to the revival of many areas of geographical research that faced insurmountable technological problems in collecting data at the end of the twentieth century. They had a particularly painful impact on the development of imaginal geography, based, according to N. Zamyatina, on a certain way of organized, internally holistic information about a place. New possibilities for using the Internet metric method, revealed and tested in the article on the example of leading global cities, made it possible to continue the traditions of the Maergoiz school of geographical study of cities of the foreign world and the figurative approach developed at the Department of Economic Geography of Foreign Socialist Countries (now Geography of World Economy) of the Geographical Faculty of Lomonosov Moscow State University more than 30 years ago. It seems useful to continue research at the intersection of international geo-urbanism and imaginary geography on the proposed principles to solve both scientific, educational and educational problems, and to develop a program for ensuring the growth of competitiveness and international influence of Russian cities in the face of ever-new global challenges.

REFERENCES

Beaverstock J.V., Smith R.G., Taylor P.J. (1999) A Roster of World Cities. Cities. 16(6), 445–458.

Bourdieu P. (2001) Practical meaning. Saint-Petersburg: Aletheia. (in Russian).

Demidova M. V. (2014) «Symbolic capital» by P. Bourdieu and «capital» by K. Marx // Bulletin of Vyatka State University for the Humanities. 11, 27-32. (in Russian).

Edelman M. (1964) The symbolic uses of politics. Urbana: Univ. of Illinois press.

Efremova V.N. (2015) Some theoretical features of the study of symbolic politics // Symbolic politics. Collection of scientific papers. Ser. «Political Science» of the Russian Academy of Sciences. INION. Issue 3 Political functions of myths. Moscow: INION RAS. P. 50-65. (in Russian).

Florida R. (2015) Cities and the creative class. New York - London, Routledge.

Friedmann J. (1986) The World City Hypothesis. Development and Change. 17(1), 69–84.

Geddes P. (1915) Cities in Evolution: An Introduction to the Town Planning Movement and to the Study of Civics. London, Williams &Norgate.

Global Cities Innovation Index: 2023, Moscow, HSE Publ., 2023, 316 p. (In Russian)

Hall P. (1966) The world cities. London: Weidenfeld & Nicholson.

Kalutskov V.N. (2008) Landscape in cultural geography. Moscow: Novyj hronograf. (in Russian).

Kiryanova L.G. (2015) The model of the image of a tourist destination within the marketing approach to the management of tourist regions. Vestnik Kemerovskogo gosudarstvennogo universiteta. 2 (62). Vol. 7. 3. 191-195. (in Russian).

Kolosov V.A., Tikunov V.S., Zayats D.V. (2000) The world in the mirror of the media: the use of anamorphoses in politico-geographical analysis. Moscow: Vestnik Moskovskogo Universiteta. Ser. 5. Geografiya. 2, 15–22. (in Russian).

Lappo G.M. The concept of the supporting frame of the territorial structure of the national economy: development, theoretical and practical significance. Izvestiya of the Academy of Sciences of the USSR. Geographic series. 1983. No. 5. pp. 16–28. (in Russian).

Malinova O.Y. (2010) Symbolic politics and the construction of macropolitical identity in post-Soviet Russia // Moscow. Polis. Political studies. 2, 90-105 (in Russian).

Meyer T. (1992) Inszenierung des Scheins.Voraussetzungen und Folgen symbolischer Politik. – Frankfurt am Main: Suhrkamp.

Mironenko N. S. (2001) Country studies: Theory and methods. Moscow: Aspekt-Press. (in Russian).

Nabilkina L.N. Paris in the Mirror of French Literature. Mir nauki, kul'tury, obrazovaniya, 2012, no. 1 (32), p. 249–251. (In Russian).

Okunev I.Y. (2020) Capitals in the mirror of critical geopolitics. Moscow: Aspect Press. (in Russian).

Potseluev S.P. (2012) «Symbolic politics»: The history of the concept // Symbolic politics. Collection of scientific papers. Center for Social Scientific and Information Research Department of Political Science; Executive Editor: Malinova O.Yu.. Moscow: INION RAS. 17-53 (in Russian).

Sarcinelli U. (1987) Symbolische Politik. Zur Bedeutung symbolischen Handelns in der Wahlkampfkommunikation der Bundesrepublik Deutschland. Opladen: Westdeutscher Verlag.

Sassen S. (1991) The Global City: New York, London, Tokyo. Princeton, New Jersey.

Sluka N., Tikunov V., Chereshnia O. (2019) The geographical size index for ranking and typology of cities. Social Indicators Research. 144(2), 981–997. DOI: 10.1007/s11205-019-02069-0

Sluka N.A., Karyakin V.V., Kolyasev E.F. (2020) Global cities as hubs of new transnational actors. Kontury global'nyh transformacij: politika, ekonomika, pravo. 13(1), 203–226. (in Russian). DOI: 10.23932/2542-0240-2020-13-1-11

Sluka N.A., Kuzovlev S.S. (2020) The modern image of Paris in the Russian-speaking segment of the Internet. Vestnik Moskovskogo universiteta. Seriya 5: Geografiya. 2, 110–114. (in Russian).

Toffler A. Power Shift. (2003) Moscow: OOO «Izdatel'stvo AST». (in Russian).

Tokbulatova ZH.E., Kolosov V.A. (2018) The image of Kazakhstan in Russia in the mirror of public opinion. Regionalnye issledovaniya. 2 (60), 58–67 (in Russian).

Vizgalov D.V. (2001) Branding of the city. Moscow: Foundation «Institute of Economics of the city». (in Russian).

Vizgalov D.V. (2008) Marketing of the city. Moscow: Foundation «Institute of Economics of the city». (in Russian).

Zamyatin D.N. (2006) Culture and space: Modeling of geographical images. Moscow: Znak. (in Russian).

Zamyatina N.Y. Harutyunyan K.M. (2005) The relationship of the images of European countries in the press (based on the newspapers The Times and The New York Times. Vestnik Moskovskogo Universiteta. Ser. 5. Geografiya. 5, 60–65. (in Russian).

RESEARCH PAPER

TRENDS IN EXTREME WEATHER EVENTS WITH SOCIO-ECONOMIC DAMAGE OVER THE PERIOD 1991-2019 IN RUSSIA AND ITS REGIONS

Anna A. Romanovskaya
Yu.A. Izrael Institute of Global Climate and Ecology, Moscow,
20B Glebovskaya str., Moscow 107258 Russian Federation
*Corresponding author: an_roman@igce.ru
Received: January 10th, 2023 / Accepted: November 14th, 2023 / Published: December 31st, 2023
https://DOI-10.24057/2071-9388-2023-2703

ABSTRACT. Increased number of extreme weather events is one of the most serious hazards of climate change over the territory of Russia. However, there is a lack of comprehensive analysis of the number of extreme weather events that caused social and economic damage in the country and its regions. This paper analyzes changes in the total number of events with damage (meteorological for the period 1991-2019 and agrometeorological – for 2004-2019), disaggregated by their types and by regions. The Mann-Kendall test is applied to detect statistical significance (0.05 level of significance, normal distribution). The results show an increase in the number of meteorological extreme events with damage for 1990-2019 in Russia from 130 to 257 events per year on average for the 1990s and 2010s, respectively, while the proportion of events with damage in relation to the total number of extreme events decreased over this period. We found statistically significant trends only for a few types of extreme events: hot and cold temperature, strong wind, heavy rain and droughts (increase by 0.9, 9.4, 11.4, 25.9 and 13.3 events/10 years, respectively). Number of heavy rain precipitation events is the only unidirectional stable growth trend. Unusual increasing trend in cold extreme events with damage in Russia can be attributed to the greater damage to the economy and population from cold extremes than hot ones. The regional distribution of trends across the territory of the Russian Federation is heterogeneous. However, significant changes in the number of extreme events of strong winds, heavy rains and soil drought by regions are statistically positive and observed mostly in some southern and central regions of European part and the Western Siberia. The development of adaptation plans to the negative effects of climate change is a first priority for these regions. A system for monitoring economic and non-economic damage from extreme events must be developed in Russia.

KEYWORDS: extreme weather events, socio-economic damage, trends, regional distribution, climate change

CITATION: Romanovskaya A. A. (2023). Trends In Extreme Weather Events With Socio-Economic Damage Over The Period 1991-2019 In Russia And Its Regions. Geography, Environment, Sustainability, 4(16), 82-90
https://DOI-10.24057/2071-9388-2023-2703

ACKNOWLEDGEMENTS: The author thanks Ms. Zhemchugova T.R. (Roshydromet) for providing the necessary primary data on agrometeorological hazards; Mr. Shamin S.I. for valuable advice and clarifications (All-Russian Research Institute of Hydrometeorological Information - World Data Center), Ms. Polumieva P. for assistance in working with geographic information systems and presenting cartographic information.

Conflict of interests: The authors reported no potential conflict of interest.

INTRODUCTION

Global climate change has increased the number and intensity of extreme weather events around the world. Continued warming will cause statistically significant changes in extreme events globally and for large regions (e.g., Masson-Delmotte et al. 2021). Many studies report observed and future increases in temperature extremes, heavy precipitation, and drought extremes and its regional distribution around the world (Spinoni et al. 2014; Donat et al. 2016; Knutson and Zeng, 2018; Sun et al. 2020; Dunn et al. 2020; Wu et al. 2021; Seneviratne et al. 2021; Rabiei et al. 2022). According to the World Meteorological Organization's report (WMO, 2021), the number of disasters increased fivefold in the 50-year period from 1970 to 2019, because of climate change, more extreme weather and improved reporting. During this period, there were more than 11,000 disasters associated with these hazards worldwide, resulting in just over 2 million deaths and $3.64 trillion in damages (WMO, 2021).

As for the Russian Federation, there is no reliable data yet on the total (economic and non-economic) damage caused by changes in climate parameters and an increase in the number of extreme events. There are sporadic reports of major disasters in Russia, such as the 2019 Irkutsk flood causing a direct economic damage of $460 million[1]. The extreme downpours in the south of the European part in the Krasnodar Territory in the summer of 2012 resulted in 177

[1]https://www.vedomosti.ru/politics/news/2019/07/06/805984-zatrati

deaths and direct losses of $250 thousand[2]. The economic damage from wildfires in 2021 estimated as high as $140 million[3]. The year 2021 was a record-breaking year for the area affected by fire. Nearly 15 thousand wildfires occurred on an area of more than 10 million hectares. Moreover, the direct potential damage from permafrost thaw in Russia may reach up to US$ 132 billion (total) and ~ US$ 15 billion for residential infrastructure alone (Melnikov et al. 2022).

The available Russian scientific literature provides analyses of changes in climatic parameters and extreme events in the country. Increased duration and intensity of heat waves and droughts are reported for central and southern European part of Russia (Bardin and Platova, 2019; Pavlova et al. 2020; Cherenkova and Semenov, 2021). Annual reports of the Federal Service for Hydrometeorology and Environmental Monitoring of the Russian Federation (Roshydromet) indicate that the changes in the precipitation regime in Russia are dominated by an increase in their annual amounts: the trend is 2.2% of the average /10 years, but the distribution is highly uneven (Report of peculiarities of climate…, 2022). Some extreme values of precipitation are observed in spring in Western Siberia (Third assessment report…, 2022; Zolina and Buligina, 2016; Khlebnikova et al. 2019); those are often followed by large flooding events. The frequency of strong winds, heavy precipitation and frost has been the highest in recent years among all weather extremes, accounting for 77% of all meteorological extreme events (Report of peculiarities of climate…, 2022). However, there is a lack of comprehensive regional analysis of the statistics on extreme events annually collected by Roshydromet that caused social[4] and economic[5] damage.

As part of the commitment to develop regional adaptation plans in 2022 (National action plan…, 2019), it is particularly relevant to assess regional trends in extreme weather events that have caused social and economic damage as well as to rank regions according to the priority of adaptation measures. Adaptation should include measures aimed at reducing damage from hazards expected in the coming decades (preventive adaptation) as well as measures responding to already observed changes in the number and intensity of extreme weather events and climatic parameters.

The purpose of this paper is a comprehensive analysis of the dynamics of extreme events causing social and material damage in the aggregate, separately by their types and by regions in Russia over the period from 1991 to 2019. Statistical significance of trends is assessed. The objectives of the study include:

- analyze trends in the total number of extreme weather events with and without socio-economic damage in 1991 - 2019 in Russia and by regions, identifying statistically significant changes;
- statistical analysis of trends in the number of extreme events with damage by its types in the country;
- statistical analysis of regional trends in the number of extreme events with damage by its types;
- identify the regions most affected by extreme events associated with socio-economic damage with the primary task of developing and implementing adaptation plans to the negative effects of climate change.

METHODS

Data sources. The data available in Roshydromet on extreme meteorological events with social and economic damage are reviewed: very strong wind; hurricane wind (hurricane); squall; tornado; heavy downpour; very heavy rain (very heavy rain with snow, very heavy wet snow, very heavy snow with rain); very heavy snow; continuous heavy rain; large hail; severe snowstorm; severe dust (sand) storm; severe fog (thick fog); severe ice and frost; severe frost; abnormally cold weather; severe heat; abnormally hot weather; extreme fire danger; avalanches. The database of the All-Russian Research Institute of Hydrometeorological Information - World Data Center of the Federal Service for Hydrometeorology and Environmental Monitoring is used (Shamin et al. 2021). Abrupt change in weather and complex adverse events are considered in our analyses as separate events.

Considering that agriculture, especially crop production, is one of the most vulnerable sectors of the economy to climate change (Third assessment report…, 2022), some agrometeorological extreme events are also included in the analysis. The corresponding data of Roshydromet on agrometeorological extreme events (including the dataset (Zhemchugova, 2016)) are obtained for the period from 2004 to 2019. Only "soil drought" event data are used in the analysis. Soil drought is defined as an event during the vegetation period of crops for a period of at least three consecutive ten-day periods with reserves of productive moisture in the soil layer 0-20 cm are not more than 10 mm or for a period of at least 20 days, if at the beginning of the drought period the reserves of productive moisture in the layer 0-100 cm were less than 50 mm. Prolonged drought (more than 1 month) is considered as a separate event in the analysis.

Hydrological extreme events are classified as secondary correlated hazards resulting from meteorological events and are excluded from the analysis. This approach also made it possible to exclude such secondary correlated consequences of climate change as an increase in the depth of seasonal thawing of permafrost soils, which is more logical to investigate separately (Edel'geriev and Romanovskaya, 2020).

Taking into account that one of the sources of this dataset is the meteorological network of Roshydromet, it should be considered that the homogeneity of the data series can be somewhat disturbed by the decrease in the number of stations in the 1990s and their growth in the beginning of the 21st century.

Heterogeneity of the data can also be determined by subjectivity in the interpretation of the single event if several threshold criteria are met (e.g., "very heavy rain" and "heavy downpour") (Chernokulsky et al. 2022). The heterogeneity of the data series used can also be determined by the fact of fixation or not of social and/or economic damage. We tried to minimize the effect of such heterogeneity of series by aggregation of data on certain types of extreme events into one indicator (e.g. sum of events with heavy downpour, very heavy rain (very heavy rain with snow, very heavy wet snow, very heavy snow with rain) and continuous heavy rain).

Period considered. The period from 1991 to 2019 is analyzed (only soil drought events from 2004 to 2019). Data for 2020 are not taken into account because of the high temperature anomaly in Russia in that year, which requires separate investigation and analysis of seasonal extreme events. Merely including 2020 could have a distorting effect on the overall trend analyses presented in this paper.

Although the considered trends of different extreme events have various durations (1991-2019; 2004-2019) this should not introduce strong distortions in our results, as our

[2]https://www.vedomosti.ru/finance/articles/2012/08/06/strahovoj_milliard

[3]https://tass.ru/ekonomika/13265341

[4]Losses associated with the life, health and spiritual values of an individual, social groups and society, associated with an increase in mortality, morbidity, disability, and a decrease in the level of life support; is defined as irretrievable and sanitary losses of people, material losses of personal property, costs for the treatment of victims and for the restoration of working capacity, moral and psychological costs and a decrease in the quality of life.

[5]Economic damage associated with material losses and damage or destruction of objects of the economy, its infrastructure and violations of production and cooperation relations.

work did not aim to aggregate all the considered trends into any single indicator.

At the same time, there is an understanding that the study period influences trend detection, i.e., climate data records may contain large-scale periodic behavior. It is especially important when analyzing data series for very large areas, when several large-scale atmospheric circulation models have the main influence on periodicity of time series. Therefore, we carry out the analysis regionally across the country and present the area of the studied regions (see Supplemental material, Table 1).

Regional analysis. Statistical processing of primary data on extreme events causing economic and social damage included summarizing the number of events by their type in each region of the Russian Federation per year. In order to avoid the possible distorting effects of incomparable regional areas we determined the specific number of events in each region per 100,000 km^2 socio-economically developed area and estimated the average 10-year change in the number of cases over the entire time series by each region. Developing an approach used in (Baburin and Badina, 2015) socio-economically developed area in our research is defined as a sum of settlements area, industrial land, agricultural land, forest land and protected areas[6] in each subject of Russia. We used that number in calculations if the sum of chosen categories of lands differed from the total area of the subject by more than 10%, in other cases the total area of the subject is used.

A total of 85 regions of the country are considered. Large events observed in several regions are considered as a separate event in each region. However, for the national total such events are counted as one.

Statistical analysis. The Mann-Kendall test is used to determine the level of significance (Gilbert 1987). Mann-Kendall is one of non-parametric tests commonly used for trend analysis of meteorological and climate data sets. Compared to parametric tests (e.g., regression coefficient test) this test requires no prior assumptions on the type of probability distribution of the data deviation from the long-term trend and is less sensitive to outliers (Wang et al. 2020). The software MAKESENS (Salmi et al. 2002) is applied for our analysis. The 0.05 significance level and normal distribution is used.

Yue et al. (2002) raises concerns about a series of hydrological events with less than 40 values for application of the Mann-Kendall test. However, according to (Salmi et al. 2002) MAKESENS software can be used for data series of 10 or more values that are normally distributed and not directly correlated with each other (Helsel and Hirsch 1992), which is valid in our case.

The results obtained are presented below in the following order from the aggregate analysis for the country as a whole to trends in single types of extreme events and their distribution across Russian regions.

RESULTS

Trends in the total number of extreme weather events associated with socio-economic damage in 1991 – 2019 in Russia and its regional distribution.

The overall dynamics of the number of extreme weather events that caused economic and social damage in Russia for the period from 1991 to 2019 indicate a sharp increase in the number of such events in the country between the 1990s and 2000s years (fig 1) from 130 to 237 events per year in average (1.8 times) with 0.001 level of significance, while for the beginning of the 21st century the trend in the number of events with social and economic damage increased to an average of 257 events and showed only 0.05 level of significance by Mann-Kendall test. A similar upward trend is obtained in (Korshunov et al. 2019) for the total number of extreme damage events, including all types of meteorological and hydrological events, in Russia in 2008-2017 compared to 1997-2008.

When comparing the data on total number of extreme weather events, including those which were not accompanied by economic damage (Panfutova, 2008; Report on the peculiarities of climate…, 2022), it can be seen that the same constant level of significance is observed for the growth between both decades: from the 1990s to the 2000s and from the 2000s to the 2010s (fig 1). The steady upward trend is consistent with climate monitoring data in Russia and the globe as a whole, where there has been a steady increase in average annual surface temperature and changes in other climatic parameters (Report of peculiarities of climate…, 2022; Masson-Delmotte et al. 2021).

The number of extreme events which are not accompanied by damage to the economy and population is gradually increasing from 1991 to 2019: in the 1990s the average share of events without associated damage was about 37% of total, and in 2010s – about 53% of the total on average over 10 years. Apparently, this can be explained either by the growth of low-intensity extreme events, the level of which reaches the criteria of extreme events, but does not cause material damage, or by methodological heterogeneity of data series: improvement in the accounting of dangerous phenomena without damage and/or imperfect determination of damage from some

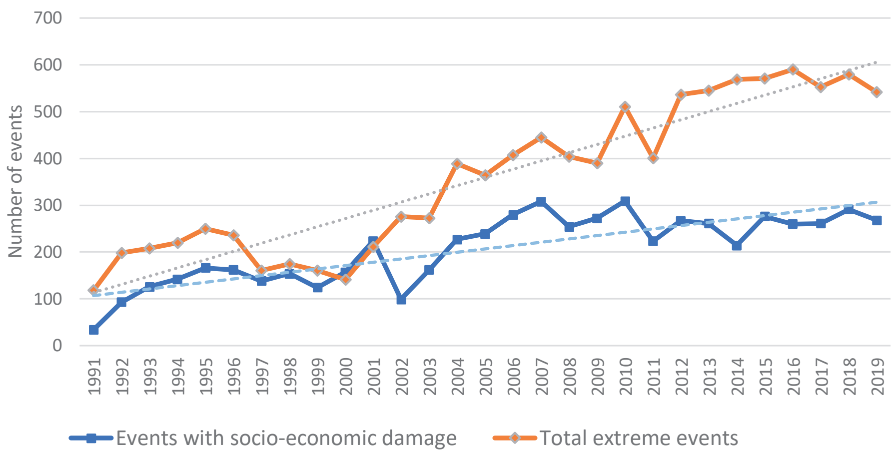

Fig. 1. Comparison of trends in the total number of extreme weather events and extreme weather events that caused economic and social damage in Russia for 1991-2019 (according to Roshydromet data)

[6]Economic damage to forests and protected areas is reflected in annual and periodic materials of the State forest registry and in reporting data on the use, protection, defense and reproduction of forests.

types of extreme events in Russia. The latter issue is discussed, for instance, by (Panfutova 2008; Chernokulsky et al. 2022).

A further possibility to explain the reasons for the observed separation of the two trends could be e.g. the improvement of early warning systems and monitoring technologies or the implementation of proactive measures to adapt the economy and population to extreme events. However, given that in Russia during the period under study we have no evidence of either, these explanations remain only at the hypothetical level.

The methodological homogeneity of data series on meteorological events with and without damage needs to be further investigated, given that the annual climate damage value is the primary justification for financing additional mitigation and adaptation measures in the country.

The total number of meteorological extreme events associated with damage has multidirectional trends across Russian regions (fig 2). The table 1 in the supplementary material presents regional data, accompanied by statistical analysis. There are regions in the country where the number of meteorological hazards is decreasing: Pskov region shows the greatest tendency to decrease by 1.8 events per 100 th. km^2 over 1991-2019 at a significance level of 0.01. There are regions where the number of hazards statistically increases at a significance level of 0.001 (see table 1 in the supplementary material). The highest growth trends are observed in 5 regions in the south of European Russia; those are marked in red in Figure 2. However, they are not always statistically significant: the trends for the Republic of North Ossetia-Alania, the Krasnodar Territory and the Republic of Crimea are significant at the 0.001 level, while the trend for the Kabardino-Balkar Republic is significant at the 0.05 level, and the trend for the Republic of Adygea is unsignificant.

Similar results were obtained in (Shamin and Sanina 2019), where a regional analysis of the same Roshydromet data for 2009-2018 demonstrates the absence of significant trends in the number of extreme events with damage for the majority of the selected 19 regions of the Russian Federation.

Trends in extreme weather events associated with socio-economic damage by type.

Applying the Mann-Kendall test, we found statistical trends in the number of events for only a few types of extreme events: hot temperature extremes, cold temperature extremes, strong wind events, heavy rain events and extreme events of droughts. No statistically significant results were found for a series of other types of extreme events. In the following, we consider only those types of events characterized by static results (Fig 3).

For **hot temperature extreme** events (which is the total of severe heat events and abnormally hot weather events) there has been a slightly increasing trend in Russia since 1991 with statistical significance (fig 3a). This trend is heavily influenced by two outliers in 1998 and 2010, and the decadal average for 2001-2010 is higher than the next decade of the 21st century.

Our results are in good agreement with the general trend of extreme hot events: many studies have shown that the number and intensity of extreme hot temperature events are significantly increasing both globally and within the territory of Russia (Donat et al. 2016; Bardin and Platova 2019; Dunn et al. 2020; Wu et al. 2021; Seneviratne et al. 2021; Report of peculiarities of climate…, 2022; Nita et al. 2022).

Cold temperature extremes on figure 3b are the totals of annual severe frost events and abnormally cold weather events. The growing number of such events in Russia is statistically significant. However, there is a high interannual variance compared with the trend of hot extremes in fig 3a in the number of cold extreme events caused damage.

The increasing trend in cold temperature extremes associated with damage found in our study is somewhat contrary to the literature: a significant decrease in the intensity and frequency of extreme cold events has been reported (Donat et al. 2016; Masson-Delmotte et al. 2021). A possible explanation for these discrepancies between our results and those in the literature is that we do not analyze all extreme temperature events, but only the part of them that caused social and economic damage (fig 1). As discussed above, there may have been an increase in the number of relatively mild extreme events with no

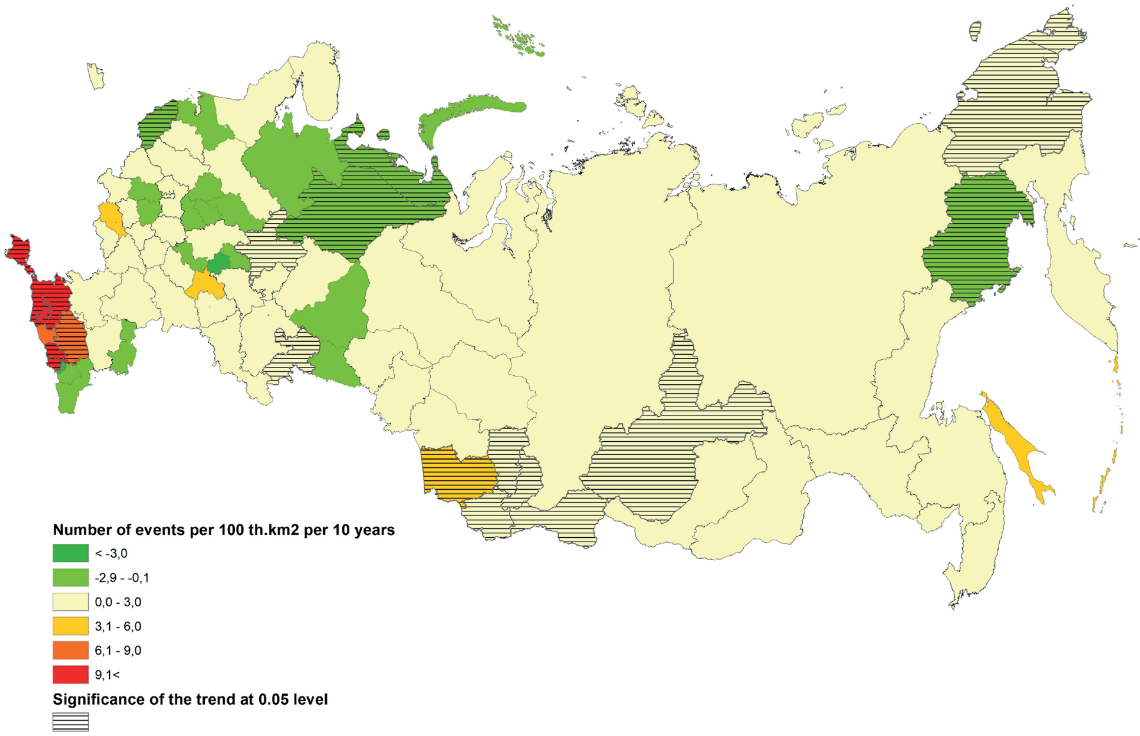

Fig. 2. Trends in the number of extreme weather events associated with socio-economic damage by regions of Russia, change in the number of events per 100 th. km^2 per 10 years during 1991-2019 period

subsequent physical loss or damage in the 21st century. Furthermore, it is logical to assume that extreme cold temperature events result in more significant damage to the economy and population than hot ones.

The clear significant trends are observed for **strong wind events** (fig 3c) and **heavy rain precipitation extreme events** with damage (fig 3d). The dynamic of heavy precipitation extremes is the only unidirectional steady growth trend.

An increase in the frequency of heavy precipitation has been observed worldwide, as well in Russia (Zolina and Buligina, 2016; Knutson and Zeng, 2018; Sun et al. 2020; Dunn et al. 2020; Seneviratne et al. 2021; Chernokulsky et al. 2022). Our results are in good agreement with this observation. The increase of heavy precipitation is obtained for the territory of the neighboring countries (e.g., Sumak and Semenova 2019).

The overall dynamics of the number of soil drought events with material damage indicates an unsignificant variations in the annual number of drought events in the Russian Federation since 2004 while atmospheric drought events as well as totals for droughts show significant increase (fig 3e). More than 90% of the recorded soil drought events in Russia were accompanied by socio-economic damage to crops and populations. Moreover, in recent years: 2012, 2013, 2015, 2017 and 2019, absolutely all registered extreme events on drought caused socio-economic damage. Thus, there is no problem separating total extreme events from events with damage in the case of a drought.

Regional trends in extreme weather events associated with socio-economic damage by types.

Analysis of the regional distribution shows that the largest changes in the number of extreme events are characteristic of the central and southern regions of the European part of Russia, as well as few regions in the central and southern parts of Western Siberia (see Figure 4 and the Table 1 in supplementary material).

Hot temperatures extremes. The regions with positive change in the numbers of hot temperature events are belong to extreme continental climate in the south of Ural and Siberia as well as central regions in European part of Russia (e.g. in Belgorod Region and Buryatia Republic increase in the number

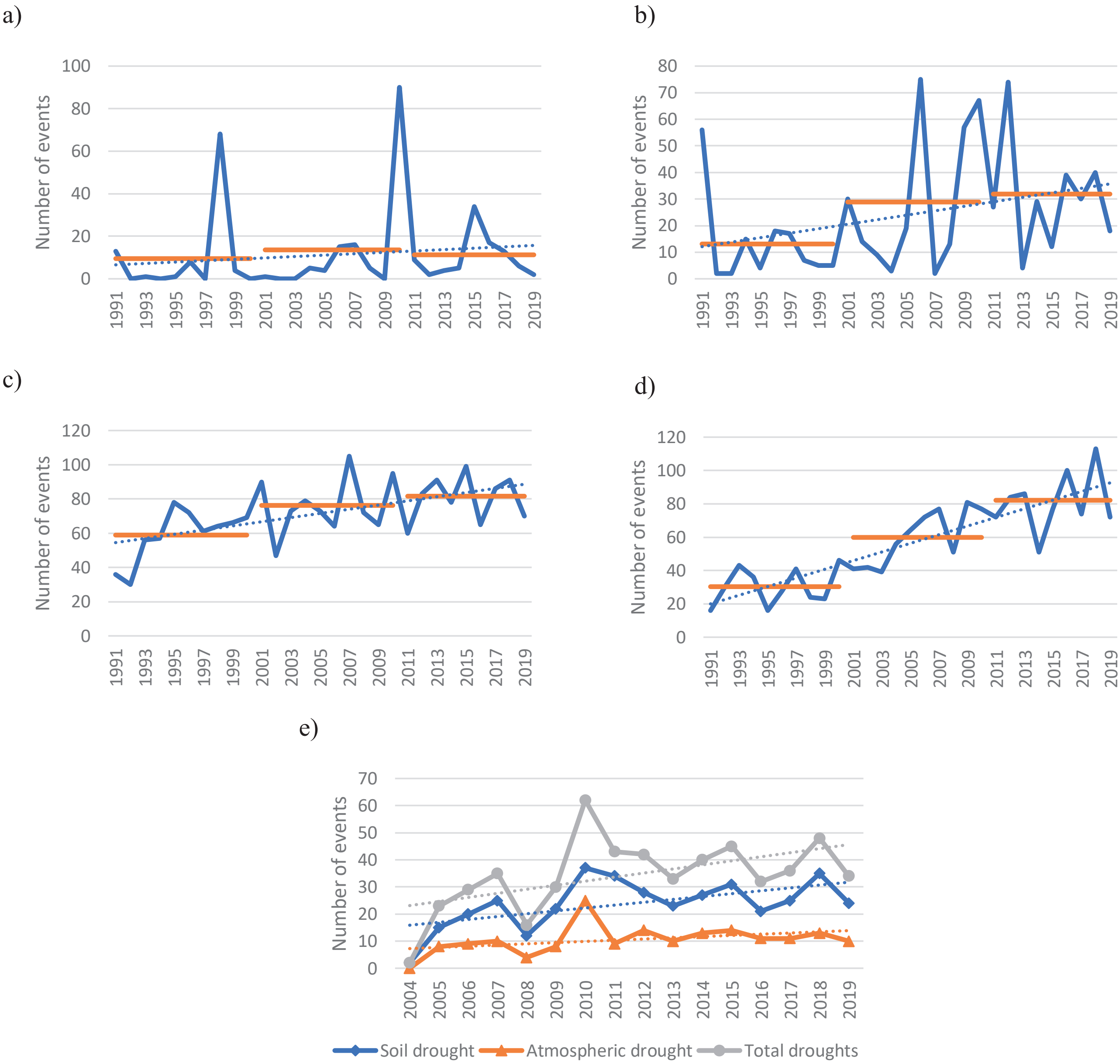

Fig. 3. Dynamic of the number of extreme events associated with social and economic damage in Russia for 1991-2019 and its decade's averages: a) the totals of severe heat events and abnormally hot weather; b) the totals of severe frost and abnormally cold weather events; c) very strong wind events; d) the totals of heavy downpour events, very heavy rain and continuous heavy rain events; e) events of soil drought, atmospheric drought and total number of drought events for 2004-2019. The dotted lines are the corresponding linear trends.

of events by 0,4 per per 100 th. km^2/10 years). Negative trends observed in the Caucasus region (e.g. in the Kabardino-Balkar Republic decreased by -0,8 in numbers of events per per 100 th. km^2/10 years) and few regions in the central part of Volga Federal District (e.g. in the Republic of Mary El change is -0,4 in numbers of events per per 100 th. km^2/10 years) (fig 4a).

Cold temperature extremes. Positive trends in cold extremes are found in few central regions in the European part of Russia, such as Bryansk (by 0,8 numbers of events per per 100 th. km^2/10 years), Lipetsk (by 0,9), Vladimir (by 0,6), Ivanovo (by 0,6), Kaluga (by 0,8), Moscow (by 0,3) regions, and south-east regions of Western Siberia: Altai Territory (by 0,3), Altai Republic (by 0,5), Novosibirsk (by 0,3), Kemerovo (by 0,6) Regions (fig 4b, Table 1 in supplementary material). The latter is in a good agreement with general dependencies in observed climate change within the territory of the Russian Federation (Report on the peculiarities of climate…, 2022). However, the Mann-Kendall test applied shows that these regional trends are not statistically significant.

The regional distribution of extreme cold temperature events (fig 4b) is well explained by the general regional time series of spatially averaged temperature anomalies for the period of 1976-2021 for all regions of country as represented in the regular Report on the peculiarities of climate on the territory of the Russian Federation of Roshydromet. The Siberian winter cooling zone in southern Western Siberia is reported here. This cooling was first detected for the period 1976-2010 and reached its maximum for the period 1976-2014 (the trend value in the center reached -0.54°C/10 years). Currently, the cooling is much less pronounced (-0.1°C/10 years in the south of Western Siberia) (Report on the peculiarities of climate…, 2022). As our study showed, the number of extreme cold temperature events that caused socio-economic damage increased in the same area.

Strong wind extremes. The largest negative significant wind trend is observed in the Karachaevo-Circassian Republic (by -2,6 numbers of events per per 100 th. km^2/10 years) and positive trends are observed in the Republic of North Ossetia-Alania (by 12,2) and the Republic of Crimea (by 3,8) (fig 4c, Table 1 in supplementary material). The high value for the Kabardino-Balkarian Republic (by 3,4), marked in dark green in Figure 4c as well, is not statistically significant. The lack of literature data on trends in extreme winds is discussed in the most recent IPCC assessment report (Masson-Delmotte et al. 2021). It is concluded that the observed intensity of extreme winds is becoming less

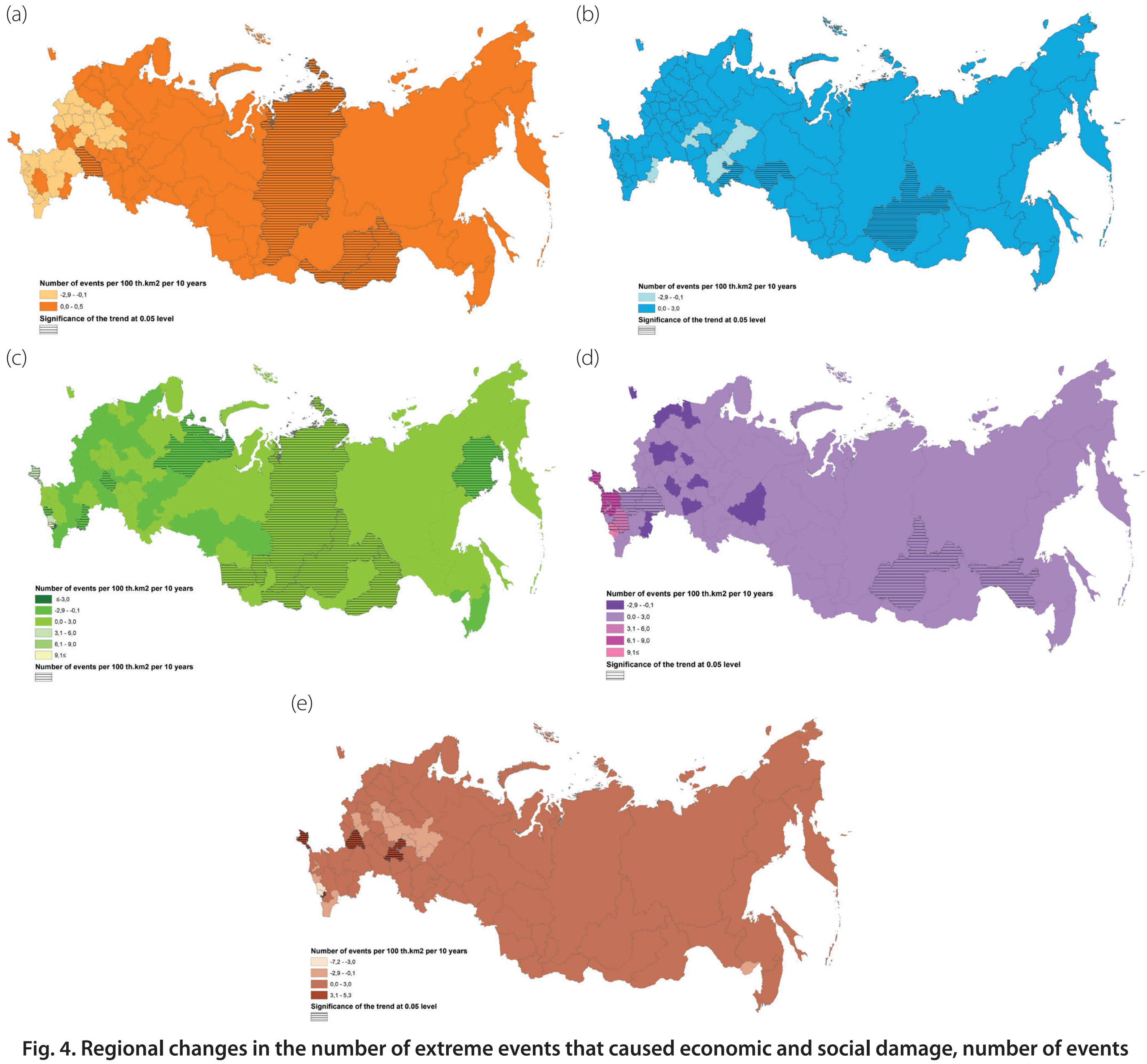

Fig. 4. Regional changes in the number of extreme events that caused economic and social damage, number of events per per 100 th. km^2/10 years: a) hot temperature extremes from 1991 to 2019; b) cold temperature extremes from 1991 to 2019; c) strong wind events from 1991 to 2019; d) heavy rains from 1991 to 2019; e) soil drought from 2004 to 2019.

severe in the lower to mid-latitudes, while becoming more severe in higher latitudes poleward of 60 degrees (low confidence). Our results show that, in general, there are no significant trends in strong winds events on the territory of the Russian Federation regardless of latitude. The only statistically significant changes are noted for several southern regions of the European part of Russia. All of them are located below 48°N.

Heavy rain extremes. In terms of heavy precipitation, the change in the extreme events is distributed unevenly across the country, with both areas with a decrease in the number of downpours that caused economic damage and with an increase (fig 4d). The Mann-Kendall test showed that statistically significant positive trends in heavy precipitation are observed for the southern regions of the European part of Russia and Caucasus region: the Kabardino-Balkar Republic (by 12,7 numbers of events per per 100 th. km^2/10 years), the Krasnodar Territory (by 7,4), Stavropol Territory (by 4,0) and the maximum for the Republic of North Ossetia-Alania[7] (by 31,7).

Significant trends in the increase of heavy rain events detected in our research in the south of Siberia and Far East are consistent with results of investigation of atmospheric severe convective events in Russia (Chernokulsky et al. 2022). At the same time, the analysis of Chernokulsky et al. for the warm period of the year found no significant increase in the number of heavy rains in the south of the European part of our country, which was found in our work. Apparently, this could be explained both by consideration of the full calendar year in our study, and by high population density and infrastructure in these regions, leading to increased frequency of fixation of socio-economic damage. However, statistically significant trends are not observed in all regions of Russia (fig 4d). The lack of significant trends in heavy rains over large areas has also been noted by other authors (Mass et al. 2011; Sun et al. 2020).

Soil drought extremes. The number of soil drought events in most of the country is unchanged or slightly decreasing (fig 4e), which, in turn, may be associated with an increase in the average annual precipitation in most regions of the Russian Federation in recent years (Report on the peculiarities of climate…, 2022). At the same time, the central and southern regions of the European part of Russia (excluding the North Caucasus republics) are particularly exposed to the increase in the number of drought events: the largest trends are observed (in descending order) in the Republics of Crimea (by 5,3 numbers of events per per 100 th. km^2/10 years), Chuvashia (by 5,3), Ingushetia (by 3,4), Ulyanovsk (by 3,4) and Voronezh (by 3,2) regions.

The largest growing trends in the frequency of soil drought extreme events is observed for central and some southern regions of the European part of Russia. The same results are reported in many studies (Pavlova et al. 2020; Bardin and Platova, 2019; Cherenkova et al. 2020; Dunn et al. 2020; Cherenkova and Semenov, 2021). The trends in frequency of soil drought extreme events in the Asian part of Russia are on average an order of magnitude lower compared to the European part. There the largest positive trend is characteristic of the Tyumen region (south of the Western Siberia), but still statistically insignificant. Most other regions in the Asian part show inconsistent, mostly decreasing trends in the number of soil drought extreme events (fig 4e). Similar results obtained for observed and projected climate regimes in Russia in other studies (Spinoni et al. 2014; Khlebnikova et al. 2019; Report on the peculiarities of climate…, 2022; Seneviratne et al. 2021).

CONCLUSION

Our results confirm global trends in the increase of extreme weather events, both with and without socio-economic damage, over the past 30 years on the territory of the Russian Federation. While the overall growth trend in the number of extreme events with damage was similar to the growth trend in the total number of extreme events (with and without damage) during the 1990s-2000s, it lags significantly behind the growth rate of the total number of extreme weather events in the country during the two decades of the 21st century. The proportion of events with damage in relation to the total number of extreme events decreased over this period. This can be explained either by the growth of low-intensity extreme events, the level of which reaches the criteria of extreme events, but does not cause material damage, or by methodological heterogeneity of data series. In any case the divergence in trends requires further methodological investigation.

Statistically significant trends in the number of events found only for a few types of extreme events: hot temperature extremes, cold temperature extremes, strong wind events, heavy rain events and extreme events of droughts. Number of heavy rain precipitation events is the only unidirectional stable growth trend. Unusual growing trend in cold extreme events with damage in Russia may be explained by more significant damage to the economy and population from cold extremes than hot ones.

The distribution of trends in changes in different types of extreme events with damage is heterogeneous over the territory of the Russian Federation: there are regions with both negative and positive trends. Statistically significant changes in the number of extreme events with strong winds, heavy rains, soil drought and total meteorological extreme events are generally positive and are observed in some southern and central regions of the European part and few regions in the Western Siberia of Russia: the Kabardino-Balkar, Crimea, Adygea, Ingushetia, Tatarstan, Khakassia and Chuvashia Republics, Altai and Krasnodar Territories, Belgorod, Bryansk, Kursk, Samara, Smolensk and Ulyanovsk regions. The development and fast implementation of regional adaptation plans is a first priority for these regions considering the density of population in these areas as well as agriculture production as a main economic activity.

Further research is needed to examine the intensity of individual extreme events and the economic and non-economic damage they cause. The latter includes losses of ecosystem services, damage to public health, forced migration, etc. The dynamics of this parameter shows the need for additional mitigation and adaptation measures, and is also an indicator of the success (effectiveness) of these measures. It would be advisable to develop methodological research in the field of climate change damage assessment in Russia and to establish annual monitoring of such losses.

[7]The outliers in North Ossetia for strong winds and heavy precipitation require additional confirmation of the reliability of statistical data on the number of extremes

REFERENCES

Baburin, V.L., and Badina, S.V.: Evaluation of socio-economic potential of the territory exposed to adverse and dangerous natural phenomena, Bulletin of Moscow University. Series 5: Geography, 5, 9–16, 2015.

Bardin, M.Y., and Platova, T.V.: Long-period variations in extreme temperature statistics in Russia as linked to the changes in large-scale atmospheric circulation and global warming, Russ. Meteorol. Hydrol., 44, 791–801, https://doi.org/10.3103/S106837391912001X, 2019.

Cherenkova, E.A., and Semenov, V.A.: A new approach to the identifying of the extreme climate effect on the wheat yield reduction in the south of European Russia, Dokl. Earth Sc., 500, 781–786, https://doi.org/10.1134/S1028334X21090075, 2021.

Cherenkova, E.A., Bardin, M.Y., Platova, T.V., and Semenov, V.A.: Influence of North Atlantic SST variability and changes in atmospheric circulation on the frequency of summer droughts in the east European Plain, Russ. Meteorol. Hydrol., 45, 819–829, https://doi.org/10.3103/S1068373920120018, 2020.

Chernokulsky, A.V., Eliseev, A.V., Kozlov, F.A. et al.: Atmospheric severe convective events in Russia: changes observed from different data, Russ. Meteorol. Hydrol., 47, 343–354, https://doi.org/10.3103/S106837392205003X, 2022.

Donat, M. G., Alexander, L. V., Herold, N., and Dittus, A. J.: Temperature and precipitation extremes in century-long gridded observations, reanalyses, and atmospheric model simulations, J. Geophys. Res. Atmos., 121, 11, 174-189, https://doi.org/10.1002/2016JD025480, 2016.

Dunn, R. J. H., Alexander, L. V., Donat M. G. et al.: Development of an updated global land in situ-based dataset of temperature and precipitation extremes: HadEX3, J. of Geoph. Res.: Atmospheres, 125, e2019JD032263, https://doi.org/10.1029/2019JD032263, 2020.

Edel'geriev, R. S. Kh., and Romanovskaya, A. A.: New approaches to the adaptation to climate change: the Arctic zone of Russia, Russ. Meteorol. Hydrol., 45, 5, 305–316, https://doi.org/10.3103/S1068373920050015, 2020.

Gilbert, R.O.: Statistical methods for environmental pollution monitoring, Van Nostrand Reinhold, New York, USA, 336 pp. 1987.

Helsel D.R., and Hirsch R.M. 1992. Statistical Methods in Water Resources. Elsevier, Amsterdam. 522 pp.

Khlebnikova, E. I., Rudakova, Y. L., and Shkolnik, I. M.: Changes in precipitation regime over the territory of Russia: Data of regional climate modeling and observations, Russ. Meteorol. Hydrol., 44, 431–439, https://doi.org/10.3103/S106837391907001X, 2019.

Knutson, T. R., and Zeng, F.: Model assessment of observed precipitation trends over land regions: detectable human influences and possible low bias in model trends, J. Clim., 31, 4617–4637, https://doi.org/10.1175/JCLI-D-17-0672.1, 2018.

Korshunov, A.A., Shaimardanov, V.M., Shaimardanov, M.Z., and Shamin, S. I.: Frequency of hydrometeorological hazards which caused socioeconomic damage in 1998–2017, Meteorol. and Hydrol., 11, 13–19, https://doi.org/10.3103/S1068373920050015, 2019 (in Russian).Mass, C., Skalenakis, A., and Warner, M.: Extreme precipitation over West Coast of North America: is there a trend?, J. of Hydrometeorology, 12, 2, 310–318, https://doi.org/10.1175/2010JHM1341.1, 2011.

Masson-Delmotte, V., Zhai, P., Pirani, A. et al. (Eds.): IPCC, 2021: Climate change 2021: the physical science basis. Contribution of Working Group I to the Sixth assessment report of the Intergovernmental Panel on Climate Change, Cambridge University Press, in press, https://www.ipcc.ch/report/ar6/wg1/, last access: 11 January 2022, 2021.

Melnikov V.P., Osipov V.I., Brouchkov A.V. et al. Climate warming and permafrost thaw in the Russian Arctic: potential economic impacts on public infrastructure by 2050. Natural Hazards, 112 (7–9), 1-21, https://doi.org/10.1007/s11069-021-05179-6, 2022.

National action plan for the first phase of adaptation to climate change for the period up to 2022, approved by the Order of the Government of the Russian Federation dated December 25, 2019 № 3183-r: http://static.government.ru/media/files/OTrFMr1Z1sORh5NIx4gLUsdgGHyWIAqy.pdf, last access: 11 January 2022, 2019 (in Russian).

Nita, I.-A., Sfîcă, L., Voiculescu, M., Birsan, M.-V., Micheu, M.-M.: Changes in the global mean air temperature over land since 1980, Atmospheric Research, Volume 279, 106392, https://doi.org/10.1016/j.atmosres.2022.106392, 2022.

Panfutova, Y. A.: Hazardous meteorological phenomena in the plain territory of the Russian Federation and the risks posed by them: author's abstract of the thesis for the degree of Candidate of Geographical Sciences, Main Geophysics Observatory, St. Petersburg, 22 pp., 2008 (in Russian).

Pavlova, V.N., Bogdanovich, A. Yu., and Semenov, S. M.: On the assessment of climate favorability for cereal cultivation based on the frequency of severe droughts, Russ. Meteorol. Hydrol., 45, 12, 864 - 869, https://doi.org/10.3103/S1068373920120079, 2020.

Rabiei, J., Khademi, M.S., Bagherpour, S., Ebadi N., Karimi A., and Ostad-Ali-Askari K. Investigation of fire risk zones using heat–humidity time series data and vegetation. Appl Water Sci 12, 216 (2022). https://doi.org/10.1007/s13201-022-01742-z

Report on the Peculiarities of Climate on the Territory of the Russian Federation for 2021, Federal service for hydrometeorology and environmental monitoring (Roshydromet), 2022. Moscow, 110 pp.: http://downloads.igce.ru/reports/Doklad_o_klimate_RF_2021sZamechIspol_VSTUPITELNOE_slovo.pdf, last access: 3 December 2022 (in Russian).

Salmi, T., Määttä, A., Anttila, P., Ruoho-Airola, T., and Amnell, T.: Detecting trends of annual values of atmospheric pollutants by the Mann-Kendall test and Sen's slope estimates – the Excel template application MAKESENS, Finnish meteorological institute, Publications on Air Quality, 31, report code FMI-AQ-31, 35 pp., 2002.

Third assessment report of Roshydromet on climate change and its consequences on the territory of the Russian Federation, 2022, Moscow, Roshydromet, 678 pp.: http://downloads.igce.ru/publications/OD_3_2022/v2022/pdf/od3.pdf, last access: 3 December 2022 (in Russian).

Seneviratne, S. I., Zhang, X., Adnan, M. et al.: Weather and climate extreme events in a changing climate, in: Climate change 2021: the physical science basis, contribution of Working group I to the Sixth assessment report of the Intergovernmental Panel on Climate Change, edited by: Masson-Delmotte, V., Zhai, P., Pirani, A. et al. Cambridge University Press, in press: https://www.ipcc.ch/report/ar6/wg1/downloads/report/IPCC_AR6_WGI_Chapter_11.pdf, last access: 11 January 2022, 2021.

Shamin, S. I., Bukhonova, L. K., and Sanina, A. T.: Information about dangerous and adverse hydrometeorological phenomena that caused material and social damage in Russia, All-Russian Research Institute of Hydrometeorological Information - World Data Center [data set] certificate of state registration of the database № 2019621326: http://meteo.ru/data/310-neblagopriyatnye-usloviya-pogody-nanjosshie-ekonomicheskie-poteri, last access: 11 January 2022, 2021 (in Russian).

Shamin, S. I., and Sanina, A. T.: Hydrometeorological hazards frequency estimated for constituent territories of the Russian Federation, Proceedings of the All-Russian research institute for hydrometeorological information – World Data Center, 184, 54 – 66, 2019 (In Russian).

Spinoni, J., Naumann, G., Carrao, H., Barbosa, P., and Vogt, J.: World drought frequency, duration, and severity for 1951-2010, Int. J. Climatol., 34, 2792–2804, https://doi.org/10.1002/joc.3875, 2014.

Sumak, E. N., and Semenova, I. G.: Cyclonic activity and recurrence of hazardous weather phenomena over the territory of Belarus, Journal of the Belarusian state university, Geography, Geology, 2, 79-93, https://doi.org/10.33581/2521-6740-2019-2-79-93, 2019 (in Russian).

Sun, Q., Zhang, X., Zwiers, F., Westra, S., and Alexander, L.V.: A global, continental, and regional analysis of changes in extreme precipitation, J. of Clim., 34, 1, 243-258, https://doi.org/10.1175/JCLI-D-19-0892.1, 2020.

Wang F, Shao W, Yu H, Kan G, He X, Zhang D, Ren M and Wang G.: Re-evaluation of the power of the Mann-Kendall test for detecting monotonic trends in hydrometeorological time series, Front. Earth Sci., 8, 14. https://doi.org/10.3389/feart.2020.00014, 2020.

WMO: WMO atlas of mortality and economic losses from weather, climate and water extremes, Publications board World Meteorological Organization (WMO), Geneva, Switzerland, 90 pp.: https://library.wmo.int/doc_num.php?explnum_id=10902, last access: 11 January 2022, 2021.

Wu, Y., Miao, C., Sun, Y., AghaKouchak, A., Shen, C., and Fan, X.: Global observations and CMIP6 simulations of compound extremes of monthly temperature and precipitation, GeoHealth, 5, e2021GH000390, https://doi.org/10.1029/2021GH000390, 2021.

Yue, S., Pilon, P., Cavadias, G. Power of the Mann-Kendall and Spearman's rho tests for detecting monotonic trends in hydrological series, J. Hydrol., 259, 254-271. https://doi.org/10.1016/S0022-1694(01)00594-7, 2002.

Zhemchugova, T. R.: Information on dangerous hydrometeorological weather phenomena. The number of dangerous natural (hydrometeorological) phenomena, which caused damage to the population and sectors of the economy, Roshydromet [data set]: http://www.meteorf.ru/opendata/7703092752-hazstat/, last access: 11 January 2022, 2016 (in Russian).

Zolina, O. G., and Buligina, O. N.: Modern climatic variability characteristics of extreme precipitation in Russia, Fundamental and applied climatology, 1, 84-103, https://doi.org/10.21513/2410-8758-2016-1-84-103, 2016 (in Russian).

RESEARCH PAPER

PHYLOGENY AND HISTORICAL BIOGEOGRAPHY OF THE ORDER PANDANALES

Nikita S. Zdravchev[1*], Alexey V. F. Ch. Bobrov[1, 2], Mikhail S. Romanov[1], Iurii M. Lebedev[2], Alexey N. Sorokin[1], Anton S. Timchenko[1], Anna A. Mikhaylova[1], Natalia D. Vasekha[1], Maxim V. Kandidov[2], Kirill V. Kuptsov[2], Petr S. Iovlev[1]

[1]Laboratory of Tropical Plants, Tsitsin Main Botanical Garden of Russian Academy of Sciences, Botanicheskaya st. 4, 127276, Moscow, Russia

[2]Department of Biogeography, Geographical Faculty, M. V. Lomonosov Moscow State University, Leninskie Gory 1, 119991, Moscow, Russia

***Corresponding author:** zdravchevnikita@yandex.ru

Received: April 25th, 2023 / Accepted: November 14th, 2023 / Published: December 31st, 2023

https://DOI-10.24057/2071-9388-2023-2870

ABSTRACT. Reconstruction of the dispersal history and formation of modern ranges of various taxa is one of the actual problems of modern biogeography. Molecular genetic biogeography based on the analysis of phylogenetic relationships of taxa of different levels began to develop actively at the end of the XX century. Currently, this method is the most objective and represents the basis for reconstruction of scenarios of the origin and dispersal of various groups of plants.

Due to recent transformation of views on the phylogenetic relationships of Pandanales, the reconstruction of tracks and modes of dispersal of representatives of the order Pandanales becomes an actual task.

Representatives of all 5 families of Pandanales sensu APG IV were selected for the study and two cladograms were constructed.

Based on the molecular-genetic cladistic method the region of hypothetical origin and probable dispersal scenarios of the families of the order Pandanales were determined. The order Pandanales is treated as originated in Laurasia and its differentiation began on the territory of Tibet. Dispersal of the representatives of the basal family Velloziaceae took place by long-distance transport via the Bering Land Bridge to South America (approximately 115 Mya). Velloziaceae dispersed in the New World vicariously in South America, then it was distributed to sub-Atlantic Africa by long-distance transport, and finally also vicariously to the east, south and north of the continent. It is shown, that the modern range of the representatives of rest Pandanales is the result of both types of dispersal – vicariously and long-distance transport.

KEYWORDS: phylogenetic biogeography, dispersal history, molecular genetic analysis, phylogeny, Pandanales

CITATION: Zdravchev N. S., Alexey V. F. Ch. Bobrov., Romanov M. S., Lebedev I. M., Sorokin A. N., Timchenko A. S., Mikhaylova A. A., Vasekha N. D., Kandidov M. V., Kuptsov K. V., Iovlev P. S. (2023). Phylogeny And Historical Biogeography Of The Order Pandanales. Geography, Environment, Sustainability, 4(16), 91-104

https://DOI-10.24057/2071-9388-2023-2870

ACKNOWLEDGEMENTS: The authors are grateful to Dr. Elena G. Suslova for valuable comments on the manuscript. This study was supported by the Russian Science Foundation (Grant № 22–24–01001, https://rscf.ru/project/22-24-01001/, for NSZ, AVFChB and AST). The authors are also grateful for the organizational and administrative support Tsitsin Main Botanical Garden of RAS (Unique Scientific Installation 'Fund Greenhouse' and research projects № 122042700002–6 and 'Reproductive biology, comparative morphology and structural evolution in key groups of seed plants'; NSZ, MSR, ANS, AST, AAM, NDV, KVK, and PSI) and M. V. Lomonosov Moscow State University (Development program of the Interdisciplinary Scientific and Educational School of M. V. Lomonosov Moscow State University 'Future Planet and Global Environmental Change' and research project №121051100137–4; AVFChB, IML, and MVK; and for support of the Program of Development of MSU (#1220) to IML, and MVK).

Conflict of interests: The authors reported no potential conflict of interest.

INTRODUCTION

At the end of the 20th century, due to the expansion of technological capabilities of molecular genetic research, phylogenetic biogeography began its active development. Phylogenetic biogeography is based now on the analysis of the phylogenetic relationships of taxa at different levels. This method is currently the most objective and is used as the basis for reconstructions of scenarios of the origin and dispersal history of different taxa of plants, as well as other living organisms (Heads 2012; Heads 2013).

In the APG IV system the families Velloziaceae, Triuridaceae, Stemonaceae, Pandanaceae and Cyclanthaceae were included in the order Pandanales. Earlier, most of these families were not considered to be related (Hutchinson 1973; Cronquist 1981; Thorne 2000; Takhtajan 2009). For example, the family Triuridaceae was considered in a separate monotypic subclass Triurididae and the family Stemonaceae was treated as closely related to Smilacaceae (Takhtajan 1987).

Within Pandanales the Velloziaceae clade (5–10 genera; 250 species) is basal. It is distributed in sub-Saharan Africa, south-western Arabia, western Madagascar, eastern Tibet, eastern, northern and central South America and Panama. Most Velloziaceae usually grow on granite or quartzite rocks, on sandy or stony soils, in more or less arid habitats (Takhtajan 1982; Kubitzki 1998a). Many species of *Vellozia* occur only on soils rich in iron in the form of hematite (Takhtajan, 1982). Some *Vellozia* species are well adapted to the unique Brazilian landscapes, their seeds are able to remain in the soil for long periods of time and maintain high germination rates. Thus, representatives of *Vellozia* form long-term stable soil seed banks, which play an important role in restoring disturbed plant communities (Garcia et al. 2017). Some representatives of the genera *Xerophyta* and *Nanuza* can survive severe drought to the point of complete leaf desiccation, consuming moisture only in the form of a dew. Almost all species of Velloziaceae are more or less xerophytic, whereas *Talbotia* is a true mesophyte (Takhtajian 1982; Kubitzki 1998a).

The next branched clade of Pandanales is the family Triuridaceae (5–9 genera; 70 species). It has a pantropical distribution, and also found in Japan and in the Midwest of the United States. Some genera are distributed in subtropical regions, including *Peltophyllum* in Argentina and Paraguay and *Sciaphila* in Japan (Maas-Van De Kamer and Weustenfeld 1998). Triuridaceae are achlorophyllous, saprophytic (mycoheterotrophic) herbaceous plants with obligate endomycorrhiza (Merckx et al. 2013). This mode of nutrition allows Triuridaceae to inhabit shaded conditions, and obtain carbon from symbionts but not from photosynthesis (Mennes et al. 2013). Triuridaceae inhabit dense and humid forests, under a closed canopy, at the base of large trees or along the banks of rivers, at altitudes ranging from 200 to 2200 m. Less commonly they are found in temporarily flooded forests, forests on coral sands, in bamboo thickets or on termite mounds (*Sciaphila purpurea* Benth., *S. africana* Becc.). They often grow in close association with other mycotrophic plants from different families (Mies-Van De Kamer and Weustenfeld 1998; Merckx et al. 2013).

The next step in the evolution of the order is the divergence of the family Stemonaceae (4 genera; 30 species). Its representatives are distributed in Malaysia, northeastern Australia, Sri Lanka, south of the Indian Peninsula, Japan (except Hokkaido Island), southern China, Indochina Peninsula and south-eastern USA. Stemonaceae inhabit tropical and subtropical highland forests, they occur on hillsides or in valleys, in shady areas and often in scrub vegetation (Velgorskaya 1982). In general, the representatives of the family prefer dry sandy or clay soils, but occasionally occur in wet areas on muddy soils in depressions in the foothills and lowlands (*Stemona tuberosa* Lour., *Pentastemona* spp.), some species of *Stemona* and *Stichoneuron* are distributed at altitudes up to 1800 m (Velgorskaya 1982; Kubitzki 1998b; Kubitzki 1998c). In Japan, *Croomia* species are often found in plantations of *Cryptomeria japonica* (Thunb. ex L. f.) D. Don. *Croomia pauciflora* (Nutt.) Torr. grows on dry, loose soils along riverbanks in the shade of forests (Vielgorskaya 1982). Seeds of representatives of most Stemonaceae have arillus or elaiosomes, which may indicate an adaptation to zoochoria. The seeds of some Stemonaceae species are light and dangle from the fruit by a long funiculus, and can probably be dispersed by wind (Velgorskaya 1982). Seeds of *Croomia* have a thick shell, which may contribute to hydrochoria (Kubitzki 1998b).

The family Stemonaceae is basal to the two sister terminal families of Pandanales – Pandanaceae (Palaeotropics; 5 genera; 750-900 species) and Cyclanthaceae (Neotropics; 12 genera; 230 species). Pandanaceae representatives are distributed from the sea level and up to altitude of ca. 3000 m on a variety of substrates: granites, limestones, ultrabasic, muddy, peaty or clay substrates. They also often participate in littoral mangrove communities or grow as epiphytes in rainforests (Stone et al. 1998). Representatives of the largest genus, *Pandanus*, are most commonly found along the shores of tropical lowlands. *Pandanus* species have an almost universal adaptability to different habitats. In addition to coasts and swamps, it is found in drier lowlands, mountainous and even high-altitude forests, on coral reefs and limestone cliffs, on the slopes of volcanoes, and in savannas (Grushvitsky 1982). Pandanaceae diaspores are dispersed by birds, mammals, sometimes turtles, and freshwater or ocean currents (Cox 1990; Stone et al. 1998). Almost all representatives of Cyclanthaceae are growing in wet and more or less shady habitats (tropical rainforests). The epiphytic Cyclanthaceae (61% of the family) dominate the epiphytic communities of the Neotropics, with only two other flowering plant families, Orchidaceae and Marcgraviaceae, having a similar ecological role (Gentry and Dodson 1987). The often brilliantly coloured spadices of Cyclanthaceae is probably an adaptation to endozoochoria (Harling et al. 1998), the agents of which are bats (Croat 1978; Hammel and Wilder 1989), monkeys (Croat 1978; Gentry and Dodson 1987) and birds (Olson and Blum 1968). Furthermore, ballistochoria (Hammel 1986) and barochoria (Hammel and Wilder 1989; Eriksson 1995) have been also described in some species of Carludovicoideae.

With the current reassessment of Pandanales phylogeny, the reconstruction of its dispersal history becomes an actual task of plant biogeography. In order to determine the region of hypothetical origin and probable dispersal scenarios of the families of Pandanales families, the representatives of all 5 families from 30 genera of the order Pandanales (sensu APG IV) were selected for conducting a phylogenetic phytogeographic reconstruction based on a molecular genetic cladistic methods of investigation.

MATERIALS AND METHODS

The cladistic method proposed by W. Hennig in 1950 was used in the present study (Crisci et al. 2003; Lukashov 2009; Hall 2011; Wiley and Lieberman 2011).

Thirty seven species from 30 genera from all five families of the order Pandanales were used in the present study (Table A.1). The sequences of four different markers were selected for each species, – matR (mitochondrial DNA), 18S (ribosomal RNA), atpA (chloroplast DNA), matK (chloroplast DNA). Since the selected nucleotide sequences had different lengths and some deletions, the multiple sequence alignment was performed using the Clustal Omega algorithm (Lukashov 2009; Sievers et al. 2011; Wiley and Lieberman 2011; Judd et al. 2016). Then, the concatenation of 4 markers to one sequence (18s–atpA–matK–matR) was made in Mega X program (Kumar et al. 2018), after which the consensus molecular genetic cladogram of Pandanales was obtained (Fig. 1).

Evolutionary models were formed in the MrBayes 3.2 program (Ronquist et al. 2012) using Bayesian inference by 4 genes for 3000000 generations. Samples were taken every 100 generations and 25% were discarded in the burning. For 18S and matR markers, the Kimura two-parameter model (Kimura 1980) was used. For atpA and matK the General time reversal (GTR) model was used (Nei, Kumar, 2000). Optimal models were selected in TOPALi v2 (Milne et al. 2009). Six species of *Dioscorea* (Dioscoreaceae–Dioscoreales, sister order to Pandanales sensu APG IV) were selected as an outgroup.

In order to clarify the relationship between representatives of the basal family Velloziaceae, we constructed a separate molecular genetic cladogram. The nucleotide sequences of three markers representing 9 species from 9 narrowly considered genera of Velloziaceae were selected from GenBank (Table A.2): two plastid (atpB with spacer atpB-rbcL and tRNA-Leu (trnL) with spacer trnL-F), and one ribosomal (5.8S ribosomal RNA with two internal spacers – 1 and 2).

Multiple sequence alignment was carried out using the Clustal X 2.0 program (Larkin et al. 2007), after which the consensus molecular genetic cladogram was obtained (Fig. 2). Evolutionary models were constructed in the Mega7 7.0.26 program (Kumar et al. 2016) using the maximum likelihood statistical method based on the Tamura 3-parameter model (Tamura 1992). The consensus cladograms were obtained using bootstrap analysis with 1000 replicates (Felsenstein 1985). The *Stemona tuberosa* Lour. from the closely related family Stemonaceae (Chase et al. 2016) was selected as an outgroup.

The charts of the correlation of the phylogenetic relationships of Pandanales genera and their geographical distribution were presented for each family separately: Velloziaceae (Fig. 3); Triuridaceae (Fig. 4); Stemonaceae (Fig. 5); Pandanaceae (Fig. 6) and Cyclanthaceae (Fig. 7).

RESULTS

As a result of our research, cladograms were obtained (Fig. 1, 2). The resulting cladograms are generally supported with high bootstrap index at most nodes. Velloziaceae is shown to be basal in Pandanales (Fig. 1). The next phylogenetic event was the separation of the clade Triuridaceae from other families. Later Stemonaceae clade and two sister terminal families – Pandanaceae and Cyclanthaceae – separated (Fig 1).

Phylogeny of Velloziaceae

The Tibetan genus *Acanthochlamys* is the most basal in Velloziaceae (Fig. 2). At the next step the American genus *Barbaceniopsis* and all other genera diverged into two branches. The first branch includes two sister African genera *Talbotia–Xerophyta*, which are basal to all other genera. Later these genera become diverged into two sister clades – *Nanuza–Vellozia* and *Pleurostima–Barbacenia–Burlemarxia*, both of which are American.

Phylogeny of Triuridaceae

In the family Triuridaceae, the Cameroon-Tanzanian clade *Kihansia–Kupea* is basal (Fig. 1, 4). It is followed by a polytomy giving rise to three clades: (1) *Seychellaria* – a genus distributed in Madagascar, Seychelles and Tanzania, (2) *Sciaphila* – a pantropical genus, and (3) *Lacandonia–Triuris* clade, whose representatives are distributed in Central America and tropical regions of South America.

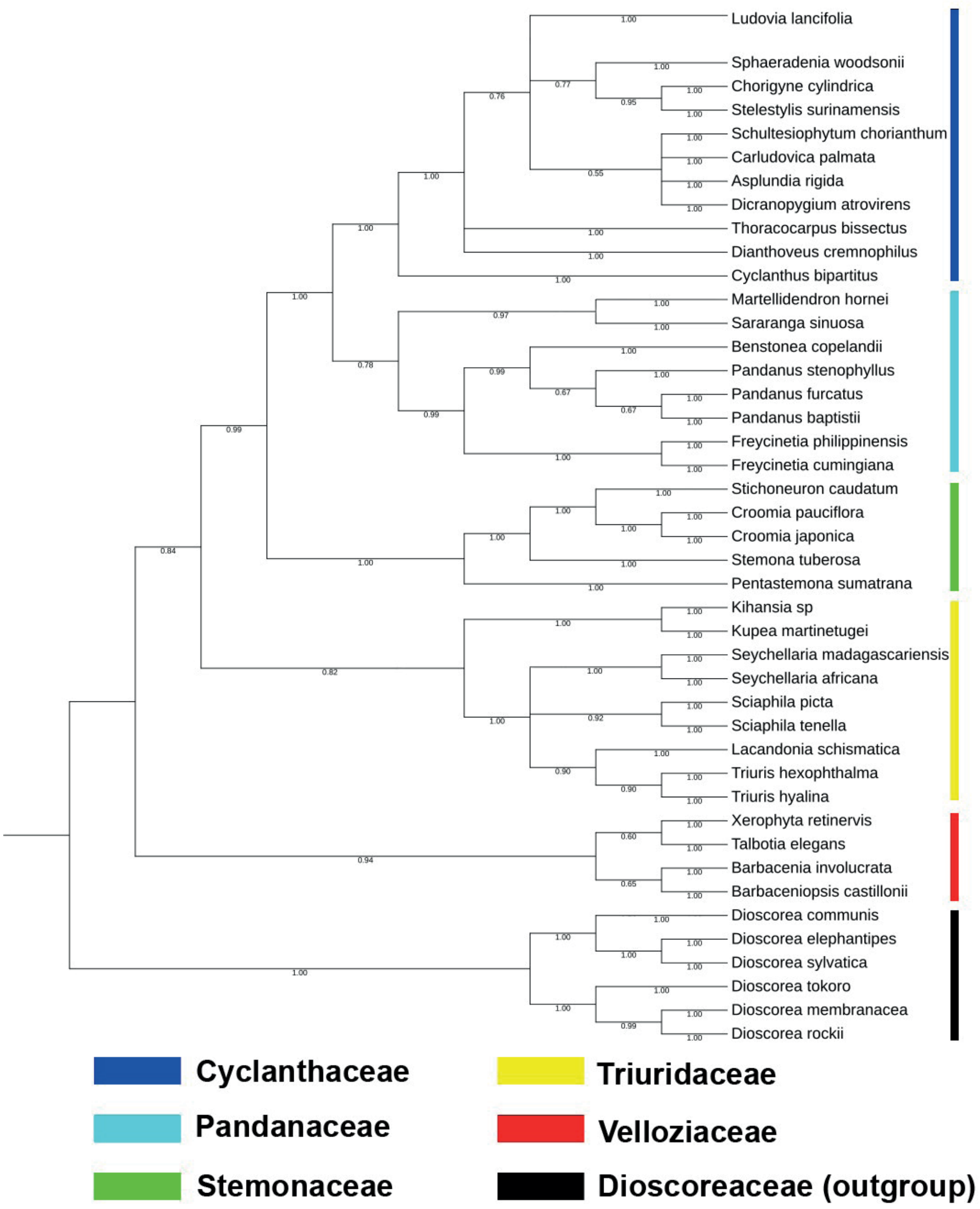

Fig. 1. Molecular genetic cladogram of Pandanales

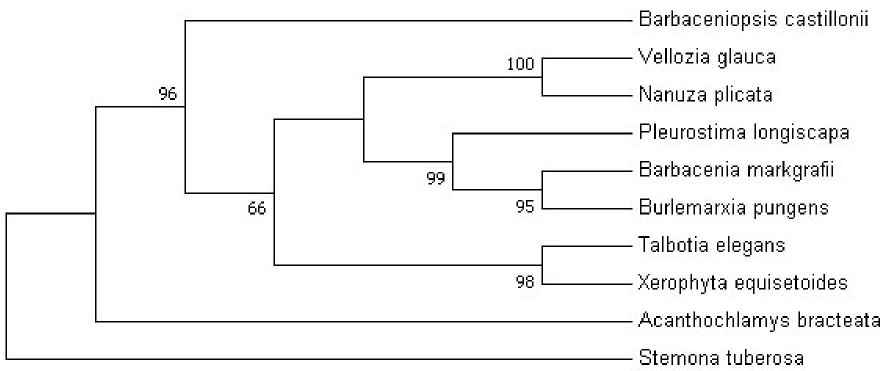

Fig. 2. Molecular genetic cladogram of Velloziaceae

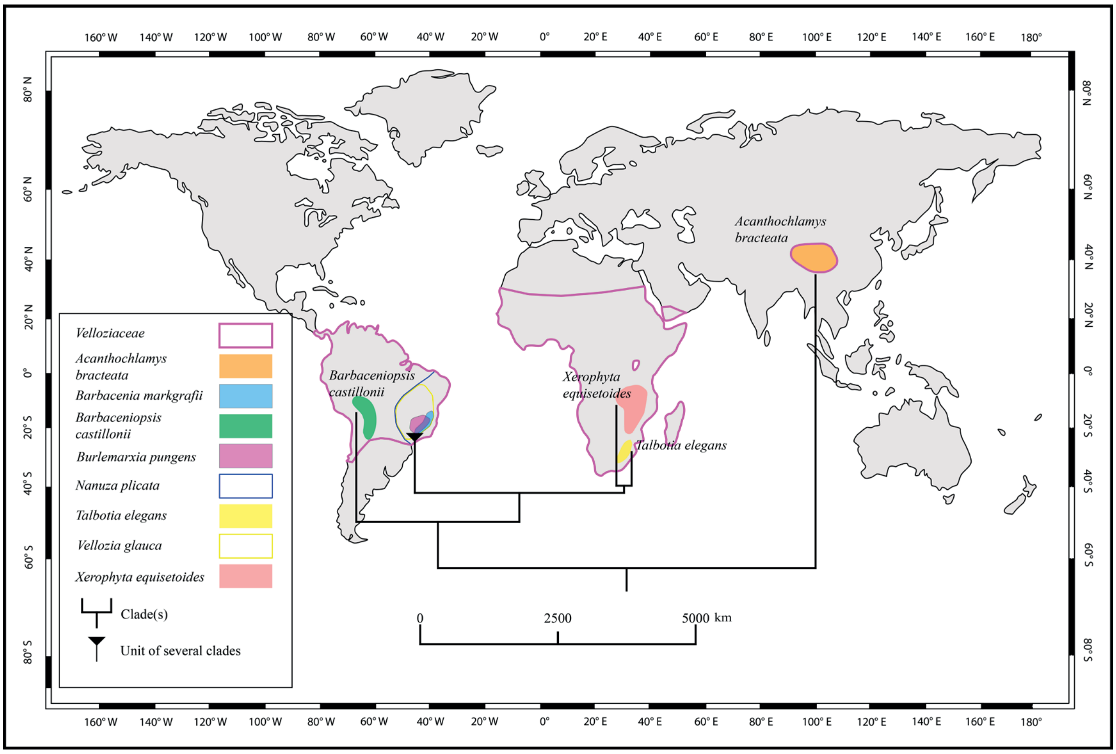

Fig. 3. Correlation of phylogeny of Velloziaceae genera and their distribution

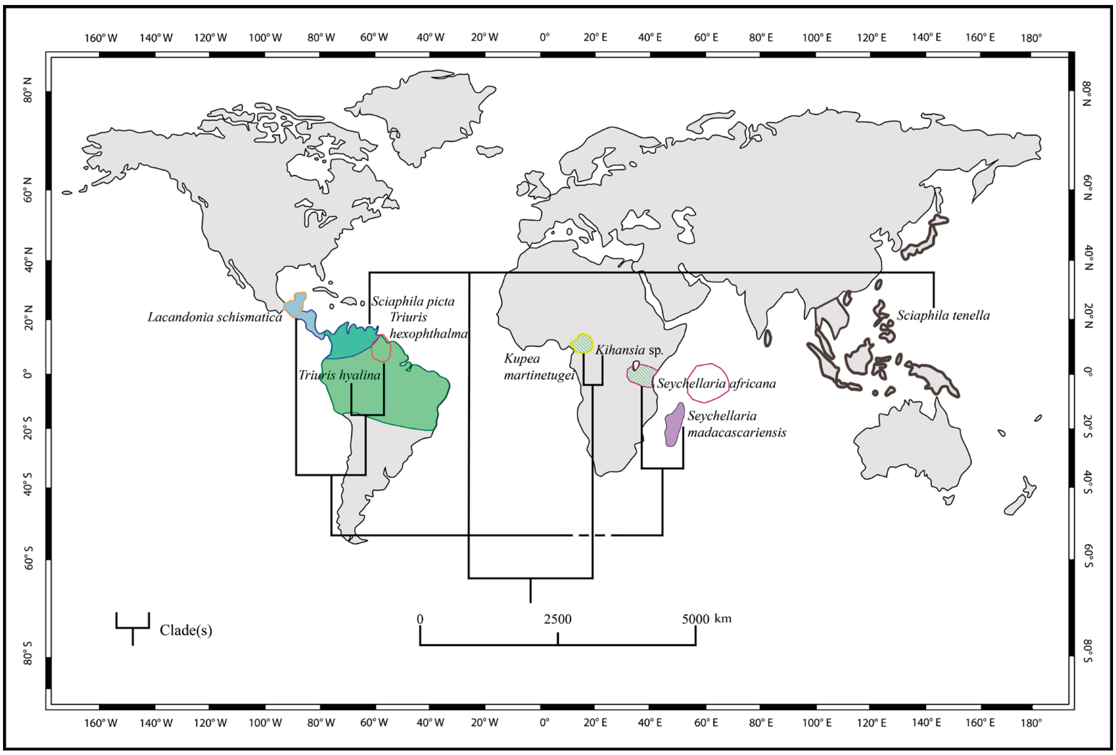

Fig. 4. Correlation of phylogeny of Triuridaceae genera and their distribution

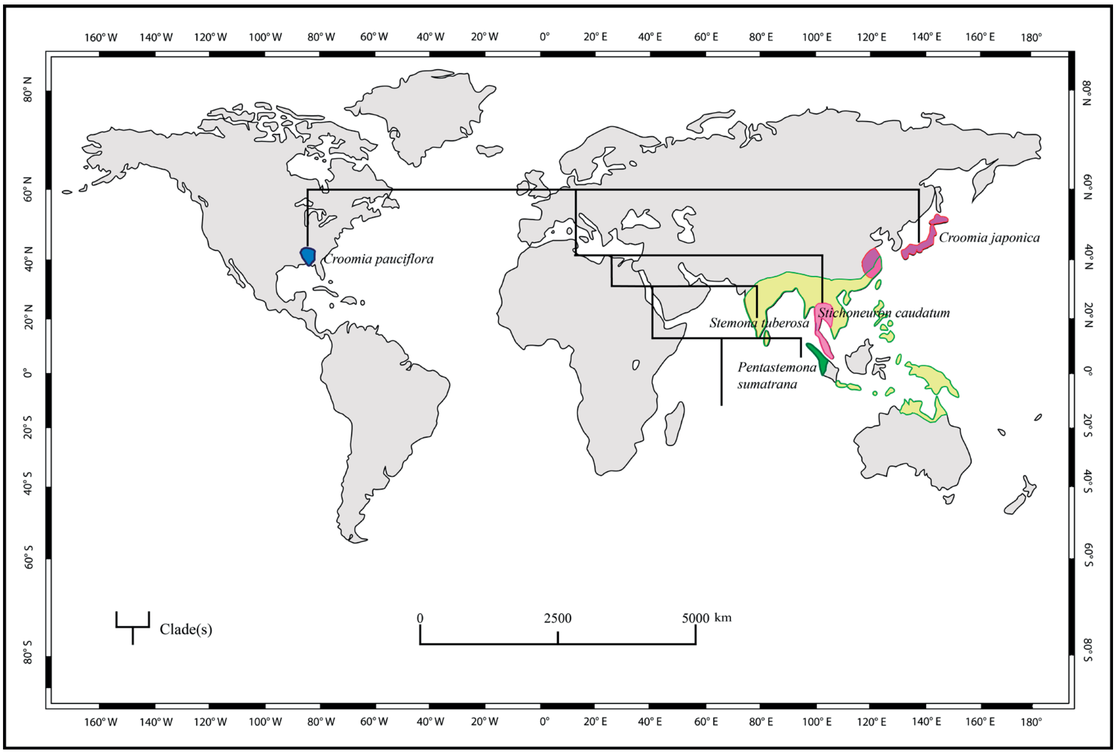

Fig. 5. Correlation of phylogeny of Stemonaceae genera and their distribution

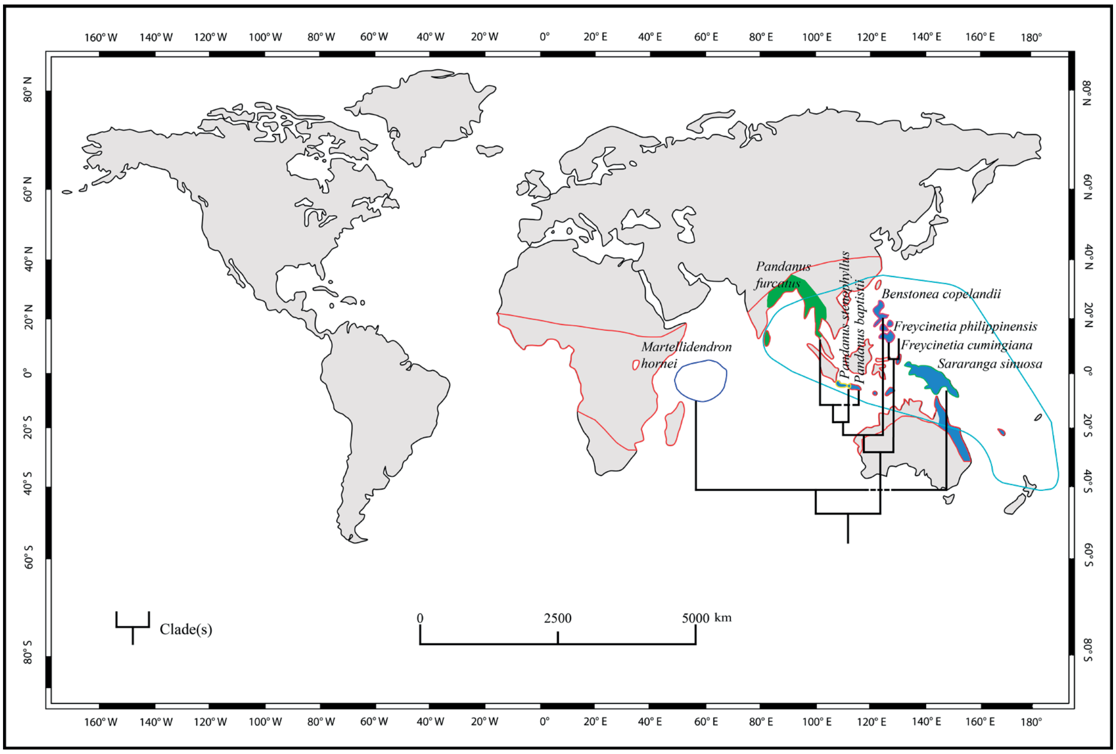

Fig. 6. Correlation of phylogeny of Pandanaceae genera and their distribution

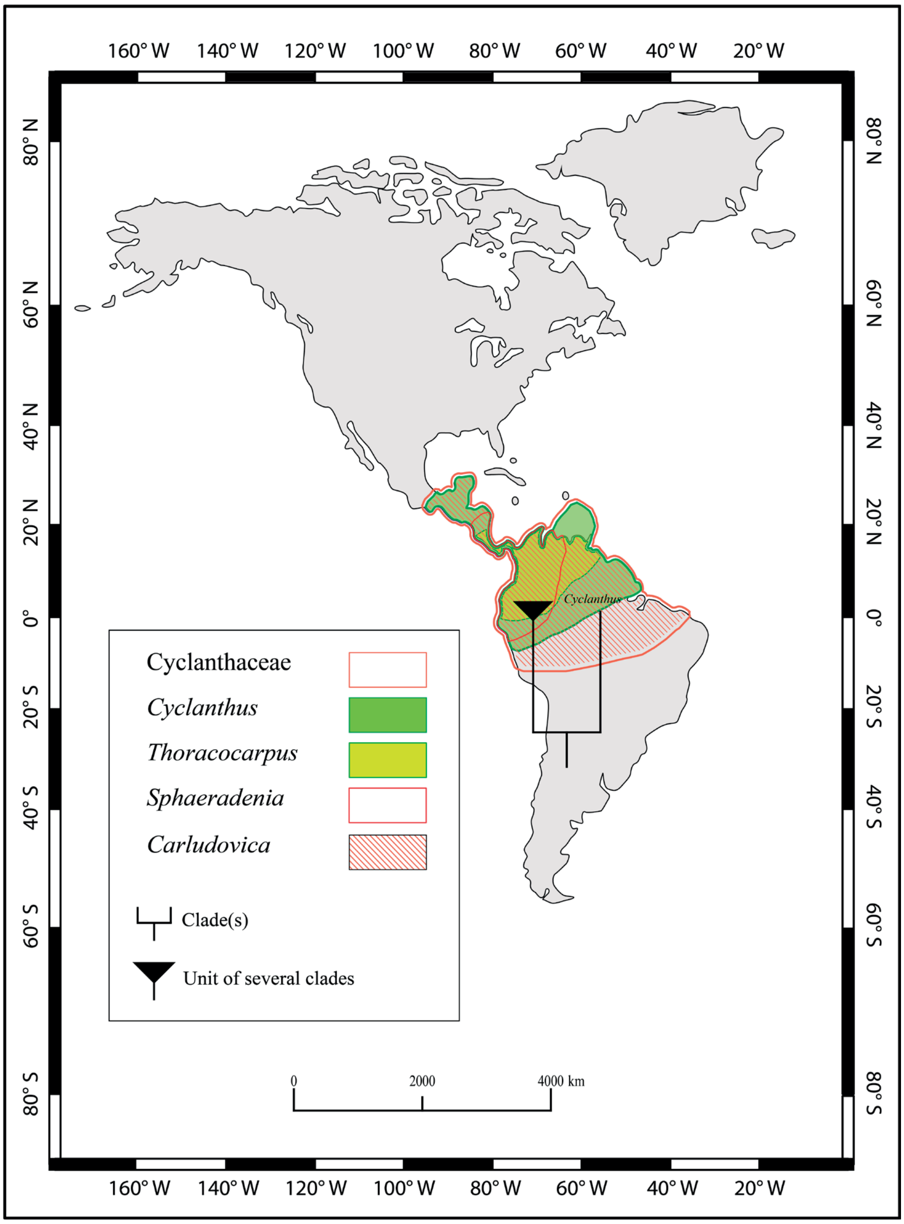

Fig. 7. Correlation of phylogeny of Cyclanthaceae genera and their distribution

Phylogeny of Stemonaceae

The genus *Pentastemona*, the endemic of Sumatra, is the basal in Stemonaceae family (Fig. 1, 5). Then the genus *Stemona*, which is widespread in the Paleotropics, diverged from the other genera of the family. The final bifurcation resulted in two sister clades: *Stichoneuron* (continental Southeast Asia) and *Croomia* (East Asia and Southeastern United States).

Phylogeny of Pandanaceae

The clade *Martellidendron–Sararanga* (Madagascar, Seychelles, New Guinea, Philippines) is basal in Pandanaceae (Fig. 1, 6). The clades of *Freycinetia* (from Sri Lanka to the Marquesas Islands, including Hawaii, Australia and New Zealand) and *Benstonea–Pandanus* (both Paleotropics) diverged at the next steps.

Phylogeny of Cyclanthaceae

The basal position in the neotropical family Cyclanthaceae was occupied by the representative of a separate monotypic subfamily – *Cyclanthus bipartitus* Poit. ex A.Rich. (Fig. 1, 7), which is distributed from northern Guatemala through Central America, the Lesser Antilles and Trinidad Island to Chile and Brazil. Polytomies were observed three times during the next evolutionary steps in the family, which may indicate the recent evolutionary divergence between the genera. (1) The first polytomy is the split of the rest genera (subfamily Carludovicoideae) into three clades: *Thoracocarpus, Dianthoveus* and all other genera. (2) The second polytomy is the split of the remaining genera into three clades as follows: *Ludovia, Sphaeradenia–Chorigyne–Stelestylis* and all other genera. (3) The third polytomy occurred at the final step and of four genera became separated: *Asplundia, Dicranopygium, Schultesiophytum* and *Carludovica*.

DISCUSSION

According to the cladogram of Pandanales, the family Velloziaceae occupies the basal position (Fig. 1). Due to the fact that the Asian genus Acanthochlamys is basal within Velloziaceae, it is suggested that the region of the hypothetical origin of the Pandanales order could be Tibet.

Phylogenetic biogeography of Velloziaceae

After the separation of *Acanthochlamys*, the basal genus of Velloziaceae, the bifurcation of the second order resulted in origin of the American genus *Barbaceniopsis* and all other genera (distributed in Neotropics and Africa). Their areas of distribution could be formed as the result of long-distance transport from Tibet to America via the existing bridge between Asia and North America (Fig. 8) around 115-100 Mya (Scotese et al. 1988; Wu 1988). After that, dispersal probably took place via the incipient Atlantic Ocean to West Africa (Scotese et al. 1988; Scotese 2014). Further on in Africa, vicarious dispersal in two directions is most probable: eastwards to the east coast of the continent (*Talbotia*) and on to Madagascar and northwards to the Arabian Peninsula (*Xerophyta*). In South America a vicarious dispersal probably occurred to the north and northeast of the continent (Fig. 8). The proposed dispersal scenario (scenario #1) suggest that the Velloziaceae originated in Laurasia, then dispersed by long-distance transport at early stages of their history via Americas to Africa and later vicariously from West Africa to east coast of the continent and to the Arabian Peninsula. Such interpretation of Velloziaceae phytogeographic history contrasts with earlier studies (Mello-Silva et al. 2011), which suggested a Gondwanan origin of Velloziaceae and recognized their modern distribution (almost exclusively) as the result of vicariance (scenario #2). This alternative interpretation (scenario #2) of the dispersal history of Velloziaceae (Mello-Silva et al. 2011) is also probable as far as more than 90% of the representatives of the family is currently distributed in the New World, two genera (*Talbotia, Xerophyta*) distributed in Africa, Madagascar and southern Arabia and only one monotypic genus in Tibet. Based on this, it can be assumed that Velloziaceae originates in the Neotropics (i. e. in Gondwana). At the same time a third scenario (scenario #3) of Velloziaceae dispersal history could be assumed. The range disjunction of the family is generally indicative of the relict nature of the taxa and molecular studies suggest that the Velloziaceae originated around 115 Mya, which is comparable to the early dicotyledons (Mello-Silva et al. 2011). So, during the Upper Cretaceous, representatives of the family could migrate from Tibet to Africa via Arabia and then from West Africa via the Atlantic to South America, where they found more suitable ecological niches.

Phylogenetic biogeography of Triuridaceae

After the separation of Triuridaceae from other Pandanales, probably in Tibet (where the basal family Velloziaceae originated), the long-distance dispersal to the Americas via the Bering Land Bridge is assumed (Fig. 9) around 100–90 Mya (Gandolfo et al. 2002; Scotese 2014), which was followed by their expansion to South America and then to Africa. In Africa the basal clade of Triuridaceae – *Kihansia–Kupea* diverged from the main tree. The representatives of *Kihansia* are distributed in Cameroon and Tanzania, whereas the studied species of *Kupea, K. martinetugei* Cheek & S.A.Williams, is distributed only in Cameroon. The revealed topology and the ranges of the basal representatives of Triuridaceae (Fig. 4) may indicate a Laurasian-Gondwanan origin of the family. The origin of Triuridaceae revealed in the present study is also supported by fossil records of plants with a high degree of attribution to Triuridaceae, reported from the modern territory of the USA and dated to 90–94 Mya (Gandolfo et al. 2002). The pantropical genus *Sciaphila*, the next clade (Fig. 4), dispersed from central West Africa in two directions (Fig. 9): (1) vicariously to north-east Africa and then – eastward via the tropical regions of Eurasia to the South-East Asia and Japan; (2) by long-distance transport to Central America. The representatives of *Seychellaria* diverge from the main tree in next turn and dispersed vicariously from central West Africa eastwards to Tanzania, Madagascar and the Seychelles. The studied representatives of the *Lacandonia–Triuris* clade dispersed vicariously, most probably, from the place of hypothetical separation from the other Triuridaceae in central West Africa into northern South America. Then they dispersed there westward via the continent to the Pacific coast, southward in South America to the boundary of the tropics, southwestward to northern Argentina and northward into Central America to the Yucatan Peninsula and the Antilles (Fig. 9).

Phylogenetic biogeography of Stemonaceae

Pentastemona, the basal genus of Stemonaceae, is distributed in North Sumatra (Fig. 5). Based on this the Stemonaceae most probably originated in West Malesia. The next stage of the evolution of the family was the differentiation of the palaeotropical genus *Stemona*, which dispersal from West Malesia supposedly took place vicariously in two directions. (1) South-eastwards via the Sunda Islands to North Australia and then eastwards along the continent to Cape York Peninsula, westwards along the northern coast of Australia and then southwards to the south-west of Australia. (2) Northward via continental South-East Asia to the tropical border, then eastward to the coast of the Taiwan Strait and westward to the Indian Peninsula. And then southward to the Indian Ocean coast and Sri Lanka Island (Fig. 10). After the branching of the terminal clade *Croomia* in tropical East Asia vicarious dispersal most likely took place northwards along the Eurasian coast to the northern cost of the East China Sea and later eastwards to the Japanese islands. The further dispersal of *Croomia* representatives was realised by long-distance transport via the Kuril Islands, the Kamchatka Peninsula and possibly via the Bering Land Bridge to North America and further southwestward (Fig. 10).

Disjunction of the ranges of closely related species has traditionally been described for representatives of various taxa, including early dicotyledons. The conservation of morphological peculiarities among taxa with such disjunctions can be the result of morphological stasis and/or low evolutionary rates (Wen 2001). This can be the reason of the morphological similarities between closely related taxa native to East Asia and eastern North America (Wen 2001). For example, one part of the species of the genus *Magnolia* sect. *Rytidospermum* is distributed in eastern Asia and the other in eastern North America. Such disjunction explained by the relatively recent differentiation of species (Eocene-Miocene) and their further migration, particularly via the Bering Land Bridge (Tiffney 1985; Qiu et al. 1995).

Phylogenetic biogeography of Pandanaceae

A clade of two sister genera, *Martellidendron* (Madagascar and Seychelles) and *Sararanga* (Philippines and New Guinea), is basal in Pandanaceae. Thus, it is possible to assume hypothetical origin of the family in Madagascar or in New Guinea. Both variants indicate a south-east Gondwanan origin of the Pandanaceae. At the first stage, after the separation from other Pandanales, representatives of Pandanaceae most probably dispersed vicariously from hypothetical range of origin in East Africa via the southern Arabian Peninsula and the Indian subcontinent into south-east Asia, where the genera *Benstonea, Pandanus* and *Freycinetia* became differentiated (Fig. 11). Then, also vicariously, they continued to disperse southwards to the north coast of Australia and southeastwards to New Guinea. Thereafter, some species of *Pandanus* repopulated Africa, probably by long-distance transport (from South-East Asia). Such dispersal tracks can be explained by the prolonged germ activity of *Pandanus* hydrochorous diaspores (Gallaher et al. 2015). Later the African *Pandanus* species vicariously dispersed westwards to the Atlantic coast of Africa and southwards to the continental margins (Fig. 11).

The Gondwanan origin of the family war earlier suggested by other researchers and it is supported hypothesis by the fossil evidence (Callmander and Laivao 2002; Callmander et al. 2003; Nadaf et al. 2012). Recent study of the biogeography of Pandanaceae, based on molecular data, has proposed that dispersal of most species occurred by long-distance transport in the late Eocene, i. e. after the divergence of the Gondwana continents (Gallaher et al. 2015).

Phylogenetic biogeography of Cyclanthaceae

The family Cyclanthaceae is most probably originated in south-west Gondwana, as the basal genus *Cyclanthus* is distributed in northern South America and Central America.

After the basal clade of Cyclanthaceae separated, polytomies of clades: *Dianthoveus, Thoracocarpus* and all other Cyclanthaceae occurred. There representatives of these clades were distributed vicariously from northern South America southwards to the tropical border in Brazil and south-westwards to northern Argentina (Fig. 12). The diversity hotspot of Cyclanthaceae is Central America, where up to 90% of the species of Cyclanthaceae are distributed. After the differentiation of the genera *Dianthoveus* and *Thoracocarpus*, polytomy has three times occurred in the family, indicating close genetic relations between different genera and their recent evolutionary divergence.

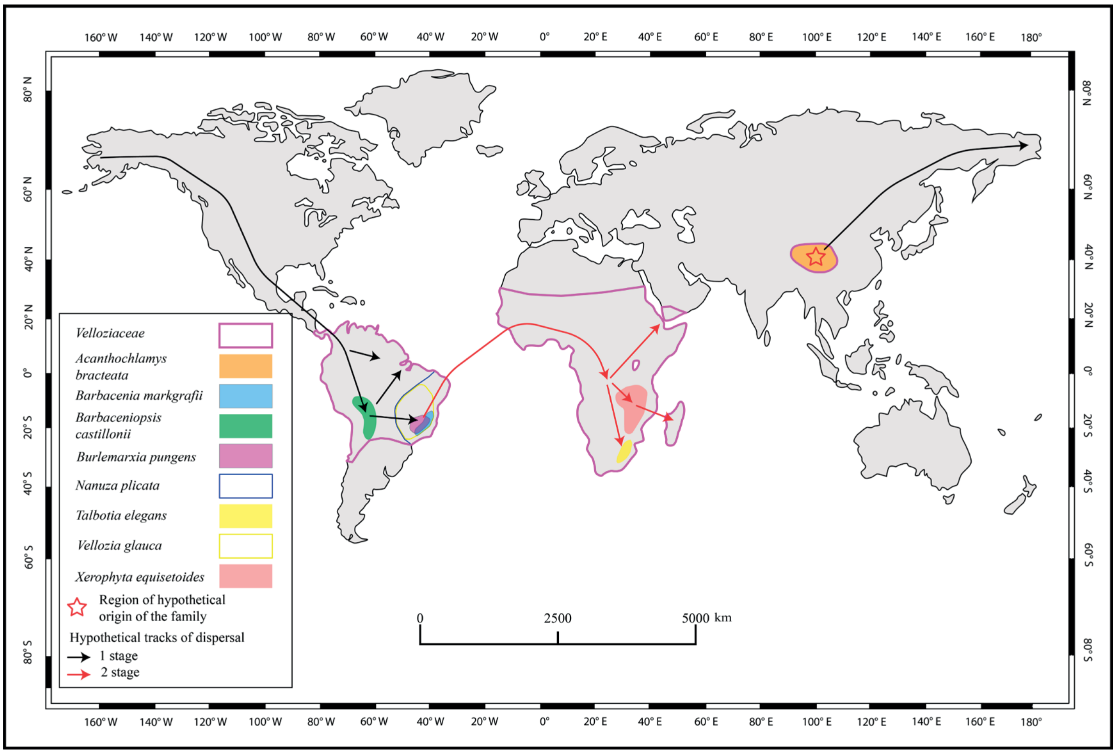

Fig. 8. The region of hypothetical origin and probable dispersal tracks of Velloziaceae

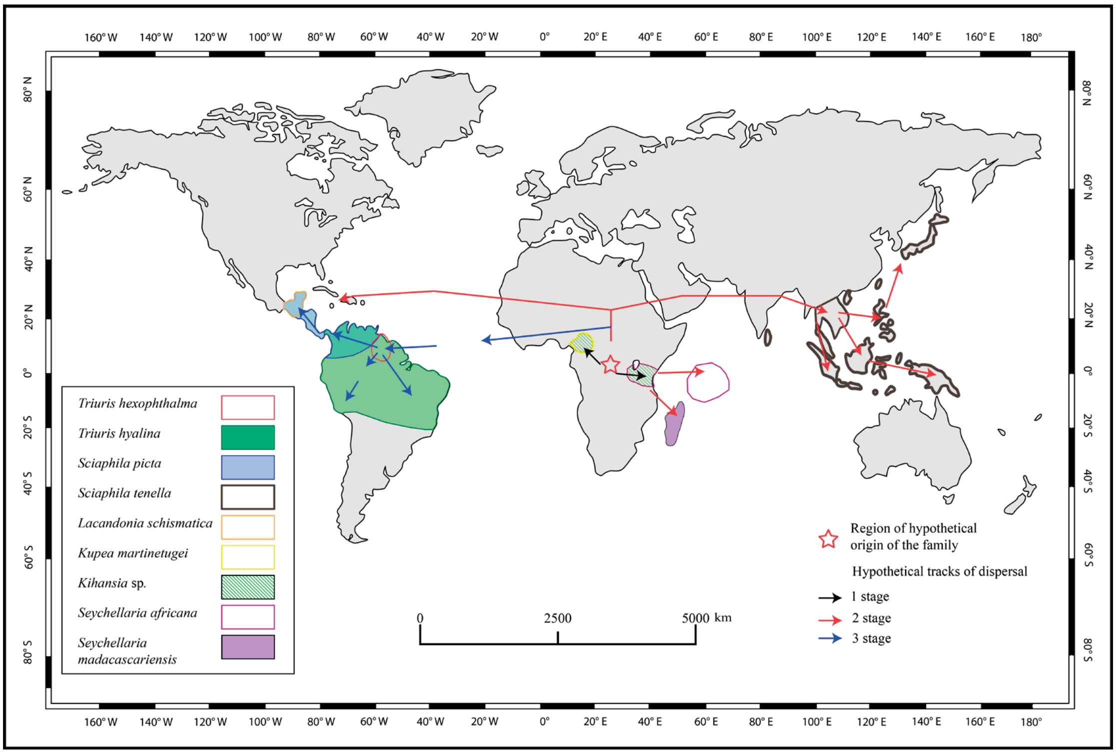

Fig. 9. The region of hypothetical origin and probable dispersal tracks of Triuridaceae

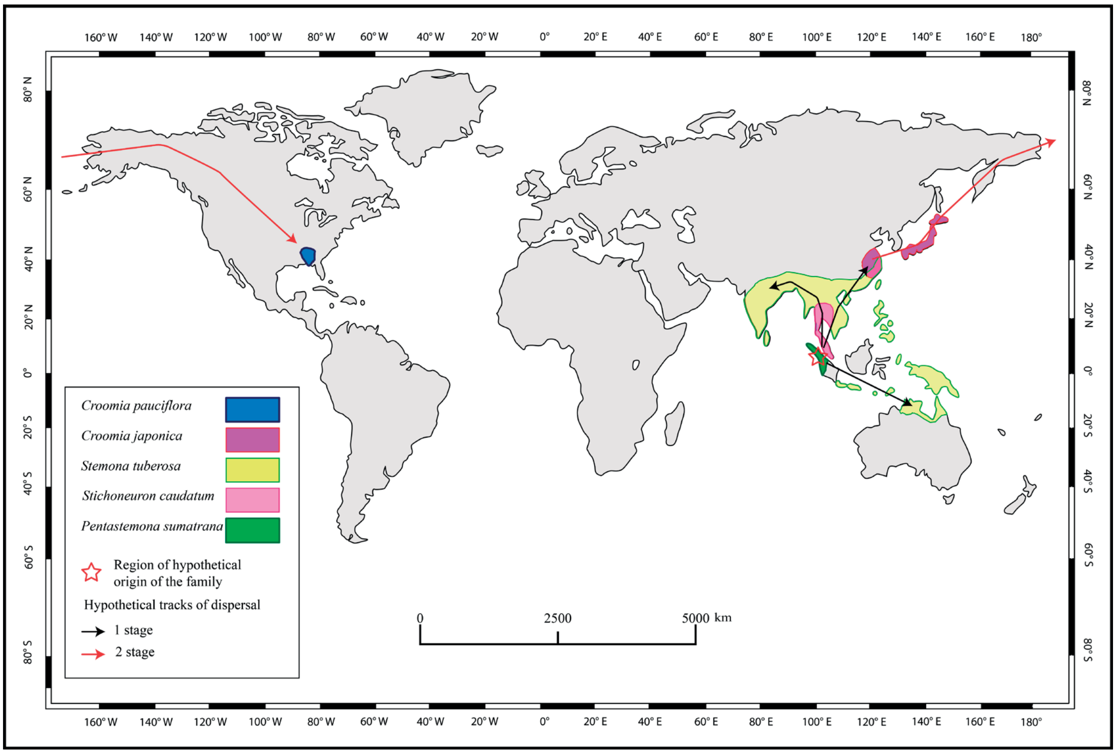

Fig. 10. The region of hypothetical origin and probable dispersal tracks of Stemonaceae

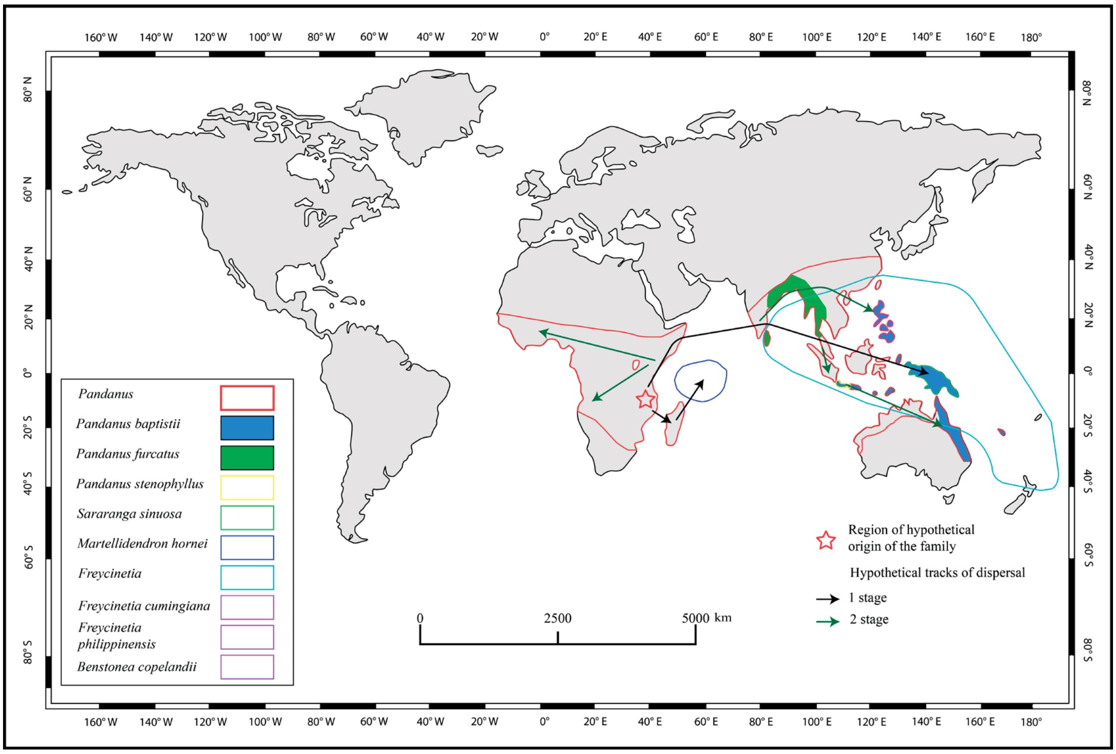

Fig. 11. The region of hypothetical origin and probable dispersal tracks of Pandanaceae

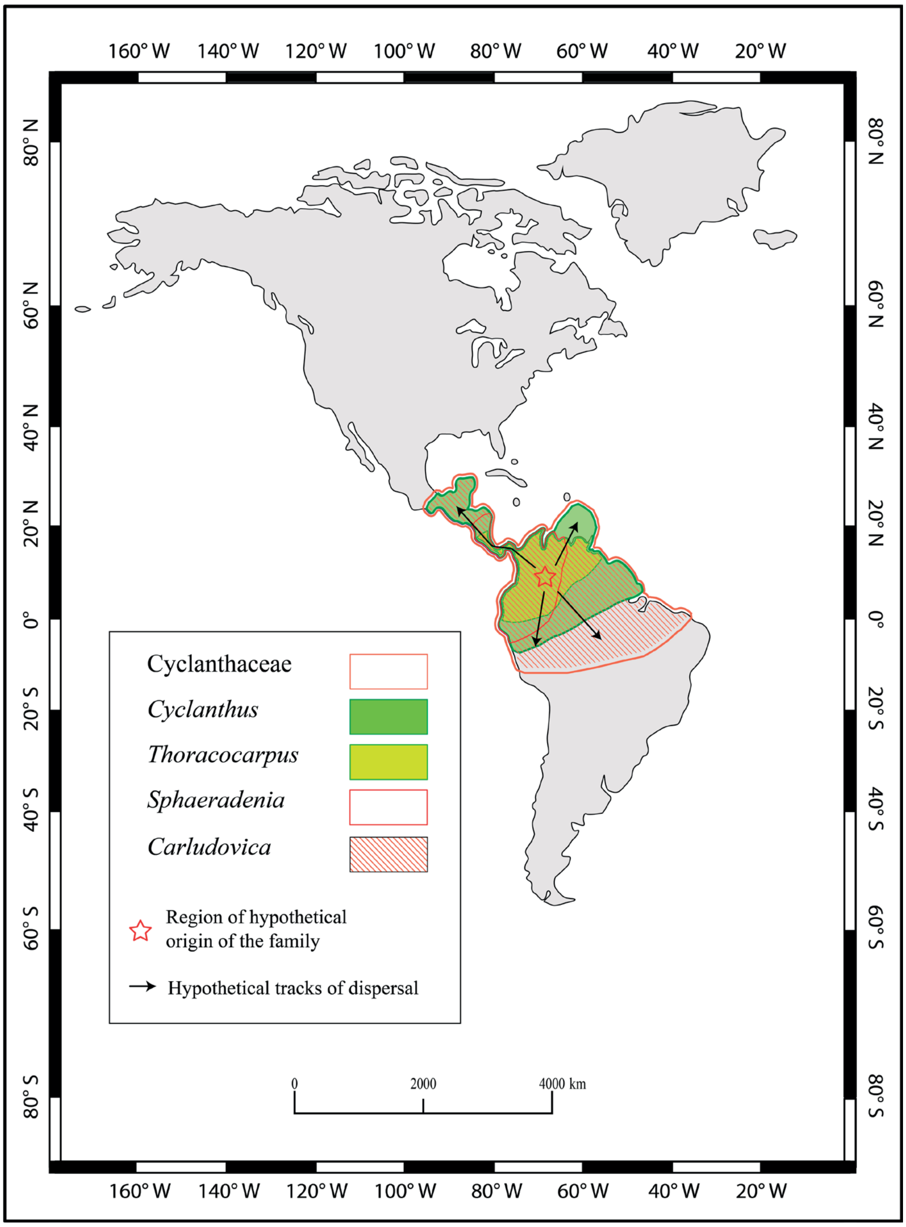

Fig. 12. The region of hypothetical origin and probable dispersal tracks of Cyclanthaceae

CONCLUSIONS

1. The order Pandanales is treated as originated in Laurasia and its differentiation began on the territory of Tibet.

2. Dispersal of the representatives of the basal family Velloziaceae took place by long-distance transport via the Bering Land Bridge to South America (approximately 115 Mya).

3. Velloziaceae dispersed in the New World vicariously in South America, then in was distributed to sub-Atlantic Africa by long-distance transport, and finally also vicariously to the east, south and north of the continent.

4. Triuridaceae, which probably originated in Africa, first dispersed vicariously along the several tracks of the tropical parts of the continent. Later two phylogenetic lines of Triuridaceae distributed to South America by long-distance transport on one side and probably vicariously – to South and South-East Asia, to North Australia and Oceania on the other.

5. Stemonaceae, having been differentiated from others Pandanales, probably, in South Malesia, dispersed vicariously from there in several tracks. Along the east track – to the coast of the Asian continent and then on to the Japanese islands; to the south-west to Hindustan and on to the island of Sri Lanka; to the south-east to the Philippines, Borneo, New Guinea and north-east Australia. Later the Stemonaceae dispersed from East Asia by long-distance transport via the Bering Land Bridge to the New World and reached eastern North America.

6. The family Pandanaceae probably diverged from the other Pandanales in West Africa. Later the representatives of the family vicariously dispersed eastwards into south-east Asia, northern Australia and New Zealand. Representatives of *Pandanus*, the largest genus in Pandanales, supposedly repopulated Africa (from south-east Asia) by long-distance transport.

7. Cyclanthaceae probably originated in south-west Gondwana (in northern South America or in Central America). The distribution of the representatives of the family most likely took place in South America vicariously: southwards to the tropical border of Brazil and south-westwards to northern Argentina.

In order to verify and clarify proposed scenario of Pandanales dispersal history the detailed comparative-morphological analysis (including studies of the carpological characters – the most conservative and, hence, informative in phylogenetic reconstructions) should be carried out. Furthermore, a detailed palaeobotanical data is needed that could verify the direction of dispersal tracks and the region of the hypothetical origin especially of the basal family Velloziaceae.

REFERENCES

Callmander M. and Laivao M. (2002). Endémisme et biogéographie du genre Pandanus (Pandanaceae) en Afrique et à Madagascar. Bioterre, Revue internationale des Sciences de la Vie et de la Terre, no spécial, 76-89.

Callmander M.W., Chassot P., Küpfer P., Lowry Ii P.P. (2003). Recognition of Martellidendron, a new genus of Pandanaceae, and its biogeographic implications. Taxon, 52(4), 747-762, DOI: 10.2307/3647349.

Chase M.W., Christenhusz M., Fay M., Byng J., Judd W.S., Soltis D., Mabberley D., Sennikov A., Soltis P.S., Stevens P.F. (2016). An update of the Angiosperm Phylogeny Group classification for the orders and families of flowering plants: APG IV. Botanical Journal of the Linnean Society, 181(1), 1-20, DOI: 10.1111/boj.12385.

Cox P.A. (1990). Pollination and the evolution of breeding systems in Pandanaceae. Annals of the Missouri Botanical Garden, 77(4), 816-840, DOI: 10.2307/2399673.

Crisci J.V., Katinas L., and Posadas P. (2003). Historical Biogeography. An Introduction. Cambridge: Harvard University Press, DOI: 10.1086/421673.

Croat T.B. (1978). Flora of Barro Colorado Island. Stanford, California, USA: Stanford University Press, DOI: 10.5962/bhl.title.153450.

Cronquist A. (1981). An Integrated System of Classification of Flowering Plants. New York: Columbia University Press, DOI: 10.2307/2806386.

Eriksson R. (1995). The genus Sphaeradenia (Cyclanthaceae). Opera Botanica, 126, 1-106.

Felsenstein J. (1985). Confidence limits on phylogenies: an approach using the bootstrap. Evolution, 39(4), 783-791, DOI: 10.1111/j.1558-5646.1985.tb00420.x.

Gallaher T., Callmander M.W., Buerki S., Keeley S.C. (2015). A long distance dispersal hypothesis for the Pandanaceae and the origins of the Pandanus tectorius complex. Molecular Phylogenetics and Evolution, 83, 20-32, DOI: 10.1016/j.ympev.2014.11.002.

Gandolfo M.A., Nixon K.C., and Crepet W.L. (2002). Triuridaceae fossil flowers from the Upper Cretaceous of New Jersey. American Journal of Botany, 89(12), 1940-1957, DOI: 10.3732/ajb.89.12.1940.

Garcia Q.S., Saraiva I.S., Soares da Mota L.A., and Bicalho E.M. (2017). Long-term persistence of Velloziaceae species in the soil seed bank in campo rupestre vegetation, Brazil. Plant Ecology & Diversity, 10(4), 323-328, DOI: 10.1080/17550874.2017.1379570.

Gentry A. and Dodson C.H. (1987). Diversity and biogeography of neotropical vascular epiphytes. Annals of the Missouri Botanical Garden, 74, 205-233, DOI: 10.2307/2399395.

Grushvitsky I.V. (1982). Pandanales order. In: A.L. Takhtajan, ed., Plant Life: In Six Volumes. Moscow: Enlightenment, 6, 451-461 (in Russian).

Hall B.G. (2011). Phylogenetic Trees Made Easy: A How to Manual. 4th ed. Sunderland: Sinauer, DOI: 10.1007/978-3-031-11958-3.

Hammel B.E. (1986). Cyclanthaceae. Selbyana, 9(1), 196-202.

Hammel B.E. and Wilder G.J. (1989). Dianthoveus: a new genus of Cyclanthaceae. Annals of the Missouri Botanical Garden, 76(1), 112-123, DOI: 10.2307/2399344.

Harling G., Wilder G.J., and Eriksson R. (1998). Cyclanthaceae. In: K. Kubitzki, ed., Flowering Plants. Berlin, etc.: Springer, 3, 202-215, DOI: 10.1007/978-3-662-03533-7_27.

Heads M. (2012). Molecular Panbiogeography of the Tropics. Berkeley: University of California Press, DOI: 10.1093/sysbio/sys040.

Heads M. (2013). Biogeography of Australasia: A Molecular Analysis. Cambridge: Cambridge University Press, DOI: 10.1017/CBO9781139644464.

Hutchinson J. (1973). The Families of Flowering Plants, Arranged According to a New System Based on their Probable Phylogeny. 3rd ed. Oxford: Oxford University Press.

Judd W.S., Campbell C.S., Kellogg E.A., Stevens P.F., Donoghue M.J. (2016). Plant Systematics: A Phylogenetic Approach. 4th ed. Sunderland: Sinauer, DOI: 10.3119/0035-4902-118.976.418.

Kimura M.A. (1980). A simple method for estimating evolutionary rates of base substitutions through comparative studies of nucleotide sequences. Journal of Molecular Evolution, 16(2), 111-120, DOI: 10.1007/BF01731581.

Kubitzki K. (1998a). Velloziaceae. In: K. Kubitzki, ed., Flowering Plants. Berlin, etc.: Springer, 3, 459–467, DOI: 10.1007/978-3-662-03533-7_60.

Kubitzki K. (1998b). Stemonaceae. In: K. Kubitzki, ed., Flowering Plants. Berlin, etc.: Springer, 3, 422–425, DOI: 10.1007/978-3-662-03533-7_53.

Kubitzki K. (1998c). Pentastemonaceae. In: K. Kubitzki, ed., Flowering Plants. Berlin, etc.: Springer, 3, 404–406, DOI: 10.1007/978-3-662-03533-7_48.

Kumar S., Stecher G., and Tamura K. (2016). MEGA7: molecular evolutionary genetics analysis version 7.0 for bigger datasets. Molecular Biology and Evolution, 33(7), 1870-1874, DOI: 10.1093/molbev/msw054.

Kumar S., Stecher G., Li M., Knyaz C., Tamura K. (2018). MEGA X: molecular evolutionary genetics analysis across computing platforms. Molecular Biology and Evolution, 35(6), 1547-1549, DOI: 10.1093/molbev/msy096.

Larkin M.A., Blackshields G., Brown N.P., Chenna R., McGettigan P.A., McWilliam H., Valentin F., Wallace I.M., Wilm A., Lopez R. (2007). Clustal W and Clustal X version 2.0. Bioinformatics, 23(21), 2947-2948, DOI: 10.1093/bioinformatics/btm404.

Lukashov V.V. (2009). Molecular evolution and phylogenetic analysis. Study guide. Moscow: BINOMIAL. Laboratory of Knowledge (in Russian).

Maas-Van De Kamer H. and Weustenfeld T. (1998) Triuridaceae. In: K. Kubitzki, ed., Flowering Plants. Berlin, etc.: Springer, 3, 452-458, DOI: 10.1007/978-3-662-03533-7_59.

Mello-Silva R. de, Santos D.Y.A., Salatino M.L.F., Motta L.B., Cattai M.B., Sasaki D., Lovo J., Pita P.B., Rocini C., Rodrigues C.D. (2011). Five vicarious [vicariant] genera from Gondwana: the Velloziaceae as shown by molecules and morphology. Annals of Botany, 108(1), 87-102, DOI: 10.1093/aob/mcr107.

Mennes C.B., Smets E.F., Moses S.N., Merckx V.S. (2013). New insights in the long-debated evolutionary history of Triuridaceae (Pandanales). Molecular Phylogenetics and Evolution, 69(3), 994-1004, DOI: 10.1016/j.ympev.2013.05.031.

Merckx V.S.F.T., Freudenstein J.V., Kissling J., Christenhusz M.J.M., Stotler R.E., Crandall-Stotler B., Wickett N., Rudall P.J., Maas-van de Kamer H., Maas P.J.M. (2013). Taxonomy and Classification. In: V.S.F.T. Merckx, ed., Mycoheterotrophy. New York: Springer, 19-101, DOI: 10.1007/978-1-4614-5209-6.

Milne I., Lindner D., Bayer M., Husmeier D., McGuire G., Marshall D.F., Wright F. (2009). TOPALi v2: a rich graphical interface for evolutionary analyses of multiple alignments on HPC clusters and multi-core desktops. Bioinformatics, 25(1), 126-127, DOI: 10.1093/bioinformatics/btn575.

Nadaf A., Zanan R., and Callmander M.W. (2012). Indian Pandanaceae - An Overview. Berlin, etc.: Springer, DOI: 10.1007/978-81-322-0753-5.

Qiu Y.L., Parks C.R., and Chase M.W. (1995). Molecular divergence in the eastern Asia–eastern North America disjunct section Rytidospermum of Magnolia (Magnoliaceae). American Journal of Botany, 82(12), 1589-1598, DOI: 10.2307/2446188.

Ronquist F., Teslenko M., Van Der Mark P., Ayres D.L., Darling A., Höhna S., Larget B., Liu L., Suchard M.A., Huelsenbeck J.P. (2012). MrBayes 3.2: efficient Bayesian phylogenetic inference and model choice across a large model space. Systematic Biology, 61(3). 539-542, DOI: 10.1093/sysbio/sys029.

Scotese C. (2014). Atlas of Late Cretaceous paleogeographic maps. Book Atlas of Late Cretaceous paleogeographic maps, 2, 16-22, DOI: 10.13140/2.1.4691.3284.

Scotese C.R., Gahagan L.M., and Larson R.L. (1988). Plate tectonic reconstructions of the Cretaceous and Cenozoic ocean basins. Tectonophysics, 155(1-4), 27-48, DOI: 10.1016/0040-1951(88)90259-4.

Sievers F., Wilm A., Dineen D., Gibson T.J., Karplus K., Li W., Lopez R., McWilliam H., Remmert M., Söding J. (2011). Fast, scalable generation of high-quality protein multiple sequence alignments using Clustal Omega. Molecular Systems Biology, 7(1), 1-6, DOI: 10.1038/msb.2011.75.

Stone B.C., Huynh K.-L., and Poppendieck H.-H. (1998). Pandanaceae. In: K. Kubitzki, ed., Flowering Plants. Berlin, etc.: Springer, 3, 397-404, DOI: 10.1007/978-3-662-03533-7_47.

Takhtajan A.L. (1982). Velloziaceae family (Velloziaceae). In: A.L. Takhtajan, ed., Plant Life: In Six Volumes. Moscow: Enlightenment, 6, 203-204 (in Russian).

Takhtajan A.L. (1987). Magnoliophyte system. Leningrad: Science (in Russian).

Takhtajan A.L. (2009). Flowering Plants. 2nd ed. Berlin, etc.: Springer, DOI: 10.1007/978-1-4020-9609-9.

Tamura K. (1992). Estimation of the number of nucleotide substitutions when there are strong transition-transversion and G+ C-content biases. Molecular Biology and Evolution, 9(4), 678-687, DOI: 10.1093/oxfordjournals.molbev.a040752.

Thorne R.F. (2000). The classification and geography of the flowering plants: dicotyledons of the class Angiospermae. Botanical Review. 66(4), 441-647, DOI: 10.1007/BF02869011.

Tiffney B.H. (1985). Perspectives on the origin of the floristic similarity between eastern Asia and eastern North America. Journal of the Arnold Arboretum, 66(1), 73-94, DOI: 10.5962/bhl.part.13179.

Velgorskaya T.V. (1982). Stemonaceae family (Stemonaceae). In: A.L. Takhtajan, ed., Plant Life: In Six Volumes. Moscow: Enlightenment, 6, 215-218 (in Russian).

Wen J. (2001). Evolution of Eastern Asian–Eastern North American Biogeographic Disjunctions: A Few Additional Issues. International Journal of Plant Sciences, 162(S6), S117-S122, DOI: 10.1086/322940.

Wiley E.O. and Lieberman B.S. (2011). Phylogenetics: Theory and Practice of Phylogenetic Systematics. 2nd ed. Hoboken: Wiley-Blackwell, DOI: 10.1093/sysbio/sys065

Wu Z. (1988). Hengduan mountain flora and its significance. Journal of Japanese Botany, 63, 297-311, DOI: 10.1016/j.pld.2017.09.004.

APPENDICES

Table A.1. Access codes for sequences used in present investigation in the gene bank database (GenBank).

Species	18S	atpA	matK	matR
Cyclanthaceae				
Asplundia rigida (Aubl.) Harling	KF264477.1	KF258578.1	–	KF258199.1
Carludovica palmata Ruiz & Pav.	AF293756.1	KF258586.1	AB088793.1	KF258204.1
Chorigyne cylindrica R. Erikss.	–	MT054857.1	MT046143.1	MT054502.1
Cyclanthus bipartitus Poit. ex A. Rich.	AF168837.1	KF258587.1	KT205206.1	MT054505.1
Dicranopygium atrovirens (H. Wendl.) Harling	KF264481.1	KF258588.1	–	KF258203.1
Schultesiophytum chorianthum Harling	–	MT054861.1	MT046149.1	MT054506.1
Sphaeradenia woodsonii Harling	–	MT054868.1	MT046150.1	MT054513.1
Stelestylis surinamensis Harling	–	MT054867.1	MT046151.1	MT054512.1
Dianthoveus cremnophilus Hammel & G. J. Wilder		MT054864.1	MT046144.1	MT054509.1
Ludovia lancifolia Brongn.	KF264482.1	KF258589.1	MT046146.1	KF258202.1
Thoracocarpus bissectus (Vell.) Harling	–	MT054865.1	MT046152.1	MT054510.1
Pandanaceae				
Benstonea copelandii (Merr.) Callm. & Buerki	–	MT054880.1	–	MT054525.1
Freycinetia philippinensis Hemsl.	KF298381.1	KF298288.1	–	KF298294.1
Freycinetia cumingiana Gaudich.	KF298366.1	KF298287.1	–	KF298293.1
Martellidendron hornei (Balf. f.) Callm. & Chassot	–	MT054878.1	MT046147.1	MT054523.1
Pandanus furcatus Roxb.	KF298358.1	KF298307.1	KR531333.1	KF298321.1
Pandanus baptistii Misonne	KF298360.1	KF298305.1		KF298319.1
Pandanus stenophyllus Kurz ex Miq.	KF298353.1	KF298313.1	–	KF298327.1
Sararanga sinuosa Hemsl.	–	MT054881.1	KT204605.1	MT054526.1
Triuridaceae				
Kihansia sp. Sainge 1620	KF197095.1	KF197072.1	–	KF197113.1
Kupea martinetugei Cheek & S. A. Williams	KF197093.1	KF298372.1	–	KF197110.1
Triuris hexophthalma Maas	KF264487.1	KF258585.1	–	KF258197.1
Triuris hyalina Miers	KF264488.1	KF258581.1	–	
Sciaphila picta Miers	KF197084.1	–	–	KF197106.1
Sciaphila tenella Blume	KF264484.1	–	–	KF258194.1
Seychellaria africana Vollesen	KF264485.1	KF258584.1	–	KF258195.1
Seychellaria madagascariensis C. H. Wright	KF264486.1	–	–	KF258196.1
Lacandonia schismatica E. Martínez & Ramos	–	AY299794.1	–	–
Stemonaceae				
Croomia japonica Miq.	AF309408.1	MT054875.1	KT204663.1	MT054520.1
Croomia pauciflora (Nutt.) Torr.	AF168835.1	AF197708.1	KP083061.1	AF197735.1
Pentastemona sumatrana Steenis	KF264490.1	MT054873.1	KT205057.1	MT054518.1
Stemona tuberosa Lour.	AB429262.1	MT054874.1	KT204764.1	MT054519.1

Stichoneuron caudatum Ridl.	AF168875.1	KT204947.1	KT205006.1	MT054521.1
Velloziaceae				
Talbotia elegans Balf.	KF197080.1	KF197075.1	MT046154.1	MT054515.1
Barbacenia involucrata L. B. Sm.	–	MT054869.1	MT046141.1	MT054514.1
Xerophyta retinervis Baker	–	MT054871.1	KT204806.1	MT054516.1
Barbaceniopsis castillonii (Hauman) Ibisch	–	MT054872.1	MT046142.1	MT054517.1
Dioscoreaceae (outgroup)				
Dioscorea membranacea Pierre ex Prain & Burkill	–	MT054854.1	AY957598.1	MT054499.1
Dioscorea rockii Prain & Burkill	DQ786090.1	EU421029.1	AY972488.1	KF264495.1
Dioscorea elephantipes (L'Hér.) Engl.	FJ215767.1	FJ215777.1	KR086958.1	KY554897.1
Dioscorea tokoro Makino ex Miyabe	DQ786088.1	FJ215776.1	HQ637586.1	KY554895.1
Dioscorea sylvatica Eckl.	FJ215768.1	FJ215778.1	KR086976.1	KY554898.1
Dioscorea communis (L.) Caddick & Wilkin	EU186223.1	AY277804.1	HM850486.1	KF298370.1

Table A.2. Access codes for sequences used in present investigation in the gene bank database (GenBank)

Species	5.8s rib. RNA	AtpB	tRNA-Leu (trnL)
Talbotia elegans Balf.	JN016957.1	JN017009.1	JN016905.1
Vellozia glauca Pohl	JN016972.1	JN017024.1	JN016920.1
Barbacenia markgrafii Schulze-Menz	JN016942.1	JN016994.1	JN016890.1
Xerophyta equisetoides Baker	JN016986.1	JN017038.1	JN016934.1
Barbaceniopsis castillonii (Hauman) Ibisch	JN016945.1	JN016997.1	JN016893.1
Acanthochlamys bracteata P. C. Kao	JN016937.1	JN016989.1	JN016885.1
Pleurostima longiscapa (Goethart & Henrard) N. L. Menezes	JN016953.1	JN017005.1	JN016901.1
Nanuza plicata (Mart.) L. B. Sm. & Ayensu	JN016951.1	JN017003.1	JN016899.1
Burlemarxia pungens N. L. Menezes & Semir	JN016947.1	JN016999.1	JN016895.1
Stemona tuberosa Lour.	KF298348.1	JQ733661.1	JQ733892.1

RESEARCH PAPER

GROUNDWATER QUALITY AND QUANTITY ANALYSIS FOR IRRIGATION PURPOSES IN OKARA, SAHIWAL AND KHANEWAL DISTRICTS OF PUNJAB, PAKISTAN

Usfa Asif[1], Aqsa Munir Ahmad[1], Muhammad Asif Javed[1], Muhammad Nasar-u-Minallah[2]*, Sajid Rashid Ahmad[1], Nusrat Parveen[3]

[1]College of Earth and Environmental Sciences, University of the Punjab, Lahore, 54000, Pakistan.

[2]Institute of Geography, University of the Punjab, Lahore, 54000, Pakistan.

[3]Department of Geography, GC University, Faisalabad, 38000, Pakistan

***Corresponding author:** Nasarbhalli@gmail.com

Received: May 21st, 2023 / Accepted: November 14th, 2023 / Published: December 31st, 2023

https://DOI-10.24057/2071-9388-2023-2901

ABSTRACT. Irrigated agriculture is the major determinant of economic growth potential as it accounts for 20% of the Gross Domestic Product (GDP) of the country. The current study focuses on the qualitative and quantitative assessment of groundwater in three districts i.e., Okara, Sahiwal and Khanewal of the Punjab province of Pakistan, which are considered highly fertile for agriculture production. The data were acquired from the Punjab Irrigation Department (PID) for 10 years (2010-2020) to assess the spatio-temporal patterns. The spatiotemporal mapping and variability of depth to the water table, electrical conductivity (EC), sodium absorption ratio (SAR), and residual sodium carbonate (RSC) were done as per the standards of the World Health Organization (WHO) and Punjab Irrigation Department using inverse distance weighting (IDW) statistical approach of GIS Techniques. The finding of the study revealed that overall water quality in the study area was reported as "fit" by following the WHO standards, whereas as per Punjab Irrigation Department standards, it was observed, as "Moderately fit". Moreover, in Sahiwal, Okara, and Khanewal districts, the average depth of the water table declined from 2010 to 2015 by 0.619, 1.286, and 0.164 metres and then increased from 2016 to 2020 by 1.698, 1.421 and 0.830 metres, respectively. Although currently the quality and quantity of groundwater were not in critical condition, with continued carelessness and the release of additional water from aquifers, these conditions could deteriorate in the near future. So, developing a suitable mechanism for supplying surface water to farmers, and adapting environmentally acceptable methods of recharging aquifers is much needed.

KEYWORDS: Groundwater, quality and quantity, Irrigation, Geospatial techniques, Pakistan

CITATION: Asif U., Ahmad A. M., Javed M. A., Nasar-u-Minallah M., Ahmad S. R., Parveen N. (2023). Groundwater Quality and Quantity Analysis for Irrigation Purposes in Okara, Sahiwal and Khanewal Districts of Punjab, Pakistan. Geography, Environment, Sustainability, 4(16), 105-119

https://DOI-10.24057/2071-9388-2023-2901

ACKNOWLEDGEMENTS: We would like to express our sincerest gratitude to the Punjab Irrigation Department for their invaluable support and assistance during the research work.

Conflict of interests: The authors reported no potential conflict of interest.

INTRODUCTION

Water quality and quantity are both crucial for crop development, agricultural land productivity, and human utilization (Farooq et al. 2019; Butt et al. 2020; Leng et al. 2021). After a crisis arises of surface water resources over time (Shahzad et al. 2020) in Pakistan, approximately 73% of water is supplied to irrigated areas through groundwater (Qureshi 2020). Groundwater is regarded as the most trustworthy alternative source for irrigation, domestic consumption, and industrial uses, particularly in dry and semi-arid countries (Awais et al. 2017). Groundwater was once thought to be safe for use in agriculture, but at that time, both its quality and quantity were vulnerable to being depleted, especially in Pakistan. But occasionally, even after rain and natural disasters like floods, the amount of water grew, but the quality of the water continued to deteriorate and be disrupted (Basharat et al. 2015). Due to population development, industrialization, and inadequate drainage systems, unrestricted and irregular groundwater consumption is depleting the aquifers, which has significant implications for the water table and saltwater intrusion (Ruzikulova et al. 2021; Riaz et al. 2016).

Studies from the past have revealed the ongoing depletion of groundwater in several areas of the Indus Basin, as well as the imbalances between abstraction and recharge (Usman et al. 2015). In Pakistan, excessive groundwater use affects agricultural production and the secondary salinization of deep groundwater (Usman et al. 2012). The physiochemical characteristics of soil and crop productivity are impacted by groundwater quality (Simsek and Gunduz 2007; Kareem et al. 2016). Both natural and artificial activities affect the quality of the water, and the discharge of wastewater into fields has become a significant issue. Poor-quality water can damage the soil's structure and reduce its ability to hold both air and water by displacing calcium and magnesium ions from the soil. As a result, crops suffered from improper growth and damage. The type of water and level of soluble salts decide whether it is suitable for irrigation. For a better knowledge of groundwater quality, scientists have used a variety of chemical indices, such as the Electric Conductivity, Sodium Absorption Ratio, and Residual Sodium Carbonate (Ramesh and Elango 2012; Zara et al. 2015).

Multiple factors are responsible for the degradation of water quality and quantity in the Okara, Sahiwal, and Khanewal districts such as agricultural pollution in which excessive application of fertilizers and pesticides, has resulted in water pollution as these chemicals are carried by runoff into rivers and streams, thereby contaminating water sources. Industries present in these districts also release untreated wastewater into water bodies. Furthermore, the process of rapid urbanization has strained the water supply due to heightened water demand, resulting in overexploitation of groundwater and subsequent aquifer depletion. The influence of climate change is significant as well, with shifting weather patterns causing irregular rainfall and negatively impacting water availability (Basharat and Ata-ur-Rehman 2013). If the annual domestic water demand of a person is taken as 33.5 m^3 then according to the population of Okara, Sahiwal, and Khanewal in the year 2015 that was 2,915,324, 2,414,994, and 730,928, respectively, the corresponding domestic water demand in 2015 for Okara, Sahiwal, and Khanewal was found to be 101.51 MCM, 80.6 MCM, and 24.45 MCM (Khanam et al., 2023). If the population growth rate is considered as 2.03% per year the water demand is increased from 101.507 MCM in 2015 to 167.9 MCM in 2040, 80.66 MCM in 2015 to 133.418 in 2040, and 25.449 MCM to 54.808 in 2015 to 89.810 in 2040 in Okara, Sahiwal, and Khanewal districts (Khanam et al., 2023).

Water demand for agriculture in Okara, Sahiwal, and Khanewal according to the agricultural land cover area was 530.3362, 1713 MCM and 445.308 MCM respectively in 2015 (Shahid et al. 2023). The assessment of water quality, and quantity and its appropriateness for irrigation purposes is a vital aspect of water management. For this purpose, GIS is a suitable technology. Its inverse distance weighted (IDW) interpolation, ordinary kriging, overlay analysis, and Geostatistical (Awais 2017) techniques are widely used for detecting the suitability of groundwater for irrigation purposes. Since mapping based on IDW is a recent breakthrough for verifying water quality and quantity for irrigation, economic growth must understand trends in water level and quality, as well as the accompanying patterns of change across time and geography. To assess the spatiotemporal fluctuations of groundwater level, mineralization, and soil salinity in irrigated areas of Uzbekistan's Syrdarya Province, maps were made using IDW techniques in GIS (Kulmatov et al. 2022). To understand the spatiotemporal distribution of fluctuations in groundwater quality and level, many studies have used Geostatistical and IDW approaches.

For irrigation reasons, it is currently necessary to offer a visual depiction of groundwater quality and quantity that can assess the scope of the issue and help us conserve water for the future (Elci and Polat 2011). There isn't much information available or published in Pakistan that focuses on the quantity and quality of groundwater for irrigation. In the districts of Okara, Sahiwal, and Khanewal, there has not been any research on the spatiotemporal fluctuations of groundwater using IDW and geo statistics. The main objectives of this study are 1. Mapping of individual groundwater irrigation parameters to assess the spatial distribution across the study region. 2. Quantification and spatial distribution of Groundwater quantity using geospatial techniques 3. Assessment of spatio-temporal variability of groundwater quantity and quality over '6-10 years' time span.

MATERIALS AND METHOD

Study Area

Khanewal, Sahiwal, and Okara districts were selected as study areas for this research (Figure 1). These districts are located in the southeast of Punjab, Pakistan. The Sahiwal, Khanewal, and Okara districts, with corresponding latitudinal extents of 30°.66'82"N, 30°.28'64"N, and 30°.81'38"N, and longitudinal extents of 73°.11'14" E, 71°.93'20"E, and 73°.45'34"E, covering 3224.2 sq. km, 4367.5 sq. km, and 4413.0 sq. km of area, respectively. Most of the Okara, Sahiwal and Khanewal districts fall in the command areas of the Lower Bari Doab Canal (LBDC) irrigation system which is the second-largest irrigation system in Punjab. The climate in these areas is semiarid. The coldest months are December through February when temperature usually drops to 2°C. Whereas, the hottest months are May, June and July, when temperature often reaches up to 50°C. The average rainfall in this region is about 2000 mm importantly, the 2010 mighty flood in the study area led to an increase in groundwater levels in aquifers.

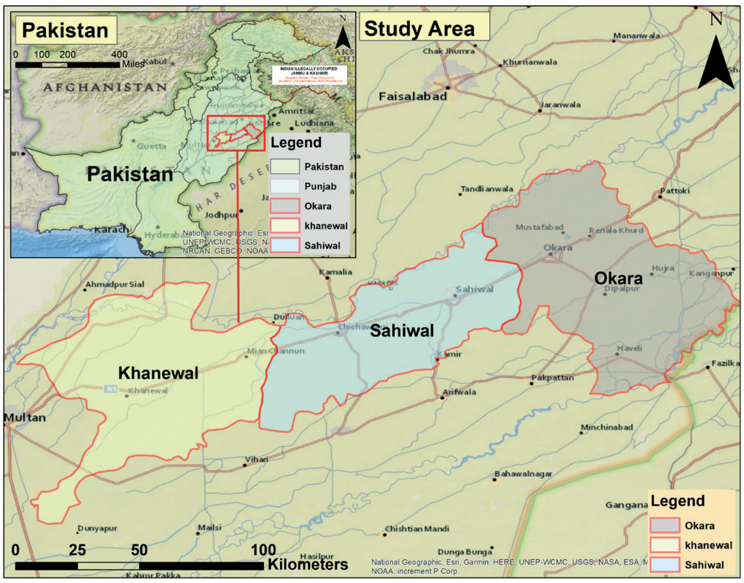

Fig. 1. Location of the study area (Okara, Sahiwal and Khanewal districts)

Data and its Sources

Three quality measures, including EC, SAR, and RSC, (Figure 2) are typically used to represent the water quality of groundwater for irrigation purposes in this study (Arshad and Shakoor 2017). Water quality of groundwater data for the years 2015 and 2020 and water quantity of groundwater data for the years 2010, 2015, 2016, and 2020 were collected from the Punjab Irrigation Department (PID). Water quality and water quantity data of groundwater were further classified as per WHO and Pakistan Council of Research in Water Resources (PCRWR) standards.

Data Processing

Geospatial and geostatistical techniques were used for spatial analysis (Nasar-u-Minallah et al. 2023) and mapping of water quality and quantity of groundwater for selected districts of Punjab Pakistan. The groundwater data was initially processed and refined to rectify the existing errors (Kareem et al. 2016; Farooq et al. 2019). A geostatistical analysis using IDW (Fatima et al., 2023) was performed which is shown in Figure 3. The spatial water quality mapping for EC, SAR, and RSC was prepared and classified into three categories as presented in the results sections. To employ discrete raster maps with a single integer value for overlay analysis, the categorized maps were reclassified (Sahar et al. 2013) using the raster overlay approach. The highest value was assigned to the class that was least favourable or unsuitable, and the lowest value was assigned to the class that was most favourable for irrigation purposes. Similarly, reclassification was carried out for water quantification. To compute the area, beneath each class, raster surfaces were created using "Raster to Polygon" (Nasar-u-Minallah et al. 2021).

Data Analysis

Toxicity, alkalinity, salinity, and sodicity are the four major problems associated with poor groundwater quality. The water quality parameters used herein are EC, SAR, and RSC, and the water quality standards of the World Health Organization and Punjab Irrigation Department are adopted to classify the irrigation water quality. The spatial and temporal changes in the groundwater levels are intended for the sustainable development of water resources (Butt et al. 2020). Geospatial techniques have been an important approach for groundwater management studies in recent years. Spatial analysis tools in the geographical information system (GIS) were used to study the spatiotemporal variation of groundwater over 10 years for water quantity, whereas changes in water quality were assessed from 2014 to 2020.

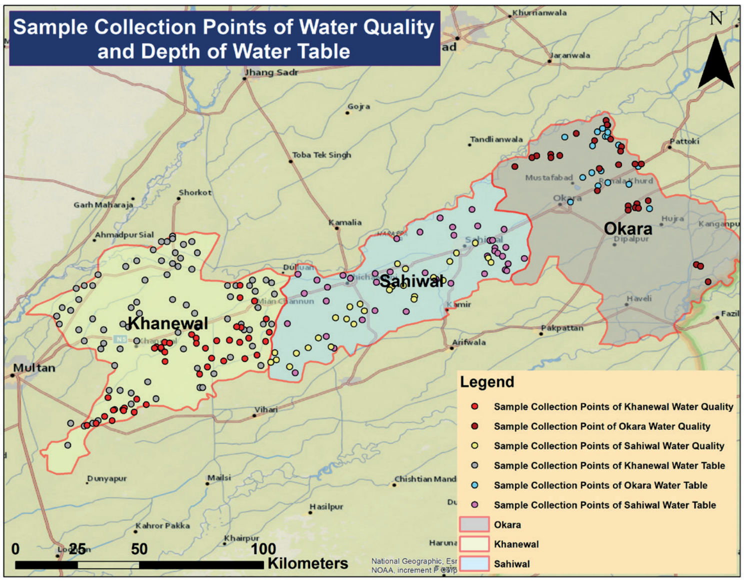

Fig. 2. Locations of the sample collection points of selected districts

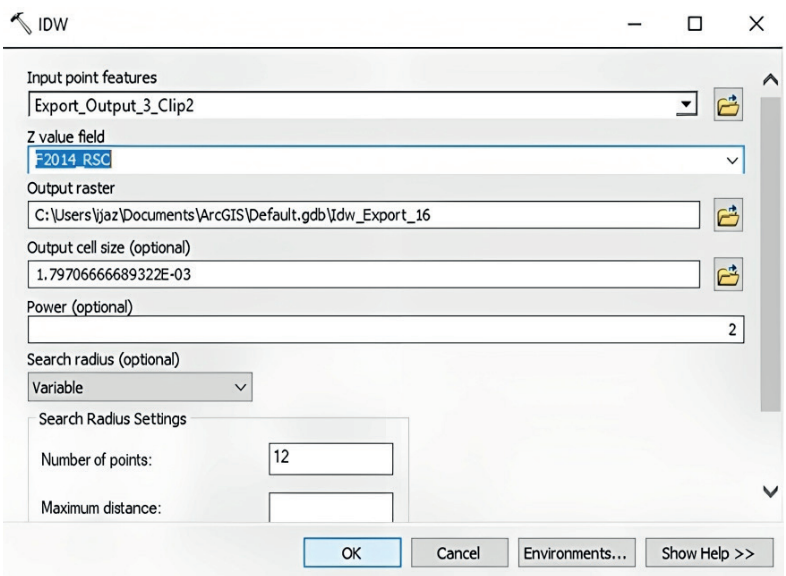

Fig. 3. "IDW" tool for interpolation of the points

With the help of the inverse distance weighted approach, the data were spatially interpolated (Fatima et al. 2023). The inverse distance weighted interpolation technique was used because the collected data was limited to a larger extent and this method is recommended and suggested for such types of data sets and studies (Kumar et al. 2018). Among all interpolation methods, including kriging, natural neighbour, spline, and trend, inverse distance weighted is the most straightforward as it has the advantage of being relatively simple to define and, hence, simple to grasp the outcomes. Figure 4 illustrates the whole methodology of performed research comprehensively.

Accuracy Assessment

Out of the total field samples for water quality and water quantity data of groundwater, 20% of samples were considered for validation and not incorporated in the analysis. These validation points were overplayed with the water quality and water quantity maps for accuracy assessment.

RESULTS AND DISCUSSION

Spatial Distribution of Groundwater Quality Parameters

The WHO groundwater quality standards for EC and SAR parameters demonstrate that the water quality in Khanewal is suitable for irrigation because the majority of the region falls under the low category and just a tiny section of the territory falls under the moderate category. In the Khanewal district, the RSC criteria for water quality exceed the severe (unfit) level, rendering the water unfit for agriculture. All three parameters (RSC, EC, and SAR) are within a tolerable range, indicating satisfactory water quality in Sahiwal. Sahiwal district relies heavily on irrigation. The Okara district's water quality falls into the low category for SAR, EC, and RSC parameters, meaning it is also suitable for growing crops and poses no risks to irrigated land. The results of different indicators are detailed below.

Electrical Conductivity (EC): Electrical conductivity is an incredibly significant parameter for determining the quality of groundwater. The evaluation or quantification of groundwater's EC content is crucial. According to WHO standards, a level of EC (dc/m) less than 1.5 is recommended for irrigation purposes. If the EC level is between 1.5 and 3, some crops can tolerate it, but not others. More than 3 is considered a severe level of EC, making it inappropriate for any type of agricultural or irrigation use. The EC concentration according to the WHO standards in Sahiwal district has not undergone any appreciable alteration throughout time. The overall area at low elevation is the same for both 2014 and 2020 i.e. 2834 sq. km, while the overall area at moderate elevation is also the same for both years i.e. 391 sq. km (Figure 5a, b). In Okara district, the area classified in the low class has decreased from 4384 sq. km to 4376 sq. km over a period i.e. 2014-2020 and the area classified as an intermediate class increased from 29 37 sq. km in this period. Okara's spatial distribution mapping reveals that the majority of the region contains high-quality water that is appropriate for agriculture (Figure 5c, d), whereas, In Khanewal, the region with suitable water quality expanded from 4034 sq. km to 4048 sq. km from 2014-2020 as a result of the water's EC level being maintained and improving over time, while the moderate zone shrank from 334 sq. km in 2014 to 319 sq. km in 2020 (Figure 5e, f).

Sodium Absorption Ratio (SAR): The sodium adsorption ratio illustrates the risk of sodium. The SAR estimation is used to determine whether water is acceptable for an irrigation system as this parameter measures how much sodium is taken up by the soil. SAR results are graded as suitable (10), moderately suitable (10–18), and not suitable (>18) by WHO standards. According to the WHO standards, the low-level zone in Sahiwal increased from 3210 sq. km of the area in 2014 to 3221 sq. km of the area in 2020. The moderate quality zone in Sahiwal was reduced from 14 sq. km of the area in 2014 to 4 sq. km of the area in 2020 (Figure 6a, b). SAR is stable in groundwater for irrigation purposes in the district of Okara (Figure 6c, d). The moderate quality zone in Khanewal increased from 1 sq. km of area in 2014 to 8 sq. km of area in 2020. The area under the low category of Khanewal is the same in the years 2014 and 2020. There is no change to be detected between 2014 and 2020 (Figure 6e, f).

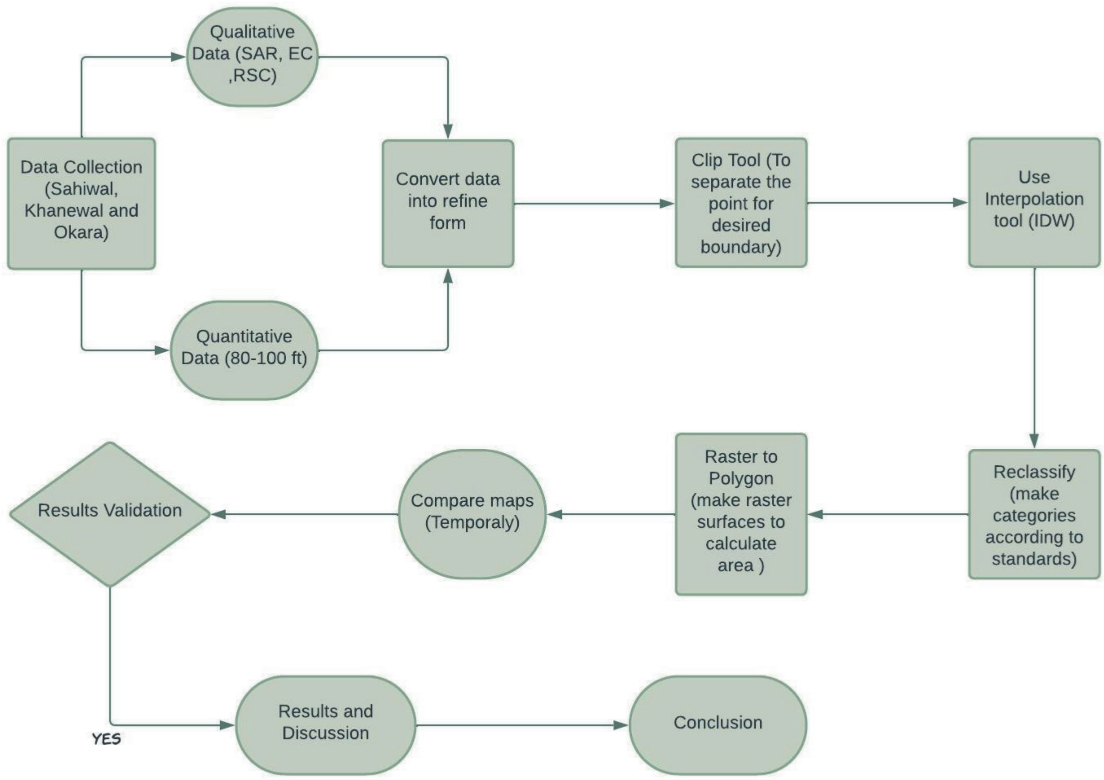

Fig. 4. The flowchart of the Research Methodology

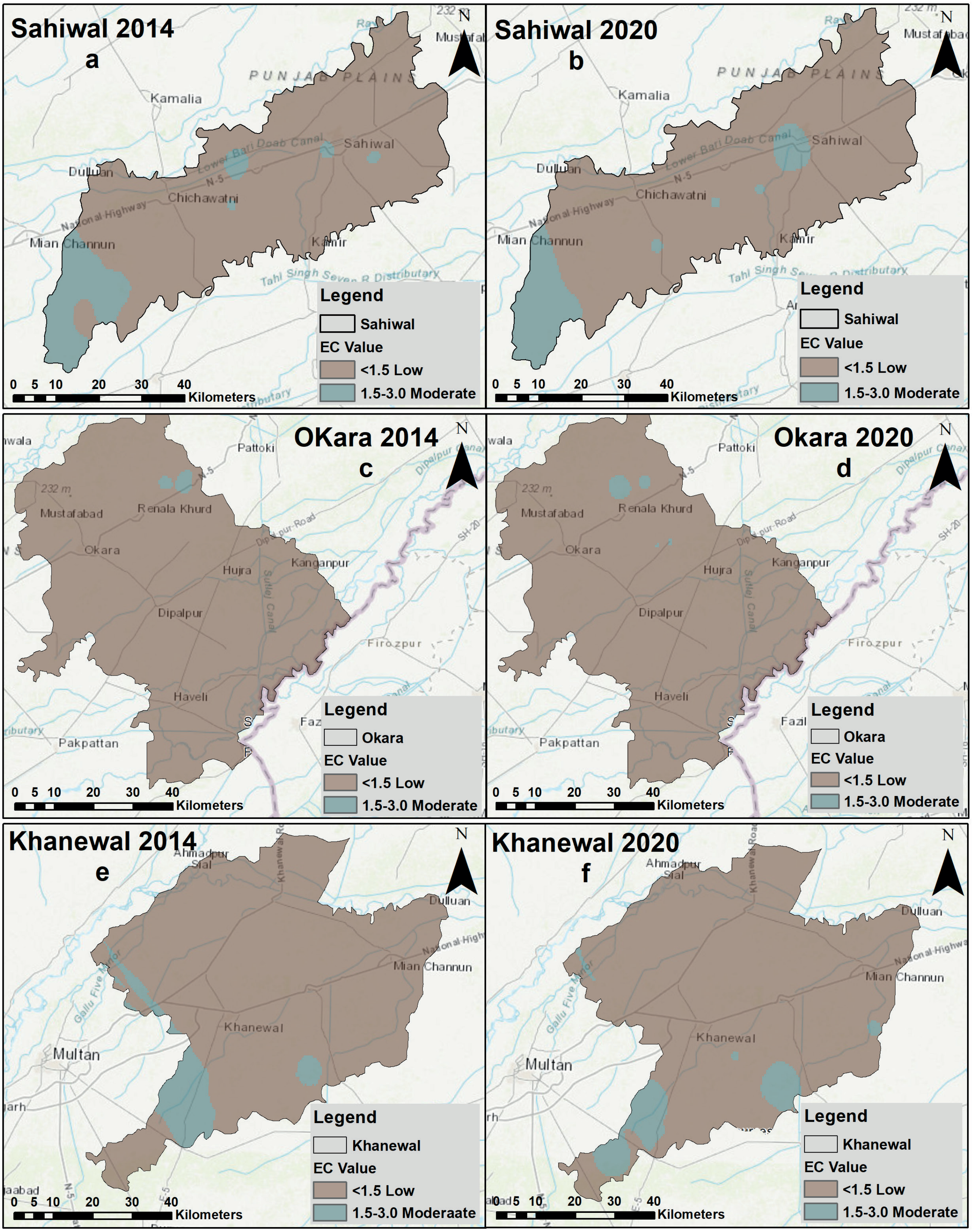

Fig. 5. The Concentration of EC (WHO Standards) in Groundwater of Sahiwal (a, b), Okara (c, d), and Khanewal (e, f) districts.

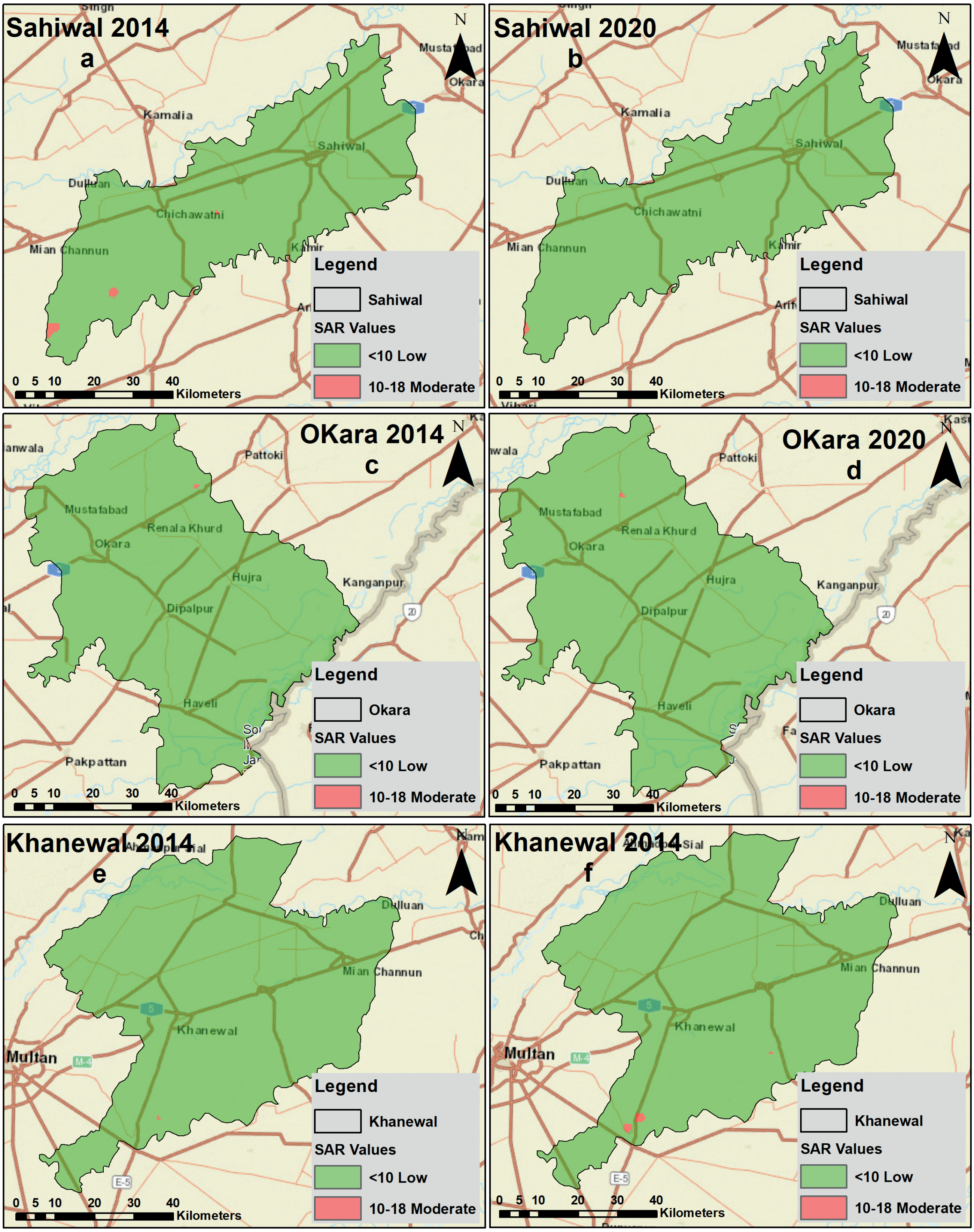

Fig. 6. The Concentration of SAR (WHO standard) in Groundwater of Sahiwal (a, b), Okara (c, d), and Khanewal (e, f) districts

AS per PID, classification is as follows; good (0–6), moderate (6–8), or poor (>10) for irrigation purposes. According to the PID standards, the spatio-temporal distribution of the SAR describes that good water quality area with no hazard to irrigation declined in Sahiwal, Khanewal, and Okara from 977 sq. km, 2996 sq. km, 4140 Sq. Km in 2014 to 424 sq. km, 1464 sq. km, and 1344 sq. km in 2020, respectively. While the moderate water quality area increased from 2233, 1371, and 272 Sq. Km on 2014 to 2797, 2895, 3068 Sq. Km in 2020 (Figure 7). The unsuitable water quality area under the severe category also moved toward declination from 14 sq. km in 2014 to 4 sq. km in 2020 in Sahiwal, which shows the level of SAR (mg/L) has been improved within the study period (Figure 7a, b). The area under the severe category has been the same for district Okara between 2014 and 2020 (Figure 7c, d). In the Khanewal district, the unsuitable water quality area under study has been increased from 1 sq. km in 2014 to 8 sq. km in 2020. This variation shows water quality moving toward an unsuitable level over time (Figure 7e, f).

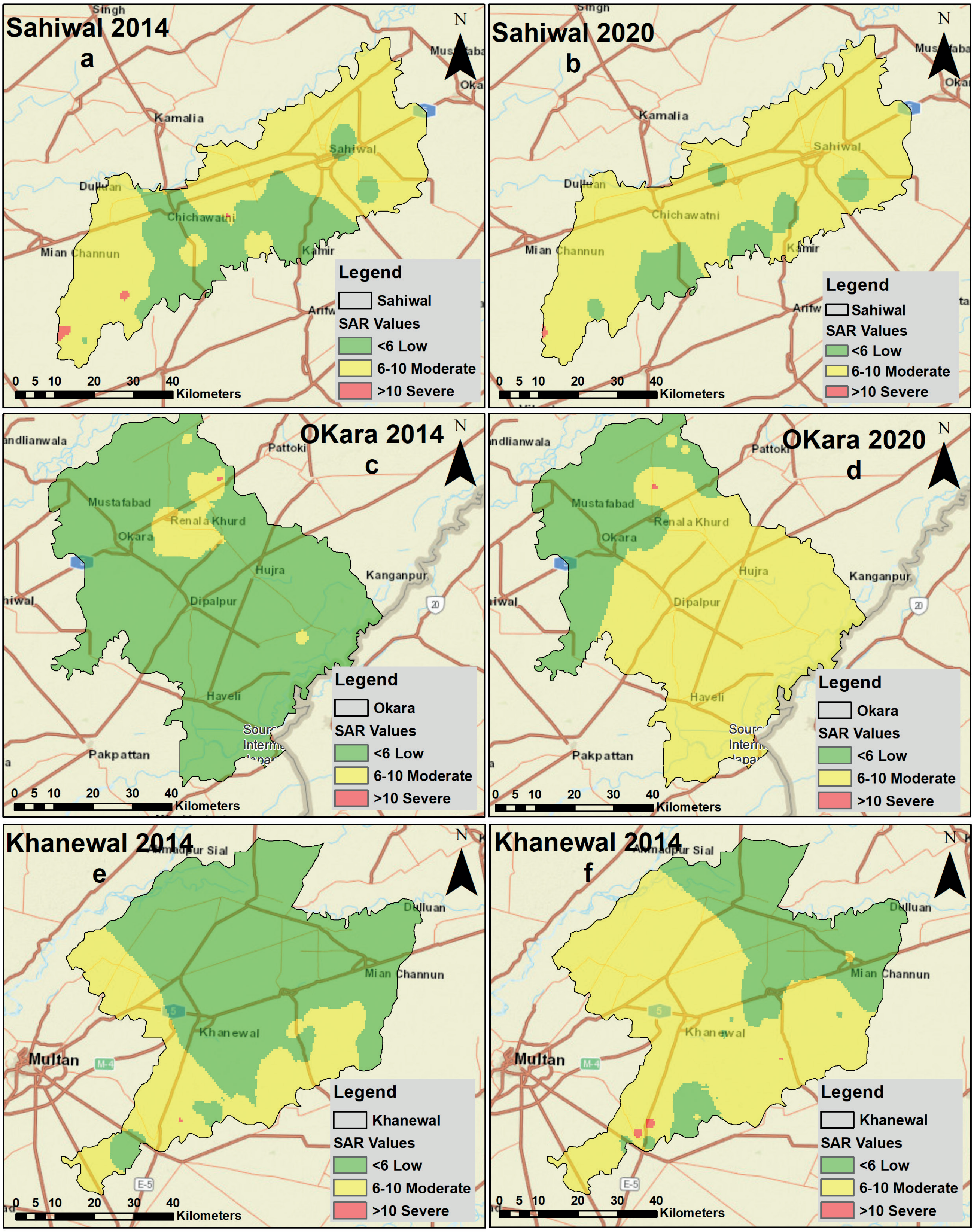

Fig. 7. The Concentration of SAR (PID Standard) in Groundwater of Sahiwal (a, b), Okara (c, d), and Khanewal (e, f) districts

Residual Sodium Carbonate (RSC): RSC variable is used to measure the water's bicarbonate content. The natural material degrades when the pH of the water is raised due to a high bicarbonate concentration. Calcium and magnesium are prone to falling into the water with high RSC estimates, which can raise the sodium content of debris. As per WHO, RSC is classified as; good (2.5), marginal (2.5–5.0), and not good (>5.0). In Sahiwal, the area under the low category increased from 3085 sq. km in 2014 to 3176 sq. km in 2020, and under the moderate category, reduced from 140 sq. km in 2014 to 48 sq. km in 2020 (Figure 8a, b). In 2020, some parts of Khanewal (4 sq. km) fall under the severe category, while the lower category has an extent of 3934 sq. km, as compared to 2014, which has an extent of 3654 sq. km. So the area under moderate level is reduced from 713 sq. km to 430 sq. km (Figure 8e, f).

According to Punjab Irrigation Department (PID) standards RSC (meq/L) is categorized as; good (0–1.25), moderate (1.25-2.5), and poor (>2.5). The visual representation shows that water quality improves within the study period. A remarkable change can be detected in Sahiwal district, which had a moderate zone of 1132 sq.

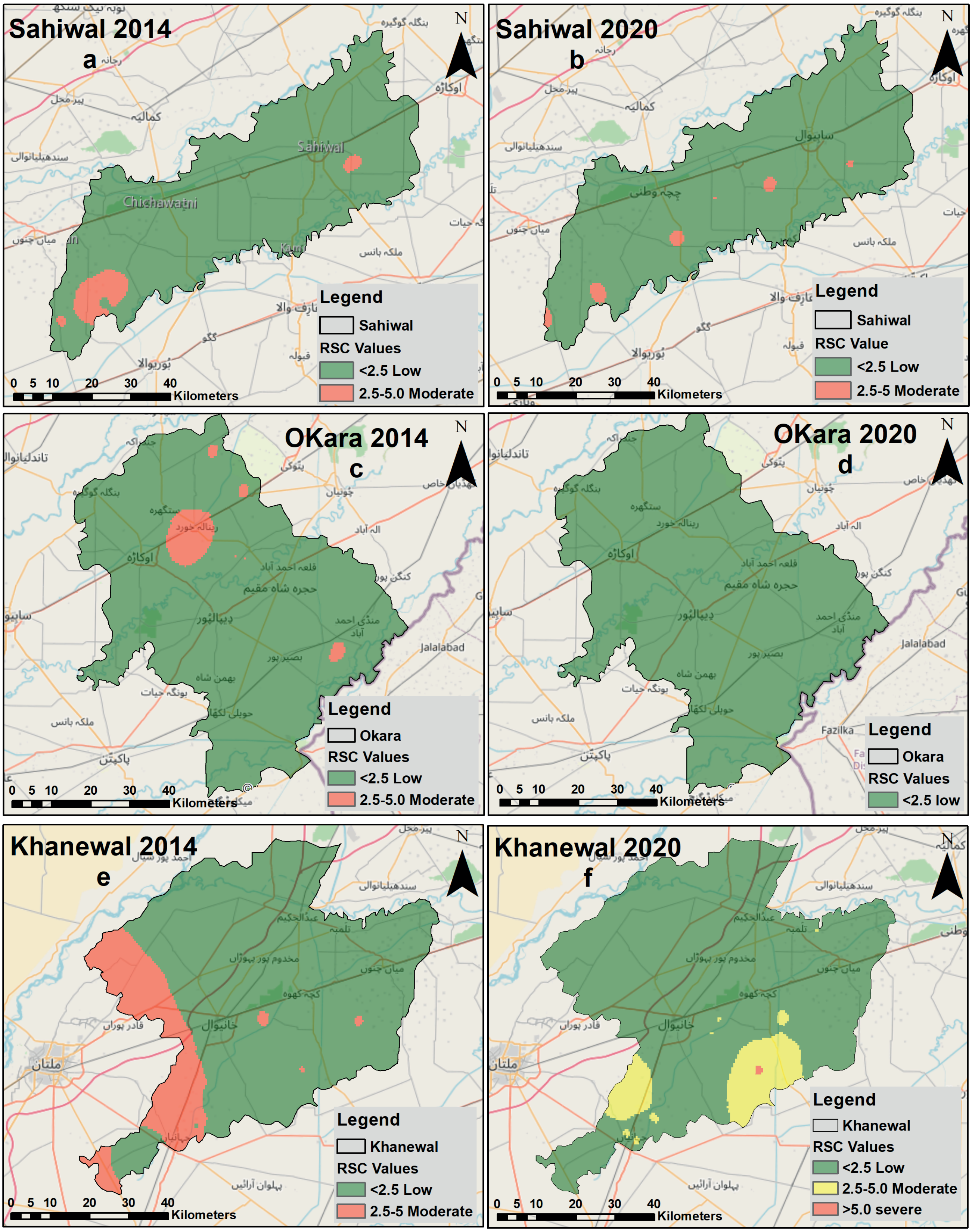

Fig. 8. The Concentration of RSC (WHO standard) in Groundwater of Sahiwal (a, b), Okara (c, d), and Khanewal (e, f) districts

km area in 2014 to 2353 sq. km area in 2020, while a severe zone decreased over time from 140 sq. km in 2014 to 40 sq. km in 2020. The low-quality zone area changed from 1953 sq. km in 2014 to 823 sq. km in 2020 (Figure 9a, b). According to the district Okara map (Figure 9c, d), water quality with the RSC parameter also improved over time. In 2014, 4247 sq. km of the area was under the low category and 166 sq. km area under the moderate level but in 2020 all areas the low category. The variation of SAR over Okara district (Figure 9c, d) elaborates that the best water quality zone for irrigation purposes falls (646 to 292 sq. km) and the moderate zone rises (3,605 to 4121 sq. km). The visual representation of Sodium Residual Carbonate in Khanewal revealed that the best water quality zone increased from 978 sq. km in 2014 to 1934 sq. km in 2020, the moderate water quality zone was reduced from 2676 sq. km to 2142 sq. km, and the highly vulnerable water quality zone dropped from 713 sq. km in 2014 to 291 sq. km in 2020 (Figure 9e, f).

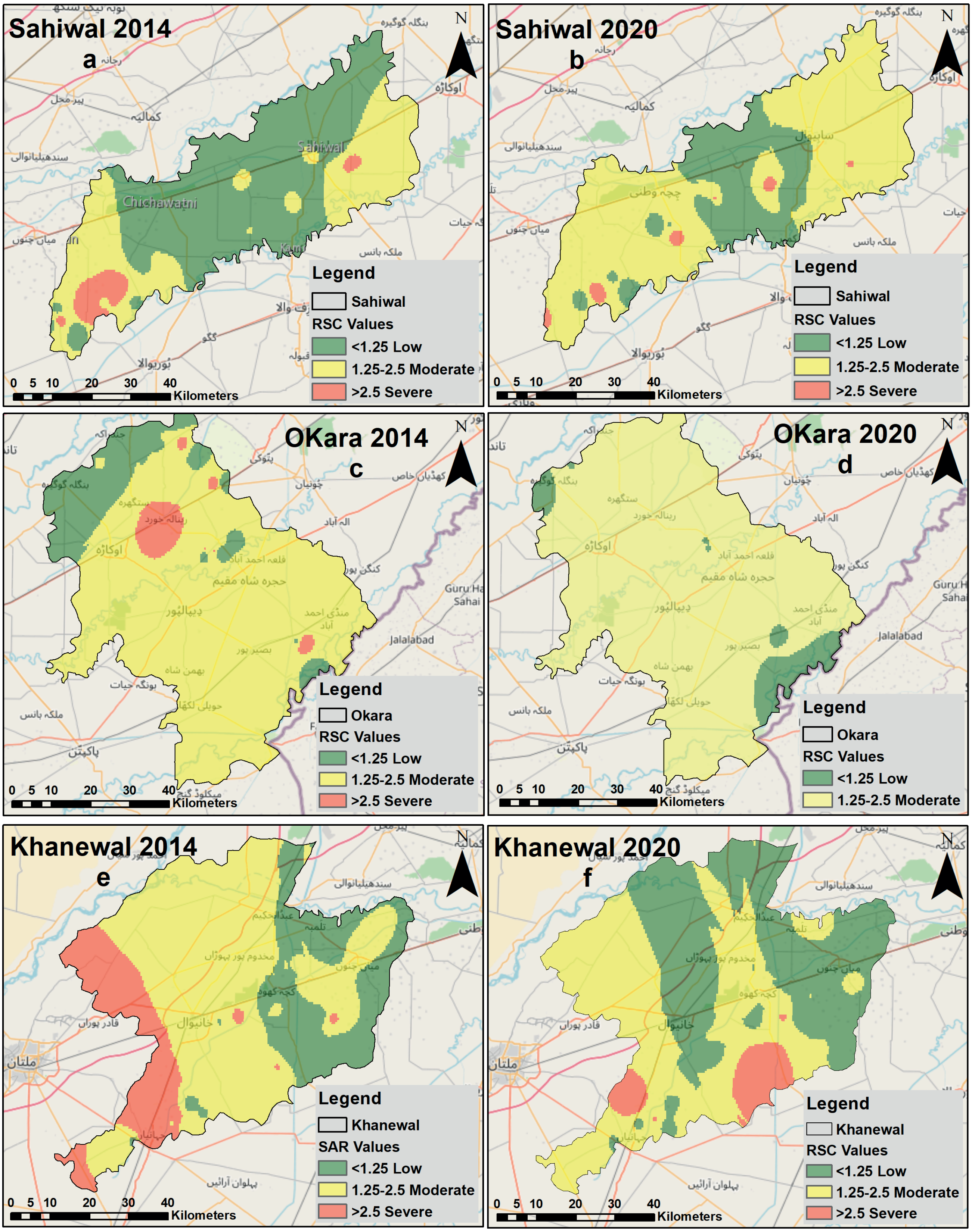

Fig. 9. The Concentration of RSC (PID standard) in groundwater of Sahiwal (a, b), Okara (c, d), and Khanewal (e, f) districts

Monitoring of Water Quantity

District Okara: Water table mapping illustrates how the water table has declined from 2010 to 2020 (Figure 10) in the Okara district. The southeast region of the study area has witnessed a significant decline in the water table as a larger portion has shifted to 6.1-7.6 meters (20-25 feet) class in 2020 where water was available below 6.1 meters (20 feet) in 2010. Similarly Northeast region has also experienced a declining trend as the water table drops up to 9.1 meters (30 feet) in the year 2020. There are four classes for a better understanding of the water table. In Okara, the area covered in the 1st, 2nd, 3rd, and 4th classes of 2010 was 1384 sq. km, 2030 sq. km, 815 sq. km, and 184 sq. km. In 2015, the area was 3099 sq. km, 611 sq. km, 639 sq. km, and 63 sq. km, while in 2016, the area was 1416 sq. km, 1384 sq. km, 1610 sq. km, and 3 sq. km, which changed to 457 sq. km, 2290 sq. km, and 1720 sq. km in 2020 (Figure 10).

District Sahiwal: Sahiwal district experienced a mixed trend in terms of the water table in 2015, some regions' water depth improved, but in 2020 a significant decline

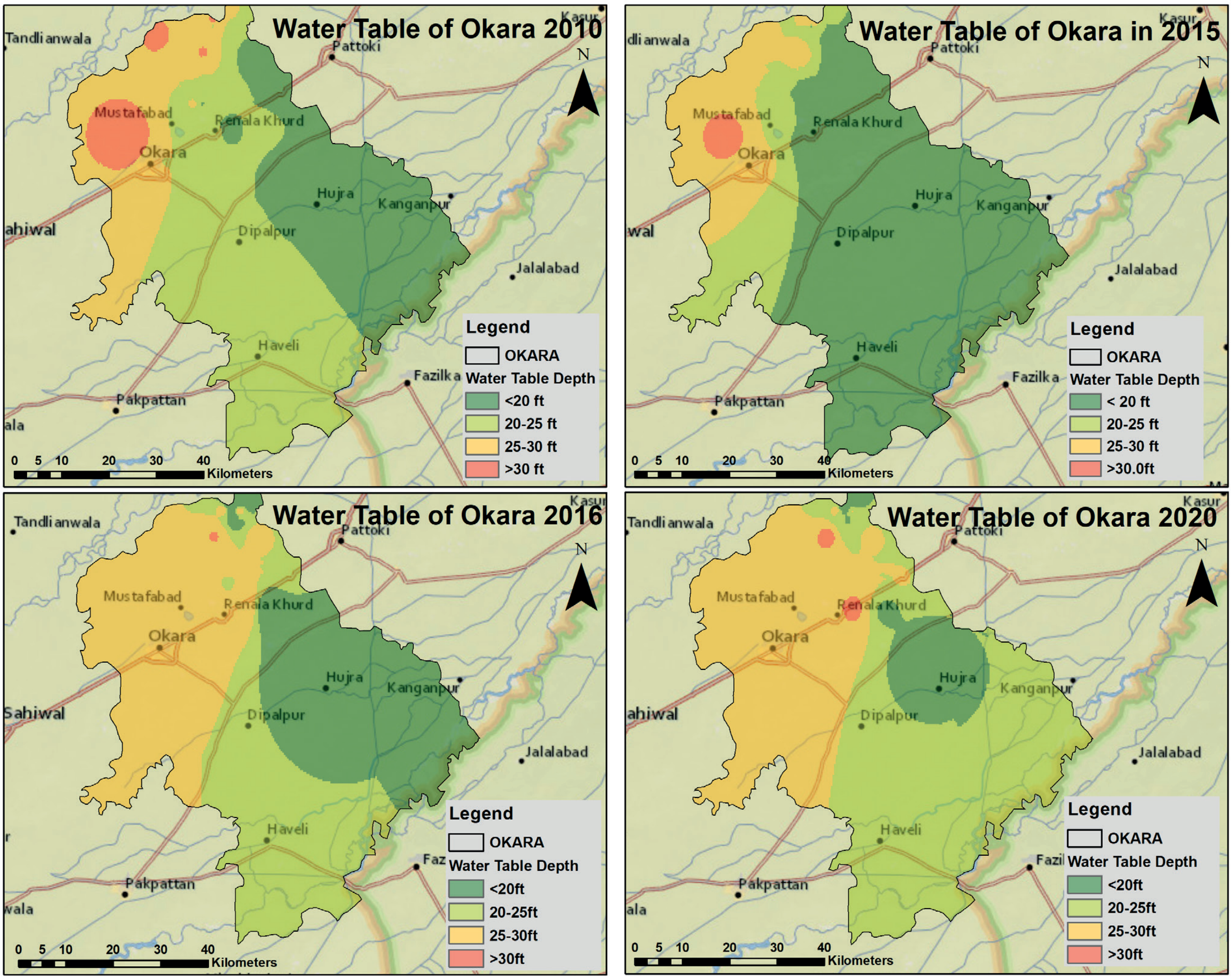

Fig. 10. Water Table Depth of Okara district from 2010-2015 & 2016-2020

in the water table was observed specifically in the north-west and south-west of the district (Figure 11). According to the classification of Sahiwal (Figure 11) and the area covered under it, in the first category, 122 sq. km of the area was covered in 2010, 181 sq. km in 2015, 709 sq. km in 2016, and 175 sq. km in 2020. 1441 sq. km of the area were covered in 2010, 1629 sq. km in 2015, 1401 sq. km in 2016, and 756 sq. km in 2020 under the second category. In the third category, 1189 sq. km of the area was covered in 2010, which was reduced to 639 sq. km in 2015, then increased to 951 sq. km in 2016 and 1679 sq. km in 2020. The fourth category shows that 473 sq. km of the area was covered in 2010, which was reduced to 144 sq. km in 2015, and 163 sq. km of area in 2010, which suddenly increased to 614 sq. km in 2020. This variation shows that the water table declined from 2016 to 2020 during drought conditions.

District Khanewal: Almost the same pattern has been observed for Khanewal district, where south-east and south-west regions undergone in decline from 2010 to 2020 (Figure 12). Five classes of different depths covering different areas are shown on the map of Khanewal (Figure 12). In the first class, 381 sq. km of the area was covered in 2010, which increased to 451 sq. km in 2015. 217 sq. km of the area was covered in 2016, which declined to 144 sq. km in 2020. In the second class, 560 sq. km of the area was covered in 2010, compared to 633 sq. km in 2015. 887 sq. km of the area were covered in 2016, compared to 794 sq. km in 2020. In the third class, 585 sq. km of the area was covered, which was reduced to 533 sq. km in 2015. 963 sq. km were covered in 2016, which decreased to 877 sq. km in 2020. In the fourth class, 1505 sq. km of the area was covered in 2010, which was reduced to 1497 sq. km in 2015. 1480 sq. km of the area was covered in 2010, which declined to 912 sq. km in 2020. In the fifth class, 1334 sq. km of the area was covered in 2010 as compared to 1254 sq. km in 2015. 821 sq. km of the area was covered as compared to 1670 sq. km in 2020.

Figure 13 illustrates the overall water table trend in three districts. Almost the same pattern exists in all districts over a one-decade period (2010-2020). As is well known, Pakistan had floods during 2015-2016, which led to the improvement of the water table this duration. Between 2010 and 2015, the water table's depth dropped, indicating an improvement in the water level during that time. This is mostly because the 2014 flood significantly replenished the aquifer in the Khanewal and Sahiwal regions (Ashraf, 2023). In contrast, the years 2016 to 2020 saw relatively little rainfall, which allowed for enough groundwater extraction to meet the needs of agriculture during this time.

VALIDATION OF RESULTS

Reclassified maps for both water quantity and quality for each year were validated with the field validation points. It was observed that classification ranges of both water quality and quantity are aligned and found consistent with the validation points as illustrated in Figures 14 and 15 respectively. The Punjab Irrigation Department has also verified the findings of this study.

DISCUSSION

The study's primary goal was to precisely map the quantity and quality of groundwater available for irrigation. Following the specific requirements, the quality of groundwater influences its usefulness for various

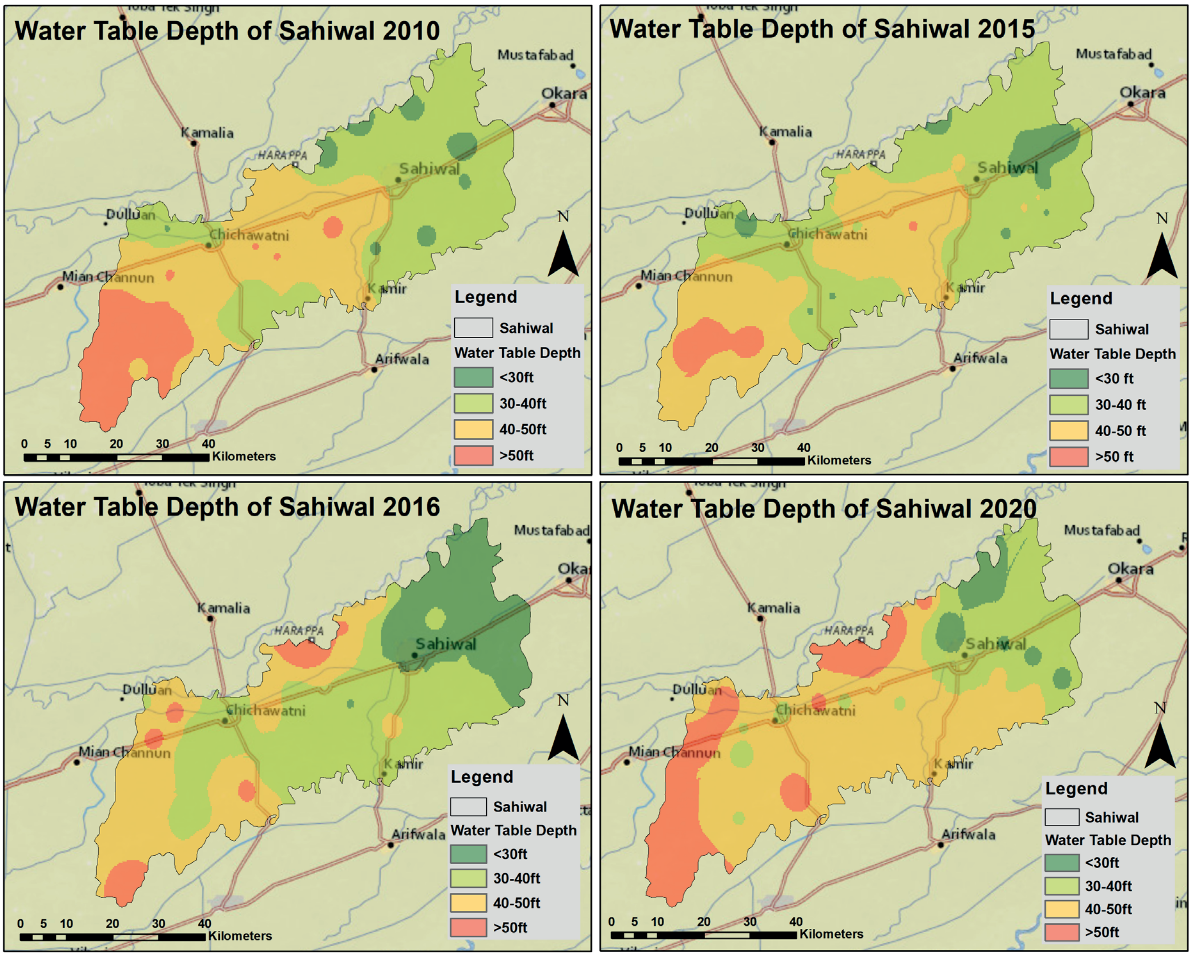

Fig. 11. Water Table Depth of Sahiwal District from 2010-2015 & 2016-2020

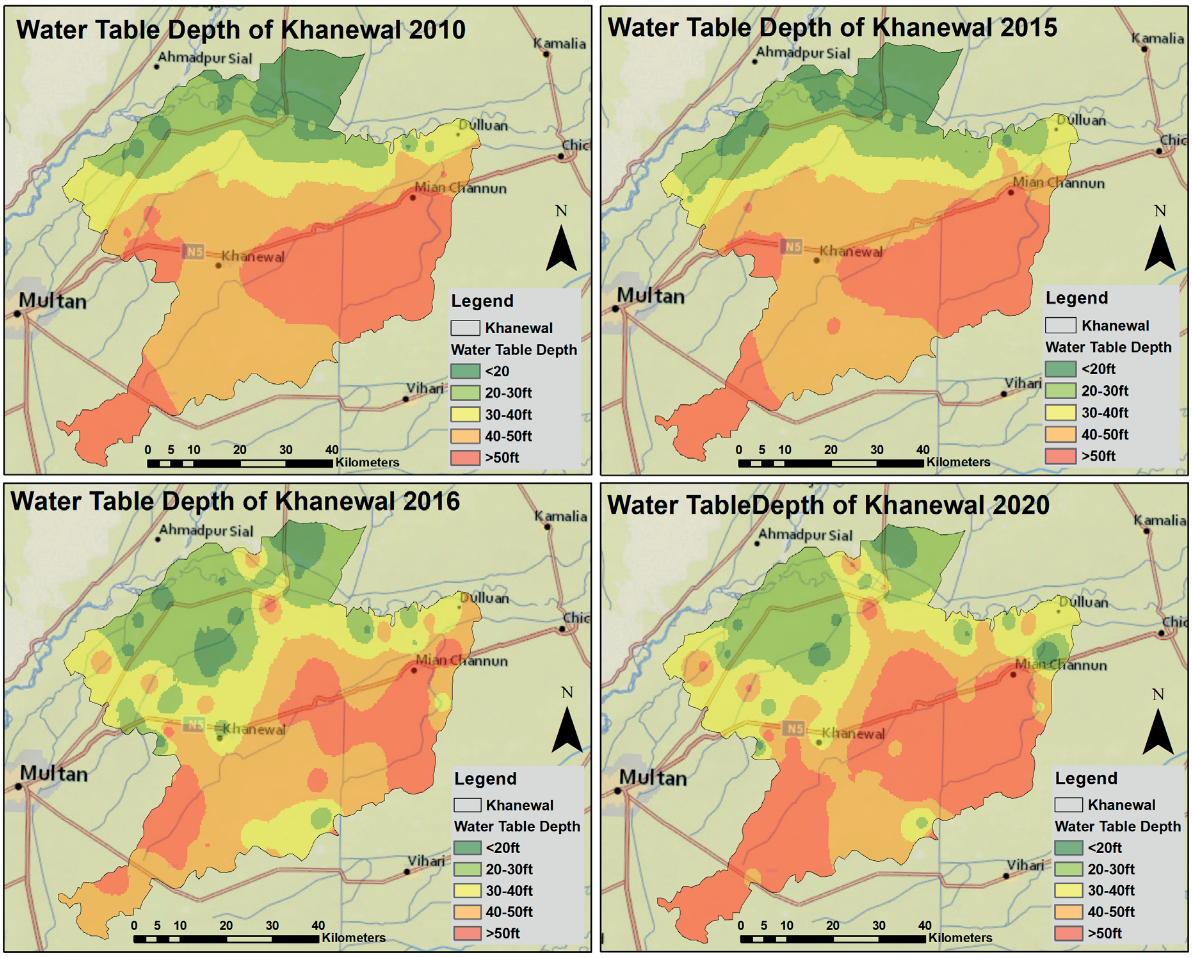

Fig. 12. Water Table Depth of Khanewal District from 2010-2015 & 2016-2020

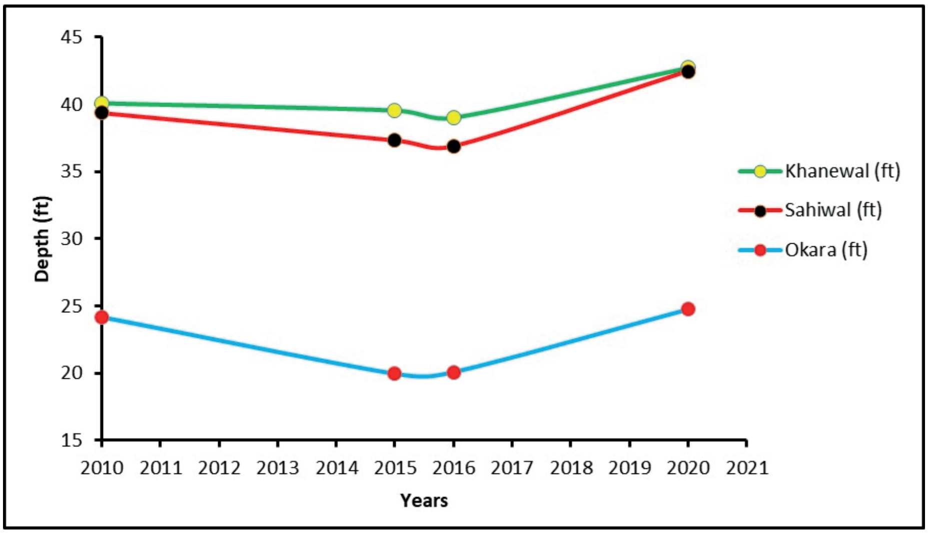

Fig. 13. Variations in water table depth of Okara, Sahiwal, & Khanewal districts

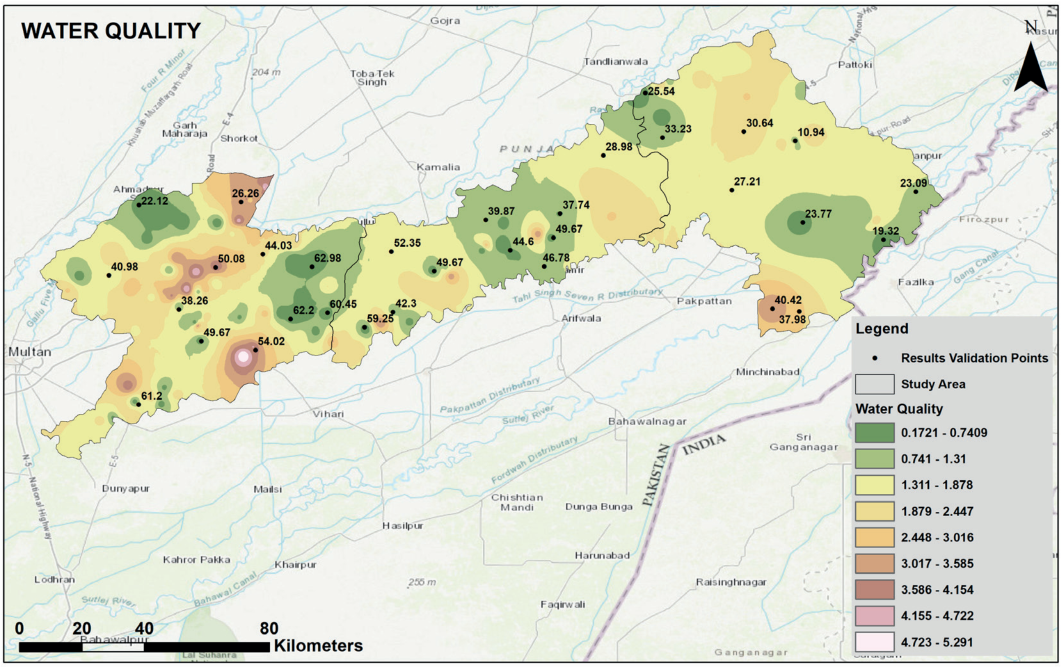

Fig. 14. Sample sites of water quality for the validation of results

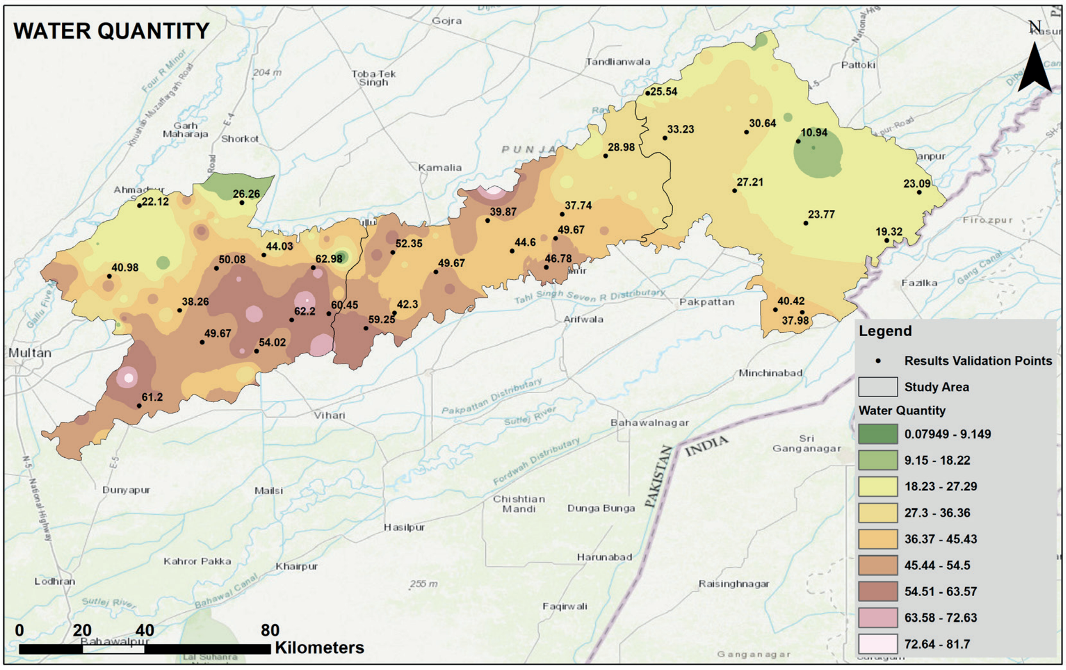

Fig. 15. Sample sites of water quantity for the validation of results

applications. For the objectives of this study, three quality measures—EC, SAR, and RSC—are commonly utilized to depict the water quality of groundwater for irrigation. When identifying irrigation water types, Electrical Conductivity is crucial. The ability of water to transport current is referred to as the concept of conductivity (Riaz et al. 2018). Plants cannot survive in highly salinized water, which also poses a risk to human health (Borecka et al. 2016). Typically, EC is used to measure water salinity. A "physiological" drought may occur when there are high salt concentrations in the soil. Osmotic pressure in soil solution is caused by high salt concentration in irrigation water (Thorne and Peterson 1954). In addition to directly affecting plant growth, salts also have an impact on soil structure, permeability, aeration, texture, and hardness (Trivedy and Geol 1984). In other words, even when it appears that the field has enough moisture, the plants begin to wilt because the roots can no longer absorb the water (Isbell 2016).

The variation in EC is primarily attributed to geochemical processes like ion exchange, reverse exchange, evaporation, silicate weathering, rock water interaction, and sulphate reduction and oxidation processes (Ramesh 2008) as well as anthropogenic activities like application of prevailing agrochemicals in the area (Ramesh & Elango 2012). The study's findings demonstrate that the EC concentration in the Sahiwal district has not significantly changed over time when compared to WHO criteria. Okara's geographical distribution mapping demonstrates that the majority of the area has high-quality water that is suitable for agriculture. Due to the water's EC level being maintained and rising over time in Khanewal, the area with suitable water quality grew from 2014 to 2020. Any region's higher groundwater EC concentration may be the result of excessive groundwater abstraction. Fragmented rocks and shale dissolve in the water as a result of excessive groundwater extraction, raising the salt level (Mabrouk et al. 2019). Additionally, strong evaporation causes salts to accumulate in dry and semi-arid regions, resulting in high-salinity groundwater that prevents plant roots from absorbing enough water to meet their metabolic needs (Chen and Feng 2013; Chen et al., 2019; Xu et al. 2019).

SAR measures the alkali/sodium threat to crops, making it a crucial criterion for establishing the appropriateness of groundwater for irrigation (Ramesh & Elango 2012). When SAR values increase, overall ground stability can drop by as much as 30%. The SAR in groundwater assesses how sodium hazards interact with calcium and magnesium concentrations (Li et al., 2020). The current study's findings demonstrate that between 2014 and 2020, the area in Sahiwal classified as a low-level zone increased following WHO standards. Sahiwal's moderate quality zone had been reduced by 10 km between 2014 and 2020. Groundwater used for irrigation in the Okara district contains constant levels of SAR during the study period between 2014 and 2020. In Khanewal, between 2014 and 2020, the moderate quality zone expanded by 7 km. There has been no change between 2014 and 2020 in the area that falls within Khanewal's low category by WHO standards. The Spatio-temporal distribution of the SAR demonstrates the good water quality class reported decline between 2014 and 2020 under PID criteria. On the other hand, Okara, Sahiwal, and Khanewal saw an increase in moderate water class observations over this period. The area in Sahiwal with poor water quality under the severe category also moved in the direction of declination, indicating that the SAR (mg/L) level has increased. Unsuitable water quality area under areas rose by 7 km in the Khanewal district between 2014 and 2020. From 2014 to 2020, the district Okara area that falls under the severe category remained the same. Seasonal variations have been observed to have an impact on groundwater SAR, which can decrease soil permeability and obstruct crops' ability to absorb water (Tahmaseb et al. 2018).

The sodicity risk is typically identified by a higher RSC value in irrigation water (Awais et al., 2017). In soil particles, sodium tends to absorb if the RSC value of the water is high (Eaton 1950). RSC has been calculated to assess the risky impact of $CO3^{2-}$ and HCO_{3-} on the quality of water for agricultural purposes (Eaton 1950). The graphic representation of the current study demonstrates the improvement in water quality during the investigation. Sahiwal district has undergone a notable transformation, with a moderate zone expanding by 1221 km between 2014 and 2020 and a severe zone decreasing by 100 km within that same period. Between 2014 and 2020, the low-quality zone's perimeter changed by 1130 km. Water quality with the RSC metric also increased over time, as seen by the district Okara map. The best water quality zone increased by 956 sq. km from 2014 to 2020, the moderate water quality zone shrunk by 543 sq. km, and the highly vulnerable water quality zone shrunk by 422 sq. km from 2014 to 2020, according to Khanewal's visual representation of Sodium Residual Carbonate. In terms of residual sodium carbonate, Richards 1954 was the only study to look at the potentially harmful effects of carbonate and bicarbonate on soil and crop health. Continuous usage of water with an excessive RSC can limit the flow of air and water through the soil and harm the soil structure, which lowers crop production (Latha and Rao 2012). As a result, based on their predicted RSC values, the majority of the groundwater samples that are currently available in the region are appropriate for irrigation.

According to the findings, the overall water quality in the study area was deemed "fit" by WHO standards but only "Moderately fit" by Punjab Irrigation Department standards. In contrast, the Sahiwal, Okara, and Khanewal districts saw an average reduction in water table depth from 2010 to 2015 of 0.61, 1.28, and 0.16 metres, respectively, and an increase from 2016 to 2020 of 1.69, 1.42 and 0.83 metres. In 2010, 2015, 2016, and 2020, the water table of the study area exhibited an inverse relationship. The visual representation demonstrates that during the first interval, from 2010 to 2015, the water level decreased while during the second, from 2016 to 2020, the depth of the water table rose. The sustainable circumstances for underground water were changed by floods in Pakistan between 2010 and 2015, which raised the level of subsurface water. This is mainly because of flood conditions in 2014 which recharged the aquifer in Khanewal and Sahiwal regions to a significant level (Ashraf et al., 2023). Whereas, the period from 2016 to 2020 remained dry comparably as fewer rainfalls have been reported which results in sufficient groundwater extraction to fulfil the agriculture needs in this period. Due to significant rains that lowered groundwater levels, Pakistan experienced a drought season from 2016 to 2020. Surface water is also impacted by this drought (Sahar et al., 2023). There isn't enough surface water left over from the drought to adequately irrigate crops. As a result, farmers use subsurface water, which also contributes to lowering the water table.

The outcome is consistent with prior research (Demeke and Andualem, 2018; Melese and Belay 2022). Okara experienced the highest depletion rate, 0.94 m/year, during the dry years of 1998 to 2002. The Okara Division's highest depletion rate during the drought also demonstrates the significantly greater contribution of rains to meeting crop water needs and groundwater recharging. For Sahiwal and Khanewal, the average rate of groundwater depletion from 1987 to 2008 was 0.36 m/year. However, there is no discernible depletion of the groundwater in either Balloki or Okara, where levels are constant (Bashrat 2012). According to Basharat and Tariq (2012), the irrigation system in the Indus Basin has experienced differential variations in rainfall, which have in turn led to changes in the demand for irrigation water. Although the quantity and quality of groundwater in the chosen district (research area) are not currently in a critical state, future deterioration is likely with continued carelessness and the release of additional water from aquifers. Therefore, it is essential to create a proper system for supplying surface water to farmers, implement water conservation measures, and use environmentally friendly methods of replenishing aquifers.

CONCLUSION

The area under good quality in Sahiwal and Okara in 2014 was 60% and 15%, respectively, but in 2020 that area had decreased to 26% and 7%. In contrast, between 2014 and 2020, water quality in the Khanewal district increased by 22% to 44%. Overall water quality has been found "good" in the study area by comparing the WHO standard with a moderate range according to the Punjab Irrigation Department standards. According to the findings, the current decline in groundwater quality in Okara, Sahiwal, and Khanewal is not a very serious issue, but over-draining an aquifer (especially in salty areas) might drastically lower groundwater quality in the coming future. The depth of the water table decreased from 2010 to 2015, which means the water level improved between these years. This is mainly because of flood in 2014 recharged the aquifer in the Khanewal and Sahiwal regions to a significant level. In comparison, the period from 2016 to 2020 remained dry as fewer rainfalls were reported which resulted in sufficient groundwater extraction to fulfil the agriculture needs in this period. A significant increase in the depth of the water table has been observed in the Khanewal and Sahiwal districts from 2016 to 2020. Contrary to expectations, Okara district showed almost consistent results in water quantity over this period. In the Sahiwal and Okara districts, respectively, 52% and 22% area covered more than 12.192 metres and 7.62 metres depth to the water table in 2014 which increased to 71% and 40% after 10 years. Therefore, in the Khanewal district, 35% of the area is less than 12.192 metres (2010), and that number rises to 41% by 2020. The depletion of groundwater increases over time. The primary problem in the current situation of rising water needs is the sustainability of groundwater irrigation. In handling this problem in future, there is a need to promote the use of artificial recharge techniques such as infiltration ponds, recharge wells, and percolation tanks to refill groundwater, as well as encourage the implementation of water-saving technology, including efficient irrigation systems and rainwater harvesting.

REFERENCES

Ashraf, A., Jabeen, M., Ditta, S. A., & Ahmad, Z. (2023). Examining groundwater sustainability through influential floods in the Indus Plain, Pakistan. Sustainable Water Resources Management, 9(2), 56.

Arshad, M., and Shakoor, A. (2017). Irrigation water quality. Water Int, 12(1-2), 145-160.

Awais, M., Arshad, M., Shah, S. H. H., and Anwar-ul-Haq, M. (2017). Evaluating groundwater quality for irrigated agriculture: spatiotemporal investigations using GIS and geo statistics in Punjab, Pakistan. Arabian Journal of Geosciences, 10, 1-15.

Basharat, M. (2012). Spatial and temporal appraisal of groundwater depth and quality in LBDC command issues and options. Pakistan Journal of Engineering and Applied Sciences.

Basharat M. and Tariq A.R, (2012). Spatial climatic variability and its impact on irrigated hydrology in a canal command. Arabian Journal for Science and Engineering, 37(8).

Basharat, M., & Tariq, A.U.R. (2013). Long-term groundwater quality and saline intrusion assessment in an irrigated environment: a case study of the aquifer under the LBDC irrigation system. Irrigation and Drainage, 62(4), 510-523.

Basharat, M., & Tariq, A.U.R. (2015). Groundwater modelling for need assessment of command scale conjunctive water use for addressing the exacerbating irrigation cost inequities in LBDC irrigation system, Punjab, Pakistan. Sustainable Water Resources Management, 1, 41-55.

Borecka, M., A. Białk-Bielińska, L.P. Haliński, K. Pazdro, P. Stepnowski and S. Stolte. (2016). The influence of salinity on the toxicity of selected sulfonamides and trimethoprim towards the green algae Chlorella vulgaris. J. Hazard. Mat., 308: 179-86.

Butt, I., Fatima, M., Nasar-u-Minallah, M., and Ali, M. (2020). Evaluation of drinking water quality and waterborne disease prevalence in children at Shah di Khoi, Lahore, Pakistan. Journal of Himalayan Earth Sciences, 53 (1), 118-125.

Chen, L., Feng, Q. (2013). Geostatistical analysis of temporal and spatial variations in groundwater levels and quality in the Minqin oasis, Northwest China. Environ. Earth Sci. 2013.

Chen, J.; Huang, Q.; Lin, Y.; Fang, Y.; Qian, H.; Liu, R.; Ma, H. (2019). Hydrogeochemical characteristics and quality assessment of groundwater in an irrigated region, Northwest China. Water, 2019, 11, 96.

Demeke, G. G., & Andualem, T. G. (2018). Application of remote sensing for evaluation of land use change responses on the hydrology of Muga Watershed, Abbay River Basin, Ethiopia. J. Earth Sci. Clim. Change, 9(2).

Eaton, F. M. (1950). Significance of carbonate in irrigation waters. Soil Science, 69, 123–133.

Elçi, A., and Polat, R. (2011). Assessment of the statistical significance of seasonal groundwater quality change in a karstic aquifer system near Izmir-Turkey. Environmental monitoring and assessment, 172, 445-462.

Fatima, M., Butt I., Nasar-u-Minallah M., Atta A., Cheng G. (2023). Assessment of Air Pollution and Its Association with Population Health: Geo-Statistical Evidence from Pakistan. Geography, Environment, Sustainability, 16(2):93-101. https://doi.org/10.24057/2071-9388-2022-155

Farooq, M.U., Batool, S., Riaz, O., Nasar-u-Minallah, M., Abbas, T., and Tayyab, M. (2019). Assessment of groundwater contamination and its impact on public health in Bhalwal City, Pakistan. Journal of Biodiversity and Environmental Sciences, 15(1), 1-11.

Isbell, R. (2016). The Australian soil classification. CSIRO publishing.

Kareem, M., Nasar-u-Minallah, M. Parveen, N. and Naqvi, S. A. A. (2016). Spatial analysis of groundwater contamination in close vicinity to solid waste sites in Faisalabad using GIS techniques (A case study). Science International, 28(2), 1051-1055.

Khanam, H., Ali, S., Zaman, M., Shahid, M. A., Muzammal, H., Khan, M. Z., & Majeed, M. D. (2023). Integrated Water Resource Management Using Water Evaluation and Planning Model: A Case Study of Lower Bari Doab Canal, Pakistan. Environmental Sciences Proceedings, 25(1), 55.

Khasanov, S., Li, F., Kulmatov, R., Zhang, Q., Qiao, Y., Odilov, S. and Akhmatov, D. (2022). Evaluation of the perennial spatio-temporal changes in the groundwater level and mineralization, and soil salinity in irrigated lands of the arid zone: as an example of Syrdarya Province, Uzbekistan. Agricultural Water Management, 263, 107444.

Latha, P.S., and Rao K.N. (2012). An integrated approach to assess the quality of groundwater in a coastal aquifer of Andhra Pradesh. India Environ Ear Sci., 66, 2143–2169

Leng, P., Zhang, Q., Li, F., Kulmatov, R., Wang, G., Qiao, Y., and Khasanov, S. (2021). Agricultural impacts drive longitudinal variations of riverine water quality of the Aral Sea basin (Amu Darya and Syr Darya Rivers), Central Asia. Environmental Pollution, 284, 117405.

Li, H., Lu, Y., Zheng, C., Zhang, X., Zhou, B., Wu, J. (2020). Seasonal and inter-annual variability of groundwater and their responses to climate change and human activities in arid and desert areas: A case study in Yaoba Oasis, Northwest China. Water, 2020(12), 303.

Mabrouk, M., Jonoski, A., Essink, G.H.P.O., (2019). Uhlenbrook, S. Assessing the fresh-saline groundwater distribution in the Nile delta aquifer using a 3D variable-density groundwater flow model. Water, 2019(11), 1946.

Kareem, M., Minallah, M.N., Parveen, N. and Naqvi, S. A. A. (2016). Spatial analysis of groundwater contamination in close vicinity to solid waste sites in Faisalabad using GIS techniques (A case study). Science International, 28(2), 1051-1055.

Khanam, H., Ali, S., Zaman, M., Shahid, M. A., Muzammal, H., Khan, M. Z., & Majeed, M. D. (2023). Integrated Water Resource Management Using Water Evaluation and Planning Model: A Case Study of Lower Bari Doab Canal, Pakistan. Environmental Sciences Proceedings, 25(1), 55.

Melese, T., & Belay, T. (2022). Groundwater potential zone mapping using analytical hierarchy process and GIS in Muga Watershed, Abay Basin, Ethiopia. Global Challenges, 6(1), 2100068.

Nasar-u-Minallah, M., Zia S., Rahman A., Riaz O. (2021). Spatio-Temporal Analysis of Urban Expansion and Future Growth Patterns of Lahore, Pakistan. Geography, Environment, Sustainability. 14(3):41-53. https://doi.org/10.24057/2071-9388-2020-215.

Nasar-u-Minallah, M., Haase, D., Qureshi, S., Zia, S. Munnaza, F. (2023). Ecological monitoring of urban thermal field variance index and determining the surface urban heat island effects in Lahore, Pakistan. Environ Monit Assess 195, 1212. https://doi.org/10.1007/s10661-023-11799-1.

Qureshi, A.S. (2020). Groundwater governance in Pakistan: From colossal development to neglected management. Water, 12(11), 3017.

Ramesh, K. (2008). Hydrochemical studies and effect of irrigation on groundwater quality in Tondiar basin, Tamil Nadu. PhD thesis (Unpublished), Anna University, Chennai, India.

Ramesh, K., and Elango, L. (2012). Groundwater quality and its suitability for domestic and agricultural use in Tondiar River basin, Tamil Nadu, India. Environmental monitoring and assessment, 184, 3887-3899.

Riaz, O., Abbas, T., Nasar-u-Minallah, M., Rehman, S. and Ullah, F. (2016). Assessment of groundwater quality: a case study in Sargodha city, Pakistan. Science International, 28(5), 4715-4721.

Riaz, U., Abbas, Z., Mubashir, M., Jabeen, M., Zulqadar, S. A., Javeed, Z., & Qamar, M. J. (2018). Evaluation of Ground Water Quality for Irrigation Purposes and Effect on Crop Yields: A GIS-Based Study of Bahawalpur. Pakistan Journal of Agricultural Research, 31(1).

Ruzikulova, O., Sabitova, N., and Kholdorova, G. (2021). The role of GIS technology in determining irrigated geosystems. In E3S Web of Conferences (Vol. 227, p. 03004). EDP Sciences.

Sahar, J., Nasar-u-Minallah, M., Parveen, N., Zia, S. (2023). Desertification vulnerability assessment through geospatial techniques in Bahawalpur division of Punjab, Pakistan. GeoJournal. https://doi.org/10.1007/s10708-023-10955-x.

Shahzad, H., Farid, H. U., Khan, Z. M., Anjum, M.N., Ahmad, I., Chen, X., and Gulakhmadov, A. (2020). An integrated use of GIS, geostatistical and map overlay techniques for spatiotemporal variability analysis of groundwater quality and level in the Punjab Province of Pakistan, South Asia. Water, 12(12), 3555.

Simsek, C., and Gunduz, O. (2007). IWQ index: a GIS-integrated technique to assess irrigation water quality. Environmental monitoring and assessment, 128, 277-300.

Tahmasebi, P.; Mahmudy-Gharaie, M.H.; Ghassemzadeh, F.; Karimi Karouyeh, A. (2018). Assessment of groundwater suitability for irrigation in a gold mine surrounding area, NE Iran. Environ. Earth Sci. 2018.

Thorne, D. W., & Peterson, H. B. (1954). Irrigated soils. London: Constable and Company.

Trivedy, R. K., & Geol, P. K. (1984). Chemical and biological methods for water pollution studies. Karad: Environ Publications.

Usman, M., Liedl, R., & Awan, U. K. (2015). Spatio-temporal estimation of consumptive water use for assessment of irrigation system performance and management of water resources in irrigated Indus Basin, Pakistan. Journal of hydrology, 525, 26-41.

Usman, M., Kazmi, I., Khaliq, T., Ahmad, A., Saleem, M. F., & Shabbir, A. (2012). Variability in water use, crop water productivity and profitability of rice and wheat in Rechna Doab, Punjab, Pakistan. Journal of Animal and Plant Sciences, 22(4), 998-1003.

Xu, P., Feng, W., Qian, H., Zhang, Q. (2019). Hydrogeochemical characterization and irrigation quality assessment of shallow groundwater in the central-Western Guanzhong basin, China. Int. J. Environ. Res. Public Health, 2019(16), 1492.

Zara, N., Bhalli, M. N. and Parveen, N. (2015). Impact assessment of sewerage drains on groundwater quality of Faisalabad, Pakistan. A Physio-chemical Analysis. Pakistan Journal of Science, 67(1), 52-58.

RESEARCH PAPER

MULTIYEAR VARIATIONS OF SOIL MOISTURE AVAILABILITY IN THE EAST EUROPEAN PLAIN

Gornyy V.I., Balun O.V., Kiselev A.V., Kritsuk S.G., Latypov I.Sh., Tronin A.A.
St. Petersburg Federal Research Center of the Russian Academy of Sciences
***Corresponding author:** v.i.gornyy@mail.ru
Received: March 21st, 2023 / Accepted: November 14th, 2023 / Published: December 31st, 2023
https://DOI-10.24057/2071-9388-2023-2811

ABSTRACT. This study aims to examine the impact of climate change on the water storage across the East European Plain, utilizing archived digital materials from several remote sensing satellites, including the Terra/Aqua (MODIS), the Global Precipitation Climatology Project, GRACE, and GRACE FO satellites, as well as data from digital maps of Selyaninov hydrothermal coefficients. The spatial resolution of the analyzed data ranged from 1x1 km to 250x250 km. Aiming to enhance the spatial resolution of Selyaninov coefficient maps, a new version of the Selyaninov hydrothermal coefficient was suggested, leveraging satellite remote sensing data. Both visual and computer analyses of these materials reveal a consistent reduction in water storage in the southern regions of the East European Plain, accompanied by a slight increase in the Novgorod Oblast. This information suggests that the non-chernozem region of the East European Plain will play a crucial role in supplying agricultural products to the population in the next decades. The observed stable water storage in the northern part of the East European Plain, encompassing the Komi Republic and the Novgorod Oblast, hints at the potential of increased agricultural production in these areas. However, achieving sustainable growth in agricultural production in these regions necessitates a focused investment policy.

KEYWORDS: East European Plain, climate change, water storage, satellite, remote sensing, digital maps, processing, trends, forecast

CITATION: Gornyy V.I., Balun O.V., Kiselev A.V., Kritsuk S.G., Latypov I.Sh., Tronin A.A. (2023). Multiyear variations of soil moisture availability in the East European Plain. Geography, Environment, Sustainability, 4(16), 120-124
https://DOI-10.24057/2071-9388-2023-2811

Conflict of interests: The authors reported no potential conflict of interest.

INTRODUCTION

Agricultural production heavily relies on meteorological factors, particularly temperature and precipitation, which are highly variable and dictate moisture levels and water storage in the region. Consequently, crop yields fluctuate from year to year due to the strong dependence on weather conditions (Gulyanov 2022, Javadinejad et al. 2021). In recent decades, climate change has significantly impacted the water storage of various regions worldwide (Tretii otsenochnyi doklad… 2022).

In Russia, the hydrothermal coefficient (K_{Sel}), developed by G.T. Selyaninov, is commonly used to assess regional water storage (Selyaninov 1928, Svoboda et al. 2016, Cherenkova, Zolotokrylin 2016). K_{Sel} is calculated using the formula $K_{Sel}= R_M \cdot 10/\Sigma t$, where R_M represents the total precipitation measured by an weather station in millimeters during the period with temperatures exceeding +10°C, and Σt denotes the total of daily average temperatures in Celsius during the same period. K_{Sel} values ranging from 1.0 to 1.3 indicate sufficient moisture, while values between 0.7 and 1.0 signify arid farming zones, and values between 0.5 and 0.7 correspond to dryland farming zones. However, K_{Sel} has limitations, as it does not consider differences in evaporation and surface runoff of areas and relies on meteorological data with low spatial resolution. In contrast, satellite monitoring systems, such as Gravity Recovery and Climate Experiment (GRACE) and GRACE Follow-On (FO), enable multi-year monitoring of water storage over large areas, automatically accounting for differences in evaporation, humidity, and surface runoff. However, these systems have a low spatial resolution of 250x250 km. Monthly values of the equivalent water thickness layer (EWTL)[1] are deduced from the detected variations of the terrestrial gravitation field. The benefit of using this method to monitor regional water storage lies in its ability to automatically account for evaporation and surface runoff, as well as its consistent observation network. Prior research has demonstrated the reliability of GRACE data in tracking soil moisture and water storage in watersheds (Kiselev et al. 2015, Kiselev et al. 2016, Velicogna et al. 2015, Sun 2013, Longuevergne et al. 2013, Cesanelli 2011, Strassberg et al. 2007, Pat et al. 2006).

The aim of this study is to assess changes in water storage within the Eastern European Plain over a 20-year period. We utilized satellite digital maps of land surface temperature and precipitation, along with GRACE and GRACE FO satellite data, and time series of meteorological station observations of air temperature and precipitation. To enhance the spatial resolution of soil moisture availability maps, the paper suggests creating a novel hydrothermal moistening criterion: K_{RS}, or Selyaninov's hydrothermal coefficient. This new criterion will rely on satellite remote sensing precipitation and land surface temperature measurements.

The study seeks to objectively assess how climate change affects water storage in various territories. Additionally, it aims to predict the economic significance of agricultural land in different zones of the East European Plain.

[1]The equivalent water thickness layer refers to the thickness of an infinite, plane-parallel layer of water situated on the surface of a geoid, whose gravitation force at the orbital level is equivalent to the gravitation field change observed by the satellite.

Data and Methods

The research utilized the following satellite data:

- infrared thermal spectral bands imagery materials from Terra/Aqua satellites (MODIS instrument), with a spatial resolution of 1x1 km, a standard product for land surface analysis. Daily maps of the Earth's surface temperature were generated four times per day (MOD11A1[2] and MYD11A1[3]) from 2003 to 2022.
- Global Precipitation Climatology Project version 3 (Huffman et al. 2022) precipitation maps with a spatial resolution of 0.5°x0.5° (~50x50 km), displaying daily precipitation totals for the period from 2002 to 2020.
- GRACE and GRACE-FO satellite gravimetric survey data covering the period from 2002 to 2022 as a standard product in the form of monthly maps that display the EWTL and changes in the terrestrial gravitation field. The maps have a spatial resolution of approximately 250 km (Swenson and Wahr 2006). A total of 168 scenes were analyzed.

The Selyaninov hydrothermal coefficient was calculated by using satellite data as $K_{RS}=R_{RS}\cdot 10/\Sigma t_{RS}$, where R_{RS} denotes the total precipitation in millimeters during the period with temperatures above +10°C. Σt_{RS} refers to the total daily average surface temperatures in Celsius during the same period, also based on the satellite data. K_{Sel} values ranging from 1.0 to 1.3 indicate sufficient moisture, while values between 0.7 and 1.0 signify arid farming zones, and values between 0.5 and 0.7 correspond to dryland farming zones. Daily average temperatures were calculated using every four scenes of the daily Terra/Aqua (MODIS) satellite imagery, while the data on precipitation were sourced from the Global Precipitation Climatology Project. For each surface element, a time series of daily average surface temperatures was created, and every year in which the daily average temperature exceeded +10°C was identified within that series. At the same time, the K_{RS} formula was implemented to calculate the overall amounts of temperature and precipitation. To compare the hydrothermal coefficient K_{RS} calculated from the remote sensing data with the traditional K_{Sel}, we used the Agroecological Atlas of Russia (Afonin et al. 2006). K_{Sel} was calculated in the atlas using the abovementioned formula, with two notable differences. Firstly, the atlas (Afonin et al. 2006) determined the growing season for average daily air temperatures exceeding +5°C. Secondly, in our case for K_{RS} calculation, land surface temperature was used instead of a daily air temperature at a 2 m height, which is used for K_{Sel}. In order for agrometeorologists to better understand the idea, it was necessary to further calibrate the K_{RS} with respect to the K_{Sel} map shown in Figure 1. Figure 2C shows the calibrated digital K_{RS} map.

Further analysis involved creating digital maps displaying trends in K_{RS}, EWTL, *p*-values, and *Var*, or coefficients of variation, between 2003 and 2022. The reliability of trend determination was judged using *p*-values, with trends having $p>0.05$ being considered unreliable. Additionally, coefficients of variation assessed the consistency of the factors in effect and were determined by dividing the standard deviation by the sample mean: $Var=\sigma V/(\bar{V})$, with $(\bar{V})$ being the sample mean.

Results and Discussion

The primary outcome of this study is a compilation of annual digital maps of the East European Plain, developed using metrologically-supported satellite measurement systems. These maps delineate fluctuations in moisture content on a subcontinental scale over a multi-year period (Fig. 2).

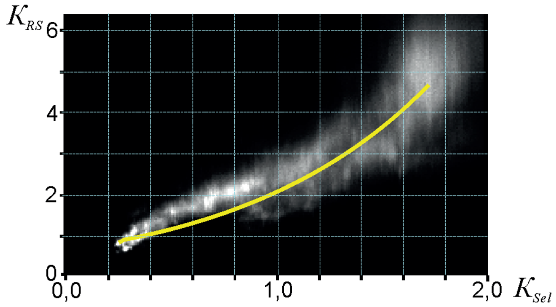

Fig. 1. Approximation of K_{RS} by the exponential function $K_{RS}=0.8\cdot exp(K_{Sel})$ of a two-dimensional distribution

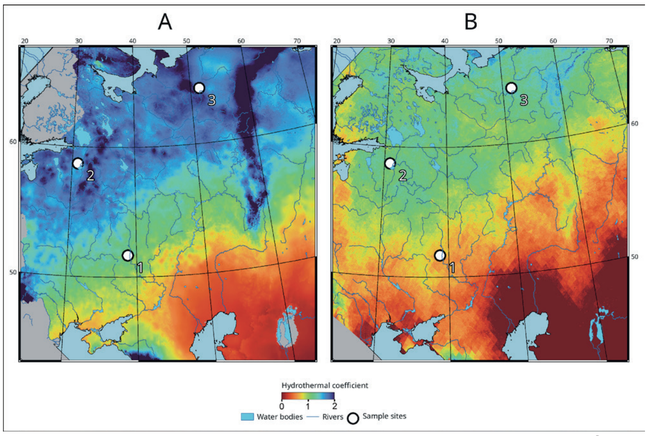

Fig. 2. Digital maps of the East European Plain. A) K_{Sel} - according to observations of air temperature and precipitation at weather stations, averaged over the period from 1965 to 1974. The initial spatial resolution is 0.25x0.25 (~250x250 km) degrees of the geographic grid, increased by reanalysis to 10x10 km (Afonin et al. 2006). B) K_{RS}, built up for 2003 according to satellite monitoring data. Spatial resolution 10x10 km

[2]Daily per-pixel Land Surface Temperature and Emissivity Product MOD11A1v006, DOI:10.5067/MODIS/MOD11A1.006, https://lpdaac.usgs.gov/products/mod11a1v006/

[3]Daily per-pixel Land Surface Temperature and Emissivity Product MYD11A1v006, DOI:10.5067/MODIS/MYD11A1.006, https://lpdaac.usgs.gov/products/myd11a1v006/

Over the last two decades, the region with low hydrothermal coefficient values in the East European Plain has exhibited a clear northward trend. Simultaneously, the southern areas of the East European Plain have become a part of the irrigated agricultural zone.

To illustrate the northward shift of the dry zone, a digital map of the K_{RS} trend from 2003 to 2020 was created (Fig. 3D). This map quantitatively confirms by the trend (Fig. 4C). Meanwhile, the non-chernozem region of the East European Plain maintains adequate moisture. The northern part of the East European Plain displays a trend of water availability (Fig. 3A) with high values of both p-value (Fig. 3B) and Var coefficient (Fig. 3C). This suggests a lack of a significant, permanent factor affecting the K_{RS} in this region.

An analysis of meteorological data for Novgorod Oblast over the past 60 years indicates a consistent increase in annual precipitation and annual average temperature. Precipitation has increased by 28 mm, and the annual temperature has risen by 0.5ºC per decade (Table). Furthermore, the sum of effective temperatures (above +10ºC), which determines the heat storage of major crops, is increasing at a rate of +54ºC per decade, while precipitation is increasing by 10 mm over the same period. Over the 60-year period, the moisture availability K_{Sel} in Novgorod Oblast has not displayed a clear dependence on time. However, during the last 30 years, there has been a consistent rise in the moisture content in the area: K_{Sel} has increased from 1.28 to 1.45 units.

Based on the analysis of K_{Sel} and K_{RS} trends, we assume that there will be no significant changes in moisture availability in the non-chernozem regions over the next decade, despite the situation in the southern regions of the East European Plain. However, a further decrease in soil moisture availability is expected in those southern regions.

The map depicting the EWTL trend across the East European Plain (Fig. 3A) provides a clearer picture. In Novgorod Oblast, there has been a slight increase in water storage over the past two decades, albeit an insignificant one (Fig. 3A, Fig. 4 A, B). Conversely, the areas south of Novgorod Oblast have experienced a decline in overall water storage in the soil, groundwater, and atmosphere.

Simultaneously, Figure 3B demonstrates a highly reliable trend estimation, while the Var coefficient map (Fig. 3C) displays a consistent factor in the southern areas of the East European Plain. Moreover, the EWTL graph (Fig.

Table 1. Meteorological indicators for the Novgorod Oblast

Period, years	Indicators				
	Annual amount of precipitation, mm	Average annual temperature, ºC	Precipitation at temperatures above +10ºC, mm	Sum of temperatures above 10ºC	K_{Sel}
1960-1969	525	3,6	280	2091	1,36
1970-1979	538	4,3	284	2141	1,34
1980-1989	577	4,6	336	2193	1,55
1990-1999	562	5,3	281	2212	1,28
2000-2009	604	5,7	316	2271	1,40
2010-2019	683	6,3	343	2389	1,45
Dependence of the indicator (y) on time (x)	y = 2,78x - 4937	y = 0,053x - 99	y = 1,017x - 1712	y = 5,43x - 8554	y = 0,001x - 0,645
Correlation coefficient	0,91	0,99	0,66	0,97	0,20

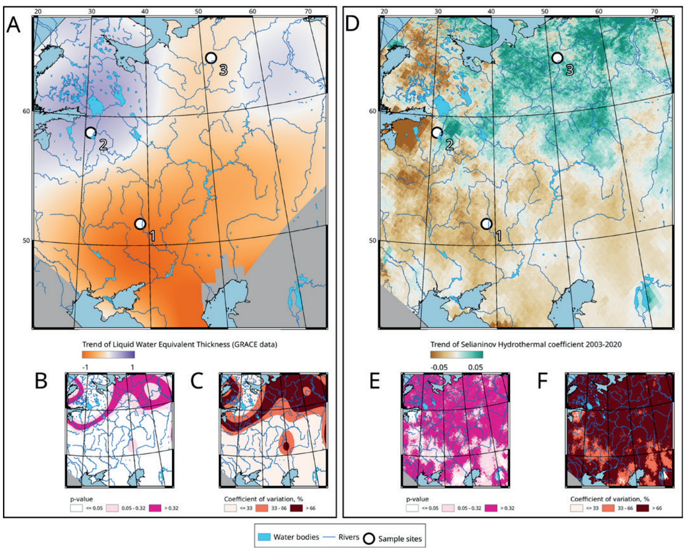

Fig. 3. Digital maps of the East European Plain.
A) EWTL trend for the period from 2002 to 2022. B) *p*-value of the EWTL trend. C) Var of EWTL. D) K_{RS} trend for the period from 2003 to 2022. E) p-value of trend of the K_{RS}. F) Var of trend for K_{RS}. Legend: Locations of graphs in fig. 4: 1. The Komi Republic (Fig. 4 A); 2. The Novgorod Oblast (Fig. 4 B); 3. The Voronezh Oblast (Fig. 4C)

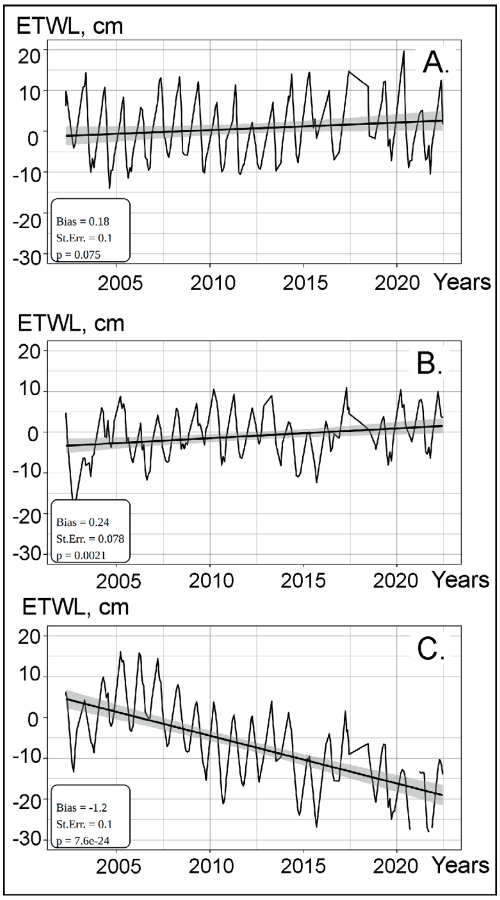

Fig. 4. EWTL changes for the period from 2002 to 2022 in points (see Fig. 3). A) The Komi Republic B) The Novgorod Oblast. C) The Voronezh Oblast

4C) demonstrates a distinct trend of decreasing multiyear moisture regime in Voronezh Oblast. It should be noted that there has been no decrease observed in the reduction rate of the EWTL in recent years (Fig. 4 C). The data, combined with the highly dependable trends observed in this area and the persistent natural driving force that diminishes water storage, suggest a forthcoming worsening of moisture availability in the southern regions and a greater role of the non-chernozem zone in agriculture of the East European Plain within the next decades.

The joint analysis of the Selyaninov remote sensing coefficient and EWTL reveals a consistently decreasing trend in moisture availability for both indicators across the southern regions of the East European Plain (Fig. 3 A, D, and Fig. 4 C). However, a slight increase in moisture content is observed in Novgorod Oblast (Fig. 3 A, D; Fig. 4 A, B and Table).

Based on the analysis of trends in the Selyaninov remote sensing coefficient and EWTL, it is hypothesized that there will be no significant changes in moisture availability in the non-chernozem zone of the East European Plain during the next decade. However, it is anticipated that water storage in the southern regions of the East European Plain will further decrease. Since moisture availability significantly affects the productivity of agricultural land (Gulyanov 2022, Javadinejad et al. 2021), the forthcoming trends may decrease agricultural productivity in the south while increasing the non-chernozem zone's importance in providing agricultural products.

CONCLUSION

1. The observed trend of the arid zone shifting northwest emphasizes the pressing need for implementing sustainable land-use management practices in affected regions. This is crucial to mitigate the impact of drought on agricultural productivity and prevent land degradation effectively.

2. The sustained moisture availability in the non-chernozem zone signals the potential for enhancing agricultural production in this region. It is advisable to formulate development policies and target investments strategically to maximize sustainable agricultural growth.

3. The results of this study provide valuable, objective insights for decision-makers involved in land use management, agricultural development, and the formulation of climate change adaptation strategies relevant for the Eastern European Plain and other regions facing similar challenges.

REFERENCES

Afonin A.N., Li Yu.S., Lipiyainen K.L., Tsepelev V.Yu. (2006). Hydrothermal coefficient of Selyaninov (HTC) for growing season (Gidrotermicheskii koeffitsient Selyaninova (GTK) za vegetatsionnyi period, V V: Afonin A.N., Grin S.L., Dzyubenko N.I., Frolov A.N. (red.) Agroekologicheskii atlas Rossii i sopredel'nykh stran: ekonomicheski znachimye rasteniya, ikh vrediteli, bolezni i sornye (In Russian). (Internet-version 2.0).

Cesanelli, A., Guarracino, L. (2011). Estimation of regional evapotranspiration in the extended Salado Basin (Argentina) from satellite gravity measurements. Hydrogeol. J., 19, 629–639, DOI:10.1007/s10040-011-0708-3.

Cherenkova, Elena & Zolotokrylin, Alexander. (2016). On the comparability of some quantitative drought indexes // Fundamental and applied climatology, 2, 79-94. DOI:10.21513/2410-8758-2016-2-79-94.

Gulyanov Yu.A. (2022). Influence of climatic changes on the dynamics of winter wheat grain production in the Orenburg region. Perm Agrarian Bulletin, 3 (39), 20-31. DOI: 10.47737/2307-2873_2022_39_20 (in Russian).

Huffman, G.J., Behrangi A., Bolvin D.T., Nelkin E.J. (2022). GPCP Version 3.2 Daily Precipitation Data Set, Edited by Huffman, G.J., A. Behrangi, D.T. Bolvin, E.J. Nelkin, Greenbelt, Maryland, USA, Goddard Earth Sciences Data and Infor-mation Services Center (GES DISC), 10.5067/ MEASURES/GPCP/DATA305

Javadinejad S., Dara R., Jafary F. (2021). Analysis and Prioritization the Effective Factors on Increasing Farmers Resilience Under Climate Change and Drought. Agricultural Research, 10, 497-513. DOI:10.1007/s40003-020-00516-w

Kiselev A. V., Muratova N.R., Gornyi V.I., Tronin A.A. (2015). Svyaz' zapasov produk-tivnoi vlagi v pochve s polem sily tyazhesti Zemli (po dannym s»emok sputnikami GRACE) (Relation-ship of productive moisture reserves in the soil with the Earth's gravity field (according to GRACE satellite survey data)) Sovremennye problemy distantsionnogo zondirovaniya Zemli iz kosmosa, 12(6), 7–16. http://d33.infospace.ru/ d33_conf/sb2015t6/7-16.pdf (in Rusian).

Kiselev A.V., Gornyy V.I., Kritsuk S.G., Tronin A.A. (2016). Indikatsiya opasnykh pri-rodnykh yavlenii variatsiyami gravitatsionnogo polya Zemli (po dannym sput-nikovykh s»emok sistemoi GRACE) (Indication of hazardous natural phenomena by variations of the Earth's gravitational field (according to satellite imagery by the GRACE system)), Sovremennye problemy distantsionnogo zondirovaniya Zemli iz kosmosa, 13(6), 13–28. (in Russian).

Longuevergne L., Wilson C. R., Scanlon B. R., and Crétaux J. F. (2013). GRACE water storage estimates for the Middle East and other regions with significant reservoir and lake storage. Hydrol. Earth Syst. Sci., 17, 4817–4830, DOI:10.5194/hess-17-4817-2013

Pat J.-F. Yeh, Swenson S. C., Famiglietti J. S., and Rodell M. (2006). Remote sensing of groundwater storage changes in Illinois using the Gravity Recovery and Climate Experiment (GRACE). Water Resources Research, 42, W12203, DOI:10.1029/2006WR005374.

Selyaninov, G.T. (1928). About climate agricultural estimation. Proceedings on Agricultural Meteorology, 20, 165–177.

Strassberg G., Scanlon B. R., and Rodell M. (2007). Comparison of seasonal terrestrial water storage variations from GRACE with groundwater-level measure-ments from the High Plains Aquifer (USA). Geophysical Research Letter, 34, L14402, DOI:10.1029/2007GL030139.

Sun, A. Y. (2013), Predicting groundwater level changes using GRACE data, Water Resour. Res., 49, 5900–5912, DOI:10.1002/wrcr.2042111.

Swenson, S. C. and Wahr J. (2006). Post-processing removal of correlated errors in GRACE data. Geophys. Res. Lett., 33, L08402, DOI:10.1029/2005GL025285.

Tretii otsenochnyi doklad ob izmenenii klimata i ikh posledstviyakh na territorii Rossiiskoi Federatsii, Obshchee rezyume. (2022). (Third assessment report on climate change and its conse-quences on the territory of the Russian Federation. General summary) (in Russian), Sankt-Peterburg: naukoemkie tekhnologii, 124p.

Velicogna I, Kimball J. S. and Kim Y. (2015). Impact of changes in GRACE derived terrestrial water storage on vegetation growth in Eurasia. Environ. Res. Lett., 10, 124024. DOI:10.1088/1748-9326/10/12/124024.

World Meteorological Organization (WMO) and Global Water Partnership (GWP). (2016). Handbook of Drought Indicators and Indices (M. Svoboda and B.A. Fuchs). Integrated Drought Management Programme (IDMP), Integrated Drought Management Tools and Guidelines Series 2. Geneva, 45.

RESEARCH PAPER

CROP RESIDUES STIMULATE YIELD-SCALED GREENHOUSE GAS EMISSIONS IN MAIZE-WHEAT CROPPING ROTATION IN A SEMI-ARID CLIMATE

Morad Mirzaei*[1,2], Manouchehr Gorji Anari[1], Maurício Roberto Cherubin[3,4], Nermina Saronjic[5], Seyed Mohammad Nasir Mousavi[6,7], Azin Rooien[8], Mohammad Zaman[9], Andrés Caballero-Calvo*[10]

[1]Department of Soil Science and Engineering, Faculty of Agricultural Engineering and Technology, University of Tehran, Karaj, Iran

[2]School of Natural Sciences, Botany Discipline, Trinity College Dublin, Dublin 2, Ireland

[3]Department of Soil Science, "Luiz de Queiroz" College of Agriculture, University of São Paulo, 11 Pádua Dias Avenue, Piracicaba, São Paulo 13418-900, Brazil

[4]Center for Carbon Research in Tropical Agriculture (CCARBON) - University of São Paulo, 11 Alameda das Palmeiras, Piracicaba, São Paulo 13418-900, Brazil

[5]Institute of Soil Research, Department of Forest and Soil Sciences, University of Natural Resources and Life Sciences (BOKU), Vienna, Austria

[6]Department of Plant, Food, and Environmental Sciences, Faculty of Agriculture, Dalhousie University, Halifax, NS B2N 5E3, Canada

[7]Institute of Land Use, Engineering and Precision Farming Technology, Faculty of Agricultural and Food Sciences and Environmental Management, University of Debrecen, 138 Böszörményi St., 4032 Debrecen, Hungary

[8]Department of Landscape Protection and Environmental Geography, Institute of Earth Science, Faculty of science and technology, University of Debrecen, 4032 Debrecen, Hungary

[9]Soil and Water Management & Crop Nutrition Section, Joint FAO/IAEA Division of Nuclear Techniques in Food & Agriculture, Department of Nuclear Sciences and Applications, International Atomic Energy Agency, Vienna, Austria

[10]Departamento de Análisis Geográfico Regional y Geografía Física, Facultad de Filosofía y Letras, Campus Universitario de Cartuja, University of Granada, 18071 Granada, Spain.

***Corresponding author:** andrescaballero@ugr.es, mirzaei.morad95@ut.ac.ir

Received: October 13st, 2022 / Accepted: November 14th, 2023 / Published: December 31st, 2023

https://DOI-10.24057/2071-9388-2023-2629

ABSTRACT. Mitigating yield-scaled greenhouse gas emissions (YSE) is beneficial for enhancing crop yield, reducing greenhouse gas (GHG) emissions, and advancing climate-smart agronomic management practices. This study aims to evaluate the impact of different crop residue rates– 100% (R_{100}), 50% (R_{50}), and residue removal (R_0) – on the YSE indicator within a maize-wheat cropping rotation under both conventional tillage (CT) and no-tillage (NT) systems in a semi-arid region. In the NT system, crop residues had a notable effect on the YSE indicator for wheat. Specifically, R_0 exhibited a 39% and 20% decrease in YSE for wheat compared to R_{100} and R_{50}, respectively. Interestingly, crop residue did not significantly influence YSE for maize under the NT system. On the other hand, in the CT system, YSE for maize in R_0 was 33% and 25% lower than that in R_{100} and R_{50}, respectively. Additionally, compared to R_0, there were observed increases of 28% and 20% in YSE for wheat in R_{100} and R_{50} under the CT system, respectively. Our findings show that crop residue removal decreases YSE under both CT and NT systems. However, given that this practice degrades soil quality and results in lower yields, it is not considered a sustainable management practice compared to residue retention options. This research highlights the importance of evaluating GHG mitigation strategies by concurrently considering both emissions and crop production. Nevertheless, it is essential to conduct off-site assessments of GHG emissions from crop residue application and also engage in long-term studies to comprehend the full potential of crop residue management on YSE.

KEYWORDS: oil health, cropping system, food security, conservation agriculture, soil management, climate change, greenhouse gas emissions

CITATION: Mirzaei M., Anari M. G., Cherubin M. R., Saronjic N., Mousavi S. M. N., Rooien A., Zaman M., Caballero-Calvo A. (2023). Crop Residues Stimulate Yield-Scaled Greenhouse Gas Emissions In Maize-Wheat Cropping Rotation In A Semi-Arid Climate. Geography, Environment, Sustainability, 4(16), 125-132

https://DOI-10.24057/2071-9388-2023-2629

Conflict of interests: The authors reported no potential conflict of interest.

INTRODUCTION

Due to anthropogenic activities, global concentrations of greenhouse gases (GHG), such as carbon dioxide (CO_2), nitrous oxide (N_2O), and methane (CH_4), have increased (O'Neill et al. 2021;IPCC, 2021). Enhancing agricultural productivity through strategic management techniques, such as reduced use of conventional agronomic practices, may mitigate GHG emissions (Ceschia et al. 2010; Radicetti et al. 2020; Mohammed et al. 2022; Mirzaei et al. 2022a, 2022b). Land management practices often determine whether cropland soils act as net sinks or sources of GHG emissions (Ceschia et al. 2010; Radicetti et al. 2019; Bossio et al. 2020).

Mitigating GHG emissions and increasing soil organic carbon sequestration are achievable through improved management practices (Paustian et al. 2016; Minasny et al. 2017; Ogle et al. 2019; Lal et al. 2021). Agricultural practices, including crop residue management, significantly influence soil C and GHG emissions, and crop productivity by impacting dynamic changes in carbon and nitrogen in soil, nutrient availability, and factors influencing GHG emissions such as soil moisture, temperature, and microbial activity (Yao et al. 2013; Jin et al. 2014; Cherubin et al. 2018; Vasconcelos et al. 2018; Battaglia et al. 2021; Drury et al. 2021; Mirzaei et al. 2021; Tenelli et al. 2021; Liu et al. 2022; Mancinelli et al. 2023). Therefore, evaluating the effect of agricultural practices is crucial for developing more sustainable approaches with high crop yields, lower potential for GHG emissions, and reduced global warming impact (Pratibha et al. 2016; Mancinelli et al. 2020; Mirzaei et al. 2023).

Metrics such as greenhouse gas intensity (GHGI) or yield-scaled metrics assess GHG emissions per unit of crop yield, considering both food production and climate change concerns (Mosier et al. 2006; Van Groenigen et al. 2010; Pratibha et al. 2016; Li et al. 2022). The yield-scaled emissions (YSE) approach is an effective integrated assessment method for evaluating changes in crop management operations destined to optimize cropping practices, achieve food security, and simultaneously reduce the impacts of climate change (Van Groenigen et al. 2010, Abalos et al. 2016).

While previous studies have assessed the effect and mitigation potential of agronomic practices on GHG emissions (Six et al. 2004; Zhao et al. 2016; Xia et al. 2017), few studies have been linked to crop yield (Van Groenigen et al. 2010; Linquist et al. 2012; Feng et al. 2013; Van Kessel et al. 2013; Zhang et al. 2015). Comprehensive assessments of cropping practices per unit yield (yield-scaled) are suggested to benefit food security and GHG mitigation goals (Van Groenigen et al. 2010; Linquist et al. 2012; IPCC, 2014). Therefore, the integrated evaluation of both crop yield and GHG emissions is crucial for optimizing cropping system practices.

The maize-wheat rotation is one of the most common grain production cropping systems (Pooniya et al. 2022), producing a substantial amount of crop residues annually (Bao et al. 2022). However, a significant portion of these residues is removed for fodder, energy production, or other purposes, or burned (Mirzaei et al. 2021). To date, there is no information about the effects of crop residue management practices on GHG emissions, especially yield-scaled GHG emissions from agricultural soil in Iran. We hypothesized that total residue removal treatment would lead to large yield-scaled GHG emissions. The objective of this study is to assess the effects of different crop residue rates (100 %, 50 %, and total residue removal) on wheat and maize yield-scaled GHG emissions under conventional tillage (CT) and no-tillage (NT) systems in a semi-arid region in Iran.

Materials and methods

Site description and experimental layout

The study took place at the Agriculture Research Station of the College of Agriculture and Natural Resources, University of Tehran, Karaj, Iran (35˚48' 32" N, 50˚ 58' 06" E, 1308 m a.s.l.) in 2018 (Fig.1). This region has semi-arid climate conditions, with an annual precipitation of 245 mm and an annual mean temperature of 13.7 °C (Tabari and Talaee, 2011). For the experiment, two fields with a wheat (*Triticum aestivum L.*) - maize (*Zea mays L.*) cropping rotation background were chosen, managed under CT and NT practices. The soil in the CT field was classified as sandy loam with 57% sand, 24.4% silt, and 18.6% clay. In the NT field, soil was classified as clay loam with 52.5% sand, 28.1% silt, and 19.4% clay. Both fields had a soil pH of 7.7 and no salinity issues. Organic carbon content was 8.9 g kg^{-1} under CT and 11.3 g kg^{-1} under NT. Total nitrogen (TN), available phosphorus (AP), and available potassium (AK) under CT were 0.8 mg kg^{-1}, 13.5 mg kg^{-1}, and 150.6 mg kg^{-1} respectively. Under the NT system, these values were 1.0 mg kg^{-1}, 15.2 mg kg^{-1}, and 258.2 mg kg^{-1} for TN, AP, and AK respectively. The experiment was set up as a randomized complete block with three replicates. In total, 18 plots (3×4 m) were designated for both fields. In this research, in order to facilitate the application of crop residue treatments and planting operations, the residue treatments were first applied to the designated plots, followed by the planting of crops. Finally, the plots were separated based on the specific dimensions.

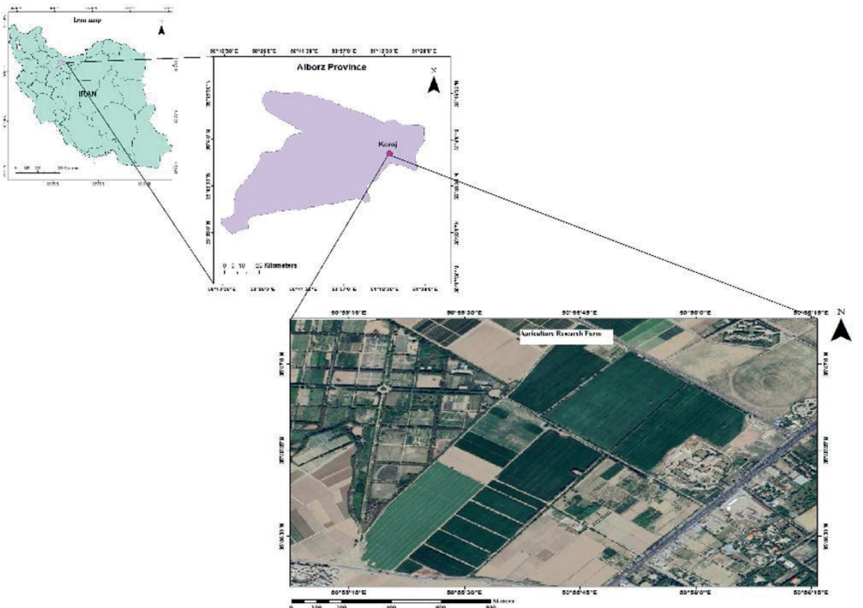

Fig. 1. Geographical location of the study area

Treatment implementation and cultivation practices

Wheat residue rates and maize planting

After harvesting wheat on July 6, 2018, three wheat residue rates – 100 % (R_{100}), 50 % (R_{50}), and no residue (R_0) – were applied to both CT and NT fields on July 11, 2018. The residue rates were achieved by weighing post-harvest crop residue samples collected across the farm at several locations using a wooden quadrat (1m×1m). The average weight per square meter was then scaled up to a hectare. For the R_{100} and R_{50} treatments, the residue was distributed over the soil surface, while for the R_0 treatment the residue was completely removed from the plots. Next, maize seeds were planted. In the NT field, sowing was carried out using a planter with a single colter. In the CT, before seed placement with a row crop planter, the soil was cultivated with a moldboard plow to a depth of 35 cm, followed by disking and leveling. Basal NPK fertilizers were applied: 23, 36, and 68 kg ha^{-1} of N, K_2O, and P_2O_5 respectively, with additional top-dressing of 37 and 125 kg ha^{-1} N at eight and ten leaves stages, post-cultivation. Plots were irrigated at 7-10 days intervals.

Maize residue rates and wheat planting

In October 2018, Maize was harvested, and three maize residue rates (R_{100}, R_{50}, and R_0) were applied to the same plots. The residue application process mirrored that of wheat residues. Winter wheat was planted in November 2018 using a drilling machine, with basal fertilization of 23, 80, and 90 kg ha^{-1} N, K_2O, and P_2O_5. Additional fertilizers of 50, 50, and 23 kg ha $^{-1}$ N were applied during late tillering, stem elongation, and spiking, respectively.

Greenhouse gas sampling and analysis

Flux measurements were performed every 7–10 days in summer, and every 14 days in winter using the static closed chamber method (De Klein and Harvey, 2013). This method is one of the most popular tools for flux measurements from agricultural soil (De Klein and Harvey., 2013). A polyvinyl chloride (PVC) chamber measured carbon dioxide (CO_2), methane (CH_4), and nitrous oxide (N_2O) efflux. Gas sampling was conducted at 9-10 am at 0, 30, and 60 min time points. At each time point, a 20 ml gas sample was taken by inserting a needle attached to a 20 ml syringe in the sampling port and transferred into 12-ml pre-vacuumed vials sealed with butyl rubber septa (Glass vials (e.g. Exetainer®, Labco Limited, High Wycombe, UK)).

Gas chromatography (Teif Gostar Faraz, TG 2552, Iran; Brucker, Germany) was used for the analysis, with concentrations of N_2O, CH_4, and CO_2 measured using an electron capture detector (ECD), a flame ionization detector (FID), and a thermal conductivity detector (TCD), respectively (Al-Shammary et al. 2022). The fluxes were calculated based on changes in linear concentration gradient over time and on the ratio between chamber volume and soil surface area (Liebig et al. 2010; De Klein and Harvey., 2013; Bayer et al. 2014). Linear interpolation of data points and the integration of the underlying area were used to calculate the cumulative rate of GHG fluxes (Sainju et al. 2012; Wegner et al. 2018).

Yield-scaled CO_2 equivalent GHG fluxes were determined by dividing the global warming potential (GWP) of GHG fluxes in CO_2 equivalents by dry yield, with CH_4 concentration assumed to be zero, as it constantly was below the detection level (Johnson et al. 2012; Bayer et al. 2014; Hurisso et al. 2016). Equations (1) and (2) were used for calculations.

$$Yield-scaled\ emission\left(MgCO_{2\_}eq.Mg\ dry\ yield^{-1}\right)=\frac{GWP\left(MgCO_{2\_}eq\right)}{Dry\ yield\,(Mg)} \quad (1)$$

$$GWP=\left(CO_2\times 1\right)+\left(N_2O\times 298\right)+\left(CH_4\times 25\right) \quad (2)$$

Yield Measurement

Maize and wheat yields within each plot were determined using a 1m×1m quadrat. The entire harvested plants were dry-weighted for each plot, and the mean was calculated as yield.

Statistical analysis

The general linear models (GLM) procedure in SAS 9.4 software (SAS Institute Inc., Cary, NC, USA) was used for data analysis. A mean comparison was performed by using the Duncan method at the 0.05 statistical significance level.

Results and discussion

Crop yield and GWP of GHG emissions in maize-wheat cropping rotation under NT and CT systems

In the NT system, the addition of crop residue positively impacted maize yield, with significant increases observed in full residue retention (R_{100}) compared to residue removal (R_0). However, no significant differences were observed between R_{50} and R_0 (Fig. 2A). Conversely, In the CT system, residue had no significant impact on maize yield (Fig. 2B). Wheat yield in the NT system increased with rising residue amounts in R_{100} and R_{50} compared to R_0 (Fig. 2C). In the CT system, wheat yield significantly increased in R_{100} compared to R_0, but no significant differences were noted between R_{50} and R_0 treatments (Fig. 2D). The enhanced crop yield attributed to crop residue can be influenced by improved soil quality, regulated soil temperature, increased soil organic matter, and higher nutrient availability (Choudhury et al. 2014; Mu et al. 2016; Pant et al. 2017; Maw et al. 2019). Conversely, the decreased crop yield in residue removal can be linked to reduced water availability, high daily soil temperature fluctuations, increased soil compaction, augmented surface runoff, and lower nutrient intake (Blanco-Canqui and Lal, 2009; Cherubin et al. 2018; Carvalho et al. 2019; Cherubin et al. 2021). For a more in-depth discussion on the crop yield response to crop residue management in this experiment, refer to Mirzaei et al. (2021).

Full retention of crop residue resulted in higher GHG emissions during the maize season under the NT system, with R_{100} showing a significant increase compared to R_0. However, no significant differences were observed between R_{100} and R_{50} treatments (Fig. 3A). In the CT system, the GWP of GHG in maize showed a significant increase in R_{100} and R_{50} compared to R_0 (Fig. 3B). The GWP index for the wheat crop, under both systems, also increased with rising residue amounts, and R_{100} and R_{50} both showed a significant increase compared to R_0 (Figs. 3C and 3D). In line with our findings, Dendooven et al. (2012) reported that, under semi-arid conditions in Mexico, removing crop residue reduced the GWP of GHG 1.3 times in a wheat-maize rotation. Similarly, Zhang et al. (2014) found that residue treatments significantly increased GWP by 9-30% relative to no residue treatment during a rice-growing season in China. Enhanced GWP in crop residue treatment is attributed to both crop residue and GHG emissions from the soil. Crop residue plays a crucial role in GHG emissions by altering carbon (C) and nitrogen (N) dynamics (Guzman et al. 2015; Nawaz et al. 2017; Seiz et al. 2019; Essich et al. 2020; Al-Shammary et al. 2023), and indirectly influencing the soil environment (Baggs et al. 2006; Taghizadeh-Toosi et al. 2021). The lower GWP of GHG in plant residue removal treatment may be due to reduced C and N uptake into the soil, along with microclimatic variations related to changes in soil cover (Jin et al. 2014). In Brazil, Gonzaga et al. (2019) also found a reduction in N2O emissions under total sugarcane straw removal. However, indiscriminate sugarcane straw removal led to reduced crop yields (Carvalho et al. 2019), soil C stocks (Tenelli et al. 2021), and soil health (Cherubin et al. 2021).

The effect of crop residue on YSE in maize-wheat cropping rotation under NT and CT systems

In the NT system, maize YSE was not significantly affected by crop residues (Fig. 4A), potentially due to the short-term duration of the corn season, insufficient for crop residue to show their true effect. However, crop residue

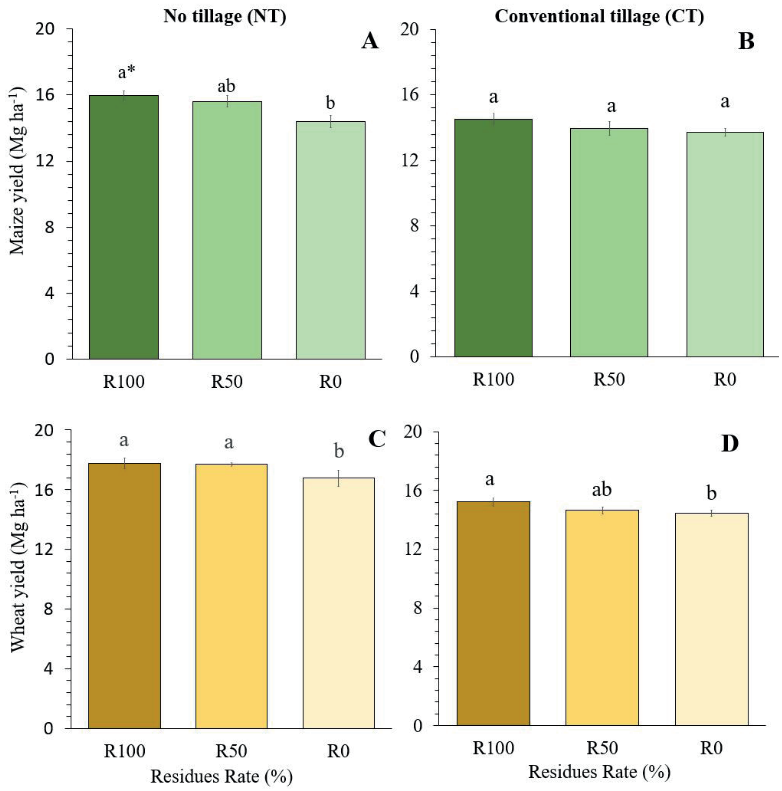

*. Similar letters indicate no significant difference. Whiskers represent standard error (n=3).

Fig. 2. Impact of residue rate on seasonal maize (A and B) and wheat (C and D) yield under NT (left) and CT (right) systems

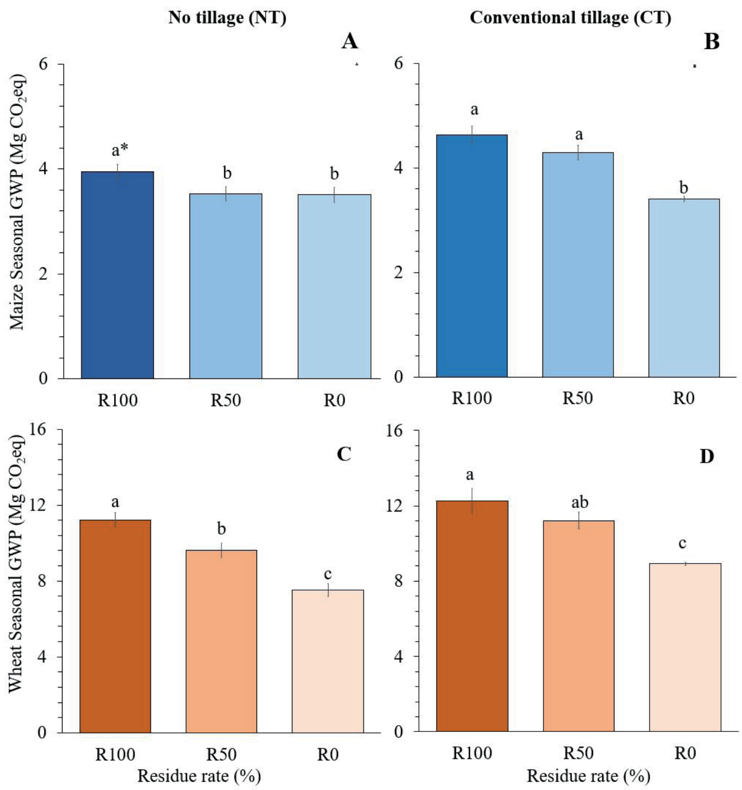

* Similar letters indicate no significant difference. Whiskers represent standard error (n=3).

Fig. 3. Impact of residue rate on maize (A and B) and wheat (C and D) seasonal GWP of GHG fluxes under NT (left) and CT (right) systems

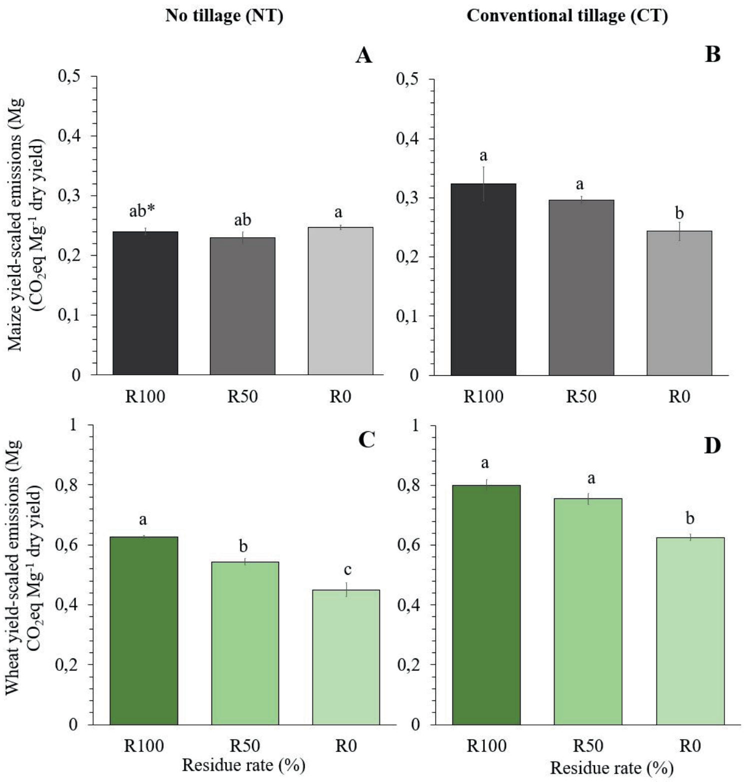

* Similar letters indicate no significant difference. Whiskers represent standard error (n=3).

Fig. 4. Impact of residue rate on maize (A and B) and wheat (C and D) YSE under NT (left) and CT (right) systems

rates significantly impacted ($p < 0.05$) YSE for wheat (Fig. 4B). The highest amount of YSE for wheat (0.62 Mg CO_2eq Mg^{-1} dry yield) was obtained from the R_{100} treatment, 39 % higher compared to the R_0 treatment (0.45 Mg CO_2eq Mg^{-1} dry yield). Additionally, R_{50} (0.54 Mg CO_2eq Mg^{-1} dry yield) resulted in a 20 % increase over R_0.

In the CT system, YSE for both maize and wheat crops increased with rising residue rates (Figs. 4C and 4D), although no significant differences were observed between R_{100} and R_{50}. For maize, R_{100} (0.32 Mg CO_2eq Mg^{-1} dry yield) and R_{50} (0.30 Mg CO_2eq Mg^{-1} dry yield) led to 33% and 25% increases in YSE compared to R_0 (0.24 Mg CO_2eq Mg^{-1} dry yield). Similarly, for wheat, 28% and 20% increases in YSE were noted in R_{100} (0.8 Mg CO_2eq Mg^{-1} dry yield) and R_{50} (0.75 Mg CO_2eq Mg^{-1} dry yield) compared to R_0 (0.62 Mg CO_2eq Mg^{-1} dry yield).

Higher YSE for wheat and maize in residue treatments compared to residue removal could be attributed to the strong influence of residue on the GWP of GHG relative to crop yield. Compared to R_0, R_{100}, and R_{50} led to 6% and ~2% increases in maize yield under the CT system, respectively (Fig. 2B), while the GWP of GHG for this crop showed 36% and 26% increases for R_{100} and R_{50} under the CT, respectively (Fig. 3B). Furthermore, under the NT system, wheat yields were 6% and 5.5% higher for R_{100} and R_{50} than R_0, respectively, whereas, in the CT system, R_{100} and R_{50} resulted in 5% and 1% higher yields than R_0 (Figs. 2C and 2D). In addition, the GWP of GHG for wheat was 50% and 28% higher in R_{100} and R_{50} than in R_0 under the NT system. These quantities were equivalent to 37% and 25% under the CT system (Figs. 3C and 3D).

In the CT system, there were no significant differences in YSE for both maize and wheat crops between R_{100} and R_{50} treatments (Figs. 4B and 4D) due to the lack of significant differences between GWP and crop yield in these two treatments (Figs. 2B and 2D; 3B and 3D). In both tillage systems, YSE was higher in wheat than in maize cultivation (Fig. 4). This difference is primarily driven by the higher GWP of GHG emissions in wheat than in maize (Fig. 3). Additionally, the longer crop season of wheat (November 2018 – July 2019) compared to maize (July 2018 – October 2018) contributes to higher emissions of GHG.

Our results, indicating higher YSE in areas with substantial crop residue maintenance, align with data reported in rice and rice-wheat cropping systems in China (e.g., Feng et al. 2013; Yao et al. 2013; Zhang et al. 2015). However, Pratibha et al. (2016) reported lower YSE with an increase in crop residue and a decrease in tillage intensity for both pigeon pea and castor crops in semi-arid regions of Southern India. Zhang et al. (2014) reported that residue mulching decreased YSE for rice by 35-72% relative to no residue treatment in China. These discrepancies with other studies highlight the importance of considering different residue management practices and their duration.

Conclusions

The assessment of cropping systems' effects on crop YSE is valuable for selecting innovative and promising management practices to balance higher yields and lower GHG emissions. Our findings demonstrate that crop residue removal mitigates wheat and maize YSE under both CT and NT systems. In addition, YSE was higher for both crops under CT compared to the NT system. Furthermore, wheat had higher YSE than maize under both tillage systems. Despite the lower YSE in crop residue removal, this practice negatively impacts crop productivity, C sequestration, soil health, and biodiversity. Additionally, residue removal accelerates soil quality degradation. Thus, considering all these aspects, retaining 50% of post-harvest crop residue in the field may be considered as a more sustainable crop residue management in the study area. Finally, considering the perspectives of farmers, particularly in terms of economic viability, is essential for the successful implementation of new management strategies.

Ethical approval statement

The authors declare no known competing financial interests or personal relationships that could have influenced the work reported in this paper.

This research does not involve human or animal participants.

All authors consent to the submission of this manuscript to this journal.

Availability of data

The data that support the findings of this study are available from the corresponding author [ACC] upon reasonable request.

REFERENCES

Abalos D., Jeffery S., Drury C.F. & Wagner-Riddle, C. (2016). Improving fertilizer management in the US and Canada for N2O mitigation: understanding potential positive and negative side-effects on corn yields. Agric. Ecosyst. Environ. 221 214–21.

Al-Shammary, A.A.G., Caballero-Calvo, A., Abbas Jebur, H., Khalbas, M.I. & Fernández-Gálvez, J. (2022). A novel heat-pulse probe for measuring soil thermal conductivity: Field test under different tillage practices. Computers and Electronics in Agriculture, 202, 107414, 1-13. https://doi.org/10.1016/j.compag.2022.107414

Al-Shammary, A. A. G., Al-Shihmani, L. S. S., Caballero-Calvo, A., & Fernández-Gálvez, J. (2023). Impact of agronomic practices on physical surface crusts and some soil technical attributes of two winter wheat fields in southern Iraq. Journal of Soils and Sediments, 1-20. https://doi.org/10.1007/s11368-023-03585-w

Baggs, E. M., Chebii, J., and J. K. Ndufa (2006). A short-term investigation of trace gas emissions following tillage and no-tillage of agroforestry residues in western Kenya. Soil and Tillage Research. 90(1-2): 69-76.

Bao, X., Wen, X., Sun, X., & Bao, G. (2022). The effects of crop residues and air temperature on variations in interannual ecosystem respiration in a wheat-maize crop rotation in China. Agriculture, Ecosystems & Environment, 325, 107728.

Battaglia, M., Thomason, W., Fike, J. H., Evanylo, G. K., von Cossel, M., Babur, E., ... & Diatta, A. A. (2021). The broad impacts of corn stover and wheat straw removal for biofuel production on crop productivity, soil health and greenhouse gas emissions: A review. Gcb Bioenergy, 13(1), 45-57.

Bayer, C., de Souza Costa, F., Pedroso, G. M., Zschornack, T., Camargo, E. S., de Lima, M. A., ... & Macedo, V. R. M. (2014). Yield-scaled greenhouse gas emissions from flood irrigated rice under long-term conventional tillage and no-till systems in a Humid Subtropical climate. Field Crops Research, 162, 60-69.

Blanco-Canqui, H., & Lal, R. (2009). Corn stover removal for expanded uses reduces soil fertility and structural stability. Soil Science Society of America Journal, 73(2), 418-426.

Bossio, D. A., Cook-Patton, S. C., Ellis, P. W., Fargione, J., Sanderman, J., Smith, P., ... & Griscom, B. W. (2020). The role of soil carbon in natural climate solutions. Nature Sustainability, 3(5), 391-398.

Carvalho, J. L. N., Menandro, L. M. S., de Castro, S. G. Q., Cherubin, M. R., Bordonal, R. D. O., Barbosa, L. C., ... & Castioni, G. A. F. (2019). Multilocation straw removal effects on sugarcane yield in south-central Brazil. BioEnergy Research, 12(4), 813-829.

Ceschia, E., Béziat, P., Dejoux, J. F., Aubinet, M., Bernhofer, C., Bodson, B., et al. (2010). Management effects on net ecosystem carbon and GHG budgets at European crop sites. Agric. Ecosyst. Environ, 139 (3), 363–383. doi:10.1016/ j.agee.2010.09.020.

Cherubin, M. R., Bordonal, R. O., Castioni, G. A., Guimaraes, E. M., Lisboa, I. P., Moraes, L. A., ... & Carvalho, J. L. (2021). Soil health response to sugarcane straw removal in Brazil. Industrial Crops and Products, 163, 113315.

Cherubin, M. R., Oliveira, D. M. D. S., Feigl, B. J., Pimentel, L. G., Lisboa, I. P., Gmach, M. R., ... & Cerri, C. C. (2018). Crop residue harvest for bioenergy production and its implications on soil functioning and plant growth: A review. Scientia Agricola, 75, 255-272.

Choudhury, S.G.; Srivastava, S.; Singh, R.; Chaudhari, S.; Sharma, D.; Singh, S.; Sarkar, D. (2014). Tillage and residue management effects on soil aggregation, organic carbon dynamics and yield attribute in rice–wheat cropping system under reclaimed sodic soil. J. Soil Tillage Res. 136, 76–83.

Collins, H.P., P.A. Fay, E. Kimura, S. Fransen, and A. Himes (2017). Intercropping with switchgrass improves net greenhouse gas balance in hybrid poplar plantations on a sand soil. Soil Sci. Soc. Am. J. 81:781–795. doi:10.2136/ sssaj2016.09.0294.

Dendooven, L., Patiño-Zúñiga, L., Verhulst, N., Luna-Guido, M., Marsch, R., & Govaerts, B. (2012). Global warming potential of agricultural systems with contrasting tillage and residue management in the central highlands of Mexico. Agriculture, Ecosystems & Environment, 152, 50-58.

De Klein, C., & Harvey, M. (2013). Nitrous Oxide Chamber Methodology Guidelines, Global Research Alliance on Agricultural Greenhouse Gases. Publisher: Ministry of Primary Industries, Wellington, New Zealand.

Drury, C. F., Woodley, A. L., Reynolds, W. D., Yang, X. M., Phillips, L. A., Rehmann, L., & Calder, W. (2021). Impacts of corn stover removal on carbon dioxide and nitrous oxide emissions. Soil Science Society of America Journal, 85(5), 1334-1348.

Essich, L., Nkebiwe, P. M., Schneider, M., & Ruser, R. (2020). Is Crop Residue Removal to Reduce N2O Emissions Driven by Quality or Quantity? A Field Study and Meta-Analysis. Agriculture, 10(11), 1-20.

Essich, L., Nkebiwe, P. M., Schneider, M., & Ruser, R. (2020). Is Crop Residue Removal to Reduce N2O Emissions Driven by Quality or Quantity? A Field Study and Meta-Analysis. Agriculture, 10(11), 1-20.

Feng, J., Chen, C., Zhang, Y., Song, Z., Deng, A., Zheng, C., & Zhang, W. (2013). Impacts of cropping practices on yield-scaled greenhouse gas emissions from rice fields in China: a meta-analysis. Agriculture, Ecosystems & Environment, 164, 220-228.

Gan, Y., Liang, C., Huang, G., Malhi, S. S., Brandt, S. A., and Katepa-Mupondwa, F. (2012). Carbon footprint of canola and mustard is a function of the rate of N fertilizer. Int. J. Life Cycle Assess. 17 (1), 58–68. doi:10.1007/s11367-011-0337-z

Gonzaga, L. C., Zotelli, L. D. C., de Castro, S. G. Q., de Oliveira, B. G., Bordonal, R. D. O., Cantarella, H., & Carvalho, J. L. N. (2019). Implications of sugarcane straw removal for soil greenhouse gas emissions in São Paulo State, Brazil. BioEnergy Research, 12(4), 843-857.

Guzman, J., Al-Kaisi, M., & Parkin, T. (2015). Greenhouse gas emissions dynamics as influenced by corn residue removal in continuous corn system. Soil Science Society of America Journal, 79(2), 612-625.

Hurisso, T. T., Norton, U., Norton, J. B., Odhiambo, J., Del Grosso, S. J., Hergert, G. W., & Lyon, D. J. (2016). Dryland Soil Greenhouse Gases and Yield-Scaled Emissions in No-Till and Organic Winter Wheat–Fallow Systems. Soil Science Society of America Journal, 80(1), 178-192.

Intergovernmental Panel on Climate Change. Agriculture, Forestry and Other Land Use (AFOLU) (2015). In Climate Change 2014, Mitigation of Climate Change; Contribution of Working Group III to the Fifth Assessment Report of the Intergovernmental Panel on Climate Change; Edenhofer, O., Pichs-Madruga, R., Sokona, Y., Farahani, E., Kadner, S., Seyboth, K., Adler, A., Baum, I., Brunner, S., Eickemeier, P., Eds.; Cambridge University Press: Cambridge, UK; New York, NY, USA, 2014; Chapter 11.

IPCC, 2021. In: Masson-Delmotte, V., Zhai, P., Pirani, A., Connors, S.L., P´ean, C., Berger, S., Caud, N., Chen, Y., Goldfarb, L., Gomis, M.I., Huang, M., Leitzell, K., Lonnoy, E., Matthews, J.B.R., Maycock, T.K., Yelekçi, W.T.O., Yu, R., Zhou, B. (Eds.), Climate Change 2021: the Physical Science Basis. Contribution of Working Group I to the Sixth Assessment Report of the Intergovernmental Panel on Climate Change. Cambridge.

Jin, V. L., Baker, J. M., Johnson, J. M. F., Karlen, D. L., Lehman, R. M., Osborne, S. L., ... & Wienhold, B. J. (2014). Soil greenhouse gas emissions in response to corn stover removal and tillage management across the US Corn Belt. BioEnergy Research, 7(2), 517-527.

Johnson, J. M., Weyers, S. L., Archer, D. W., & Barbour, N. W. (2012). Nitrous oxide, methane emission, and yield-scaled emission from organically and conventionally managed systems. Soil Science Society of America Journal, 76(4), 1347-1357.

Li, Y., Feng, H., Wu, W., Jiang, Y., Sun, J., Zhang, Y., Cheng, H., Li, C., Siddique, K.H. and Chen, J., 2022. Decreased greenhouse gas intensity of winter wheat production under plastic film mulching in semi-arid areas. Agricultural Water Management, 274, p.107941.

Linquist, B., Groenigen, K. J., Adviento-Borbe, M. A., Pittelkow, C., and Kessel, C. (2012). An agronomic assessment of greenhouse gas emissions from major cereal crops. Glob. Change Biol. 18 (1), 194–209. doi:10.1111/j.1365- 2486.2011.02502.x.

Lal, R., Mello, F. F. D. C., Damian, J. M., Cherubin, M. R., & Cerri, C. E. P. (2021). Soil carbon sequestration through adopting sustainable management practices: potential and opportunity for the American countries. Ed. Instituto Interamericano de Cooperación para la Agricultura.

Liu, W., Liu, Y., Liu, G., Xie, R., Ming, B., Yang, Y., ... & Hou, P. (2022). Estimation of maize straw production and appropriate straw return rate in China. Agriculture, Ecosystems & Environment, 328, 107865.

Mancinelli, R., Marinari, S., Allam, M. and Radicetti, E., 2020. Potential role of fertilizer sources and soil tillage practices to mitigate soil CO2 emissions in mediterranean potato production systems. Sustainability, 12(20), p.8543.

Mancinelli, R., Marinari, S., Atait, M., Petroselli, V., Chilosi, G., Jasarevic, M., Catalani, A., Abideen, Z., Mirzaei, M., Allam, M. and Radicetti, E., 2023. Durum Wheat–Potato Crop Rotation, Soil Tillage, and Fertilization Source Affect Soil CO2 Emission and C Storage in the Mediterranean Environment. Land, 12(2), 326.Maw, M.J.; Goyne, K.W.; Fritschi, F.B. (2019). Soil carbon changes following conversion to annual biofuel feedstocks on marginal lands. Agron. J., 111, 4–13.

Minasny, B., Malone, B. P., McBratney, A. B., Angers, D. A., Arrouays, D., Chambers, A., et al. (2017). Soil carbon 4 per mille. Geoderma, 292, 59–86. doi:10.1016/j.geoderma.2017.01.002.

Mirzaei, M., Gorji Anari, M., Razavy-Toosi, E., Asadi, H., Moghiseh, E., Saronjic, N., & Rodrigo-Comino, J. (2021). Preliminary Effects of Crop Residue Management on Soil Quality and Crop Production under Different Soil Management Regimes in Corn-Wheat Rotation Systems. Agronomy, 11(2), 302.

Mirzaei, M., Anari, M. G., Razavy-Toosi, E., Zaman, M., Saronjic, N., Zamir, S. M., ... & Caballero-Calvo, A. (2022). Crop residues in corn-wheat rotation in a semi-arid region increase CO2 efflux under conventional tillage but not in a no-tillage system. Pedobiologia, 93, 150819. https://doi.org/10.1016/j.pedobi.2022.150819

Mirzaei, M., Gorji Anari, M., Saronjic, N., Sarkar, S., Kral, I., Gronauer, A., Mohammed, S. and Caballero-Calvo, A., 2023. Environmental impacts of corn silage production: influence of wheat residues under contrasting tillage management types. Environmental Monitoring and Assessment, 195(1), 171. https://doi.org/10.1007/s10661-022-10675-8

Mirzaei, M., Gorji Anari, M., Taghizadeh-Toosi, A., Zaman, M., Saronjic, N., Mohammed, S., Szabo, S., Caballero-Calvo, A. (2022). Soil nitrous oxide emissions following crop residues management in corn-wheat rotation under conventional and no-tillage systems. Air, Soil and Water Research, 15, 1-12. https://doi.org/10.1177/11786221221128789

Mohammed, S., Mirzaei, M., Pappné Törő, Á., Anari, M. G., Moghiseh, E., Asadi, H., ... & Harsányi, E. (2022). Soil carbon dioxide emissions from maize (Zea mays L.) fields as influenced by tillage management and climate. Irrigation and Drainage, 71(1), 228-240.

Mosier, A.R., Halvorson, A.D., Reule, C.A., Liu, X.J.J. (2006). Net global warming potential and greenhouse gas intensity in irrigated cropping systems in northeastern Colorado. Journal of Environmental Quality 35, 1584–1598.

Mu, X.; Zhao, Y.; Liu, K.; Ji, B.; Guo, H.; Xue, Z.; Li, C. (2016). Responses of soil properties, root growth and crop yield to tillage and crop residue management in a wheat–maize cropping system on the North China Plain. Eur. J. Agron, 78, 32–43.

Nawaz, A., Lal, R., Shrestha, R. K., & Farooq, M. (2017). Mulching Affects Soil Properties and Greenhouse Gas Emissions Under Long-Term No-Till and Plough-Till Systems in Alfisol of Central Ohio. Land Degradation & Development, 28(2), 673-681.

O'Neill, M., Lanigan, G. J., Forristal, P. D., & Osborne, B. A. (2021). Greenhouse Gas Emissions and Crop Yields From Winter Oilseed Rape Cropping Systems are Unaffected by Management Practices. Frontiers in Environmental Science, 377.

Ogle, S. M., Alsaker, C., BaldockBernoux, J. M., Bernoux, M., Breidt, F. J., McConkey, B., et al. (2019). Climate and Soil Characteristics Determine where No-Till Management Can Store Carbon in Soils and Mitigate Greenhouse Gas Emissions. Sci. Rep. 9, 11665. doi:10.1038/s41598-019-47861-7.

Pant, P.K.; Ram, S.; Singh, V. (2017). Yield and soil organic matter dynamics as affected by the long-term use of organic and inorganic fertilizers under rice–wheat cropping system in subtropical mollisols. J. Agric. Res, 6, 399–409.

Paustian, K., Lehmann, J., Ogle, S., Reay, D., Robertson, G. P., & Smith, P. (2016). Climate-smart soils. Nature, 532(7597), 49-57.

Pooniya, V., Zhiipao, R. R., Biswakarma, N., Kumar, D., Shivay, Y. S., Babu, S., ... & Lama, A. (2022). Conservation agriculture based integrated crop management sustains productivity and economic profitability along with soil properties of the maize-wheat rotation. Scientific reports, 12(1), 1-13.

Pratibha, G., Srinivas, I., Rao, K. V., Shanker, A. K., Raju, B. M. K., Choudhary, D. K., ... & Maheswari, M. (2016). Net global warming potential and greenhouse gas intensity of conventional and conservation agriculture system in rainfed semi arid tropics of India. Atmospheric Environment, 145, 239-250.

Radicetti, E., Campiglia, E., Langeroodi, A.S., Zsembeli, J., Mendler-Drienyovszki, N. and Mancinelli, R., 2020. Soil carbon dioxide emissions in eggplants based on cover crop residue management. Nutrient Cycling in Agroecosystems, 118, 39-55.

Radicetti, E., Osipitan, O.A., Langeroodi, A.R.S., Marinari, S. and Mancinelli, R., 2019. CO2 flux and C balance due to the replacement of bare soil with agro-ecological service crops in Mediterranean environment. Agriculture, 9(4), 71.

Seiz, P., Guzman-Bustamante, I., Schulz, R., Müller, T., & Ruser, R. (2019). Effect of crop residue removal and straw addition on nitrous oxide emissions from a horticulturally used soil in South Germany. Soil Science Society of America Journal, 83(5), 1399-1409.

Six, J.; Ogle, S.M.; Conant, R.T.; Mosier, A.R.; Paustian, K. (2004). The potential to mitigate global warming with no-tillage management is only realized when practised in the long term. Glob. Chang. Biol, 10, 155–160.

Tabari, H., & Talaee, P. H. (2011). Analysis of trends in temperature data in arid and semi-arid regions of Iran. Global and Planetary Change, 79(1-2), 1-10.

Taghizadeh-Toosi, A., Janz, B., Labouriau, R., Olesen, J. E., Butterbach-Bahl, K., & Petersen, S. O. (2021). Nitrous oxide emissions from red clover and winter wheat residues depend on interacting effects of distribution, soil N availability and moisture level. Plant and Soil, 1-18.

Tenelli, S., Bordonal, R. O., Cherubin, M. R., Cerri, C. E. P., & Carvalho, J. L. N. (2021). Multilocation changes in soil carbon stocks from sugarcane straw removal for bioenergy production in Brazil. GCB Bioenergy, 13(7), 1099-1111.

Trumbore, S. (2000). Age of soil organic matter and soil respiration: radiocarbon constraints on belowground C dynamics. Ecol. Appl. 10 (2), 399–411.

Van Groenigen, J. W., Velthof, G. L., Oenema, O., Van Groenigen, K. J., Van Kessel, C., (2010). Towards an agronomic assessment of N2O emissions: a case study for arable crops, European Journal of Soil Science, 61, 903–913.

Van Kessel, C.; Venterea, R.; Six, J.; Adviento-Borbe, M.A.; Linquist, B.; Van Groenigen, K.J. (2013). Climate, duration, and N placement determine N2O emissions in reduced tillage systems: A meta-analysis. Glob. Chang. Biol., 19, 33–44.

Vasconcelos, A. L. S., Cherubin, M. R., Feigl, B. J., Cerri, C. E., Gmach, M. R., & Siqueira-Neto, M. (2018). Greenhouse gas emission responses to sugarcane straw removal. Biomass and Bioenergy, 113, 15-21.

Xia, L.; Lam, S.K.; Chen, D.; Wang, J.; Tang, Q.; Yan, X. (2017). Can knowledge-based N management produce more staple grain with lower greenhouse gas emission and reactive nitrogen pollution? A meta-analysis. Glob. Chang. Biol., 23, 1917–1925.

Yao, Z., Zheng, X., Wang, R., Xie, B., Butterbach-Bahl, K., & Zhu, J. (2013). Nitrous oxide and methane fluxes from a rice–wheat crop rotation under wheat residue incorporation and no-tillage practices. Atmospheric Environment, 79, 641-649.

Zhang, L., Zheng, J., Chen, L., Shen, M., Zhang, X., Zhang, M., ... & Zhang, W. (2015). Integrative effects of soil tillage and straw management on crop yields and greenhouse gas emissions in a rice–wheat cropping system. European Journal of Agronomy, 63, 47-54.

Zhang, Z. S., Cao, C. G., Guo, L. J., & Li, C. F. (2014). The effects of rape residue mulching on net global warming potential and greenhouse gas intensity from No-Tillage paddy fields. The Scientific World Journal, 2014.

Zhao, X.; Liu, S.; Pu, C.; Zhang, X.; Xue, J.; Zhang, R.; Wang, Y.; Lal, R.; Zhang, H.; Chen, F. (2016). Methane and nitrous oxide emissions under no-till farming in China: A meta-analysis. Glob. Chang. Biol., 22, 1372–1384.

RESEARCH PAPER

ASSESSING SPATIAL DISTRIBUTION AND ACCESSIBILITY OF PUBLIC PRIMARY SCHOOLS IN MAFRAQ CITY, JORDAN: A GIS-BASED APPROACH

Abed Alhameed AlFanatseh*
Al-Hussein Bin Talal University, Faculty of Arts, Department of Geography, P.O. Box, 20, Ma'an, Jordan
***Corresponding author:** abdalhamed.A.Alfanatsa@ahu.edu.jo
Received: January 26st, 2023 / Accepted: November 14th, 2023 / Published: December 31st, 2023
https://DOI-10.24057/2071-9388-2023-2750

ABSTRACT. The spatial accessibility of educational services is important in planning and managing educational services. This study seeks to evaluate the spatial distribution of basic schools, find the optimal location for the distribution of those schools, and develop solutions and proposals to improve accessibility by creating new schools. p-median models were applied to allocate sites. After analysing the locations of schools and demand points (residential buildings) in the city of Mafraq, where this model tries to provide recommendations regarding the area that service should cover, the standards of the Ministry of Education were adopted; they stipulate that the distance between the site of the basic school and the residential building should range 750 m. Accordingly, two models were applied: The first scenario was applied to evaluate the current school sites, whereas the second suggested the establishment of new schools in underserved areas and the evaluation of the effectiveness of accessibility after the construction of new schools. The results of the study showed that the number of unserviced demand points according to the optimal criterion for distance of access is approximately 58.9%, while it decreased to 38% after proposing the establishment of 10 schools in new locations. The study concluded that the analysis of site allocation using p-median models is an effective method in the spatial planning of schools. It can assist decision-makers and urban planners in improving accessibility to primary schools by establishing new schools and upgrading access to existing schools in underserviced areas..

KEYWORDS: accessibility, spatial analysis, p-median models, primary schools, Mafraq city

CITATION: Abed Alhameed AlFanatseh (2023). Assessing Spatial Distribution And Accessibility Of Public Primary Schools In Mafraq City, Jordan: A Gis-Based Approach. Geography, Environment, Sustainability, 4(16), 133-143
https://DOI-10.24057/2071-9388-2023-2750

ACKNOWLEDGEMENTS: Thanks for Al-Hussein Bin Talal University and Ministry of Education for their logistic help.

Conflict of interests: The authors reported no potential conflict of interest.

INTRODUCTION

Public services are a human activity, and many sciences are involved in the study of this phenomenon; hence, the concept of public services differs according to the different sciences and encompass education, health, parks, and social and cultural centres. The importance of public services is highlighted when they are able to meet the needs of the population with the least effort, time and cost. This means that the service location should be close to the centre of the population density (Murray & Tong 2009). Educational service is one of the essential services to provide the city residents with. It is significant to take care of this service, plan for it, and follow up on it. Also, an attention must be paid to this service in terms of its distribution and its relationship to both population growth and distribution; this will considerably provide a geographical vision that contributes to urban planning and development programs. (Duwaikat, 2013).

In geography, there are two types of optimization techniques: (1) location–allocation models and (2) spatial suitability maps (Murray 2010). They both take a different path. The first method approaches it as a mathematical problem that must be solved in phases to identify acceptable methods. The second approach chooses a set of candidate places based on established spatial parameters. Location-allocation is a location theory development model that can be used to locate facilities spatially based on demand (Yasenovskiy & Hodgson 2007). The location–allocation model has mathematical characteristics and is a normative model to solve location problems (Utami et al. 2022) Location-allocation models in GIS are divided into seven main problems, which can be simplified into three subgroups: (1) p-median problems, (2) coverage problems and (3) competition problems.

Educational services in the Hashemite Kingdom of Jordan in general and the city of Mafraq in particular face difficulty in access. In recent years, Mafraq, similar to other Jordanian cities, has experienced an increase in population growth rates and urban expansion. This reflects negatively on the poor distribution of public services in it, especially educational services. What Mafraq city has witnessed as a result of the natural increase of the population and the influx of forced migration by Syrians to the city has put pressure on educational services, and there is an urgent need for educational services for all residents due to the increasing importance of education in our time.

The subject of this study is to improve the ease of access to the sites of primary public schools in Mafraq city using geographic information systems in accordance with the local standards of the Hashemite Kingdom of Jordan. The study relies on the standards of the Ministry of Education, requiring that the distance between the location of the basic school and the application points (residential building) range between 500-750 m. (Al-Dulaimi 2015). The current study utilizes the application of modern technologies such as GIS to build a spatial information base through which to produce applied maps to improve the ease of access to the locations of primary schools.

Thus, this study seeks to develop a geographic approach based on GIS to improve the accessibility and coverage of primary schools of Mafraq using the p-median model of site allocation. In addition, it endeavours to identify the number of candidate schools required to cover all or most of the demand points (for population) by identifying the proposed new optimal locations for basic schools. The study also aims to determine whether new schools should be established, leading to improving the ease of access to schools and helping to identify the future needs of the population of schools in light of the urban expansion witnessed in recent years by the city of Mafraq.

LITERATURE REVIEW

A literature review shows that researchers have much interest in educational services studies; some are interested in highlighting the spatial distribution pattern of schools. Abdul Jabbar & Laffta (2020) addressed the use of GIS in identifying differences in accessibility to private schools. Jiang et al. (2022) discussed the spatial pattern and factors influencing basic education resources in rural areas around major cities. Abraha (2019) also studied the evaluation of the spatial distribution pattern of schools by studying the characteristics of beneficiaries and analysing the obstacles that affect the efficiency of this service and the impact of location on different educational facilities. Another trend was concerned with the spatial distribution of schools in relation to population growth rates and evolution of the number of school centres Bulti et al. (2019), while others used some theories to evaluate school distribution, such as central place theory and efficiency distribution Yang et al. (2017). Some authors also suggested school mapping and geographic analysis of schools through spatial analysis and GIS (for example, the study of (Al-Enazi et al. 2016).

Site allocation models added another dimension in the development of studies related to the selection of school sites, as they benefited from the application of advanced algorithms. A series of recent studies indicated that some have shifted to the use of GIS-based site allocation models, which has been discussed by a large number of authors in previous studies. One study Menezes & Pizzolato (2014) examined locating public schools in fast expanding areas, applying the capacitated p-median and maximal covering location models. Mindahun & Asefa, (2019)applied a GIS-based location allocation model to improve geographic location and access to urban services. Utami et al. (2022) aimed to provide an alternative solution to the problem of empty space in the school division system and applied the p-median model (site allocation analysis) and service area analysis within the road network analysis within the GIS environment. In the same direction, some studies have focused on the use of geographic information systems as an educational decision support system and for the management of educational services. Iubadewo et al. (2013) examined the spatial distribution of primary schools to create a geographic database of schools and analyzed the pattern of distribution of schools. Al-Rasheed & El-Gamily, (2013) studied the use geographic information systems in the inventorying, mapping and analysis of educational facilities and unoccupied land reservations to improve planning and decision-making.

Some authors have also suggested providing a practical model for evaluating school sites in a way that helps planners improve access to school sites, the extent of their commitment to the conditions for choosing the optimal location and the effectiveness of providing these services in light of urban development to reach the optimal distribution of schools. Al-Sabbagh (2022) discussed site allocation as a model for establishing new schools and examined the appropriateness of location–allocation models for improving primary school access. Meena et al. (2022)applied site allocation models to primary school assessment and accessibility and applied the travelling salesman problem (TSP) to help choose the best path to school access. Fabiyi& Ogunyemi (2015) discussed post primary spatial re-engineering to enhance access to schools.

In previous studies, a large number of authors have presented a multi-objective model for site allocation that takes into account the reduced overall cost of travel, uneven access to schools, and incompatibility of uses. Mustapha et al. (2015) addressed assessing accessibility to private primary schools. Data analysis was performed using neighbour nearest analysis by performing a set of origin and destination (OD) matrices on the network dataset to assess the distance travelled to school by students. Rekha et al. (2020)studied site customization and accessibility models to improve spatial planning for educational services. Sumari et al. (2019)addressed the integration of accessibility models and location allocation in GIS as a proposed strategy for improving spatial planning for educational services. Batsaris et al. (2021) used the spatial decision support system (SDSS) to assist school location allocation decisions with the goal of reducing commuting distance to school from the perspective of capacity and proximity constraints.

Through the presentation of previous studies, we find that the present study constitutes a basis on which decision-makers can design a model to be used in planning and replanning the locations of primary schools in the future. It represents the first of its kind for Mafraq city, since the spatial distribution of school locations there has never been studied using GIS technology.

Study area

The city of Mafraq is located in the Hashemite Kingdom of Jordan 69 km to the northeast of the capital Amman, as shown in Fig.1. The total area of the city is 42 km^2, and the population of the city is 122785 (Department of General Statistics 2022), constituting 19.27% of the population of the Mafraq Governorate; the number of families in the city is 23590, and the population density of Mafraq City is 2923 inhabitants/km^2.The city of Mafraq is administratively divided into twenty-six residential neighbourhoods; the city centre is located within the old neighbourhoods, which contain most commercial and administrative activities. The city's name "Mafraq" stems from the fact that it is located at the crossroads of international roads heading to Syria in the north, Saudi Arabia in the south and Iraq in the east. Mafraq city played a historical role in the Islamic era since it has served on a major route for the Levantine pilgrimage. The city became one of the public transportation stations in the Ottoman Empire because of the presence of a Hejaz railway station there. From 1945 on, the city began to accelerate the local development process and witnessed a comprehensive service development renaissance that had the greatest impact on improving the features of life in the city and sparking urban advancement.

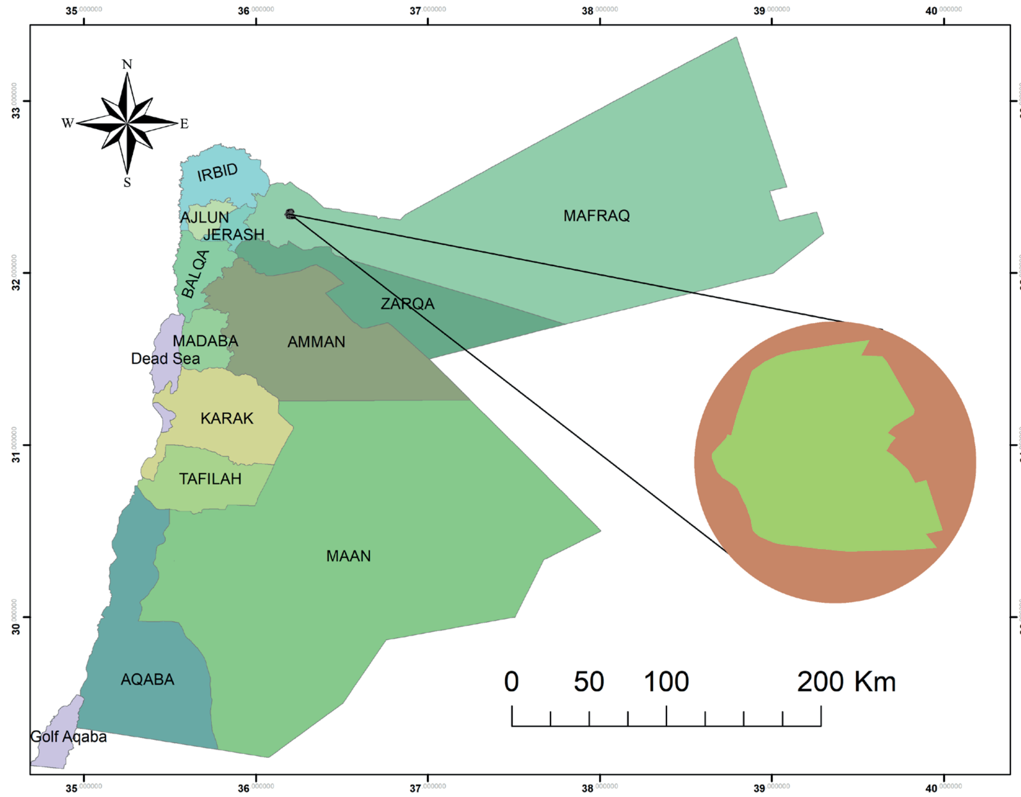

Fig. 1. Area targeted by the present study

MATERIALS AND METHODS

Spatial analysis of the accessibility of approach schools is attempted through geospatial techniques and includes data collection, spatial database creation, modelling and analysis of results to assess the location of schools in the city, as well as the development of candidate reality for improving the overall performance of the city's approach schools. The procedures used to carry out this study are summarized in Fig. 2. The methodology flow chart is shown. It involved collecting spatial and attribute data, including boundary data, road data, school location data, school raw data and census data.

Data sources

In any model for allocating sites, the location of the facilities, the sum of the demand points, and the supply network that meets the needs of the demand points are necessary to build the model. Accordingly, the present model applied here has used five basic maps with the coordinate reference system, Jordan Transverse Mercator (JTM) is a grid system created by the Royal Jordan Geographical Center (RJGC). The system is based on a 6° zone with the central meridian at 37° East. JTM is based on the 1924 International Hayford ellipsoid: School data were obtained from the school map of Mafraq City for 2021from the Ministry of Education, the road network for Mafraq City was obtained from the GIS Department at the Ministry of Public Works and Housing, and the location and administrative boundaries and population buildings of Mafraq City for 2021 were obtained from the GIS Section at the Department of Statistics. The data on population were obtained from the Department of Statistics, the General Population and Housing Census for 2015 and the population estimates for the city of Mafraq for 2021.Table 1. Data used in spatial analysis.

Preparing for analysis and processing study data

Conducting network analysis and location–allocation of primary schools in Mafraq city through tools a network analysis within the ArcGIS 10.4.1 software environment requires the preparation of the following maps

A- Preparing a base map of the city of Mafraq, (Fig. 3), with the coordinate reference system, (JTM) where the following layers appear:

1. The administrative boundary layer of the city of Mafraq in the form of an area (polygon)

2. The current school layer, in the form of points.

3. Road network layer: At this stage, the road map for Mafraq city has been prepared in the form of a polyline.

4. Preparing the map of residential buildings was prepared by relying on the ARC GIS program, where the built area was divided into a network of cells of equal dimensions (100 x100 m), These dimensions are suitable for the study area, numbering 4383 cells. A total of 2144

Table 1. Data used in spatial analysis

Data	Data Source	Type Data	Purpose of data
Map of the location	Department of statistics (2021)	shapefile (Polygon)	Showing the administrative divisions
Location of schools	Ministry of Education (2021)	shapefile (Points)	Identifying the available facilities
Residential buildings	Editing by Google Earth	shapefile (Polygon)	Identifying the residential areas to clarify the demand points
Road networks	Ministry of Public Works and Housing	shapefile (Polyline)	Clarifying the service coverage area

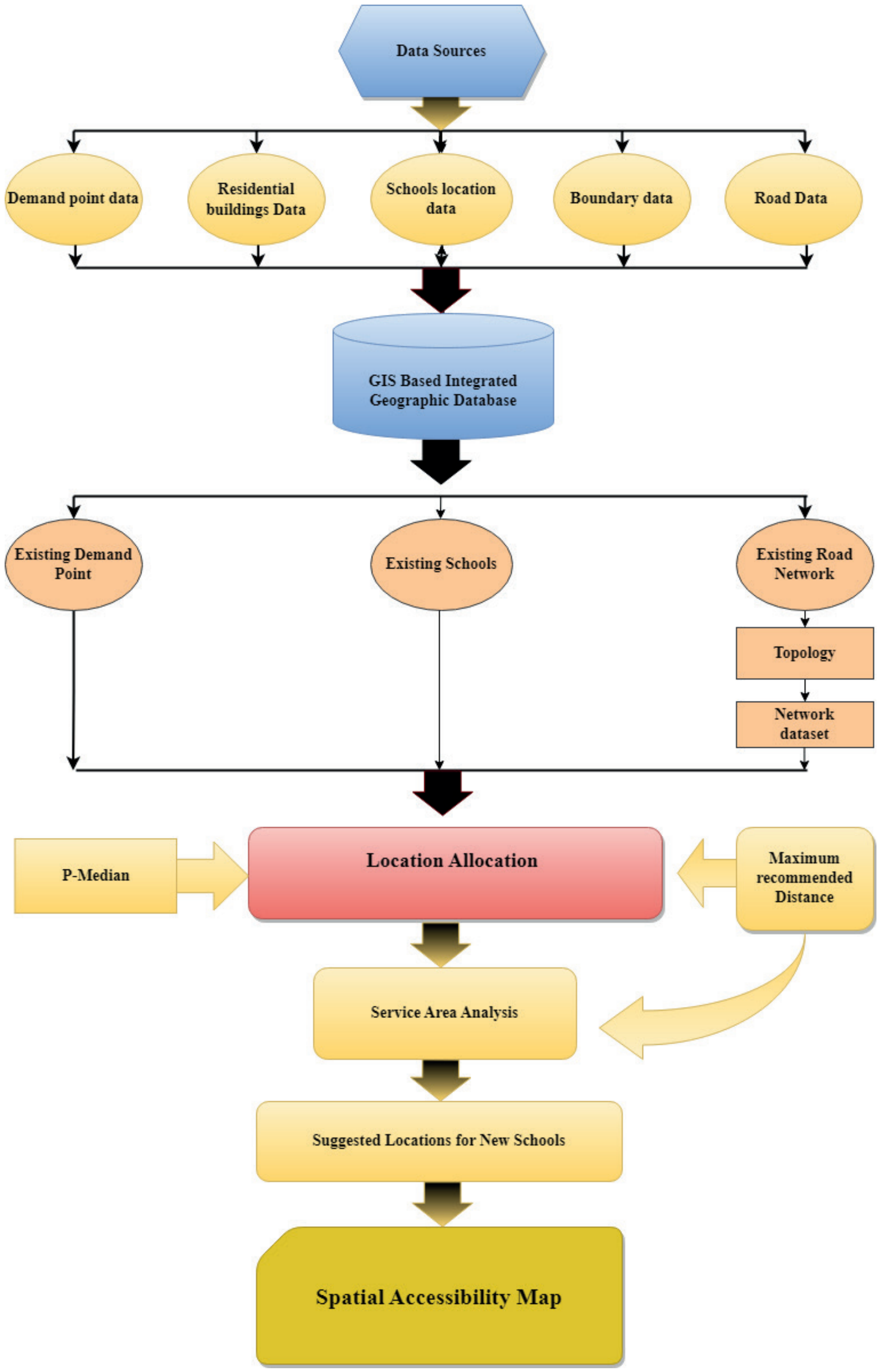

Fig. 2. Flowchart of the methodology used in the study

cells were excluded because they were not residential areas, while 2239 cells were retained for the purpose of determining demand points. The data (residential building network layer) have been converted from a cadastral layer (polygon) to a point layer (points)to be used as demand points to analyse the current locations of schools and study the proposed locations of schools and demand points at the same time.

B. It is necessary to build a dataset network that contains data tables, while working, the study classifies the roads into three types (i.e., main roads, side roads and secondary roads). The data related to the classified types of roads are grouped in columns in a table. These columns include: data about the names and the length of the roads in metres, data about the directions of the roads (i.e., one side or two-side roads), and the types of roads (main roads, side roads or highways) (AlFanatseh and Sababhi, 2023)

c. According to p-median problem, for specific demand points, the number (x) of facilities is calculated for the minimum total weights of the distances moving between facilities and demand. This assumes that the recipients of the service are using the nearest facility, and the equation of the p-median problem can be formulated as follows (Polo et al. 2015):

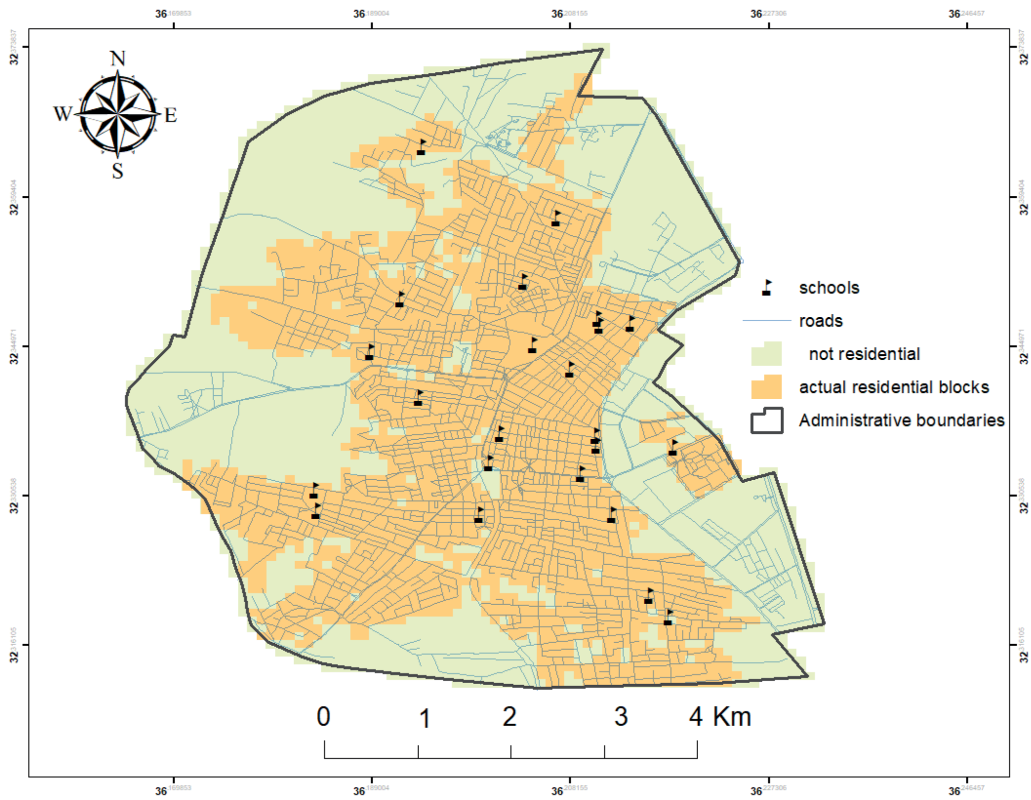

Fig. 3. Administrative divisions, road networks and the location of schools and the residential building areas in Mafraq

Maximize:

$$Z = \sum_{i} \sum_{j} a_i d_i jx_j$$

Subject to:

$$\sum_{j} xij = 1 \quad \forall i,$$

$$xij \le yj, \quad \forall i, \quad \forall j,$$

$$\sum_{jyj} = p,$$

$$xij, yi = \in \{0, 1\}.$$

Where:
i : Locations of demand.
j : Service sites.
dij: The shortest distance from the site (*i*) to the site(*j*).
x j: if the site is assigned (*i*) to site (*j*) 0 otherwise.
ai: Population on site (*i*)

RESULTS

Spatial Analysis Model for Choosing Appropriate Locations for New Schools

Building a spatial analysis model to choose the best place to establish a service is one of the proposed effective solutions for choosing the appropriate location for establishing a school at the city level. Spatial analysis methods are the most important planning tools for determining the proposed location's suitability. Designing a model to determine appropriate locations for new schools in Mafraq entailed completing the following steps:

Creating information layers for geographical variables related to the conditions for suitable locations for new schools. The most important criteria that were considered are summarized in Table 2.

This study used the Euclidean distance tool, which works at the expense of distances from the centre of the source cell (location) to the centres of all the surrounding cells. Each cell is appointed a value that represents the value of the source cell.

After defining the necessary parameters and determining spatial suitability, reclassifying all the informational layers was required. To achieve the goal for which the model was built, the distances were divided into ten periods using the equal interval method, and each period was given a specific value from one to ten. If the value was nine or ten, the distances would be of a large and close value. From the proposed location to be created, it will be highly convenient. If the value is one or two, the distance will be great, and it will be permanently inappropriate.

A weighted overlay was used on all the information layers, which were reclassified to produce a single information layer. The researcher accurately determines these using the weighted matching tool, and the program relies on them. The result of deriving a new information layer classified into new categories is that the categories of each layer overlap with others in all input layers. The criteria weighting and the relative importance of each were determined based on previous studies and research, in addition to the researcher's vision after reviewing the conditions of the study area and the lessons learned from the current school location. Next, Model Builder was utilized to determine appropriate locations for new schools. Model Builder is an application used to produce the final map, which includes areas that meet the selection conditions for the optimal location that were previously identified and excludes all areas that fail to meet these conditions (Fig. 4).

The final location suitability map divides the study area into two categories of suitable locations for establishing new schools in Mafraq. sites that were deemed suitable and sites that were deemed highly suitable. As shown in Fig. 5, which provides the results of the weighted map matching analysis, it determines the location's degree of suitability for establishing new schools

Table 2. Standards for new school locations in Mafraq

General Standards	Description
Land uses	It is not ideal to locate a construction site for educational institutions near commercial, industrial, religious or administrative districts. Therefore, such districts are accorded low weight values, while high weight values are given to residential, recreational and health districts, due to their high level of attractiveness for educational services.
Current school locations	The new location must be far from extant schools.
Slope	Choose flat areas to build new schools and avoid steep areas.
Population	Since the goal of building new schools is to serve the population, it is necessary to choose high-density areas and avoid new school construction in low-density areas.
Unused areas	Schools occupy urban land areas. When building the suitability model, construction priority is given to empty and unused areas.
Roads	It is necessary to determine the construction location for primary education schools. The proposed location must be easily accessible via the main roads.
Drainage networks	Avoid locating new school construction near watercourses and river valleys.
Dangerous locations	The construction site must be as far as possible from any source of potential risk or danger (e.g., fuel and gas stations).

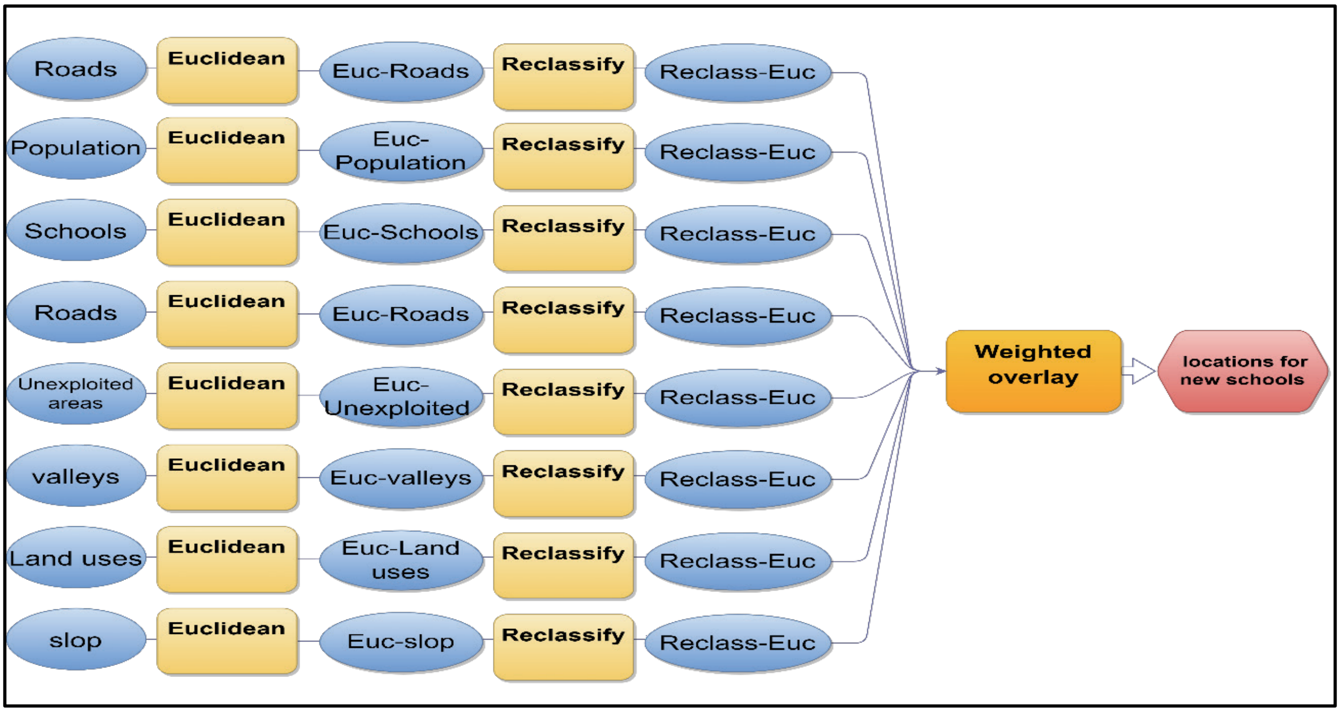

Fig. 4. Structural model for analysing the spatial suitability of new school locations in Mafraq

P-median modelling analysis

The site allocation model was created to improve accessibility to approach schools, such as by including the school layer and the request points layer in the created site specification form. It also helped to determine the type of problem to be solved through this analysis, where the issue of reducing weighted impedance p-median was used here to identify the assessment of the geographical distribution of the locations of basic schools within the neighbourhoods of the city; two scenarios were used to assess the accessibility of basic schools. This analysis has been used in a number of geographical studies that have dealt with the planning of educational services and other services to improve access to schools. For example, see the studies by Al-Sabbagh (2022), Utami et al. (2022) and Sánchez-Partida et al. (2020),in addition to the study by Mindahun & Asefa (2019). This method was used to assess school accessibility by proposing the redistribution of existing schools to increase the efficiency of accessibility.

The first scenario focused on the current geographical distribution of schools Fig.6.

The second scenario centred on the proposed distribution through the establishment of new schools in neighbourhoods not served by schools Fig. 6. The result of the analysis of the allocation models for primary schools in the city of Mafraq can be noted from the data contained in Table 3.

With reference to Table 3 and Fig.6, the results of the allocation of sites for accessibility assessment for the first scenario (current geographical distribution of schools) are given. The Minimize impedance model showed that the total network lengths were 403 km, and the average distance was 439 m. In the second scenario (proposed distribution of schools through the establishment of 10 new schools, the total network length was 602 km, with an average distance of 334 m.

The analysis of the data of Table (4) showed that there are five neighbourhoods where the points of demand constitute (57.76%), where the reach distance is 480 m, 519

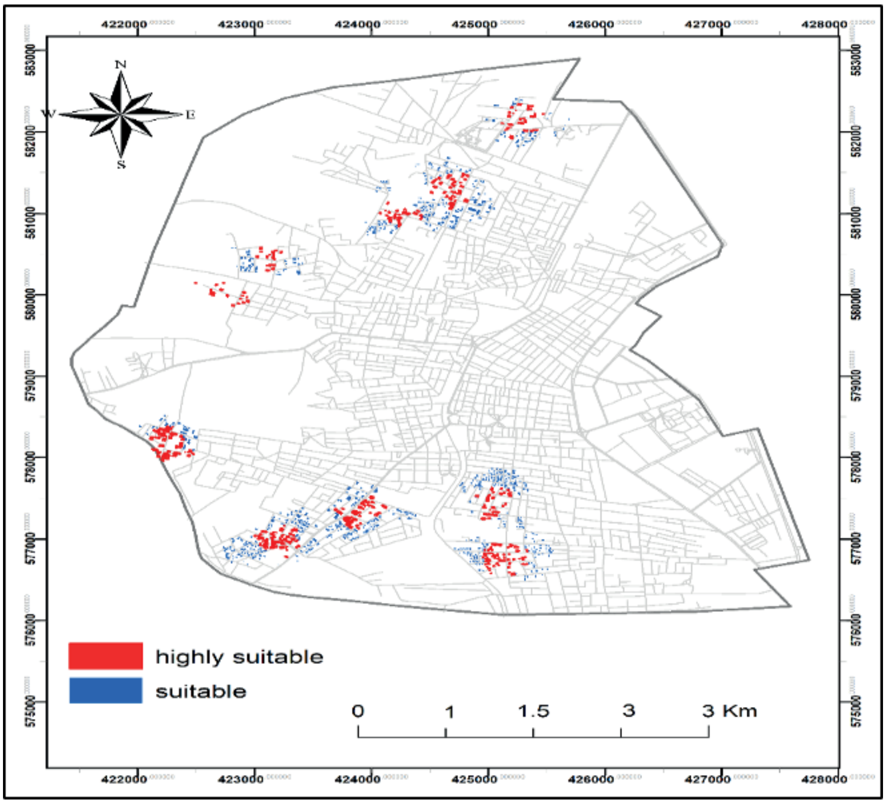

Fig. 5. Outputs of weighted map matching analysis to determine the degree of suitability of a location for new schools

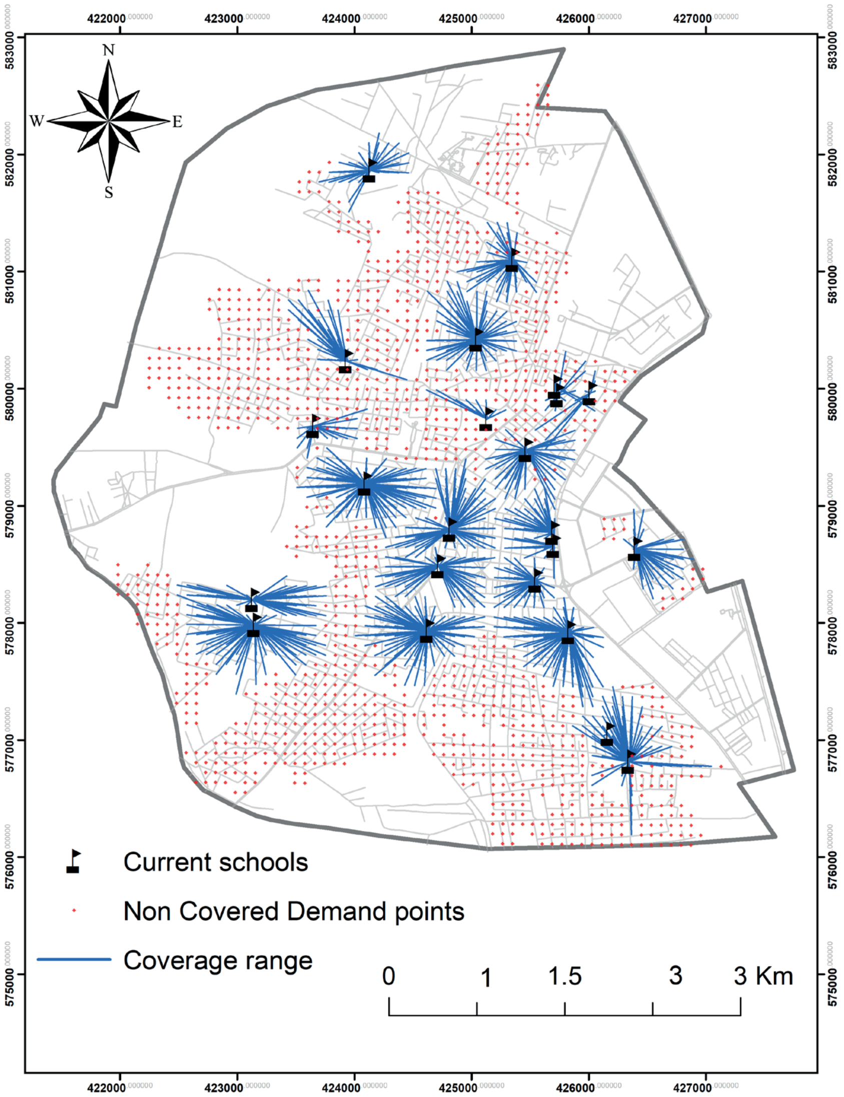

Fig. 6. The results of the proposed location–allocation models for primary schools in Mafraq

Model	Scenario No. 1			Scenario No. 2		
	No. Schools	Total network lengths/km	Average distance/m	No. Schools	Total network lengths/km	Average distance/m
Minimize Impedance	23	403	439	33	602	334

m, 442 m, 426 m, 471 m, and 574 m for the neighbourhoods Alhusban, Alsafwa, West Hashemi, Alnahda, King Abdullah, and Almizh, respectively. These neighbourhoods extend continuously in a westwards direction on the margins of the city, Despite the existence of numerous residential structures, the paucity of schools in these neighborhoods is attributable to the fact that these neighborhoods were developed recently as a result of Mafraq's fast urban development, and constituting 36% of the city's total area, while the rest of the city's neighbourhoods (twenty areas) comprise 42.24% of the demand points.

It was found from the analysis of Table 4. According to the proposed impedance reduction model for the geographical distribution of school locations where it was proposed to establish 10 new schools at the level of the city's neighbourhoods, there are four neighbourhoods that have witnessed an increase in the number of schools to their current status, namely, Aljundiu neighbourhood,

Table 4. The pointers of accessibility for reaching the main schools in the districts

No	District name	Minimize impedance model (current geographical distribution)			Minimize Impedance Model (Proposed geographical distribution)		
		Schools	Demand Points	Average distance/m	Schools	Demand Points	Average distance/m
1	Alzuhur	0	0	0	0	0	0
2	Craft area	0	0	0	0	0	0
3	Hamza	0	81	0	1	81	0
4	Industrial	0	0	0	0	0	0
5	Prince Hassan	3	67	284	3	67	221
6	Alfadayn	1	64	385	1	64	292
7	Alnasr	1	74	411	1	74	313
8	Princess Ealia	1	95	507	2	95	314
9	Aldubaat	0	9	397	0	9	325
10	Nwarat East	1	85	456	1	85	336
11	East Hashemi	1	93	479	1	93	343
12	Wasfi Altal	1	55	466	1	55	350
13	Aljaysh	0	30	459	0	30	351
14	Aljundiu	0	46	492	1	46	354
15	West Hashemi	2	146	442	3	146	360
16	Alnahda	6	196	426	6	196	372
17	Alqadisia	1	53	456	1	53	372
18	Alhusban	2	253	480	3	253	377
19	King Abdullah	2	469	471	4	469	389
20	Alhusayn	1	58	445	1	58	390
21	Ghazi	0	84	585	1	84	435
22	Alkarama	0	11	589	0	11	436
23	Alsafwa	0	111	519	0	111	450
24	Nwarat West	0	83	635	1	83	474
25	Almizh	0	120	574	1	120	464
26	Alnuzha	0	48	565	0	48	492

from 0 to 1 school, Princess Ealia from 1 to 2 schools, Ghazifrom0 to 1 school, Nwarat West from 0 to 1 school, Alhusban from 2to 3 schools, West Hashemi from 2to 3 schools, King Abdullah neighbourhood from 2to 3 schools, Hamza neighbourhood from 0 to 1 school, and Almizhneighbourhoodfrom0to 1 school.

Nine neighbourhoods witnessed stability in the number of schools, Alfadayn, Alhusayn, Wasfi Altal, Alnasr, Nwarat East, East Hashemi and Alqadisia, with one school for each neighbourhood, and Prince Hassan neighbourhood, with three schools. Alnahda neighbourhood has 6 schools, while eight neighbourhoods have remained without schools due to the lack of demand points in these areas because these areas are low in population density or are not qualified as rugged, industrial, military, and agricultural areas.

As a result of the establishment of new schools between the areas of the city, accessibility indicators have improved in areas that were far from the nearest school. As per the average distance (Table4) and (Fig. 7): Princess Ealia decreased from 507 m to 314 m, Ghazi from 585 m to 435 m, Nwarat West from 635 m to 474 m, Alsafwa from 519 m to 450 m, West Hashemi from 652 m to 360 m, and Almizh from 574 m to 464 m. In general, all indicators of access to basic schools have been improved in all neighbourhoods of the city compared to those of the current distribution. (Fig. 8)

DISCUSSION AND CONCLUSION

This study demonstrated the dynamic capabilities of geographic information system (GIS) applications in the spatial distribution and accessibility of primary schools in Mafraq. This study will help the Ministry of Education visualize the locations of primary schools on the map, guide them in establishing new schools to benefit unserved areas and consider the nature of primary school accessibility. We employed a GIS-based optimization model based on the P-median tool to allocate primary school services to ideal locations in Mafraq.

The results show the integration of site allocation and spatial suitability analysis. Therefore, a P-median site allocation model and spatial analysis based on a GIS are the best methods for determining the most suitable sites for new schools and other relevant public services. Site allocation technology and land suitability analysis enhance the efficiency of school sites more than traditional methods. However, reorganizing existing primary schools will not be possible because doing so consumes resources and the state may be unable to bear the additional costs.

Network analysis, both P-median, can run optimally if the road network data (network data set) is correct and detailed - in the sense that it includes information about the direction of the road (one or two directions, turning, etc.), However, a notable limitation of construction-level analysis was the lack of detailed data for the road network in the city; this limitation may seriously affect the results of the study.

The study presents two scenarios for the development of accessibility to schools. The first scenario was applied to evaluate the current school sites, whereas the second suggested the establishment of new schools in underserved areas and evaluation of the effectiveness of accessibility after the construction of new schools. The results of the study show that all indicators of access to primary schools in all neighbourhoods of the city have been improved when compared to the current distribution. This result is consistent with previous studies, whose findings showed that the integration of spatial accessibility and site allocation models represents an alternative solution to the problems associated with spatial planning and distribution. The study presented a model for spatial analysis of basic schools using spatial planning methods and standards for choosing new school sites. Planning standards related to the conditions for suitable sites for new schools were introduced, and among the most important standards that were considered were the following: current school sites, slope, population, road networks, drainage network, land uses, and hazardous sites. The results of the spatial analysis allowed for the derivation of a map of suitable sites for establishing new schools in the study area. Sites

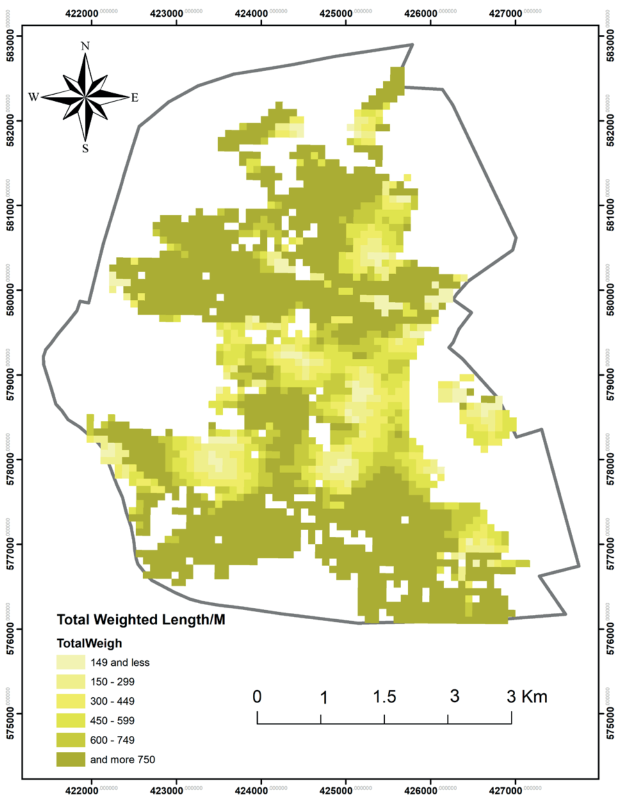

Fig. 7. Accessibility indicators of current location-allocation models for Mafraq city districts

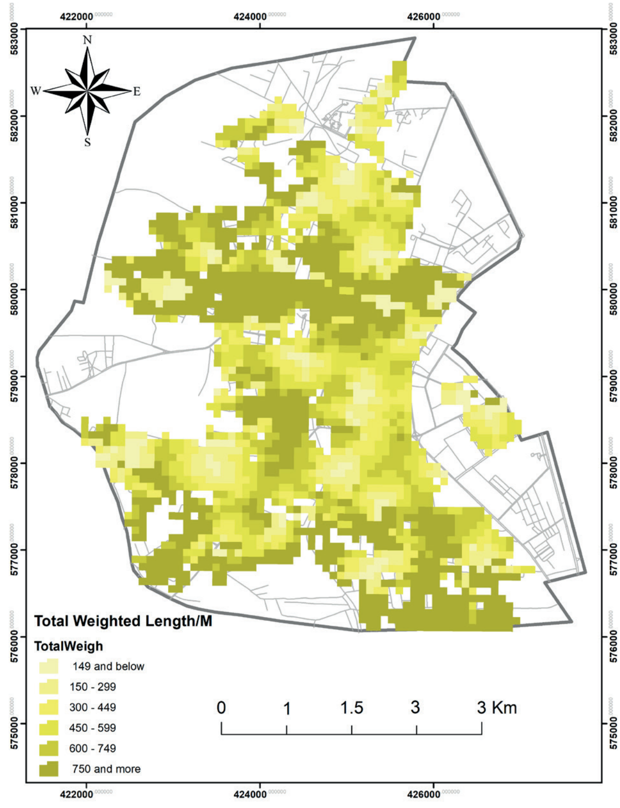

Fig. 8. Accessibility indicators of proposed location-allocation models for Mafraq city districts

in the study area were divided into two different suitability categories: sites that were deemed suitable and sites that were deemed highly suitable.

The study was able to demonstrate the dynamic capabilities of (GIS) for improving access to primary schools. The study results were analysed through the following site allocation models: the p-median impedance reduction model problem and a spatial suitability analysis. This approach helped the developer determine the type of problem to be solved, as the problem of reducing the p-median impedance was used to determine suitable places for establishing new schools in the Mafraq city. Residential buildings (demand points) that fell within the scope of primary school services were also identified.

By applying the proposed impedance reduction model, the number of schools needed to cover the needs of the population was determined, and it became clear that for improving access to primary schools, 10 new schools would need to be created to cover all or most of the residential buildings (demand points) in the city. According to the proposed impedance reduction model According to the proposed impedance reduction model and because of the establishment of new schools in model, accessibility indicators improved in areas where the distance to schools was high.

The results of the study showed the average access distance to primary schools decreased after the implementation of the proposal to establish new schools, which led to an improvement in all indicators regarding access to primary schools in all neighbourhoods of the city.

The high cost of establishing new schools in the city is one of the biggest problems facing the process of improving access to primary schools as a result of the meagre financial resources available in Jordan, which is a developing country. Another issue is infrastructure problems represented by the road network. The Ministry of Education can resort to temporary solutions, such as renting residential buildings for the purpose of providing schools in appropriate areas and identifying locations that need new roads to ensure better access to schools.

The location–allocation p-median models' approach can be applied in other countries and cities of the world while considering the planning standards specific to each country, and this method can be useful in distributing other related public facilities, such as hospitals, public health care centres, warehouses and markets. The adoption of spatial decision support models can also help countries improve the selection of locations for public facilities, especially with the proliferation of decision support models that have become more widely used as GIS programmes mature.

Based on the findings of the study, we recommend making use of GIS techniques in making planning decisions, especially spatial planning decisions. With the possibility of benefiting from this model, planners, especially in the field of services in general and primary services in particular, can formulate the appropriate plan for best and proper development in the region involving easy access to these services. Further research on several fronts and additional studies are recommended in other cities in Jordan. Comparative analysis would provide a growing empirically based understanding of effective social service planning.

REFERENCES

Abdul Jabbar S. and Laffta S. (2020). Spatial analysis of Private School Sites in Al-Jihad Neighborhood in Baghdad-Iraq by Using Geographic Information Systems. IOP Conference Series: Materials Science and Engineering, 737(1), DOI: 10.1088/1757-899X/737/1/012247.

Abraha T. (2019). Analyzing spatial and non-spatial factors that influence Educational Quality of Primary Schools in Emerging Regions of Ethiopia: Evidence from Geospatial Analysis and Administrative Time Series Data. Journal of Geography and Regional Planning, 12(1), 10–19, DOI: 10.5897/jgrp2018.0705.

Al-Dulaimi K. (2015). Planning Community Services and Infrastructure: Foundations Standards Techniques, 2nd ed. Dar Safaa for Printing Publishing and Distribution.

Al-Enazi M., Mesbah S., Anwar A. (2016). Schools Distribution Planning using GIS in Jeddah City. International Journal of Computer Applications, 138(1), 33–36, DOI: 10.5120/ijca2016908693.

AlFanatseh A. and Sababhi S. (2023). Applying GIS using location allocation models for improved spatial planning of Civil Defence Services: a Case Study of the Karak Governorate, Jordan. GeoJournal, 88(1), 691–710. DOI: 10.1007/s10708-022-10632-5

Al-Rasheed K. El-Gamily H. (2013). GIS as an Efficient Tool to Manage Educational Services and Infrastructure in Kuwait. Journal of Geographic Information System, 05(01), 75–86, DOI: 10.4236/jgis.2013.51008.

Al-Sabbagh T. (2022). GIS Location-Allocation Models in Improving Accessibility to Primary Schools in Mansura City-Egypt. GeoJournal, 87(2), 1009–1026, DOI: 10.1007/s10708-020-10290-5.

Batsaris M., Kavroudakis D., Hatjiparaskevas E., Agourogiannis P. (2021). Spatial Decision Support System for Efficient School Location Allocation. European Journal of Geography, 12(4), 31–044, DOI: 10.48088/ejg.m.bat.12.4.031.044

Bulti D., Bedada T., Diriba L. (2019). Analyzing Spatial Distribution and Accessibility of Primary Schools in Bishoftu Town, Ethiopia. Spatial Information Research, 27(2), 227–236, DOI: 10.1007/s41324-018-0227-6.

Duwaikat Q. (2013). Spatial analysis of Public-School Sites in the City of Irbid using geographic information systems. Journal of Mu'tah for Research and Studies: Humanities and Social Sciences Series, 28(6), 273–314.

Fabiyi O. Ogunyemi S. (2015). Spatial Distribution and Accessibility to Post Primary Educational Institution in Ogun State, Southwestern Nigeria: Case Study of Yewa South Local Government Area, Nigeria. Journal of Scientific Research and Reports, 5(7), 542–552, DOI: 10.9734/jsrr/2015/12328.

Jiang L., Chen J., Tian Y., Luo J. (2022). Spatial Pattern and Influencing Factors of Basic Education Resources in Rural Areas around Metropolises A Case Study of Wuhan City's New Urban Districts. ISPRS International Journal of Geo-Information, 11(11), DOI: 10.3390/ijgi11110576.

Meena D., Tripathi R., Agrawal S. (2022). An evaluation of Primary Schools and its Accessibility Using GIS Techniques: A Case Study of Prayagraj district, India. GeoJournal, 88, 1921–1951, DOI:10.1007/s10708-022-10715-3.

Menezes R. Pizzolato N. (2014). Locating Public Schools in fast Expanding Areas: Application of the Capacitated P-median and Maximal Covering Location Models. Pesquisa Operacional, 34(2), 301–317.

Mindahun W. Asefa B. (2019). Location Allocation Analysis for Urban Public Services Using GIS Techniques: A Case of Primary Schools in Yeka sub-city, Addis Ababa, Ethiopia. American Journal of Geographic Information System, 8(1), 26–38.

Murray A. (2010). Advances in Location Modeling: GIS Linkages and Contributions. Journal of Geographical Systems, 12(3), 335–354, DOI: 10.1007/s10109-009-0105-9.

Murray A. Tong D. (2009). GIS and Spatial Analysis in the Media. Applied Geography, 29(2), 250–259.

Mustapha O., Akintunde O., Alaga A., Sharafdeen O., Sunday K., Isal b., Hafeez S., Muibi K. (2015). A Geospatial Approach to Evaluation of Accessibility to Government Primary Schools in Ilorin West Local Government. European International Journal of Science and Technology, 4(8), 2304–9693.

Polo G., Acosta C., Ferreira F., Dias R. (2015). Location-Allocation and Accessibility Models for Improving the Spatial Planning of Public Health Services. PLOS ONE, 10(3), 1–14, DOI: 10.1371/journal.pone.0119190.

Rekha R., Radhakrishnan N., Mathew S. (2020). Spatial Accessibility Analysis of Schools Using Geospatial Techniques. Spatial Information Research, 28(6), 699–708, DOI: 10.1007/s41324-020-00326-w.

Sánchez-Partida D., Sánchez-Castro M., Martínez-Flores J., Cano-Olivos P., Straka M. (2020). Territorial Sales Redesign Using Geotechnical Tools. Advances in Science, Technology and Engineering Systems, 5(2), 368–376, DOI: 10.25046/AJ050248.

Sumari N., Tanveer H., Shao Z., Kira E. (2019). Geospatial Distribution and Accessibility of Primary and Secondary Schools: A Case of Abbottabad City, Pakistan. In Proceedings of the ICA, 2(July), 1-11,DOI: 10.5194/ica-proc-2-125-2019.

Utami R., Khakhim N., Jatmiko R., Kurniawan A., Halengkara L. (2022). GIS Network Analysis to Optimize Zoning System Implementation for Public Junior high Schools in Yogyakarta city. IOP Conference Series: Earth and Environmental Science, 1089(1), DOI: 10.1088/1755-1315/1089/1/012035.

Yang P., He R., Hou H. (2017). Distribution of Primary School Based on Spatial Network Comprehensive Model in Low Income Mountainous Cities: A Case Study in Wanyuan, China. Journal of Mountain Science, 14(10), 2082–2096, DOI: 10.1007/s11629-016-4316-5.

Yasenovskiy V. Hodgson J. (2007). Hierarchical Location Allocation with Spatial Choice Interaction Modeling. Annals of the Association of American Geographers, 97(3), 496–511.

RESEARCH PAPER

MODELING SEDIMENT PRODUCTION IN URBAN ENVIRONMENTS: CASE OF RUSSIAN CITIES

Andrew V. Shevchenko[1,2*], Andrian A. Seleznev[1,2], Georgy P. Malinovsky[1], Ilia V. Yarmoshenko[1]
[1]Institute of Industrial Ecology, Ural Branch of Russian Academy of Sciences, 620108, Ekaterinburg, Russia
[2]Ural Federal University, 620002, Ekaterinburg, Russia
***Corresponding author:** sav@ecko.uran.ru
Received: August 25th, 2023 / Accepted: November 14th, 2023 / Published: December 31st, 2023
https://DOI-10.24057/2071-9388-2023-3022

ABSTRACT. The aim of this study is to provide a tool to assess sediment production in an urban area. The urban environment is affected by a variety of anthropogenic and natural factors that, in particular, lead to the sediment production. The storage of sediments in the urban landscape negatively affects the quality of the urban environment.

The model was developed on the basis of landscape studies conducted in residential areas of six Russian cities. The model takes into account (1) the influence of precipitation, spring snowmelt, and vehicles, (2) the influence of erosion factors for two seasons: warm (t>5°C) and cold (t<5°C), and (3) the presence of disturbed surfaces.

The application of the developed model to Ekaterinburg city conditions returned sediment production equal to 1.2 kg/m^2/y. A comparison of seasonal values shows that sediment production in cold season is 2.5 times higher than in the warm season. In the absence of the disturbed surfaces, sediment production decreases to 0.44 kg/m^2/y. Modeling showed a correlation between sediment production in Russian cities and duration of the cold season. The efficiency of various urban area maintenance practices and cleaning measures were evaluated in terms of sediment production and storage.

The developed model presented in this paper is based on research in Russian cities, but can be applied to assess the formation of sediment and measures to reduce the value of its accumulation in the urban environment in different regions of the world.

KEYWORDS: urban environment, residential area, contemporary sedimentation, urban surface deposited sediments, pollution, accumulation, sediment production, soil, erosion

CITATION: Shevchenko A. V., Seleznev A. A., Malinovsky G. P., Yarmoshenko I. V. (2023).Modeling Sediment Production In Urban Environments: Case Of Russian Cities. Geography, Environment, Sustainability, 4(16), 144-155
https://DOI-10.24057/2071-9388-2023-3022

Conflict of interests: The authors reported no potential conflict of interest.

INTRODUCTION

The large cities are subjected to the constant impact of various negative anthropogenic factors: landscape transformations, construction, motor transport, high population density, concentration of industries, etc. (Silveira et al. 2016; Owens 2020b). The above factors cause the destruction of road surfaces, lawns, sidewalks, abrasion of the road bed by tires (including studded ones), earthwork and repair work and construction (Murakami et al. 2007; Corradini et al. 2019; Pereira et al. 2016; Silveira et al. 2016; Stojiljkovic et al. 2019; US EPA 2022, 2023).

In the natural-technogenic urban landscape catenary complex, the process of sedimentation takes place according to the principle of cascade, and a part of the loose sediment remains deposited on a variety of urban surfaces, including sidewalks, driveways, lawns, playgrounds, and parking lots (Taylor et al. 2007, 2009; Owens et al. 2011; Seleznev et al., 2019a, b; Yarmoshenko et al. 2020). Urban sediment includes particles of soil, leaf litter, atmospheric solid particles, as well as solid material of vehicle emissions, building materials, road salt, road paint, and pedestrian debris (Pereira et al. 2016; Haynes et al. 2020). This object can be referred to as urban surface deposited sediments (USDS) (Seleznev et al. 2021).

The USDS reduces the quality of the urban environment. It causes deterioration of the urban infrastructure, siltation of storm water drainage systems, decrease of the fertility of the urban soils, wearing of mechanisms, vehicles, clothes and shoes, increases financial costs for sediment removal, cleaning of the territories (Pereira et al. 2016; Hewett et al. 2018; Yarmoshenko et al. 2020, Owens 2020b). These aspects of sediment storage cause many people to view sediment as a nuisance and typically have negative connotations (Owens 2020b; Seleznev et al. 2021).

Fine fractions of sediments can accumulate substances potentially harmful for human health (Landrigan et al. 2018; Stojiljkovic et al. 2019; Seleznev et al. 2020; Haynes et al. 2020). The urban sediments represent a secondary, non-point source of pollution and poses a significant risk to the environment due to high content of dust particles and other pollutants (Taylor et al. 2007; Martínez & Poleto 2014; Pereira et al. 2016; Li et al. 2019; Lee et al. 2021). Sediment generated in urban areas can be transported to streams, rivers, and reservoirs (Restrepo & Syvitski 2006; Najafi et al. 2021; Cendrero et al. 2022). These contributes to suspended sediment in water bodies. The potential of sediment as a geo-indicator component in ecological and geochemical studies has recently been under consideration (Kasimov 2013; Crosby et al. 2014; Dias-Ferreira et al. 2016; Owens 2020b).

The problem of sediment production and accumulation on the urban surfaces is of great importance for urban environment quality management. However, there is currently no comprehensive assessment of sediment production in Russian cities. There is also no recommended tool for such an assessment. There are verified models for estimating soil loss on agricultural land due to precipitation, for example Revised Universal Soil Loss Equation (RUSLE), but the experimental assessment of sediment production in urban environments is difficult due to the heterogeneity of the urban landscape. Vehicle traffic is a significant contributor to total sediment production in this type of landscape (Stojiljkovic et al. 2019; Seleznev et al. 2021). There are a number of methods currently available to assess pavement wear, but they assess this wear from a road safety perspective rather than a sediment production perspective. A multi-factorial system such as the urban environment requires an appropriate model that considers all aspects of the environment's erosion potential.

The aim of this study is to develop a model for estimating sediment production in urban areas. In order to achieve the aim, the following tasks were formulated:

1. To create a model object that reflects the typical structure of residential blocks in Russian cities by averaging previous landscape studies.
2. Modify the RUSLE model for use in an urbanized environment and calculate sediment production.
3. To propose a method for estimating the amount of sediment production by pavement wear from studless and studded tires.
4. To perform model estimation of sediment production in urban environments in different climatic conditions.
5. To perform model estimation of sediment production in Ekaterinburg conditions.

MATERIALS AND METHODS

Data source

In recent years, the Institute of Industrial Ecology of the Ural Branch of the Russian Academy of Sciences has collected significant experimental material on surface sediments in the urban environment in a large number of Russian cities: Moscow, Rostov-on-Don, Nizhniy Novgorod, Tyumen, Ekaterinburg, Murmansk, Chelyabinsk, Vladivostok and other. Surface sediments were sampled in residential areas and the adjacent network of streets and roads (Seleznev et al. 2019a, 2019b, 2020, 2021, 2022, 2023; Yarmoshenko et al. 2020). In total, more than 500 samples were taken. The selected samples were analyzed for granulometric, chemical, and mineral composition. In cold season, snow and snow-dirt sludge, which is a mixture of snow and surface sediment from vehicle and pedestrian traffic, were sampled.

A description of the landscape conditions was made at the sampling locations, taking into account the type of use of the landscape areas, the type of pavement, the technical condition, the quality of cleaning and other parameters. Based on the results of the studies, the accumulated stock of surface sediments was estimated. In the fourth populated Russian city Ekaterinburg, the amount of solid sediment storage was found to be 3.2 kg/m^2 (Seleznev et al. 2019).

Elementary Urban Residential Landscape

The paper (Yarmoshenko et al. 2020) describes a study conducted in six Russian cities: Ekaterinburg, Rostov-on-Don, Nizhniy Novgorod, Tyumen, Murmansk, Chelyabinsk. In each city, six experimental sites in residential land use areas in different parts of each city and at different stages of development were selected for field survey. Each site represents a part of the residential yard with an adjacent street and road network area of a block of multi-story apartment buildings. After analyzing the field survey data, which covered about 350,000 m^2, an averaged version of all experimental sites is presented in the paper (Yarmoshenko et al. 2020) and called Elementary Urban Residential Landscape (EURL). The EURL is an elementary part of the typical residential block of most large Russian cities, mostly built during the Soviet era.

The model EURL (Fig. 2.1) was defined as an area of 10 000 m^2 and divided into 14 segments according to the criteria suggested by Yarmoshenko et al. (2020). The typical EURL consists of external (street) and internal (yard) parts and include the following functional zones: road, driveways, parking lots, lawns, sidewalks, playground, and illegal parking. Illegal parking is a part of the city territory that was not originally designed and arranged to accommodate vehicles. During the field surveys the illegal parking were detected on lawns and playgrounds (red cars on Fig. 2.1). The field surveys included the characterization of the segments by several parameters which describe, in particular, the type of pavement, proportion of disturbed surface, state of cleaning, presence of elevation, and others.

The typical EURL includes 50 parking lots and 12 illegal parking lots in the internal part (Yarmoshenko et al. 2020). The intensity of traffic on a three-lane road within the city limits averages 3,000 cars per day, according to the Ekaterinburg city administration. The length of the road adopted in the EURL is 100 m, which is roughly the length of the side of the block.

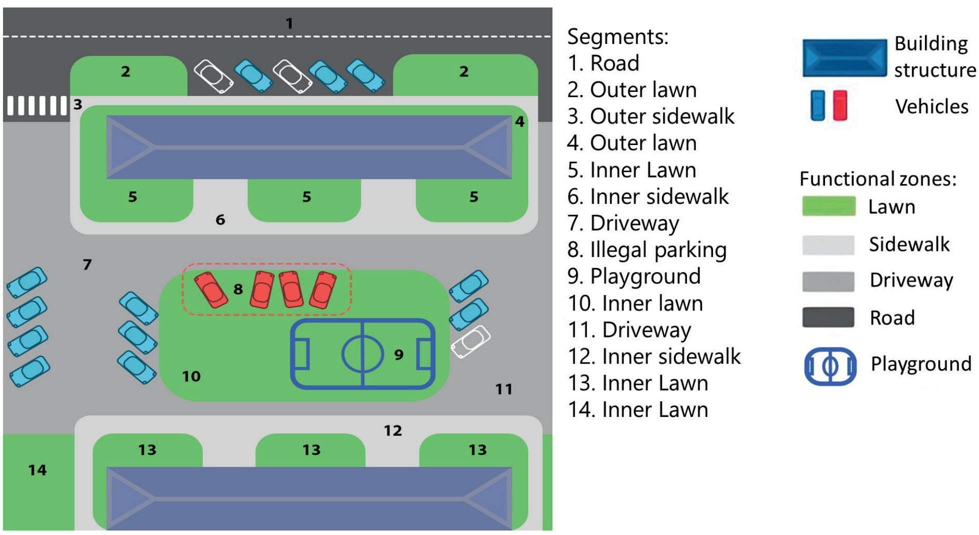

Fig. 1. Scheme of the typical elementary urban residential landscape (EURL) in Russian cities divided into segments and functional zones

Surface types of the elementary urban residential landscape

Three types of surfaces were defined within the EURL: asphalt, lawn, and bare soil. However, this paper considers two variants of the condition and use of functional zone surfaces: real conditions – surfaces are partially disturbed, ideal conditions –surfaces are completely undisturbed. The percentage of the area of each segment that is attributable to disturbed pavement is accepted equal to 16% and 27% for the external and internal segments, respectively. For the road, this percentage is 3.6%. On the average, according to (Yarmoshenko et al. 2020), in the residential areas of the large cities of Russia, the percentage of the disturbed pavement is 24%.

Atmospheric precipitation cannot have a significant effect on undisturbed segments of hard surfaces of roads, driveways, and sidewalks, so there is no natural erosion from the effects of rain and snowmelt. The calculation of erosion from the impact of non-studded tires considers only the segments on which the vehicle is moving. For studded tires, the calculation is for the road only. This is because in the cold season yard driveways are covered with a layer of compacted snow or ice and in most cases are not shoveled to a hard surface, so there is no effect of the studs on them. For ideal conditions, it is assumed that there is no illegal parking and it is an inner undisturbed lawn, and the use of studded tires is prohibited.

Descriptions of the studied cities

As a main object of application of the developed model of estimation of sediment production the city of Ekaterinburg, fourth most populated city in Russia, was chosen. Ekaterinburg is characterized by a high concentration of industrial enterprises, a high traffic load on the road network, and a high population density.

In calculations that take into account temperature and snow cover, two seasons are defined: warm and cold. The warm season is the period when the air temperature is >5°C and the cold season is <5°C. This choice is due to the fact that at air temperatures <5°C it is recommended to equip cars with winter tires. The cold season in Ekaterinburg, lasts on average from November to March (5 months). The average air temperature during this period is -11.2°C. Atmospheric precipitation in the form of snow accumulates at negative temperatures. The average temperature over several years is -15.3°C in January and +17.4°C in July.

In addition, calculations were made for seven major Russian cities located in climatic zones different from Ekaterinburg. For this purpose, cities with cold period duration (t<5°C) from 1 to 9 months were selected: Sochi (1 month), Novorossiysk (2 months), Rostov-on-Don (3 months), Vladivostok (4 months), Khabarovsk (6 months), Novosibirsk (7 months), Salekhard (8 months), Norilsk (9 months).

Ekaterinburg receives an average of 535 mm of precipitation per year, but the RUSLE model considers only liquid precipitation, which is 405 mm/y. For other cities, this value varies from 341 to 1648 mm/y. The average value is about 600 mm/y, against which Sochi stands out with a value of 1648 mm/y.

The average height of the snow cover in Ekaterinburg is 440 mm (Seleznev et al. 2020). This value was used in calculations for such areas as lawns and playgrounds. These areas are not cleared of snow during the cold season. For areas with paved surfaces (roads, driveways, sidewalks) a height of 220 mm of snow cover was used because these areas are subject to regular snow removal. Snow cover height at illegal parking was also assumed to be 220 mm. Parked cars prevent the free accumulation of snow. In other cities, a different snow cover height was selected from reference climate data. The snow cover height on unpaved surfaces is from 100 to 600 mm, on paved surfaces - from 50 to 300 mm.

Soils in urban areas are predominantly altered by human activities. These are urban soils. Therefore, the K-factor for these soils should be determined experimentally for each site for which calculations are made. Sod-podzolic soils containing 20-30% clay and about 40% sand are typical for the Ekaterinburg region (Gafurov 2008). The K-factor of the RUSLE was calculated using these characteristics. This type of soil was used for all cities, because urban topsoil does not differ much in granulometric composition, being an anthropogenically transformed soil.

Empirical model for soil loss assessment

There are three categories of models for the assessment of soil loss on agricultural land: empirical models, conceptual models, and physically based models (Igwe et al. 2017). Empirical models have the advantage that they can be applied to situations with limited data and parameters and are particularly useful as a first step in the identification of sources of sedimentation (Merritt at al. 2003). One of the empirical models is the Revised Universal Soil Loss Equation (RUSLE) (Renard et al. 1991). RUSLE provide a long-term average annual estimate of soil loss due to precipitation. It was developed for small slopes, but can be used to model catchment-scale erosion and sediment transport.

The Revised Universal Soil Loss Equation (RUSLE) model is a soil erosion model that predicts the average annual soil loss due to precipitation and surface runoff from agricultural fields and pastures (Renard et al. 1991). The RUSLE model contains six factors:

$$A_p = R \times K \times LS \times C \times P \qquad (1)$$

where A_p is the annual average rainfall soil loss, t/ha/y; R is the rainfall erosivity factor, MJ mm/ha per hour; K is the soil erodibility factor, t ha h/MJ mm, *LS* is the slope length and slope steepness factor (dimensionless), *C* is the land-use (cover management) factor (dimensionless), *P* is the supporting practices factor (dimensionless).

The R-factor depends on the climatic conditions of the area. The key factor is the amount and intensity of atmospheric precipitation that causes erosion (Renard et al. 1991). To calculate the R-factor, data on the average annual liquid precipitation were used for the model site. The following formula is used to calculate the R-factor (Yu et al. 1996; Renard et al. 1997):

$$R = 0.0438 \times P^{1.61} \qquad (2)$$

where *P* is average annual liquid precipitation, mm/y.

The K-factor determines the resistance of the soil to erosion under standard conditions. It depends on the granulometric composition of the soil, its sand, clay and silt content (Renard et al. 1997; Knijff et al. 1999). The soil erodibility factor – K-factor, is usually estimated using the nomographs and formulae that are published in for example Wischmeier & Smith (1978). While these equations are suitable for large parts of the USA (for which the USLE was originally developed), they produce unreliable results when applied to soils with textural extremes as well as well-aggregated soils (Romkens et al. 1986). Therefore, they are not ideally suited for use under European conditions.

Romkens et al. (1986) performed a regression analysis on a world-wide dataset of all measured K-values, which yielded the following equation (revised in Renard et al., 1997):

$$K = 0.0034 + 0.0405 \times exp\left[-0.5 \times \left(\frac{\log D_g + 1.659}{0.7101}\right)^2\right] \qquad (3)$$

where D_g is the geometric mean weight diameter of the primary soil particles, mm.

D_g is a function of surface texture, and its value can be calculated as follows (Renard et al. 1997; Knijff et al. 1999):

$$D_g = exp\left(f_i \times \ln\left(\frac{d_i + d_{i-1}}{2}\right)\right) \quad (4)$$

where d_i is the maximum diameter, mm; d_{i-1} is the minimum diameter, mm; f_i is the corresponding mass fraction, mm, for each particle size class (clay, silt, sand).

The LS-factor is a factor of the length and slope of a landscape segment, taking into account the effect of sloping processes on erosion (Wischmeier et al. 1978). Eq. 5 was used for the calculation of the LS-factor (Moore et al. 1992):

$$LS = \left(\frac{A_S}{22.13}\right)^m \times \left(\frac{\sin\beta}{0.0896}\right)^n \quad (5)$$

where A_S is the specific catchment area, m^2/m; $sin\beta$ is the slope angle, deg.; m and n are constants, 0.4 and 1.3 respectively (Moore et al. 1992).

The C-factor in the soil-loss equation is the ratio of soil loss from land cropped under specified conditions to the corresponding loss from tilled, continuous fallow (Renard et al. 1997). This factor measures the combined effect of all the interrelated cover and management variables. The higher the value, the less the crop stands inhibit erosion.

The P-factor in the soil-loss equation is the ratio of soil loss with a support practice like contouring, stripcropping, or terracing to soil loss with straight-row farming up and down the slope (Renard et al. 1997). If there is no support practice, the P-factor is not used in the calculation and is equal to 1.

RESULTS

RUSLE adaptation for urban environments

The RUSLE model has been used in this study for the estimation of surface solid material production as a result of the impact of precipitation on urban pavements. This model implies the presence of a slope in the study area, but the relief of urban areas is many times more complicated than that of natural areas, since there are a huge number of obstacles in the way of its formation, and at the same time there are even more areas of artificial concentration of runoff. The RUSLE model is designed exclusively for soils that can be used in some form of agriculture. Therefore, the model cannot be used for urban environment without significant modifications. For this reason, the RUSLE model was modified based on a study conducted in the city of Ekaterinburg, one of the objectives of which was to select a C-factor that would allow the model to be transferred to urban conditions (Seleznev et al. 2022). It is important to note that the RUSLE model was used only for areas with ground cover or other forms of open ground, such as road potholes. Any calculations with its help on asphalt and other hard surfaces are meaningless.

In this study, slope angle values are assumed to be 0.5 degrees for areas with hard impervious surfaces (roads, sidewalks, driveways) and 5 degrees for areas with permeable surfaces. These slope angle values have been chosen as examples and approximate the actual slopes of landscape sections in urban environments. If other slopes are present, any value other than zero can be used.

The C-factor reflects the effect of vegetation cover and land use type on erosion rate (Wischmeier et al. 1978; Renard et al. 1991; Renard et al. 1997). The values of the factors range from 0 to 1, depending on the type of land cover. The lower the value, the more resistant to erosion (Lisbôa et al. 2017; Aouichaty et al. 2022; Chen et al. 2023). The C-factor values are in accordance with the paper (Seleznev et al. 2022). Within the framework of this study (Seleznev et al. 2022), two drainless small water bodies were selected in Ekaterinburg. The water bodies are located in different areas of the city, are of anthropogenic origin, the purpose of the water bodies is recreation. The catchment areas are located at the interfaces of different functional zones of the city. In the work was carried out field survey and analysis of cartographic materials of territories of watersheds, determination of bathymetric and morphometric parameters of water bodies, sampling columns of bottom sediments. The assessment of bottom sediments in water bodies was carried out using a three-dimensional triangulation model. Assessment of sediment transport from the catchment area was carried out using the RUSLE model. The parameters of the RUSLE model, in particular the C-factor, were obtained based on the calculated amount of bottom sediments (Table 2.1).

For the C-factor, we used two variants of values reflecting surface condition: undisturbed and disturbed. Disturbed surfaces are surface areas that have been subjected to anthropogenic or other impacts, as a result of which the integrity of the surface has been disturbed. Potholes in roads and other hard surfaces, trampled or unvegetated lawns, illegal parking lots, etc. are examples of such segments.

In urban residential areas, these measures are not implemented, so the P-factor was assumed as 1 (Renard et al. 1997; Lisbôa et al. 2017; Taoufik et al. 2020; Michalek et al. 2021).

A modified Larionov (1993) model of the Russian State Hydrological Institute was used for the estimation of sediment production during snowmelt following the same principles as RUSLE model. Eq. 6 (Larionov 1993; Maltsev et al. 2020) was used for the calculation of material runoff during spring snowmelt:

$$A_{sm} = h \times K \times LS \times C \times P \quad (6)$$

where A_{sm} is the average annual snowmelt soil loss, t/ha/y; h is the overland surface flow during snowmelt.

K, LS, C, and P factors are assumed to be the same as for liquid precipitation erosion calculations. The value of surface runoff h is calculated based on Eq. 7 as follows (Larionov 1993; Maltsev et al. 2020):

$$h = H \times D \times I^E \quad (7)$$

Table 1. The values of the C-factor used in the developed model

Functional zone	C-factor	
	undisturbed site	disturbed site
road	0	0.5
driveway	0	0.5
sidewalk	0	0.5
lawn	0.01	0.1
playground	0.1	0.2
illegal parking	0.5	0.5

where H is the water content in snow, mm; D and E are coefficients depending on the landscape zone and soil texture (Table 2.2); I - slope, %.

Methods for estimating sediment production from vehicles

Studless tires

The interaction of a moving vehicle with the road surface results in tire wear and abrasion of the top layer of the road surface. A factor similar to the rainfall erosivity factor (R-factor) of the RUSLE model (Renard et al. 1991) can be used to estimate pavement wear from tire abrasion during warm periods. The R-factor principle has been used to determine the amount of abrasion products from vehicle wheels. It is suggested that instead of precipitation energy, an estimate of the amount of energy transferred from the vehicle to the surface should be used.

The following forces that act on the surface as the vehicle moves are considered to estimate the amount of energy transferred from the vehicle to the surface:

• traction force – resulting from the operation of the engine and the interaction between the drive wheels and the road,

• rolling resistance force – the force that results from the deformation of the tire as it grips the surface of the road,

• friction force – occurs when the vehicle's wheels come into contact with the road surface.

The energy from the engine is transferred to the wheels through the transmission. Part of the energy is used to overcome friction and to move the units. The amount of energy that is lost depends on the efficiency factor of the transmission η_{ts}. According to Turevsky (2005), for passenger cars η_{ts} is taken to be equal to 0.88-0.92, depending on the gear that is engaged.

The torque Tq_s causes the tangential reaction of the road at the point of contact of the wheel with the road, which moves the car, i.e. the traction force F_{tr} (Turevsky 2005):

$$F_{tr} = \frac{Tq_s}{r_{sw}} \quad (8)$$

where Tq_s is the total torque on the driving wheels, N·m; r_{sw} is the static wheel radius, m.

The value of r_{sw} changes under the influence of other forces, but to simplify the calculations, it is considered constant. It is equal to the distance from the axis of the stationary wheel to the road surface (Turevsky 2005). In this case, Tqs equals:

$$Tq_s = \eta_{ts} \times Tq \times r_{gb} \times r_{mg} \quad (9)$$

where η_{ts} is the efficiency factor of the transmission; T_q is the engine torque, N·m; r_{gb} is the gear ratio of the gearbox; r_{mg} is the gear ratio of the main gear.

When a vehicle maneuvers while driving, it generates a rolling resistance force F_r. This force depends on the tire's traction coefficient with the road surface and the load on the wheels (Turevsky 2005; Filkin 2016). The rolling resistance force can be calculated by using the formula:

$$F_r = f \times G_v \quad (10)$$

where F_r is the rolling resistance force, N; f is the rolling resistance coefficient; G_v is the force of gravity acting on the vehicle, N.

According to Filkin (2016), the coefficient of rolling resistance f is considered constant at speeds up to 50 km/h. For roads with asphalt or asphalt cement pavement in excellent condition it is 0.012-0.018, and for roads in satisfactory condition it's 0.018-0.020. For unpaved roads in a dry and rolled condition it is 0.025-0.035 (Turevsky 2005). The characteristics of the vehicle and the accepted speeds for each of the functional zones that are used in the calculations are shown in Table 2.3.

The friction force is a mechanical resistance force that occurs for two reasons: the attraction of the molecules

Table 2. Values of coefficients D and E depending on conditions (Maltsev et al. 2020)

Landscape zone	Soil texture	D	E
forest	clay, loam	2.6953	0.89836
	sandy loam	2.1118	0.63475
forest-steppe	clay, loam	3.1219	0.96103
	sandy loam	2.4472	0.73120
steppe	clay, loam	3.0235	0.99758
	sandy loam	1.37	0.60474

Table 3. Characteristics of the model car and accepted speeds of its movement

Characteristics	Value
weight, kg	1500
engine torque, N·m	155
gear ratio of main gear	4.3
gear ratio of 1st gear	3.769
gear ratio of 2nd gear	2.045
gear ratio of the 4th gear	1.036
tire width, mm	195
driveway, km/h	20
road, km/h	50
illegal parking, km/h	10

to each other at the point of contact and the presence of a surface roughness. The frictional force is calculated according to the following equation:

$$F_{fr} = \mu \times m \times g \quad (11)$$

where μ is the coefficient of friction (adhesion); m is the vehicle mass, kg; g is the gravitational constant, m/s^2.

The coefficient of friction (adhesion) μ was taken from Turevsky (2005) for dry asphalt cement pavement and is equal to 0.7.

Using the data from Table 2.3 to calculate equations 8-11, we obtain the values of the energy transferred to the surface as the car moves. This value corresponds to the size units of the RUSLE model. Table 2.4 shows the values obtained for each functional zone.

In order to take into account the type of surface, it is necessary to introduce into the calculations the coefficient of intensity of wear – I-factor. It depends on the resistance of the surface to various influences. The coefficient was determined by Korsunsky M. B. (Vasiliev 1989) on the basis of the formula for the calculation of the average annual decrease in the thickness of the pavement due to wear:

$$h_{an} = a + b \times \frac{N}{1000} \quad (12)$$

where h_{an} is the annual average value of the reduction in pavement thickness due to wear, mm; a is a coefficient that depends mainly on the resistance of the pavement to adverse climatic conditions (Table 2.5); b is a coefficient that depends on the strength of the pavement material, its moisture content, composition and traffic speed (Table 2.5); N is the traffic intensity, vehicle/day.

Values representing wear per unit of energy transmitted to the pavement were calculated from data on the reduction in pavement thickness due to wear and the energy transmitted to the pavement by the vehicle during travel. The I-factor values for disturbed and undisturbed pavements are shown in Table 2.6. The area of the illegal parking lot is considered to be completely disturbed.

The final equation for calculating pavement wear for studless tires is as follows:

$$A_{sl} = \left(E \times N_w \times P_{us} \times I_{us}\right) + \left(E \times N_w \times P_{ds} \times I_{ds}\right) \quad (13)$$

where A_{sl} is the average annual production of sediment from studless tire abrasion, kg/m^2/y; E is the energy transmitted to the surface during the movement of a car, MJ/m^2/y; N_w is the number of cars per warm season; P_{us} and P_{ds} is the undisturbed and disturbed surface area, respectively, %; I_{us} and I_{ds} is the factor of intensity of wear for undisturbed and disturbed surface area, respectively, kg/MJ (Table 2.6).

Studded tires

Studded tires cause significant road wear (Stojiljkovic et al. 2019). In most parts of Russia in cold season car owners use studded tires. That said, 77% of them are studded (Autostat Omnibus, 2020). Arrojo (2000) and Carlsson (1995) have studied pavement wear for roads with different traffic intensities of vehicles with studded tires. Proposed by Carlsson (1995), SPS index indicates the actual wear from a certain amount of traffic with studded tyres during a particular measuring period, usually one cold season. The SPS index was used in the model without modification.

Table 4. Values of energy transferred to the surface during car movement

Functional zone	Energy of 1 car, MJ/ha/h
road	54
driveway	62
illegal parking	70

Table 5. Values of coefficients a and b depending on the type of pavement (Lugov et al. 2013)

No.	Pavement type	a	b
1	Asphalt-concrete	0.4…0.6	0.25…0.55
2	Crushed stone and gravel, treated with binders with a layer of wear:		
	a) double surface treatment	1.3…2.7	3.5…5.5
	b) single surface treatment	1.4…2.8	4.0…6.0
3	Crushed stone:		
	a) from firm rocks	4.5…5.5	15.0…20.0
	b) from low-strength rocks	5.5…6.5	19.0…25.0
4	Gravel:		
	a) of strong gravel	3.0…4.0	20.0…30.0
	b) gravel of low strength	4.0…6.0	

Table 6. I-factor values by functional zone (kg/MJ)

Functional zone	Undisturbed surface	Disturbed surface
road	0.0000107	0.00128
driveway	0.00000462	0.000555
illegal parking	–	0.000486

The calculations do not take into account cars equipped with studded tires in the warm period, as this is a violation of the law and is rather an exception to the rules. This type of all-season tires is common in the southern regions of Russia, but since this type of tires is not equipped with studs, it is not included in the calculations for the cold period.

The SPS index (Carlsson et al. 1995) can be used to calculate the wear of hard surfaces under the influence of studded tires. The SPS index is the Swedish abbreviation for specific wear. It can be represented as follows:

1. SPS = number of tons of asphalt abrasion per kilometer of road and one million cars with studded tires;
2. SPS = number of grams of asphalt abrasion per kilometer of road and car with studded tires.

The SPS index is based on three different methods of wear measurement: measurement on the road, measurement on slabs laid in the road and measurement on slabs in the VII's road simulator (Carlsson et al. 1995). SPS can be calculated as:

$$SPS = \frac{AW \times LW \times RL \times BD}{AADT \times WP \times SF} \quad (14)$$

where *AW* is the average wear, m/vehicle; *LW* is the lane width, m; *RL* is the road length (1 km), m; *BD* is the bulk density, g/m^3; *AADT* is the average annual daily traffic, vehicles/day, *WP* is the wear period, cold season days/y; *SF* is the stud frequency, %.

The material or type of pavement and the average annual daily traffic will affect the amount of wear. It has also been determined on a road simulator that the weight of a stud can have a 50% increase in wear (Carlsson et al. 1995). Modern studs are mostly lightweight and bi-component. The stud body is made of aluminum instead of steel and the core is made of a hard alloy material.

Developed model for estimating sediment production in urban environments

The final equation for estimating sediment production in an urban area is as follows:

$$USP = \left(\frac{A_p + A_{sm}}{10}\right) + A_{sl} + \left(SPS \times N_c \times k\right) \quad (15)$$

where *USP* is the urban sediment production, kg/m^2/y, A_p is the average annual soil loss from precipitation, t/ha/y; A_{sm} is the average annual snowmelt soil loss, t/ha/y; A_{sl} is the average annual production of sediment from studless tire abrasion, kg/m^2/y; *SPS* is the road wear caused by studded tires, g/km/car; N_c is the number of cars per cold season; *k* is the road length and width correction factor.

Calculations

Sediment production in Ekaterinburg conditions

Estimations of sediment production in warm and cold seasons for different functional zones under real and ideal conditions for Ekaterinburg obtained using the developed model (15) are presented in Table 7. The figures presented in Table 7 refer to areas of the EURL segments that belong to a specific functional zone. The Table 7 includes the areas of different functional zones which are assigned within the EURL model. Under real conditions annual sediment production varies from 0.02 at sidewalks to 6.74 kg/m^2 at roads.

The total sediment production for the entire EURL by seasons for Ekaterinburg is presented in Fig. 2. After summation of the warm and cold seasons estimations the sediment production is equal to 1.2 and 0.44 kg/m^2/y for the real and ideal conditions, respectively. There is a significant difference between estimations obtained for the real and ideal conditions during cold season due to the use of studded tires when considering the real seasonal conditions of sediment production. The model predicts a 3.5-fold increased sediment production in cold season. At the same time, the increase in the sediment production in the warm season is lower – 1.7 times. In the yard part of the EURL, the sediment production under real conditions is 0.34 kg/m^2/y, that is about three times higher than under ideal conditions. The highest sediment production is observed on illegal parking lots. According to the applied model, the sediment production in the legal parking lots and in the driveways of the yards is ten times lower than in the illegal parking lots.

The contributions of the main groups of factors of the sediment production at the model site for Ekaterinburg are shown in Fig. 3. The following groups of factors are considered: 1) ideal conditions of urban land maintenance, 2) exploitation of the urban road network during the cold period, 3) real conditions of internal and 4) external part of the EURL. According to the modeling performed, the exploitation of the urban road network during the cold period contributes 44% to the total annual supply of solid sediment. It can also be noted that 37% of the total sediment production is related to sediment generated even with high requirements to land maintenance are met. The disturbed areas of the functional zones at the external part of the EURL contribute 5% to the total sediment production, while the disturbed areas in the yard part, which mainly include illegal parking lots, contribute 14%. The dynamics of the USDS accumulation can be estimated using a simple differential model:

Table 7. Annual sediment production in warm and cold seasons under real and ideal conditions

No.	Functional zone	Area, m^2	Real conditions		Ideal conditions	
			warm, kg/m^2/y	cold, kg/m^2/y	warm, kg/m^2/y	cold, kg/m^2/y
1	road	1353	1.64	5.10	1.26	1.30
2	driveway	2744	0.08	0.02	0	0
3	lawn (external part)	984	0.07	0.13	0.03	0.05
4	lawn (internal part)	2335	0.10	0.19	0.03	0.06
5	sidewalks (external part)	367	0.01	0.01	0	0
6	sidewalks (internal part)	1348	0.02	0.02	0	0
7	playground	594	0.43	0.85	0.34	0.67
8	illegal parking	275	1.33	1.28	–	–

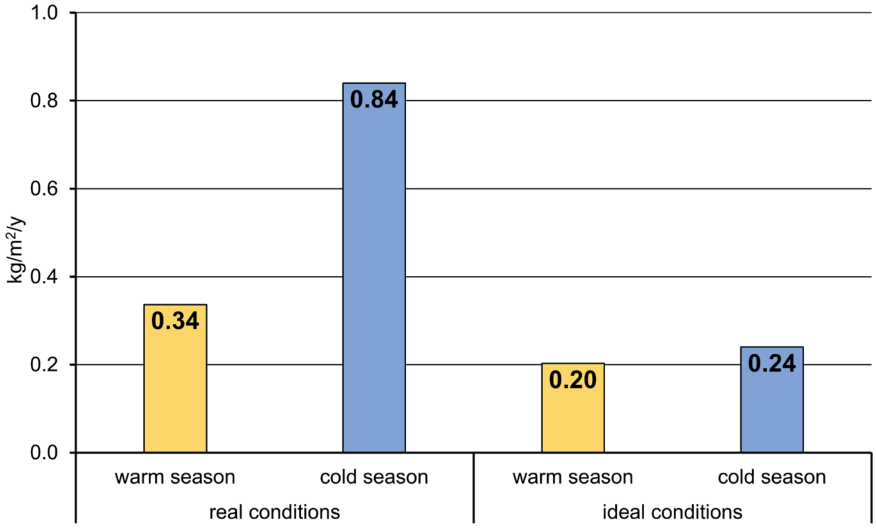

Fig. 2. Total sediment production in typical EURL

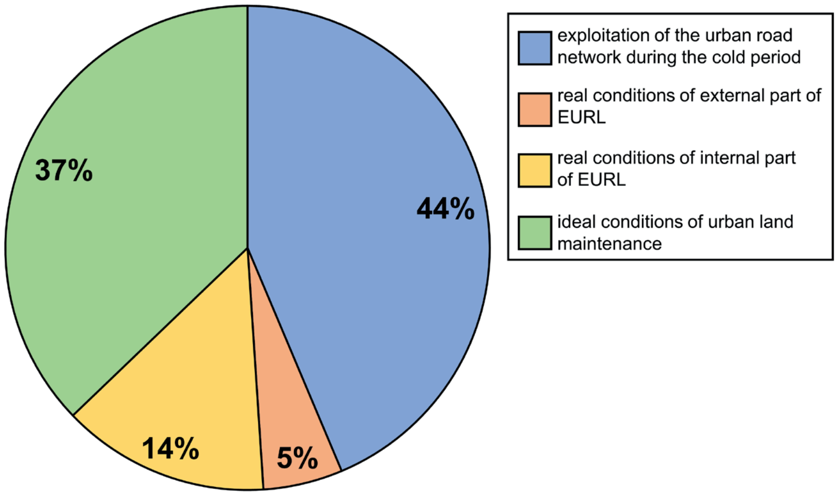

Fig. 3. Contribution of the different groups of factors to the process of sediment production in the urban environment

$$\frac{dC}{dt} = a - b \cdot C(t) \tag{16}$$

where C is the USDS storage, kg/m^2; t is the time, year; $a = 1.2$ kg/m^2/y is sediment production obtained in current study; b is the removal rate, year^{-1}. Under constant a and b, this function approaches an equilibrium value C_{eq}.

Previously, data on the storage of the USDS in the residential part of Ekaterinburg were obtained based on the study of the content of solid material in snow-dirt sludge sampled during cold season. The value of 3.2 kg/m^2 was obtained (Seleznev et al. 2019). Assuming constant conditions of sediment production and removal this value can be accepted as C_{eq}. Various landscaping activities including earthworks and construction, which may contribute to the sediment production process in the residential areas, are not considered in the developed model (USP). Such a contribution can be tentatively estimated as 10%. Thus, 2.9 kg/m^2 can be accepted as the estimation of sediment storage C_{eq} due to natural and anthropogenic processes, excluding earthworks. Solving equation (16) under such boundary conditions leads to b equal to 0.41 year^{-1}. Thus, the actual rate of removal of the USDS outside the residential area due to both anthropogenic and natural processes is almost two times lower than that required to minimize accumulation. The low removal rate leads to a significant accumulation of the USDS within the residential areas. For new urban landscapes, at such removal rate, an equilibrium between sediment production and removal will be reached in about six years.

Sediment production depending on the duration of the cold period

The results of the calculations of the sediment production in Russian cities with different duration of cold period (winter season) (from 1 to 9 months) are shown in Fig. 4. According to the results of the model calculations, the sediment production in Russian cities is in the range from 0.74 to 1.7 kg/m^2/y. Fig. 3.3 shows a clear correlation between the sediment production and cold period duration. The longer the cold period, the more solid material formed due to the abrasive effect of the studs on the paved surface. Calculations were made for the same traffic intensity (1300 cars per hour). The example of the city of Sochi in Fig. 3.3 shows the influence of atmospheric precipitation on the process of sediment formation. The relative increase in sediment production in this city is associated with the maximum amount of atmospheric precipitation of more than 1500 mm/y, which exceeds the same values in other cities by 2-4 times.

DISCUSSIONS

The factors and conditions of sediment production in Russian cities are considered in the developed model. The model is based on the RUSLE model modified for the urban environment, a model for estimating pavement abrasion production by studless tires based on the general principle of the RUSLE model, and other unmodified models. Using the developed model and the EURL, estimates of sediment production were obtained for the city of Ekaterinburg and

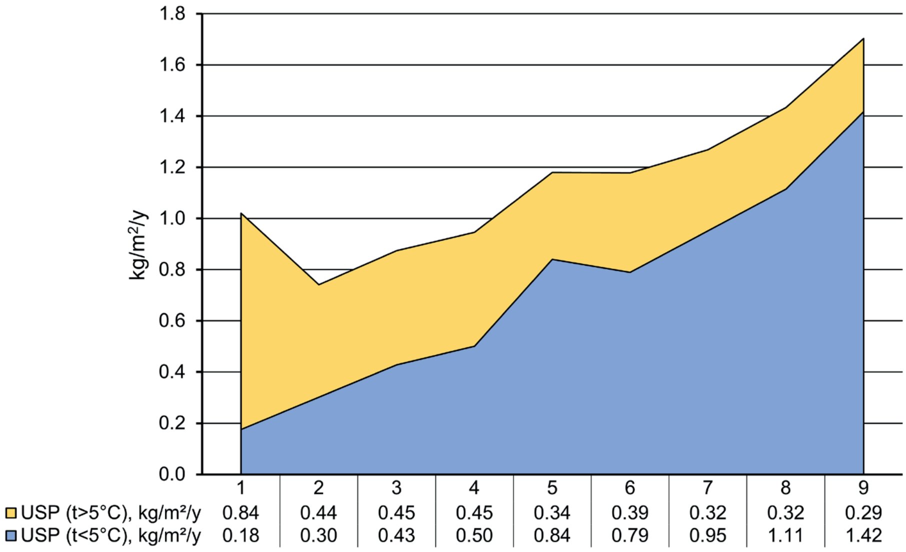

Fig. 4. Sediment production in urban environment depending on the cold season duration

seven other large Russian cities located in different climatic conditions. The dependence of sediment production on the duration of the cold period was verified.

Findings in the context of sediment production in urban environments

In the development of the model we have taken into account the conditions that are typical for large cities with a population of millions of people in Russia. The majority of the urban population live in multi-family, multi-storey buildings. A large part of the modern housing stock was built in the period from 1950 to 1991, taking into account the requirements of the building standards valid in the Soviet Union. The predominant part of the buildings has five floors and more that causes a fairly high density of the population. Throughout the country, residential areas of large cities are arranged in a similar manner: residential buildings face the street and road network, several residential buildings limit the common yard area. The basic elements of the residential block landscape (EURL) are the yard, the residential buildings, and the nearby street and road network. On average, such an element has an area of 10000 m^2, as shown in (Yarmoshenko et al. 2020). The developed modification of the sedimentation model is designed to be applied to such an element of the landscape. It is assumed that for territories of residential blocks of a large city the calculations for one element of the landscape are representative for estimation of sediment production in the entire residential land use area.

For the modification of the model of sediment production in the urban landscape, both experimental data and model results of vehicle impact on different types of pavements under different operating conditions have been used. The fact that in Russian cities a large number of cars are parked in internal parts of the blocks of multi-storey buildings is taken into account when modeling the impact of vehicles on different parts of the landscape. Before 1991, a small number of parking lots in yards was provided in standard projects of improvement of development with multi-storey buildings. In the modern conditions with the explosion of automobilization, which took place in the last decade, the yards were overcrowded with cars, even though the underground parking lots and the surface parking lots were organized away from the residential blocks. With the overcrowding of yards, some cars are parked in yards in the areas that are not intended for this purpose. Self-parking on lawns and playgrounds is widespread in all the cities surveyed, despite the fact that Russian society perceives such parking practices negatively.

A specific condition of the sediment production in the cities of Russia is the long period of cold weather. Temperatures below 0°C and permanent snow cover are established over a large area during the cold period. During the long cold period, most vehicles are equipped with studded tires. The height of the snow cover can reach several tens of centimeters. In spring, the snow melts intensively for 1-2 weeks, which significantly intensifies the weathering process.

According to the results of the calculation made for Ekaterinburg, the average sediment production in a modern Russian city is 1.2 $kg/m^2/y$. According to Russel et al. (2017) the sediment yield in urban areas without pronounced cold season conditions is defined in the range up to 1.8 $kg/m^2/y$ with a median of 0.33 $kg/m^2/y$. During the active period of construction - up to 27 $kg/m^2/y$ with a median of 5.4 $kg/m^2/y$ (Russel et al. 2017). More than 1 kg of sediment is found along 1 meter of road curb in a study conducted in British Columbia, Canada (Owens et al. 2011). Though the relationship between the sediment production and sediment yield is indirect, it can be noted that these estimates are close to the results obtained in this paper, while the average sediment production in large Russian cities is above the median and close to the maximum sediment yield in other countries.

The use of studded tires in cold period, illegal parking, disturbed lawns, asphalt and other pavements are the main causes of increased sediment production. Sedimentation is increased by a factor of 2.7 due to the intense anthropogenic impact associated with these factors. In the absence of these causes, the sediment production would be 0.44 $kg/m^2/y$. This is close to the median value obtained by (Russel et al. 2017).

Yards contribute approximately 14% of solid sediment. In internal parts of the EURL, parking on lawns and the poor condition of asphalt and lawn surfaces are the main causes of higher than ideal sediment production.

In general, Russian cities have a high sediment production. As shown by the modeling, the structure of the causes of the sediment production is to a large extent attributed to negative anthropogenic impacts. The intensive sediment production occurs both on the network of streets and roads, and in the areas of yards.

Increased sediment production is one of the major factors reducing the quality of the urban environment. The sediment storage is associated with negative environmental, medical, infrastructural, psychological and other issues. Reduction of sediment production is an important task of urban environment improvement and, more generally, of modern urbanism as a trend of social life.

Sediment surface storage depends on the rate of sediment production and removal of stored sediment. In the urban catena, the sediment removal is assumed to occur by two ways – natural and anthropogenic. Applying catena simplification, the EURL is located within the hill top and hill slope parts. The lower part of the urban catena is represented by a storm drain system and a waterway bed which is located outside of the EURL. In this way, sediment removal occurs through natural runoff. Wind lifting of the dust sediment fraction also contributes to surface sediment removal. The anthropogenic way involves the removal of the surface sediments during cleaning and other landscaping services. Anthropogenic removal also includes the transport of the USDS by the wheels of vehicles.

Measures to reduce sediment production in urban environment

The developed model of sediment production in the urban environment and further estimations allow to evaluate the effectiveness of various measures for the reduction of sediment production in the cities.

The restriction on the use of studded tires can be considered as a priority measure for the reduction of sediment production in regions with long cold season. In situation when studded tires are banned, the sediment production will decrease from 1.2 kg/m^2/y to 0.44 kg/m^2/y However, this solution involves a number of organizational and technical difficulties. Currently, there are no sufficiently inexpensive innovative type road pavements that can be used to provide the necessary grip with studless tires in freezing and icy conditions. The studless tires do not provide the necessary grip on icy parts of roads and yard driveways. If cold season traffic is reduced, the impact of studs will also be reduced. For example, total sediment production can be decreased from 1.2 to 0.92 kg/m^2/y and the contribution of studded tires would decrease from 44% to 28% if the proportion of cars (or the number of cars in the city) with studded tires is reduced by half. In general, it should be noted that a change in cold season vehicle use practices requires further researches and technological innovations.

Qualitative performance of pavements and lawns repairs on time can reduce the sediment production through the reduction of anthropogenic and natural influences on the disturbed surfaces. In Ekaterinburg, sediment production can be reduced by 19% if the technical conditions of all pavements are properly maintained.

One of the measures for reduction of the USDS accumulation in residential areas can be the increase of the cleaning efficiency. Calculations based on the model (16) show that the amount of the USDS will be reduced to 0.5 kg/m^2 in about 4 years if additional cleaning with the intensity of 1.2kg/m^2/y (i.e. equal to the annual supply) on the territory with the initial level of accumulation of 3.2 kg/m^2 is organized.

Introducing a total ban on parking in residential yards will reduce the anthropogenic impact on surfaces, exclude parking on lawns, and consequently reduce the sediment production of disturbed surfaces. For complexes of new residential buildings, this approach to solving the problem of pollution of residential yards with sediment material is widely used. In this case, such complexes are equipped with large underground and external parking lots. In the residential areas that were built earlier, e.g. before the year 2000, surface and underground parking lots were often not provided. Therefore, measures to restrict vehicle access to internal parts of the EURL designed before 2000 will cause a negative response of car owners, and thus are unlikely to be accepted by the majority of society.

As can be seen from solving equation (16), proper organization of surface runoff plays a certain role in sediment transport and deposition processes. A part of the USDS can be transported out of the yards and get into the storm water drainage system and into other artificial and natural streams. The proper organization of surface runoff is usually a consideration at the design stage of construction of new residential complexes. Previous landscape surveys (Yarmoshenko et al. 2020) have shown that, in general, in most courtyards of multi-storey buildings in Russian cities the runoff is properly arranged, especially the formation of huge puddles is prevented. However, the formation of local low-lying areas (relief depressions) with small puddles and the accumulation of the USDS is not excluded.

Sediment reduction measures must be applied to different parts of the urban landscape. In modern Russian cities, streets and adjacent sidewalks and lawns are the responsibility of the city government. The quality of internal parts and yards are under the responsibility of homeowners. The lack of consistency in environmental quality management may be one of the reasons for the ineffectiveness of sediment production reduction measures.

Full implementation of strict requirements for reduction of sediment production in urban conditions is equivalent to approaching the ideal conditions. Achieving the ideal conditions allow the pollution of the urban environment with the USDS to be reduced to 0.44 kg/m^2/y in Ekaterinburg.

Limitations of the developed model

A number of assumptions and simplifications were made in constructing the model and modeling the sediment production process in this study. These assumptions and simplifications are associated with the uncertainty in the estimates obtained. The main sources of uncertainty of the model are the following ones:

• uncertainty of the coefficients R, K, LS, C, P, h in RUSLE model;

• uncertainty of coefficients describing the dependence of warm season pavement wear on warm and cold seasons vehicle loads;

• lack of qualitative data on vehicle loadings and traffic;

• the variability of the landscape characteristics of the yards and roads.

In general, the above sources of uncertainty can have a significant impact on the results of sediment production estimation for specific real sites. At the same time, with the help of the developed model, the average characteristics for the residential areas of the city can be returned correctly enough for the estimation of the total amount of generated USDS and the contribution of different functional zones and factors.

Generally, there is no strong limitation to apply the developed model of sediment production in the urban environment in other regions of the world. However, not all countries have a residential block organization similar to the Russian one. The situation is quite different in some countries where people live mainly in single-family homes in the suburbs. In this case, it is necessary to apply another model of elementary urban landscape developed in accordance with the conditions of the area under study. The use of different model sites does not change the principles of the model structure, if all estimated factors are taken into account. It is important to note that many factors in the models are also necessary to be adjusted for a specific territory.

CONCLUSIONS

1. A model of sediment production in the urban environment has been developed. The model takes into account both natural and anthropogenic factors and

processes. The model is built using empirical coefficients that take into account the characteristics of natural and anthropogenic influences.

2. According to the results of the modeling, the sediment production in Ekaterinburg is about 1.2 kg/m^2/y and, in other Russian cities, varies from 0.74 to 1.7 kg/m^2/y.

3. The sediment production in a modern Russian city estimated using the model corresponds to the previous assessment of the USDS storage taking into account a reasonable equilibrium between production and removal. The obtained results of the modeling logically explain the differences in the rates of sediment production in the Russian cities and the data on other regions, taking into account the climatic conditions, the greater anthropogenic load in the blocks of multy-storey buildings and the quality of urban management.

4. The quantitative contribution of the different factors in the sediment production in the urban conditions has been determined. It was found that cold season exploitation of vehicles equipped with studded tires account for 44% (about 0.51 kg/m^2/y) of the sediment production. At the same time, even in the case of high requirements for the territory maintenance, the expected sediment production reaches 0.44 kg/m^2/y.

5. Measures to reduce the sediment production in the modern urban environment have been analyzed: restriction on the use of studded tires, cold season traffic reduction, reduction of vehicle load on yard spaces, higher requirements for the technical condition of infrastructure and maintenance of residential areas, etc.

6. The reference USDS removal rate that ensures a high efficiency of the measures to reduce the sediment accumulation is defined.

Declarations All authors certify that they have no affiliations with or involvement in any organization or entity with any financial interest or non-financial interest in the subject matter or materials discussed in this manuscript.

REFERENCES

Aouichaty N., Bouslihim Y., Hilali S., Zouhri A., Koulali Y. (2022). Estimation of water erosion in abandoned quarries sites using the combination of RUSLE model and geostatistical method. Scientific African, 16, e01153, DOI: 10.1016/j.sciaf.2022.e01153.

Arrojo G.M. (2000). Pavement wear caused by the use of studded tyres. DIVA. https://urn.kb.se/resolve?urn=urn:nbn:se:vti:diva-1204.

AUTOSTAT OMNIBUS – 2020. Winter car tires: car owners' preferences (fourth wave). Surveys | AUTOSTAT. Available at: https://www.autostat.ru/research/product/384/.

Basic Information about Nonpoint Source (NPS) Pollution | US EPA. (2022, December 22). US EPA. Available at: https://www.epa.gov/nps/basic-information-about-nonpoint-source-nps-pollution.

Carlsson A., Centrell P., Öberg G. (1995). Studded tyres: socio-economic calculations. Statens väg- och transportforskningsinstitut, Linköping.

Cendrero A., Remondo J., Beylich A.A., Cienciala P., Forte L.M., Golosov V., Gusarov A.V., Kijowska-Strugała M., Laute K., Li D., Navas A., Soldati M., Vergari F., Zwoliński Z., Dixon J., Knight J., Nadal-Romero E., Płaczkowska E. (2022). Denudation and geomorphic change in the Anthropocene; a global overview. Earth-Sci Rev, 233, 104186, DOI: 10.1016/j.earscirev.2022.104186.

Chen C., Zhao G., Zhang Y., Bai Y., Tian P., Mu X., Tian X. (2023). Linkages between soil erosion and long-term changes of landscape pattern in a small watershed on the Chinese Loess Plateau. CATENA, 220, 106659, DOI: 10.1016/j.catena.2022.106659.

Chin A., Beach T., Luzzadder-Beach S., Solecki W. (2017). Challenges of the "Anthropocene." Anthropocene, 20, 1–3, DOI: 10.1016/j.ancene.2017.12.001.

Corradini F., Meza P., Eguiluz R., Casado F., Huerta-Lwanga E., Geissen V. (2019). Evidence of microplastic accumulation in agricultural soils from sewage sludge disposal. Sci Total Environ, 671, 411-420, DOI: 10.1016/j.scitotenv.2019.03.368.

Crosby C.J., Fullen M.A., Booth C.N., Searle D.E. (2014). A dynamic approach to urban road deposited sediment pollution monitoring (Marylebone Road, London, UK). J Appl Geophys, 105, 10–20, DOI: 10.1016/j.jappgeo.2014.03.006.

Di Miceli Da Silveira A., Pereira J.A., Poleto C., De Lima J., Gonçalves F.S., Alvarenga L.A., Isidoro J. (2016). Assessment of loose and adhered urban street sediments and trace metals: a study in the city of Poços de Caldas, Brazil. J Soils Sediments, 16:2640–2650, DOI: 10.1007/s11368-016-1467-5.

Dias-Ferreira C., Pato R.L., Varejão J.M., Tavares A.O., Ferreira A. (2016). Heavy metal and PCB spatial distribution pattern in sediments within an urban catchment—contribution of historical pollution sources. J Soils Sediments, 16(11), 2594–2605, DOI: 10.1007/s11368-016-1542-y.

Filkin N.M., Shaikhov R.F., Buyanov I.P. (2016). Teoriya transportnyh i transportno-tekhnologicheskih mashin: Uchebnoe posobie [Theory of transport and transport-technological machines: Textbook], Perm: FGBOU VO Perm State Agricultural Academy, 230 p. (in Russian)

Gafurov F.G. (2008). Pochvy Sverdlovskoj oblasti [Soils of the Sverdlovsk Region], Ekaterinburg: Urals-University Publishing House, 396 p. (in Russian)

Golosov V., Tsyplenkov A. (2021). Factors Controlling Contemporary Suspended Sediment Yield in the Caucasus Region. Water, 13(22), 3173, DOI: 10.3390/w13223173.

Haynes H.M., Taylor K.G., Rothwell J.J., Byrne P.J. (2020). Characterisation of road-dust sediment in urban systems: a review of a global challenge. J Soils Sediments, 20(12), 4194–4217, DOI: 10.1007/s11368-020-02804-y.

Hewett C.J.M., Simpson C., Wainwrigh J., Hudson S. (2018). Communicating risks to infrastructure due to soil erosion: A bottom-up approach. Land Degrad. Dev., 29(4), 1282–1294, DOI: 10.1002/ldr.2900.

Igwe P.U., Onuigbo A.A., Chinedu O.C., Ezeaku I.I., Muoneke M.M. (2017). Soil Erosion: A Review of Models and Applications. IJAERS, 4(12), 138–150, DOI: 10.22161/ijaers.4.12.22.

Kasimov N.S. (2013). Ekogeohimiya landshaftov [Ecogeochemistry of Landscapes], Moscow, IP Filimonov M.V., p. 208 (in Russian).

Knijff J.M., Jones R.J.A., Montanarella L. (1999). Soil erosion risk assessment in Italy. European Soil Bureau, 19044, 52.

Landrigan P.J., Fuller R.A., Acosta N.J.R., Adeyi O., Arnold R.M., Basu N., Baldé A.B., Bertollini R., Bose-O'Reilly S., Boufford J.I., Breysse P.N., Chiles T.C., Mahidol C., Coll-Seck A.M., Cropper M.L., Fobil J.N., Fuster V., Greenstone M., Haines A., Zhong M. (2017). The Lancet Commission on pollution and health. The Lancet, 391(10119), 462–512, DOI: 10.1016/s0140-6736(17)32345-0.

Larionov G.A. (1993). Eroziya i deflyatsiya pochv: osnovnyye zakonomernosti i protivoerozionnykh meropriyatiy [Experience in calculating soil erosion for the construction of a set of anti-erosion measures], Eurasian Soil Sci., 4, 92–104.

Li X., Liu B., Zhang Y., Wang J., Ullah H., Zhou M., Peng L., He A., Zhang X., Yan X., Yang T., Wang L., Yu H. (2019). Spatial Distributions, Sources, Potential Risks of Multi-Trace Metal/Metalloids in Street Dusts from Barbican Downtown Embracing by Xi'an Ancient City Wall (NW, China). IJERPH, 16(16), 2992, DOI: 10.3390/ijerph16162992.

Lisbôa É.G., Blanco C.J.C., Maia R., Bello L.L. (2017). A stochastic estimation of sediment production in an urban catchment using the USLE model. Hydrolog Sci J, 62(15), 2571–2586, DOI: 10.1080/02626667.2017.1395031.

Lugov S.B. (2013). Vozmozhnosti raschetnoj ocenki iznosa pokrytij pri prognozirovanii koleeobrazovaniya [Possibilities of Calculated Assessment of Wear of Coatings in Predicting Rutting], Bulletin of the Moscow State Automobile and Road Technical University (MADI), No. 4(35), 53-59. (in Russian)

Maltsev K.A., Yermolaev O. (2020). Assessment of soil loss by water erosion in small river basins in Russia. CATENA, 195, 104726, DOI: 10.1016/j.catena.2020.104726.

Merritt W., Letcher R., Jakeman A. (2003). A review of erosion and sediment transport models. Environ Modell Softw, 18(8–9), 761–799, DOI: 10.1016/s1364-8152(03)00078-1.

Michalek A.J., Zarnaghsh A., Husic A. (2021). Modeling linkages between erosion and connectivity in an urbanizing landscape. Sci Total Environ, 764, 144255, DOI: 10.1016/j.scitotenv.2020.144255.

Moore I.D., Wilson J. (1992). Length-slope factors for the Revised Universal Soil Loss Equation: simplified method of estimation. J Soil Water Conserv, 47(5), 423–428. https://www.jswconline.org/content/47/5/423.

Murakami M., Nakajima F., Furumai H., Tomiyasu B., Owari M. (2007). Identification of particles containing chromium and lead in road dust and soakaway sediment by electron probe microanalyser. Chemosphere, 67(10), 2000–2010, DOI: 10.1016/j.chemosphere.2006.11.044.

Najafi S.K., Dragovich D., Comiti F., Sadeghi S.H. (2021). Sediment connectivity concepts and approaches. CATENA, 196, 104880, DOI: 10.1016/j.catena.2020.104880.

Owens P.N. (2020b). Soil erosion and sediment dynamics in the Anthropocene: a review of human impacts during a period of rapid global environmental change. J Soils Sediments, 20(12), 4115–4143, DOI: 10.1007/s11368-020-02815-9.

Owens P.N., Caley K.A., Campbell S.N., Koiter A.J., Droppo I.G., Taylor K.G. (2011). Total and size-fractionated mass of road-deposited sediment in the city of Prince George, British Columbia, Canada: implications for air and water quality in an urban environment. J Soils Sediments, 11(6), 1040–1051, DOI: 10.1007/s11368-011-0383-y.

Pereira Pa.A., Ferreira A., Sarah P., Cerdà A., Walsh R.P.D., Keesstra S. (2016). Preface. J Soils Sediments, 16(11), 2493–2499, DOI: 10.1007/s11368-016-1566-3.

Polluted Runoff: Nonpoint Source (NPS) Pollution | US EPA (2023, March 16) US EPA. Available at: https://www.epa.gov/nps.

Renard K.G., Foster G.R., Weesies G.A., Porter J.I. (1991). RUSLE: Revised universal soil loss equation. J Soil Water Conserv., 46(1). 30–33.

Renard K.G., Foster G.W., Weesies G.A., McCool D.K., Yoder D.C. (1997). Predicting soil erosion by water: a guide to conservation planning with the Revised Universal Soil Loss Equation (RUSLE).

Restrepo J.M., Syvitski J.P.M. (2006). Assessing the Effect of Natural Controls and Land Use Change on Sediment Yield in a Major Andean River: The Magdalena Drainage Basin, Colombia. AMBIO, 35(2), 65–74, DOI: 10.1579/0044-7447(2006)35.

Romkens M.J.M., Baumhardt R.L., Parlange M.B., Whisler F.D., Parlange J.Y., Prasad S.N. (1986). Rain-induced surface seals: their effect on ponding and infiltration. Annales Geophysicae, 4, B(4), 417–424.

Russell K.M., Vietz G., Fletcher T.D. (2017). Global sediment yields from urban and urbanizing watersheds. Earth-Sci Rev, 168, 73–80, DOI: 10.1016/j.earscirev.2017.04.001.

Seleznev A.A., Ilgasheva E., Yarmoshenko I.V., Malinovsky G. (2021). Coarse Technogenic Material in Urban Surface Deposited Sediments (USDS). Atmosphere, 12(6), 754, DOI: 10.3390/atmos12060754.

Seleznev A.A., Shevchenko A.V., Gluhov V.S., Malinovsky G.P. (2022). Assessment of the sediment supply from the catchment into a water body in an urban area. TR-MNT, 4, 13–29, DOI: 10.56564/27825264_2022_4_13.

Seleznev A.A., Teterin A., Yarmoshenko I.V. (2020). Meteorological conditions of surface sediment runoff formation during spring snowmelt in urban areas. IZVESTIYA, DOI: 10.18799/24131830/2020/2/2476.

Seleznev A.A., Toropov A.S., Okuneva T.G., Kiseleva D.V., Yarmoshenko I.V., Ryanskaya A.D. (2023). Migration of natural radionuclides in the system «hydrocriogenic components - water - ground waters of born waters» in citizens' waters. Proceedings of Tomsk Polytechnic University, 334(5), 189-204, DOI: 10.18799/24131830/2023/5/3969.

Seleznev A.A., Yarmoshenko I.V., Malinovsky G. (2019a). Assessment of Total Amount of Surface Sediment in Urban Environment Using Data on Solid Matter Content in Snow-Dirt Sludge. Environ. Process., 6(3), 581–595, DOI: 10.1007/s40710-019-00383-w.

Seleznev A.A., Yarmoshenko I.V., Malinovsky G. (2020). Urban geochemical changes and pollution with potentially harmful elements in seven Russian cities. Sci Rep, 10(1) , DOI: 10.1038/s41598-020-58434-4.

Seleznev A.A., Yarmoshenko I.V., Malinovsky G., Ilgasheva E., Baglaeva E., Ryanskaya A., Kiseleva D., Gulyaeva T. (2019b). Snow-dirt sludge as an indicator of environmental and sedimentation processes in the urban environment. Sci Rep, 9(1) , DOI: 10.1038/s41598-019-53793-z.

Stojiljkovic A., Kauhaniemi M., Kukkonen J., Kupiainen K., Karppinen A., Denby B., Kousa A., Niemi J.K., Ketzel M. (2019). The impact of measures to reduce ambient air PM10 concentrations originating from road dust, evaluated for a street canyon in Helsinki. Atmos. Chem. Phys., 19(17), 11199–11212, DOI: 10.5194/acp-19-11199-2019.

Syvitski J., Ángel J.R., Saito Y., Overeem I., Vörösmarty C.J., Wang H., Olago D. (2022). Earth's sediment cycle during the Anthropocene. Nat Rev Earth Environ, 3(3), 179–196, DOI: 10.1038/s43017-021-00253-w.

Taoufik M., Loukili I., Hadi H.E, Baghdad B. (2020). Soil erosion risk assessment in an extraction area: Case of abandoned quarries in the Akreuch region (Morocco). IEEE International conference of Moroccan Geomatics (Morgeo), DOI: 10.1109/morgeo49228.2020.9121910.

Taylor K. (2007). Urban environments. In: Perry C, Taylor K (eds) Environ Sediment, Wiley-Blackwell, Hoboken, 190–222.

Taylor K.G., Owens P.N. (2009). Sediments in urban river basins: a review of sediment–contaminant dynamics in an environmental system conditioned by human activities. J Soils Sediments, 9(4), 281–303, DOI: 10.1007/s11368-009-0103-z.

Turevsky I.S. (2005). Teoriya avtomobilya: Ucheb. posobie [Car Theory: Textbook], Moscow: Vyssh. shk. 240 p., ISBN 5-06-004615-X.

Vasiliev A.P., Balovnev V.I., Korsunsky M.B. (1989). Remont i soderzhanie avtomobil'nyh dorog: Spravochnik inzhenera-dorozhnika [Repair and maintenance of highways: Handbook of road engineer], edited by A. P. Vasiliev, M.: Transport, 287 p. (in Russian)

Waters C.N., Zalasiewicz J., Summerhayes C., Barnosky A.D., Poirier C., Gałuszka A., Cearreta A., Edgeworth M., Ellis E.C., Ellis M., Jeandel C., Leinfelder R., McNeill J.R., Richter D.D., Steffen W., Syvitski J., Vidas D., Wagreich M., Williams M., Wolfe A.P. (2016). The Anthropocene is functionally and stratigraphically distinct from the Holocene. Science, 351(6269) , DOI: 10.1126/science.aad2622.

Wischmeier W.H., Smith D.J. (1978). Predicting rainfall erosion losses: a guide to conservation planning. In Predicting rainfall erosion losses - a guide to conservation planning, vol. 537, p. 62.

Yarmoshenko I.V., Malinovsky G., Baglaeva E., Seleznev A.A. (2020). A Landscape Study of Sediment Formation and Transport in the Urban Environment. Atmosphere, 11(12), 1320, DOI: 10.3390/atmos11121320.

Yu B., Rosewell C. (1996). Rainfall erosivity estimation using daily rainfall amounts for South Australia. Soil Res, 34(5), 721, DOI: 10.1071/sr9960721.

RESEARCH PAPER

THE AEROSOL POLLUTION OF THE ATMOSPHERE ON THE EXAMPLE OF LIDAR SENSING DATA IN ST. PETERSBURG (RUSSIA), KUOPIO (FINLAND), MINSK (BELARUS)

Dmitriy A. Samulenkov, Maxim V. Sapunov
St. Petersburg University, 7-9 Universitetskaya Embankment, St Petersburg, Russia, 199034
*Corresponding author: samulenkov_da@mail.ru
Received: February 15th, 2023 / Accepted: November 14th, 2023 / Published: December 31st, 2023
https://DOI-10.24057/2071-9388-2023-2772

ABSTRACT. The results of lidar sensing of aerosol pollution in St. Petersburg (Russia) were compared with ones located in Minsk (Belarus) and Kuopio (Finland) to assess the impact of large cities on atmospheric pollution by aerosol particles. For comparison, aerosol optical depth (AOD) data obtained at the three stations from 2014 to 2021 were used. Lidar sounding of atmospheric aerosols was carried out using aerosol Nd:YAG lasers operating at three wavelengths: 355, 532 and 1064 nm. Due to differences in the lidar station equipment characteristics and, consequently, in the lower limit for determining aerosols, the aerosol optical depth was compared in the range of heights from 800 to 1600 m at 355 and 532 nm. Since the compared stations do not have data for all years, the period from 2014 to 2016 was analyzed separately. The average annual AOD 355 in Minsk in the period 2014-2016 is almost the same as the average annual AOD in St. Petersburg. When comparing data in St. Petersburg and Minsk for the period 2014-2020, AOD 355 in St. Petersburg exceeds AOD 355 in Minsk by 1.46 times. AOD 532 nm in Minsk is larger than in St. Petersburg, regardless of the chosen comparison period. The average annual AOT 355 in Kuopio is lower than in Minsk and St. Petersburg by 2.1 times, while at a wavelength of 532 nm they are 3.6 times lower than in Minsk and 2.6 times in St. Petersburg. The calculated Angstrom exponent coefficient shows that the coarse mode in Minsk is higher than in St. Petersburg. The atmosphere over Kuopio has a lower content of aerosol particles. Since 2017, there was a steady excess of aerosol content over St. Petersburg compared to Minsk. Additionally, a comparison of the lidar data with the total AOD of AERONET stations located in Kuopio, Minsk and Peterhof (25 km from the lidar station in St. Petersburg) was carried out. The AOD obtained by lidar and AERONET method is in good agreement.

KEYWORDS: aerosol, air pollution, aerosol optical depth, environmental monitoring of the atmosphere, lidar

CITATION: Samulenkov D. A., Sapunov M. V. (2023). The Aerosol Pollution Of The Atmosphere On The Example Of Lidar Sensing Data In St. Petersburg (Russia), Kuopio (Finland), Minsk (Belarus). Geography, Environment, Sustainability, 4(16), 156-163
https://DOI-10.24057/2071-9388-2023-2772

ACKNOWLEDGEMENTS: The work was performed using the equipment of the resource center "Observatory of Environmental Safety", Research Park of St. Petersburg State University This research was funded by Saint Petersburg State University, project ID: 101662710 (GZ_MDF-2023-1)

Conflict of interests: The authors reported no potential conflict of interest.

INTRODUCTION

The formation of atmospheric pollution in megacities is influenced by various factors – the number of sources of pollution, patterns of emissions distribution due to different landscapes, weather conditions, type of development, and other factors. Currently, the pollution from transport, emissions from industrial enterprises, as well as organic fuel combustion products can be distinguished from the main sources of anthropogenic air pollution. Naturally formed aerosols also contribute to atmospheric pollution (Kondratyev 2006). The natural sources of pollution are those whose formation does not depend on human activity. For example, the release of salt particles during evaporation of sea foam drops, production of pollen by plants, dispersion of soil particles and dust by wind (Zuev 1992).

In megacities, an aerosol cap is often formed in a layer up to one or two kilometers due to the rise of aerosol particles. The presence of windless weather worsens the situation: the resulting dense aerosol layer leads to environmental degradation, as well as an increase in surface temperature results in adverse effects on the health of population living in megacity.[1]

Back in the late 18th century, it was found that dust carried by air adversely affects human health. Thus, it was observed that chimney sweepers who often came into contact with high concentrations of soot often had cancer. In the second half of the 20th century, active research began, which showed the relationship between lung diseases and airborne aerosol particles. A large number of studies has been and is being currently conducted all over the world to assess the impact of aerosol particles on human health. The relationships between human exposure to aerosol particles and cardiovascular diseases, eye diseases, allergies, asthma, cancer, well-being and hospitalization of the population, and mortality among residents of aerosol-contaminated territories have been established. It also has been established that the smaller the diameter of aerosol particles in the atmosphere, the greater

[1]Doklad ob ekologicheskoj situacii v Sankt-Peterburge (Report on the environmental situation in St. Petersburg) // 2022.

the danger they pose to health (Agarwal 2017; Pandey 2020; Schraufnagel 2016; Schraufnagel 2020; Subramanian 2020; Wei 2019). Aerosol particles less than 1 micrometer penetrate deep into the lungs, reaching the alveoli. Recently, more and more studies are focused specifically on the effects of the smallest aerosol particles PM2.5, PM1 (Chen 2017; Hext 1999; Sharma 2020). Also, the danger of aerosols is associated with their ability to accumulate other pollutants on their surface, including carcinogens. It is worth noting that the effects caused by aerosol particles separately are often discussed in the literature, while their interaction with other pollutants taking the form of a synergistic effect, can have a much more significant impact on human health (Forest 2021). Another reason to pay special attention to pollution by aerosols is their ability to have an impact over hundreds of kilometers from the place of their formation due to their atmospheric transfer (Mallone 2011; Mona 2006).

Due to the extensive increase in the number of cars, the road transport is currently one of the main sources of pollution in the surface layer of the atmosphere in St. Petersburg, as well as in many other large cities (Nagy 2014). Constant traffic jams make things worse, because the discharge of pollutants mainly occurs at the time a car sets speed. Additionally, due to friction, a large number of abrasion products of automobile spikes, tires and asphalt is formed, which, in turn, are mixed with exhaust gases (Fussell 2022; Baensch-Baltruschat 2020; Kovochich 2021). Also, the soil layer brought onto the road by cars gets into this mixture. Further, all this multicomponent dust rises into the air and can be transferred by wind over long distances. In St. Petersburg in 2021, compared with 2020, the total number of motor vehicles increased by 1.67% (33886 units), while the number of passenger cars increased by 1.65% (29180 units), and the number of trucks – by 2.14% (4948 units).[2] There is an increase in the number of road transport in St. Petersburg. So in 2021, compared to 2020, the number of passenger cars increased by 1.65%, which is 29,180 cars, the number of trucks - by 2.14%, which is 4,948 units of trucks.

One of the methods that currently allow monitoring the aerosol pollution is the lidar method (Chazette 2023; Ma 2019). Lidar systems are an effective method for tracking the transport of aerosol particles. Lidar complexes find their applications for assessing the current state of the atmosphere and monitoring environmental pollution. (Aggarwal 2018; Ansmann 2005; Flamant2000; Ma 2019; McGill 2003; Yin 2021) The use of remote methods makes it possible to conduct research on the transfer of aerosol particles (Campbell 2016), calculate the atmospheric aerosol particle size distribution (Shi 2022; Samulenkov 2020).

Lidar data are used to obtain the addition information on the aerosol pollution of the atmosphere, including for spatial distribution of aerosol particle emissions in industrial areas and aerosol characteristics around highways (Yegorov 1995; Lisetskii 2019). Multiwave lidar complexes are used to monitor the transfer of aerosols of natural formation, which can also play an important role in total aerosol content under certain conditions (Ansmann 2021; Di Girolamo 2012; Kovalev 2009; Mona 2012; Vaughan 2021), and depend on the difference in air mass route and the ambient atmospheric conditions (Xie 2008). AOD studies provide an important information about the aerosol content in the atmosphere, understanding aerosol properties and improving the incorporation of aerosol effects into climate models (Kafle 2013; Khor 2014; Kong 2022; Xie 2010).

The lidar method is actively used and, therefore, there are many lidar measuring networks in the world: the Network for the Detection of Atmospheric Composition Change (NDACC, https://www.ndsc.ncep.noaa.gov) for global control of aerosol, ozone, temperature and humidity; the European Aerosol Research Lidar Network (EARLINET), the purpose of which is to track aerosol pollution on the European continent (Papagiannopoulos 2020); the NASA Micro-Pulse Lidar Network (MPL-Net) (Welton, 2018) for monitoring tropospheric aerosol. Studies of dust aerosol from the desert territory of China are carried out within the framework of the Asian Dust and aerosol lidar observation network (AD-Net) (Nishizawa, 2016); the Regional East Atmospheric Lidar Mesonet (REALM) in the Eastern USA was designed to monitor air quality (Hoff, 2002). Atmospheric aerosol monitoring in the Commonwealth of Independent States (CIS) is carried out by the CIS Lidar Network (CIS-LiNet), located in Russia, Belarus and Kyrgyzstan (Chaikovsky, 2006).

At the Resource Center “Observatory of Environmental Safety” of the St. Petersburg State University Science Park, the studies of aerosol pollution have been conducted since December 2013;the lidar station became a part of the EARLINET in 2014 . The station is located in the center of St. Petersburg on Vasilievsky Island, which is one of the most polluted parts of the city. This allows obtaining unique data on the aerosol pollution of the urban atmosphere. Minsk and St. Petersburg have the most extensive network of industrial enterprises, as well as a large population. About 5.4 million people lives in St. Petersburg, and 2 million people – in Minsk. The industry of St. Petersburg is based on more than 750 large and medium-size enterprises, some of which are among the leading manufacturing companies in Russia. Economic activity in the field of industrial production is also carried out by more than 23 thousand small enterprises, including microenterprises[3]. There are more than 3,100 industrial enterprises in Minsk, and more than 2,700 in the Minsk region[4], which also has a serious impact on the environment.

Kuopio is the eighth largest city in Finland, which is located in the Savo district near numerous lakes. The number of residents is about 120 thousand people. The city is included in the comparison as an example of a relatively environmentally safe territory[5].

The aerosol optical depth (AOD) of the atmosphere is one of the main characteristics determining the total aerosol air pollution (Cogliani 2001; Zhu 2011; Chubarova 2022; Zhdanova 2020). The influence of aerosols on atmospheric processes, the high variability of aerosol particles and harmful effects on humans determines the importance of studying the optical characteristics of aerosols. The purpose of this paper is to analyze the AOD data obtained by lidar stations in St. Petersburg, Minsk and Kuopio in order to assess the level of aerosol particle pollution in different regions, namely in two megacities, such as St. Petersburg and Minsk, and to perform a comparison with the pollution level in the relatively small city of Kuopio located in an environmentally safe region of Finland. The stations were selected based on their location. Minsk and Kuopio are the aerosol observation sites closest to St. Petersburg and have different levels of anthropogenic load. Our study will provide more information about the patterns of aerosol distribution in the studied regions.

MATERIALS AND METHODS

The main technical characteristics of three lidar systems are presented in Table 1.

The lidar equipment is used in conjunction with specialized software that allows processing the backscattered signal received by the telescope. The magnitude of the signal depends on the amount of

[2]World Health Organization. Regional Office for Europe & Joint WHO/Convention Task Force on the Health Aspects of Air Pollution. (2006). Health risks of particulate matter from long-range transboundary air pollution. Copenhagen : WHO Regional Office for Europe.
[3]Promyshlennost' i innovacii Sankt-Peterburga (Industry and innovations of St. Petersburg), 2017.
[4]Promyshlennost' respubliki Belarus' statisticheskij sbornik (Industry of the Republic of Belarus statistical compilation), 2019.
[5][Internet] – https://www.kuopio.fi/en/etusivu (date of access: 07.02.2023).

Table 1. Characteristics of lidar stations in Russia, Finland and Belarus

Parameter	St. Petersburg, Russia	Kuopio, Finland	Minsk, Belarus
Geographical coordinates	59.9427 N, 30.2730 E	62.7333 N, 27.5500 E	53.9170 N, 27.6050 E
Height above sea level, m	35	190	200
Used wavelengths, nm	355, 532	355, 532	355, 532
Initial height resolution, m	7.5	30; 60	7.5; 15
Minimum detection height, m	300-500	800-1000	455-800

aerosol present in the atmosphere. The attenuation and backscattering coefficients of the aerosol obtained from lidar sensing data were calculated using the Klett method (Klett 1985).

The lidar equation formulates the relationship between the sum of photons emitted by the laser and the sum of photons absorbed. Laser beam is transmitted in the atmosphere and there is a physical reaction between the laser beam and the probed object. The lidar equation characterizes the mathematical model of the physical processes that occur in the atmosphere when exposed to the laser beam (Kovalev 2004; Tuan 2017):

$$N_S(\lambda,R) = N_L(\lambda_L)\cdot\left[\beta\left(\lambda,\lambda_L,\theta,R\right)\cdot\Delta R\beta\right] \cdot\frac{A}{R^2}\cdot\left[T\left(\lambda_L,R\right)\cdot T(\lambda,R)\right]\cdot\left[\eta\left(\lambda,\lambda_L\right)\cdot G(R)\right]+N_B \quad (1)$$

where $N_S(\lambda, R)$ is the photon counts registered at a wavelength λ and distance R; $N_L(\lambda_L)$ is the number of transferred photons; $[\beta(\lambda, \lambda L, \theta, R)\Delta R]$ is the probability that a transferred photon is scattered into a unit solid angle at an angle θ; β is the volume scatter coefficient; ΔR is the layer thickness; A is the receiver aperture; A/R^2 is the probability that a scattered photon is collected by the receiving telescope; $[T(\lambda_L, R)T(\lambda, R)]$ is the light transmission during its propagation from a laser source to distance R and from distance R to a receiver; $\eta(\lambda, \lambda_L)$ is the hardware optical efficiency; $G(R)$ is the geometrical form factor; N_B is the background and detector noise.

The basic equation of lidar sensing is used for the calculation (Zuev, 1992):

$$P(z) = A\frac{\beta(z)}{z^2}exp\left[-2\int_0^z \alpha(z')\,dz'\right] \quad (2)$$

where $P(z)$ is the power of the detected backscattered signal from height z, A is the instrumental constant that includes all range-independent instrumental parameters (as the detector's efficiency, receiving telescope area and laser pulse width), $\beta(z)$ is the backscattering coefficient, $\alpha(z')$ is the extinction coefficient. The AOD from z_{min} to z_{max} can be calculated as:

$$AOD = \int_{z_{min}}^{z_{max}} \alpha(z)\,dz \quad (3)$$

The errors in calculating the attenuation and backscattering coefficients by the Klett method are about 20 % (Althausen 2000; Klett 1985; Klett 1981) and depend on the state of the atmosphere, the type and amount of aerosols. The range of lidar sensing also depends on atmospheric conditions.

The Angstrom exponent coefficient was calculated using the formula below to understand the nature of the aerosol particle size distribution:

$$a = -\frac{\ln\left(\frac{AOD_i}{AOD_j}\right)}{\ln\left(\frac{\lambda_i}{\lambda_j}\right)} \quad (4)$$

where a is the Angstrom exponent coefficient, $AOD_{i,j}$ is the aerosol optical depth at wavelength λ_i and λ_j.

A large array of data obtained during measurements in the most polluted part of St. Petersburg, as well as Minsk and Kuopio, allows analyzing changes in the AOD over time, and identifying sequences in the distribution of aerosols for the period from 2014 to 2021. The variability of aerosol pollution over such large megacities as St. Petersburg and Minsk and comparing the data with the relatively environmentally safe area of Kuopio, allows assessing the degree of urban pollution.

The limitation in the height of determining the aerosol optical depth is due to differences in the lower limit of measurements by the instruments (Guerrero-Rascado 2010; Halldórsson 1978). In Kuopio, the data in most cases are provided from 800 m, therefore, the lower limit of observations at all three stations is a height of 800 m. The upper level of observations is limited by 1600 m. This is due to the fact that a part of the available data ends at an altitude of 1600 m.

The number of processed measurements to obtain the AOD average values is presented in Table 2.

The distance between the observation station is: between St. Petersburg and Kuopio 343 km, between Kuopio and Minsk 980 km, and 689 km between St. Petersburg and Minsk.

Due to the coronavirus restrictions, the number of measurements performed in 2019-2021 decreased significantly.

RESULTS AND DISCUSSION

Table 3 and Figure 1 show the median values of AOD 355 and AOD 532 obtained at three monitoring stations in St. Petersburg, Minsk, and Kuopio from 2014 to 2021 at altitudes from 800 to 1600 m. The median is a stable estimate of the distribution center and does not tend to shift with significant deviations from the main data array. Unfortunately, due to the complexity of research equipment that requires periodic maintenance and repair, data for comparison in Kuopio and Minsk were not obtained for each year.

Unfortunately, the data at 800 m at the station in Kuopio are available only for three years from 2014 to 2016. According to the processed AOD data at 355 nm (Fig. 1a), the atmosphere at the location of the station in Kuopio has a lower content of aerosol particles. The AOD at 355 nm in St. Petersburg is higher than that in Minsk, with the exception of 2016. Since 2017, there was a steady excess of aerosol content over St. Petersburg compared to Minsk, with a maximum excess by 2.4 times in 2020 (Fig. 1a).

Table 2. Number of measurements by year[6]

City	Channel, nm	2014	2015	2016	2017	2018	2019	2020	2021	Total
Saint-Petersburg	355	40	40	18	50	21	9	9	5	192
	532	40	45	18	50	21	9	9	5	197
Minsk	355	3	29	26	16	15	12	7	-	108
	532	7	29	28	17	16	13	8	-	118
Kuopio	355	7	22	20	-	-	-	-	-	49
	532	12	42	30	-	-	-	-	-	84

Table 3. Distribution of optical depth median value by year during the 2014-2021 period for three stations in the layer from 800 to 1600 m.

Year	St. Petersburg, Russia		Minsk, Belarus		Kuopio, Finland	
	355 nm	532 nm	355 nm	532 nm	355 nm	532 nm
2014	0.043	0.017	0.040	0.019	0.015	0.005
2015	0.053	0.019	0.040	0.029	0.020	0.007
2016	0.030	0.018	0.045	0.028	0.025	0.009
2017	0.052	0.022	0.028	0.018	-	-
2018	0.052	0.018	0.029	0.022	-	-
2019	0.071	0.028	0.036	0.030	-	-
2020	0.053	0.021	0.022	0.018	0.013*	0.010*
2021	0.064	0.020	-	-	0.048*	-
Mean	0.052	0.020	0.034	0.023	0.020	0.007

* – data only from 1000 m.

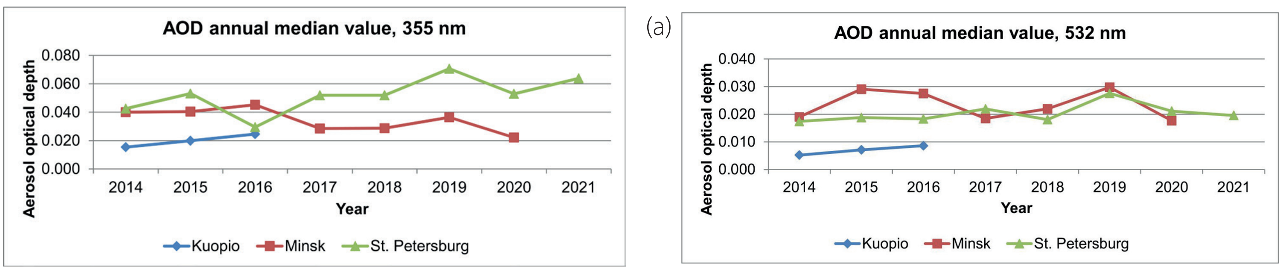

(b)

Fig. 1. Distribution of optical depth median value by year in the period from 2014 to 2021 for three stations in a layer from 800 to 1600 m at wavelengths of 355 nm (a) and 532 nm (b)

The Angstrom parameter at wavelengths of 355 and 532 nm was also considered, separately for the period 2014-2016 for all three stations and from 2014 to 2020 for lidar stations in St. Petersburg and Minsk. The Angstrom parameter allows us to conclude about the nature of the particle size distribution. The Angstrom parameter above 2 indicates the prevalence of a fine aerosol, whereas the values below 1 indicate the predominance of large aerosol particles. In the period from 2014 to 2016, the value of the Angstrom parameter was 2.60 in Kuopio, 1.26 in Minsk and 2.05 in St. Petersburg. In the period from 2014 to 2020, the average Angstrom parameter has values of 0.92 in Minsk and 2.18 in St. Petersburg. This indicates the predominance of fine aerosol over St. Petersburg.

As an additional source of information on the annual course of the AOD near St. Petersburg, we used the data from the AERONET station in Peterhof located 25 km from the lidar station, as well as data from the AERONET stations in Kuopio and Minsk (Filonchyk 2021; Volkova 2018). On average, for the measurement period from 2013 to 2016, the AOD in Peterhof at a wavelength of 500 nm is 0.12 ± 0.05 with maximum values in summer 0.14–0.19. For the AERONET station in Kuopio, the average AOD at a wavelength of 500 nm is 0.10 ± 0.03. Authors of this study also notes that the AOD values in Peterhof are higher than the results of observations in Kuopio, which is associated with the contribution of anthropogenic aerosol, which is typical for large metropolitan areas. The AOD distribution patterns obtained in work (Volkova 2018) are in good agreement with the data obtained by the lidar method for stations in Kuopio and St. Petersburg. The Angstrom parameter (440–870 nm) in Peterhof according to the AERONET changes from 1.0 to 1.6 with maximum values in the warm season. This indicates a mixed bimodal distribution of aerosol, with a finely dispersed fraction up to 60%. Taking into account the distance between the observation sites, an additional contribution of the secondary fine aerosol of anthropogenic origin in St. Petersburg is possible, which gives higher values of the Angstrom parameter. At the AERONET station in Kuopio, a similar relationship is observed.

[6][Internet] – https://data.earlinet.org (date of access: 07.02.2023).

The high summer values of the Angstrom parameter in Peterhof are attributed by the authors (Volkova 2018) to an increase in the amount of finely dispersed secondary aerosol. The overestimation of the angstrom parameter in St. Petersburg and Kuopio, obtained from lidar data in relation to the AERONET angstrom parameter, is apparently due to the limitation of the observation height from 800 to 1600 m, the location of the lidar station in the center of St. Petersburg also affects.

In Minsk, the Angstrom parameter (440-870 nm) calculated according to AERONET station data from 2002 to 2019 (Filonchyk 2021) changes significantly throughout the year, while the average annual values of the Angstrom parameter according to AERONET data exceed 1.3, which also indicates the predominance of fine aerosols, and is not entirely consistent with the results obtained by the lidar method. The average daily AOD 440 nm and Angstrom exponent (440-870 nm) values of the AERONET station in Minsk vary from 0.03 to 2.08 and from 0.11 to 2.35, and the average monthly values vary from 0.14 to 0.27 and from 1.19 to 1.58, respectively. The obtained annual mean AOD 440 is 0.22 ± 0.17. The average Angstrom parameter (355–532 nm) in Minsk according to lidar data is 0.92, which is much lower than the coefficient in St. Petersburg and Kuopio, and not quite typical for Minsk. The resulting discrepancy can be attributed to a small number of lidar observations in Minsk in the period from 2018 to 2020. Measurements during this period were carried out mainly in early spring and winter, and the Angstrom parameter (355-532 nm) shows underestimated values – 0.54, which undoubtedly affects the final value of the AOD and the Angstrom parameter for the entire period from 2014-2020. At the same time, the average Angstrom parameter (355–532 nm) for the period from 2014 to 2017 is 1.23, which is close to the readings of the AERONET station in Minsk. It can be noted that both AOD 355 and AOD 532 in St. Petersburg and Minsk on average exceed the AOD values in the city of Kuopio by 2-3 times. The results obtained allow the conclusion that the atmosphere in the city of Kuopio is less polluted by aerosol particles, which, according to the authors of this article, is due to the low number of industrial plants located in this region, as well as the low intensity of automobile traffic. At the same time, it should be noted that the natural aerosol can also contribute to the total content of aerosol pollution in cities (Chubarova 2022). The increased content of aerosols over St. Petersburg and Minsk may lead to an additional adverse effects on the health of the population due to the processes of aerosol deposition.

Since the compared stations do not have data for all years, the comparison was carried out according to the following procedure. The period from 2014 to 2016 was analyzed separately, since for these three years all three stations have measurements (fig. 2a). A separate comparison was made for Minsk and St. Petersburg from 2014 to 2020 (fig. 2b). Figure 2 clearly shows the predominance of the Minsk and St. Petersburg average AOD at 355nm and 532 nm over Kuopio. Average AOD 355 in St. Petersburg and Minsk exceeds AOD 355 in Kuopio by 2.1 times. Average AOD 532 in Minsk exceeds AOD 532 in Kuopio by 3.6 times, in Saint-Petersburg AOD 532 higher in Kuopio in 2.6 times. The average AOD values for all the years of measurements are shown in Figure 2.

As follows from the processed data, the average AOD in the selected height range in Kuopio is less than in St. Petersburg and Minsk. At the same time, in Minsk AOD 532 exceeds St.Petersburg's AOD 532, with the exception of 2017 and 2020. In the period from 2014 to 2016, there is no difference between AOD 355 in St. Petersburg and Minsk, while for AOD 532 it was clearly expressed.. AOD 355 in St. Petersburg is 1.43 times higher than AOD 355 in Minsk, and lower by 1.25 times at a wavelength of 532 nm.

CONCLUSION

The available AOD data for three stations in St. Petersburg, Minsk and Kuopio, located in three regions with different levels of anthropogenic impact and natural aerosol content, made it possible to evaluate the optical characteristics of aerosol and compare the level of atmospheric air pollution. In St. Petersburg, the location of the lidar station is in the center of the city in the most polluted area.

The average AOD 355 in St. Petersburg and Minsk over the 2014-2016 period exceeds this value in Kuopio by 2.1 times. The average value of AOD 532 in Minsk and St. Petersburg is 3.6 and 2.6 times higher than in Kuopio, respectively. For the 2014–2020 period, AOD 355 shows the following average values: 0.050±0.012 in St. Petersburg and 0.034±0.008 in Minsk, while the average AOD 532 values are: 0.020±0.004 in St. Petersburg and 0.023±0.005 in Minsk. The average AOD 355 and AOD 532 are 1.46 times higher and 1.14 times lower in St. Petersburg than those in Minsk, respectively.

Additionally, a comparison was made with the data of AERONET stations in Peterhof, Minsk, Kuopio with an analysis of the optical characteristics, the Angstrom parameter and an assessment of their variations. The smallest AOD according to AERONET data is recorded in Kuopio, the largest in Minsk, which is consistent with the received lidar data. The station in Peterhof is located far from St. Petersburg, which affects the AOD readings downwards. AOD 355 according to lidar data from 2014 to 2020 in St. Petersburg is gradually increasing, in Minsk there is a decrease.

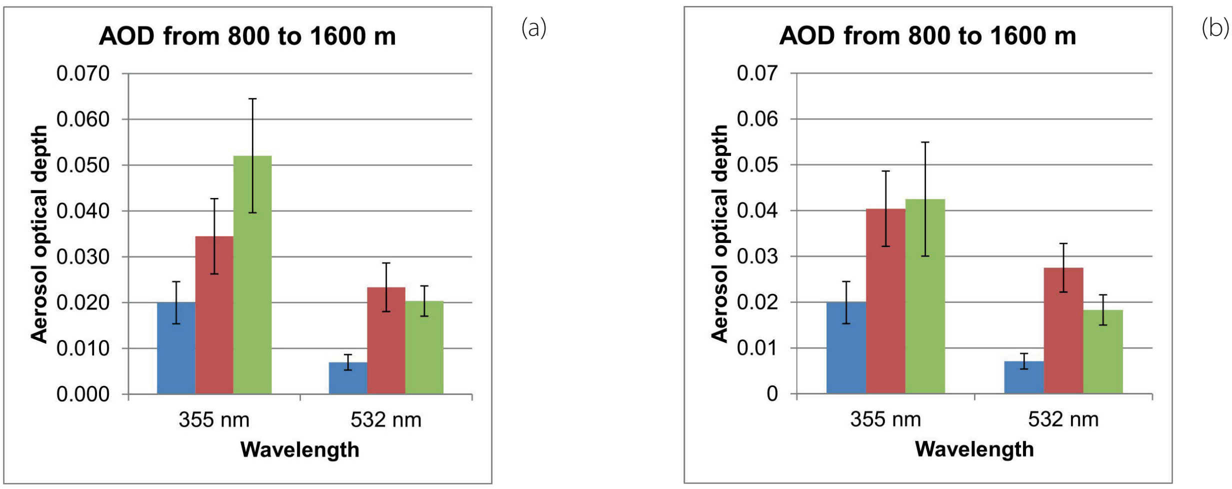

Fig. 2. The average AOD values from 2014 to 2016 (a) and from 2014 to 2020 (b) at wavelengths of 355 nm and 532 nm (black lines are standard deviations)

The distributions of the Angstrom parameter from lidar data in St. Petersburg and Kuopio are in good agreement with the Angstrom parameter obtained from the AERONET data. At the same time, higher values of the Angstrom parameter are noted in St. Petersburg and Kuopio, which can be explained by the limited height of the AOD study from 800 to 1600 m.

In Minsk, according to AERONET data, the Angstrom parameter 440-870 nm from 2002 to 2019 exceeds 1.3, which indicates the predominance of fine aerosols and does not quite agree with the data obtained from lidar measurements if we take the period from 2014 to 2020, for the average parameter. The Angstrom is influenced by data from 2018 to 2020 when there is a small number of measurements that were carried out only in early spring and winter, and the Angstrom parameter 532-355 nm was significantly underestimated - 0.54, and indicates the predominance of coarse aerosol. The calculated Angstrom parameter 532-355 nm for the period from 2014 to 2017 is 1.23, which is already close and consistent with the data obtained in the AERONET network.

The values of both AOD 355 and 532 in the city of Kuopio are significantly lower than those in St. Petersburg and Minsk due to the smaller number of aerosol particles in the atmosphere. Note that both AOD values in St. Petersburg and Minsk exceed the AOD values in Kuopio by 2-3 times (Fig. 2b), which allows us to conclude about the predominant content of aerosol particles over megacities compared to smaller cities. In this paper, the AOD was compared in a layer from 800 to 1600 m. If it was possible to compare AOD at lower heights, it seems that the differences between St. Petersburg, Minsk and Kuopio would be even greater. The main contribution to air pollution in the big cities is most likely to be made by road transport and industrial enterprises with some effects of natural aerosol.

REFERENCES

Agarwal A., Mangal A., Satsangi A., Lakhani A., Kumari K. M. (2017). Characterization, sources and health risk analysis of PM2.5 bound metals during foggy and non-foggy days in sub-urban atmosphere of Agra. Atmospheric Research, 197, 121-131. DOI: 10.1016/j.atmosres.2017.06.027.

Aggarwal M., Whiteway J., Seabrook J., Gray L., Strawbridge K., Liu P., O'Brien J., Li S.-M. and McLaren R., (2018). Airborne lidar measurements of aerosol and ozone above the Canadian oil sands region. Atmospheric Measurement Techniques, 6, 3829-3849, DOI: 10.5194/amt-11-3829-2018.

Althausen D., Müller D., Ansmann A., Wandinger U., Hube, H., Clauder, E., Zoerner, S. (2000). Scanning 6-wavelength 11-channel aerosol lidar. Journal of Atmospheric and Oceanic Technology, 17, 1469–1482.

Ansmann A. and Müller D. (2005). Lidar and Atmospheric Aerosol Particles. In: C. Weitkamp, ed., LIDAR: range-resolved optical remote sensing of the atmosphere, W. T. Rhodes. ed. Singapore: Springer, 476, DOI: 10.1007/b106786.

Ansmann A., Ohneiser K., Mamouri R.-E., Knopf D. A., Veselovskii I., Baars H., Engelmann R., Foth A., Jimenez C., Seifert P. and Barja B. (2021). Tropospheric and stratospheric wildfire smoke profiling with lidar: mass, surface area, CCN, and INP retrieval. Atmospheric Chemistry and Physics, 21(12), 9779–9807, DOI: 10.5194/acp-21-9779-2021.

Baensch-Baltruschat B., Kocher B., Stock F., Reifferscheid G. (2022). Tyre and road wear particles (TRWP) - A review of generation, properties, emissions, human health risk, ecotoxicity, and fate in the environment. Science of the Total Environment, 2020, 733, 137823. DOI: 10.1016/j.scitotenv.2020.137823.

Campbell, J. R., Ge, C., Wang, J., Welton, E. J., Bucholtz, A., Hyer, E. J., Reid, E. A., Chew, B. N., Liew, S. C., Salinas, S. V., Lolli, S., Kaku, K. C., Lynch, P., Mahmud, M., Mohamad, M. and Holben, B. N. (2016). Applying advanced ground-based remote sensing in the Southeast Asian maritime continent to characterize regional proficiencies in smoke transport modeling. J. Appl. Meteor. Climatol. 55: 3–22

Chaikovsky A., Ivanov A., Balin Yu., Elnikov A., Tulinov G., Plusnin I., Bukin O., Chen B. (2006). Lidar network CIS-LiNet for monitoring aerosol and ozone in CIS regions. Proceedings of SPIE - The International Society for Optical Engineering, 6160, 616035. DOI: 10.1117/12.675920. Available at: https://www.spiedigitallibrary.org/conference-proceedings-of-spie/6160/1/Lidar-network-CIS-LiNet-for-monitoring-aerosol-and-ozone-in/10.1117/12.675920.short [Accessed 30 March. 2023].

Chazette P., Totems J. (2023). Lidar Profiling of Aerosol Vertical Distribution in the Urbanized French Alpine Valley of Annecy and Impact of a Saharan Dust Transport Event. Remote Sensing, 15, 1070. DOI: 10.3390/rs15041070.

Chen G., Li Sh., Zhang Y., Zhang W., Li D., Wei X., He Y., Bell M. L., Williams G., Marks G. B., Jalaludin B., Abramson M. J., Guo Y. (2017). Effects of ambient PM1 air pollution on daily emergency hospital visits in China: an epidemiological study. Lancet Planet Health, 1(6), 6, e221–229. DOI: 10.1016/S2542-5196(17)30100-6.

Chubarova N., Vogel H., Androsova E., Kirsanov A., Popovicheva O., Vogel B. and Rivin G. (2022). Columnar and surface urban aerosol in the Moscow megacity according to measurements and simulations with the COSMO-ART model. Atmospheric Chemistry and Physics, 22(16), 10443–10466. DOI: 10.5194/acp-22-10443-2022.

Cogliani E. (2001). Air pollution forecast in cities by an air pollution index highly correlated with meteorological variables. Atmospheric Environment, 35, 2871–2877. DOI: 10.1016/S1352-2310(01)00071-1.

Di Girolamo P., Summa D., Bhawar R., Di Iorio T., Cacciani M., Veselovskii I., Dubovik O., Kolgotin A. (2012). Raman lidar observations of a Saharan dust outbreak event: Characterization of the dust optical properties and determination of particle size and microphysical parameters. Atmospheric Environment, 50, 66-78. DOI: 10.1016/j.atmosenv.2011.12.061.

Filonchyk M., Peterson M., Yan H., Yang Sh., Chaikovsky A. (2021). Columnar optical characteristics and radiative properties of aerosols of the AERONET site in Minsk, Belarus. Atmospheric Environment, 249(15), 118237. DOI: 10.1016/j.atmosenv.2021.118237.

Flamant C., Pelon J., Chazette P., Trouillet V., Quinn P. K., Frouin R., Bruneau D., Leon J. F., Bates T. S., Johnson J. & Livingston J., (2000). Airborne lidar measurements of aerosol spatial distribution and optical properties over the Atlantic Ocean during a European pollution outbreak of ACE-2. Tellus B: Chemical and Physical Meteorology, 52B, 662-677. DOI: 10.3402/tellusb.v52i2.17126.

Forest V. (2021) Combined effects of nanoparticles and other environmental contaminants on human health - an issue often overlooked. NanoImpact, 23, art. 100344. DOI: 10.1016/j.impact.2021.100344.

Fussell J. C., Franklin M., Green D. C., Gustafsson M., Harrison R. M., Hicks W., Kelly F. J., Kishta F., Miller M. R., Mudway I. S., Oroumiyeh F., Selley L., Wang M. and Zhu Y. (2022). A Review of Road Traffic-Derived Non-Exhaust Particles: Emissions, Physicochemical Characteristics, Health Risks, and Mitigation Measures. Environmental Science & Technology, 56(11), 6813-6835. DOI: 10.1021/acs.est.2c01072

Guerrero-Rascado J. L., João Costa M., Bortoli D., Silva A. M., Lyamani H. and Alados-Arboledas L. (2010). Infrared lidar overlap function: an experimental determination. Optics Express, 18(19), 20350–20369. DOI: 10.1364/OE.18.020350.

Halldórsson T., Langerholc J. (1978) Geometrical form factors for the lidar function. Applied Optics, 17(2), 240–244. DOI: 10.1364/AO.17.000240.

Hext P.M., Rogers K.O., Paddle G.M. (1999). The health effects of PM2.5 (including ultrafine particles). Report no. 99/60. Brussels: CONCAWE Reports.

Hoff R. M., McCann K. J., Demoz B., Reichard J., Whiteman D. N., McGee T., McCormick M. P., Philbrick C. R., Strawbridge K., Moshary F., Gross B., Ahmed S., Venable D., Joseph E. (2002). Regional East Atmospheric Lidar Mesonet: REALM. ILRC, European Space Agency (ESA), 1–4. Available at: https://pdfs.semanticscholar.org/a7a3/e0d3e92e8fe89f1ff8738e2116a41f14e0a1.pdf [Accessed 30 March. 2023].

Kafle D. N., Coulter R. L. Micropulse lidar-derived aerosol optical depth climatology at ARM sites worldwide. (2013). Journal of Geophysical Research (Atmospheres), 118(13), 7293-7308, DOI: 10.1002/jgrd.50536.

Khor W. Y., Hee W. Sh., Tan F., Lim Hw. S., Mat Jafri M. Z., Holben B. (2014). Comparison of Aerosol optical depth (AOD) derived from AERONET sunphotometer and Lidar system. IOP Conference Series: Earth, Environmental Science, 20(1), 012058, DOI: 10.1088/1755-1315/20/1/012058.

Klett J. D. (1981). Stable analytical inversion solution for processing lidar returns. Applied Optics, 20(2), 211–220. DOI: 10.1364/AO.20.000211.

Klett J. D. (1985). Lidar inversion with variable backscatter/extinction ratios. Applied Optics, 24, 1638–1643.

Kondratyev K. Ya., Ivlev L. S., Krapivin V. F., Varotsos C. A. (2006). Atmospheric Aerosol Properties: Formation, Processes and Impacts. Berlin: Springer. DOI: 10.1007/3-540-37698-4.

Kong D., He H., Zhao J., Ma J., Gong W. (2022). Aerosol Property Analysis Based on Ground-Based Lidar in Sansha, China. Atmosphere , 13(9), 1511, DOI: 10.3390/atmos13091511.

Kovalev V. A., and Eichinger W. E. (2004). Elastic lidar: theory, practice, and analysis methods. Hoboken: John Wiley & Sons.

Kovalev V. A., Petkov A., Wold C., Urbanski Sh. and Hao W. M. (2009). Determination of smoke plume and layer heights using scanning lidar data. Applied Optics, 48(28), 5287-5294. DOI: 10.1364/AO.48.005287.

Kovochich M., Parker J. A., Oh S. Ch., Lee J. P., Wagner S., Reemtsma T. and Unice K. M. (2021). Characterization of Individual Tire and Road Wear Particles in Environmental Road Dust, Tunnel Dust, and Sediment. Environmental Science & Technology Letters, 8, 1057–1064. DOI: 10.1021/acs.estlett.1c00811

Lisetskii F., Borovlev A., (2019). Monitoring of Emission of Particulate Matters and Air Pollution using Lidar, Belgorod, Russia. Aerosol and Air Quality Research, 19, 504–515. DOI:10.4209/aaqr.2017.12.0593.

Ma X., Wang C., Han G., Ma Y., Li S., Gong W., Chen J., (2019). Regional Atmospheric Aerosol Pollution Detection Based on LiDAR Remote Sensing. Remote Sensing, 11(20):2339. DOI: 10.3390/rs11202339.

Mallone S., Stafoggia M., Faustini A., Gobbi G. P., Marconi A. and Forastiere F. (2011). Saharan Dust and Associations between Particulate Matter and Daily Mortality in Rome, Italy. Environmental Health Perspectives, 119(10), 1409–1414. DOI: 10.1289/ehp.1003026.

McGill M. J., Hlavka D. L., Hart W. D., Welton E. J. and Campbell J. R. (2003). Airborne Lidar Measurements of Aerosol Optical Properties during SAFARI-2000. Journal of Geophysical Research: Atmospheres, 108 (D13), 8493. DOI: 10.1029/2002jd002370.

Mona L., Amodeo A., Pandolfi M. and Pappalardo G. (2006). Saharan dust intrusions in the Mediterranean area: Three years of Raman lidar measurements. Journal Of Geophysical Research, [online] 111(D16203). DOI:10.1029/2005JD006569. Available at: https://agupubs.onlinelibrary.wiley.com/doi/epdf/10.1029/2005JD006569 [Accessed 30 March. 2023].

Mona L., Liu Z., Muller D., Omar A., Papayannis A., Pappalardo G., Sugimoto N. and Vaughan M. (2012). Lidar Measurements for Desert Dust Characterization: An Overview. Advances in Meteorology, [online] 2012, 356265, DOI:10.1155/2012/356265. . Available at: https://downloads.hindawi.com/journals/amete/2012/356265.pdf [Accessed 30 March]. 2023].

Nagy G., Merényi A., Domokos E., Rédey Á., Yuzhakova T. (2014), Monitoring of air pollution spread on the car-free day in the city of Veszprém. International Journal Of Energy And Environment, 5(6), 679–684.

Nishizawa T., Sugimoto N., Matsui I., Shimizu A., Higurashi A. and Jin Y. (2016). The Asian Dust and Aerosol Lidar Observation Network (AD-NET): Strategy and Progress. EPJ Web of Conferences, [online] 119, 19001. DOI: 10.1051/epjconf/201611919001. Available at: https://www.epj-conferences.org/articles/epjconf/pdf/2016/14/epjconf_ilrc2016_19001.pdf [Accessed 30 March. 2023].

Pandey A. et al. (2020). Health and economic impact of air pollution in the states of India: the Global Burden of Disease Study 2019. Lancet Planet Health, 5(1), e25–38. DOI: 10.1016/S2542-5196(20)30298-9.

Papagiannopoulos N. et al. (2020). An EARLINET early warning system for atmospheric aerosol aviation hazards. Atmospheric Chemistry and Physics, 20, 10775–10789. DOI: 10.5194/acp-20-10775-2020.

Samulenkov D. A., Sapunov M.V, Mel'nikova I. N. (2020). Lidarnoe zondirovanie aerozol'nyh zagryaznenij v atmosfere po marshrutu Sankt-Peterburg – Voronezhskaya oblast'–Belgorodskaya oblast'. Current Problems in Remote Sensing of the Earth from Space, 17(3), 223–230, (in Russian). DOI: 10.21046/2070-7401-2020-17-3-223-230.

Schraufnagel D. E. (2020). The health effects of ultrafine particles. Experimental & Molecular Medicine, 52, 311–317. DOI:10.1038/s12276-020-0403-3.

Schraufnagel D. E., Balmes J. R., Cowl C. T., De Matteis S., Jung S.-H., Mortimer K., Perez-Padilla R., Rice M. B., Riojas-Rodriguez H., Sood A., Thurston G. D., To T., Vanker A., Wuebbles D. J. (2016). Air Pollution and Noncommunicable Diseases: A Review by the Forum of International Respiratory Societies' Environmental Committee, Part 1: The Damaging Effects of Air Pollution. CHEST, 155(2), 409–416. DOI: 10.1016/j.chest.2018.10.042.

Sharma Sh., Chandra M. & Kota S. H. (2020). Health Effects Associated with PM2.5: a Systematic Review. Current Pollution Reports, 6(4), 345–367. DOI: 10.1007/s40726-020-00155-3.

Shi Y., Liu W., Dong Y., Zhao X., Xiang Y., Zhang T., Lv L., (2022). Atmospheric aerosol particle size distribution from Lidar data based on the lognormal distribution mode. Heliyon, 8(8), e09975. DOI: 10.1016/j.heliyon.2022.e09975.

Subramanian R., Kagabo A. S., Baharane V., Guhirwa S., Sindayigaya C., Malings C., Williams N. J., Kalisa E., Li H., Adams P., Robinson A. L., DeWitt H. L., Gasore J. and Jaramillo P. (2020). Air pollution in Kigali, Rwanda: spatial and temporal variability, source contributions, and the impact of car-free Sundays. Clean Air Journal, 30(2), 15. DOI: 10.17159/caj/2020/30/2.8023.

Tuan A. D., Anh N. X., Hung T. P. (2017). The simulation of aerosol Lidar developed at the Institute of Geophysics. Journal of Marine Science and Technology, 17(4B), 51–57. DOI: 10.15625/1859-3097/17/4B/12991.

Vaughan G., Wareing D. and Ricketts H. (2021). Measurement Report: Lidar measurements of stratospheric aerosol following the 2019 Raikoke and Ulawun volcanic eruptions. Atmospheric Chemistry and Physics, 21(7), 5597–5604, DOI: 10.5194/acp-21-5597-2021.

Volkova K.A., Poberovsky A.V., Timofeev Yu.M., Ionov D.V., Holben B.N., Smirnov A., Slutsker I. (2018). Aerosol optical characteristics retrieved from measurements of CIMEL sun photometer (AERONET) near Saint Petersburg. Оптика атмосферы и океана, 6, 425-431, (in Russian) DOI: 10.15372/AOO20180601.

Wei Y., Wang Y., Di Q., Choirat Ch., Wang Y., Koutrakis P., Zanobetti A., Dominici F., Schwartz J. D. (2019). Short term exposure to fine particulate matter and hospital admission risks and costs in the Medicare population: time stratified, case crossover study. BMJ, 367, l6258. DOI: 10.1136/bmj.l6258.

Welton E. J., Stewart S. A., Lewis J. R., Belcher L. R., Campbell J.R. and Lolli S. (2018). Status of the NASA Micro Pulse Lidar Network (MPLNET): overview of the network and future plans, new version 3 data products, and the polarized MPL. EPJ Web of Conferences, [online] 176, 09003. DOI: 10.1051/epjconf/201817609003. Available at: https://www.epj-conferences.org/articles/epjconf/pdf/2018/11/epjconf_ilrc28_09003.pdf [Accessed 30 March. 2023].

Xie Ch., Nishizawa T., Sugimoto N., Matsui I. and Wang Z. (2008). Characteristics of aerosol optical properties in pollution and Asian dust episodes over Beijing, China. Applied Optics, 47(27), 4945–4951. DOI: 10.1364/AO.47.004945.

Xie Ch.-B., Zhou J., Sugimoto N., Wang Z.-F. (2010). Aerosol Observation with Raman LIDAR in Beijing, China. Journal of the Optical Society of Korea, 14(3), 215-220.

Yegorov A. D., Kopp I. Z., Perelma A. Y., (1995). Air aerosol pollution and lidar measurements. Proceedings of SPIE - The International Society for Optical Engineering, 2505, 38–43. DOI: 10.1117/12.219649.

Yin Zh., Yi F., Liu F., He Y., Zhang Y., Yu Ch., Zhang Y., (2021). Long-term variations of aerosol optical properties over Wuhan with polarization lidar. Atmospheric Environment, 259,118508, DOI: 10.1016/j.atmosenv.2021.118508.

Zhdanova E. Yu., Chubarova N. Ye., Lyapustin A. I. (2020). Assessment of urban aerosol pollution over Moscow megacity by MAIAC aerosol product. Atmospheric Measurement Techniques, 13(2), 877-891. DOI: 10.5194/amt-2019-325.

Zhu J., Liu D., Zeng Q. (2011). Analysis of the Aerosol Optical Depth and the Air Quality in Qingdao, China. Journal Of Software, 6(7), 1194–1200. DOI: 10.4304/jsw.6.7.1194-1200.

Zuev V. E., Zuev V. V. (1992). Distancionnoe opticheskoe zondirovanie atmosfery (Remote optical sensing of the atmosphere). St. Petersburg: Gidrometeoizdat.

RESEARCH PAPER

LONG-TERM AIR QUALITY EVALUATION SYSTEM PREDICTION IN CHINA BASED ON MULTINOMIAL LOGISTIC REGRESSION METHOD

Yang. He[1]*, Dongfang. Qi[1], V M. Bure[1,2]

[1]St. Petersburg State University, 7-9, Universitetskaya nab., St Petersburg, 199034, Russian Federation

[2]Agrophysical Research Institute, 14, Grazhdanskiy pr, St Petersburg, 195220, Russian Federation

***Corresponding author:** st082131@student.spbu.ru

Received: January 18th, 2023 / Accepted: November 14th, 2023 / Published: December 31st, 2023

https://DOI-10.24057/2071-9388-2023-2719

ABSTRACT. The aim of this article evaluate the long-term air quality in China based on the air quality index (AQI) and the air quality composite index (AQCI) though the multinomial logistic regression method. The two developed models employ different dependent variables, AQI and AQCI, while maintaining the same controlled variables gross domestic product (GDP), and a primary pollutant. Explicitly, the primary impurity is associated with one or more contaminants among six pollutant factors: O_3, $PM_{2.5}$, PM_{10}, NO_2, SO_2, and CO. Model quality verification is an integral part of our analysis. The results are illustrate d using real air quality data from China. The developed models were applied to predict AQI and ACQI for the 31 capital cities in China from 2013 to 2019 annually. All calculations and tests are conducted using R-studio. In summary, both models are able to predict China's long-term air quality. A comparison of the AQI and AQCI models using the ROC curve reveals that the AQCI model exhibits greater significance than the AQI model.

KEYWORDS: Multinomial logistic regression, Air Quality Index, Air Quality Composite Index, ROC curve

CITATION: Yang. He, Dongfang. Qi, V M. Bure (2023). Long-Term Air Quality Evaluation System Prediction In China Based On Multinomial Logistic Regression Method. Geography, Environment, Sustainability, 4(16), 164-171

https://DOI-10.24057/2071-9388-2023-2719

ACKNOWLEDGEMENTS: Authors are highly thankful to two anonymous reviewers and the principal editor for their positive constructive advices for the manuscript.

Conflict of interests: The authors reported no potential conflict of interest.

INTRODUCTION

In China, with the continuous improvement in people's quality of life, there is a growing awareness of their living environment (Fann N, et al.2013). In March 2012, the State Environmental Protection Administration of China established the National Ambient Air Quality Standard and introduced a new air quality evaluation standard for public health, known as the Air Quality Index (AQI). The AQI is derived from various pollutants, including particulate matter 2.5 ($PM_{2.5}$), inhalable particulate matter (PM_{10}), ozone (O_3), carbon monoxide (CO), nitrogen oxides (NO_2), sulfur dioxide (SO_2), among others. Government agencies use the AQI to communicate current or forecasted pollution levels to the public (Wang K, et al. 2019). In 2016, the State Environmental Protection Administration introduced another air quality evaluation method, the Comprehensive Air Quality Index (AQCI) (Wang S, et al. 2012). Both indexes have become widely popular for quick air quality assessments in China. Higher AQI or AQCI values are associated with improved public health. The World Health Organization states that 9 out of 10 people worldwide breathe polluted air, which contributes to more than 4.2 million deaths per year, and overall negatively affects the population's health, especially children and elderly (Schachter E N, Moshier E, Habre R, et al. 2016). Therefore, an accurate air pollution prediction system can help government agencies inform the public about air pollution levels (Zaib S, et al. 2022).

To the best of the authors' knowledge, the methods outlined in the referenced papers prove effective in air quality prediction problems, typically categorized into deterministic and uncertainty models. Deterministic models, are usually based on traditional statistic or economic models, such as multiple linear regression, multiple logistic regression, and time series model (Bure V. M. et al. 2007; 2013; 2019, Iakushev V. P. et al. 2020, 2021). Uncertainty models employ the state of the art machine learning techniques, and return the probability of different air quality levels. Data-driven methods, like deep learning, and ensemble learning, generally outperform, deterministic models, as reported by (R. Stern, P. Builtjes, M. Schaap, R. Timmermans, R. Vautard, A. Hodzic, M. Memmesheimer, H. Feldmann, E. Renner, R. Wolke, et al. 2008).

Moreover, (Karimian H, Li Q, Wu C, et al. 2019) explore three models: multiple additive regression trees (MART), deep feed-forward neural network (DFNN), and a new hybrid model based on long-term memory (LSTM), with LSTM emerging as the highest-performing one. (Di Q, Amini H, Shi L, et al. 2019) incorporate the geographic factor as a controlled variable, combining $PM_{2.5}$ to construct a neural network using random forest and gradient boosting. (Li X, Peng L, Hu Y, et al. 2016) employ LSTM, convolutional neural networks (CNN), and one-dimensional convolutional neural network (ID-CNN), achieving 78% accuracy in air pollution predictions. Additionally, (Li X, Peng L, Hu Y, et al.2016), combine CNN and LSTM to create a CNN-LSTM model for predicting $PM_{2.5}$ concentrations in any capital city in China. (Tong W, Li L, Zhou X, et al. 2019) take a unique approach, transforming air quality data into sequences of images using the Conv-LSTM model to interpolate the predicted air quality data for the entire cities, demonstrated over Seoul City in Korea. (Nadeem I., Ilyas A.M., Uduman P.S) employ an ARMA/ARIMA modelling approach for forecasting Respirable Suspended Particular Matter (RSPM), Sulphur dioxide (SO_2), and Nitrogen dioxide (NO_2) concentrations in Chennai City, India. (Senarathna M, et al.) utilize intelligent sensor technology to detect $PM_{2.5}$ and NO_2 in Kandy City, Sri Lanka.

Furthermore, it is intriguing to determine the model for predicting air quality, especially considering that most research focus on short-term prediction per day or per hour (Stojov V, Koteli N, Lameski P, et al.2018, Tao Q, et at al. 2019, Le V D, et at al. 2020). Therefore, proposing a new model for long-term air quality prediction in China becomes necessary (He Y, et al. 2023). Additionally, there is another significant question: do economic factors, such as GDP, affect air quality? In contrast to previous research, this study considers essential pollution items and combines them with financial aspects. In this paper, two new models based on the multinomial logistic regression algorithm are constructed, classifying 31 capital cities into different GDP states, (high, medium, and low), and combining polluting factors as controlled variables and AQI and AQCI as dependent variables. The dataset contains air quality information on 31 capital cities in China, including six air pollutants, (O_3, $PM_{2.5}$, PM_{10}, NO_2, SO_2, and CO.) per year from 2013-2019. In summary, both models provide essential outcomes that can be used for air quality prediction and assessment.

This contribution is organized as follows: Section 2 details AQI and AQCI calculation. Section 3 focuses on Date and economic model, while Section 4 and 5, present Experiment results and draw conclusions.

AQI AND AQCI CALCULATION

The calculation of AQI in China follows these steps:

$$AQI=max\left\{IAQI_1, IAQI_2, IAQI_3, IAQI_4, IAQI_5, IAQI_6,\right\}$$

Where AQI is the air quality index, $IAQI_i$ is the individual air quality index for each of the pollutants (i from 1 to 6, 1 for SO_2, 2 for NO_2, 3 for PM_{10}, 4 for CO, 5 for O_3, 6 for $PM_{2.5}$). When one of these six pollutants reaches its maximum value, and resulting AQI is above 50, that specific pollutant becomes the primary contributor to pollution.

The individual air quality index (IAQI) for each pollutant

$$IAQI=\frac{IAQI_{h_i}-IAQI_{l_o}}{BP_{h_i}-BP_{l_0}}\left(C_i-BP_{l_o}\right)+IAQI_{l_o}$$

is calculated using the formula:

Where $IAQI_i$ is the Sub Air Quality Index for Pollutant Project i, i represents the pollutant item. C_i is the mass concentration value of the pollutant item i.

BP_{h_i} is the high value of the pollutant concentration limit close to C_i in the concentration limit table (Table 1) corresponding to the air quality sub-index. BP_{l_0} is the low value of the pollution concentration limit close to C_i in the concentration limit table corresponding to the air quality sub-index. $IAQI_{h_i}$ is the air quality sub-index corresponding to BP_{h_i} in the concentration limit table corresponding to the air quality sub-index. $IAQI_{l_0}$ is the air quality sub-index corresponding to BP_{l_0} in the concentration limit table corresponding to the air quality sub-index.

China air quality composite index:

The China Air Quality Composite Index encompasses the pollutants considered in the evaluation during the assessment period. The comprehensive index is determined by summing the individual quality indexes, and a higher value indicates a greater degree of urban air pollution. This index is calculated using the concentrations of six pollutants but with different weighing factors. The key pollutants involved in the air quality composite index assessment are O_3, $PM_{2.5}$, PM_{10}, NO_2, SO_2, and CO.

$$I_i=\frac{C_i}{S_i}$$

Individual China air quality Index:

Where C_i is the concentration value of index i. S_i is the secondary standard value of Index i. The index i can be SO_2, NO_2, PM_{10}, or $PM_{2.5}$, each with its respective secondary standard limit for the annual average concentration; For O_3, S_i represent the biggest 8 hours average secondary standard limit; For CO, S_i signifies the level 2 standard for the quasi-limit of daily average concentration, as detailed in Table 2.

$$I_{sum}=\sum_{i=1}^{6} I_i$$

Where I_{sum} is the China Air Quality Composite Index, and I_i is the individual index for indicator i, covering all

Table 1. Pollution item concentration limit table

IAQI	$PM_{2.5}$	PM_{10}	SO_2	NO_2	CO	O_3
0	0	0	0	0	0	0
50	35	50	50	40	2	100
100	75	150	150	80	4	160
150	115	250	470	180	14	215
200	150	350	800	280	24	265
300	250	420	1600	565	36	800
400	350	500	2100	750	48	1000
500	500	600	2620	940	60	1200

six pollutants (O_3, $PM_{2.5}$, PM_{10}, NO_2, SO_2, and CO). When I_i represents the maximum value among all six pollutants, i is termed the primary pollutant.

DATA AND ECONOMIC MODEL

Data description

All controlled variables were sourced from the National Bureau of Statistics of China (http: //www.stats.gov.cn/tjsj/ndsj/), while the dependent variables AQI and AQCI were calculated using the national air quality calculation platform. Figure 1 illustrates the AQI and the AQCI values for the 31 capital cities in China in 2019. The dataset spans from 2013 to 2019 and includes information on six air pollutants and the economic state. According to technical regulations, AQI values are categorized into six classes: 0–50 (Excellent), 51–100 (Good), 101–150 (Lightly polluted), 151–200 (Moderately Polluted), 201– 300 (Heavily Polluted), and more than 300 (Severely Polluted). AQCI values are classified into six classes as well: 0–2 (Excellent), 2–4 (Good), 4–6 (Light Polluted), 6–10 (Moderately Polluted), 10–12 (Heavily Polluted), and more than 12 (Severely Polluted). Capital cities have their own AQI or AQCI standards aligned with national air quality standards. In Fig.1, the air quality is depicted with a colour scale, where darker shades indicate higher pollution rates. As shown in Fig. 1, the majority of cities exhibit low AQI, i.e. having good or lightly polluted air. As for the AQCI, most cities fall in "Good" and "lightly Polluted" categories, except for those in Hebei, Shanxi and Shandong provinces, which show a significant variation between light and heavy polluted under both standards.

Economic model

Multinomial logistic regression is employed for predicting categorical placement or the probability of category membership on a dependent variable based on multiple independent variables. The independent variables can be dichotomous (binary) or continuous (interval or ratio in scale). This method is an extension of binary logistic regression, accommodating more than two categories of the dependent or outcome variable. Similar to binary logistic regression, multinomial logistic regression uses maximum likelihood estimation to access the probability of specific membership. Variable selection or model specification methods are similar to those used in standard multiple regression, including sequential or nested logistic regression analysis. These methods are applied when one dependent variable serves as criteria for placement or choice on subsequent dependent variables. The multinomial logistic regression method is employed for predicting China's air quality based on the AQI and AQCI criteria. The economic model is shown below:

$$Pr\left(Y_k\right) = \frac{e^{\beta_k \cdot x_i}}{1 + \sum_{j=1}^{k-1} e^{\beta_j \cdot x_i}}$$

Here, $Pr(Y_k)$ is the probability of category k occurring, Y_k is the dependent variable (AQI or AQCI) representing one of the pollution categories observed in actual cases. k signifies the air quality level, including "Excellent", "Good", "Light polluted", "Median polluted", "Heavy" and "Serious polluted". x_i denotes controlled variables, with, x_1

Table 2. Limitation of the secondary standards for each pollution concentration

Pollution items	Time	Concentration limit	
		Level one	Level two
SO_2	Annual average	20	60
NO_2	Annual average	40	40
CO	24 hour average	4	4
O_3	8 hour average	100	160
PM_{10}	Annual average	40	70
$PM_{2.5}$	Annual average	35	75

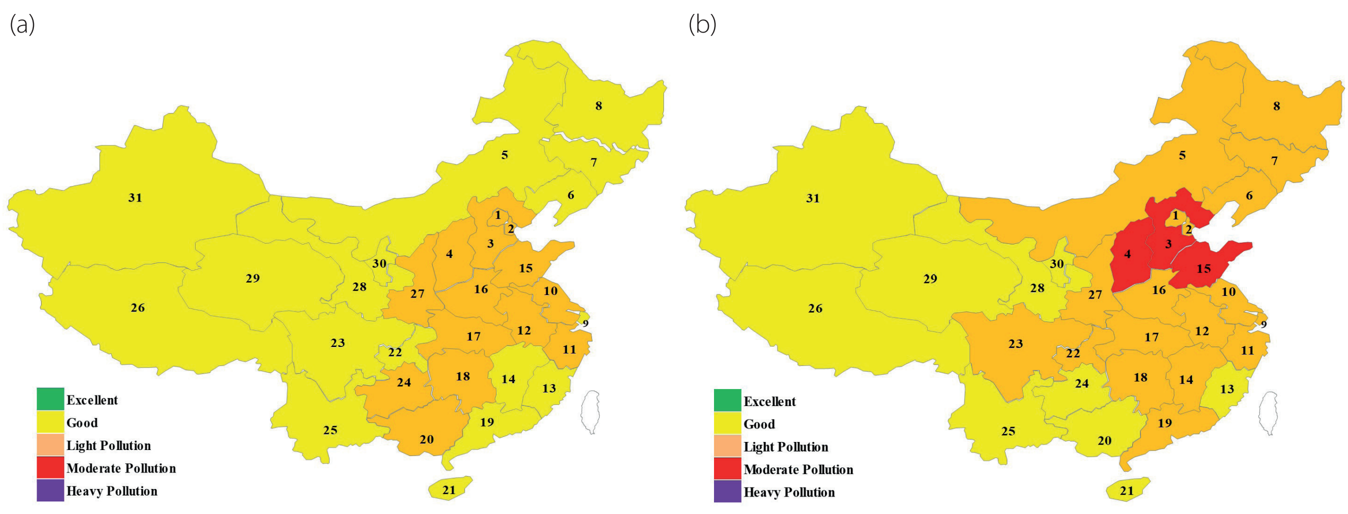

Fig. 1. AQI (a) and AQCI (b) values in Chinese capital cities. 1--Beijing, 2--Tianjin, 3--Shijiazhuang, 4--Taiyuan, 5--Hohhot, 6--Shenyang, 7--Changchun, 8--Harbin, 9--Shanghai, 10--Nanjing, 11--Hangzhou, 12--Hefei, 13--Fuzhou, 14--Nanchang, 15--Jinan, 16--Zhengzhou, 17--Wuhan, 18--Changsha, 19--Guangzhou, 20--Nanning, 21--Haikou, 22-- Chongqing, 23--Chengdu, 24--Guiyang, 25--Kunming, 26--Lhasa, 27--Xi'an, 28--Lanzhou, 29--Xining, 30--Yinchuan, 31--Urumqi

representing the primary pollutant, x_2 indicating low-level GDP status. x_3 representing middle level GDP status, and x_4 denoting high level GDP status. The β_k and β_j are the parameters in the model.

Figures 2 and 3 illustrate the primary pollutants influencing AQI and AQCI during the period 2013-2019, showcasing the proportion of the primary contaminant in the total annual pollution. $PM_{2.5}$ and O_3 were consistently identified as the primary pollutants for AQI and AQCI, respectively, comprising 71.4% and 73.3%. The second primary pollutants for AQI was O_3, one-quarter. Conversely, PM_{10} and CO contributed insignificantly, representing only 6.5% and 0.9%, over the years. As for AQCI, PM_{10} was the second primary pollutant, at 15.2%, followed by O_3 and NO_2 at 8.3% and 3.2%, respectively. The proportion of $PM_{2.5}$ as the primary pollutant in AQCI exhibited fluctuations and an overall decreasing trend. In contrast, the concentration of O_3 as primary pollutant in AQI increased annually, reaching 100% in 2018-2019. The challenging nature of controlling ozone, among six air pollutants, warrants careful consideration.

MODEL RESULTS

The multinomial logistic model, involves choosing one outcome as a "pivot" and deflecting other outcomes relative to the pivot outcome. Similarly, in the AQI model, we use "Heavily polluted" as the pivot. The process is as follows:

$$In\frac{Pr(Y_1)}{Pr(Y_4)}=10.545=0.0525x_a+10.298x_b+10.226x_c$$

$$In\frac{Pr(Y_2)}{Pr(Y_4)}=3.531+9.09\cdot 10^{-4}x_a+8.219x_b+9.098x_c$$

$$In\frac{Pr(Y_3)}{Pr(Y_4)}=5.767-3.444\cdot 10^{-2}x_a+4.848\cdot 10^{-1}x_b+4.742\cdot 10$$

Where $x_a=\log\frac{x_1}{x_4},\ x_b=\log\frac{x_2}{x_4},\ x_c=\frac{x_3}{x_4}$

$$RHS_1=In\frac{Pr(y_1)}{Pr(y_4)},\ RHS_2=In\frac{Pr(y_2)}{Pr(y_4)},\ RHS_3=In\frac{Pr(y_3)}{Pr(y_4)}$$

if we exponentiate both sides, and solve for the probabilities, we get

$$Pr(Y_1)=Pr(Y_i=Y_4)*RHS_1$$

$$Pr(Y_2)=Pr(Y_i=Y_2)*RHS_2$$

$$Pr(Y_3)=Pr(Y_i=Y_4)*RHS_3$$

$$Pr(Y_4)=1-\sum_{k=1}^{3}Pr(Y_i=Y_k)=\frac{1}{1+\sum_{1}^{k-1}e^{RHS_k}}$$

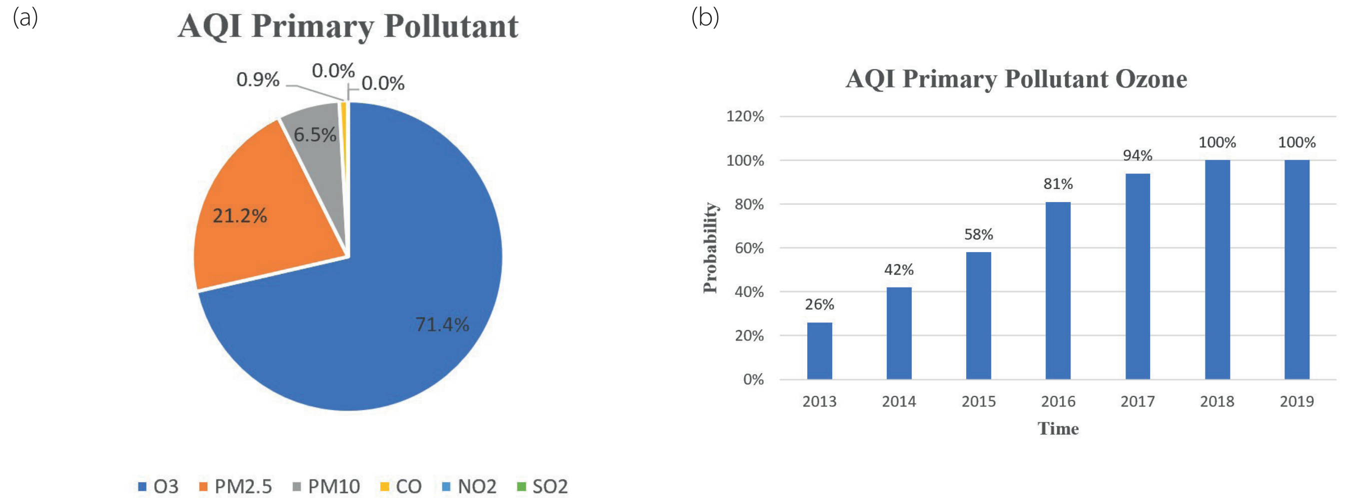

Fig. 2. AQI Pollutant Composition (2013-2019).

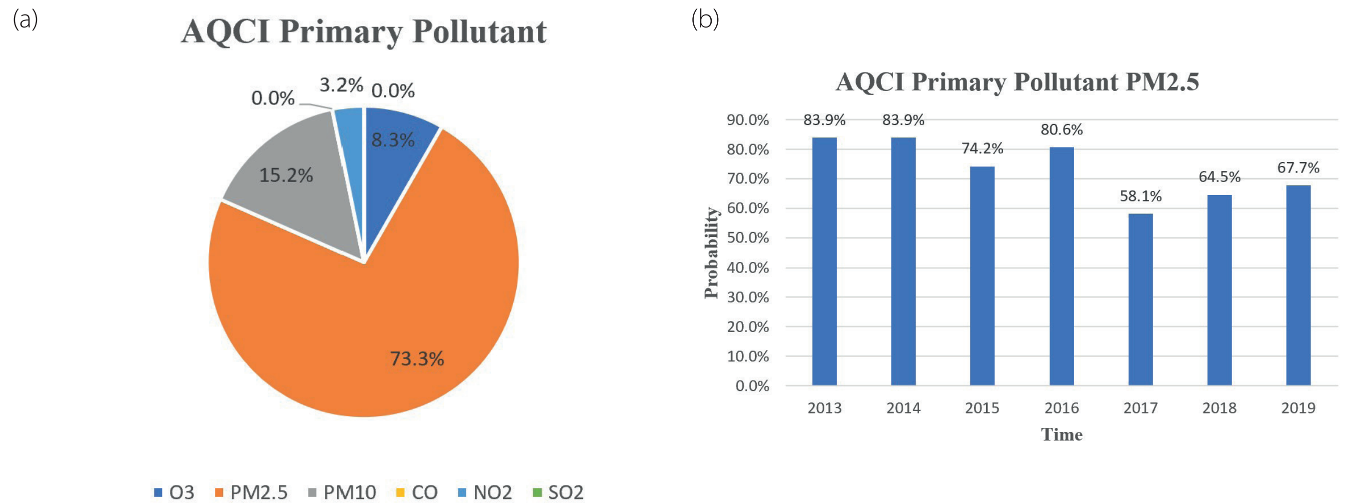

Fig. 3. AQCI pollutant Composition (2013-2019).

In AQI model, we choose the "Serious pollution" as the pivot. The process is as follows:

$$In\frac{Pr(Y_1)}{Pr(Y_4)} = 111.824 - 1.585x_a + 20.369x_b + 69.724x_c$$

$$In\frac{Pr(Y_2)}{Pr(Y_4)} = 72.642 - 0.524x_a + 4.86x_b + 49.127x_c$$

$$In\frac{Pr(Y_3)}{Pr(Y_4)} = 111.897 - 1.085x_a + 4.064x_b + 52792x_c$$

Where $x_a = \log\frac{x_1}{x_4}$, $x_b = \log\frac{x_2}{x_4}$, $x_c = \log\frac{x_3}{x_4}$,

Two tailed tests.

H0: the parameter of coefficient $x_{l,l=a,b,c}$ is significant.

H1: the parameter of coefficient $x_{l,l=a,b,c}$ is not significant.

Two-tailed tests were employed to assess the significance coefficient parameters. The null hypothesis stated that the coefficient was significant, while the alternative hypothesis suggested otherwise. The results, detailed in Tables 3 and 4, indicate that the most absolute z-value exceeded 1.96, corresponding to p-value less than 0.05. Therefore, we could reject the alternative hypothesis, confirming the significance of the coefficients.

The multiple logistic regression models were designed to predict the likelihood of China's air quality categories, including predictions for good air or light, moderate, and heavy polluted. This confusion matrix results, shown cased in Tables 5 and 6 in Appendices, offer a detailed breakdown based on the classification of the four categorical variables.

To assess the model's performance, Receiver Operating Characteristic curve (ROC) combined with Area Under the Curve (AUC) and F-1 score are employed. An AUC value above 0.8 and an F1-score exceeding 0.8 generally indicate high model quality. The AQI model demonstrates an F1-score greater than 0.8, while the AQCI model's F1-score approaches 0.8, affirming their high-quality predictions. Additionally, AUC values exceeding 0.8 in Table 5 and Table 6 further support the models' efficacy. Figure 4 visually presents the ROC curve results for AQI and AQCI models.

In Figure 5(a), the horizontal axis represents ozone concentration, with the maximum concentration value of 211 μg/m^3, and the minimum concentration value of 69 μg/m^3 adjusted to 65 μg/m^3 and 215 μg/m^3, respectively. The vertical axis represents the probability of each category, with the high GDP status shown in red. The low GDP status in green, the middle GDP status in blue. Notably, as ozone levels increase, the probabilities of various air quality levels fluctuate, revealing distinct opportunities for additional GDP and air quality levels in different regions. The application of multinomial logistic regression to predict the probability of each pollution level is considered, incorporating pollutant concentration (μg/m^3) and GDP state (Dummy) as control variables. The results showed changes in air quality with increase of ozone concentration.

The AQCI model, focusing on $PM_{2.5}$ demonstrated the results similar to the AQI model. The $PM_{2.5}$ concentration

Table 3. Two-tailed test for the AQI model

	Intercept		Ozone/High		Low/High		Middle/High	
	Z-value	P-value	Z-value	P-value	Z-value	P-value	Z-value	P-value
Good/Heavy	3.57	3.5E-4	-2.89	4.0E-3	31.59	0	39.82	0
Light/Heavy	1.19	0.231	0.05	0.959	25.27	0	35.53	0
Moderate/Heavy	1.20	0.228	-1.10	0.271	34.94	0	36.49	0

Table 4. Two-tailed test for the AQCI model

	Intercept		Ozone/High		Low/High		Middle/High	
	Z-value	P-value	Z-value	P-value	Z-value	P-value	Z-value	P-value
Good/Heavy	559.22	0	-4.96	7.2E-7	-3.08	2.1E-3	5.96	0
Light/Heavy	554.99	0	-4.77	1.8E-6	-14.33	0	51.41	0
Moderate/Heavy	57305	0	-2.39	1.7E-2	9.6E+6	0	7.1E+9	0

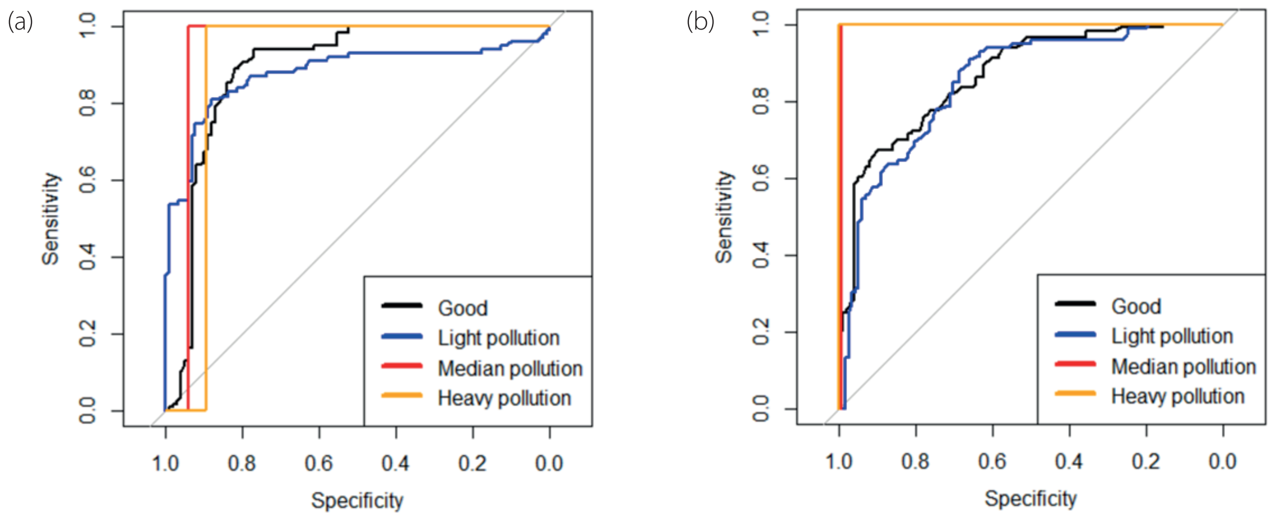

Fig. 4. The AQI model (a) and AQCI (b) model ROC curve results

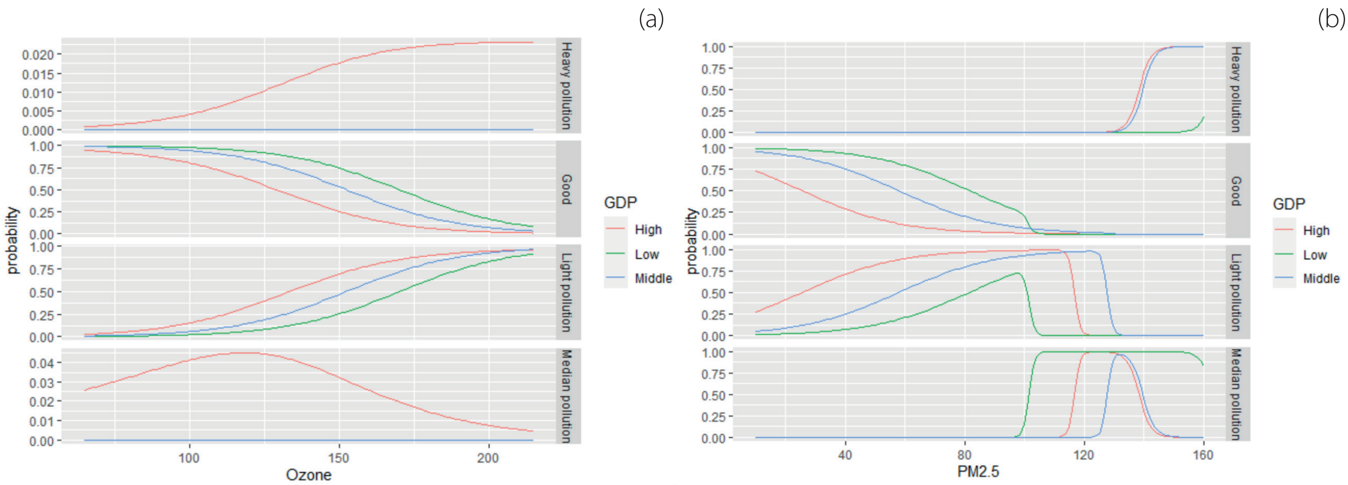

Fig. 5. The AQI model (a) and AQCI model (b) results

range limits of 12 μg/m³ and 154 μg/m³ were adjusted to 5 μg/m³ and 165 μg/m³, respectively. This analysis suggests that, under similar pollution sources, higher GDP status correlates with increased probabilities of air quality pollution across different economic statuses.

CONCLUSIONS AND DISCUSSION

The study's conclusions emphasize the suitability of multinomial logistic regression for predicting air quality in China, especially when considering different evaluation systems. The economic status of a region emerges as a significant determinant of air quality, with regions exhibiting high GDP associated with a higher probability of experiencing light or heavy air pollution rather than excellent and good air quality. This finding highlights the importance of integrating economic factors into air quality assessments.

Furthermore, the result reveals the variability in primary pollutants or influential factors across different air quality evaluation systems, warranting further exploration.

Consequently, this study advocates for the development of diverse criteria for air quality assessment, emphasizing the need for precise performance standards and the application of uncertainty models to evaluate long-term trends comprehensively. By addressing these aspects, more adequate measures are expected to be taken to tackle air pollution issues.

In conclusion, these findings provide valuable insights to future research in air quality assessment. Further investigations should focus on the development of improved performance standards and the exploration of the complex interplay between economic factors, primary pollutants, and air quality evaluation systems.

REFERENCES

Bure V. M, Parilina E. M., (2013). Probability theory and mathematical statistics, 1st ed. St Petersburg, Lan Publ., 416 p. (in Russian).

Bure V. M., Parilina E. M., Sedakov A.A., (2019) Applied statistic methods in R and Excel. 3rd ed. St Petersburg, Lan Publ., 196 p. (in Russian).

Bure V.M., (2007). Methodology for statistical analysis of empirical data. St Petersburg, Lan Publ. (in Russian).

Di Q, Amini H, Shi L, et al. (2019). An ensemble-based model of PM2. 5 concentration across the contiguous United States with high spatiotemporal resolution. Environment international, 2019, 130: 104909, DOI: 10.1016/j.envint.2019.104909.

Fan, J., Li, Q., Hou, J., Feng, X., Karimian, H., and Lin, S. (2017). A Spatiotemporal Prediction Framework for Air Pollution Based on Deep RNN, ISPRS Ann. Photogramm. Remote Sens. Spatial Inf. Sci., IV-4/W2, 15–22, DOI:10.5194/isprs-annals-IV-4-W2-15-2017.

Fann N, Risley D. (2013). The public health context for PM2. 5 and ozone air quality trends. Air Quality, Atmosphere & Health, 6(1): 1-11, DOI:10.1007/s11869-010-0125-0.

Guo Q, He Z, Li S, et al. (2020). Air pollution forecasting using artificial and wavelet neural networks with meteorological conditions. Aerosol and Air Quality Research, 20(6): 1429-1439, DOI: 10.4209/aaqr.2020.03.0097.

He Y., Qi D., Bure V. M. (2023). New application of multiple linear regression method-A case in China air quality. Vestnik of Saint Petersburg University. Applied Mathematics, Computer Sciences, Control Processes, 18(4), 516-526. DOI:10.21638/11701/spbu10.2022.406

Iakushev V. P., Bure V. M., Mitrofanova O. A., Mitrofanov E. P. K voprosu avtomatizatsii postroeniia variogramm v zadachakh tochnogo zemledeliia [On the issue of semivarigrams constructing automation for precision agriculture problems]. Vestnik of Saint Petersburg University. Applied Mathematics, Computer Sciences, Control Processes, 2020, 16(2), 177-185, (in Russian). DOI:10.21638/11701/spbu10.2020.209.

Iakushev V. P., Bure V. M., Mitrofanova O. A., Mitrofanov E. P. Theoretical foundations of prababilistic and statistical forecasting of agrometerological risks. Vestnik of Saint Petersburg University. Applied Mathematics, Computer Sciences, Control Processes, 2021, 17(2), 174-182, (in Russian). DOI:10.21638/11701/spbu10.2021.207.

Karimian H, Li Q, Wu C, et al. (2019). Evaluation of different machine learning approaches to forecasting PM2. 5 mass concentrations. Aerosol and Air Quality Research, 19(6): 1400-1410, DOI: 10.4209/aaqr.2018.12.0450

Le V D, Bui T C, Cha S K. (2020). Spatiotemporal deep learning model for citywide air pollution interpolation and prediction. 2020 IEEE international conference on big data and smart computing (BigComp). IEEE, 55-62, DOI: 10.1109/BigComp48618.2020.00-99.

Li X, Peng L, Hu Y, et al. (2016). Deep learning architecture for air quality predictions. Environmental Science and Pollution Research, 23(22): 22408-22417, DOI:10.1007/s11356-016-7812-9.

Nadeem I., Ilyas A.M., Uduman P.S. Analyzing and forecasting ambient air quality of Chennai city in India. (2020) GEOGRAPHY, ENVIRMENT, SUSTAINABILITY.13(3), 13-21, https:// doi.org/10.24057/2071-9388-2019-97.

Pan B. (2018). Application of XGBoost algorithm in hourly PM2. 5 concentration prediction, IOP conference series: earth and environmental science. IOP publishing, 2018, 113(1): 012127, DOI: 10.1088/1755-1315/113/1/012127.

R. Stern, P. Builtjes, M. Schaap, R. Timmermans, R. Vautard, A. Hodzic, M. Memmesheimer, H. Feldmann, E. Renner, R. Wolke, et al., (2008). A model inter-comparison study focussing on episodes with elevated pm10 concentrations, Atmospheric Environment, 42(19), 4567–4588, DOI: 10.1016/j.atmosenv.2008.01.068.

Schachter E N, Moshier E, Habre R, et al. (2016). Outdoor air pollution and health effects in urban children with moderate to severe asthma. Air Quality, Atmosphere & Health, 9(3): 251-263. DOI:10.1007/s11869-015-0335-6.

Senarathna M., Priyankara S., Jayaratne R., Weerasooriya R., Morawska L., Bowatte G. (2022). Measuring Traffic Related Air Pollution Using Smart Sensors In Sri Lanka: Before And During A New Traffic Plan. GEOGRAPHY, ENVIRONMENT, SUSTAINABILITY. 15(3):27-36. https://doi.org/10.24057/2071-9388-2022-011

Stojov V, Koteli N, Lameski P, et al. (2018). Application of machine learning and time-series analysis for air pollution prediction. Proceedings of the CIIT.

Tao Q, Liu F, Li Y, et al. (2019). Air pollution forecasting using a deep learning model based on 1D convnets and bidirectional GRU. IEEE access, 7: 76690-76698, DOI: 10.1109/ACCESS.2019.2921578

Tong W, Li L, Zhou X, et al. (2019). Deep learning PM2.5 concentrations with bidirectional LSTM RNN. Air Quality, Atmosphere & Health, 12(4): 411-423, DOI: 10.1007/s11869-018-0647-4.

Wang K, Yin H, Chen Y. (2019). The effect of environmental regulation on air quality: A study of new ambient air quality standards in China. Journal of Cleaner Production, 215: 268-279, DOI:10.1016/j.jclepro.2019.01.061

Wang, S., & Hao, J. (2012). Air quality management in China: Issues, challenges, and options. Journal of Environmental Sciences, 24(1): 2-13, DOI:10.1016/S1001-0742(11)60724-9.

Zaib S, Lu J, Bilal M. (2022). Spatio-Temporal Characteristics of Air Quality Index (AQI) over Northwest China. Atmosphere, 13(3): 375, DOI:10.3390/atmos13030375.

APPENDICES

Table 5. AQI model confusion matrix results

	Good	Light Polluted	Moderate Polluted	Heavy polluted
F1 score	0.8858	0.8247	0	0
AUC	0.8894	0.8783	0.9560	0.9398

Table 6. AQCI model confusion matrix results

	Good	Light Polluted	Moderate Polluted	Heavy polluted
F1 score	0.7644	0.7688	1	1
AUC	0.8665	0.8508	1	1

RESEARCH PAPER

IMPACT OF METEOROLOGICAL PARAMETERS ON THE DAILY VARIABILITY OF THE GROUND-LEVEL $PM_{2.5}$ CONCENTRATIONS ACCORDING TO MEASUREMENTS IN THE MIDDLE URALS

Anna P. Luzhetskaya[1*], Ekaterina S. Nagovitsyna[1,2], Vassily A. Poddubny[1]
[1]Institute of Industrial Ecology, Ural Branch of the Russian Academy of Sciences, ul. Sofi Kovalevskoy, 20, Yekaterinburg, 620990, Russian Federation
[2]Ural Federal University named after the first President of Russia B.N. Yeltsin, ul. Mira, 19, Yekaterinburg, 620002, Russian Federation
*Corresponding author: luzhanka@mail.ru
Received: March 29th, 2023 / Accepted: November 14th, 2023 / Published: December 31st, 2023
https://DOI-10.24057/2071-9388-2023-2824

ABSTRACT. The results of a comparison of the $PM_{2.5}$ aerosol concentration daily variability for the summer and winter seasons at the urban and background monitoring sites in the Middle Urals for 2016–2019 are presented. The cluster analysis method revealed a statistically significant difference between the two groups corresponding to higher and lower concentrations of fine aerosol during the day. Studies of the daily variation of the $PM_{2.5}$ particle concentration in the Middle Urals indicate the leading role of meteorological characteristics (in particular, air temperature, pressure and wind speed) in changing the level of aerosol suspension in the air surface layer. Distinctive typical average daily concentrations of $PM_{2.5}$ for the Middle Urals region, corresponding to the cluster of lower values, are observed in the summer and are on average ~ 5.2 μg/m^3 for the urban area and ~ 3.4 μg/m^3 for the background site. In winter, these parameters are 12.8 μg/m^3 for urban conditions and 10.5 μg/m^3 for background site. The higher content of $PM_{2.5}$ particles, corresponding to the cluster of higher values, are identified in winter and are on average ~32.2 μg/m^3 in urban conditions and ~ 30.3 μg/m^3 in the background area. In summer, these parameters are 13.6 μg/m^3 for urban site and 9.6 μg/m^3 for background area. Simultaneous analysis of the fine aerosol concentrations and the meteorological parameters in the surface atmospheric layer allowed to define of weather conditions, at which the occurrence of higher $PM_{2.5}$ values is possible.

KEYWORDS: mass concentration of $PM_{2.5}$ aerosol particles, meteorology, cluster analysis, air quality, Middle Urals

CITATION: Luzhetskaya A. P., Nagovitsyna E. S., Poddubny V. A. (2023). Impact Of Meteorological Parameters On The Daily Variability Of The Ground-Level $Pm_{2.5}$ Concentrations According To Measurements In The Middle Urals. Geography, Environment, Sustainability, 4(16), 172-179
https://DOI-10.24057/2071-9388-2023-2824

ACKNOWLEDGEMENTS: The authors of the research express their gratitude to their colleagues Yu. I. Markelov, Y. Matsumi, R. Imasu for their assistance in the measurements.

Conflict of interests: The authors reported no potential conflict of interest.

INTRODUCTION

In recent decades, the interest in the problem of atmospheric air pollution with fine suspended particles has been growing due to the significance of their impact on human health, the state of ecosystems, and global climate change. Aerosol particles with aerodynamic diameters less than 2.5 microns ($PM_{2.5}$) are a complex, heterogeneous mixture of many components suspended in the air. It is well known that $PM_{2.5}$ particles are able to penetrate into the internal environment of the body and accumulate in the upper and lower parts of the bronchi, inducing diseases of the human respiratory and cardiovascular systems (e.g., Pope et al. 2020; Vohra et al. 2021; Zhang et al. 2018; Seinfeld and Pandis 2006; Kim et al. 2015).

$PM_{2.5}$ particles can affect shortwave radiation coming from the Sun to the Earth and longwave radiation emitted by the Earth's surface into space, participating in the processes of absorption and scattering of radiation in the atmosphere, on the one hand, and in cloud formation, on the other hand (IPCC, 2021; Ginzburg et al. 2009)

The National Hydrometeorological Services monitor the concentration of suspended particles. As a criterion for the pollution level by fine aerosol, Russia has put into effect a hygienic standard that regulates the maximum permissible concentrations of suspended particles in the atmospheric air. According the hygienic standard, the average daily level of $PM_{2.5}$ particles concentrations in the air should not exceed 35 μg/m^3, and the average annual level should not exceed 25 μg/m^3 (SanPiN 1.2.3685-21, 2021).

One of the effective methods of protecting the health of the population is the forecast of unfavorable meteorological conditions contributing to an increase in the concentration of atmospheric impurities. According to the estimates of various authors (e.g., Hooyberghs et al. 2005; Stern et al. 2008; Tai et al.

2010), a significant part of the average daily variability of aerosol concentration is determined by the entire set of meteorological parameters.

The air pollution forecast schemes are developed based on the results of theoretical and experimental studies, in which the statistical relationships between atmospheric pollution and the corresponding meteorological factors are studied. For example, Gubanova et al. (2018) have investigated the relationships between $PM_{2.5}$ and meteorological factors in the Moscow. According to the correlation analysis results, $PM_{2.5}$ concentrations was negatively correlated with wind speed (correlation coefficient R= - 0.56), positively correlated with air temperatures (0.55).

Many studies have already proven that the correlations between $PM_{2.5}$ concentration and meteorological factors vary with the seasons. For example, Chen et al. (2016) have determined that the correlation between $PM_{2.5}$ and air temperature was negative in summer (- 0.03) and autumn (- 0.26) and then turned to positive in spring (0.22) and winter (0.35).

However, besides seasonal variations, it has also been found that the relationships between PM2.5 concentration and meteorological factors vary between regions (Yang et al. 2017; Novikova et al. 2017; Li et al. 2017; Kermani et al. 2020, Zhou et al. 2023; Gao et al. 2022).

In our resent work (Luzhetskaya et al. 2022) was created a prognostic model for estimating the surface $PM_{2.5}$ concentrations in the Middle Urals. The aerosol optical depth ($\tau_{0.5}$), meteorological and geographical parameters were considered as predictors. As a result, was obtained the ranked lists of the possible predictors usable in statistical models for estimating the logarithm of $PM_{2.5}$ values (the pairwise correlation coefficients between a corresponding quantity and $\ln PM_{2.5}$ are given in parentheses). The significant predictors for urban area were boundary layer height (–0.51), $\ln\tau_{0.5}$ (0.31), pressure (0.31), relative air humidity (0.29), and Normalized Difference Vegetation Index (–0.27). The possible predictors for background monitoring site were boundary layer height (–0.48), $\ln\tau_{0.5}$ (0.44), Normalized Difference Vegetation Index (–0.29), relative air humidity (0.26), and pressure (0.25).

This research is aimed at studying the impact of meteorological parameters not on the values of single concentrations, but on the daily variability of the concentration of fine $PM_{2.5}$ aerosols in the air surface layer by means of the cluster analysis method. Based measurement data set accumulated at the urban and background monitoring sites in the Middle Urals during 2016–2019, an attempt was made to reveal the specific type of daily variation and the typical values of particle concentrations depending on a set of parameters – air pressure and air temperature, wind speed, and boundary layer height.

The results obtained can be used in numerical modeling of air quality in Yekaterinburg and other cities of the Middle Urals.

MATERIALS AND METHODS

Study area and data

The Middle Urals is located inside the Eurasian continent at the junction of two parts of the world – Europe and Asia, within the Ural ridge – the Northern and Southern Urals, as well as the East European and West Siberian plains. All seasons of the year are dominated by westerly winds, northerly winds are not uncommon, and easterly winds are a rarer occurrence. The remoteness from the Atlantic Ocean and the proximity of Siberia make the climate of the Middle Urals continental, which induces sharp changes in air temperature. The average monthly air temperature in January is -16.2 °C and in July – +16.7 °C. (Morokova and Shver, 1981; Shalaumova et al. 2010; Scientific and application oriented handbook…1990).

Yekaterinburg is the fourth most populous city in Russia, located in the central part of the Middle Urals. The main sources of industrial air pollution in Yekaterinburg are ferrous and non-ferrous metallurgy, energy, mechanical engineering, construction and chemical industries, as well as road and rail transport (mprso.midural.ru, 2019).

The results of long-term measurements of the mass concentration of atmospheric aerosols of the $PM_{2.5}$ fraction performed at the background and urban monitoring sites in the Middle Urals during 2016–2019 are used in this research. The urban monitoring site is located in Yekaterinburg on the territory of the Institute of Industrial Ecology of the Ural Branch of the Russian Academy of Sciences (56.850° N, 60.655° E). The background monitoring site is located in a forest ~ 65 km northwest of Yekaterinburg at the site of the Kourovka Astronomical Observatory (KAO) of the Ural Federal University (57.036° N, 59.546° E).

Measurements of the concentration of fine particles in the surface air layer are performed using two sets of Panasonic $PM_{2.5}$ optical sensors, which allowed estimating the concentration of aerosol particles in the size range between 0.3 and 2.5 μm (Nakayama et al. 2018). Observations of $PM_{2.5}$ particle concentrations at the urban and background monitoring sites are performed at the same height (~ 9 m above the ground).

Fig. 1 shows the schematic location of two monitoring sites of the $PM_{2.5}$ fraction of aerosol particles in the Middle Urals.

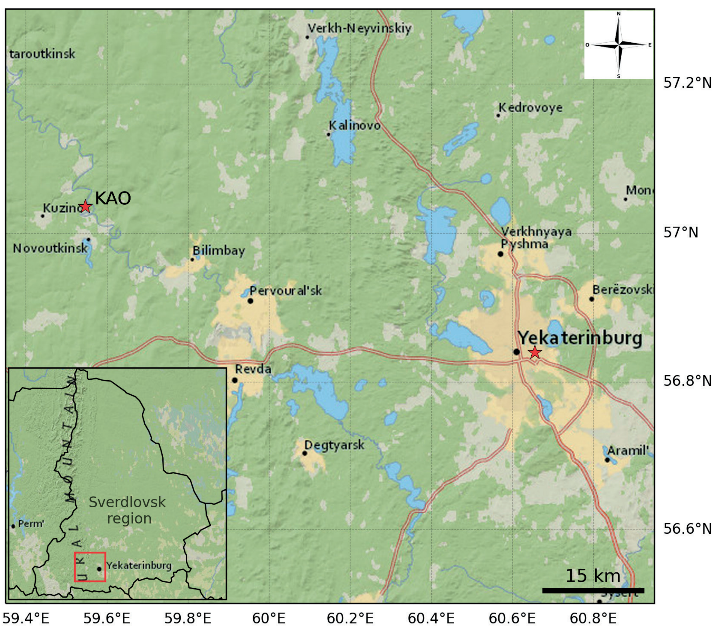

Fig. 1. Schematic location of urban (Yekaterinburg) and background (KAO) monitoring sites in the Middle Urals

The meteorological information used in the research was extracted from the reanalysis databases of the European Center for Medium-Range Weather Forecasts (ECMWF) (www.ecmwf.int). Weather data from the ECMWF Reanalysis v5 (ERA 5) database were available on a regular coordinate grid with a spatial resolution of 0.25°x0.25° and a temporal resolution of 1 hour. The following parameters were selected from the whole variety of reanalysis data: pressure (*P*, hPa); air temperature at 2 m (T, ºC); dew point temperature (*d2m*, K); horizontal wind speed components at a height of 10 m (*Vx, Vy, m/s*); boundary layer height (*blh*, km). The dew point temperature is used to calculate the relative air humidity (*Hu, %*). The horizontal wind speed w_s (m/s) and direction w_d (deg) are calculated from the horizontal wind components.

Cluster analysis method

Based on the selected data for each monitoring site, samples of $PM_{2.5}$ aerosol concentrations and meteorological parameters are formed with averaging over a time interval of 1 hour, corresponding to the calendar summer and winter periods. In spring and autumn, a transition of the daily variation features of the $PM_{2.5}$ aerosol concentration from winter to summer ones and vice versa occurs (Luzhetskaya et al. 2022), and such transient processes are not considered within the framework of this research.

The cluster analysis method is used to study the daily variability of $PM_{2.5}$ aerosol concentration. Recently, cluster analysis methods have become widespread for the analysis of aerosol pollution. For example, Rozwadowska et al. (2010), Hafner et al. (2007) have used air mass backward trajectory cluster analysis to investigate the transport pathways and potential sources of atmospheric aerosols at Spitsbergen island and in the Western U.S. Omar et al. (2005), Aladodo (2022) have identified main clusters of aerosol types and determined microphysical properties of aerosol groups using cluster analysis of Aerosol Robotic Network (https://aeronet.gsfc.nasa.gov) measurements.

In this research, the clustering procedure is performed not on the entire set of average hourly values, but on samples characterizing the daily variation of aerosol pollution of the atmosphere. Therefore, the initial time series of values of ground-level concentrations of aerosol particles iss divided into samples by day. As a result, an array is formed consisting of a set of time series, each of which contained 24 average hourly values. Time series with gaps are removed. Then the time series clustering method is applied, as a result of which each such time series belonged to one or another cluster. Thus, different types of daily variation of $PM_{2.5}$ concentrations are revealed. The K-means method is used for clustering time series in this research (Aghabozorgi et al. 2015; MacQueen 1967). K-Means is the most popular unsupervised algorithm of clustering for several reasons. It is easy to use, algorithm is computationally efficient and results are easy to interpret. The method certainly has disadvantages, among which is sensitivity to outliers. For this reason, high aerosol concentrations ($PM_{2.5}$ > 80) are excluded from consideration. Clustering is performed using the *TimeSeriesKMeans* method of the Python tslearn. clustering module (https://tslearn.readthedocs.io/en/stable/). The metric applied to determine the centers of clusters is the Euclidean distance.

In order to assess the quality of clustering, the average silhouette coefficient is used, which is calculated using the average distance between points within the cluster and the average distance to the points of another nearest cluster (Rousseeuw, 1987). The value of the average silhouette coefficient is in the range between - 1 and + 1. If the average silhouette coefficient is positive, the cluster points are on average closer to their group than to the neighboring one. The higher the value of the silhouette coefficient is, the higher is the quality of clustering.

The number of clusters is set equal to two, since with an increase in the number of clusters, the values of the silhouette coefficients noticeably decreased, which means a decrease in the quality of clustering.

The values of the average silhouette coefficients for the measurement data samples in Yekaterinburg are 0.47 and 0.50 for the summer and winter periods, respectively. In KAO the average silhouette coefficients for the summer and winter periods are 0.42 and 0.48, respectively.

RESULTS AND DISCUSSION

The clustering results are shown in Fig. 2.

Since the initial time series are not scaled in any way, the most significant feature characterizing the two groups of samples obtained during clustering is the average value in the daily variation of concentrations. As a result of the procedure described above, clusters with typical low (cluster 1) and high values (cluster 2) of $PM_{2.5}$ aerosol concentrations are identified. It should be noted that in all the cases considered, clusters with high concentrations of $PM_{2.5}$ particles are smaller in number.

Fig. 2 demonstrates the daily variations of ground-level $PM_{2.5}$ particle concentrations, which, as a result of the procedure, are assigned to a specific cluster (gray lines), and the centers of the corresponding clusters (red lines). The figure also reveals information on how many time series fell into a particular cluster.

Fig. 3 demonstrates the daily variability of hourly mean values of ground-level $PM_{2.5}$ particle concentrations and some meteorological parameters for each of the two selected clusters. The upper and lower bounds of the boxes mark the values of the first and third quartiles of the data samples. The horizontal bar in the box corresponds to the median, and the slanted serifs at the median were a rough estimate of the 95% confidence interval for median differences. The overlap of slanted serifs allows revealing the statistical indistinguishability of the medians of the compared measurement data samples corresponding to a certain hour.

According to Fig. 3, the most pronounced changes in the daily variations are characteristic of high aerosol concentrations (cluster 2). The curves of daily variations of $PM_{2.5}$ aerosol concentrations in summer are characterized by the presence of two periods of increased values. Both in Yekaterinburg and KAO the higher values of $PM_{2.5}$ aerosol concentrations are observed in the morning and evening hours, which are separated by a segment with a lower content of particles in the afternoon hours. In summer, the maximum of daily average variations of fine aerosol concentration exceeds the minimum 1.6 times in Yekaterinburg and 2.4 times in KAO.

If the winter period is considered, then the segments of lower values in the curves of the daily variation at both monitoring sites was less pronounced. It should be noted that during the cold period, the daily variations in the $PM_{2.5}$ particle concentrations in the background region for cluster 2 are more pronounce. The maximum of daily average variations of fine aerosol concentration exceeds the minimum 1.4 times. For Yekaterinburg the difference of these values is less pronounced and their ratio is 1.2

It should be noted that smaller changes in the daily variations in the concentrations of fine particles both in winter and in the summer period in the city could be associated with the formation of an urban heat island, which reduced daily fluctuations in the boundary level height. The research used meteorological parameters, including the height of the boundary layer, taken from the ECMWF reanalysis data with a spatial resolution of 0.25°x0.25°. Therefore, the graphs shown in Fig. 3 do not illustrate a fundamental difference in the daily variation

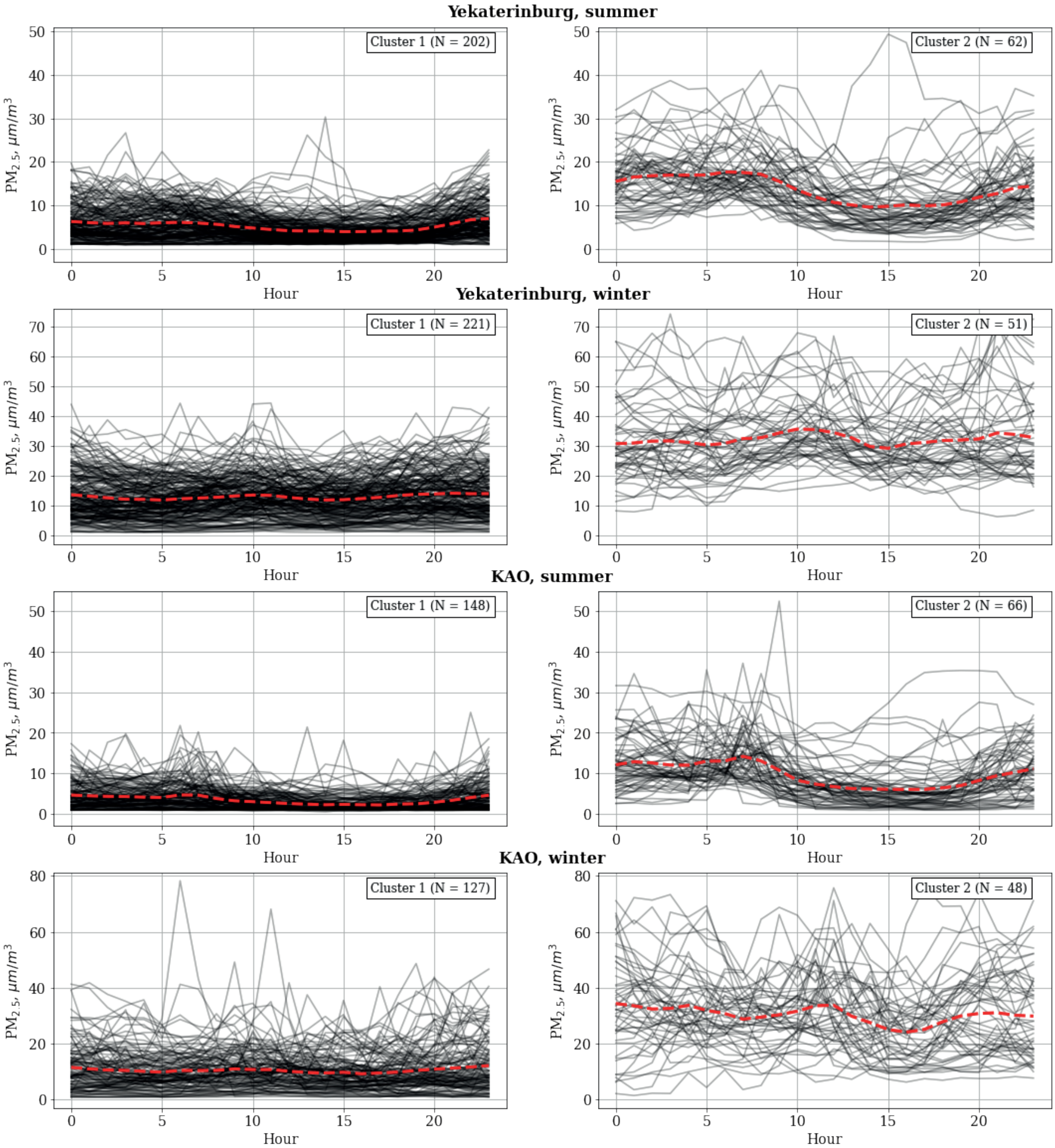

Fig. 2. Clusters identified by the K-mean method based on daily variability in the concentration of $PM_{2.5}$ particles

of boundary layer heights for urban and background monitoring sites.

A comparison of the daily variability of $PM_{2.5}$ particle concentrations with meteorological characteristics confirm the fact that meteorological parameters significantly influenced the level of pollution of the lower atmospheric layer with fine aerosol.

Fig. 3 shows that in all cases, the differences of median values of wind speed, air temperature, and pressure corresponding to clusters of low (cluster 1, blue boxes) and high (cluster 2, orange boxes) ground-level aerosol concentrations are statistically significant. Also, the differences between median values of the boundary layer height are statistically significant in the winter period for the entire daily variation curve. At the same time, in the summer period no statistically significant difference is revealed both in the city and in the background territory during the daytime. Therefore, in the summer period, the boundary layer height during the daytime have the same impact on the aerosol concentration values in both groups – an increase in the boundary layer height is accompanied by a decrease in the $PM_{2.5}$ particles concentrations and vice versa.

For the daily variation of relative air humidity (*Hu, %*) and wind direction (*wd*, deg.), no statistically significant difference was found between the medians of the samples corresponding to different clusters. For this reason, Fig. 3 does not show graphs for *Hu* and *wd*.

The graphs in Fig. 3 demonstrate that in summer, both in Yekaterinburg and in KAO, the cluster with higher content of $PM_{2.5}$ particles corresponded to clusters with higher values of air temperature (*T*, ºC) and pressure (*P*, hPa), as well as to clusters with lower values of wind speed (w_s, m/s) and boundary layer height (*blh*, km).

It should be noted that in winter, when compared with the summer period, both in Yekaterinburg and in KAO, a cluster with higher content of $PM_{2.5}$ particles correspond to a cluster of lower air temperature values. This is probably due to temperature inversions, which led to a weakening of the active atmospheric circulation, a decrease in the boundary layer height, and a weak manifestation of its daily variation. In winter, an increase in air temperature lead to an increase in vertical convection (boundary layer height) and, as a result, to a decrease in ground-level aerosol concentrations. In summer, higher air temperatures, on

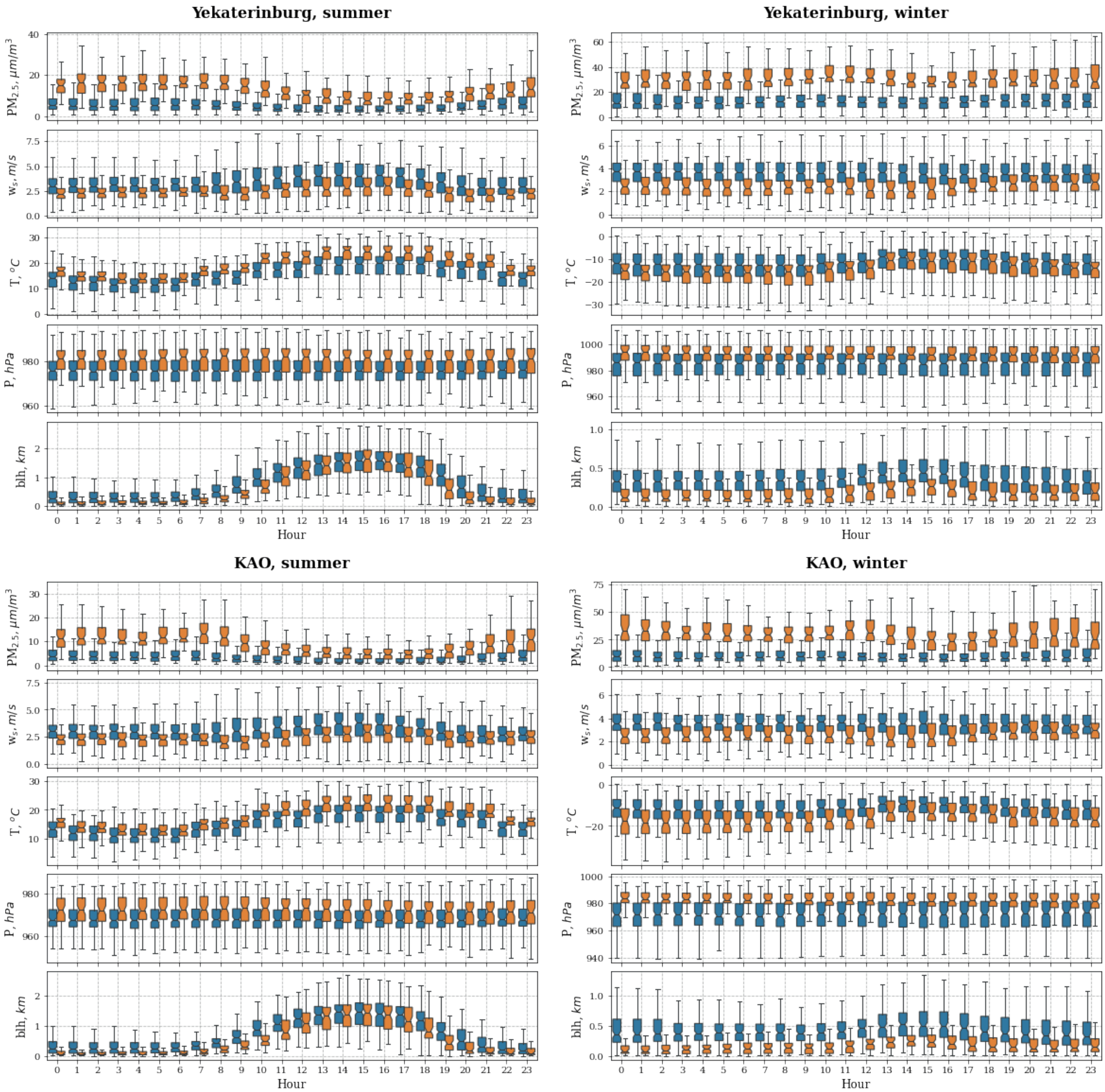

Fig. 3. Daily variability of statistical characteristics of ground-level $PM_{2.5}$ aerosol concentrations and some meteorological parameters for clusters of low (cluster 1, blue boxes) and high (cluster 2, orange boxes) values

the one hand, also caused an increase in convection, but at the same time, on the other hand, contributed to the intensification of natural fires. Wildfires lead to an increase in the aerosol content in the total atmospheric column, including in the lower atmospheric layer.

In the winter season, the range of pressure changes is wider than in the summer period, and for the atmospheric boundary layer, it is vice versa. For summer conditions, changes in the boundary layer height are significant for both the city and the background monitoring sites. At the same time, it is during the winter period that the values of atmospheric pressure and boundary layer height for clusters 1 and 2 have significant differences.

Table 1 shows the average daily values of $PM_{2.5}$ aerosol concentrations and meteorological parameters for two clusters with typical and high content of fine particles for the Middle Urals region.

Higher levels of ground-level aerosol concentrations in winter (cluster 2) are associated with the so-called unfavorable meteorological conditions – high pressure, weak winds, low air temperatures, and low atmospheric boundary layer heights. In these situations, aerosol particles cannot rise to the upper atmosphere and accumulate in the surface air.

Moreover, a group of meteorological conditions for winter and summer, which contribute to the emergence of higher concentrations of surface aerosol for the Middle Urals region can be selected. The scatter diagrams of the average daily values of meteorological parameters of the concerned clusters were analyzed for this purpose (Fig.4).

Table 2 shows the ranges of meteorological parameters corresponding to the cluster of higher surface concentrations, which are determined on the basis of Figure 4. The higher $PM_{2.5}$ aerosol concentrations (on average ~32 μg/m^3 for the urban area, ~ 30 μg/m^3 for the background area) are observed in winter and are associated with pressure > 962 hPa, weak winds < 5 m/s, air temperatures < -5.0 ºC, and low boundary layer heights < 0.5 km. In summer, higher $PM_{2.5}$ aerosol concentrations reach values ~13.6 μg/m^3 in the urban area, ~ 9.6 μg/m^3 in the background area. Higher of aerosol concentrations are concerned with pressure > 954 hPa, weak winds < 5 m/s, air temperatures > 12.0 ºC, and boundary layer heights < 1 km.

Table 1. Average daily (± standard deviation) values of $PM_{2.5}$ aerosol concentrations and meteorological parameters for two clusters with typical and high content of fine particles for the Middle Urals region

Typical values of $PM_{2,5}$ (cluster 1)				
parameters	Yekaterinburg, summer	KAO, summer	Yekaterinburg, winter	KAO, winter
$PM_{2,5}$, μg/m^3	5.2 ±2.7	3.4±0.7	12.8±5.7	10.5±5.6
blh, km	0.8 ± 0.5	0.7±0.5	0.4±0.2	0.4±0.2
w_s, m/s	3.5 ± 1.1	3.2±1.0	3.6±1.0	3.6±0.9
T, ºC	15.4 ± 4.1	15.0±3.9	-12.0±5.4	-11.6±4.9
P, hPa	976.0 ± 5.5	967.8±5.5	984.5±9.7	971.4±9.8
High values of $PM_{2,5}$ (cluster 2)				
	Yekaterinburg, summer	KAO, summer	Yekaterinburg, winter	KAO, winter
$PM_{2,5}$, μg/m^3	13.6±4.3	9.6±4.9	32.2±9.1	30.3±11.0
blh, km	0.6±0.5	0.5±0.5	0.2±0.1	0.2±0.1
w_s, m/s	2.5±1.1	2.4±0.8	2.5±0.9	2.6±0.9
T, ºC	19.2±4.3	17.6±4.0	-14.6±5.1	-16.7±5.8
P, hPa	981.0±5.9	971.9±6.3	991.7±7.6	982.3±5.7

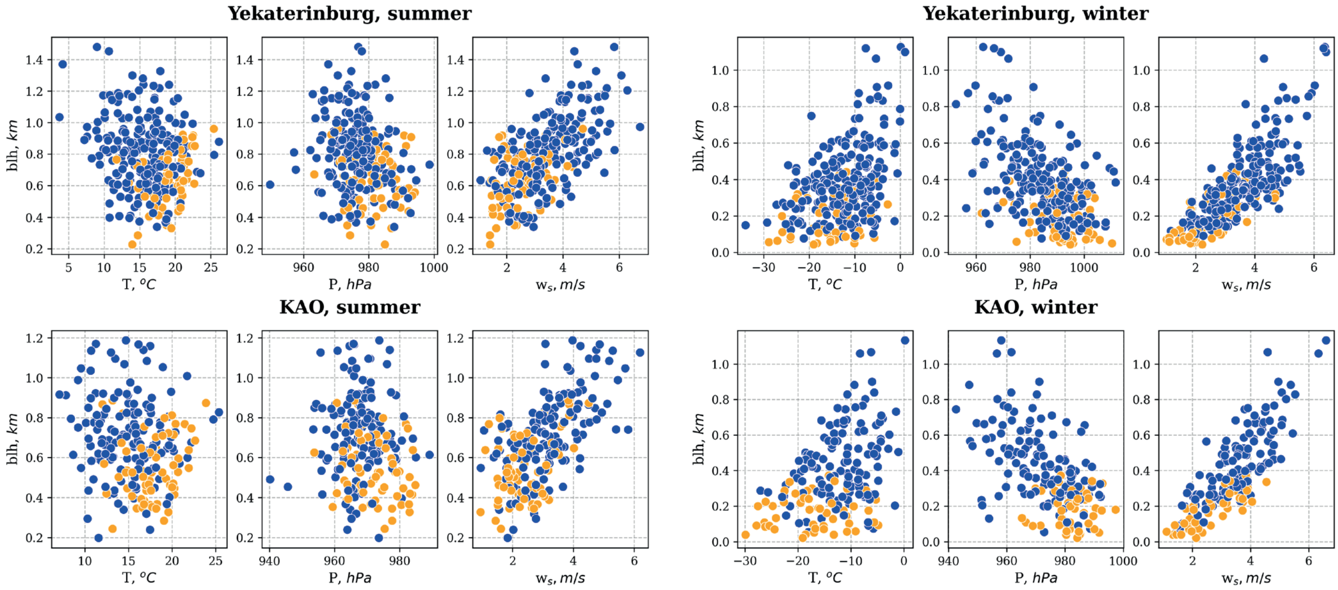

Fig. 4. Scatter diagram of average daily values of meteorological parameters for clusters of low (cluster 1, blue dots) and high (cluster 2, orange dots) values

Table 2. Meteorological conditions contributing to the appearance of higher $PM_{2.5}$ aerosol surface concentrations for the Middle Urals region for the Middle Urals region

parameters	summer	winter
blh, km	<1	<0.5
w_s, m/s	<5	<5
T, ºC	>12	<-5
P, hPa	>954	>962

The physical sense of this group of meteorological conditions is as follows. Under such meteorological conditions, increased surface concentrations are likely in the presence of sources of aerosol release into the atmosphere. From the point of view of mathematical logic, this is a necessary condition for the appearance of increased surface aerosol concentrations in the daily variation, but not a sufficient one. On the contrary, when implementing meteorological parameters, the values of which do not satisfy the conditions, even in the presence of atmospheric aerosol sources, $PM_{2.5}$ surface concentration increase cannot be realized. Thus, we can speak of a necessary and sufficient condition for the appearance of typical aerosol surface concentrations in the daily variation.

CONCLUSION

This work presents a clustering approach using the K-means method to studying the daily variability of $PM_{2.5}$ aerosol concentration of measurements at the urban and background monitoring sites in the Middle Urals region.

Cluster analysis identifies a statistically significant difference between the two groups corresponding to higher and lower concentrations of fine aerosol during the day.

The study reveals a significant dependence of the daily variability of $PM_{2.5}$ particles concentrations on meteorological characteristics (in particular, air temperature, pressure, wind speed and boundary layer height).

Results show that distinctive typical average daily concentrations of $PM_{2.5}$ in the air atmospheric layer for the Middle Urals region, corresponding to the cluster of lower values, are observed in the summer and were on average ~ 5.2 μg/m^3 for the urban area and ~ 3.4 μg/m^3 for the background area. In winter, these parameters are 12.8 μg/m^3 for Yekaterinburg and 10.5 μg/m^3 for KAO. Higher concentrations of $PM_{2.5}$ aerosols, corresponding to the cluster of higher values, were observed in winter and were on averaged ~ 32.2 μg/m^3 for the urban area, ~ 30.3 μg/m^3 for the background area. In summer, these parameters are 13.6 μg/m^3 for Yekaterinburg and 9.6 μg/m^3 for KAO.

The obtained results allow us to formulate threshold values of meteorological parameters, at which the occurrence of higher fine aerosol concentrations is possible. In summer, higher values are associated with pressure > 954 hPa, wind < 5 m/s, air temperature > 12 ºC and boundary layer height < 1 km. In winter, higher values are possible with pressure > 962 hPa, wind < 5 m/s, air temperature < -5 ºC and boundary layer height < 0.5 km.

The statistical regularities of the influence of meteorological parameters on the daily variability of the $PM_{2.5}$ particles concentrations revealed during the research can be used as the basis for developing methods for assessing atmospheric pollution by fine aerosol in the Middle Urals based on weather forecasts, as well as for improving the air basin monitoring system.

The proposed approach can be used to determine the basic "background" type of weather conditions under which the levels of pollution of the lower atmospheric layer with fine $PM_{2.5}$ aerosols can be considered typical for the analyzed region.

REFERENCES

Aghabozorgi S., Seyed Shirkhorshidi A. and Ying Wah T. (2015). Time-series clustering – A decade review. Information Systems, 53, 16–38, DOI:10.1016/j.is.2015.04.007.

Aladodo S.S., Akoshile C.O., Ajibola T.B. Sani M., Iborida O. A. and Fakoya A. A (2022). Seasonal Tropospheric Aerosol Classification Using AERONET Spectral Absorption Properties in African Locations. Aerosol Sci Eng, 6, 246–266, DOI: 10.1007/s41810-022-00140-x.

Chen, T.; He, J.; Lu, X.; She, J.; Guan, Z. (2016). Spatial and Temporal Variations of PM2.5 and Its Relation to Meteorological Factors in the Urban Area of Nanjing, China. Int. J. Environ. Res. Public Health, 13(9), 921, DOI:10.3390/ijerph13090921.

Gao X., Ruan Z.; Liu J.; Chen Q.; Yuan Y. (2022). Analysis of Atmospheric Pollutants and Meteorological Factors on PM2.5 Concentration and Temporal Variations in Harbin. Atmosphere 13(9), 1426, DOI: 10.3390/atmos13091426.

Ginzburg A. S., Gubanova D. P. and Minashkin V. M. (2009). Influence of natural and anthropogenic aerosols on global and regional climate. Russian Journal of General Chemistry, 79(9), 2062–2070, DOI:10.1134/S1070363209090382.

Gubanova D. P., Belikov I. B., Elansky N. F., Skorokhod A. I. and Chubarova N. E. (2018). Variations in PM2.5 Surface Concentration in Moscow according to Observations at MSU Meteorological Observatory. Atmospheric and Oceanic Optics, 31(3), 290–299, DOI:10.1134/S1024856018030065.

Hafner W. D., Solorazano N. N., Jaffe D. A. (2007). Analysis of rainfall and fine aerosol data using clustered trajectory analysis for National Park sites in the Western U.S. Atmos. Environ., 41, 3071–3081, DOI:10.1016/j.atmosenv.2006.11.049.

Hooyberghs J., Mensink C., Dumont G., Fierens F. and Brasseur O. (2005). A neural network forecast for daily average PM concentrations in Belgium. Atmospheric Environment, 39(18), 3279–3289, DOI:10.1016/j.atmosenv.2005.01.050.

IPCC. (2021). Climate Change 2021: The Physical Science Basis. Contribution of Working Group I to the Sixth Assessment Report of the Intergovernmental Panel on Climate Change (Vol. In Press). Cambridge, United Kingdom and New York, NY, USA: Cambridge University Press, DOI:10.1017/9781009157896.

Kermani M., Jafari A.J., Gholami M., Fanaei F., Arfaeinia H. (2020). Association between meteorological parameter and PM2.5 concentration in Karaj, Iran, International Journal of Environmental Health Engineering, 9, 4, DOI: 10.4103/ijehe.ijehe_14_20

Kim K.-H., Kabir E. and Kabir S. (2015). A review on the human health impact of airborne particulate matter. Environment International, 74, 136–143, DOI:10.1016/j.envint.2014.10.005.

Li X., Feng Y. J., Liang H. Y. (2017). The impact of meteorological factors on PM2. 5 variations in Hong Kong. In: IOP Conference Series: Earth and Environmental Science, IOP Publishing, 78 (1), 012003.

Luzhetskaya A. P., Nagovitsyna E. S., Omelkova E. V. and Poddubny V. A. (2022). Temporal variability and relationship between the surface concentration of PM2.5 and aerosol optical depth according to measurements in the Middle Urals. Atmospheric and Oceanic Optics, 35(1), S133–S142, DOI:10.1134/S1024856023010098.

MacQueen J. (1967). Some Methods for Classification and Analysis of Multivariate Observations. Proceedings of the 5th Berkeley Symposium on Mathematical Statistics and Probability, 1, 281–297.

Morokova V.V., and Shver Ts.A. (1981). Climate of Sverdlovsk. Leningrad: Gidrometeoizdat (in Russian).

Mprso.midural.ru (2019). State report on the state and protection of the environment Sverdlovsk region in 2019 [online] Available at: https://mprso.midural.ru/article/show/id/1126 [Accessed 1 March 2023] (in Russian).

Nakayama T., Matsumi Y., Kawahito K. and Watabe Y. (2018). Development and evaluation of a palm-sized optical PM 2.5 sensor. Aerosol Science and Technology, 52(1), 2–12, DOI:10.1080/02786826.2017.1375078.

Novikova K. N., Shagidullin A. R., Tunakova Yu. (2017). A. Models for calculating the concentrations of fine dust fractions in the surface layer of atmospheric air from a set of easily determined meteorological parameters. In: Chemistry and Engineering Ecology: XVII International Scientific conference: Collection of articles, 27–29 September 2017., Kazan: Brig Publishing House, 151-154 (In Russian).

Omar A. H., Won J. G., Winker D. M., Yoon S. C., Dubovik O., and McCormick M. P. (2005). Development of global aerosol models using cluster analysis of Aerosol Robotic Network (AERONET) measurements. Journal of Geophysical Research: Atmospheres, 110, D10S14. , DOI: 10.1029/2004JD004874.

Pope C. A., Coleman N., Pond Z. A. and Burnett R. T. (2020). Fine particulate air pollution and human mortality: 25+ years of cohort studies. Environmental Research, 183, 108924, DOI:10.1016/j.envres.2019.108924.

Rousseeuw P. J. (1987). Silhouettes: A graphical aid to the interpretation and validation of cluster analysis. Journal of Computational and Applied Mathematics, 20, 53–65, DOI:10.1016/0377-0427(87)90125-7.

Rozwadowska A., Zieliński T., Petelski T., Sobolewski P. (2010). Cluster analysis of the impact of air back-trajectories on aerosol optical properties at Hornsund, Spitsbergen. Atmos. Chem. Phys.,10, 877-893, DOI:10.5194/acp-10-877-2010.

SanPiN 1.2.3685-21 (2021). Hygienic Standards and Requirements for Ensuring the Safety and (or) Harmlessness of Environmental Factors for Humans. I. Maximum Permissible Concentrations (MPC) of Pollutants in Urban and Rural Atmospheric Air (in Russian).

Scientific and application oriented handbook on the USSR climate. Series 3, Parts 1–6, 9. (1990). Leningrad: Gidrometeoizdat (In Russian).

Seinfeld J. H. and Pandis S. N. (2006). Atmospheric Chemistry and Physics: From Air Pollution to Climate Change (2nd ed.). New York: Wiley-Interscience.

Shalaumova Yu. V., Fomin V. V. and Kapralov D. S. (2010). Spatiotemporal dynamics of the Urals' climate in the second half of the 20th century. Russian Meteorology and Hydrology, 35(2), 107–114, DOI:10.3103/S1068373910020044.

Stern R., Builtjes P., Schaap M., Timmermans R., Vautard R., Hodzic A., Memmesheimer M., Feldmann H., Renner E. and Wolke R. (2008). A model inter-comparison study focussing on episodes with elevated PM10 concentrations. Atmospheric Environment, 42(19), 4567–4588, DOI:10.1016/j.atmosenv.2008.01.068.

Tai A. P. K., Mickley L. J. and Jacob D. J. (2010). Correlations between fine particulate matter (PM2.5) and meteorological variables in the United States: Implications for the sensitivity of PM2.5 to climate change. Atmospheric Environment, 44(32), 3976–3984, DOI:10.1016/j.atmosenv.2010.06.060.

Vohra K., Vodonos A., Schwartz J., Marais E. A., Sulprizio M. P. and Mickley L. J. (2021). Global mortality from outdoor fine particle pollution generated by fossil fuel combustion: Results from GEOS-Chem. Environmental Research, 195, 110754, DOI: 10.1016/j.envres.2021.110754.

Yang Q, Yuan Q, Li T, Shen H, Zhang L. (2017). The Relationships between PM2.5 and Meteorological Factors in China: Seasonal and Regional Variations. International Journal of Environmental Research and Public Health, 14(12), 1510, DOI: 10.3390/ijerph14121510.

Zhang H., Li Z., Liu Y., Xinag P., Cui X., Ye H., Hu B. and Lou L. (2018). Physical and chemical characteristics of PM2.5 and its toxicity to human bronchial cells BEAS-2B in the winter and summer. Journal of Zhejiang University-SCIENCE B, 19(4), 317–326, DOI:10.1631/jzus.B1700123.

Zhou L., Wu T., Pu L., Meadows M., Jiang G, Zhang J, Xie X. (2023). Spatially heterogeneous relationships of PM2.5 concentrations with natural and land use factors in the Niger River Watershed, West Africa. Journal of Cleaner Production, 394, 136406, DOI: 10.1016/j.jclepro.2023.136406.

RESEARCH PAPER

MONITORING FOR ELEMENTAL COMPOSITION OF PARTICULATE MATTER DEPOSITED IN SNOW COVER AROUND COAL-FIRED THERMAL POWER PLANT (KARAGANDA, CENTRAL KAZAKHSTAN)

Anna V. Talovskaya, Tamara E. Adil'bayeva, Egor G. Yazikov
National Research Tomsk Polytechnic University, 30 Lenin Ave., 634050, Tomsk, Russia
*Corresponding author: talovskaj@yandex.ru

Received: April 1st, 2023 / Accepted: November 14th, 2023 / Published: December 31st, 2023
https://DOI-10.24057/2071-9388-2023-2829

ABSTRACT. Studies on thermal power plant areas with respect to chemical composition of particulate matter deposited in snow cover are limited. This study aims to monitor (2014–2022) particulate load and trace elements associated with the particulate matter distributed around (0.5-4.5 km) the coal-fired thermal power plant in Karaganda. In this study, snow cover was used as an effective scavenger of atmospheric pollutants. Using instrumental neutron activation analysis and atomic absorption spectrometry, the content of 26 elements and Hg, respectively, was determined in the particulate phase of snow. The results showed that particulate load varied from 26 to 1751, with mean of 427 and a background of 47 mg m^{-2} d^{-1}. Anthropogenic impact caused a significant increase in content of U, Hg, Ta, Zn, Na, Cr, Co, Sr, Rb, Cs, Sc, Ca, Fe, Nd, Ba (2–30 times) in the samples compared to the background. Metal-bearing phases of Zn, Ba, As, U-Ta-Nb were detected through scanning electron microscope. The highest levels of particulate load (169–1032 mg m^{-2} d^{-1}) and element contents in the samples were localized up to 0.7 km from the thermal power plant. The changes of particulate load and element composition of snow deposits during the monitoring period were connected with temperature, modernization of dust-collecting equipment, composition of coal and fly ash, long-range transport of emissions from other industries. The element content and metal-bearing phases in the particulate phase of snow can be used as markers for identifying emission sources from coal combustion.

KEYWORDS: urban snow pollution; rare elements; heavy metals; metal-bearing phases; atmospheric deposition; coal combustion

CITATION: Talovskaya A. V., Adil'bayeva T. E., Yazikov E. G. (2023). Monitoring For Elemental Composition Of Particulate Matter Deposited In Snow Cover Around Coal-Fired Thermal Power Plant (Karaganda, Central Kazakhstan). Geography, Environment, Sustainability, 4(16), 180-192
https://DOI-10.24057/2071-9388-2023-2829

ACKNOWLEDGEMENTS: The experimental procedures were carried out at Tomsk Polytechnic University within the framework of Tomsk Polytechnic University Competitiveness Enhancement Program Grant in the Group of Top Level World Research and Academic Institutions.

This work was performed on the unique scientific IRT-T equipment. The authors thank Alexander Sudyko and Larisa Bagydskaya for the performing of instrumental neutron activation analysis, Ekaterina Filimonenko and Nina Osipova for their help in Hg measurements in the Uranium Geology International Centre (Tomsk Polytechnic University), Natalia Savelyevna for her assistance in SEM-EDX analysis (Karaganda State Technical University).

Conflict of interests: The authors reported no potential conflict of interest.

INTRODUCTION

Atmospheric pollution is largely associated with the development of thermal power, about 38–40 % of the world's energy demand is met by coal-fired power plants (International… 2023). Despite the various benefits it suggests, the operation of a thermal power plant can contribute to environmental pollution. Coal contains various trace elements, including heavy metals, rare-earth elements and radioactive elements (Arbuzov and Ershov 2007; Córdoba et al. 2012; Dai et al. 2012; Ambade 2014; Finkelman et al. 2018; Arbuzov et al. 2019; Hou et al. 2023). Consequently, coal combustion is considered as one of the main sources of anthropogenic inputs of trace elements in the atmosphere (Carpi 1997; Zereini et al. 2005; Jayasekhe 2009; Finkelman et al. 2018; Zhao et al. 2018). Many of the trace elements in the suspended particulate matter create serious environmental problems due to their toxicity (Schwarze 2006). Particulate matter which result from combustion processes is a potential contributor to human health (Nemmar et al. 2002).

It is important for environmental monitoring purposes to identify trace element contents in the particulate matter emitted by coal-fired thermal power plant and to assess their distribution at long distances from the source.

Snow cover as a natural environment is widely used by many researchers to study pollutants and identify sources of anthropogenic air pollution. Most studies have focused on the concentration of chemical and ionic components in the snow cover in urbanized and background areas, for example, in Russia

(Kasimov et al. 2012; Ianchenko et al. 2016; Grebenshchikova et al. 2017; Eremina and Vasil'chuk 2019; Pozhitkov et al. 2020; Vlasov et al. 2020; Krickov et al. 2022), Republic of Kazakhstan (Temirzhanova et al. 2021), Lithuania (Krastinytė et al. 2012; Baltrėnaitė et al. 2014; Taraškevičius et al. 2018), Slovenia (Gaberšek and Gosar 2020). However, studies for areas of thermal power plants with respect to the element composition of particulate matter deposited in the snow cover (particulate phase of snow) are limited. For example, the anthropogenic impact of the Novosibirsk thermal power plant (Russia) was connected with high concentrations of Sn, As, Ge, Sb, Nb, U, Th in the particulate phase of snow (Bortnikova et al. 2009; Raputa et al. 2020; Artamonova 2020). In Irkutsk (Russia) some elements (Si, Fe, Mg, Mn) were identified as dominant elements in the vicinity of the thermal power plant (Filimonova et al. 2015). In Ulaanbaatar (Mongolia), the main source of As, Cd, Cu, Mo, Ni, Pb, Sr, V, W in the snow cover were emissions from a thermal power plant (Sorokina et al. 2013). In the particulate phase of snow collected in the vicinity of Pavlodar thermal power plant (Republic of Kazakhstan) heavy metals (Hg, Bi, Sr, Ni, V) were identified as dominant elements (Panin and Azhaev 2006). However, the content of a wider range of trace elements, including rare-earth and radioactive elements, in the particulate matter deposited in the snow cover and their transport on the different distances in the vicinity of coal-fired thermal power plants were insufficiently studied.

A large thermal power plant located in the Central Kazakhstan (Karaganda city) was chosen as an object for the investigation, because high-ash coal is combusted there, which can lead to an increase in anthropogenic emissions of particulate matter into the urbanized area. Additionally, anthropogenic particles generated in the industrial locations transport to the nearby residential areas of the city based upon the meteorological factors.

The investigations of the snow cover and soil were carried out within industrial areas of Karaganda city and its fellow town in the period of 1991–1993 (Kalmykov and Malikova 2017). This study showed that the particulate load varied from 1500 to 4300 mg m^{-2} d^{-1} and exceeded the background value (60 mg m^{-2} d^{-1}) 25–75 times at the distance of 1 to 3 km from the thermal power plant. It was identified the high content of Se, P, Hg, Mo in the solid airborne particles deposited in the snow cover around the thermal power plant. It was also determined that soil in this area was polluted by some heavy metals and metalloids (Pb, Zn, Cd, Hg, Se, Cr, Cu, Mo, Sb, Mn, Bi, P).

Some authors (Arbuzov et al. 2014; 2016; 2019; Amangeldykyzy et al. 2021) showed that coal of Central Kazakhstan, which is used in the studied thermal power plant, include high contents of some elements (e.g. Sc, Cr, Co, Zn, Sr, Ba, Ce, Nd, Rb, Th, U). These elements could be emitted into the air during high temperature combustion and then deposited on the snow cover around the plant.

The deposition rates of particulate matter and the environmentally relevant chemicals on the snow cover were insufficiently studied during the last 30 years around the thermal power plant located in Karaganda city. Additionally, there are still some gaps with respect to quantification of rare elements, including rare-earth and radioactive elements, in the particulate phase of snow cover within areas impacted by the thermal power plant.

The aim of this study is to monitor (2014–2022) particulate load and trace elements associated with particulate matter distributed within 0.5–4.5 km of the coal-fired thermal power plant in Karaganda using snow cover. Consequently, the main objectives of this study were: (a) to determine the level of particulate load; (b) to analyze 27 elements, including metals and metalloids (As, Hg, Cr, Sr, Ba, Co, Zn, Sb), rare-earth (La, Ce, Eu, Lu, Yb, Sm, Tb, Nd), radioactive elements (U, Th), Cs, Hf, Rb, Sc, Ta, Ca, Na, Fe, Br associated with the particulate phase of snow; (c) to identify metal-bearing phases of dominant elements in the particulate phase of snow; (d) to study the spatial and temporal changes of particulate load and elemental composition of particulate phase of snow considering some meteorological parameters and stages of modernization of dust-collecting equipment at the thermal power plant.

MATERIALS AND METHODS

Study area

The study area is the vicinity of the coal-fired thermal power plant. It is located in the city of Karaganda, Central Kazakhstan, with a population of 502 964 (data for 2022). Karaganda is one of the largest industrial, economic, scientific and cultural centers of the Republic of Kazakhstan. The city is located in the steppe landscape. Karaganda has a humid continental climate with harsh and long winters.

Blizzards and snowstorms are not uncommon in the winter season, with temperatures ranging from -15.1 to -34.7°C (open source: weather in the city of Karaganda). Snow cover usually covers the ground from mid-October to the end of February. During the monitoring period, snow cover averaged 38 cm in 2014–2017, 24 and 28 cm in 2021 and 2022, respectively. Southwestern (36%), southern (19%), and eastern (19%) winds prevail in the study area during the winter season (open source: weather in the city of Karaganda).

The thermal power plant has been in operation since 1977 and is located in the northern part of Karaganda, in 1.5 km from the residential areas of the city (Fig. 1).

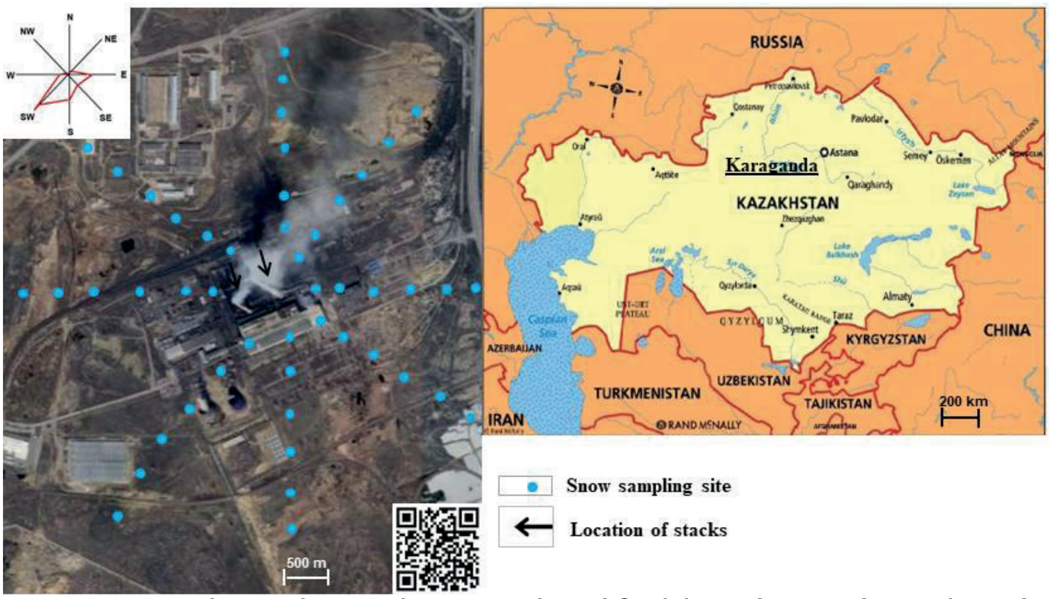

Fig. 1. Study area showing the Karaganda coal-fired thermal power plant and sampling sites (source: Google Earth, Republic of Kazakhstan, modified)

The heating season is from October 15 to April 15. The power plant operates on the high-ash coal from the Ekibastuz basin (Republic of Kazakhstan) and fuel oil. This thermal power plant uses $25x10^5$ tons of coal and 35 tons of fuel oil per year. The thermal power plant generates an energy capacity of 670 MW and a heat capacity of 1174 Gcal/hour. The pollutants, including particulate matter, discharged through two tall stacks (180 and 270 m) (open source: Karaganda thermal power plant).

Sampling and sample preparation

The collection and analysis of snow cover samples in the vicinity of the thermal power plant were carried out from 2014 to 2017, from 2020 to 2021. Sampling and sample preparation were carried out according to Russian State Standard for air pollution control and several studies (Saet et al 1990; Kasimov et al. 2012; Baltrėnaitė et al. 2014; Filimonova et al., 2015; Grebenshchikova et al. 2017; Taraškevičius et al. 2018; Artamonova 2020; Ianchenko and Kotova 2022).

The samples were collected in seven directions from the thermal power plant (northeast, northwest, north, east, south, southeast and southwest) at a distance of 0.5; 0.7; 1.6; 2.2; 3.2 and 4.5 km from the stacks. Additionally, for the selection of monitoring sites locations following factors were considered: 1) prevailing wind direction; 2) extension of emissions depending on stack heights; 3) flat terrain; 4) accessibility of the sampling sites; and 5) distance from roads and other emission sources. The background area was chosen at a distance of 55–80 km from Karaganda to be sufficiently distant from the city to avoid its polluting influence.

Snow sampling was carried out in the period from 2014 to 2022. Every year snow samples were taken at once in the period from the end of January to the beginning of February, during the maximum thickness of the snow cover and before the period of snow melting. In total, 101 samples were collected during the monitoring period, each weighing approximately 15 kg.

At each monitoring site, a pit was made along the vertical profile from the top of the snow cover to 5 cm above the land in order to avoid contact with the soil. This sampling approach allowed us to obtain representative data on the accumulation of particulate matter in the snowpack over the winter season. Snow samples were taken with a plastic shovel, then stored and transported in polyethylene bags. Snow samples were melted at room temperature, then the snow water was filtered ("Blue Line" filter type) to obtain the particulate phase of snow, which was then sieved (1 mm sieve) and weighed in the laboratories. The filtration of snow-melted water was also conducted to separate particulate metals from dissolved metals in the samples. Therefore, the content of the elements was determined in the particulate phase of snow.

Laboratory analysis

Chemical and mineralogical analyses the particulate phase of snow samples were performed in the laboratories of the Uranium Geology International Centre and research nuclear reactor in Tomsk Polytechnic University (Russia). The analyses were conducted using replicates, method blanks and standard reference materials in order to maintain the standard quality.

It was used the instrumental neutron-activation analysis (INAA) and atomic absorption spectrometry (AAS) for analytical investigations of the particulate phase of snow samples collected in the vicinity of the thermal power plant and background area. These methods do not need for special sample preparation and have a low detection limit of elements which are shown in Appendix A.

Method of INAA was used to measure content of some heavy metals and metalloids (As, Cr, Sr, Ba, Co, Zn, Sb), rare-earth (La, Ce, Eu, Lu, Yb, Sm, Tb, Nd), radioactive elements (U, Th), Cs, Hf, Rb, Sc, Ta, Ca, Na, Fe, Br in the samples. These laboratory measurements were carried out on the unique scientific IRT-T equipment (nuclear geochemical laboratory, accreditation certificate № RA.RU.21АБ27 from 08.04.2015). The weight of 100 mg sample was used for measure of element content. When applying INAA the digestion of the samples was not necessary (Witkowska et al. 2005). The samples were irradiated with reactor neutrons for 3 to 18 hours followed by cooling from 7 days to 3 weeks (Sudyko 2016). The gamma-ray activate was measured with Ge-detector (GX3518, Canberra Inc.). The quality of INAA was controlled using a certified standard for particulate phases (Baikal silt BIL-1 GSO 7126-94). INAA is effective used for determination of element composition in different natural objects (Witkowska et al. 2005; Mezhibor et al. 2009; Soktoev et al. 2014; Sudyko 2016; Arbuzov et al. 2019; Farkhutdinov et al. 2021).

Content of mercury in the samples was measured by AAS with pyrolytic volatilization using an atomic absorption spectrometer RA-915+ with pyrolyzer PYRO-915 (Lumex, Russia) and software package RA915R. In samples, Hg compounds were atomized at 850°C in a cuvette connected with an open absorption cell. Three replicate measurements were performed for each sample, weighted 150 mg. From these replicates average content of Hg in each sample were calculated. The relative measurement error is within 20–28%. A standard soil sample (SDPS-3) with a mercury concentration of 290±58 ng/g was used as a standard reference material. A number of papers have been published in which the mercury content in snow samples was determined using atomic absorption spectrometry (Filimonenko et al. 2014; Grebenshchikova et al. 2017; Gustaytis et al. 2018; Talovskaya et al. 2019).

The mineralogical composition of the samples was determined by X-ray diffraction (XRD) analysis on a D2 PHASER powder diffractometer (Bruker, Germany) with Cu-Kα radiation (30 kV and 10 mÅ). The diffractometer was monitored by means of a computer, using software package DIFFRACplus v.15.0. The samples (1 g each) were compressed and placed on plastic sample holder for XRD analysis. XRD patterns were recorded over a 2θ interval of 3–70°, at a rate of 3º (2θ)/min and a sampling distance of 0.02° (2θ). The mineral phases and its content (in %) in the samples was identified using Diffrac. Eva V3.2 software, based on the calibration curves obtained from different standard samples of known mineral composition. The detection limit for mineral content was 1% in the samples (Talovskaya et al. 2018). The precision of the diffractometer was controlled before and after the experiments, using the Si standard.

The mineral and anthropogenic particles abundance in the samples were studied using binocular microscope (Leica ZN 4Dr). On this microscope we first determined the percentage content of each particle type, then the percentage of the group of mineral and anthropogenic particles, so that the content of all identified particles in total was 100 %.

Some published research applying the scanning electron microscopy (SEM) with energy dispersive spectroscopy (EDS) to identify and characterize solid metal-bearing phases in the snow deposits (Golokhvast and Shvedova 2014; Miler and Gosar 2015; Gustaytis et al. 2018; Shevchenko et al. 2020). The samples of particulate phase of snow were analyzed by SEM-EDS in the laboratories of Karaganda State Technical University, Republic of Kazakhstan. Scanning electron microscope (Tescanr Orsayr Holdingr, Czech) coupled with an Oxford INCA EDS system was used to study the morphology and chemical composition of some individual particles in the samples. Samples were mounted on double-sided carbon type with the surface area of 25 mm^2 and sputter coated with a thin layer of carbon for conductivity. The SEM-EDS analysis was carried out in a high vacuum, at 20 kV accelerating voltage, magnifications of 3.00 kx and 15 mm working distance. The INCA Energy software was used to identified element content in some individual particles. It is based on semi-quantitative analysis with 5-15% relative accuracy depending on identified element.

Data analysis

STATISTICA 8.0 was used to calculate the mean values±SE (standard error of mean), median, Spearman correlation coefficients and their significance as well as to perform cluster analysis (Ward's method of amalgamation with 1-r distance), revealing the differences between groups using Mann–Whitney U and test Kruskal-Wallis non-parametric test when comparing more than two groups. The differences were considered significant at p = ≤ 0.01 at the 0.05 level. Nonparametric tests were used, because Lilliefors and Kolmogorov-Smirnov tests had shown that the variables do not correspond to normal distribution.

Following indexes were calculated to assess particulates pollution in accordance with research studies by some authors (Saet et al. 1990; Kasimov et al. 2012; Baltrėnaitė et al. 2014; Filimonova et al. 2015; Taraškevičius et al. 2018; Vlasov et al. 2020). The calculations of *particulate load* (P_n, mg m^{-2} d^{-1}) were made using Equation 1:

$$P_n = \frac{P_o}{S \times t} \tag{1}$$

where P_o is the mass of the particulate phase (mg); S is the square of the snow pit (m^2); t is the time representing the stable snow cover formation duration up to sampling day (d).

The concentration coefficient (K_c) representing the level of element enrichment in the particulate phase of snow in relation to the background content was determined using Equation 2:

$$K_c = \frac{C_i}{C_b} \tag{2}$$

where C_i is the element content in the particulate phase of snow (mg/kg); C_b is the background element content in the particulate phase of snow (mg/kg).

It can be stated that, if K_c values are higher than 1.5, element could be of anthropogenic origin (Saet et al. 1990).

The total levels of contaminants from a particular group of elements or the general contamination levels were expressed by the *total pollution of snow cover* (Z_c), calculated according to the Equation 3:

$$Z_c = \sum K_c - (n - 1) \tag{3}$$

where K_c is concentration coefficients for elements with $K_c \geq 1.5$, n is the number of elements, having $K_c \geq 1.5$.
Classification of pollution level based on the particulate load and total pollution of snow cover are shown in Table 1.

RESULTS

Particulate load and mineral composition of particulate phase of snow

Particulate load in the vicinity of the thermal power plant between 2014 and 2022 ranged from 26 to 1751 mg m^{-2} d^{-1}, with a background of 47 mg m^{-2} d^{-1}. During the monitoring period, the mean of particulate load was 427 mg m^{-2} d^{-1}, which corresponds to moderately hazardous and highly hazardous level of pollution.

The spatial and temporary changes of particulate load both in was revealed during the six-year monitoring period.

In the period from 2014 to 2022, there was a statistically significant (p ≤ 0.001) decreasing of particulate load from 1.5 to 5 times (Fig. 2a). A sharp decrease in particulate load has been identified since 2015. In subsequent years (2016–2021), no significant changes in particulate load were observed. It was observed the changes in particulate load from hazardous pollution level and dangerous risk level in 2014 to moderately hazardous and highly hazardous levels in 2015–2017. In 2021 and 2022, allowable pollution level and non-dangerous risk level were identified.

Table 1. Pollution level based on the particulate load (P_n) and total pollution of snow cover (Z_c) (Saet et al. 1990; Kasimov et al. 2012; Baltrėnaitė et al. 2014)

Pollution level	Risk level	P_n, mg m^{-2} d^{-1}	Z_c
Allowable	Non-dangerous	≤250	≤64
Moderately hazardous	Highly hazardous	250-450	64-128
Hazardous	Dangerous	450-850	128-256
Highly hazardous	Very dangerous	≥850	≥256

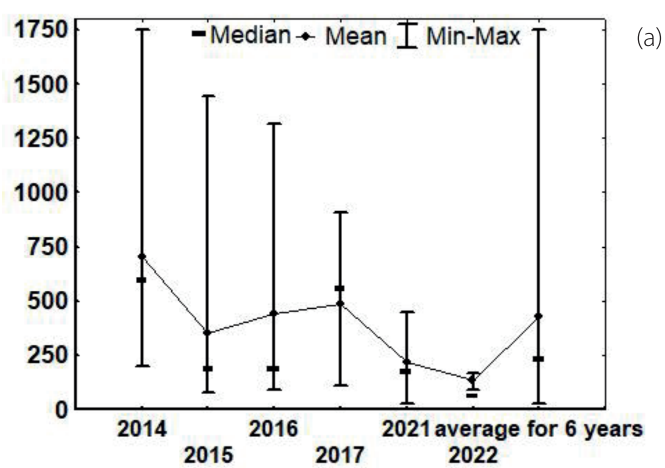

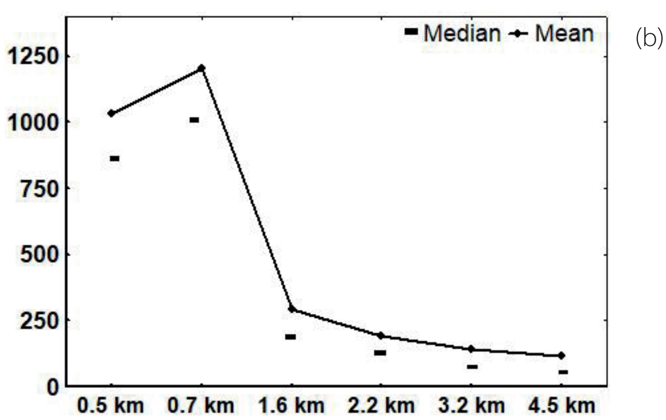

Fig. 2. Particulate load (mg m^{-2} d^{-1}) around the coal-fired thermal power plant: a) dynamics from 2014 to 2022 (according to the non-parametric Kruskal-Wallis test p-value is less 0.001 at the 0.05 level); b) distribution in the north-east direction (mean for 2014–2022)

Particulate load was decreased with distance from the thermal power plant in the northeastern direction of the main mass transport of pollutants (Fig. 2b). Over a six-year monitoring period, the highest level of particulate load was observed at a distance of up to 0.7 km (169–1032 mg m^{-2} d^{-1}), and within 1.6–4.5 km the particulate load was decreased on average from 1.5 to 4 times (118–276 mg m^{-2} d^{-1}).

It was determined the content of mineral (6–13%) and anthropogenic (87–94%) particles in the particulate phase of snow. Mineral particles include such minerals as quartz (3–6%) and feldspars (2–5%). Anthropogenic particles include soot and coal dust (18–20%), slag and ash (20–22%), Fe-rich (21–25%) and Al-Si-rich spherules (23–25%). It was also identified plant residues (1–2%). The content of the identified particles in the samples did not change significantly during the monitoring period.

According to X-ray diffraction data, the content of mineral phases was 73.5%, and the amorphous phase was 26.5%. Mullite (21.9%) was identified as the predominant mineral phase, which associated with Al-Si-rich spherules. The content of quartz (14.2%), albite (12.1%), kaolinite (12.7%), and chlorite (15.2%) was detected by XRD on a smaller proportion in the samples.

Elemental composition of particulate phase of snow

Average content of the elements in the particulate phase of snow around studied plant for the monitoring period and in the background area are given in Table 2. Geochemical peculiarities of the samples were connected with the high content of U, Hg, Ta, Zn, Na, Cr, Co, Sr, Rb, Cs, Sc, Ca, Fe, Nd, Ba relatively to background (Fig. 3). Results shown that the content of elements in the samples exceeded the background from 1.5 to 30 times during period of 2014–2022 (Table 3).

During the monitoring period, high concentrations of U (K_c=3...24), Hg (K_c=8.8...29), Ta (K_c=1.6...14), Zn (K_c=1.5...6.6), Na (K_c = 1.9...3.4) were observed relative to the background in the particulate phase of snow. Another elements (Cr, Co, Sr, Rb, Cs, Sc, Ca, Fe, Nd, Ba) were less concentrated in the samples (K_c=1.5...3). The content of Th, Br, Sb, As and some lanthanides was determined at the background level (K_c≤1.5) in the particulate phase of snow. Content of elements exceeding the background by more than 2 times indicate local anthropogenic sources of element origin.

Table 2. Mean element contents in the particulate phase of snow around coal-fired thermal power plant (2014–2022) and in background area (mg/kg)

Element	Mean±SE	Background content*	Element	Mean±SE	Background content*
Na, %	0.6±0.05	0.2	Cs	2.3±0.3	1.1
Ca, %	2.6±0.2	1.3	La	20.8±0.8	19.9
Fe, %	2.7±0.1	1.7	Hf	4.3±0.1	4.4
Hg	0.45±0.1	0.03	Ce	50.3±2.8	47.5
As	7.5±0.4	8.6	Nd	22.6±2.0	15.9
Zn	235±40.3	86.4	Ta	2.1±0.9	0.3
Sb	3.4±0.4	3.4	Sm	5.1±0.3	4.5
Co	17.1±1.4	9.6	Eu	1.2±0.05	1.0
Cr	74.2±10.7	34.5	Tb	0.8±0.05	0.6
Ba	595±25.3	467	Yb	2.7±0.1	2.7
Sr	263±19.6	85.1	Lu	0.5±0.03	0.4
Sc	23.2±7.4	11.1	Th	4.5±0.2	4.3
Br	8.8±0.8	9.3	U	8.3±3.5	0.7
Rb	30.5±3.3	13.1			

* - background levels of elements in the samples are the authors' data

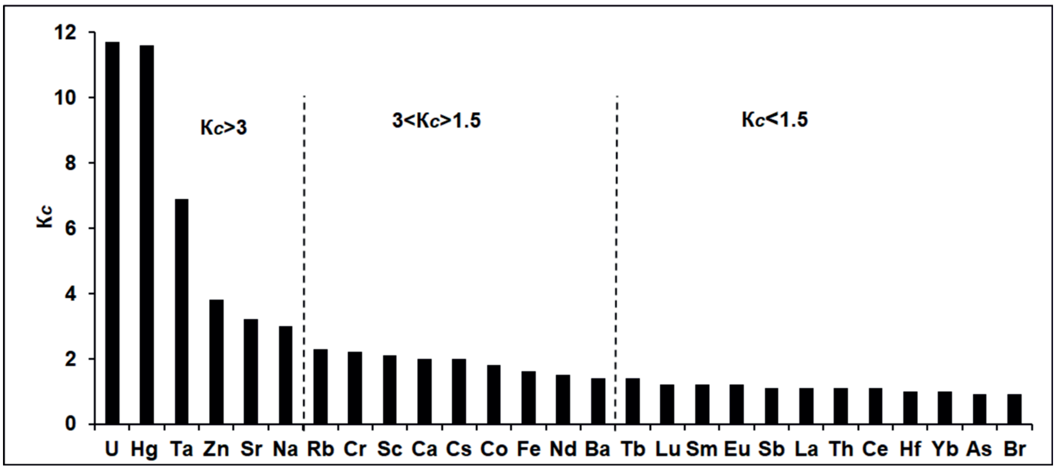

Fig. 3. Accumulation of elements in the particulate phase of snow relative to the background around the coal-fired thermal power plant (mean for 2014–2022, Z_c=68)

During the monitoring period, the total pollution of snow cover changed from moderately hazardous pollution level and highly hazardous risk level in 2014-2016 to allowable pollution level and non-dangerous risk level in 2021-2022 (Table 3).

Cluster analysis was identified 7 significant geochemical associations of elements (Fig. 4) in the particulate phase of snow in the vicinity of the thermal power plant during the monitoring period: 1) Tb-Sm-Eu-Ce-La (r~0.69...0.96), 2) Lu-Yb-Hf-Br (r~0.65...0.88), 3) U-Ta-Nd-Ba (r~0.82...0.99), 4) Cr-Co-Zn-Sb-As (r~0.78...0.89), 5) Sr-Ca (r~0.48), 6) Rb-Hg (r~0.41), 7) Fe-Na (r~0.77).

During the monitoring period (2014–2022), significant correlations of U-Ta-Nd (r~0.71...0.88), Sm-Ce-La-Hf (r~0, 65...0.88), Cr-Co (r~0.77...0.95) were remained in the particulate phase of snow.

The identified geochemical associations could indicate the common sources of the elements in the snow cover and the modes of their occurrence in the particulate phase of snow. It was identified the metal-bearing phases of U, Ba, As, and Zn in the particulate phase of snow using the scanning electron microscope. Additionally, it was determined U-Ta-Nb-bearing phases with Ti, Fe, Ca impurities (average size: 42 μm) (Fig. 5a). Particles (size: 2.0-2.3 μm) consisting of S, Ba and As were assumed as mixture of As sulphides and Ba sulphate (Fig. 5b). Particles (size: 9.8 μm) containing S and Zn were assigned to be Zn sulphides. Particles of Zn sulphides were also found in the particulate phase of snow in the vicinity of thermal power plants in the south of the Western Siberia (Talovskaya et al. 2018).

The temporal changes of the element contents in the samples was shown in Table 3 as the concentration coefficients. During the monitoring period, it was determined that from 2015 to 2022 there was a statistically significant ($p \leq 0.01$) decrease in the content of Na (0.7...0.4 mg/kg), Fe (2.9...2.1 mg/kg), Zn (318...86.4 mg/kg) Sb (3.9...2.9 mg/kg), Co (21.2...11.3 mg/kg), Cr (105...42 mg/kg), Sc (38.2...12.2 mg/kg), Cs (2.9...1.6 mg/kg) in the particulate phase of snow. Uneven statistically significant distribution ($p \leq 0.001$) of Hg, U, Ta, Nd, Rb, As content was determined in samples collected in different years during the monitoring period. In the samples no significant change ($p \geq 0.1$) in the content of Ca, Ba, Sr, Th and lanthanides over the years was revealed, which may indicate constant sources of element emissions into the environment.

Table 3. Changes of element concentration coefficients (K_c) in the particulate phase of snow and total pollution of snow cover (Z_c) around the coal-fired thermal power plant (2014–2022)

Period of monitoring	K_c				Z_c
	>10	3–10	1.5–3	≤1.5	
2014	Hg_{17}	$Sc_{3.5}Na_{3.5}$ $Ca_{3.5}Zn_4$	Ta_2Co_2 Cs_3Sr_3 $U_3Cr_3Rb_3$	Fe, As, Sb, Ba, Br, La, Hf, Ce, Nd, Sm, Eu, Tb, Yb, Lu, Th	71
2015	$Ta_{14}U_{25}$	$Na_3Sr_3Hg_6$	$Co_2Cr_2Cs_2$ $Nd_2Rb_2Ca_2Zn_2$	Fe, As, Sb, Ba, Sc, Br, La, Hf, Ce, Sm, Eu, Tb, Yb, Lu, Th	77
2016	Hg_{29}	$Cs_3Rb_3U_3$ $Sr_{3,4}Na_{3,5}$	$Ca_{1.6}Zn_{1.6}Nd_{1.6}$ $Ta_{1.6}Tb_{1.6}$ $Fe_2Cr_2Co_2$	As, Sb, Ba, Sc, Br, La, Hf, Ce, Sm, Eu, Yb, Lu, Th	75
2021	$U_{10}Hg_{24}$	Sr_4Ta_6	$Fe_{1.6}Lu_{1.7}$ $Zn_2Na_2Ca_{2.5}$	As, Sb, Co, Cr, Ba, Sc, Br, Rb, Cs, La, Hf, Ce, Nd, Sm, Eu, Yb, Th	56
2022	$Ta_{13}U_{21}Hg_{24}$	–	$Lu_2Na_2Ca_2Sr_{2.5}$	Fe, As, Zn, Sb, Co, Cr, Ba, Sc, Br, Rb, Cs, La, Hf, Ce, Nd, Sm, Eu, Tb, Yb, Th	62

* subscripts correspond to the average value of K_c

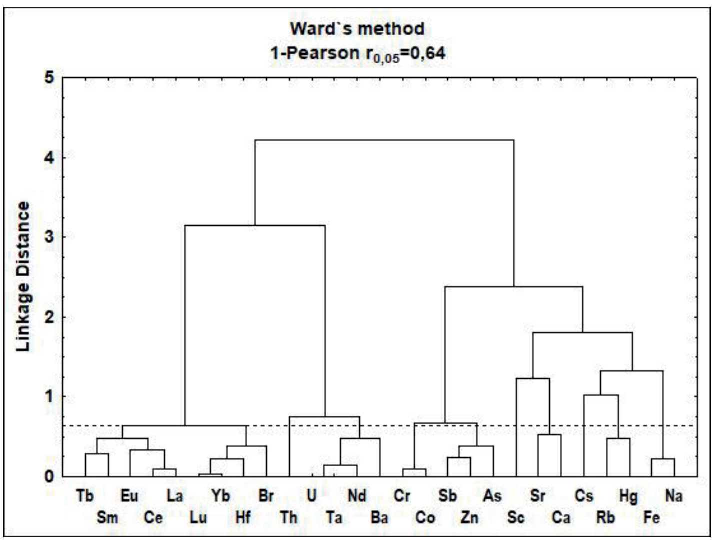

Fig. 4. Clusters of related elements in the particulate phase of snow around the coal-fired thermal power plant (2014–2022, n=39)

It was determined that the element contents in the samples collected in 2021–2022 were significant lower in comparison with the results for the period of 2014–2016.

In the period of 2021–2022, it was revealed the statistically reliable 2–6 times increasing of Ce, Ta and U content in the particulate phase of snow in comparison with the data for the period of 2014–2016. This was due to the different distribution of elements with distance to the northeast from the thermal power plant (0.5–4.5 km) during the monitoring period. In 2021-2022 a peak of Ce, Ta, and U content in samples collected at a distance of 1.6 km was determined.

During the monitoring period (2014–2022), it was revealed the significant decrease of Hg, Br, La, Hf, Eu, Cs, Tb, Yb, U content in the samples collected in the northeastern direction at a distance of 0.5 to 4.5 km from the thermal power plant. In addition, the maximum content of these elements were determined in the samples collected at distances of up to 1.6 km. The content of Th, Lu, Nd, Ba in the samples did not change significantly with distance from the thermal power plant. As content in the samples was increased at a distance of 0.5 to 4.5 km, which was explained by volatility of this element. It was observed peak of Zn, Co, Cr, Ca content in the samples taken at a distance of 4.5 km from the thermal power plant. As an example, Fig. 6 shows the distribution of Co, Cr, Hg, La, Ce, Rb, Nd, Sc, Th, U content in the particulate phase of snow in the north-east direction from the plant.

DISCUSSION

During the observation period around the thermal power plant in Karaganda, the decrease in particulate load and the contents of elements in the samples was due to various factors. Firstly, dust-collecting equipment were reconstructed with fly ash collection efficiency of 96.5–99.5% at the thermal power plant in 2014-2016. In addition, in 2016, a new power unit with an electrostatic precipitator was installed with fly ash collection efficiency of 99.75%, which made it possible to reduce the inputs of dust and gas emissions (open source: Ensuring reliable and high-quality energy supply).

Secondly, the identified changes over monitoring period could be connected with the meteorological parameters and the depth of the snow cover. The average values of these parameters over the years are shown in the tables in the Appendix B. The impact of these factors was observed in 2021 and 2022, when particulate load (219 and 135 mg m^{-2} d^{-1}, respectively), the element contents in the samples and snow cover depth (24 and 28 cm, respectively; open source: weather in the city of Karaganda) were the lowest during the monitoring period. Consequently, 2021 and 2022 were sparsely snowy, which could affect the ratio of the processes of "dry" and "wet" deposition of pollutants from the atmosphere. It was determined the significant positive correlation (r~0.55...0.66) between particulate load and temperature in the winter seasons. Additionally, between 2014 and 2017, the average temperature during the winter season was -15.6ºC, in 2021–2022 the temperature was 10.5ºC (open source: weather in the city of Karaganda). This could have an impact on the consumption of coal burning at the plant, as a consequence, on the level of particulate load during these periods.

The highest level of particulate load, that was observed at a distance of up to 0.7 km from the stacks of the thermal power plant, on the one hand, was due to the close location of the open coal warehouse, where the coal was unloaded, crushed and transported on conveyors to the boiler house bunkers. On the other hand, an additional factor could be the processes of scavenging the emitted fine particles by ice pellets formed when water vapor freeze in the smoke plume of the thermal power plant. This effect was investigated and confirmed for the coal-fired thermal power plant in Kyzyl (Russia) (Belyaev et al. 1997). Due to this phenomenon, most of the particulate emissions in the winter could be deposited nearby to the thermal power plant.

Previous studies on snow cover pollution in Karaganda (1991–1993) showed that particulate load within a radius of 1–3 km from the thermal power plant was on average 2500 mg m^{-2} d^{-1} (Kalmykov and Malikova 2017). It can be seen that over a 30-year period (from 1991–1993 to 2014–2022) particulate load was decreased into six times in the impacted area of the thermal power plant. Additionally, the average particulate load in the vicinity of Karaganda thermal power plant (427 mg m^{-2} d^{-1}) was slightly higher than in the vicinity of Pavlodar thermal power plant located in Kazakhstan (338 mg m^{-2} d^{-1} (Panin and Azhaev 2006)); in two-three times higher than in the vicinity of some thermal power plants located in cities of Western Siberia

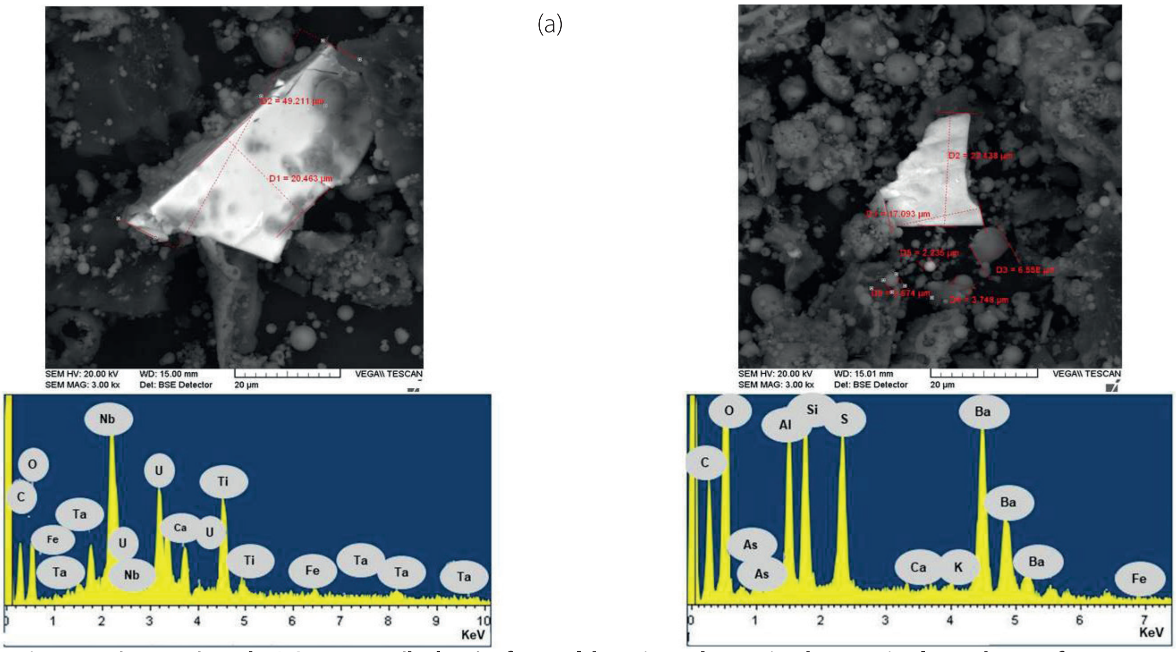

Fig. 5. SEM images (on top) and EDS spectra (below) of metal-bearing phases in the particulate phase of snow around the coal-fired thermal power plant: a) U-Ta-Nb-bearing phases with Ti, Fe, Ca impurities; b) mixture of sulphides of As and sulphate of Ba

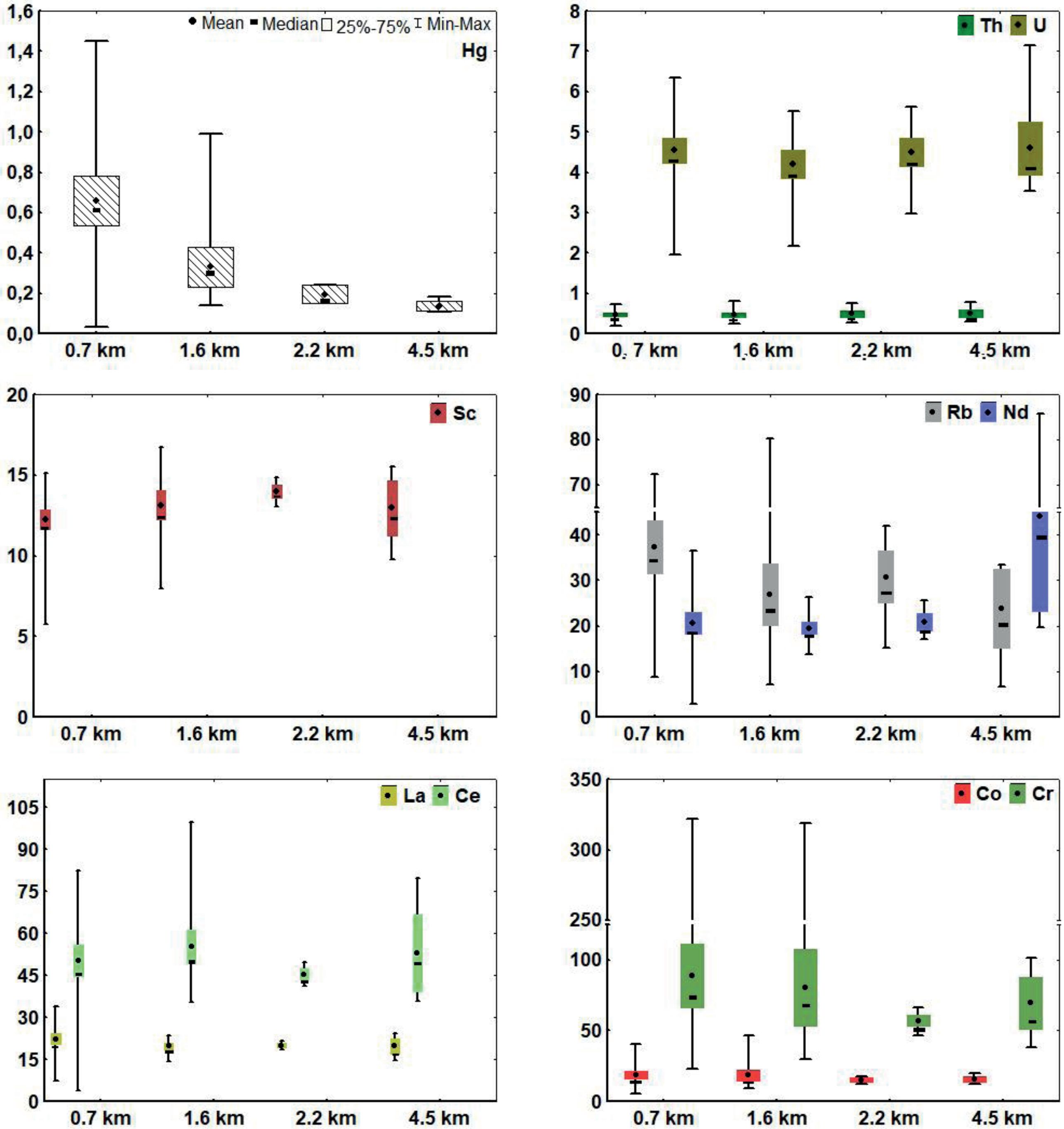

Fig. 6. The distribution of element content (mg/kg) in the particulate phase of snow in the north-east direction from the coal-fired thermal power plant (average for 2014–2022)

(201–555 mg m^{-2} d^{-1} (Talovskaya et al. 2019); 143 mg m^{-2} d^{-1} (Artamonova 2020)).

The content of the identified mineral phases and spherules in the particulate phase of snow could be related to the composition of fly ash. Earlier we determined that Al-Si-rich spherules and Fe-rich spherules with sizes of 0.2–41.7 μm in the particulate phase of snow correspond in their morphology to the same spherules with sizes of 1.5-126 μm in fly ash (Adil'bayeva et al. 2017). Some studies (e.g. Goodarzi 2006; Magiera et al. 2011; Zyryanov et al. 2011) also show that fly ash is characterized by the content of the spherules. Valeev D. and co-authors (2019) showed that Ekibastuz coal fly ash consists mainly of quartz, mullite and magnetite. Consequently, spherules and mineral phases contained in the fly ash might be released into the air and then deposited in the snow cover.

The changes of some element contents in the particulate phase of snow with distance from the thermal power plant could be related to the impact of local anthropogenic sources, on the one hand, and the particle sizes that transport these elements in the air, on the other hand.

The identified peak of Ce, Ta, and U content in samples collected at a distance of 1.6 km could be associated with the impact of the local anthropogenic sources, which began to actively operate since 2017 at a distance of more than 2 km from the thermal power plant. The identified peak of Zn, Co, Cr, Ca content in the samples collected at a distance of 4.5 km was probably associated with the long-range transport of emissions from industries located in the city of Karaganda and its fellow town. In the industrial and coal combustion processes, fine particles can be formed and released into the atmosphere (Dai et al. 2012; Lanzerstorfer 2018; Czech et al. 2020). Wu J. and coauthors (2022) showed that Fe- and Ti-containing particles (>100 nm) were dominated in the metal-containing emissions of thermal power plants. The most volatile-toxic elements (Sb, As, Hg) were contained mainly in submicron fraction (<0.05

microns) or vapor-gas phase of aerosol (Lanzerstorfer 2018; Czech et al. 2022). Ba, Sr, Zn, Rb, Cr, Co, Th, U condense on fine particles (<1 μm), which are not retained by electrostatic precipitators, escaping its and then emit into the air (Krylov 2017; Lanzerstorfer 2018). Therefore, large particles might be deposited nearby to the plant; otherwise fine particles could be transported far from the source. As a result, anthropogenic geochemical areas could be formed at different distances from the industries and thermal power plants.

Identified geochemical peculiarities of the particulate phase of snow in the vicinity of the thermal power plant, on the one hand, was associated with the impact of the emission sources of the plant, on the other hand, with the long-range transport of emissions from other industries and transport of the city, and its fellow cities. Some studies were shown that the possible source of some heavy metals in the air could be exhaust and non-exhaust vehicle emissions (Golokhvast et al. 2015; Vlasov et al. 2020).

In the research (Kalmykov and Malikova 2017) performed in 1991–1993 in the vicinity of Karaganda thermal power plant, in the particulate phase of snow high Hg content were determined due to the impact of coal combustion. It was also identified that Zn, Hg, Cr, Sb content was exceeded the background in soil. It was suggested that the emissions of the elements into the air was related due to the complex impact of the thermal power plant and the diffuse pollution.

The identified geochemical peculiarities (high levels of some rare-earth elements, Sc, U, Hg, Ba, Sr) of the particulate phase of snow in the vicinity of the thermal power plant was probably due to the composition of the used coal and fly ash. We determined that the content of Na, As, Sc, Br, Cs, Th and lanthanides in dust from electrostatic precipitators was in 2–17 times higher than their content in fly ash. Additionally, the content of Zn and U in the fly ash was 2–3 times higher than in the dust from the electrostatic precipitators. These facts might also indicate the sources of elements in particulate matter emitted into the air.

Coal ash was more enriched with trace elements compared to coal (Arbuzov and Ershov 2007). Levels of elements in the fly ash of the same coal at different thermal power plants could vary significantly. Some published researches were identified the high concentrations of rare elements (rare-earth, Sc, Ta, Nb, Hf, Zr, Ba, Sr, Ce) in the coal of Central Kazakhstan (Arbuzov et al. 2014; 2016; Amangeldykyzy et al. 2021). In addition, Arbuzov S.I. and coauthors (2014; 2019) showed that coal basins of Kazakhstan were significantly enriched in siderophile group of elements (Fe, Co, Cr), rare-earth elements (Sc, lanthanides), Ba, Sr, U, Th. Moreover, coals of Ekibastuz basin (Kazakhstan) contained very high Hg concentration (Kalmykov and Malikova 2017). Micromineral modes of rare-earth elements, Hf, Sc, Ta, Ba, native and intermetallic compounds were found in coals (Arbuzov et al. 2019; Amangeldykyzy et al. 2021). These elements could be emitted into the air during coal combustion.

CONCLUSIONS

The results of long-term snow cover monitoring (2014–2022) made it possible to study the spatial and temporal changes of particulate load and element contents in particulate matter deposited in snow cover in the vicinity of the coal-fired thermal power plant.

During the six-year monitoring period, U, Hg, Ta, Zn, Na, Cr, Co, Sr, Rb, Cs, Sc, Ca, Fe, Nd, Ba were the main pollutants around the coal-fired thermal power plant. The content of these elements in the particulate phase of snow and particulate load were 2–30 times higher than the background. Metal-bearing phases of Ba, As, U-Ta-Nb, anthropogenic particles (coal particles, slag, ash) and mullite were found in the particulate phase of snow, reflecting the impact of the thermal power plant.

This study demonstrated a decrease in particulate load and content of some elements (Na, Fe, Zn, Sb, Co, Cr, Sc, Cs) in the particulate phase of snow from 2015 to 2022. Comparison of the results obtained for 2014–2016 with data from 2021–2022 showed significantly high content of U, Ce, Ta in the samples collected in the last two years of monitoring. It was determined that the content of Ca, Ba, Sr, Th and some lanthanides in the particulate phase of snow did not change from year to year.

The results showed moderately hazardous and hazardous levels of particulate pollution in 2014–2017, which changed to allowable level in 2021–2022.

The revealed variability of particulate load and elemental composition of the samples were connected, on the one hand, with modernization of dust-collecting equipment from 2015 at the thermal power plant to reduce emissions into the air. On the other hand, it was found the correlation between particulate load and temperature in the winter seasons.

Particulate load and content of Hg, Br, La, Hf, Eu, Cs, Tb, Yb, U in the particulate phase of snow were determined to decrease with distance of 0.5-4.5 km from the thermal power plant in the northeast direction. We found significantly high particulate load and element contents in the samples collected at distances up to 0.7 km. This could be connected, on the one hand, with the impact of open coal warehouse located close to the monitoring sites. On the other hand, the processes of scavenging of fine solids by ice pellets in the stacks of the plant could contribute to the deposition of emissions at close distances.

The peculiarities of the element composition of the particulate phase of snow were caused by the composition of fly ash, the emitted dust, and the geochemical specificity of coals used at the thermal power plant. During the monitoring period, identified peaks in the content of some elements in samples were probably associated with the long-range transport of emissions from industries of the city and its fellow town.

The identified trace elements (e.g. rare-earth, Sc, U, Hg, Ba, Sr) in the particulate phase of snow could be used as markers of pollution from coal combustion in the urban atmosphere.

REFERENCES

Adil'Bayeva T.E., Talovskaya A.V., Yazikov E.G. (2017). Estimation of aerotechnical pollution in the vicinity of the thermal power plant (TPP-3) in Karaganda according to snow survey (Republic of Kazakhstan). News of the National Academy of Sciences of the Republic of Kazakhstan, Series of Geology and Technical Sciences, 4(424), pp. 237–247

Amangeldykyzy A., Kopobayeva A., Askarova N., Ozhigin D., Portnov V. S. (2021). Study of rare earth elements in the coals of the Shubarkol deposit. Complex Use of Mineral Resources, 4, 319, pp. 48-56, DOI:10.31643/2021/6445.40

Ambade B. (2014). Seasonal variation and sources of heavy metals in hilltop of Dongargarh, Central India. Urban Climate, 9, pp. 155–165, DOI: http://dx.doi.org/10.1016/j.uclim.2014.08.001

Arbuzov S.I. and Ershov V.V. (2007). Geochemistry of rare elements in coals of Siberia. Tomsk: D-Print (in Russian)

Arbuzov S.I., Chekryzhov R.B., Finkelman Y.Z., Sun C., Zhao L., Il'enok S.S., Blokhin M.G., Zarubina N.V. (2019). Comments on the geochemistry of rare-earth elements (La, Ce, Sm, Eu, Tb, Yb, Lu) with examples from coals of north Asia (Siberia, Russian far East, North China, Mongolia, and Kazakhstan). International Journal of Coal Geology, 206, pp. 106–120, DOI:10.1016/J.COAL.2018.10.013

Arbuzov S.I., Il'enok S.S., Mashenkin V.S., Sun Y. (2016). Rare earth elements in the late Paleozoic coals of north Asia (Siberia, Northern China, Mongolia, Kazakhstan). Bulletin of the Tomsk Polytechnic University Geo Assets Engineering, 327, 8, pp. 74-88 (in Russian with English summary)

Arbuzov S.I., Volostnov A.V., Mezhibor A.M., Rybalko V.I., Ilenok S.S. Scandium (Sc) geochemistry in coals (Siberia, Russian Far East, Mongolia, Kazakhstan, and Iran) (2014). International Journal of Coal Geology, 125, pp. 22–35, DOI: http://dx.doi.org/10.1016/j.coal.2014.01.008

Artamonova Yu. (2020). Uranium and thorium in aerosol fallout of Novosibirsk city and its vicinity (West Siberia). Bulletin of the Tomsk Polytechnic University, Geo Assets Engineering, 331 (7), pp. 212–223, DOI: 10.18799/24131830/2020/7/2731 (in Russian with English summary)

Baltrėnaitė E., Baltrėnas P., Lietuvninkas A., Šerevičienė V. and Zuokaitė E. (2014). Integrated evaluation of aerogenic pollution by air-transported heavy metals (Pb, Cd, Ni, Zn, Mn and Cu) in the analysis of the main deposit media. Environmental science and pollution research, 21, pp. 299–313, DOI: 10.1007/s11356-013-2046-6

Belyaev S.P., Beschastnov S.P., Khomushku G.M., Morshina T.I., Shilina A.I. (1997). Some patterns of pollution of the natural environment by combustion products of coal on the example of Kyzyl. Meteorology and hydrology, 12, pp. 54–63 (in Russian)

Bortnikova S.B., Raputa V.F., Devyatova A.Yu., Yudakhin F.N. (2009). Methods of analyzing data on the snow cover contamination in the areas affected by industrial enterprises (by the example of Novosibirsk). Geologiya. Gidrogeologiya. Geokriologiya, 6, pp. 515–525 (in Russian)

Carpi A. (1997). Mercury from combustion sources: A review of the chemical species emitted and their transport in the atmosphere. Water, air and soil pollution, 98, 3–4, pp. 241–254, DOI: 10.1007/BF02047037

Córdoba P., Ochoa-González R., Font O., Izquierdo M., Querol X., Leiva C., López-Antón M.A., Díaz-Somoano M., Martinez-Tarazona M.R., Fernandez C., Tomás A. (2012). Partitioning of trace inorganic elements in a coal-fired power plant equip pedwithawet flue gas desulphurization system. Fuel, 92, pp. 145–157

Czech T., Marchewicz A., Sobczyk A.T., Krupa A., Jaworek A., Śliwiński Ł., Rosiak D. (2020). Heavy metals partitioning in fly ashes between various stages of electrostatic precipitator after combustion of different types of coal. Process Safety and Environmental Protection, 133, pp. 18–31, DOI:10.1016/j.psep.2019.10.033

Dai S., Ren D., Chou C.-L., Finkelman R. B., Seredin V. V., Zhou Y. (2012). Geochemistry of trace elements in Chinese coals: A review of abundances, genetic types, impacts on human health, and industrial utilization. International Journal of Coal Geology, 94, pp. 3–21, DOI: 10.1016/j.coal.2011.02.003

Ensuring reliable and high-quality energy supply. Kazakhstan Municipal Systems LLP (KKS), Annual Report 2016. Available at: https://kus.kz/ru/investori/godovye-otchety [Accessed 12 Feb. 2023] (in Russian)

Eremina I.D., Vasil'chuk J.Yu. (2019). Temporal variations in chemical composition of snow cover in Moscow. Geography, Environment, Sustainability, 12(4), pp. 148–158, DOI: 10.24057/2071-9388-2019-79

Farkhutdinov I., Soktoev B., Zlobina A., Farkhutdinov A., Zhang C., Chesalova E., Belan L., Volfson I. (2021). Influences of geological factors on the distribution of uranium in drinking water limescale in the junction zone of the East European platform and the Southern Urals. Chemosphere, 282, article number 131106, DOI: 10.1016/j.chemosphere.2021.131106

Filimonenko E.A., Lyapina E.E., Talovskaya A.V., Parygina I.A. (2014). Eco-geochemical peculiarities of mercury content in solid residue of snow in the industrial enterprises impacted areas of Tomsk. In: Proc. of SPIE 9292, 20th International Symposium on Atmospheric and Ocean Optics: Atmospheric Physics, Volume 929231. Available at: https://doi.org/10.1117/12.2075637

Filimonova L.M., Parshin A.V., Bychinskii V.A. (2015). Air pollution assessment in the area of aluminum production by snow geochemical survey. Russian Meteorology and Hydrology, 40 (10), pp. 691–698, DOI:10.3103/S1068373915100076

Finkelman R.B., Palmer C.A., Wang P. (2018). Quantification of the Modes of Occurrence of 42 Elements in Coal. International Journal of Coal Geology, 185, pp. 138–160

Gaberšek M. and Gosar M. (2021). Meltwater chemistry and characteristics of particulate matter deposited in snow as indicators of anthropogenic influences in an urban area. Environ Geochem Health, 43, pp. 2583–2595, DOI: 10.1007/s10653-020-00609-z

Goodarzi F. (2006). Morphology and chemistry of fine particles emitted from a Canadian coal-fired power plant. Fuel, 85(3), pp. 273–280, DOI:10.1016/j.fuel.2005.07.004

Golokhvast K.S. and Shvedova A.A. (2014). Galvanic manufacturing in the cities of Russia: potential source of ambient nanoparticles. PLOS ONE, 9(10), number of article e110573, DOI: 10.1371/journal.pone.0110573

Golokhvast K.S., Chernyshev V.V., Chaika V.V., Ugay S.M., Zelinskaya E.V., Tsatsakis A.M., Karakitsios S.P., Sarigiannis D.A. (2015). Size-segregated emissions and metal content of vehicle-emitted particles as a function of mileage: implications to population exposure. Environmental Research, 142, pp. 479–485, DOI: 10.1016/j.envres.2015.07.018

Grebenshchikova V.I., Efimova N.V., Doroshko A.A. (2017). Chemical composition of snow and soil in Svirsk city (Irkutsk Region, Pribaikal'e). Environmental Earth Sciences, 76, 712, DOI: https://doi.org/10.1007/s12665-017-7056-0

Gustaytis M.A., Myagkaya I.N. Chumbaev A.S. (2018). Hg in snow cover and snowmelt waters in high-sulfide tailing regions (Ursk tailing dump site, Kemerovo region, Russia). Chemosphere, 202, pp. 446–459, DOI: 10.1016/j.chemosphere.2018.03.076

Hou Y., Dai S., Nechaev V.P., Finkelman R.B., Wang H., Zhang S., Di S. (2023). Mineral matter in the Pennsylvanian coal from the Yangquan Mining District, northeastern Qinshui Basin, China: Enrichment of critical elements and a Se-Mo-Pb-Hg assemblage. International Journal of Coal Geology, 266, p. 178, DOI: 10.1016/j.coal.2022.104178

Ianchenko N.I. and Kotova E.I. (2022). Methodological aspects of snow cover sampling for chemical analysis. Pure and Applied Chemistry, 94(3), pp. 303–307, DOI: 10.1515/pac-2021-0310

Ianchenko N.I., Kondratiev V.V., Verkhoturov V.V. (2016). Features of the elemental composition of snow cover in the area of production primary aluminum emissions. In the collection: Proceedings of SPIE. The International Society for Optical Engineering, p. 1003563, DOI: 10.1117/12.2248867

International Energy Outlook (IEO), (2023). International Energy Outlook Official Website. [online] Available at: https://www.iea.org/reports/world-energy-outlook-2022 [Accessed 13 Feb. 2023]

Jayasekher T. (2009). Aerosols near by a coal fired thermal power plant: Chemical composition and toxic evaluation. Chemosphere, 75, pp. 1525–1530, DOI: 10.1016/j.chemosphere.2009.02.001

Kalmykov D.E. and Malikova A.D. (2017). Driven into coal. Center for the Introduction of New Environmentally Friendly Technologies (KINECT). Available at: https://bankwatch.org/wp-content/uploads/2018/01/KZ-Coal_RU.pdf (in Russian)

Karaganda thermal power plant. Available at: https://ru.wikipedia.org/wiki [Accessed 07 Feb. 2023] (in Russian)

Kasimov N.S., Kosheleva N.E., Vlasov D.V., Terskaya E.V. (2012). Geochemistry of snow cover within the eastern district of Moscow. Vestnik Moskovskogo Unviersiteta, Seriya Geografiya, 4, pp. 14–24 (in Russian with English summary)

Krastinyte V., Baltrenaite E., Lietuvninkas A. (2013). Analysis of snow-cap pollution for air quality assessment in the vicinity of an oil refinery. Environmental Technology, 34 (6) pp. 757–763, DOI: 10.1080/09593330.2012.715758

Krickov I.V., Lim A.G., Vorobyev S. N., Shevchenko V.P., Pokrovsky O.S. (2022). Colloidal associations of major and trace elements in the snow pack across a 2800-km south-north gradient of western Siberia. Chemical Geology, 610, article number 121090, DOI: https://doi.org/10.1016/j.chemgeo.2022.121090

Krylov D.A. (2017). Negative impact impurity elements from coal-fired thermal power plants to the environment and human health. Gornyy informatsionno-analiticheskiy byulleten (12), pp. 77–87, DOI: 10.25018/0236-1493-2017-12-0-77-87 (in Russian)

Lanzerstorfer C. (2018). Fly ash from coal combustion: Dependence of the concentration of various elements on the particle size. Fuel, 228, pp. 263–271, DOI: 10.1016/j.fuel.2018.04.136

Magiera T., Jabnska M., Strzyszcz Z., Rachwal M. (2011). Morphological and mineralogical forms of technogenic magnetic particles in industrial dusts. Atmospheric Environment, 45, pp. 4281–4290, DOI: 10.1016/j.atmosenv.2011.04.076

Mezhibor A.M., Arbuzov S I., Rikhvanov L.P. (2009). Accumulation and average contents of trace elements in the high-moor peat of Tomsk Region (Western Siberia, Russia). Energy Exploration & Exploitation, 27 (6), pp. 401–410, DOI: 10.1260/0144-5987.27.6.401

Miler M. and Gosar M. (2015). Chemical and morphological characteristics of solid metal-bearing phases deposited in snow and stream sediment as indicators of their origin. Environmental Science Pollution Research, 22(3), pp. 1906–1918, DOI: 10.1007/s11356-014-3589-x

Nemmar A., Hoet P.H., Vanquickenborne B. (2002). Passage of inhaled particles into the blood circulation in humans. Circulation, 105, pp. 411–414, DOI: 10.1161/hc0402.104118

Panin M.S. and Azhaev G.S. (2006). Geochemical characteristics of solid atmospheric precipitation on the territory of Pavlodar, Republic of Kazakhstan according to the study of snow cover pollution. Bulletin of Tomsk State University, 292 (1), pp. 163–170 (in Russian)

Pozhitkov R., Moskovchenko D., Soromotin A., Kudryavtsev A., Tomilova E. (2020). Trace elements composition of surface snow in the polar zone of northwestern Siberia: the impact of urban and industrial emissions. Environmental Monitoring Assessment, 192(4), pp. 192–215. DOI: https://doi.org/10.1007/s10661-020-8179-4

Raputa V.F., Kokovkin V.V., Shuvaeva O.V. (2020). The study of aerosol deposition in the environ of TPP-5 in Novosibirsk. Proceedings of SPIE - 26th International Symposium on Atmospheric and Ocean Optics, Atmospheric Physics, article num. 115604R, DOI: 10.1117/12.2575606

Russian State Standard for air pollution control. RD 52.04.186-89. Available at: http://docs.cntd.ru/document/1200036406 [Accessed 15 Dec. 2012] (in Russian)

Saet Y, Revich B.A, Janin E.P, et al. (1990). Environmental geochemistry. Moscow: Nedra (in Russian)

Shevchenko V.P., Vorobyev S.N., Krickov I.V., Boev A.G., Lim A.G., Novigatsky A.N., Starodymova D.P., Pokrovsky O.S. (2020). Insoluble particles in the snowpack of the Ob river basin (Western Siberia) a 2800 km submeridional profile. Atmosphere, 11, article number 1184, DOI: 10.3390/atmos11111184

Schwarze P.E. (2006). Particulate matter properties and health effects: consistency of epidemiological and toxicological studies. Human & Experimental Toxicology, 25 (10), pp. 559– 579, DOI: 10.1177/096032706072520

Soktoev B.R., Rikhvanov L.P., Taisaev T.T., Baranovskaya N.V. (2014). Geochemical characteristics of drinking water salt deposits of Baikal region. Bulletin of the Tomsk Polytechnic University, Geo Assets Engineering, 324 (1), pp. 209–223 (in Russian with English summary)

Sorokina O.I., Kosheleva N.E., Kasimov N.S., Golovanov D.L., Bazha S.N., Dorzhgotov D., Enkh-Amgalan S. (2013). Heavy metals in the air and snow cover of Ulan Bator. Geography and Natural Resources, 34 (3), pp. 291–300, DOI: 10.1134/S1875372813030153

Sudyko A.F. (2016). Determination of uranium, thorium, scandium and some rare earth elements in twenty-four standard samples of comparison by instrumental neutron activation method. Radioactivity and radioactive elements in the human environment: proceedings of the V International conference. Tomsk: STT, pp. 620–624 (in Russian)

Talovskaya A.V., Yazikov E.G., Filimonenko E.A., Lata J.-C., Kim J., Shakhova T.S. (2018). Characterization of solid airborne particles deposited in snow in the vicinity of urban fossil fuel thermal power plant (Western Siberia), Environmental Technology, 39 (18), pp. 2288–2303, DOI: 10.1080/09593330.2017.1354075

Talovskaya A.V., Yazikov E.G., Osipova N.A., Lyapina E.E., Litay V. V., Metreveli G., Kim J. (2019). Mercury pollution in snow cover around thermal power plants in cities (Omsk, Kemerovo, Tomsk Regions, Russia). Geography, Environment, Sustainability, 12(4), pp. 132–147, DOI-10.24057/2071-9388-2019-58

Taraškevičius R., Zinkut R., Gedminien L., Stankevičius Z. (2018). Hair geochemical composition of children from Vilnius kindergartens as an indicator of environmental conditions. Environmental Geochemistry and Health, 40(5), pp. 1817–1840, DOI: 10.1007/s10653-017-9977-7

Temirzhanova E., Dyusembaeva M.T., Lukashenko S.N., Yazikov E.G., Shakenov E.Z. (2021). Elemental composition of snow cover solid phase in small settlements (the case of Dolon Village, Republic of Kazakhstan). Bulletin of the Tomsk Polytechnic University, Geo Assets Engineering, 331 (12), pp. 41–50, DOI: 10.18799/24131830/2020/12/2937 (in Russian with English summary)

Valeev D., Kunilova I., Alpatov A., Mikhailova A., Goldberg M., Kondratiev A. (2019). Complex utilisation of ekibastuz brown coal fly ash: Iron & carbon separation and aluminum extraction. Journal of Cleaner Production, 218, pp. 192–201, DOI: 10.1016/j.jclepro.2019.01.342

Vlasov D., Vasil'chuk N., Kosheleva N., Kasimov N. (2020). Dissolved and suspended forms of metals and metalloids in snow cover of megacity: Partitioning and deposition rates in western Moscow. Atmosphere, 11, article number 907, DOI: 10.3390/atmos11090907

Weather in the city of Karaganda. Available at: http://weatherarchive.ru [Accessed 15 Feb. 2023] (in Russian)

Witkowska E., Szczepaniak K., Biziuk M. (2005). Some applications of neutron activation analysis: a review. Journal of radioanalytical and nuclear chemistry, 265, pp. 141–150, DOI: 10.1007/s10967-005-0799-1

Wu J., Tou F., Guo X., Liu C., Sun Y., Xu M., Liu M., Yang Y. (2021). Vast emission of Fe- and Ti-containing nanoparticles from representative coal-fired power plants in China and environmental implications. Science of The Total Environment, 838, pp. 156–157, DOI: 10.1016/j.scitotenv.2022.156070

Zereini F., Alt F., Messerschmidt J., Feldmann I., Bohlen A.V., Muller J., Libel K., Puttmann W. (2005). Concentration and distribution of heavy metals in urban airborne particulate matter in Frankfurt am Main, Germany. Environmental Science Technology, 39, pp. 2983–2989, DOI: 10.1021/es040040t

Zhao S., Duan Y., Li Y., Liu M., Lu J., Ding Y., Gu X., Tao J., Du M. (2018). Emission characteristic and transformation mechanism of hazardous trace elements in a coal-fired power plant. Fuel, 214, pp. 597–606, DOI: 10.1016/j.fuel.2017.09.093

Zyryanov V.V., Petrov S.A, Matvienko A.A. (2011). Characterization of spinel and magnetospheres of coal fly ashes collected in power plants in the former USSR. Fuel, 90, pp. 486–492, DOI: https://doi.org/10.3390/min10121066

Appendix A.

Table 1. The instrumental neutron activation analysis detection limit of 27 elements (Soktoev et al. 2014) and atomic absorption spectrometry detection limit of Hg (Talovskaya et al. 2019) in particulate phases

Element	Detection limit, mg/kg	Element	Detection limit, mg/kg
Na	10	Ta	0.01
Ca	300	Sc	0.02
Fe	100	Tb	0.005
As	0.3	Sm	0.01
Co	0.1	Eu	0.004
Cr	0.2	La	0.01
Sb	0.05	Ce	0.06
Ba	10	Yb	0.009
Zn	10	Nd	1.0
Br	0.3	Lu	0.001
Rb	0.5	U	0.06
Cs	0.01	Th	0.01
Sr	100	Au	0.005
Hf	0.009	Hg	0.005

Appendix B.

Table 1. The average values of snow cover depth in Karaganda in the winter season of 2014–2022

Snow cover depth, cm	Year					
	2014	2015	2016	2017	2021	2022
Annual	34	38	36	38	24	28
December	27	29	28	28	25	26
January	41	48	44	51	32	35
February	35	36	34	36	16	23

Open source: https://ldas.gsfc.nasa.gov/data

Table 2. The average values of temperature in Karaganda in the winter season of 2014–2022

Temperature, (oC)	Year					
	2014	2015	2016	2017	2021	2022
Annual	-16,8	-15,1	-14,8	-14,4	-10,2	-10,5
December	-15,7	-14,4	-14,1	-13,8	-10,1	-10,0
January	-19,9	-18,2	-17,2	-16,7	-12,3	-12,2
February	-14,5	-13,1	-11,6	-12,3	-9,1	-9,8

Open source: https://www.kazhydromet.kz/

RESEARCH PAPER

ATMOSPHERIC AIR DUST CONCENTRATION, COMPOSITION AND SIZE DISTRIBUTION DATA AT BREATHING HEIGHTS IN YEKATERINBURG

Irina E. Subbotina*, Alexander G. Buevich, Aleksandr P. Sergeev, Elena M. Baglaeva, Andrey V. Shichkin, Anastasia S. Butorova

Institute of Industrial Ecology, Ural Branch of the Russian Academy of Sciences, Yekaterinburg, Russia

*Corresponding author: iesub@mail.ru

Received: February 1st, 2023 / Accepted: November 14th, 2023 / Published: December 31st, 2023

https://DOI-10.24057/2071-9388-2023-2760

ABSTRACT. Accurate information on air quality serves as the foundation for making regulatory and legal decisions aimed at reducing air pollution. This study investigates the vertical distribution of dust particle concentration, their elemental composition, and size distribution in the atmospheric surface layer in Yekaterinburg. Over eight days in April 2021, 64 dust samples were collected on filters at heights ranging from 0.5 m to 10 m at a single site using a mobile post. The mass concentration of the dust, characterized by heterogeneous data with a coefficient of variation exceeding 30%, exhibited a weak tendency to decrease with height. The proportion of particles smaller than 1 μm decreased with increasing altitude, except for 10 m, where their proportion increased. Conversely, the concentration of p articles ranging from one to two microns decreased closer to the surface. Dust grains of other sizes were nearly evenly distributed at various heights. Dust particles smaller than $PM_{2.5}$ accounted for approximately 45% of the total particles. X-ray fluorescence analysis identified 12 elements in dust particles, with S, Ca, and Fe showing the most substantial content. The proportion of most metals and Ca in solid particles decreased with height, while the content of S and As increased. The Cu, Zn, and Sb content in dust particles remained constant at all measured heights.

KEYWORDS: air pollution, mobile post, dust, particulate matter, particulate composition, vertical distribution, particle-size distribution, urban environment

CITATION: Subbotina I. E., Buevich A. G., Sergeev A. P., Baglaeva E. M., Shichkin A. V., Butorova A. S. (2023). Atmospheric Air Dust Concentration, Composition And Size Distribution Data At Breathing Heights In Yekaterinburg. Geography, Environment, Sustainability, 4(16), 193-199

https://DOI-10.24057/2071-9388-2023-2760

Conflict of interests: The authors reported no potential conflict of interest.

INTRODUCTION

Understanding the content of various impurities in the atmosphere and their spatial distribution is crucial for assessing the state of atmospheric air and its impact on the health of urban populations (Baglaeva et al. 2019; Cachon et al. 2014; Hornberg et al. 1998; Jia et al. 2022; Laiman et al. 2022; Lim et al. 2012; Wu et al. 2022; Xu et al. 2021; Yang et al. 2022). Recently, the World Health Organization updated its air quality guidelines, reducing the annual exposure limit to fine particulate matter ($PM_{2.5}$) from 10 to 5 μg/m^3, citing global health considerations (WHO, 2022). Exposure to $PM_{2.5}$ harms human health and is a leading environmental source of premature mortality (Cohen A.J. 2017; Lim S.S. 2012). Monitoring air pollution is vital not only for citizens, raising awareness of health risks associated with air pollutants, but also for policymakers, aiding in the development of regulations and laws aimed at minimizing these risks.

The selection of suitable control methods for these pollutants depends mainly on their nature and size. Predicting the composition of contaminants without direct measurements is challenging since gas and aerosol impurities emitted by anthropogenic sources undergo significant changes in the atmosphere. The chemical composition of atmospheric dust includes compounds of silicon, beryllium, aluminum, cadmium, and other metals, coal particles, and soot aerosol, spores of microorganisms and plant pollen, and other particles of organic origin. Additionally, chemical reactions in the atmosphere form secondary inorganic compounds like nitrates, sulfates, and ammonium (Isidorov 2001; Zaikov 1991).

Roshydromet collects, processes, and analyzes information on the state of the environment, particularly atmospheric air, and its pollution in Russia. The assessment of air pollution in cities is carried out in combination with an evaluation of the meteorological and climatic parameters of the territories under consideration. Industrial enterprises that pollute the atmospheric air of residential areas are involved in the state monitoring of environmental pollution. Alongside regular observations, additional surveys are conducted in some cities, including those under the auspices of industrial enterprises. The location of atmospheric observation points is determined by the objectives related to obtaining data on the characteristics of pollution at global, regional, territorial, and local levels (Federal Service for Hydrometeorology 2020; State Committee for Hydrometeorology of the USSR 1991; Klyuev N.N. 2019; Ministry of Natural Resources 2020). Such monitoring is characterized by recording the concentration of $PM_{2.5}$ and PM_{10} as bulk density, with no determination of size distribution, shape, or chemical composition of PM.

Currently, studies of the particle-size distribution of atmospheric dust are, in most cases, carried out using various types of sensors. However, despite the high level of development of computer technology and measuring equipment, the accuracy and reproducibility of mass and quantitative concentrations reported by different models vary significantly. Studies (Dubey 2022b; Tryner 2020) have shown that particle count data are unreliable, with the distribution of the number and size of dust particles obtained with different sensors not agreeing with each other. Thus, measurements based on direct counting of the number of particles settled on filters remain relevant (Beddows D.C.S. 2023).

The Institute of Industrial Ecology of the Ural Branch of the Russian Academy of Sciences has developed and patented a mobile dust sampling station (Baglaeva 2017). The station consists of a pump powered by a battery, a set of gas meters showing the volume of air that has passed through them, and pipes with filter holders oriented in different directions. In 2016, using a mobile post, a series of measurements of the particulate matter (PM) concentration in the surface layer of the atmosphere of Yekaterinburg at different heights was carried out. The minimum PM value was found at 1 m compared to the values of concentrations at other heights from 0.5 m to 2 m (Baglaeva 2019).

The purpose of the study is to determine the concentration, size, and chemical composition of particulate matter in the ground layer of atmospheric air in Yekaterinburg at different heights. Additionally, this study aims to compare the features of the vertical distribution of dust concentrations amassed by filters based on measurements taken in 2016 and 2021.

DATA AND METHODS

Study area

Dust content measurements in the atmospheric air were conducted in Yekaterinburg, Russia (N56°51', E60°36'). Located in the central part of the Eurasian continent on the border of Europe and Asia, Yekaterinburg is nestled on the eastern slope of the Ural Mountains in the Iset River valley. The city is characterized by temperate continental climate, marked by sharp variability in weather conditions and well-defined seasons. Throughout the year, western and southern winds prevail. The primary contributors to air pollution in Yekaterinburg are road transport and industrial enterprises situated within the city and its vicinity.

Air dust sampling

We adapted the mobile station (Baglaeva 2017) to investigate the distribution of low dust concentrations at a 1-meter height (Baglaeva 2019). The number of filters for sampling was increased to eight on each measurement day, with five filters covering the height interval of 0.5-1.5 m, enabling a detailed study of dust concentration distribution. Filters were positioned at heights of 0.5 m, 0.75 m, 1 m, 1.25 m, 1.5 m, 2 m, 4 m, and 10 m. The appearance of the mobile sampling station is illustrated in Fig. 1.

Measurements were conducted over eight days, from April 9 to April 20, 2021. During the spring months, from early April to mid-May, before trees are covered with leaves and lawns are overgrown, there is a peak in atmospheric air pollution (Goskomgidromet SSSR 1991). The air pollution observation point was situated on an open, dust-free asphalt site, ventilated from all sides, minimizing measurement result distortion by wind shadows from green spaces, buildings, and

Fig. 1. The mobile sampling station

Table 1. Time and meteorological conditions of sampling

Date	Time		Pressure, mmHg	Temperature, °C	Humidity, %	Cloud cover, %	Wind	
	Start	Finish					Direction	Speed, m/s
09.04.2021	11:47	20:47	749.3	12	29%	50	SE	1-2
12.04.2021	11:48	20:52	756.8	13.9	10%	70	NW	2-3
13.04.2021	11:13	20:30	756.8	21.4	9%	10	SW	1-2
14.04.2021	12:10	21:10	749.3	18.1	10%	60	W	3-4
15.04.2021	11:45	21:05	739.8	22.4	12%	20-30	W	5-6
16.04.2021	11:15	20:40	743.8	11.6	23%	10	E	1-2
19.04.2021	12:00	21:00	748	5	18%	5	N	2-3
20.04.2021	11:51	20:51	746	11.2	15%	40	W	3-4

other obstacles. All measurements were carried out at a single site; Table 1 details the weather conditions and sampling times.

The mobile station (Baglaeva 2017) operated for approximately 9 hours a day and pumped an average of 30 m^3 of air daily. To ensure accuracy, we initially pumped 10 m^3 through the connected series of counters (according to the readings of the first counter in the row) before the start of the experiment. A check of the meter readings showed a difference of 0.7%; hence, no correction factors were introduced for subsequent calculation.

Data preparation procedure

Before air pumping, we measured the filter's mass and determined the elemental composition of each clean filter, averaging three different measurements. After air pumping, we re-weighed the filters and determined the mass of the settled dust as the difference between the masses before and after air pumping. Daily recordings of temperature, atmospheric pressure, relative humidity, wind speed and direction were made at the measurement site.

The qualitative elemental composition of pure filters and filters with atmospheric dust was determined using an INNOV X Systems X-5000 X-ray fluorescence spectrometer, with a systematic measurement error ranging from 20% for most elements to 30% for arsenic.

Particle size distribution

Each dust filter was photographed with an XJP-H100 metallographic microscope (Wuzhou New Found Instrument Co., Ltd) and processed for easy analysis. An example of a filtered photograph is shown in Fig. 2. Dust particles on each filter were counted in five fields of view to determine their disperse composition. Subsequently, the total number of dust particles was distributed over 11 size intervals: less than 1 μm, 1–2 μm, 2–3 μm, 3–4 μm, 4–5 μm, 5–6 μm, 6–7 μm, 7–8 μm, 8– 9 μm, 9– 10 μm, and more than 10 μm.

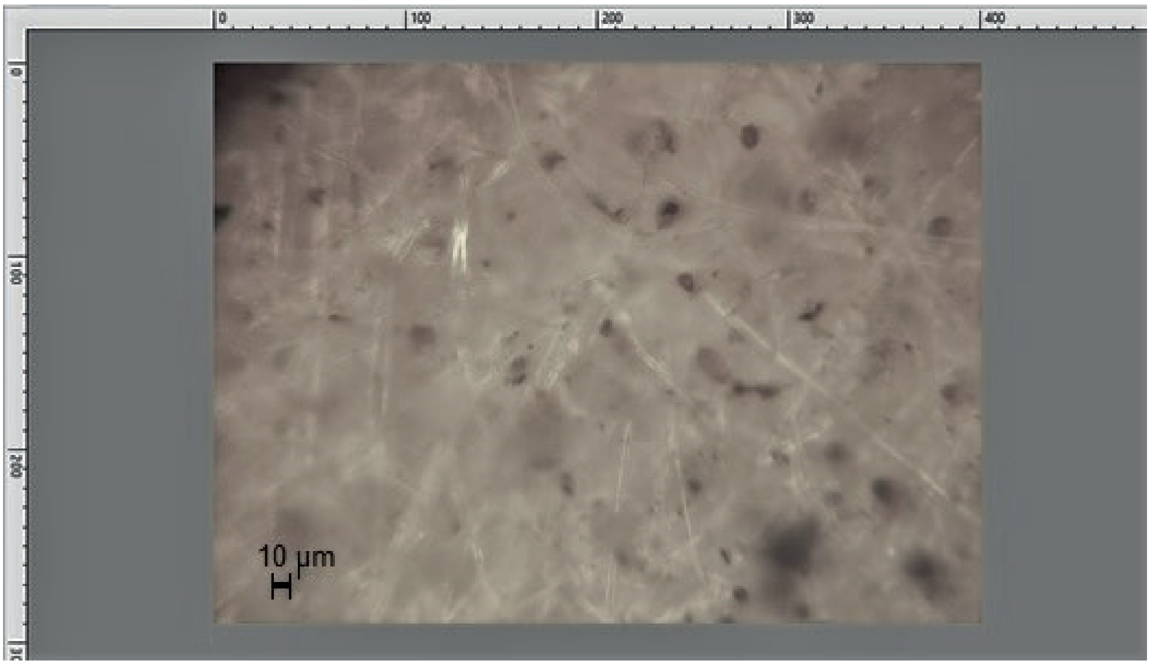

Fig. 2. Photograph of the filter with deposited dust (dark spots)

RESULTS

The calculated dust concentrations averaged over eight days of measurements are presented in Table 2. Dust content is observed to be higher at heights of ≤ 2 m from the ground compared to heights of ≥ 4 m, with no significant differences found within the 2 m range. Coefficients of variation were determined to assess the homogeneity of the data.

Figure 3 shows a comparison of the dust content in the air of Yekaterinburg in 2021 at heights ranging from 0.5 to 10 m with the results of a series of the PM concentration measurements from 2016 (I, II, III seasons) (Baglaeva 2019).

The images of the filters captured in 5 fields of view using a metallographic microscope (similar to Fig.2) were processed. The settled dust grains were counted and distributed over size intervals from 0 µm to 10 µm with a step of 1 µm; the last interval encompassed all dust particles larger than 10 µm. A homogenous dispersed composition was identified for all filters. Figure 4 demonstrates the size distribution of dust particles deposited on the filter for each sampling height, averaged over eight days. The particle size value represents the arithmetic mean over the interval, 10.5 µm corresponds to the maximum PM size. The proportion of the smallest particles (<1 µm) decreased with height, except for 10 m, where their proportion increased. Particles ranging in size from 1 micron to 2 microns, on the contrary, decreased in number the closer they were to the earth's surface. Dust grains of other sizes exhibited almost even distribution along the height.

Subsequently, we identified the elemental composition of the filter with deposited dust using an X-ray fluorescence spectrometer. Chemical elements that were either fixed on the filter with dust or exhibited an increased proportion compared to the clean filter were deemed a part of the chemical composition of the dust.

An analysis conducted on an X-ray fluorescence spectrometer unveiled 12 elements on filters with settled dust. Table 3 presents the averaged content of these elements over all days of measurements. The numbers indicate the mass fraction of the element in the dust. Based on the calculated average dust content in 1 m^3 of air, equal to 0.15 mg/m^3, to calculate the content of each individual element in 1 m^3 of atmospheric air, the value obtained by the XRF method must be multiplied by $0.15*10^{-6}$.

Table 2. The value of dust concentration

Height, m	Mean dust concentration ± Standard deviation, mg/m^3	Coefficient of variation	Min dust concentration, mg/m^3	Max dust concentration, mg/m^3
0.5	0.155 ± 0.052	0.34	0.085	0.220
0.75	0.163 ± 0.058	0.36	0.069	0.250
1	0.170 ± 0.053	0.31	0.080	0.220
1.25	0.162 ± 0.049	0.31	0.078	0.213
1.5	0.168 ± 0.058	0.35	0.094	0.259
2	0.167 ± 0.054	0.32	0.081	0.224
4	0.084 ± 0.029	0.35	0.044	0.122
10	0.115 ± 0.043	0.37	0.058	0.178

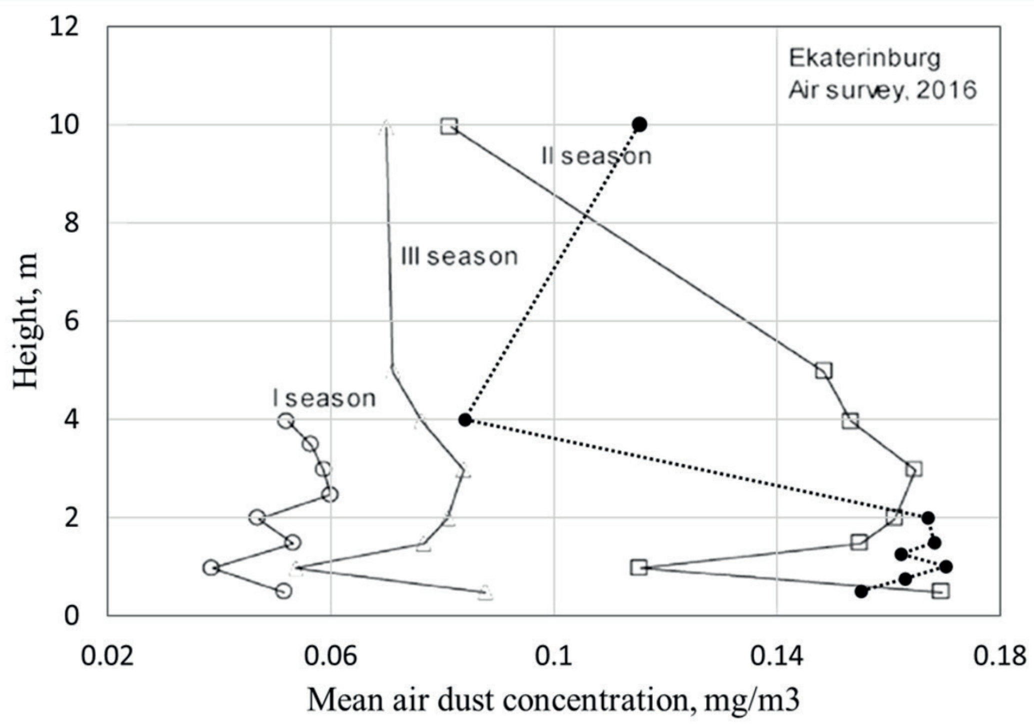

Fig. 3. Relation between the dust content in the atmospheric air and height (average dust concentration for all days of measurements is given. Solid lines refer to 2016, and dotted line refers to 2021)

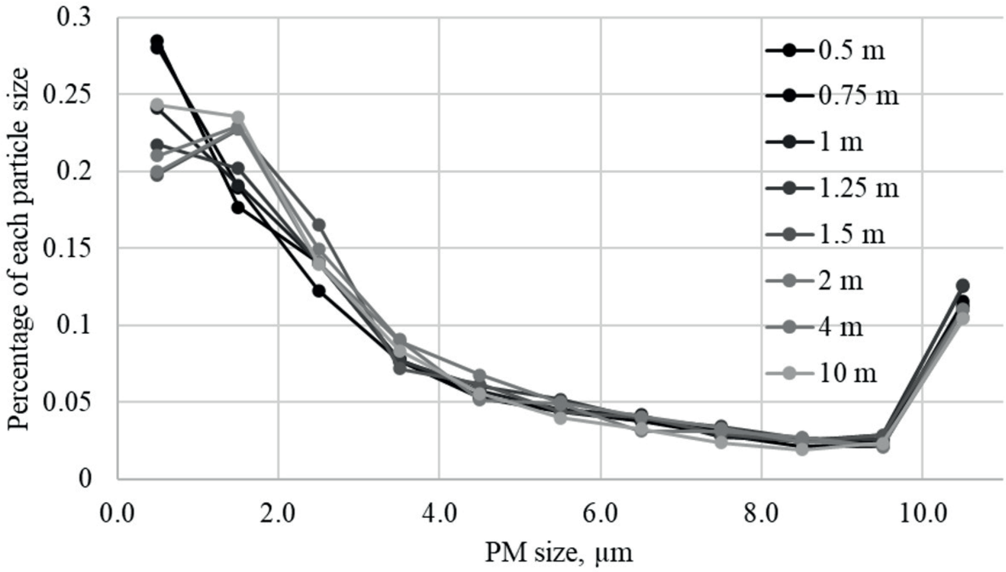

Fig. 4. Dispersed dust composition deposited on the filter

Table 3. The elements' content on filters with settled dust

	S	Ca	K	Fe	Ti	Cr	Mn	Ni	Cu	Zn	Sb	As
ppm	90150	$1.1*10^5$	23220	83313	4190	417	737	430	380	353	700	56

DISCUSSION

In contrast to the previous study (Baglaeva 2019), the minimum dust concentration averaged over 8 days of measurements for the studied human breathing zone (0.5–2 m) turned out to be at a height of 0.5 m (Figure 4). However, on some measurement days, the minimum occurred at heights of 0.75 m, 1.0 m, and 1.25 m. Such results may be associated with the features of air flows in the surface layer of the atmosphere during warm, sunny, calm weather. No statistically significant relationship was found between the obtained data and the main weather conditions (temperature, atmospheric pressure, relative humidity, wind speed and direction (Table 1)). On the days of measurements, there was calm weather (5 days out of 8) or a weak wind, no more than 4-5 m/s. A probable unaccounted parameter is the vertical component of wind speed and force. A slight increase in dust concentration at a height of 10 m (compared to data at a height of 4 m) may be attributed to the peculiarities of the filter location. Unlike others, it was positioned on the edge of the building 3 meters above the roof, which could impact the distribution of dust in that area.

The obtained values of the coefficients of variation for the surface concentration of dust exceeding 0.3 (Table 2) indicate strong deviations of the measured values of concentrations from the arithmetic mean, highlighting the heterogeneity of the data. This result aligns with the information on significant observed diurnal changes in dust content in the surface layer of atmospheric haze up to 70 m high (Kondratiev 1983).

The minimum value of the concentration of dust particles in the surface layer of atmospheric air up to 2 m was observed at a height of 0.5 m, in contrast to the measurement results from 2016, when the PM minimum at a height of 1 m was a special point (Figure 3).

This study's average dust concentration did not exceed 0.17 mg/m^3 (Table 2). The maximum permissible concentration (MPC) for particulate matter in the atmosphere of populated areas according to hygienic standards SanPiN 1.2.3685-21 is 0.5 mg/m^3. The maximum dust concentration obtained at a height of 1.5 m (Table 2) did not exceed this critical value. Additionally, the MPC for dust consisting of particles with a diameter of 10 microns or less is 0.3 mg/m^3. For dust with particles of 2.5 microns or less, it is 0.16 mg/m^3.

Figure 4 shows that the proportion of the smallest particles (<1 μm) decreases with height, except at 10 m where the proportion increases. The proportion of particles whose size varies from 1 to 2 microns, on the contrary, decreases as they approach the earth's surface. Dust grains of other sizes exhibited almost even distribution along the height. The proportion of $PM_{2.5}$ particles is approximately 0.45, and the proportion of PM_{10} reaches 0.89. We do not have the ability to calculate the distribution of mass concentrations of particles by size, since the density of particles of different sizes is unknown, and the assumption about density sameness is incorrect.

Note the similarity of the distributions of the elements' proportion by height for metals. The proportion of most metals and calcium in solid particles decreased with height, following a distribution pattern similar to Fig. 5 (right). The content of sulfur and arsenic at 4 m and 10 m was higher than at heights not exceeding 2 m (Fig. 5 (left)). The copper, zinc, and antimony content in dust particles remained constant at all measured heights.

To estimate the content of some chemical elements in the surface layer of atmospheric air, an average dust content of 1 m^3 was used. The content of toxic elements turned out to be significantly lower than the maximum permissible concentration. In particular, one element of the first hazard class was detected (As). Hygienic standards (SanPiN 1.2.3685-21) establish the average daily maximum concentration limit for As in the atmospheric air of urban settlements at the level of $3*10^{-4}$ mg/m^3. In this study, the calculated average value of arsenic content is $8.4*10^{-6}$ mg/m^3.

CONCLUSIONS

1. Inhomogeneities in the dust concentration distribution in the human breathing zone were identified. The average dust concentration in the study area, 0.155 mg/m^3, was observed at a height of 0.5 m. The obtained dust concentration values remained below the highest

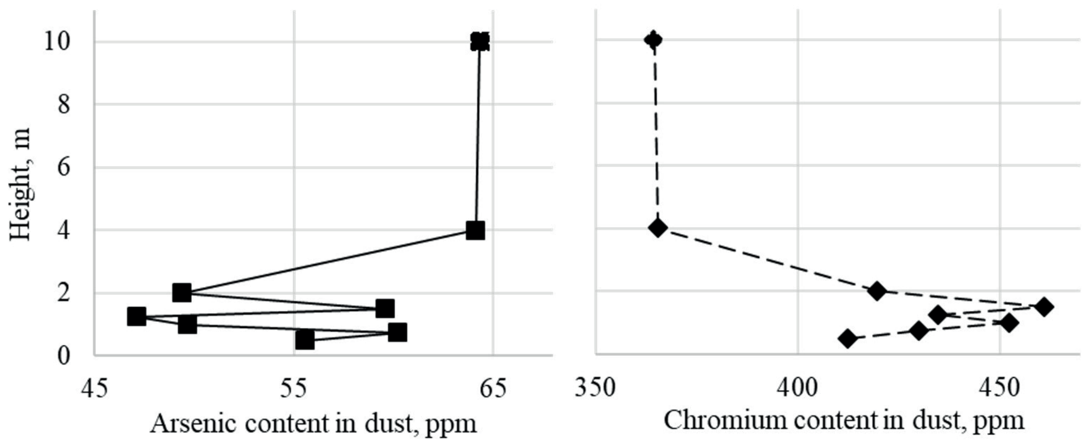

Fig. 5. Relation between the content of chemical elements in dust and height

permissible values according to the hygienic standards (SanPiN 1.2.3685-21). To comprehend the nuances of the dust's vertical distribution, it is advisable to employ a device to monitor the vertical wind speed.

2. The primary chemical elements in the composition of dust sampled at the height of human breathing were identified (Table 3). The 8-day average of dust content is provided in parentheses: Ca (106,140 ppm), S (90,150 ppm), Fe (83,313 ppm), K (23,220 ppm), Ti (4,190 ppm), Mn (737 ppm), Sb (700 ppm), Ni (430 ppm), Cr (417 ppm), Cu (380 ppm), Zn (353 ppm), As (56 ppm).

3. The dispersed composition of dust in the human breathing zone was determined. The proportion of $PM_{2.5}$ particles was approximately 0.45. The fraction of the smallest particles (<1 μm) decreased with height, except at the height of 10 m, where their fraction increased. Particles ranging from 1 to 2 microns, on the contrary, decreased in number, the closer they were to the earth's surface. Dust grains of other sizes exhibited almost even distribution along the height.

4. The mobile station can be effectively utilized in the urban environmental monitoring system to assess the level of dust pollution in the atmospheric air, including at the height of human breathing, in specific local areas.

REFERENCES

Baglaeva E.M., Sergeev A.P., Buevich,A.G., et. al. (2019). Particulate matter size distribution in air surface layer of Middle Ural and Arctic territories. Atmospheric Pollution Research, 4, 1220-1226.

Baglaeva E.M., Buevich A.G., Subbotina I.E., and Sergeev A.P. (2017). Mobile station for dust sampling of the surface layer of atmospheric air with height stratification. Ecological Systems and Devices (ESIP), 7, 23-32. [in Russian]

Beddows D.C.S., Harrison R.M., Gonet T. Measurement of road traffic brake and tyre dust emissions using both particle composition and size distribution data. Environmental Pollution, (2023), 331(1), 121830. https://doi.org/10.1016/j.envpol.2023.121830

Cachon B.F., Firmin S., Verdin A., et.al. (2014). Proinflammatory effects and oxidative stress within human bronchial epithelial cells exposed to atmospheric particulate matter (PM2.5 and PM>2.5) collected from Cotonou, Benin. Environmental Pollution, 185, 340-351, https://doi.org/10.1016/j.envpol.2013.10.026.

Cohen A. J., Brauer M., Burnett R., et al. Estimates and 25-year trends of the global burden of disease attributable to ambient air pollution: an analysis of data from the Global Burden of Diseases Study 2015. Lancet, (2017), 389, 1907–1918. https://doi.org/10.1016/S0140-6736(17)30505-6.

Isidorov, V.A. (2001). Ecological chemistry. St. Petersburg: Himizdat. [in Russian]

Dubey R., Patra A.K., Joshi J., et.al. (2022a). Evaluation of vertical and horizontal distribution of particulate matter near an urban roadway using an unmanned aerial vehicle. Science of The Total Environment, 836, 155600, https://doi.org/10.1016/j.scitotenv.2022.155600.

Dubey R., Patra A.K., Joshi J., et.al. (2022b). Evaluation of low-cost particulate matter sensors OPC N2 and PM Nova for aerosol monitoring. Atmospheric Pollution Research, 13(3), 101335, https://doi.org/10.1016/j.apr.2022.101335.

Federal Service for Hydrometeorology and Environmental Monitoring. (2020). Overview of the state and pollution of the environment in the Russian Federation for 2019. Moscow. http://downloads.igce.ru/publications/reviews/review2019.pdf. [in Russian].

Goskomgidromet SSSR. (1991). RD 52. 04. 186-89. Guidance document. Air Pollution Control Guide. Input: 1991-07-01. Moscow, 693 p, https://fcgie.ru/download/osnovnye_dokumenty_po_vedeniyu_sgm/186_89.pdf.

Hornberg C., Maciuleviciute L., Seemayer N.H., et.al. (1998) Induction of sister chromatid exchanges (SCE) in human tracheal epithelial cells by the fractions PM-10 and PM-2.5 of airborne particulates. Toxicology Letters, 96-97, 215-220, https://doi.org/10.1016/S0378-4274(98)00075-7.

Klyuev N.N. (2019). Atmospheric air quality in Russian cities in 1991-2016. Regional Research of Russia, 9, 204–212.

Kondratiev K.Y., Moskalenko N.I., and Pozdnyakov D.V. (1983). Atmospheric aerosol. Leningrad: Gidrometeoizdat. [in Russian].

Laiman V., Hsiao Ta-Ch., Wang Yu-H., at.al. (2022). Contributions of acidic ions in secondary aerosol to PM2.5 bioreactivity in an urban area. Atmospheric Environment, 275, 119001, https://doi.org/10.1016/j.atmosenv.2022.119001.

Lim S.S., Vos T., Flaxman A.D., et al. (2012). A comparative risk assessment of burden of disease and injury attributable to 67 risk factors and risk factor clusters in 21 regions, 1990-2010: a systematic analysis for the global burden of disease study 2010. Lancet, 380 (9859), 2224-2260, https://doi.org/10.1016/S0140-6736(12)61766-8.

Ministry of Natural Resources and Ecology of the Russian Federation. (2020). Order N 524 from July 30, «On approval of the requirements for monitoring the state of the environment, its pollution» (Entering into force on January 1, 2021 and valid until January 1, 2027.). [in Russian].

SanPiN 1.2.3685-21 «Hygienic standards and requirements for ensuring the safety and (or) harmlessness of environmental factors to humans». [in Russian]. URL: https://docs.cntd.ru/document/573500115#6560IO

Tryner J., Mehaffy J., Miller-Lionberg D., et.al. (2020). Effects of aerosol type and simulated aging on performance of low-cost PM sensors. Journal of Aerosol Science, 150, 105654, https://doi.org/10.1016/j.jaerosci.2020.105654.

WHO. Ambient (Outdoor) Air Pollution. World Health Organisation (2022) https://www.who.int/news-room/fact-sheets/detail/ambient-(outdoor)-air-quality-and-health

Wu H., Zhang B., Wei J., et.al. (2022). Short-term effects of exposure to ambient PM1, PM2.5, and PM10 on ischemic and hemorrhagic stroke incidence in Shandong Province, China. Environmental Research, 212, part C, 113350, https://doi.org/10.1016/j.envres.2022.113350.

Yang M., Jalava P., Hakkarainen H., et.al. (2022). Fine and ultrafine airborne PM influence inflammation response of young adults and toxicological responses in vitro. Science of The Total Environment, 836, 155618, https://doi.org/10.1016/j.scitotenv.2022.155618.

Zaikov G.E., Maslov S.A., and Rubailo V.P. (1991). Acid rains and the environment. Moscow: Chemistry. [in Russian]

ges.rgo.ru/jour/

ISSN 2542-1565 (Online)